MULTIDIMENSIONAL MAGNETOTELLURICS

A 2D CASE STUDY AND A 3D APPROACH TO SIMULTANEOUSLY INVERT FOR RESISTIVITY STRUCTURE AND DISTORTION PARAMETERS

MARION PETRA MIENSOPUST

A thesis submitted to the Faculty of Science,
National University of Ireland, Galway
in fulfilment of the requirements for the degree of

Doctor of Philosophy

February 2010

School of Cosmic Physics
Geophysics Section
Dublin Institute for Advanced Studies
Dublin, Ireland
and
Faculty of Science
Department of Earth and Ocean Sciences
National University Ireland
Galway, Ireland

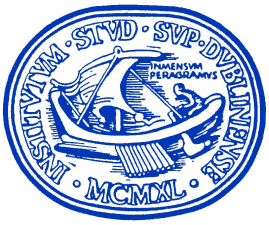

SUPERVISION BY:
Prof. Dr. Alan G. Jones, Dublin Institute for Advanced Studies, Dublin, Ireland,
and
Dr. Colin Brown, National University of Ireland, Galway, Ireland

CONTENTS

LIST OF FIGURES

LIST OF TABLES

ACRONYMS

1D	one-dimensional
2D	two-dimensional
3D	three-dimensional
AMT	Audio-magnetotellurics
BBMT	Broad-band magnetotellurics
BCGSTAB	stablised biconjugate gradient method
CG	conjugate gradient method
DQGMRES	direct versions of quasi generalized minimum residual method
EM	electromagnetics
FD	finite difference (method)
FE	finite element (method)
GMRES	generalized minimum residual method
GN	Gauss-Newton (method)
IE	integral equation (method)
ILU/ILU(0)	incomplete LU matrix decompositon (with zero fill-in)
LMT	Long period magnetotellurics
MCMT3DID	Marion and Colin's MT 3D Inversion code including Distortion
MPI	message passing interface
MT	magnetotellurics
NLCG	nonlinear conjugate gradients (method)
SAMTEX	Southern African MagnetoTelluric EXperiment
SASE	Southern African Seismic Experiment
TE	transverse electric (TE) mode / E-polarisation
TFQMR	transpose-free quasi-minimum residual method
TM	transverse magnetic (TM) mode / B-polarisation

LIST OF SYMBOLS

Below is a list of symbols and nomenclature used within this thesis and their meanings as well as their SI units. Vectors are denoted by a single underline whereas matrices /tensors are denoted by a double underline.

SYMBOL	SI UNIT	DENOTATION
$\underline{B}$	nT or T $= \frac{Vs}{m^2}$	magnetic induction
C	m (or km)	Schmucker-Weidelt transfer function
$\underline{\underline{C}}$		galvanic distortion matrix (electric effects)
$\underline{D}$	$\frac{As}{m^2}$	electric displacement
$\underline{\underline{D}}$		galvanic distortion matrix (magnetic effects)
δ	m (or km)	skin depth
$\underline{E}$	$\frac{V}{m}$	electric field
E_x, E_y, E_z	$\frac{V}{m}$	elements of $\underline{E}$ in Catesian coordinates
$\varepsilon = \varepsilon_0 \cdot \varepsilon_r$	$\frac{As}{Vm}$	electrical permittivity
ε_0	$8.854 \cdot 10^{-12}\ \frac{As}{Vm}$	electrical permittivity of the vaccum
ε_r		relative electric permittivity
η	$\frac{C}{m^3}$	electric charge density
η_f	$\frac{C}{m^3}$	electric charge density of free charges
f	$Hz = \frac{1}{s}$	frequency
$\underline{H}$	$\frac{A}{m}$	magnetic intensity
H_x, H_y, H_z	$\frac{A}{m}$	elements of $\underline{H}$ in Catesian coordinates
I	A	current
$\underline{j}$	$\frac{A}{m^2}$	electric current density
$\underline{j}_f$	$\frac{A}{m^2}$	electric current density of free charges
$\underline{\underline{M}}$	$\frac{mV}{km}/nT$ (or $\frac{V}{m}/T$)	complex magnetotelluric tensor
$M_{xx}, M_{xy},$ M_{yx}, M_{yy}	$\frac{mV}{km}/nT$ (or $\frac{V}{m}/T$)	elements of $\underline{\underline{M}}$ in Catesian coordinates
μ	$\frac{Vs}{Am}$	magnetic permeability
μ_0	$4\pi \cdot 10^{-7}\ \frac{Vs}{Am}$	magnetic permeability of the vaccum
$\underline{\underline{R}}$		rotation matrix
ρ	$\Omega m\ (= \frac{Vm}{A})$	electric resistivity
ρ_a	Ωm	apparent electric resistivity
ρ	$\frac{C}{m^n}$	charge density (n=2 surface; n=3 volume)

SYMBOL	SI UNIT	DENOTATION
σ	$\frac{S}{m}$ (= $\frac{1}{\Omega m}$)	electric conductivity
T	s	period
$\underline{T}$		geomagnetic transfer function/tipper
T_x, T_y		elements of $\underline{T}$ in Catesian coordinates
t	s	time
ω	$\frac{1}{s}$	angular frequency
x, y, z		Cartesian coordinates (z pos. downwards)
$\underline{\underline{Z}}$	$\Omega = \frac{V}{A}$	complex impedance tensor
Z_{xx}, Z_{xy}, Z_{yx}, Z_{yy}	Ω	elements of $\underline{\underline{Z}}$ in Catesian coordinates
z	m (or km)	depth
i		complex number
Re		real part of a complex number
Im		imaginary part of a complex number
$\frac{\partial}{\partial t}$		time derivative
∇		Nabla operator
Δ		Laplace operator
π		Ludolf's number
∞		infinite
$\lvert \cdot \rvert$		absolute value
$\lVert \cdot \rVert$		norm
$\underline{\mathbf{x}}$		vector x
$\underline{\underline{\mathbf{X}}}$, $\underline{\underline{\mathbf{X}}}^T$		matrix X, transpose matrix X
$\underline{\underline{\mathbf{I}}}$		identity matrix
Ar		Argon
Nd		Neodynium
Pb		Lead (Plumbum)
Sm		Samarium
Sr		Strontium
Rb		Rubidium
U		Uranium

ABSTRACT

Within the framework of the Southern African Magnetotelluric EXperiment (SAMTEX) the aim of this study was to gain a better understanding of the southern African geology and tectonic setting using deep-probing magnetotellurics (MT) with a particular focus on the westerly extension of the Zimbabwe Craton into Botswana. The area of interest is located in northeastern Botswana, where Kalahari sands cover most of the geological terranes, and very little is known about the lithospheric structures and thickness. Some of the terrane boundary locations based on potential field data are also questionable.

Investigation of the 600 km long ZIM line profile crossing the Zimbabwe Craton (ZC), Magondi Mobile Belt (MMB) and Ghanzi-Chobe Belt (GCB) showed that the ZC is characterised by thick (~ 220 km) resistive lithosphere, consistent with geochemical and geothermal estimates from kimberlite samples of the Orapa and Letlhakane pipes (~ 175 km west of the profile). The lithospheric mantle of the GCB is resistive but the lithosphere is only about 180 km thick. At crustal depths a northwards-dipping boundary between the GCB and the MMB was identified and two mid- to lower-crustal conductors were found in the MMB. The crustal terrane boundary between MMB and GCB was found to be located further to the north, and the southwestern boundary of the ZC might be further to the west, than previously estimated using potential field data.

MT data from sites above the highly resistive Okavango dyke swarm showed that in the area close to Maun the dilatation of dykes estimated from the magnetic anomaly is too small (2.6%) to enhance resistivity significantly, and that conductive near-surface layers mask its minor effect. An anisotropic or fault-like structure was found to be orientated perpendicular to the dyke swarm direction and extending from about 10 - 15 km depth down into the lithospheric mantle, to 120 km or deeper.

The second part of this research was to develop a 3D inversion code for MT data based on the finite-element forward solver by Colin Farquharson. The new developments of the inversion code, compared to other codes, are that electric galvanic distortion is taken into account during the inversion process and that the noise-free synthetic data are rotated into the local coordinate system of the observed data in order to avoid rotation of noisy observed data prior to modelling.

PUBLICATIONS

Preliminary results, some ideas and figures of the work conducted have been presented to the scientific community as follows (note, as per the agreement in the SAMTEX consortium, there is a member from each organisation represented on any SAMTEX publications):

PEER-REVIEWED PAPERS:

- Colin G. Farquharson and Marion P. Miensopust, *Three-dimensional finite-element modelling of magnetotelluric data with a divergence correction. Submitted to Geophysical Journal International.*

CONFERENCE TALKS:

- Miensopust, Marion P., Alan G. Jones, Mark R. Muller, Mark P. Hamilton, Xavier Garcia, Rob L. Evans, Patrick Cole, Tiyapo Ngwisanyi, David Hutchins, C.J.S. Fourie, Hielke Jelsma, Theo Aravanis, Wayne Pettit, Susan Webb, Jan Wasborg, and The SAMTEX Team, 28 September - 2 October 2009. *Magnetotelluric study in northeastern Botswana*. EMTF, Seddiner See, Germany.

- Miensopust, Marion P., Alan G. Jones, Mark R. Muller, Mark P. Hamilton, Xavier Garcia, Rob L. Evans, Patrick Cole, Tiyapo Ngwisanyi, David Hutchins, C.J.S. Fourie, Hielke Jelsma, Theo Aravanis, Wayne Pettit, Susan Webb, Jan Wasborg, and The SAMTEX Team, 16 - 18 September 2009. *Magnetotelluric study in northeastern Botswana*. SAGA meeting, Swaziland.

- Miensopust, Marion P., Colin G. Farquharson and Alan G. Jones, 23 - 30 August 2009. *Inverting MT 3D data using local coordinates and taking distortion parameters into account: progress and preliminary results*. IAGA meeting, Sopron, Hungary.

- Miensopust, Marion P., Colin G. Farquharson and Alan G. Jones, 19 - 24 April 2009. *Inverting MT 3D data using local coordinates and taking distortion parameters into account: progress and preliminary results*. Annual EGU meeting, Vienna, Austria.

- Miensopust, Marion P., Colin G. Farquharson and Alan G. Jones, 15 - 19 December 2008. *MCMT3DID - a finite-element, 3D MT inversion code using local coordinates for each site and solving for distortion parameters*. Annual AGU fall meeting, San Francisco, USA.

- Miensopust, Marion P., Pilar Queralt and Alan G. Jones, 23 - 29 October 2008. *MT 3D inversion - a recapitulation of a successful workshop*. 19th Electromagnetic Induction in the Earth workshop, Beijing, China.

- Miensopust, Marion P., Pilar Queralt and Alan G. Jones, 6 - 14 August 2008. *Three-dimensional models for MT code testing: Preliminary results and comparison*. 33th International Geological Congress, Oslo, Norway.

POSTER PRESENTATIONS:

- Miensopust, Marion P., Colin G. Farquharson and Alan G. Jones, 20 - 22 February 2009. *MCMT3DID - a finite-element, 3D MT inversion code using local coordinates for each site and solving for distortion parameters*. Annual IGRM meeting, Dublin, Ireland.
- Miensopust, Marion P., Colin G. Farquharson and Alan G. Jones, 23 - 29 October 2008. *A finite-element, 3D MT inversion code using local coordinates for each site and solving for distortion parameters*. 19th Electromagnetic Induction in the Earth workshop, Beijing, China.
- Miensopust, Marion P., Alan G. Jones, Mark R. Muller, Mark P. Hamilton, Jessica E. Spratt, Xavier Garcia, Rob L. Evans, Shane F. Evans, Andy Mountford, Wayne Pettit, Patrick Cole, Tiyapo Ngwisanyi, Dave Hutchins, C.J.S. Fourie, and the SAMTEX Team, 21 - 26 October 2007. *Magnetotelluric profile across the Zimbabwe craton*. 10th SAGA Biennial Technical Meeting and Exhibition, Wild Coast Sun, South Africa.
- Miensopust, Marion P., Alan G. Jones, Mark R. Muller, Mark P. Hamilton, Jessica E. Spratt, Xavier Garcia, Rob L. Evans, Andy Mountford, Wayne Pettit, Patrick Cole, Tiyapo Ngwisanyi, Dave Hutchins, C.J.S. Fourie, and the SAMTEX Team, 1 - 5 October 2007. *Effects of the chosen strike angle on the two-dimensional modelling of magnetotelluric data*. EMTF meeting, Decin, Czech Republic.
- Miensopust, Marion P. and Alan G. Jones, 27 - 30 September 2007. *Testing of the 3D inversion routine engine - the 3D forward algorithm - by comparison with 2D modelling results*. 4th International Symposium on Three-Dimensional Electromagnetics, Freiberg, Germany.

FOR DAD

Nothing is easier than being busy,
and nothing is more difficult
than being effective.

— R. Alec Mackenzie

ACKNOWLEDGEMENTS

I would like to thank many kind and helpful colleagues, many of whom I now regard as friends rather than colleagues, who helped me to make my time as PhD student not just busy but also effective and this thesis to what it is now. It is impossible to name them all here, but I would like to take the opportunity to thank some who have been of particular help during the last few years.

I would like to thank my supervisors Alan Jones and Colin Brown for their guidance, inspiration, constructive and thorough advice and continual encouragement throughout my studies. Their doors were always open and they have given me the opportunity to work with scientists around the world and present my work on many occasions. Beside my supervisors, Colin Farquharson, Mark Muller and Xavi Garcia were always there when help and advice was needed. I sincerely would like to thank them for their time and help, I found the discussions with them constructive and encouraging. I am deeply grateful for Mark's constructive and thorough comments and suggestions he made to the draft of my thesis. And special thanks go to Colin, who would deserve to be listed as supervisor of this thesis (but unfortunately that would break a NUI rule). He not just made his 3D MT forward code available to me but always helped with words and deeds. His constructive and thorough advice, encouragement and guidance was essential for my work on the 3D MT inversion (Part III of this thesis).

The SAMTEX project has been a pleasure and privilege to work on not least because of the support and enthusiasm shown by the many co-workers and helpers during the field work. I sincerely like to thank all of them for having such a great time in southern Africa, particularly I like to thank Jessica Spratt, Mark Muller, Xavi Garcia, Colin Hogg, Pieter Share and David Khoza.

In March 2008 we had a great workshop on MT 3D inversion in Dublin, which encouraged me to become more engaged in the whole 3D modelling and inversion business and, eventually, is partly responsible for taking the second part of my thesis in the direction of code development. Therefore, I would like to thank all workshop attendees from all over the world for making the workshop such a great success and an unforgettable event that allowed me to talk to other students as well as the 'big-names' of this business face to face. A special thank goes to Pilar Queralt and Alan Jones who were co-organising this workshop with me.

I would like to thank Randy Mackie, Greg Newman and Michael Commer for taking the time to meet me and let me pick their brains, and Ian Ferguson for an interesting and constructive discussion on my work during his stay at DIAS as well as for his thorough and useful suggested corrections how to improve the final version of this thesis.

Certainly everyone at DIAS has helped me in some way or another during my time there. I would particularly like to thank the DIAS MT group for many useful and enlightening discussions, the DIAS students for making even the hard times a bit enjoyable, and everyone in the Blue room (Max Moorkamp, Mark Hamilton, Mark Muller, Estelle Roux), where I spent most of my time, for the friendly and lively work environment.

I would like to thank Randy Mackie and Phil Wannamaker for making their COMMEMI 3D-2A data available to me for comparison. I also would like to thank André Miede who is the originator of the Latex style template bundle CLASSICTHESIS, which is freely available and is used (slightly modified) for the typesetting of my thesis. I acknowledge Wessel and Smith (1991, 1998) for their Generic Mapping Tools (GMT), which is used for plotting numerous figures in this thesis. I also would like to acknowledge the developers of VALGRIND, which was a great help detecting memory issues in the 3D code. And, as such a work cannot be realised with out any computing power, I would like to thank all the people who are operating in the shadows, namely Sean O'Sullivan (DIAS system administrator), Clyde Clements and Daniel Vasiliu (keeping the MUN cluster ROX alive) and the team of the ACEnet (Atlantic Computational Excellence Network).

I would like to thank all my friends for their continued support and their persuasion to relax every now and then. I would like to thank my family, especially to Mum, Dad and Gerald, thank you for your continual faith, love and support. I know you tried to keep the sorrow off me as much as possible to give me the chance to stay in Dublin and finish my thesis. And thank you to Alan for being so understanding and supporting that I always could fly home when times got toughest there and I was needed most. And last but not least thank you, Micha, simply for everything.

1

INTRODUCTION

Magnetotellurics (MT) is an electromagnetic method that detects the resistivity structure of the crust and upper mantle. As the resistivity at depths in the upper mantle is strongly correlated to the thermal conditions, MT has been applied successfully to determine the depth to the lithosphere-asthenosphere boundary of cratons and their surrounding mobile belts (e.g., Jones et al., 2003; Muller et al., 2009; Spratt et al., 2009). As part of the Southern African Magnetotelluric EXperiment (SAMTEX), the work presented in this thesis investigates a data set acquired above the Zimbabwe Craton and its neighbouring belts. An approximately 600 km long 2D profile across the area of interest (called the ZIM line) has been modelled at crustal and upper-mantle depths, and the crustal structure at the northern end of the profile formed the focus of a more detailed investigation. The MT responses of sites located in the vicinity of the 2D profile were also examined to help constrain the locations of significant terrane boundaries. One-dimensional (1D) and two-dimensional (2D) inversion strategies have been applied to the data. Three-dimensional (3D) inversion is not yet a standard procedure for modelling MT data. Various 3D forward routines have been developed in recent years, but 3D inversion codes are still in their infancy. As a contribution to the advancement of 3D MT inversion codes, a part of the research described in this thesis deals with the development of a 3D inversion code that takes distortion parameters into account during the inversion process. The new code is also able to rotate the noise-free synthetic data into the local coordinate system of the observed data in order to avoid the conventional approach of decomposition and/or rotation of noisy observed data prior to modelling.

The thesis is divided into four parts, namely THEORY AND BACKGROUND INFORMATION (Part I), INTERPRETATION OF THE 2D ZIM PROFILE (Part II), 3D FORWARD MODELLING AND INVERSION (Part III) and CONCLUSION, BIBLIOGRAPHY AND APPENDICES (Part IV).

The first part, THEORY AND BACKGROUND INFORMATION, consists of two chapters (MT THEORY and SOUTHERN AFRICA). Chapter 2 summarises MT theory. MT sources (Section 2.1) and the electromagnetic properties of Earth materials (Section 2.2) are discussed. Assumptions and fundamental equations of the MT method follow in Sections 2.3 and 2.4, respectively. Section 2.5 introduces the MT transfer functions, and their characteristics, that depend on dimensionality (and anisotropy), are reviewed in Section 2.6. In Section 2.7 the causes and effects of distortion are explained. Finally, the data acquisition (Section 2.8) and strategies of data processing, analysis, modelling and inversion (Section 2.9) are described.

Chapter 3 provides information about the geology of the field area, introduces SAMTEX and reviews previous geophysical work undertaken in southern Africa. The aim of SAM-

TEX is to improve the understanding of the southern African geological framework and the history of the tectonic processes involved in the formation of the southern part of the continent. MT is used to map the lithospheric structure and the geometry of various terranes. The focus of the thesis is an area in northeastern Botswana, where most of the geological terranes are covered by Kalahari sands. Only a few outcrops and magnetic and gravity surveys are available to allow the estimation of rough outlines of these terranes. The only information about the lithospheric mantle structure in northeastern Botswana is provided by the kimberlites of the Orapa and Letlhakane pipes, which are located about 150 - 200 km to the west of the ZIM line. It is uncertain which geological terrane these pipes belong to, as they are located on the boundary (based on the potential field data) between the Magondi Mobile Belt and the Zimbabwe Craton.

Prior to the SAMTEX work, northeastern Botswana has been mostly terra incognita, especially at lithospheric mantle depths. For none of the terranes was the thickness of the lithosphere known, nor the location or nature (e.g., sharp or smooth transition, dip, different location at crustal than lithospheric mantle depths) of the terrane boundaries at lithospheric depths. Although the terrane boundaries drawn based on the potential field data are adequate for a larger regional scale picture, focussing locally, the positions of these boundaries might need adjustment. Especially the western boundary of the Zimbabwe Craton is of great interest, but the boundary drawn there based on the potential field data is questionable.

In crustal depths de Beer et al. (1975, 1976) and van Zijl and de Beer (1983) mapped a conductor that extends from northern Namibia, through northern Botswana into Zimbabwe/Zambia. In north-south direction they were not able to localise the position and lateral extent of the conductor more accurately than to within a range of 150 - 200 km. The lateral extent of the Okavango Dyke Swarm is known from magnetic data but there is no control on its depth extent prior to this work. Section 3.1 reviews the geology and tectonic setting of southern Africa in general and of the areas of interest (i.e., the Limpopo Belt, Zimbabwe Craton, Magondi Belt, Ghanzi-Chobe Belt, Okavango giant mafic dyke swarm and Makgadikgadi Pans Complex) in more detail. Section 3.2 provides information about SAMTEX and results published to date. Previous geophysical work in southern Africa is summarised in Section 3.3.

The second part, INTERPRETATION OF THE 2D ZIM PROFILE, is focussed on the applied work undertaken for the thesis. A subset of the SAMTEX data set, located in northeastern Botswana, is used for the study. The so-called ZIM profile consists of 31 MT stations (only broad-band MT sites, recording a period range of 0.001 s to a few 1000 s) that cross the geological terranes of the Limpopo Belt, Zimbabwe Craton, Magondi Mobile Belt and Ghanzi-Chobe Belt. The sites are in close proximity to the Makgadikgadi Pans (a huge salt pan complex most likely associated with a brine aquifer) and cross the dominant magnetic anomaly related to the Okavango dyke swarm. Chapter 4 includes sites from neighbouring profiles for data imaging (Section 4.1) and strike angle analysis (Section 4.2). The imaging suggests that the boundary between the Magondi Mobile Belt and the Ghanzi-Chobe Belt is located further to the north, and the western boundary of the Zimbabwe Craton further to the west, than defined using the potential field data. The imaging also showed that two groups of sites, both located above the Okavango dyke swarm, exhibit significantly different resistivities. The sites related to the ZIM line and nearby sites are highly resistive,

whereas a group of sites further west (close to the town of Maun) have low resistivities. Section 4.3 addresses the search for an explanation, showing that a 2.6% dilatation of the dykes, observed in the field geology, does not enhance the resistivity significantly and that its small effect is masked by the conductive near-surface layers.

The 2D inversion results of the ZIM profile are discussed in Chapter 5. Section 5.1 describes the inversion strategy applied and discusses the chosen inversion parameters (including trade-off curves to search for the regularisation parameter τ). As the crustal and mantle components of the lithosphere are characterised by different electrical strike directions, first a separate inversion of the northern end of the profile at crustal depths was conducted (using its appropriate strike direction of 55° E of N; Section 5.2). Then the inversion of the whole profile (Section 5.3) using the lithospheric strike direction (35° E of N) followed. Results are compared to known geology, another SAMTEX profile, other geophysical data (e.g., magnetic and gravity data) and geothermal and geochemical data from the kimberlite pipes at Orapa and Letlhakane. The Zimbabwe Craton is found to be characterised by thick, resistive lithosphere (lithosphere-asthenosphere boundary (LAB) at about 220 km) and the Ghanzi-Chobe Belt has about a 40 km thinner resistive lithosphere (LAB at about 180 km). Due to the poor data coverage, no information about the lithospheric mantle beneath the Magondi Mobile Belt is possible. At crustal depths, the boundary between the Magondi and Ghanzi-Chobe Belts was found to be dipping northwards and the crustal conductors found can be associated with the Magondi Mobile Belt.

The third part, 3D FORWARD MODELLING AND INVERSION, concentrates on the development of a 3D inversion code for MT data. The existing forward routine by Colin Farquharson, described in Chapter 6, is used as the driving engine for the inversion code. It is a finite-element code implemented for a rectilinear mesh using Dirchlet boundary conditions. Nodal- and edge-element basis functions (Section 6.1) are applied to the finite-element forward problem (Section 6.2) and the divergence correction (Section 6.3), respectively.

The forward algorithm was thoroughly tested using different approaches (Chapter 7). Section 7.1 shows the comparison of different 2D forward responses to 3D results, while Section 7.2 presents the comparison of 3D response curves to 3D responses calculated with several other codes, using the COMMEMI models 3D-1A and 3D-2A (Zhdanov et al., 1997) as well as the Dublin Test Model 1 (DTM1), which was designed for the 3D MT inversion workshop held at DIAS in March 2008. In summary (Section 7.3), the forward code has been found to work reliably and is therefore considered suitable as the engine for the inversion code.

Chapter 8 describes the 3D inversion algorithm. Section 8.1 explains the new developments in the inversion code compared to other codes, namely taking electric galvanic distortion into account during the inversion process and avoiding noise propagation from one data component into the others due to rotation of the observed data. The latter is addressed by rotation of the noise-free synthetic data instead, and the distortion matrix is implemented as an optional choice between either fixed distortion parameters or inverting for distortion parameters simultaneously with the subsurface resistivity structure. The inversion scheme applied is a Gauss-Newton approach and the objective function is modified to accommodate the inversion for distortion parameters jointly with the resistivity structure (Section 8.2). If the distortion parameters are considered during the inversion, the Jacobian matrix also

needs to be adapted (Section 8.3). Section 8.4 addresses the required modifications associated with the rotation of the synthetic data, instead of the observed data prior to the inversion.

Chapter 9 shows the first preliminary inversion test results. The code is not yet running perfectly due to a problem with the coding of the Jacobian matrix with respect to the resistivity structure in which the Jacobian is not calculated correctly. Therefore, as a short-term solution, the part of the code calculating the Jacobian has been replaced by the 'brute-force' Jacobian. The brute-force Jacobian matrix contains the derivatives of the data with respect to the conductivity structure and is calculated by changing the model parameter (i.e., the conductivity of a cell) one at a time and then dividing the difference in the predicted data by the change in the model parameter that caused the change in the data. The brute-force method of calculating the Jacobian is expensive in terms of computation time and is therefore only executed once for the starting model. In the following iteration steps the Jacobian matrices (which normally should be recalculated using the updated model) are approximated by applying the brute-force Jacobian of the starting model. This approach has demonstrated that the inversion with respect to the conductivity structure results in a inversion model that gives a suggestion of the location of the conductive block, although neither the exact shape nor the correct resistivity can be obtained due to the approximation using the starting model brute-force Jacobian. Unfortunately the model remains so fuzzy that none of the distortion aspects of the code nor the rotation of the synthetic data into the local measurement coordinate systems of each site can be tested.

The fourth part, CONCLUSION, BIBLIOGRAPHY AND APPENDICES, consists of an overall conclusion and an outlook to the future (Chapter 10), the bibliography and several appendices. Appendix A shows the derivation of the unit conversion from field units to SI units and the rotation of the transfer functions. Appendices B and C show additional figures related to data imaging, analysis and inversion of the ZIM line (related to Chapters 4 and 5, respectively). Detailed equations of the edge- and nodal-element basis functions, their rotation and gradients and their multiplication as required for the forward problem (see Chapter 6) are presented in Appendix D. Complementary figures to the 3D forward modelling tests shown in Chapter 7 are assembled in Appendix E. The derivation of the derivatives of the data with respect to the resistivity structure and with respect to the distortion parameters, as needed for the inversion (see Chapter 8), are detailed in Appendix F.

Part I

THEORY AND BACKGROUND INFORMATION

2

MT THEORY

The magnetotelluric (MT) method is a natural-source (passive), frequency-domain electromagnetic method. As with almost all electromagnetic methods it is also based on the fundamental equations of electromagnetics - the Maxwell equations. Tikhonov (1950, reprinted: Tikhonov, 1986) and independently in more detail Cagniard (1953) were the first who propounded the fundamental theory of MT. Wait (1954) questioned Cagniard's (1953) assumption of a plane wave source, because finite ionospheric sources cannot generate normally incident plane waves. Therefore Price (1962) developed a general theory for the MT method based on finite dimensions of the source field. However, computer modelling studies by Madden and Nelson (1964) and Srivastava (1965) indicated that for realistic earth conductivity profiles, Cagniard's (1953) plane wave assumption remains valid for periods up to 10^3 s; in mid-latitudes it even is valid for periods up to 10^5 s (Srivastava, 1965; Swift, 1967). The original scalar representation (Cagniard, 1953) of the impedance relationship failed in areas of lateral conductivity variation. Therefore it was replaced by a tensor relationship between the magnetic and electric fields: the admittance tensor (Neves, 1957; Bostick and Smith, 1962) or the impedance tensor (Berdichevsky, 1960; Tikhonov and Berdichevsky, 1966). Bostick and Smith (1962) showed that the admittance tensor can be rotated to minimise the diagonal elements and thus can be reduced, as far as possible, to the scalar representation by Cagniard (1953). In the following years many statistical and spectral techniques became available to estimate the impedance tensor. After the first papers on MT theory, it took about 20 years before MT was brought into practise. Since then, MT has developed fast in all fields (e.g., theory, field instrumentation and interpretation philosophy) and the scientific and industrial interest grew rapidly. Within only a few decades, interpretation philosophies, processing tools, modelling and inversion codes evolved from a one-dimensional (1D) Earth to a three-dimensional (3D) understanding, although the latter is still in its infancy regarding modelling and inversion. Today MT is used for scientific purposes as well as for industrial exploration. Industry seems to have recognised the advantages of MT, which is useful in areas where seismics cannot be practically or economically applied or where the target is characterised by an electrical properties contrast, rather than a change in seismic velocity or a density contrast. The environmental impact of MT is negligible and the costs are relative low when using the method for exploration.

In the field, time variations of the electric and magnetic field components are recorded simultaneously: this data set is called the time series, which is converted into the frequency domain using, normally, Fourier-transformation, although some wavelet-based approaches are appearing. The resulting frequency-dependent electric and magnetic field components are used to calculate the complex 2x2 impedance matrix relating the two components. Taking into account that the frequency dependence of the impedance matrix is related to an

investigation distance (depth and length) variation, it is possible to derive the subsurface conductivity distribution with depth and also sense laterally, which can provide information about the electrical structure of the crust and lithosphere and even deep into the mantle.

This chapter will present the basic concepts of MT theory including the sources and the relevant properties of the Earth's materials as well as data processing and analysis schema, distortion effects and strategies for dealing with them.

2.1 THE MAGNETOTELLURIC SOURCES

Natural electromagnetic (EM) signals are generated from sources ranging from the core of the Earth to distant galaxies and they are produced by an large number of different processes. For MT signals the important source region is the ionosphere. The ionosphere is the boundary between the neutral atmosphere and the magnetosphere and it contains gases, especially oxygen and nitrogen, which are ionized by ultraviolet and other solar radiation. The very complex system of the magnetosphere and ionosphere is constantly buffeted by a solar wind of highly energetic ions, a plasma of electrons and protons, ejected from the sun. Therefore the time behaviour of magnetic field pulsation is essentially chaotic, but includes features localized in frequency and/or space and the Earth's main magnetic dipole field imposes a global pattern on the behaviour (Vozoff, 1991). The interaction of the different processes described above provide the source of the long-periodic signal (>1 s), which penetrates deep (100 km or more) into the Earth.

The short period signals (>8 Hz) have their origin in meteorological activity; thunderstorms worldwide are associated with lightning discharges, which radiate EM fields propagating to great distances. These signals are known as SFERICS and contain a broad range of EM frequencies. The most significant lightning discharges are the ones from the highly disturbed equatorial regions. These sferics propagate around the world within the wave guide bounded by the ionosphere and the Earth's surface (Garcia and Jones, 2002a; Simpson and Bahr, 2005). If the sferics are in phase after surrounding the Earth, constructive interference amplifies the signal, otherwise destructive interference will erase them. The resulting resonance frequencies (7.8 Hz, 14.1 Hz, 20.3 Hz and higher orders) are called SCHUMANN RESONANCE (Garcia and Jones, 2002a). Local lightning discharges may saturate the instrumentation amplifiers and will appear as spikes in the data. In the transition between the meteorological and the solar caused source processes (at about 1 Hz) the signal amplitude is very low and is referred to as the MT DEAD-BAND.

For the interpretation of MT data the PLANE WAVE ASSUMPTION can be considered valid (e.g. Cagniard, 1953; Wait, 1954; Madden and Nelson, 1964), when the distance to the source is much larger than the depth of interest and when the horizontal wavelength of the source is much larger than the horizontal scale of the study region. The assumption of uniform sources is most valid at mid-latitude sites distant from the equatorial and auroral electrojets. At high and low latitude regions the complexities of the electro jet current system cause instabilities in the forms of the source fields that do not fulfil the plane wave assumption. Lezaeta et al. (2007) discuss the source field effects in the auroral zone using an example data set from the Slave craton in north-western Canada. They discovered lateral changes of source signal across the study area, as well as daily and seasonal variations, which are different for different frequency ranges. They consider a complex system of

various overlapping, non-homogeneous sources. Compared to shorter time windows, the responses obtained from over eight month long recording periods seem to average out the source-effect variability. Lezaeta et al. (2007) point out that it is impossible to be certain that even the long time-period responses are equal to the hypothetical source-free values and devoid of the relative seasonal bias.

Different papers describe ways of reducing or eliminating source-field disturbance in data sets measured in the auroral zone using, e.g., a robust processing procedure (Garcia et al., 1997) or the vertical magnetic field component (Jones and Spratt, 2002). Since only data from mid-latitude sites (approx. 17°S - 33°S) are used in this research, the problems associated with auroral and equatorial zone data will not be discussed further.

Vozoff (1991) mentioned that the dependence of the MT method on natural fields is both its major attraction and its greatest weakness. In comparison with MT, a controlled source EM method of the same investigation depth would required massive - probably truck-mounted - installations, which restrict the access in many circumstances or cause undesirable environmental damage. Also the geometry of the source field in the controlled source case makes the interpretation of the data more complicated (compared to MT), because in the near field the plane wave assumption is not fulfilled in the near field. On the other hand, natural sources do not provide equally strong signals at all the times, so that the signal to noise ratio will not always be optimal, especially in the MT dead-band.

2.2 ELECTROMAGNETIC PROPERTIES OF EARTH MATERIALS

Since MT is an EM method, the rock properties of interest are the material specific electric and magnetic properties describing the behaviour of a medium in relation to a penetrating EM field.

2.2.1 *Electrical properties of rocks and minerals*

The electrical properties of a material are described by the conductivity σ - or the reciprocal parameter resistivity ρ - and the electrical permittivity ε.

Electrical conductivity

The electrical conductivity σ measures the ability of a material to conduct an electrical current. This parameter is a rock and mineral property, that - for common Earth's materials - spans many orders of magnitude (see Fig. 2.1). The variations in the observed conductivity values are not only related to the different electrical conductivities of various rock types and compositions, but also to the overall physical condition of the medium. An increase in temperature will decrease the resistivity (laboratory studies on dry granites, basalts and gabbros by Kariya and Shankland (1983) showed a decrease in resistivity by two orders of magnitude for a temperature increase from 500° C to 1000° C), whereas a wet environment is more likely to be more conductive than a dry environment. For example Karato's (1990) studies on dry olivine showed that implausibly high temperatures (over 1500°C) would be required in the asthenosphere to explain the high conductivity observed. Therefore he takes this result as indication of hydrogen (or water) incorporation into olivine, which would

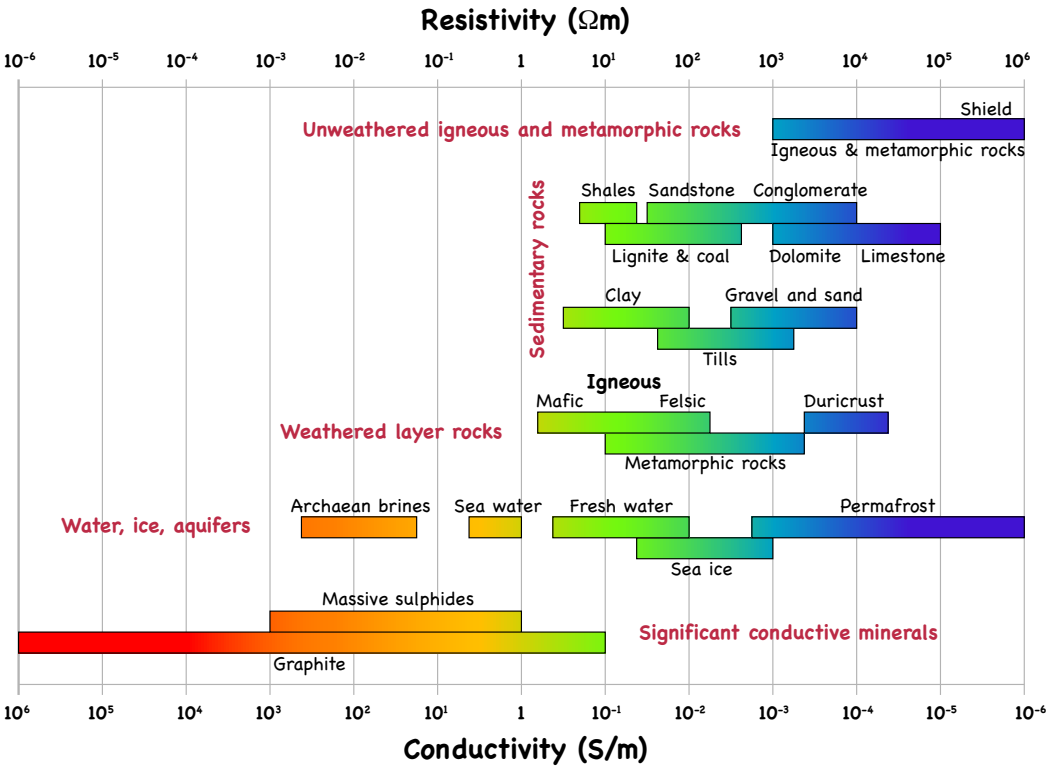

Figure 2.1: Ranges in electrical conductivity (and resistivity) of some common Earth materials. Modified from Martí (2006) and Palacky (1987).

increase the conductivity. Table 2.1 shows the effects of water content on the bulk resistivity of rocks. Another factor is the connectivity of the minerals - strongly interconnected minerals will enhance the conductivity when compared with the same minerals with poor connectivity.

Ohm's Law - the first constitutive equation - relates the electric current density $\underline{j}$ to the electric field $\underline{E}$ by taking the material's property - the conductivity σ - into account:

$$\underline{j} = \sigma \underline{E} \quad . \tag{2.1}$$

Since both the electrical field $\underline{E}$ and the current density $\underline{j}$ are vectors, the quantity σ must be a tensor. If two of the orthogonal coordinate directions of the tensor are selected to lie in the direction of the maximum and minimum conductivities, all non-diagonal elements of the tensor are zero. Considering isotropic (uniform in all directions) minerals or rocks, the three principal values of the conductivity are the same and conductivity can be treated as scalar.

Electrical permittivity

The permittivity ε describes how an electric field affects, and is affected by, a dielectric medium, and is a measure of the material's ability to become polarized by the external electrical field, thereby reducing the total electric field inside the medium; it relates to the material's nature of transmitting or 'permitting' an electric field.

Table 2.1: Bulk resistivities of some selected rock types with different percentages of water content (taken from Telford et al. (1990)). A higher water content results in a lower bulk resistivity.

ROCK TYPE	% H_2O	BULK RESISTIVITY (Ωm)
Siltstone	0.54	$1.5 \cdot 10^4$
Siltstone	0.38	$5.6 \cdot 10^8$
Coarse grain sandstone	0.39	$9.6 \cdot 10^5$
Coarse grain sandstone	0.18	10^8
Medium grain sandstone	1.0	$4.2 \cdot 10^3$
Medium grain sandstone	0.1	$1.4 \cdot 10^8$
Graywacke sandstone	1.16	$4.7 \cdot 10^3$
Graywacke sandstone	0.45	$5.8 \cdot 10^4$
Peridotite	0.1	$3 \cdot 10^3$
Peridotite	0	$1.8 \cdot 10^7$
Granite	0.31	$4.4 \cdot 10^3$
Granite	0.19	$1.8 \cdot 10^6$
Basalt	0.95	$4 \cdot 10^4$
Basalt	0.95	$4 \cdot 10^4$
Olivine-pyrox.	0.028	$2 \cdot 10^4$
Olivine-pyrox.	0	$5.6 \cdot 10^7$

The second constitutive equation, which relates the electric field $\underline{E}$ to the electrical displacement $\underline{D}$, is given by:

$$\underline{D} = \varepsilon \underline{E} \quad , \tag{2.2}$$

where ε is the electrical permittivity, which is given by the electrical permittivity of a vacuum $\varepsilon_0 = 8.854 \cdot 10^{-12}$ As/Vm and the unitless, relative electrical permittivity ε_r, which is specific to the material:

$$\varepsilon = \varepsilon_r \cdot \varepsilon_0 \quad . \tag{2.3}$$

The relative electrical permittivity varies from $\varepsilon_r = 1$ for a vacuum to $\varepsilon_r = 80.36$ for water (at 20° C (Telford et al., 1990)). Table 2.2 lists the relative electrical permittivities of some common Earth materials.

The total current density $\underline{j}$ is given by the current density of the free charges $\underline{j}_f$ plus the displacement currents:

$$\underline{j} = \underbrace{\sigma \underline{E}}_{\underline{j}_f \text{ (diffusion part)}} + \underbrace{\frac{\partial \underline{D}}{\partial t}}_{\text{displacement currents}} \quad . \tag{2.4}$$

The EM induction process becomes diffusive if the second term on the right hand side of Equation 2.4 (the displacement currents) is negligibly small compared to the first term. Using the relations in Equations 2.1 and 2.2, as well as the fact that the period $T = \frac{2\pi}{\omega}$,

Table 2.2: Relative electrical permittivities of some common Earth materials. Most of these values have been measured at 100 kHz and higher (taken from Telford et al. (1990) and Keller (1987)), but permittivity tends to be about 30% higher for very low frequencies.

MATERIAL	RELATIVE PERMITTIVITIES ε_r
Vacuum	1
Air	$\simeq 1$
Peridotite	8.6
Biotite	4.7 - 9.3
Muscovite	6.19 - 8.0
Quartz	4.2 - 5
Granite (dry)	4.8 - 18.9
Gabbro	8.5 - 40
Gneiss	8.5
Basalt	12
Dolomite	6.8 - 8.0
Sandstone (dry to moist)	4.7 - 12
Plagioclase feldspar	5.4 - 7.1
Water (20° C)	80.36

where ω is the oscillation frequency of the electric field, the limits of the assumption of negligible displacement current become clear:

$$\sigma \underline{E} \gg \frac{\partial \underline{D}}{\partial t} \Rightarrow 1 \gg \frac{\frac{\partial \underline{D}}{\partial t}}{\sigma \underline{E}} = \frac{\varepsilon \frac{\partial \underline{E}}{\partial t}}{\sigma \underline{E}} \simeq \frac{\varepsilon}{\sigma T} \quad , \tag{2.5}$$

and therefore the displacement current term becomes only small enough to be neglected, if

$$T \gg \frac{\varepsilon}{\sigma} \quad . \tag{2.6}$$

Even at very high frequencies (optimistic frequency range for MT: 10^{-5} s - 10^{5} s) and in very resistive environments, the displacement currents are likely to be at least one order of magnitude smaller than the diffusion term. As discussed above, the maximum electrical permittivity is about $100 \cdot \varepsilon_0$, which together with a minimal conductivity value of 10^{-6} S/m (as for example picked by Price (1973)) makes the displacement currents comparable with the conduction currents if the period of interest is about 10^{-4} s or less. Taking into account that larger conductivity values are more likely (see Figure 2.1) and that most MT measurements may not record data at 10^{-5} s, Equation 2.6 is valid for (almost) all MT data. Therefore the displacement currents can be neglected and the EM induction in the Earth may be treated as a pure diffusion process in what is called the QUASI-STATIC APPROXIMATION.

In the RadioMagnetoTelluric (RMT) case, where EM fields in the VLF (3 -3 kHz) and LF (30-300 kHz) frequency ranges are used, the validity of the quasi-static assumption is questionable. Kalscheuer et al. (2008) show that for frequencies between 10 - 300 kHz

and a structure with resistivities greater than 1000 Ωm, the quasi-static approximation causes increasingly inaccurate forward responses and leads to inverse models with artificial structures.

2.2.2 *Magnetic properties of rocks and minerals*

The permeability μ is the degree of magnetization of a material that responds linearly to an applied magnetic field. If the medium is isotropic, permeability is a scalar, whereas for an anisotropic linear medium it becomes a second rank tensor.

The third constitutive equation describes the relation between the magnetic induction $\underline{B}$, the magnetic intensity $\underline{H}$ and the magnetic permeability μ:

$$\underline{B} = \mu \underline{H} \quad . \tag{2.7}$$

Magnetic permeability μ is a combination of the permeability of a vacuum $\mu_0 = 4\pi \cdot 10^{-7}$ Vs/Am and the unitless relative permeability μ_r, which is specific to the material:

$$\mu = \mu_r \cdot \mu_0 \quad . \tag{2.8}$$

For most Earth materials, permeability is very close to the free-space (vacuum) value, except for those rocks containing a large quantity of iron. For example, the relative permeability of basalt containing 2 vol % magnetite (Fe_3O_4) is $\mu_r = 1.08$, and that of basalt with 5 vol % magnetite is $\mu_r = 1.18$. Gabbros and peridotites, with typical magnetite contents, have similar relative permeability values (Carmichael, 1989). Kao and Orr (1982) showed that the common assumption of $\mu = \mu_0$ can cause misleading interpretation of MT data if a layer of highly magnetized minerals is present. They demonstrated that a magnetized layer could be misinterpreted as an unmagnetized layer, which is (μ_r-times) more resistive and (μ_r-times) thicker than the magnetized one. This becomes a problem particularly when a local area hosting a mineral deposit, that has a permeability many times higher than the free-space value μ_0, is studied using high frequencies.

2.3 THE ASSUMPTIONS OF THE MT METHOD

A number of simplifying assumptions (some have already been discussed in earlier sections) apply when considering EM induction in the Earth for the MT case. These assumptions have been discussed in several publications (e.g. Cagniard, 1953; Price, 1962, 1973; Vozoff, 1991; Simpson and Bahr, 2005) and are summarised here (modified from Simpson and Bahr, 2005):

i Maxwell's equations (Equations 2.9, 2.10, 2.11, 2.12) are obeyed (see Section 2.4).

ii The Earth does not generate EM energy, but it only absorbs or dissipates it.

iii Away from their source, all fields can be presumed to be conservative and analytic, i.e., they are differentiable at all points.

iv The EM source fields utilised by the MT method may be treated as being uniform, plane-polarised EM waves, which are generated at a relatively distant (from the Earth surface) source and have near-vertical angle of incidence to the Earth's surface. This plane-wave approximation may be violated if measurements were made in the polar

or equatorial regions or, if for other reasons, the source is considered to be too close (see Section 2.1).

v No accumulation of free charges is sustained in a 1D layered Earth. In a 2D or 3D Earth, non-inductive static shift effects can be caused by charges that are accumulated and dissipated along conductivity discontinuities.

vi The Earth acts as ohmic conductor and charges are conserved, i.e., $\underline{j} = \sigma\underline{E}$ and $\frac{\partial \rho}{\partial t} + \nabla \cdot \underline{j} = 0$, where $\underline{j}$ is the electric current density, ρ is the charge density, σ is the conductivity of the medium and $\underline{E}$ is the electric field.

vii The quasi-static approximation: for the period range used in MT (approximately 10^{-5} s - 10^{5} s) the time-varying displacement currents (Maxwell's term in Equation 2.12: $\frac{\partial \underline{D}}{\partial t}$) are small compared to the time-varying conduction currents ($\underline{j}_f$ in Equation 2.12) and can be neglected (see Section 2.2).

viii Any variations in the electrical permittivities and magnetic permeabilities of rocks and minerals are negligible compared with variations in the bulk rock conductivities (see Section 2.2).

It is worth noting that there are no known cases where (i) and (iii) are invalid. With regards to (viii), electrical permittivity ε and magnetic permeability μ can both be interpreted, but unlike the permittivity ε, the permeability μ cannot be separated from the conductivity in terms of the inductive (wavenumber) parameter (i.e., μ will always be part of the term $i\omega\mu\sigma$). However, a localised surface zone of increased magnetic susceptibility would increase the measured magnetic field independently of the conductivity and also galvanic distortion depends primarily on conductivity and is approximately independent of the near-surface magnetic susceptibility distribution, and therefore, at least in theory, permeability and conductivity could be discriminated in some cases.

2.4 THE FUNDAMENTAL EQUATIONS OF THE MT METHOD

The fundamental equations of EM theory are Maxwell's equation that describe the behaviour of both the electrical and magnetic fields and their interaction. Therefore, at any frequency, the physical principles of the MT method are based on these four equations:

i Gauss' Law for the electric field: The electric field (or the electric displacement $\underline{D} = \varepsilon_0\underline{E}$) is a field with the charge density as its source. The electric displacement through a closed surface of a volume is equal to the electric charges inside the volume,

$$\nabla \cdot \underline{E} = \frac{q}{\varepsilon_0} \quad . \tag{2.9}$$

ii Faraday's Law: Any time variation of the magnetic field causes an electric vortex field. Or, in other words, time variations of the magnetic field induce corresponding changes in the electric field flowing in a closed loop with the axis oriented in the direction of the inducing field,

$$\nabla \times \underline{E} = -\frac{\partial \underline{B}}{\partial t} \quad . \tag{2.10}$$

iii Gauss' Law for the magnetic field: The magnetic field is source free. There are no free magnetic charges, i. e., magnetic monopoles do not exist,

$$\nabla \cdot \underline{B} = 0 \quad . \tag{2.11}$$

iv Ampère-Maxwell's Law: The magnetic field depends on the electrical current density of free charges and the time variation of the electric displacement. The magnetic field along the edges of a surface is equal to the sum of the electric currents and the time variations of the current displacement through the surface,

$$\nabla \times \underline{H} = \underline{j}_f + \frac{\partial \underline{D}}{\partial t} \quad . \tag{2.12}$$

In an EM problem, each of the fields must satisfy Maxwell's Equations, and equations derived therefrom. In addition, appropriate conditions need to be applied at boundaries between the homogeneous regions involved in the problem, e.g., at the air-Earth interface. Ward and Hohmann (1987) give an overview of the commonly-used boundary-value problems. They show that the boundary conditions can be derived from the integral forms of Maxwell's Equation, which can be derived by applying Stokes' theorem. It assumes that the normal component of the curl of a vector, integrated over a surface, is equal to the contour integral of the tangential component of the vector, i.e.,

$$\int_S (\nabla \times \underline{A}) \cdot \underline{n} ds = \oint_C \underline{A} \cdot d\underline{l} \quad . \tag{2.13}$$

Therefore, assuming that the surface S does not vary with time, Faraday's Law (Equation 2.10) and Ampère's Law (Equation 2.12) become

$$\oint_C \underline{E} \cdot d\underline{l} = -\frac{\partial}{\partial t} \int_S \underline{B} \cdot \underline{n} ds \quad , \tag{2.14}$$

and

$$\oint_C \underline{H} \cdot d\underline{l} = I + \frac{\partial}{\partial t} \int_S \underline{D} \cdot \underline{n} ds \quad , \tag{2.15}$$

in which the current I is defined as $I = \int_s \underline{J} \cdot \underline{n} ds$. Using the divergence, or Gauss, theorem,

$$\int_V \nabla \cdot \underline{A} dv = \oint_S \underline{A} \cdot \underline{n} ds \quad , \tag{2.16}$$

where S denotes a closed surface enclosing the volume V and $\underline{n}$ is a unit outward oriented normal, Gauss' Laws (Equation 2.9 and 2.11) become

$$\oint_S \underline{E} \cdot \underline{n} ds = \frac{q}{\varepsilon_0} \tag{2.17}$$

and

$$\oint_S \underline{B} \cdot \underline{n} ds = 0 \quad . \tag{2.18}$$

Therefore, the boundary conditions are the following (e.g., Stratton, 1941), given two regions, medium 1 and medium 2:

- The normal component B_n of the magnetic field $\underline{B}$ is continuous across an interface separating medium 1 from medium 2, i.e.,

$$B_{n1} = B_{n2} \quad . \tag{2.19}$$

- Due to the accumulation of a surface-charge density, ρ_s, the normal component of displacement current $\underline{D}$, D_n, is discontinuous across an interface separating the two media, i.e.,

$$D_{n2} - D_{n1} = \rho_s \quad . \tag{2.20}$$

- The tangential components of the electrical field $\underline{E}$, E_t, are continuous across an interface, i.e.,

$$E_{t1} = E_{t2} \quad . \tag{2.21}$$

- If there is no surface current, the tangential components H_t of the magnetic field $\underline{H}$ are continuous across an interface of two media, i.e.,

$$H_{t1} = H_{t2} \quad . \tag{2.22}$$

- If displacement currents may be neglected, the normal component j_n of the current density $\underline{j}$ is continuous across an interface, i.e.,

$$j_{n1} = j_{n2} \quad . \tag{2.23}$$

- The scalar potentials, appropriate to static fields only, V and U defined by: $\underline{E} = -\nabla V$ and $\underline{H} = -\nabla U$, are continuous across an interface, i.e.,

$$V_1 = V_2 \qquad \text{and} \qquad U_1 = U_2 \quad . \tag{2.24}$$

Taking all of these assumptions into account, Maxwell's Equations can be simplified as described in the following. Assuming a plane wave with an harmonic time dependence of the form $e^{+i\omega t}$ results in

$$\frac{\partial \underline{B}}{\partial t} = i\omega \underline{B} \quad . \tag{2.25}$$

Applying assumption vi from Section 2.3 and Ohm's Law (Equation 2.1) to Ampère-Maxwell's Law (Eq. 2.12) and taking the divergence (making use of the vector identity $\nabla \cdot (\nabla \times \underline{A}) = 0$ for any vector field $\underline{A}$) gives

$$\begin{aligned} \underbrace{\nabla \cdot (\nabla \times \underline{H})}_{0} &= \underbrace{\nabla (\sigma \underline{E})}_{} \\ &= \sigma \nabla \underline{E} + \underline{E} \nabla \sigma \quad . \end{aligned} \tag{2.26}$$

Substituting with Gauss' Law for the electrical field (Eq. 2.9) results in

$$0 = \sigma \frac{q}{\varepsilon_0} + \underline{E} \nabla \sigma \qquad \Rightarrow \qquad \frac{q}{\varepsilon_0} = -\underline{E} \frac{\nabla \sigma}{\sigma} = -\underline{E} \nabla \ln \sigma \quad . \tag{2.27}$$

Using Equations 2.25 and 2.27, and applying Equations 2.2 and 2.7 and Ohm's Law (Equation 2.1), the Maxwell equations can be written as:

$$\nabla \cdot \underline{E} = -\underline{E} \nabla \ln \sigma \quad , \tag{2.28}$$

$$\nabla \times \underline{E} = -i\omega \underline{B} \quad , \tag{2.29}$$

$$\nabla \cdot \underline{B} = 0 \quad , \tag{2.30}$$

and

$$\nabla \times \underline{B} = \mu_0 \sigma \underline{E} \quad . \tag{2.31}$$

To derive the diffusion equations in terms of the electrical and magnetic fields, the curl needs to be taken of Equations 2.29 and 2.31 respectively. Therefore we can make use of the following two proven vector identities:

$$\nabla \times (\nabla \times \underline{A}) = \nabla(\nabla \cdot \underline{A}) - \nabla^2 \underline{A} \quad , \tag{2.32}$$

and

$$\nabla \times (\zeta \underline{A}) = \zeta \nabla \times \underline{A} - \underline{A} \times \nabla \zeta \quad , \tag{2.33}$$

where $\underline{A}$ is any vector field and ζ is any scalar field.
The diffusion equation of the electrical field is given by

$$\nabla \times (\nabla \times \underline{E}) = \nabla \times (-i\omega \underline{B})$$

$$\Rightarrow \quad \underbrace{\nabla \cdot \underbrace{\nabla \cdot \underline{E}}}_{= -\underline{E} \nabla \ln \sigma} - \nabla^2 \underline{E} = -i\omega \underbrace{\nabla \times \underline{B}}_{= \mu_0 \sigma \underline{E}}$$

$$\Rightarrow \quad \nabla^2 \underline{E} = i\omega \mu_0 \sigma \underline{E} - \nabla (\underline{E} \nabla \ln \sigma) \quad , \tag{2.34}$$

and the one for the magnetic field by

$$\nabla \times (\nabla \times \underline{B}) = \nabla \times (\mu_0 \omega \underline{E})$$

$$\Rightarrow \quad \underbrace{\nabla \cdot \underbrace{\nabla \cdot \underline{B}}_{= 0}}_{} - \nabla^2 \underline{B} = \mu_0 \nabla \times (\sigma \underline{E}) = \mu_0 \sigma \underbrace{\nabla \times \underline{E}}_{= -i\omega \underline{B}} - \mu_0 \underline{E} \times \nabla \sigma$$

$$\Rightarrow \quad \nabla^2 \underline{B} = i\omega \mu_0 \sigma \underline{B} + \mu_0 \underline{E} \times \nabla \sigma \quad . \tag{2.35}$$

In the case of an isotropic and homogeneous space, the conductivity σ is constant (i.e., $\nabla \sigma = 0$), therefore the diffusion Equations 2.34 and 2.35 simplify to

$$\nabla^2 \underline{E} = i\omega \mu_0 \sigma \underline{E} \tag{2.36}$$

and

$$\nabla^2 \underline{B} = i\omega\mu_0\sigma\underline{B} \quad . \tag{2.37}$$

These are second order differential equations with solutions that are valid for an vertical, external source field (i.e., source geometry is a function of z only and $\frac{\partial \underline{E}}{\partial x} = \frac{\partial \underline{E}}{\partial y} = 0$) and of the form

$$\underline{E} = \underline{E}_1 e^{i\omega t - qz} + \underline{E}_2 e^{i\omega t + qz} \qquad \text{and} \tag{2.38}$$

$$\underline{B} = \underline{B}_1 e^{i\omega t - qz} + \underline{B}_2 e^{i\omega t + qz} \quad . \tag{2.39}$$

The second term on the right-hand side increases with depth z. Because the Earth does not generate EM energy, but only dissipates or absorbs it (assumption (ii) in Section 2.3), the amplitudes of these terms should be set to $\underline{E}_2 = 0$ and $\underline{B}_2 = 0$ respectively. In the case of an homogeneous halfspace (where $\frac{\partial \underline{E}}{\partial x} = \frac{\partial \underline{E}}{\partial y} = 0$), applying the solution as described in Equation 2.38 to the left side of Equation 2.36 yields

$$\nabla^2 \underline{E} = \frac{\partial^2 \underline{E}}{\partial z^2} = q^2 \underline{E}_1 e^{i\omega t - qz} = q^2 \underline{E} \quad , \tag{2.40}$$

therefore Equation 2.36 becomes

$$q^2 \underline{E} = i\omega\mu_0\sigma\underline{E} \tag{2.41}$$

$$\Rightarrow q^2 = i\omega\mu_0\sigma \tag{2.42}$$

or

$$q = \sqrt{i\omega\mu_0\sigma} = \sqrt{i}\sqrt{\omega\mu_0\sigma} = \frac{\pm(1+i)}{\sqrt{2}}\sqrt{\omega\mu_0\sigma} = \pm\left(\sqrt{\frac{\omega\mu_0\sigma}{2}} + i\sqrt{\frac{\omega\mu_0\sigma}{2}}\right) \tag{2.43}$$

using

$$\sqrt{i} = \frac{\pm(1+i)}{\sqrt{2}} \Rightarrow i = \frac{(\pm(1+i))^2}{2} = \frac{1+2i+i^2}{2} = \frac{1+2i-1}{2} \quad . \tag{2.44}$$

The inverse of the real part of q is known as the frequency-dependent, EM SKIN DEPTH δ:

$$\delta = \frac{1}{\mathrm{Re}(q)} = \sqrt{\frac{2}{\mu_0\sigma\omega}} \quad , \tag{2.45}$$

and the inverse of q is referred to as the SCHMUCKER-WEIDELT TRANSFER FUNCTION (Schmucker, 1970; Weidelt, 1972; Schmucker, 1973)

$$C = \frac{1}{q} \quad . \tag{2.46}$$

The Schmucker-Weidelt transfer function is complex and frequency dependent and has the dimensions of length. Using the assumption of a homogeneous halfspace ($\frac{\partial \underline{E}}{\partial x} = \frac{\partial \underline{E}}{\partial y} = 0$) and Faraday's law (Equation 2.10 and 2.29 respectively) we obtain relationships of q to the different electric and magnetic field components

$$\begin{aligned} -\frac{\partial E_y}{\delta z} = -\frac{\partial B_x}{\partial t} \quad &\Rightarrow \quad qE_y = -i\omega B_x \quad , \\ \frac{\partial E_x}{\delta z} = -\frac{\partial B_y}{\partial t} \quad &\Rightarrow \quad qE_x = i\omega B_y \quad . \end{aligned} \tag{2.47}$$

Therefore the Schmucker-Weidelt transfer function also can be expressed as a relationship between the electric and magnetic field components

$$C = \frac{1}{q} = \frac{E_x}{i\omega B_y} = -\frac{E_y}{i\omega B_x} \quad . \tag{2.48}$$

Combining Equation 2.48 with the definition of q (Equation 2.43) yields,

$$\rho = \frac{1}{\sigma} = \frac{1}{|q|^2(\omega)}\mu_0\omega = |C|^2\mu_0\omega \quad , \tag{2.49}$$

where ρ and σ are the resistivity and conductivity respectively of the homogeneous half-space. Since C is complex, a phase ϕ can also be derived and written as

$$\phi = \tan^{-1}\left(\frac{\text{Im } C}{\text{Re } C}\right) \quad . \tag{2.50}$$

2.5 THE MAGNETOTELLURIC TRANSFER FUNCTIONS

A MT transfer function is defined as a function that relates the measured EM fields at a given frequency. It depends only on the electrical properties of the material the EM waves propagate through and not on the EM source. (Note, this definition is only true for the narrower sense of MT transfer functions by the means of passive MT as used in the presented work, but excluding, e.g., controlled source MT.) Beside the above mentioned Schmucker-Weidelt transfer function, several others are also in use. The most common MT transfer functions are represented by the impedance tensor or MT tensor and the geomagnetic transfer function (also known as the tipper vector or the vertical magnetic transfer function).

2.5.1 *The impedance tensor and the magnetotelluric tensor*

The impedance tensor $\underline{\underline{Z}}$ is a complex second-rank, frequency-dependent matrix. It is a phenomenological description of the relation of the orthogonal horizontal electric (E_x, E_y) and magnetic field components (H_x, H_y or $B_x/\mu_0, B_y/\mu_0$ respectively) at a given frequency:

$$\underline{E} = \underline{\underline{Z}}\,\frac{\underline{B}}{\mu_0} \quad \text{or} \quad \begin{pmatrix} E_x \\ E_y \end{pmatrix} = \begin{pmatrix} Z_{xx} & Z_{xy} \\ Z_{yx} & Z_{yy} \end{pmatrix} \begin{pmatrix} \frac{B_x}{\mu_0} \\ \frac{B_y}{\mu_0} \end{pmatrix} \quad , \tag{2.51}$$

or applying the relation of $\underline{B} = \mu_0\,\underline{H}$ (see Equation 2.7), results in the equivalent equation

$$\underline{E} = \underline{\underline{Z}}\,\underline{H} \quad \text{or} \quad \begin{pmatrix} E_x \\ E_y \end{pmatrix} = \begin{pmatrix} Z_{xx} & Z_{xy} \\ Z_{yx} & Z_{yy} \end{pmatrix} \begin{pmatrix} H_x \\ H_y \end{pmatrix} \quad . \tag{2.52}$$

Weaver et al. (2000) introduced the term MT tensor ($\underline{\underline{M}}$), which is an identical description of the transfer function, except that it uses the $\underline{B}$ instead of the $\underline{H}$ field:

$$\underline{E} = \underline{\underline{M}}\,\underline{B} \quad \text{or} \quad \begin{pmatrix} E_x \\ E_y \end{pmatrix} = \begin{pmatrix} M_{xx} & M_{xy} \\ M_{yx} & M_{yy} \end{pmatrix} \begin{pmatrix} B_x \\ B_y \end{pmatrix} \quad . \tag{2.53}$$

Both tensors ($\underline{\underline{Z}}$ and $\underline{\underline{M}}$) are complex, and thus each matrix element is a complex number containing real and imaginary parts, i.e., each component not only has a magnitude, but also a phase.

2.5.2 *The geomagnetic transfer function*

The geomagnetic transfer function $\underline{T}$ describes the relationship between the horizontal and the vertical magnetic field component as

$$H_z = (T_x, T_y) \begin{pmatrix} H_x \\ H_y \end{pmatrix} \quad . \tag{2.54}$$

The geomagnetic transfer function is a complex, frequency-dependent vector. A commonly used representation of this vector is the induction arrow, the concept of which goes back to Parkinson (1959, 1962) and Wiese (1962). Induction arrows are two real, dimensionless vectors

$$\underline{T}_{Re} = (\mathrm{Re}\ T_x, \mathrm{Re}\ T_y) \quad , \tag{2.55}$$

and

$$\underline{T}_{Im} = (\mathrm{Im}\ T_x, \mathrm{Im}\ T_y) \quad , \tag{2.56}$$

which represent the real and imaginary parts of the geomagnetic transfer function on the xy plane. The induction arrows can be used to indicate the presence or absence of lateral variations in conductivity, since the vertical magnetic fields are generated by lateral conductivity gradients (Jones and Price, 1970; Jones, 1986; Simpson and Bahr, 2005). (Also non-uniform sources affect the vertical magnetic fields; see Section 2.1 and Jones and Spratt (2002).) There are two conventions used for plotting the induction arrows:

i The PARKINSON CONVENTION (Parkinson, 1959), where the vectors generally point *towards* the anomalous current concentration (i.e., a good conductor). The real or in-phase arrow is given by $(-\mathrm{Re}\,T_x\,i - \mathrm{Re}\,T_y\,j)$ and the imaginary or quadrature arrow by $(\mathrm{Im}\,T_x\,i + \mathrm{Im}\,T_y\,j)$, where i, j are the Cartesian unit vectors towards magnetic north and east, respectively (Jones, 1986).

ii The WIESE CONVENTION (Wiese, 1962), where the vectors point *away* from the anomalous current concentration.
The induction arrow of the real part is given by the magnitude of $\sqrt{\mathrm{Re}\,T_x^2 + \mathrm{Re}\,T_y^2}$ and the angle $\arctan\left(\frac{\mathrm{Re}\,T_y}{\mathrm{Re}\,T_x}\right)$, whereas the magnitude for the imaginary induction arrow is given by $\sqrt{\mathrm{Im}\,T_x^2 + \mathrm{Im}\,T_y^2}$ and the angle by $\arctan\left(\frac{\mathrm{Im}\,T_y}{\mathrm{Im}\,T_x}\right)$.

Although both conventions can be found in publications and presentations, the Parkinson convention is the more commonly used (Jones, 1986; Simpson and Bahr, 2005).

2.6 DIMENSIONALITY

The complexity of the impedance tensor depends on the dimensionality of the subsurface medium. In the 1D and 2D case there are a few simplifications that become invalid once the complexity of the structure increases. It is important to keep in mind that the dimensionality always depends on the scale. A 3D body of conductivity σ_2 embedded in a homogeneous halfspace of conductivity σ_1 will have a 1D response as long as the periods are sufficiently short and their skin depths are small compared to the shortest dimension of the 3D body. With increasing periods the skin depths increase and become comparable to at least one

of the body's dimensions, resulting in a multidimensional MT response. For very long periods, where the skin depth is much larger than the dimensions of the body, the anomaly caused by the body becomes weak, but the frequency independent, so-called GALVANIC DISTORTION (see Section 2.7), remains. Figure 2.2 shows a sketch of the dimensionality change from a 1D Earth (see Section 2.6.1) to a 2D (see Section 2.6.2) and 3D Earth (see Section 2.6.3) and finally to a distortion effect. It is worth noting, that depending on the structure and its location, not all four stages of dimensionality will always occur (e.g., for a sphere at a depth greater than its radius, the 2D effect will be absent in the sounding curve).

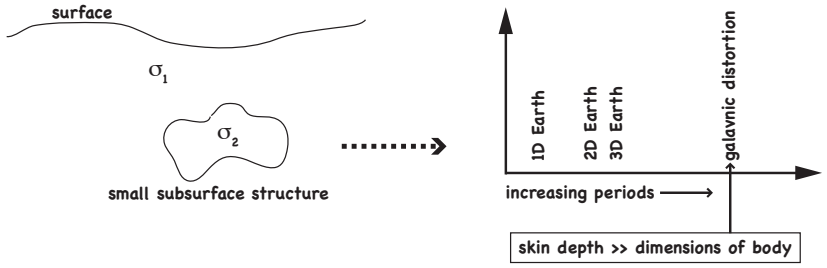

Figure 2.2: Sketch to illustrate the dependence of dimensionality on scale. The 3D body of σ_2 is embedded in a homogeneous halfspace of σ_1. Depending on the skin depth - and therefore the period - compared to the dimensions of the body, the MT response will be 1D, 2D or 3D and for very long periods only the galvanic distortion effects remain. Redrawn from Simpson and Bahr (2005).

2.6.1 *The 1D Earth*

For the simple case of a 1D, isotropic layered Earth (i. e., the conductivity changes only with depth) the diagonal components (Z_{xx} and Z_{yy}) of the impedance tensor, which are related to the parallel electric and magnetic fields, are zero. Since there is no lateral conductivity variation, the off-diagonal elements (Z_{xy} and Z_{yx}) have the same amplitude, but are of different sign to preserve the right hand rule. Therefore the simplified impedance tensor for the 1D Earth can be represented by:

$$\underline{\underline{Z}}_{1D} = \begin{pmatrix} Z_{xx} & Z_{xy} \\ Z_{yx} & Z_{yy} \end{pmatrix} = \begin{pmatrix} 0 & Z_{xy} \\ -Z_{xy} & 0 \end{pmatrix} \quad . \tag{2.57}$$

Applying the 1D assumption of the impedance tensor to Equation 2.51 yields

$$\begin{pmatrix} E_x \\ E_y \end{pmatrix} = \begin{pmatrix} 0 & Z_{xy} \\ -Z_{xy} & 0 \end{pmatrix} \begin{pmatrix} \frac{B_x}{\mu_0} \\ \frac{B_y}{\mu_0} \end{pmatrix} \quad . \tag{2.58}$$

or written as components

$$E_x = \frac{1}{\mu_0} Z_{xy}\, B_y \qquad \text{and} \qquad E_y = -\frac{1}{\mu_0} Z_{xy}\, B_x \quad . \tag{2.59}$$

Solving these equations for Z_{xy} gives

$$Z_{xy} = \mu_0 \frac{E_x}{B_y} = -\mu_0 \frac{E_y}{B_x} \quad . \tag{2.60}$$

This result is analogous to the Schmucker-Weidelt transfer function in Equation 2.48 and therefore can also be derived from Maxwell's Equations for the 1D case (and also for 2D along strike). The difference is only in the definition of the transfer function itself. In the case of the Schmucker-Weidelt transfer function $C = 1/q$, whereas the impedance tensor is $Z = i\omega\mu_0/q$. Therefore these two transfer functions are related by:

$$Z = i\omega\mu_0 C \quad . \tag{2.61}$$

The apparent resistivity, analogous to Equation 2.49, can be written as

$$\rho_a = \frac{1}{\mu_0 \omega} |Z|^2 \quad , \tag{2.62}$$

where ρ_a - the apparent resistivity - is defined as the average resistivity of an equivalent homogeneous halfspace, and the impedance phase, analogous to Equation 2.50, is given by

$$\phi = \tan^{-1}\left(\frac{\mathrm{Im}\ Z}{\mathrm{Re}\ Z}\right) \quad . \tag{2.63}$$

For an isotropic, homogeneous halfspace - a special case of the 1D Earth - the apparent resistivity ρ_a is equal to the actual resistivity value of the halfspace:

$$\begin{array}{ccccc} \rho_a = \frac{1}{\mu_0\omega}|Z|^2 & = & \frac{1}{\mu_0\omega} & |\frac{i\omega\mu_0}{q}|^2 & = \frac{\omega\mu_0}{q^2} = \rho \\ & & \Uparrow & & \Uparrow \\ & & Z = \frac{i\omega\mu_0}{q} & & \text{Eq. 2.49} \end{array} \quad . \tag{2.64}$$

Equation 2.43 showed that for the special case of a homogeneous halfspace, the real and imaginary parts of the impedance tensor elements will have the same magnitude. Therefore the impedance phase is equal to 45°. MT phases that are greater than 45° indicate a substratum in which the resistivity decreases with depth, whereas a phase of less than 45° is related to an increasing resistivity with depth. Figure 2.3 shows apparent resistivity and phase curves for layered halfspace models (top: decreasing resistivities with depth; middle: increasing resistivities; bottom: 3-layer model with a 10 km thick high conductivity layer). The right column shows the 1D model as solid black line and the corresponding resistivity and phase values for periods from 10^{-2} to 10^3 are plotted on the left next to each model. Also included are two different depth and resistivity estimates, which are plotted as dots within the resistivity-depth plot on the right hand side (Niblett-Bostick and $\rho^* - z^*$ transform; for more details about these two approximations see the next subsection). All three models have a 5 Ωm halfspace beneath 410 km and phases above 45° correspond clearly with decreasing resistivity values, whereas increasing resistivities are found where the phase is below 45°.

Tikhonov (1965) and Bailey (1970) proved that the solution of the inverse problem is unique in the 1D case, assuming that the MT data are error- and noise-free and sampled continuously at all frequencies.

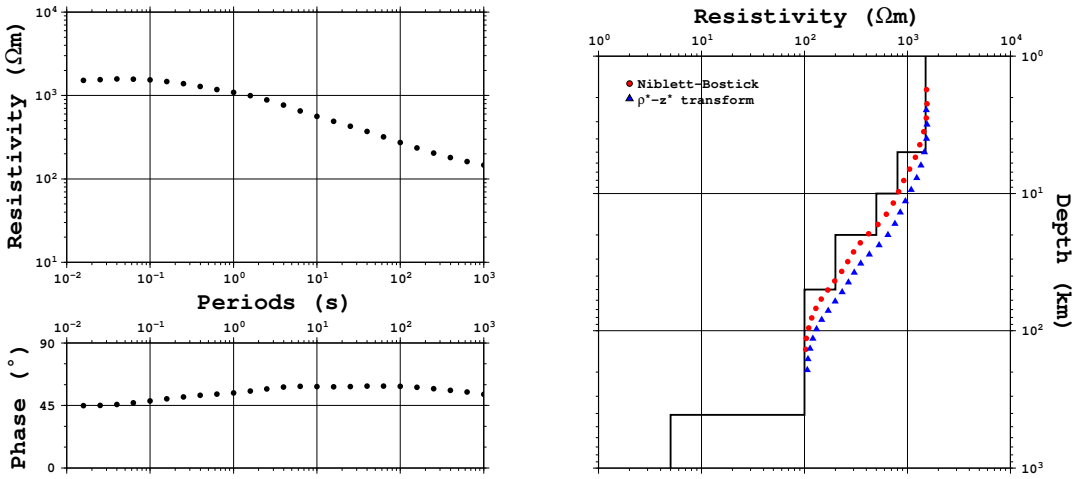

(a) 1D model A - decreasing resistivity

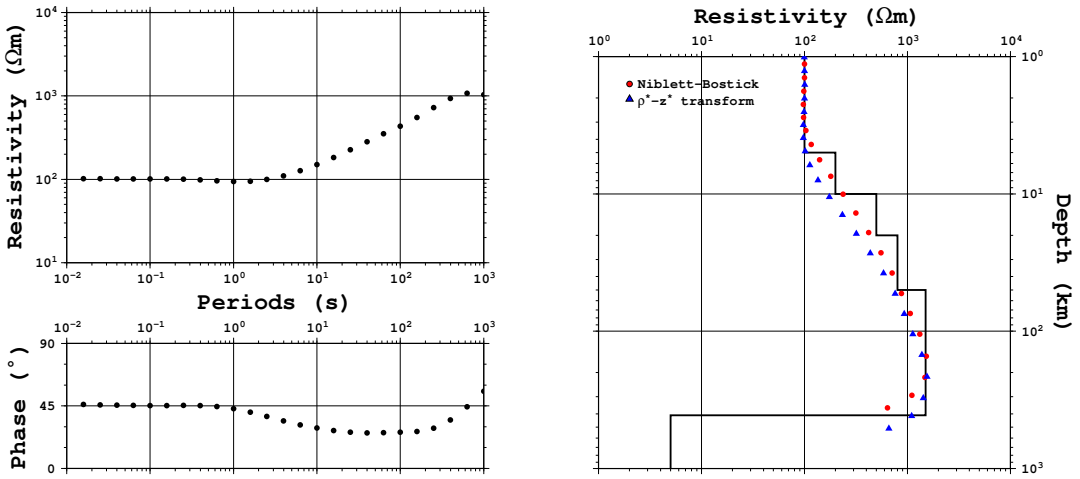

(b) 1D model B - increasing resistivity

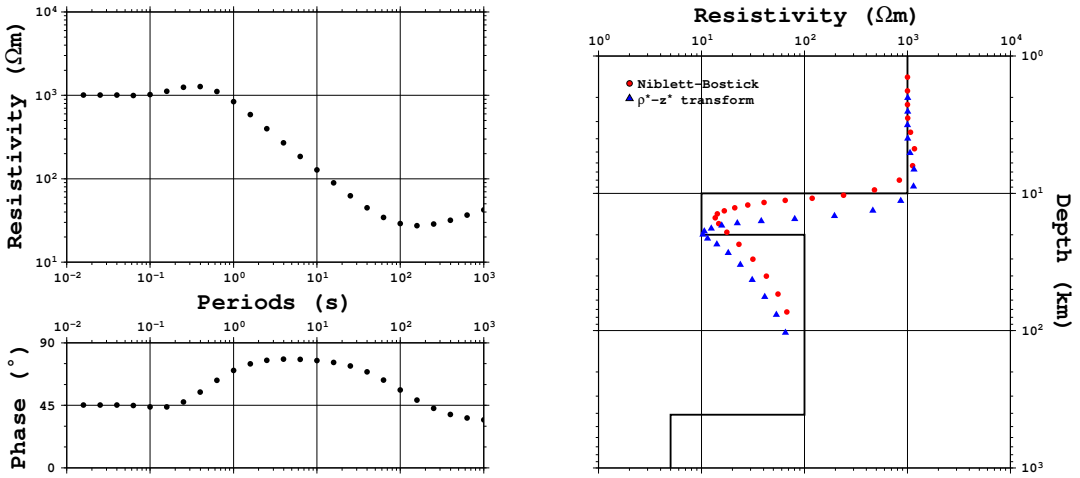

(c) 1D model C - 3 layer model

Figure 2.3: The left column of the figure shows the resistivity and phases curves calculated from the 1D models shown in the right column (solid black line). The symbols are the resistivity and depth estimates calculated from the data curves shown on the left using the Niblett-Bostick and the $\rho^* - z^*$ transform approaches (see 'Resistivity and depth approximations'). From top to bottom: (a) is a model where the resistivity decreases with depth, (b) shows a model of increasing resistivity with depth and (c) is a 3 layer model. All three models have a 5 Ωm halfspace as base model beneath 410 km. Modified from Simpson and Bahr (2005)

Resistivity and depth approximations

Often it is useful to determine a reasonable first-order approximation of the investigation depth. These approximations are all based on the homogeneous halfspace approach. One of these depth estimations is the skin depth δ (Eq. 2.45) introduced earlier

$$\delta(T) = \sqrt{\frac{2}{\mu_0 \sigma(T) \omega(T)}} \approx 503\sqrt{\rho_a(T)T} \quad , \tag{2.65}$$

where $\rho_a = \frac{1}{\sigma}$ is the apparent resistivity at the period $T = \frac{1}{f}$ with $\omega = 2\pi f$. For each chosen period Equation 2.65 will give the depth where the amplitude of the penetrating fields would be attenuated to $\frac{1}{e}$ in a homogeneous halfspace of resistivity equal to the apparent resistivity measured at that period. Instead of assuming the apparent resistivity of the chosen period to be the resistivity value at the estimated depth, there is an estimation for the apparent resistivity value at a certain depth, based on the Schmucker-Weidelt transfer function; it is called $\rho^* - z^*$ TRANSFORM (Schmucker, 1987). The depth z^* is defined by the real part of the Schmucker-Weidelt transfer function (see Equation 2.45 and 2.46; $z^* = \delta$). The estimated resistivity ρ^* is given by

$$\rho^* = \begin{cases} 2\rho_a \cos^2\theta & \text{for} \quad \theta > 45° \\ \frac{\rho_a}{2\sin^2\theta} & \text{for} \quad \theta < 45° \end{cases} \quad . \tag{2.66}$$

These resistivity estimates become $\rho^* = \rho$ for the homogeneous halfspace, where $\theta = 45°$.

Niblett and Sayn-Wittgenstein (1960) and Bostick (1977) developed different penetration depth estimates that imply an attenuation factor at each period of approximately $\frac{1}{2}$. Jones (1983a) showed that these two approximations are equivalent and it is therefore called the NIBLETT-BOSTICK DEPTH APPROXIMATION. For the Niblett-Bostick approximation the penetration depth δ_{NB} is given by

$$\delta_{NB} = \sqrt{\frac{\rho_a(T)T}{2\pi\mu_0}} \quad . \tag{2.67}$$

The Niblett-Bostick resistivity at the depth δ_{NB} is estimated as

$$\rho_{NB}(\delta_{NB}) = \rho_a(T)\frac{1 + m(T)}{1 - m(T)} \quad , \tag{2.68}$$

where $m(T)$ is the gradient of the apparent resistivity curve on a log-log scale, i.e.

$$m(T) = \frac{\partial \log(\rho_a(T)))}{\partial \log(T)} = \frac{T}{\rho_a(T)}\frac{\partial \rho_a(T)}{\partial T} \quad . \tag{2.69}$$

Jones (1983a) pointed out, that an alternative expression for the resistivity at depth δ_{NB} is also in use, where

$$\tilde{\rho}_{NB}(\delta_{NB}) = \rho_a(T)\left(\frac{\pi}{2\phi(T)} - 1\right) \tag{2.70}$$

using the phase information $\phi(T)$. The advantage of the approach using Equation 2.70 is that an estimate of the gradient $m(T)$ is not required; but $\tilde{\rho}_{NB}(\delta_{NB}) \neq \rho_{NB}(\delta_{NB})$. For a homogeneous halfspace, both approximations of the resistivity value $\rho_{NB}(\delta_{NB})$ (Equation 2.68) and $\tilde{\rho}_{NB}(\delta_{NB})$ (Equation 2.70) become $\rho_{NB}(\delta_{NB}) = \rho$ and $\tilde{\rho}_{NB}(\delta_{NB}) = \rho$

respectively, because for this special case the gradient $m(T) = 0$, the phase $\phi(T) = 45°$ and the apparent resistivity ρ_a is equal to the resistivity ρ of the homogeneous halfspace, as for the $\rho^* - z^*$ transform. Figure 2.3 shows the resistivity-depth estimates of both approximations for the different models in comparison to the true 1D models. In general the Niblett-Bostick approach (using ρ_{NB}; Eq. 2.68) fits the real model better than the $\rho^* - z^*$ transform. Although, for the 3-layer model (bottom model) the $\rho^* - z^*$ transform gives the correct resistivity value for the second layer at its lower boundary, whereas the Niblett-Bostick approach seems to estimate the depth extent better, but does not estimate the correct resistivity value. Keeping in mind that these are approximations based on a homogeneous halfspace assumption, both approaches give very good estimates of the true structure.

2.6.2 *The 2D Earth - along strike approach*

Other than for the 1D case, in a 2D or 3D Earth the resistivity not only varies with depth but also with lateral extent. Jones (1983b) explored the conditions under which structure may be treated as 2D and when a 3D approach is required. When a 2D or 3D approach might be required depends largely on the length extent of the body (L) and the skin depth of the periods of interest in the host rock (δ_h). If the ratio $\frac{L}{\delta_h}$ is far greater than 1, then a 2D interpretation of the structure for this period should give approximately the correct conductivity structure. If the ratio is smaller than 1, i.e., either the body is too small (small L) or the period is too long (large δ_h), then a 2D interpretation will not be valid and a 3D interpretation becomes necessary. A geological setting where the 2D approach would be appropriate could, for example, be a transect across a laterally long fault structure, that is in a fairly conductive environment, where the skin depth of the period of interest δ_h is far smaller than the extent of the fault (L).

In Section 2.4 the boundary conditions at a contact between two media of different conductivity, as, for example, at a fault structure, were listed. Since one boundary condition (Equation 2.23) requires that the current density $\underline{j}$ is continuous across the interface and the two media have different conductivities σ_1 and σ_2, Ohm's Law (Equation 2.1) implies that the normal component of the electrical field is discontinuous, i.e.,

$$j_{n1} = j_{n2} \quad \Rightarrow \quad \sigma_1 E_{n1} = \sigma_2 E_{n2} \quad \text{with} \quad \sigma_1 \neq \sigma_2 \quad \Rightarrow \quad E_{n1} \neq E_{n2} \quad . \tag{2.71}$$

A discontinuous normal component of the electric field means it has different amplitudes on either side of the boundary, and is achieved by charge build-up on the boundary surface, which deflects or refracts the electric fields at the boundary (Jones and Price, 1970). The current density decreases with the skin depth and therefore the amount of charge build-up at the contact is larger in shallow regions. All magnetic field components of $\underline{H}$ are continuous across the interface, but only the tangential components of the electric field $\underline{E}$ (Jones and Price, 1970). Figure 2.4 sketches the effect of these boundary charges on the electric current. Note also that the current flows closer to the surface on the more conductive side of the discontinuity (σ_1). Dawson et al. (1982) introduced 'adjustment distances' or 'equilibrium distances' y_1 and y_2, which are the distances from the contact on either side, where the current flow has adjusted to the one expected in a homogeneous halfspace of σ_1 and σ_2 respectively. Within the bounds $-y_1 < y < y_2$ the current flow is perturbed by the surface charges at the boundary.

If the interface is the Earth's surface (z=0), i.e., the boundary between the air and the Earth, the normal electric field, E_z, becomes zero: because the air is a good insulator (i.e., very

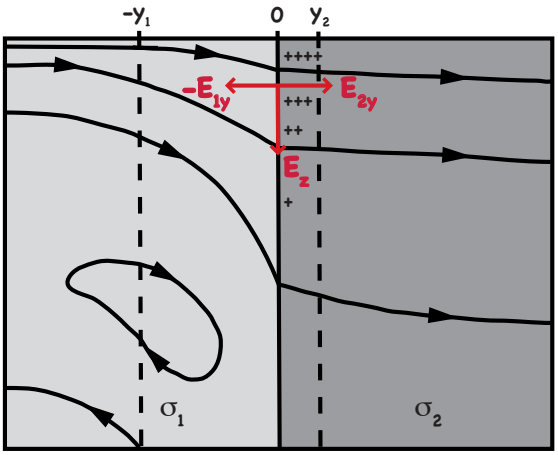

Figure 2.4: Current lines and surface charge distributions near a vertical conductivity discontinuity, where $\sigma_1 > \sigma_2$. Redrawn from Price (1973) including modifications from Jones (1983b).

high resistivity $\Rightarrow$ conductivity $\sigma_{air} \approx 0$), and Ohm's Law and the continuity of the current density apply, Equation 2.71 is only true if E_z inside the conductor, i.e., the Earth, is equal to zero at the contact.

For a body of infinite (or significantly longer than the penetration depth) along-strike extension, the fields do not vary along-strike (defined as the x-direction), i.e., $\frac{\partial}{\partial x} = 0$ (see Figure 2.5). Therefore Equations 2.29 and 2.31 become

$$\begin{pmatrix} \frac{\partial}{\partial x} \\ \frac{\partial}{\partial y} \\ \frac{\partial}{\partial z} \end{pmatrix} \times \begin{pmatrix} E_x \\ E_y \\ E_z \end{pmatrix} = \begin{pmatrix} \frac{\partial E_z}{\partial y} - \frac{\partial E_y}{\partial z} \\ \frac{\partial E_x}{\partial z} - 0 \\ 0 - \frac{\partial E_x}{\partial y} \end{pmatrix} = -i\omega \begin{pmatrix} B_x \\ B_y \\ B_z \end{pmatrix} \quad , \tag{2.72}$$

$$\Uparrow$$

$$\frac{\partial}{\partial x} = 0$$

and

$$\begin{pmatrix} \frac{\partial}{\partial x} \\ \frac{\partial}{\partial y} \\ \frac{\partial}{\partial z} \end{pmatrix} \times \begin{pmatrix} B_x \\ B_y \\ B_z \end{pmatrix} = \begin{pmatrix} \frac{\partial B_z}{\partial y} - \frac{\partial B_y}{\partial z} \\ \frac{\partial B_x}{\partial z} - 0 \\ 0 - \frac{\partial B_x}{\partial y} \end{pmatrix} = \mu_0 \sigma \begin{pmatrix} E_x \\ E_y \\ E_z \end{pmatrix} \quad . \tag{2.73}$$

$$\Uparrow$$

$$\frac{\partial}{\partial x} = 0$$

In the ideal 2D case, as shown in Figure 2.5, the electric and magnetic fields are orthogonal to each other, where an electric field parallel to strike (E_x) only induces magnetic fields in the vertical plane perpendicular to strike (H_y,H_z or B_y,B_z), whilst a magnetic field parallel to strike (H_x or B_x) only induces electrical fields in the vertical plane perpendicular to strike (E_y,E_z). This decoupling into two independent modes also becomes obvious when treating Equations 2.72 and 2.73 component by component. One mode, which describes the currents flowing parallel to the strike direction (i.e., in the x-direction), is called the

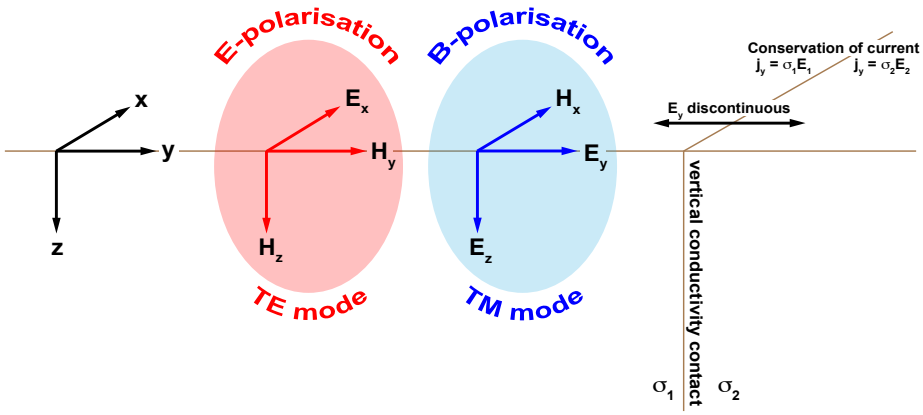

Figure 2.5: A simple 2D model composed of 2 quarterspaces with different conductivities σ_1 and σ_2. Due to conservation of current across the vertical discontinuity, the y-component of the electrical field E_y is discontinuous across the contact. For the ideal 2D case, the EM fields can be decoupled into the two independent modes, known as TE and TM modes. Redrawn and modified from Simpson and Bahr (2005).

TRANSVERSE ELECTRIC (TE) MODE or E-POLARISATION and is composed of E_x, B_y and B_z:

$$\left.\begin{aligned} \frac{\partial E_x}{\partial y} &= i\omega B_z \\ \frac{\partial E_x}{\partial z} &= -i\omega B_y \\ \frac{\partial B_z}{\partial y} - \frac{\partial B_y}{\partial z} &= \mu_0 \sigma E_x \end{aligned}\right\} \quad \text{TE mode/E} - \text{polarization} \tag{2.74}$$

The other mode, which describes currents flowing perpendicular to the strike direction, is known as the TRANSVERSE MAGNETIC (TM) MODE or B-POLARISATION and is composed of B_x, E_y and E_z:

$$\left.\begin{aligned} \frac{\partial B_x}{\partial y} &= \mu_0 \sigma E_z \\ -\frac{\partial B_x}{\partial z} &= \mu_0 \sigma E_y \\ \frac{\partial E_z}{\partial y} - \frac{\partial E_y}{\partial z} &= -i\omega B_x \end{aligned}\right\} \quad \text{TM mode/B} - \text{polarization} \tag{2.75}$$

In the ideal 2D case the along-strike impedance tensor (Equation 2.52) can be simplified, because the diagonal elements are zero, since the electric components are related to orthogonal magnetic components only (and vice versa). The off-diagonal elements (Z_{xy} and Z_{yx}) represent essentially the two modes: TE and TM respectively.

$$\underline{\underline{Z}}_{2D} = \begin{pmatrix} 0 & Z_{xy}(\omega) \\ Z_{yx}(\omega) & 0 \end{pmatrix} = \begin{pmatrix} 0 & Z_{TE}(\omega) \\ Z_{TM}(\omega) & 0 \end{pmatrix} \tag{2.76}$$

They are normally of opposite sign and have different magnitudes. The opposite sign causes the phases of xy and yx to be in different quadrants (1st and 3rd, if a positive time dependency $e^{+i\omega t}$ is used).

Since the electric field E_y is discontinuous across the contact, the impedances associated with E_y are also discontinuous: $Z_{yx} = \frac{E_y}{H_x}$ (and $Z_{yy} = \frac{E_y}{H_y}$, which is zero for the ideal 2D case). From Ohm's Law (Equation 2.1) the discontinuity of E_y, and therefore of Z_{yx}, is equal to the ratio of the two conductivity values of either side of the discontinuity σ_2/σ_1. There

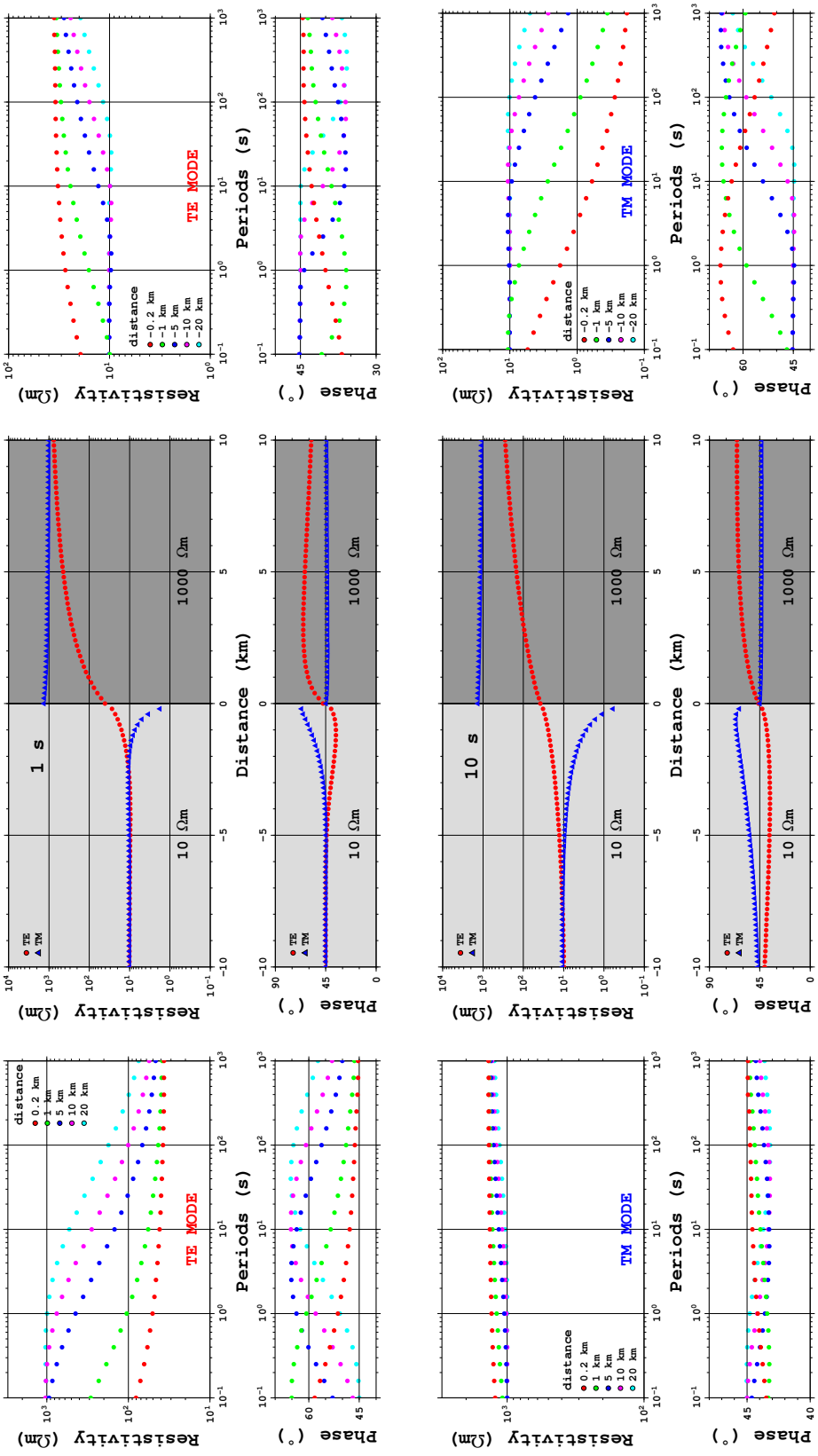

Figure 2.6: Resistivity and phase curves obtain over 2 quarterspaces. In the middle are the resistivity and phase values across a contact between a 10 Ωm (left) and 1000 Ωm quarterspace (right) shown for 1 s (top) and 10 s (bottom) periods. While the apparent resistivity curve for the TE mode is continuous across the contact, the TM mode is discontinuous. Sounding curves are plotted on either side of the quarterspace model and correspond with sites located 0.2 km, 1 km, 5 km, 10 km and 20 km from the contact to either side (left: 1 Ωm, right: 1000 Ωm, TE on top, TM in the bottom graph).

will also be a discontinuity in the apparent resistivity perpendicular to the strike direction, ρ_{yx}, of magnitude $(\sigma_2/\sigma_1)^2$ (see Equation 2.62). Figure 2.6 shows apparent resistivity and phase curves for a range of frequencies and distances from the conductivity contrast for a 2D model similar to Figure 2.4 and 2.5. As a consequence of the discontinuous behaviour of ρ_{yx} across a vertical boundary, the TM mode tends to resolve lateral conductivity variations better than the TE mode resistivities ρ_{xy}. The geomagnetic transfer function describes the ratio of vertical to lateral magnetic fields, therefore it is only associated with the TE mode. Since the geomagnetic transfer function is sensitive to lateral conductivity variations, it is possible to identify lateral variation from the TE mode (see Figure 2.7).

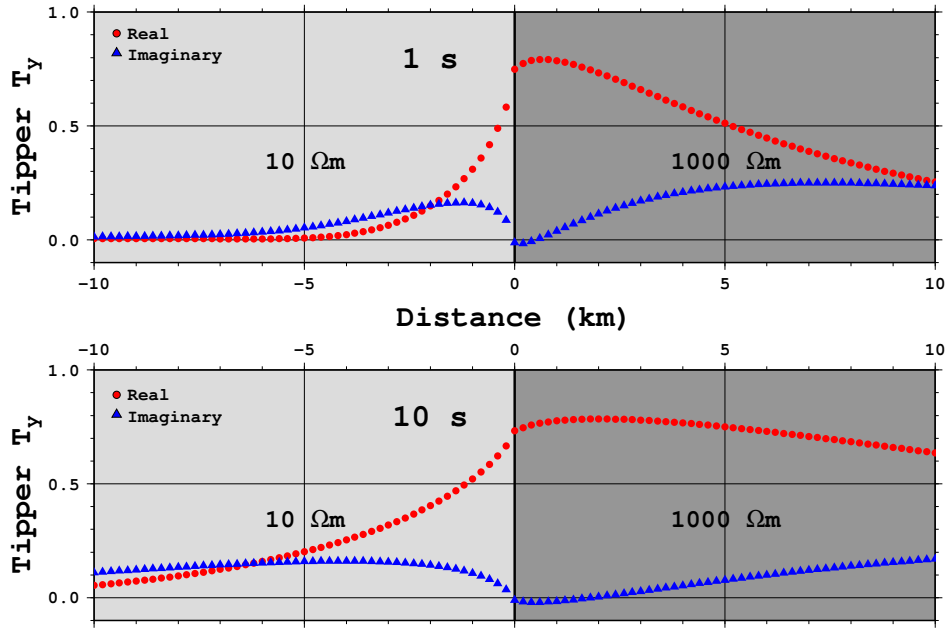

Figure 2.7: Real and imaginary tipper (T_y) curves obtain over 2 quarterspaces (same model as in Figure 2.6: 10 Ωm (left) and 1000 Ωm (right)) shown for 1 s (top) and 10 s (bottom) periods.

If the impedance tensor is not in the electrical strike coordinates, as it is the case for most recorded data, the diagonal elements of the impedance matrix will not be zero, and the TE and TM modes will be mixed in the tensor. For an ideal 2D structure and noise-free data it is possible to rotate the impedance tensor by an angle θ around a vertical axis using a Cartesian rotation matrix $\underline{\underline{R}}_\theta$ until the diagonal components are zero. (The derivation of the rotation for the impedance tensor and the geomagnetic transfer function can be found in Appendix A.2.) A 2D impedance tensor $\underline{\underline{Z}}_{2D}$, which has been rotated through an angle θ to the strike coordinates, can be calculated as follows

$$\underline{\underline{Z}}_{2D} = \underline{\underline{R}}_\theta \underline{\underline{Z}}_{obs} \underline{\underline{R}}_\theta^T \quad , \tag{2.77}$$

where

$$\underline{\underline{\mathbf{R}}}_\theta = \begin{pmatrix} \cos\theta & \sin\theta \\ -\sin\theta & \cos\theta \end{pmatrix} \quad \text{and} \quad \underline{\underline{\mathbf{R}}}_\theta^T = \begin{pmatrix} \cos\theta & -\sin\theta \\ \sin\theta & \cos\theta \end{pmatrix} \tag{2.78}$$

are the rotation matrix $\underline{\underline{R}}_\theta$ and its transpose $\underline{\underline{R}}_\theta^T$, and $\underline{\underline{\mathbf{Z}}}_{obs}$ is the recorded impedance tensor in the observational reference frame. For a non-ideal 2D case and/or noisy data, it will not be possible to find a rotation angle in which the diagonal elements are zero, and one could try to minimize the values of the diagonal elements. However, such amplitude-based methods are to be avoided, since the amplitude can be affected by galvanic distortion (see Section 2.7).

2.6.3 *The 3D Earth*

If the conductivity distribution varies with depth and in both lateral directions, the problem becomes 3D. In this case no rotation by any angle is able to result in an impedance tensor where the diagonal elements approach zero. Also the decoupling into two separate modes, discussed above, is no longer valid. The 3D Earth requires the determination of a full impedance tensor with four complex elements for each frequency. But a disturbing near surface 3D structure can produce modes that can be discerned in TE and TM modes using the vertical magnetic transfer function on a dense and large grid (Becken et al., 2008).

2.6.4 *The anisotropic Earth*

Under a number of circumstances and for a number of reasons Earth materials can be electrically anisotropic - i. e., the electrical properties of the material vary depending on the direction in which the electric fields are propagating. In near-surface or upper crustal regions, anisotropy can be caused by the preferential orientation of a mineral fabric, e.g., graphite in a shear zone (Ji et al., 1996), although anisotropy is also possible at greater depths (Jones, 1992). It is necessary for a mineral phase to be well-interconnected to give rise to electrical anisotropy, or at least be partially interconnected in a significant manner over distances of the order of the inductive scale length (Everett, 2005). Graphite phases can form along grain boundaries and therefore along foliations and lineations, which causes a shape-preferred orientation (Jones, 1992; Mareschal et al., 1995). Other causes of electrical anisotropy in a crustal environment are interconnected saline fluid-filled cracks and geological structures such as dykes and sills.

Hydrogen diffusion in mantle minerals, such as olivine, has been proposed not only as a mechanism for reducing the electrical resistivity (e.g., Karato, 1990; Hirth et al., 2000) but also for causing electrical anisotropy because the rate of hydrogen diffusion is different along one mineral axis than along the others (e.g., for olivine the a-axis [100] has the highest rate of hydrogen diffusion (Schock et al., 1989; Mackwell and Kohlstedt, 1990)). Olivine crystals align preferentially when under strain, and therefore many crystals with similar alignment contribute to an overall anisotropic effect. Although the influence of hydrogen in mantle minerals is qualitatively known, the debate about the quantitative effects is still ongoing (e.g., Karato, 1990; Hirth et al., 2000; Hirth, 2006; Yoshino et al., 2006, 2008). Yoshino et al. (2008) state that the conductivity-depth profiles of oceanic and continental mantle in the mantle transition zone (from 410 km to 660 km) do not require any water in the mantle minerals (but less than 0.1 wt% cannot be excluded); only if the water content is larger 0.1 wt% can electrical conductivity be used to estimate the water content. In contrast, Karato (1990) states that amounts as low as 200 - 2000 ppm H/Si (i.e., 0.02 - 0.2 wt%) can increase the conductivity significantly.

The resistivity of an anisotropic body or layer cannot be specified by a scalar but by a full 3×3 tensor, such as

$$\rho(x,y,z) = \begin{pmatrix} \rho_{xx} & \rho_{xy} & \rho_{xz} \\ \rho_{yx} & \rho_{yy} & \rho_{yz} \\ \rho_{zx} & \rho_{zy} & \rho_{zz} \end{pmatrix} \quad , \tag{2.79}$$

which is a symmetric (i.e., $\rho_{xy} = \rho_{yx}$, $\rho_{xz} = \rho_{zx}$ and $\rho_{zy} = \rho_{yz}$) and positive-definite tensor (Pek and Verner, 1997). The symmetric and positive-definite conditions allow the matrix to be expressed by a diagonal matrix of the three principal resistivities (ρ_1, ρ_2 and ρ_3, all positive) and three rotation angles (Pek and Verner, 1997; Pek and Santos, 2002; Heise et al., 2006). Pek and Verner (1997) (and also Pek and Santos, 2002) use three angles in the Cartesian coordinate system (α_S, α_D and α_L) to describe the anisotropic resistivity by

$$\rho(x,y,z) = \underline{\underline{R}}_z^T(\alpha_S)\,\underline{\underline{R}}_{x'}^T(\alpha_D)\,\underline{\underline{R}}_{z'}^T(\alpha_L) \begin{pmatrix} \rho_1 & 0 & 0 \\ 0 & \rho_2 & 0 \\ 0 & 0 & \rho_3 \end{pmatrix} \underline{\underline{R}}_{z'}(\alpha_L)\,\underline{\underline{R}}_{x'}(\alpha_D)\,\underline{\underline{R}}_z(\alpha_S), \tag{2.80}$$

where $\underline{\underline{R}}$ is the Cartesian rotation matrix and $\underline{\underline{R}}^T$ its transpose. The subscript of the rotation matrix and its transpose describes the respective rotation axis as sketched in Figure 2.8. The matrix for a rotation around the z-axis is given by

$$\underline{\underline{R}}_z(\alpha) = \begin{pmatrix} \cos\alpha & \sin\alpha & 0 \\ -\sin\alpha & \cos\alpha & 0 \\ 0 & 0 & 1 \end{pmatrix} \quad , \tag{2.81}$$

and around the x-axis by

$$\underline{\underline{R}}_x(\alpha) = \begin{pmatrix} 1 & 0 & 0 \\ 0 & \cos\alpha & \sin\alpha \\ 0 & -\sin\alpha & \cos\alpha \end{pmatrix} \quad . \tag{2.82}$$

Figure 2.8 illustrates the rotation successively, which starts with a rotation around the z-axis by the anisotropic strike angle α_S, then a rotation around the new x-axis (x'), the anisotropic dip angle α_D, and finally a rotation by the anisotropic slant angle, α_L, around the most recent z-axis (z') (Pek and Verner, 1997). The sequence of applying the anisotropy angles is a non-cummutative mathematical construct without a physical meaning (unlike, e.g., the twist, shear and anisotropy which have a physical meaning).

Under the plane wave assumption for MT sources, there is no vertical magnetic field for induction in a 1D Earth. Because of the asymptotic limit of, e.g., infinite thin dykes, the absence of the vertical magnetic field under the plane wave assumption is also valid for an anisotropic 1D Earth. The horizontally varying magnetic fields diffusing downwards in the Earth will induce horizontal electric fields at right angles, which drive the telluric currents. Therefore, the primary current induced in a 1D Earth has only horizontal components.

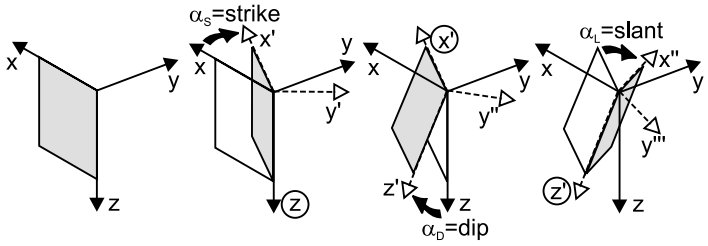

Figure 2.8: Sketch to illustrate the basic anisotropy parameters. An x-directed dyke is transformed into a more general position by successively applying the three elementary Cartesian rotations by α_S (anisotropic strike), α_D (anisotropic dip) and α_L (anisotropic slant). Taken from Pek and Santos (2002).

Consequently, without any additional information available, the MT field of a plane wave does not allow reconstruction of the full resistivity tensor in a 1D medium (Pek and Santos, 2002). That means, only the projection of the principal resistivities onto the horizontal plane (Earth's surface) can be resolved and therefore, if the principal axes of the resistivity tensor are not parallel and perpendicular to the surface (i.e., the dip is non-zero) the MT response cannot be distinguished from an equivalent laterally anisotropic resistivity (i.e., the dip and slant are zero) (Heise et al., 2006). As MT is measuring a bulk resistivity, it is impossible to resolve the scale of the anisotropic structure (microscopic or macroscopic) at great depth (Wannamaker, 2005).

The descriptions of electrical anisotropy are generally based on a background resistivity and an anomalous resistivity of the mineral phase, dyke or sill. As the resistivity of an anisotropic body is specified by the three principal resistivities, the background and anomalous resistivities need to be transformed into the principal resistivities. Figure 2.9 (left) shows a sketch of a dyke-like anisotropic structure. Assuming that all three angles (i.e., strike, dip and slant) of the anisotropy are zero, the principal resistivities are the ones obtained for an x-, y- and z-directed current flow, respectively. Currents that flow in x-direction or z-direction, i.e., parallel to the dyke direction, experience the anisotropic body as a parallel connection of the background and the dyke resistivities (sketch in the middle of Figure 2.9). For currents flowing in y-direction, i.e., perpendicular to the dyke direction, the principal resistivity can be obtained from a serial connection of the background and the dyke resistivities (sketch on the right-hand side in Figure 2.9).

If the anisotropic structure is more pipe-like, as sketched in Figure 2.10 (left), the currents flowing in the x-direction are still parallel to the anomalous structure and therefore the principal resistivity can be calculated by a parallel connection of background and pipe resistivities (sketch in the middle of Figure 2.10). The other two principal resistivities cannot be obtained that easily; for the y- and z-directions, the currents have to be treated as being 'parallel or perpendicular' to the structure depending on the location in the body. One would have to treat the currents flowing in the y-direction first in parallel slices of the model, separating the ones containing the anomalous structure and calculating the serial connection resistivity for each of these slices. The individual slices of background resistivity and serial connection resistivity then have to be treated as a parallel connection to finally obtain the principal resistivity in the y-direction (sketch on the right-hand side of Figure 2.10). By analogy, the z-directed principal resistivity, ρ_z, can also be calculated. Note that ρ_y and ρ_z are only equal for the special case where the cumulative extent of

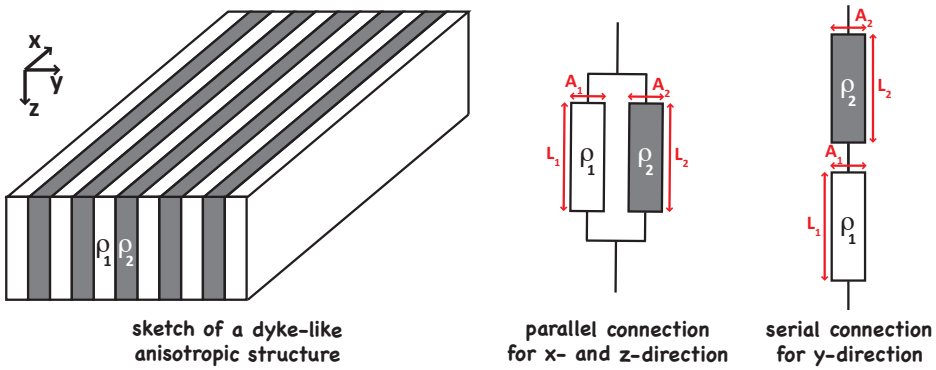

Figure 2.9: Sketch of a dyke-like anisotropic structure and its equivalent schematic circuit diagrams. The left-hand side figure shows an anisotropic body that has vertical, x-directed dykes. For currents flowing in x- and z-direction the anisotropic body acts as a parallel connection as shown in the middle figure. In this case the equivalent resistivities ρ_x and ρ_z can be calculated by applying Kirchhoff's Law for parallel connection to ρ_1 and ρ_2. (Note, ρ_x is equal to ρ_z.) Currents flowing in the y-direction experience the anisotropic body as a serial connection, as shown in the right-hand side figure, and therefore Kirchhoff's Law for serial connections can be used to calculate an equivalent resistivity ρ_y from ρ_1 and ρ_2.

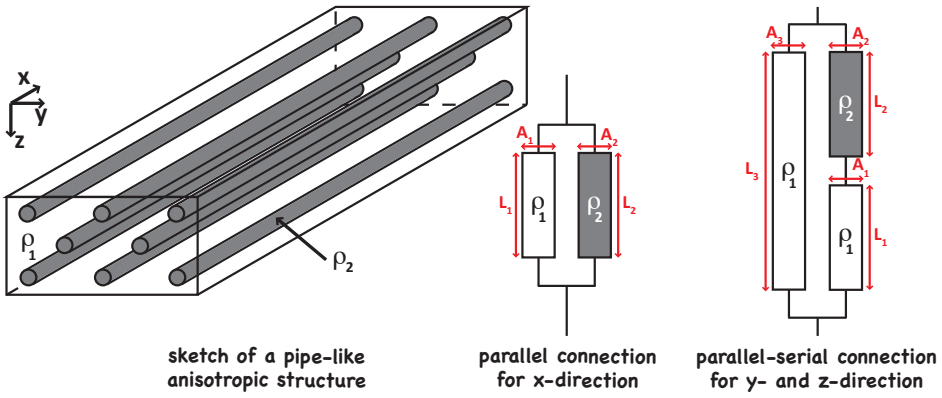

Figure 2.10: Sketch of a pipe-like anisotropic structure and its equivalent schematic circuit diagrams. The left-hand side figure shows an anisotropic body which contains serial pipe-like structures (note that the shape of the pipes can be different, the identical round shape of the cross-sectional areas was only chosen to simplify the sketch). For currents flowing in x-direction the anisotropic body acts as a parallel connection as shown in the middle figure. In this case an equivalent resistivity ρ_x can be calculated by applying Kirchhoff's Law for parallel connection to ρ_1 and ρ_2. Currents flowing in the y- and z-directions experience the anisotropic body as a parallel-serial connection, as shown on the right-hand side, and therefore a combination of Kirchhoff's Laws for serial and parallel connections can be used to calculate the equivalent resistivities ρ_y and ρ_z from ρ_1 and ρ_2. (Note, ρ_y is not necessarily equal to ρ_z.)

the pipes is equal in the y- and z-directions. (Note that Schön (2004) gives a similar and useful review of sheet, channel and film resistivity models (without transverse resistivity of channel models) based on one conductive component (pore water) and the empirical Archie equation.)

The equivalent parallel and serial resistivities can be calculated based on Kirchhoff's Laws. The conductance, G, is given by

$$G = \frac{\sigma A}{l} = \frac{A}{\rho l} \quad , \tag{2.83}$$

where l is the length of the object, A is its cross-sectional area and σ is the conductivity of the object (or ρ its resistivity). For a parallel connection, the equivalent conductance G_p is given by

$$G_p = G_1 + G_2 \qquad \rightarrow \qquad \frac{A_p}{\rho_p l_p} = \frac{A_1}{\rho_1 l_1} + \frac{A_2}{\rho_2 l_2} \quad , \tag{2.84}$$

where the equivalent length of the body, l_p, is equal to the lengths, l_1 and l_2, of the two individual objects, and the equivalent cross-sectional area is the sum of the two individual cross-sectional areas ($A_p = A_1 + A_2$). Therefore

$$\frac{A_1 + A_2}{\rho_p l_p} = \frac{1}{l_p}\left(\frac{A_1}{\rho_1} + \frac{A_2}{\rho_2}\right) \qquad \rightarrow \qquad \frac{A_1 + A_2}{\rho_p} = \frac{A_1}{\rho_1} + \frac{A_2}{\rho_2} \quad , \tag{2.85}$$

which yields

$$\rho_p = \frac{A_1 + A_2}{\frac{A_1}{\rho_1} + \frac{A_2}{\rho_2}} = \frac{A_1 + A_2}{\frac{A_1\rho_2}{\rho_1\rho_2} + \frac{A_2\rho_1}{\rho_1\rho_2}} = \frac{(A_1 + A_2)\rho_1\rho_2}{A_1\rho_2 + A_2\rho_1} \quad . \tag{2.86}$$

In the case of Kirchhoff's Law for serial connection, the equivalent conductance, G_s, is given by

$$\frac{1}{G_s} = \frac{1}{G_1} + \frac{1}{G_2} \qquad \rightarrow \qquad \frac{\rho_s l_s}{A_s} = \frac{\rho_1 l_1}{A_1} + \frac{\rho_2 l_2}{A_2} \quad , \tag{2.87}$$

where this time the cross-sectional areas are equal ($A_s = A_1 = A_2$) and the equivalent length is the sum of the lengths of the two bodies ($l_s = l_1 + l_2$). Using these relations yields

$$\rho_s(l_1 + l_2) = \rho_1 l_1 + \rho_2 l_2 \tag{2.88}$$

and therefore

$$\rho_s = \frac{\rho_1 l_1 + \rho_2 l_2}{(l_1 + l_2)} \quad . \tag{2.89}$$

Although MT deals with AC problems, the DC approach to calculate the principal anisotropic resistivities in all the directions, based on Kirchhoff's Laws, will be used as an approximation of appropriate principal resistivities based on known background and dyke resistivities (see e.g., Section 4.3). As a dyke swarm has an increased surface area to volume ratio compared to a simple single contact the charge dissipation and accumulation time probably gives arise to the complex conductivity responses if this time is comparable to the signal period.

2.7 DISTORTION EFFECTS

Distortion comprises all the small-scale, near-surface conductivity inhomogeneities that cannot be resolved within the conductivity model of the subsurface, but still affect the MT responses, i.e., distort them. The complex process of distortion has been classified by Berdichevsky et al. (1973) into two major effects: the galvanic and the inductive effects. The galvanic effect is caused by primary electric fields that produce electrical charges where conductivity variations occur, i.e., at distinct boundaries (similar to that described in Section 2.6.2) or at continuous transitions. The primary electric field is distorted because the excess charges result in secondary electric fields that add vectorially to the primary field. The inductive effects are related to time-varying magnetic fields inducing currents that flow in closed loops. These vortex currents produce secondary magnetic fields that also add vectorially to the primary magnetic field (Jiracek, 1990). The galvanic distortion affects not only the electric field, but also the magnetic fields. Although these effects on the electric and magnetic fields are not entirely separate, they are often considered as different and are called galvanic electric and galvanic magnetic distortion (e.g. Garcia and Jones, 2002b; Chave and Smith, 1994; Chave and Jones, 1997; Smith, 1997). Galvanic distortion is also known as current gathering, current deflection, current leakage, current concentration or current channelling (Jones, 1983b). For a conductive inclusion, the boundary charges cause a secondary field, that is antiparallel to the primary along the sides of the body and over it, so that the total field is reduced, whereas off the ends of the body the total field is enhanced. The resistive case is exactly the opposite: the total field is enhanced over the body and along its sides, and reduced off the end of the body. Figure 2.11 shows a sketch of this behaviour (Jiracek, 1990). The galvanic electric field effectively channels the current into conductive inhomogeneities and around resistive inhomogeneities (Smith, 1997). Therefore the apparent resistivities recorded in MT soundings directly above a surficial resistive body (CURRENT DEFLECTION) are shifted upwards, whereas they are shifted downwards over a conductive patch (CURRENT CHANNELLING). This upward or downward shift is asymptotically a constant - or static - shift of the MT log-log apparent resistivity versus period curve. Therefore these effects are known as STATIC SHIFT. No distortion occurs in the impedance phase.

Jiracek (1990) showed that these galvanic effects are not only produced by resistive or conductive inclusions but also by 2D topography that can cause the so-called galvanic topographic effect. The topographic galvanic effect occurs when the primary electric field is perpendicular to the trend of the topography, which is the case for the TM mode, that is therefore associated with these effects. There are no surface charges at the top of a hill nor at the bottom of a valley; the maximum charge concentration can be found where the topography is steepest. The total electric field causes a current flow tangential to the topography beneath the surface . The electric fields are reduced at the top of a hill and increased in a valley, and therefore the apparent resistivity values are highest in valleys and lowest on topographic peaks. Unlike the 'normal' galvanic distortion effects, the galvanic topographic effects do not require a conductivity inhomogeneity to be present.

The inductive distortion effects are dependent on frequency, the electrical properties and the geometry of the subsurface. Unlike the galvanic effect, where the secondary field is in phase with the causative primary electric field, for the inductive case the phase of the secondary magnetic field varies between 0 (the resistive limit) and $\frac{\pi}{2}$ (the inductive limit)

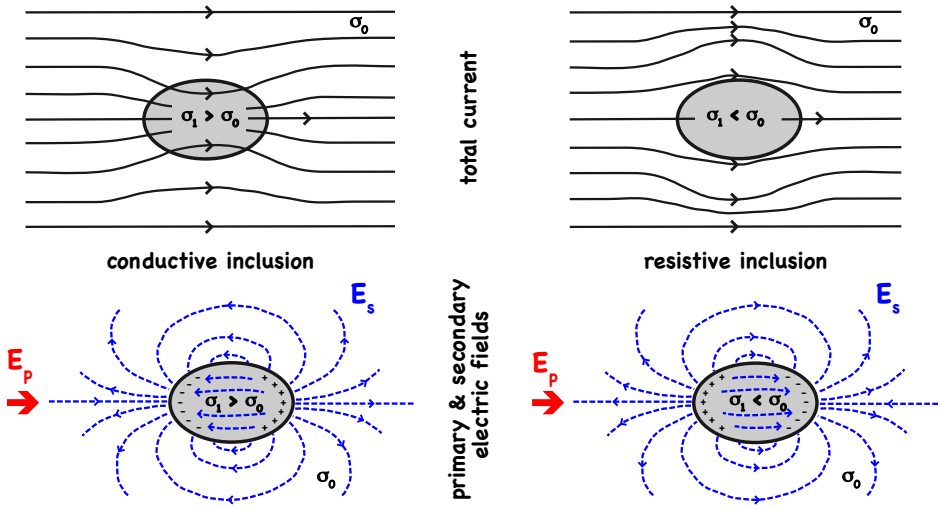

Figure 2.11: Galvanic effects for a conductive (left) and a resistive inclusion (right). Charge build-up on the surface of the body causes secondary electric fields $\underline{E}_s$, which add vectorially to the primary electric field $\underline{E}_p$ (bottom) resulting in current channelling (top, left) and current deflection (top, right). Redrawn from Jiracek (1990).

relative to the primary magnetic field. The major difference between inductive and galvanic effects is that the former increases to saturation as frequency increases and the magnetic field has the leading role, whereas the electric field is the more important one for the latter, which increases towards saturation with decreasing frequency (Jiracek, 1990). For the quasi-stationary approximation ($\sigma = \varepsilon/T$), which is one of the assumptions in MT, inductive distortion can be ignored (Berdichevsky and Dmitriev, 1976a).

Chave and Smith (1994) and Smith (1997) explain how the galvanic distortion can be described mathematically. The measured electric field $\underline{\underline{E}}_{obs}$ is proportional to the regional, 2D electric field $\underline{\underline{E}}_{2D}$

$$\underline{\underline{E}}_{obs} = \underline{\underline{C}}\,\underline{\underline{E}}_{2D} \quad , \tag{2.90}$$

where the matrix $\underline{\underline{C}}$ is the electric galvanic distortion matrix. Since the magnetic field of the galvanic distorted currents $\underline{\underline{B}}_{dist}$ are proportional to, and in phase with, the currents, which are proportional and in phase with the regional electric field, they can be written as

$$\underline{\underline{B}}_{dist} = \underline{\underline{D}}\,\underline{\underline{E}}_{2D} \quad , \tag{2.91}$$

where the matrix $\underline{\underline{D}}$ is the magnetic galvanic distortion matrix. Both the electric and the magnetic distortion matrix are real and frequency independent. They can be written as

$$\underline{\underline{C}} = \begin{pmatrix} C_{11} & C_{12} \\ C_{21} & C_{22} \end{pmatrix} \text{ and } \underline{\underline{D}} = \begin{pmatrix} D_{11} & D_{12} \\ D_{21} & D_{22} \end{pmatrix} \quad . \tag{2.92}$$

The observed magnetic field $\underline{\underline{B}}_{obs}$ itself is the sum of the regional magnetic field $\underline{\underline{B}}_{2D}$ and the galvanic distorted magnetic field $\underline{\underline{B}}_{dist}$, i.e.,

$$\underline{\underline{B}}_{obs} = \underline{\underline{B}}_{2D} + \underline{\underline{B}}_{dist} = \underline{\underline{B}}_{2D} + \underline{\underline{D}}\,\underline{\underline{E}}_{2D} \quad . \tag{2.93}$$

The measured impedance $\underline{\underline{Z}}_{obs}$ is related to the observed electric $\underline{\underline{E}}_{obs}$ and magnetic fields $\underline{\underline{B}}_{obs}$:

$$\underline{\underline{E}}_{obs} = \underline{\underline{Z}}_{obs}\,\underline{\underline{B}}_{obs} \quad . \tag{2.94}$$

By analogy, the regional impedance $\underline{\underline{Z}}_{2D}$ is given by

$$\underline{\underline{E}}_{2D} = \underline{\underline{Z}}_{2D}\,\underline{\underline{B}}_{2D} \quad . \tag{2.95}$$

In Equation 2.94, replacing $\underline{\underline{E}}_{obs}$, $\underline{\underline{B}}_{obs}$ and $\underline{\underline{E}}_{2D}$ with Equations 2.90, 2.93 and 2.95 yields

$$\underline{\underline{C}}\,\underline{\underline{Z}}_{2D}\,\underline{\underline{B}}_{2D} = \underline{\underline{Z}}_{obs}\,\underline{\underline{B}}_{2D} + \underline{\underline{Z}}_{obs}\,\underline{\underline{D}}\,\underline{\underline{Z}}_{2D}\,\underline{\underline{B}}_{2D} \quad . \tag{2.96}$$

This holds for all polarizations of the regional magnetic field $\underline{\underline{B}}_{2D}$, therefore

$$\underline{\underline{C}}\,\underline{\underline{Z}}_{2D} = \underline{\underline{Z}}_{obs} + \underline{\underline{Z}}_{obs}\,\underline{\underline{D}}\,\underline{\underline{Z}}_{2D} = \underline{\underline{Z}}_{obs}\left(\underline{\underline{I}} + \underline{\underline{D}}\,\underline{\underline{Z}}_{2D}\right) \tag{2.97}$$

$$\Rightarrow \qquad \underline{\underline{Z}}_{obs} = \underline{\underline{C}}\,\underline{\underline{Z}}_{2D}\left(\underline{\underline{I}} + \underline{\underline{D}}\,\underline{\underline{Z}}_{2D}\right)^{-1} \quad , \tag{2.98}$$

where $\underline{\underline{I}}$ is the identity matrix. Assuming that the observation coordinate system is not identical to the strike or 2D regional reference frame, a rotation by an angle θ needs to be applied (similar to Equation 2.77), i.e.

$$\underline{\underline{Z}}_{obs}(\theta) = \underline{\underline{R}}(\theta)\underline{\underline{C}}\,\underline{\underline{Z}}_{2D}\left(\underline{\underline{I}} + \underline{\underline{D}}\,\underline{\underline{Z}}_{2D}\right)^{-1}\underline{\underline{R}}^{T}(\theta) \quad . \tag{2.99}$$

The galvanic magnetic distortion is given by the frequency dependent (due to the frequency dependence of $\underline{\underline{Z}}_{2D}$) product of $\underline{\underline{D}}\,\underline{\underline{Z}}_{2D}$ and vanishes for low frequencies (long periods). Therefore the magnetic galvanic distortion is usually neglected for the MT case (Garcia and Jones, 2002b) and Equation 2.99 simplifies to

$$\underline{\underline{Z}}_{obs}(\theta) = \underline{\underline{R}}(\theta)\,\underline{\underline{C}}\,\underline{\underline{Z}}_{2D}\,\underline{\underline{R}}^{T}(\theta) \quad . \tag{2.100}$$

The assumption that magnetic galvanic distortion is negligible is not always correct, as Chave and Smith (1994) demonstrated using two different examples. The first one is data from a site in Carty Lake (electrodes at the bottom of the lake, magnetometer on the shore of the lake) in central Ontario, Canada. In this case the electric galvanic distortion decomposition was not sufficient to describe the distortion of the MT response at higher frequencies (shorter periods). Only taking both the electric and magnetic galvanic distortion effect into account allowed them to adequately describe the distortion affecting the response. Their second example shows that the magnetic field galvanic distortion is significant for seafloor MT data, probably because of the relatively resistive rocks immediately beneath the oceanic crust causing a strong electric current concentration and channelling within the highly conductive ocean (Chave and Smith, 1994). Note that the seafloor case is different from the land case as the measurement site for the magnetic field is beneath the distorting current sheet, which causes significantly modifications of the fields even in absence of any distortion compared to the surface (background) values. Galvanic distortion reduces the amount of this attenuation.

Several distortion correction techniques have been proposed to deal with or to remove the unwanted galvanic distortion due to near-surface inhomogeneities and topography: mathematically, statistically or physically based approaches have been used (for more details on the different approach see e.g., Groom and Bahr (1992), Jiracek (1990)). Some of these approaches will be discussed in a later section (Section 2.9.2).

In the 3D case, the same distortion effects can also be observed. Furthermore, several additional galvanic distortion effects appear, as result of field curvature, that can be reduced to two types: flow-around (the current flows around resistive structures) and concentration (the current concentrates in conductive structure). (Berdichevsky and Dmitriev, 1976b)

2.8 DATA ACQUISITION

The acquisition of MT data involves the recording of the time variations of the natural electric and magnetic fields simultaneously. In the logistically ideal case, both horizontal and the vertical magnetic fields are recorded, but if necessary one can omit the vertical component. For the electric field only the two horizontal components are recorded. In the first place, setting up a 100 m vertical electrical dipole is logistically very expensive (or impossible), but the main reason is that the vertical electric field at the air-Earth interface is (per boundary condition) zero (see Section 2.6.2).

There are various types of instruments used to measure MT data. The equipment used for the broad-band sites within the SAMTEX project was a system from Phoenix Geophysics. The receivers, MTU5s and MTU5As, are able to record data in the MT range (0.001 s - 50 000 s) and the AMT-MT range (0.0001 s - 50 000 s) respectively. The MTU5s/MTU5As record up to two electric and three magnetic channels simultaneously. A GPS antenna provides the geographic coordinates and the elevation of the site, and - more importantly - a continuous time signal, that allows accurate recording of the time series to allow synchronization with remote reference stations. The broad-band magnetotelluric (BBMT) magnetic field sensors used were the 1,41 m long MTC-50 induction coils. According to the manufacturer's specifications, these coils provide data in the range 0.0025 s to 50 000 s. However, the longest usable periods recorded in the SAMTEX project are 'only' a few 1000 s, because of the short acquisition time of 2-3 days at each site, relative low signal due to a minimum in the solar cycle and cultural noise. The sensors used for measuring the electric field were non-polarising lead, lead-chloride ($Pb - PbCl$) electrodes.

A number of long period MT (LMT) sites were also installed during the SAMTEX project. So-called LIMS instruments developed by, and borrowed from, the Geological Survey Canada as well as Ukrainian instruments called LEMIs and copper, copper-sulphate ($Cu - CuSO_4$) electrodes were used to record the long period data. Since the work for this thesis is only based on BBMT data, the LMT equipment will not be discussed further (more details about the LEMIs can be found on the manufacturer's webpage *http://www.isr.lviv.ua/lemi417.htm*).

The ideal location for recording MT data is far from human interference, far from electrical noise (e.g., DC train lines, electric fences, power lines and mining activity) and in an area with minimal topography, that allows equipment protection (i.e., soft soil that allows the burying of all sensors and cables, but also has a shady spot for the recording unit to protect it from the sun and overheating). Figure 2.12 shows a typical setup used for the sites in the SAMTEX project. The recording unit and a ground electrode were at the centre of the layout. Four other electrodes were located in geographical orientation with respect to magnetic north - typically 50 m each - north, south, east and west of the ground electrode. To lower the contact resistance with the ground and to keep the electrodes moist for longer in the hot and dry climate, they were put into buckets filled with mud made from local soil and salt water. This electrode-bucket set was buried in the ground. The magnetic sensors were also buried in the ground once they were aligned north-south or east-west (horizontal coils) and levelled (all coils). The sensors were buried to protect them against human and animal interference, avoid movement caused by wind or animals dragging on the cables and to minimize temperature effects. Daily temperatures in the field area varied from above 40°C during the day to several degrees below zero during the night. The temperature changes

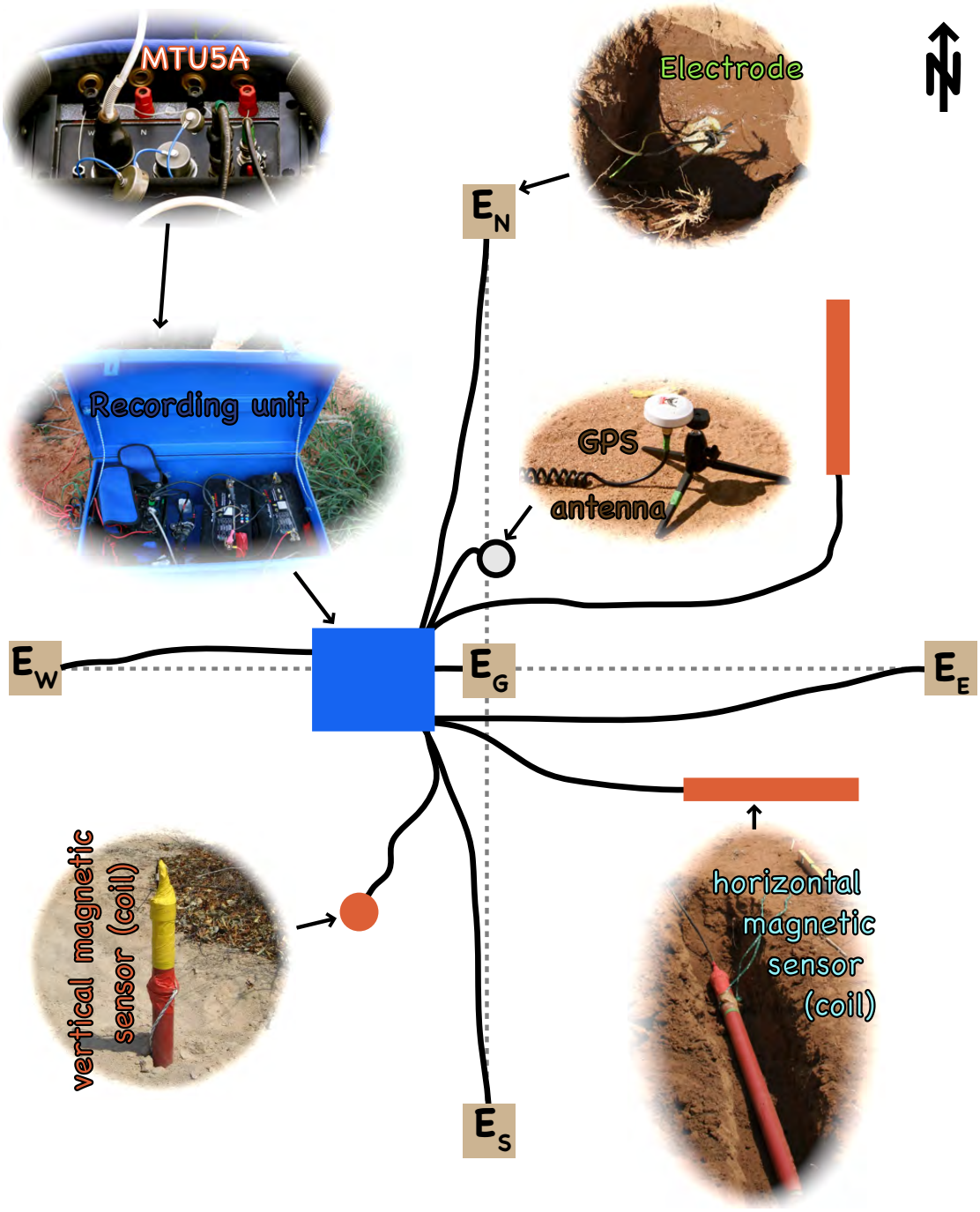

Figure 2.12: Sketch of a broad-band MT site layout including photos of the instrument components in the field. In the centre of the layout is the recording unit, which consists of a MTU5A powered by car batteries protected in a blue metal box. Four electrodes, to record the variation of horizontal electric fields, are orientated N-S and E-W and are buried typically 50 m away from the ground electrode (photo: electrode in mud, ready to be buried). The fluctuations of the magnetic field components are recorded by two N-S and E-W oriented horizontal coils (photo: levelled and aligned coil, ready to be buried) and one vertical broad-band coil (photo: levelled coil, ready to be covered by a protective bin). The GPS antenna provides the MTU5A with the site geographic coordinates and more importantly with a continuous time signal, which is essential for recording the times series and later for remote reference processing with other sites (photo: GPS antenna, not yet buried).

are damped beneath the ground surface: at only a few decimetres depth below the surface the variation is less than 1°C in the daily cycle.

2.9 DATA PROCESSING, ANALYSIS, MODELLING AND INVERSION

A typical workflow for 2D data processing, analysis, decomposition and modelling is described by Spratt et al. (2009) using the example of data from the Wopmay orogen, Northwest Territories, Canada. First the time series data were inspected and bad or null data removed. Next, a robust, remote-reference code is used to convert the time series into MT response estimates. If broadband and long periodic data were available at the same site, they were merged to produce a single response curve per site. An analysis for distortion effects resulting from auroral and equatorial electrojets followed, if the data were recorded at high or low latitudes respectively.

Jones (2006) showed that 1D depth estimates are valid in the 2D case if the two 2D modes, TE and TM, are totally decoupled. Therefore, they can be used to derive a first order estimate of the maximum investigation depth at each site. The next important step is to analyse the MT responses for galvanic distortion and to determine the most consistent geoelectric strike direction. With the results of the distortion analysis, a single site, frequency independent decomposition can be applied to derive the most accurate regional 2D impedances. D^+ or ρ^+ (more details in Subsection 2.9.3) approaches can then be used to support the selection and removal of unreliable data points that have larger scatter and large error bars. The data set can then be inverted for subsurface electrical resistivity structure. For the inversion, different parameters (e.g., regularization and smoothing factors) have to be chosen carefully and separate inversions of different parts of the data set may be required as well.

In the following sections, most of these processing and analysis steps are described in more detail, expect for the depth approximations (see earlier section), the merging of broad-band and long period data (the data set used for this thesis contains broad-band data only) and the correction for distortion due to source effects related to high or low latitudes (as mentioned earlier, the data were recorded in mid-latitudes and do not require this treatment).

2.9.1 *Time series to transfer functions*

The MT transfer functions are obtain by processing the time series of the acquired data. Jones et al. (1989) describe several methods of deriving transfer function estimates. All these processing schemes involve the following steps (in one way or another): preconditioning of the data, conversion from the time to frequency domain and estimation of the transfer functions.

Pre-conditioning is done to reduce the effects of trends and to remove severe noise (spikes). Also part of pre-conditioning is the splitting of the time series into segments of different length, depending on the period being calculated. The statistical result will be the better the more segments are used. Since the segments are of finite length, a Fourier Transform would cause spectral distortion by permitting 'leakage' of power (Jones, 1977). To avoid spectral distortion, a window function (such as e.g., Parzen window or Hamming window) is generally applied to the time segments.

Once pre-conditioned, the windowed time series segments are converted into the frequency domain using a (Discrete or Fast) Fourier Transform or a wavelet transform. Each of the measured field components must be calibrated with respect to the particular instrument's sensitivity. Calibration is achieved by applying the instrument calibration functions that are either frequency dependent (e.g., induction coil) or frequency independent (e.g., fluxgate magnetometer). Because the dispersion relation of Weidelt (1972) predicts that neighbouring frequencies provide similar transfer functions, evaluating about six to ten frequencies per decade will give reasonable result, but less could lead to aliasing effects in the frequency domain (Simpson and Bahr, 2005). One should keep in mind that the more frequency estimates that are available, the higher the resolution of the resulting transfer function at the expense of increasing variance.

Once in the frequency domain, the raw power spectra for each time segment for each channel are used to calculate the auto and cross spectra, which are the products of the field components and their complex conjugates. These spectra are stored in the so-called SPECTRAL MATRIX:

B_x	B_y	B_z	E_x	E_y	
$B_x \cdot B_x^*$	$B_y \cdot B_x^*$	$B_z \cdot B_x^*$	$E_x \cdot B_x^*$	$E_y \cdot B_x^*$	B_x
	$B_y \cdot B_y^*$	$B_z \cdot B_y^*$	$E_x \cdot B_y^*$	$E_y \cdot B_y^*$	B_y
		$B_z \cdot B_z^*$			B_z
			$E_x \cdot E_x^*$	$E_y \cdot E_x^*$	E_x
				$E_y \cdot E_y^*$	E_y

For the same evaluation frequency, several spectral matrices will be stacked and potentially manually edited or weighted using statistical techniques.

The next step is the estimation of the transfer functions - the impedance tensor and tipper vector:

$$E_x(\omega) = Z_{xx}(\omega) \cdot H_x(\omega) + Z_{xy}(\omega) \cdot H_y(\omega) + \delta Z(\omega) \quad , \tag{2.101}$$

$$E_y(\omega) = Z_{yx}(\omega) \cdot H_x(\omega) + Z_{yy}(\omega) \cdot H_y(\omega) + \delta Z(\omega) \quad , \tag{2.102}$$

$$H_z(\omega) = T_x(\omega) \cdot H_x(\omega) + T_y(\omega) \cdot H_y(\omega) + \delta T(\omega) \quad , \tag{2.103}$$

where $\delta Z(\omega)$ and $\delta T(\omega)$ represent uncorrelated noise (in this case electrical noise), that is required because measurement errors make the transfer function equations inexact (Simpson and Bahr, 2005).

Jones et al. (1989) state that there are two types of error estimates in the estimation of transfer functions: statistical and biased errors. The statistical error estimate gives a quantitative measure of precision of an estimate and generally will be reduced by analysing more data or by using robust methods, which eliminate errors due to Gaussian residuals. Sims et al. (1971) discuss the biased error. They state that there are six possible ways to estimate each impedance element: two of them turn out to be unstable for the 1D case, whereas the other four are quite stable. Two of the four stable estimates are biased down by random noise in the magnetic field $\underline{H}$ but are not affected by noise in the electric field $\underline{E}$, whereas the other two are biased up by noise in $\underline{E}$, but are unaffected by noise in $\underline{H}$. Goubau et al. (1978) and Gamble et al. (1979) introduced remote reference processing to avoid these biased errors due to noise. They measure two extra channels (electric and/or magnetic) at a site remote

from the local MT site to use as references. Often several MT sites, that were recording simultaneously, are used as remote references for each other.

Correlated noise components between the local and remote fields are not removed by the remote reference processing approach and can cause bias effects. Remote reference results always have larger associated statistical noise than the standard single station methods (Jones et al., 1989).

Commonly used least-squares and robust processing techniques are based on statistical processing methods, which solve Equations 2.101, 2.102 and 2.103 as a bivariate linear regression problem, to remove noise from MT data (Simpson and Bahr, 2005). Therefore the impedance elements can be estimated as

$$Z_{xx} = \frac{\langle E_x R_x^* \rangle \langle H_y R_y^* \rangle - \langle E_x R_y^* \rangle \langle H_y R_x^* \rangle}{DET} \quad , \tag{2.104}$$

$$Z_{xy} = \frac{\langle E_x R_y^* \rangle \langle H_x R_x^* \rangle - \langle E_x R_x^* \rangle \langle H_x R_y^* \rangle}{DET} \quad , \tag{2.105}$$

$$Z_{yx} = \frac{\langle E_y R_x^* \rangle \langle H_y R_y^* \rangle - \langle E_y R_y^* \rangle \langle H_y R_x^* \rangle}{DET} \quad , \tag{2.106}$$

$$Z_{yy} = \frac{\langle E_y R_y^* \rangle \langle H_x R_x^* \rangle - \langle E_y R_x^* \rangle \langle H_x R_y^* \rangle}{DET} \quad , \tag{2.107}$$

and the tipper elements are given by

$$T_x = \frac{\langle H_z R_x^* \rangle \langle H_y R_y^* \rangle - \langle H_z R_y^* \rangle \langle H_y R_x^* \rangle}{DET} \quad , \tag{2.108}$$

$$T_y = \frac{\langle H_z R_y^* \rangle \langle H_x R_x^* \rangle - \langle H_z R_x^* \rangle \langle H_x R_y^* \rangle}{DET} \quad , \tag{2.109}$$

where

$$DET = \langle H_x R_x^* \rangle \langle H_y R_y^* \rangle - \langle H_x R_y^* \rangle \langle H_y R_x^* \rangle \quad . \tag{2.110}$$

The complex conjugate quantities R_x^* and R_y^* theoretically represent any reference field, either local or remote, but also either of the electric or magnetic field components. In practise, the most commonly used reference fields are the horizontal magnetic fields from a remote site (often called remote H). Remote H is the generally preferred choice because the magnetic field is usually less affected by noise than the electric field (except for frequencies within the MT dead-band). Therefore a remote H estimate is usually the least biased and statistically the best.

There are several commercial as well as free processing codes available (e.g., Egbert and Booker (1986), Egbert (1997), Chave and Thomson (2004). Phoenix commercial software is based on Jones and Jödicke (1984)/method 6 in Jones et al. (1989)). These various different codes perform with varying degrees of success depending on the nature and quantity of the noise contained within the recorded signal and the chosen parameter settings (e.g., coherence threshold) in the code. Therefore, it is sometimes useful to apply different processing codes (or the same code with different parameters) to the same data, or only use parts of the data, because the noise contamination might vary during the recording time window (often the night-time is quieter/less noisy - especially at high frequencies). Deriving a final set of transfer functions for modelling and inversion is a time consuming

procedure that requires much trial-and-error. In the end it is also a relatively subjective decision as to whether the final transfer function is acceptable or whether more work is needed.

2.9.2 *Distortion analysis and removal*

The distortion problem was described in Section 2.7. In order to remove the distortion effects, different approaches of distortion analysis and decomposition or correction can be applied to the data. For example Sternberg et al. (1988), Pellerin and Hohmann (1990) and Sternberg (1993) proposed using transient electromagnetic (TEM) data to correct for static shifts in MT responses, either by joint inversion allowing vertical shifts in the MT apparent resistivity curves or by using a correction scheme that is based on 1D inversion of TEM soundings. From the estimated 1D structure, a synthetic MT response is computed for short periods ($\leqslant 1$s). The observed MT curves are then shifted to match the computed curves in order to eliminate static shifts. This strategy is only accurate if the overlapping region between MT and TEM is 1D; for multidimensional environments the approach might provide a useful indication of a static shift problem, but often there are no TEM data available at MT sites. A different approach is described by de Groot-Hedlin (1991) and de Groot-Hedlin (1995), where she tries to invert for the static shift (de Groot-Hedlin, 1991) or the full electric galvanic distortion matrix (de Groot-Hedlin, 1995) and the resistivities (in 2D) simultaneously to find the smoothest model.

One of the most commonly used decomposition technique to obtain the regional 2D strike direction, a measure of the anisotropy, a measure and description of the galvanic distortion effects from distorted, measured data is the one by Groom and Bailey (1989) (see below). But there are also several other techniques available, e.g., Swift (1967), Bahr (1988), Weaver et al. (2000) and Martí et al. (2005), which will not be discussed in more detail. Unlike previous approaches, where a 2D regional structure is assumed, Utada and Munekane (2000), Garcia and Jones (2002b) and Becken et al. (2008) tried to solve the problem of distortion removal for a 3D environment. Another approach allowing for a 3D background structure is the phase tensor proposed by Caldwell et al. (2004), which is not a decomposition technique but a diagnostic and characterisation procedure that will be described later in this section.

Groom-Bailey decomposition

Bailey and Groom (1987), Groom (1988) and Groom and Bailey (1989) were the first to propose a distortion tensor decomposition that is based on a physical model of distortion for a 2D regional impedance (based on Larsen's (1977) decomposition for model consisting of a local, small-scale 3D anomaly over a layered Earth). The approach neglects the magnetic galvanic distortion and only deals with the real and frequency independent electric galvanic distortion matrix. The aim of the Groom-Bailey decomposition is to factorise the measured impedance $\underline{\underline{Z}}_{obs}$ into a rotation matrix $\underline{\underline{R}}$, the distortion matrix $\underline{\underline{C}}$ and a scaled regional 2D impedance tensor $\underline{\underline{Z}}_{2D}$, as given by Equation 2.100, and therefore to separate the local 3D distortion from the regional 1D or 2D response.

Groom (1988) and Groom and Bailey (1989) use a parametrisation of the distortion matrix that has a physical meaning, but also separates determinable and indeterminable parts. The

parametrisation is a product of a scaling or GAIN factor, g, and three tensors: TWIST, $\underline{\underline{T}}$, SHEAR, $\underline{\underline{S}}$ and local ANISOTROPY, $\underline{\underline{A}}$:

$$\underline{\underline{C}} = g\,\underline{\underline{T}}\,\underline{\underline{S}}\,\underline{\underline{A}} \quad . \tag{2.111}$$

These matrices are given by modified Pauli spin matrices, which have been normalised to ensure that the elements of $\underline{\underline{T}}$, $\underline{\underline{S}}$ and $\underline{\underline{A}}$ remain bounded during computations (Groom and Bailey, 1989).

Figure 2.13 illustrates the effects of twist, shear and distortion by the delocation and/or deformation of a group of unity vectors, if these effects are applied. The anisotropy tensor (or splitting tensor) stretches the two field components by different factors:

$$\underline{\underline{A}} = \frac{1}{\sqrt{1+a^2}} \begin{pmatrix} 1+a & 0 \\ 0 & 1-a \end{pmatrix} \quad . \tag{2.112}$$

The shear tensor is given by

$$\underline{\underline{S}} = \frac{1}{\sqrt{1+s^2}} \begin{pmatrix} 1 & s \\ s & 1 \end{pmatrix} \quad , \text{ where } s = \tan\phi_s \quad , \tag{2.113}$$

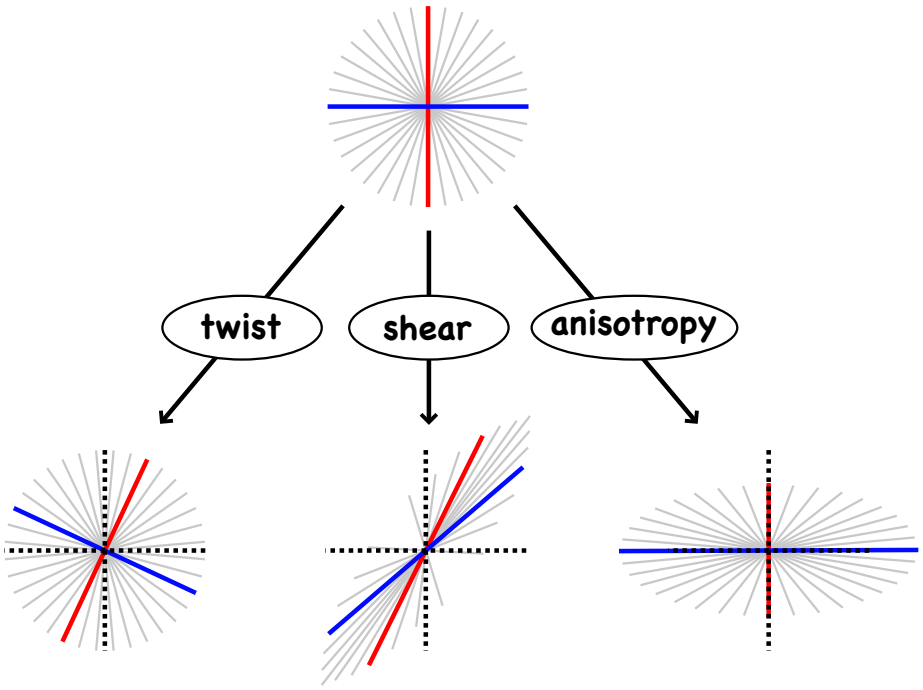

Figure 2.13: Sketch to illustrate the effects of twist, shear and anisotropy. On the top is a group of unity vectors with 2 reference vectors in red and blue. On the bottom are the groups of vectors after application of (from left to right) twist (Eq. 2.114), shear (Eq. 2.113) and anisotropy (Eq. 2.112). The black dashed lines indicate the original position and length of the two reference vectors (red and blue), which are now delocated and/or deformed. Redrawn from Groom (1988) and Groom and Bailey (1989).

and imposes an anisotropy on the axes that bisects the principle axes of the regional induction. In Figure 2.13 the sketch of the shear effect shows that the red vector is deflected clockwise by an angle ϕ_s, whereas the blue one experience a counter-clockwise deflection by the same angle. Therefore the shear s is characterised by the shear angle ϕ_s. Note that shear results in non-orthogonal axes. The twist tensor

$$\underline{\underline{T}} = \frac{1}{\sqrt{1+t^2}} \begin{pmatrix} 1 & -t \\ t & 1 \end{pmatrix} \quad , \text{ where } \; t = \tan\phi_t \quad , \tag{2.114}$$

simply rotates the electric field through a clockwise angle ϕ_t. The gain g finally performs an overall scaling of the electric field. Neither the gain nor the anisotropy can be determined separately from $\underline{\underline{Z}}_{2D}$, i.e., $\underline{\underline{Z}}'_{2D} = g\underline{\underline{A}}\,\underline{\underline{Z}}_{2D}$ both look like equally valid ideal 2D impedance tensors. The fact that gain and anisotropy cannot be separated results in apparent resistivity curves that are shifted by an unknown scaling factor, while the shapes of the apparent resistivity and impedance phase curves remain unchanged. These are the so-called STATIC SHIFTS.

The factorisation of the distortion matrix can be stated explicitly as

$$\underline{\underline{C}} = \frac{g}{\sqrt{(1+t^2)(1+s^2)(1+a^2)}} \begin{pmatrix} 1 & -t \\ t & 1 \end{pmatrix} \begin{pmatrix} 1 & s \\ s & 1 \end{pmatrix} \begin{pmatrix} 1+a & 0 \\ 0 & 1-a \end{pmatrix} \tag{2.115}$$

$$= \frac{g}{\sqrt{(1+t^2)(1+s^2)(1+a^2)}} \begin{pmatrix} (1+a)(1-ts) & (1-a)(s-t) \\ (1+a)(s+t) & (1-a)(1+ts) \end{pmatrix} \quad . \tag{2.116}$$

Groom and Bailey (1989) approximate the case of 'weak' distortion, where t, s and a are all much less than unity and therefore all the second and third order terms of t, s and a can be neglected, as

$$\underline{\underline{C}} \approx g \begin{pmatrix} 1+a & s-t \\ s+t & 1-a \end{pmatrix} \quad . \tag{2.117}$$

Groom and Bailey (1989) showed that in general two solutions exist, but only one is meaningful. One solution results in $|s| < 1$ and the other in $|s| > 1$. An intuitive consideration of the effect of the shear operator (Equation 2.113) indicates that a shear angle larger than $45°$ is not meaningful (because it implies a reversal of the current flow direction), and it is therefore reasonable to require, for a physically meaningful solution, that $|s| \leqslant 1$.

Jones and Groom (1993) demonstrated that the determination of strike angle from MT data has to be treated with care if both noise and local galvanic distortion are present. They stated that twist and shear are more stable over a wide period band than the regional strike direction, as distortion, caused by charge effects, dominates over induction, caused by currents. They warn that the choice of distortion parameters imposes a coordinate system on the MT data, which leads to erroneous strike determination. Therefore they iterated between constraining the distortion parameters and the strike until a self-consistent result was obtained. High twist and shear indicate strong distortion; if the shear is unity, the local current channelling is so severe that the MT data only contain information from a single electric field direction, and no method will ever be able to extract the regional impedances from both modes (Jones and Groom, 1993).

McNeice and Jones (2001) proposed an extension to the Groom-Bailey decomposition method in which a global minimum is sought to determine the most appropriate strike direction and distortion parameters for a range of frequencies and a set of MT sites. This multisite, multifrequency analysis is useful to find an appropriate strike direction over the whole profile length (or segments of it) and at all frequencies to allow modelling the data in 2D. McNeice and Jones (2001) developed a freely available computer program called STRIKE that decomposes data using this extended Groom-Bailey approach. The most recent version of STRIKE also allows an analysis of a depth band (using the Niblett-Bostick depth approximation) to accommodate the fact that in certain areas the penetration depth of neighbouring sites may be very different. The same period might sense completely different depths, e.g., in trying to find a common strike angle, a 10 s period might investigate crustal depths at one site, whereas at the next site 10 s might have a lithospheric mantle investigation depth. In such cases it is very useful to define a depth range instead of a frequency range for the analysis.

It is worth noting that decomposition to strike is not equivalent to a simple rotation into that direction. When applying a decomposition, the impedance elements are recalculated, most distortion effects are removed and only static shifts remain. Spratt et al. (2009) use the maximum phase difference in decomposed data as an indication of dimensionality, saying they can treat their data as 1D if the maximum phase difference is well below 10° over a broad period band.

Phase tensor analysis

The MT phase tensor approach was first published by Caldwell et al. (2004). It is based on the fact that only the amplitudes of the observed electric field are distorted by near-surface heterogeneities and that the phase relationship between the horizontal electric and magnetic field vectors will be virtually unaffected if the distortion is purely galvanic. In contrast to other MT distortion analysis approaches, the phase tensor method also allows both the heterogeneity and regional conductivity structure to be 3D. Caldwell et al. (2004) prove that the phase tensor is independent of the galvanic distortion as follows:
The real, second-rank phase tensor $\underline{\underline{\Phi}}$ is defined as the ratio of the real $\underline{\underline{X}}$ and imaginary parts $\underline{\underline{Y}}$ of the complex impedance $\underline{\underline{Z}} = \underline{\underline{X}} + i\,\underline{\underline{Y}}$, i.e.,

$$\underline{\underline{\Phi}} = \underline{\underline{X}}^{-1}\underline{\underline{Y}} \quad . \tag{2.118}$$

In the presence of galvanic distortion, the observed impedance $\underline{\underline{Z}} = \underline{\underline{C}}\,\underline{\underline{Z}}_R$, where $\underline{\underline{Z}}_R = \underline{\underline{X}}_R + i\,\underline{\underline{Y}}_R$ is the regional impedance and $\underline{\underline{C}}$ is the distortion tensor. Therefore the distorted real part may be written as $\underline{\underline{X}} = \underline{\underline{C}}\,\underline{\underline{X}}_R$, and the distorted imaginary part as $\underline{\underline{Y}} = \underline{\underline{C}}\,\underline{\underline{Y}}_R$. Based on these relations, it is obvious that the observed and regional phase tensor are identical and independent of the galvanic distortion tensor:

$$\begin{aligned}
\underline{\underline{\Phi}} &= \underline{\underline{X}}^{-1}\,\underline{\underline{Y}} \\
&= \left(\underline{\underline{C}}\,\underline{\underline{X}}_R\right)^{-1}\left(\underline{\underline{C}}\,\underline{\underline{Y}}_R\right) \\
&= \underline{\underline{X}}_R^{-1}\,\underline{\underline{C}}^{-1}\underline{\underline{C}}\,\underline{\underline{Y}}_R \\
&= \underline{\underline{X}}_R^{-1}\,\underline{\underline{Y}}_R \\
&= \underline{\underline{\Phi}}_R \quad .
\end{aligned} \tag{2.119}$$

In a Cartesian coordinate system (x_1,x_2) the phase tensor may be written in terms of the real and imaginary parts of the impedance tensor $\underline{\underline{Z}}$

$$\begin{pmatrix} \Phi_{11} & \Phi_{12} \\ \Phi_{21} & \Phi_{22} \end{pmatrix} = \frac{1}{\det(\underline{\underline{X}})} \begin{pmatrix} X_{yy}Y_{xx} - X_{xy}Y_{yx} & X_{yy}Y_{xy} - X_{xy}Y_{yy} \\ X_{xx}Y_{yx} - X_{yx}Y_{xx} & X_{xx}Y_{yy} - X_{yx}Y_{xy} \end{pmatrix} \quad , \tag{2.120}$$

where $\det(\underline{\underline{X}}) = X_{xx}X_{yy} - X_{yx}X_{xy}$ is the determinant of $\underline{\underline{X}}$.

Like a vector which is characterized by its direction and magnitude, a real second-rank tensor is characterized by a direction and three coordinate invariants, which are scalar quantities that are independent of the coordinate system. Caldwell et al. (2004) define the three invariants of the phase tensor as maximum (Φ_{max}) and minimum (Φ_{min}) tensor values and the skew angle β. The direction is given by the angle α, which expresses the tensor's dependence on the coordinate system (x_1, x_2). Figure 2.14 shows a sketch of the graphical representation - an ellipse - defined by these four quantities. The major and minor axes of the ellipse represent the principal values of the tensor (Φ_{max} and Φ_{min}) with the orientation of the major axis specified by the angle $\alpha - \beta$.

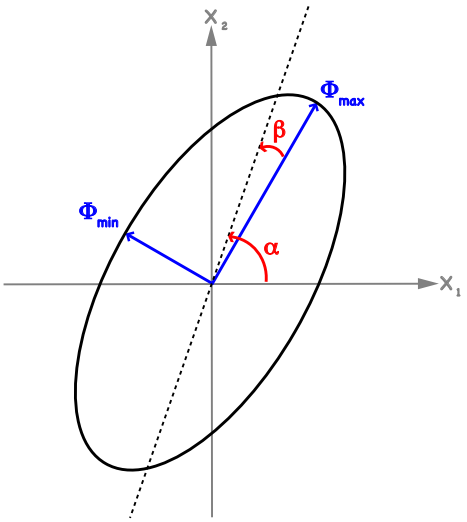

Figure 2.14: Graphical representation of the phase tensor. The lengths of the ellipse axes, which represent the principle axes of the tensor, are proportional to the principle values of the tensor: Φ_{max} and Φ_{min}. If the phase tensor is non-symmetric, a third coordinate invariant is needed to characterize the tensor: the skew angle β. The direction of the major axis of the ellipse is given by $\alpha - \beta$ and defines the relationship between the tensor and the observational reference frame (x_1, x_2). Redrawn from Caldwell et al. (2004).

The phase tensor can be written in terms of its invariants Φ_{max}, Φ_{min} and β and the angle α:

$$\underline{\underline{\Phi}} = \underline{\underline{R}}^{T}(\alpha - \beta) \begin{pmatrix} \Phi_{max} & 0 \\ 0 & \Phi_{min} \end{pmatrix} \underline{\underline{R}}(\alpha + \beta) \quad , \tag{2.121}$$

where $\underline{\underline{R}}^T$ is the transpose or inverse of the rotation matrix, i.e., $\underline{\underline{R}}^T(\theta) = \underline{\underline{R}}^{-1}(\theta) = \underline{\underline{R}}(-\theta)$, and the rotation matrix $\underline{\underline{R}}(\alpha+\beta)$ is given by

$$\underline{\underline{R}}(\alpha+\beta) = \begin{pmatrix} \cos(\alpha+\beta) & \sin(\alpha+\beta) \\ -\sin(\alpha+\beta) & \cos(\alpha+\beta) \end{pmatrix} \quad . \tag{2.122}$$

The two angles α and β can be expressed by

$$\alpha = \frac{1}{2}\tan^{-1}\left(\frac{\Phi_{12}+\Phi_{21}}{\Phi_{11}-\Phi_{22}}\right) \quad , \tag{2.123}$$

and

$$\beta = \frac{1}{2}\tan^{-1}\left(\frac{\Phi_{12}-\Phi_{21}}{\Phi_{11}+\Phi_{22}}\right) \quad . \tag{2.124}$$

The principals Φ_{max} and Φ_{min} of the tensor are given by

$$\Phi_{max} = \left(\Phi_1^2+\Phi_3^2\right)^{1/2} + \left(\Phi_1^2+\Phi_3^2-\Phi_2^2\right)^{1/2} \quad , \tag{2.125}$$

$$\Phi_{min} = \left(\Phi_1^2+\Phi_3^2\right)^{1/2} - \left(\Phi_1^2+\Phi_3^2-\Phi_2^2\right)^{1/2} \quad , \tag{2.126}$$

where Φ_1, Φ_2 and Φ_3 are related to the trace ($tr(\Phi)$), the determinant ($det(\Phi)$) and the skew ($sk(\Phi)$) of the tensor respectively,

$$\begin{aligned} \Phi_1 &= \frac{tr(\Phi)}{2} = \frac{\Phi_{11}+\Phi_{22}}{2} \quad , \\ \Phi_2 &= \left(det(\underline{\underline{\Phi}})\right)^{1/2} = (\Phi_{11}\Phi_{22}-\Phi_{12}\Phi_{21})^{1/2} \qquad \text{and} \\ \Phi_3 &= \frac{sk(\Phi)}{2} = \frac{\Phi_{12}-\Phi_{21}}{2} \quad . \end{aligned}$$

In the simplest case of a uniform conductivity halfspace, a circle of unit radius represents the phase tensor at all periods. For the more general case of an isotropic, 1D structure, $\Phi_{max}-\Phi_{min}$ still should be zero, and the tensor will be represented by circles in which the radius will vary with period. For example, the radius will increase, if the conductivity increases with depth (Caldwell et al., 2004). In the 2D case, $\Phi_{max}-\Phi_{min}$ will not be zero, and the phase tensor will be represented by an ellipse. A necessary, but not significant, condition for a 2D regional conductivity structure is that $\beta = 0$, i.e., the phase tensor is symmetric. For the 3D case the phase tensor is not symmetric and accordingly the skew angle β will be non-zero. Figure 2.15 shows phase tensor maps at three different periods (0.0316 s, 0.316 s and 3.16 s) with the colour representing the skew angle β. The model used is Caldwell et al.'s (2004) 3D structure of a small 10 Ωm, near-surface cube and a much larger (regional) 1 Ωm body at depth, both embedded in a 100 Ωm halfspace. Although the resistivity structure is clearly 3D, most of the skew angles are relatively small. Caldwell et al. (2004) state that while a large value of the skew angle necessarily implies a 3D regional conductivity structure (assuming perfect, noise-free data), a small value of the skew angle is not necessarily a good indication of the closeness of the conductivity structure to 2D. They recommend that the constancy of the direction of the principle axes of the phase tensor with period and with location along strike is a much more reliable indicator of two-dimensionality.

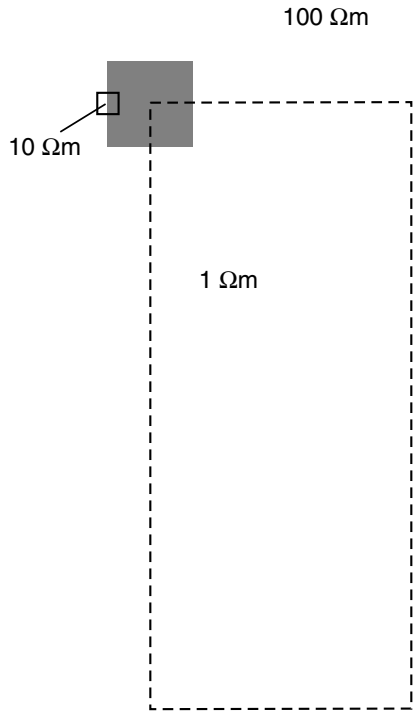

(a) Sketch of the 3D model, taken from Caldwell et al. (2004)

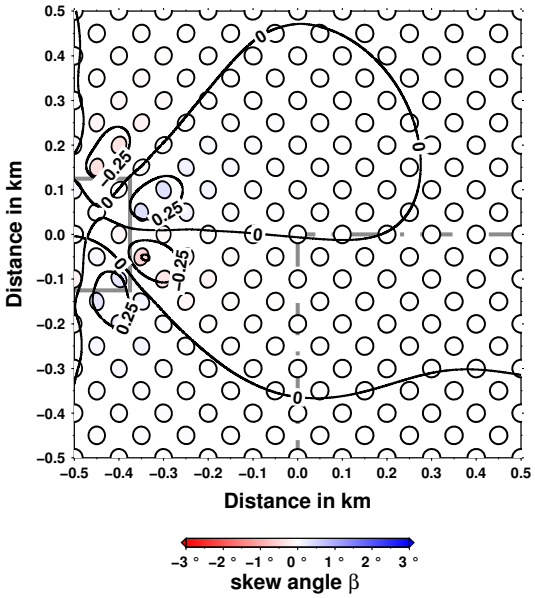

(b) Phase tensor map at 0.0316 s

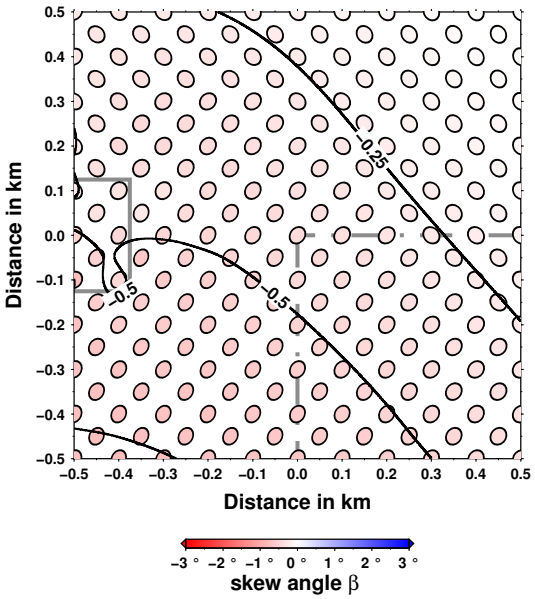

(c) Phase tensor map at 0.316 s

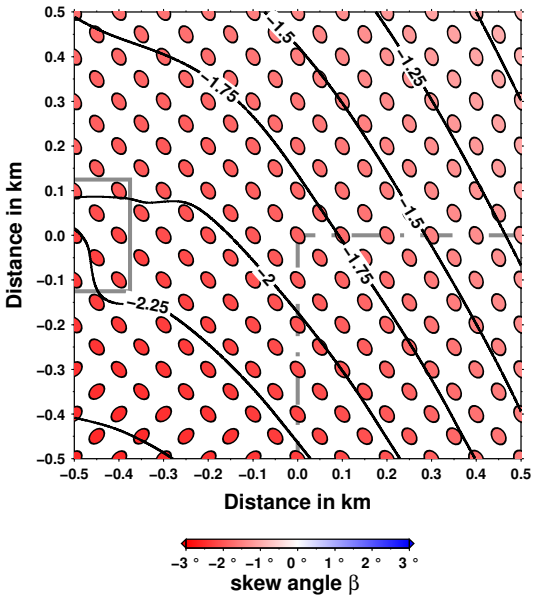

(d) Phase tensor map at 3.16 s

Figure 2.15: Example phase tensor maps after Caldwell et al. (2004). Panel (a) shows a plan view of the 3D resistivity structure that consists of a small (250 m x 250 m x 250 m) 10 Ωm cube with its top 50 m below the surface and a larger (7 km x 3 km x 3 km) rectangular 1 Ωm body buried 1.5 km below the surface. Both bodies are embedded in a 100 Ωm halfspace. The grey area (in (a)) indicates the region covered by phase tensor ellipse maps in (b) to (d) for three different periods (0.0316 s in (b), 0.316 s in (c) and 3.16 s in (d)). The colour filling of the phase tensor ellipses (normalised by Φ_{max}) in (b) to (d) show the skew angle β. The lateral extent of the two bodies is indicated by grey lines.

Heise et al. (2006) and Caldwell et al. (2004) showed that the presence of anisotropy does not cause a phase split, it only affects the amplitudes of the MT responses. The observation of a phase split between the principle phase values indicates only that a conductivity gradient (lateral or vertical) exists. Phase splits that are coincident with an anisotropic layer are produced by the interface between the overlying isotropic and the deeper anisotropic material.

Although the phase tensor method cannot be used to recover an undistorted impedance tensor, it has potential as a data imaging and modelling tool, since the principle axes of the phase tensor ellipse (Φ_{max}, Φ_{min}) indicate the horizontal directions of the maximum and minimum induction current, which reflects lateral variations in the conductivity structure (Caldwell et al., 2004). The phase tensor skew angle (β), and the variation of the direction of the major axis of the phase tensor ellipse can help in determining the dimensionality of the structure. Heise et al. (2006) successfully used the phase tensor approach for a trial-and-error forward modelling of a data set from the Taupo Volcanic Zone, New Zealand.

2.9.3 *D^+ and ρ^+*

The D^+ approach is work published by Parker (1980), Parker and Whaler (1981) and Parker (1982). The D^+ method is based on the fact that the discrete MT response of any one-dimensional conductivity profile can be matched arbitrarily well at a finite number of frequencies by the response of a finite system of delta functions. They perform 1D modelling of the admittance c. In a further development of the approach, called ρ^+, Parker and Booker (1996) use the logarithm of the admittance, $\log(c)$, rather than the admittance itself. The admittance is related to the apparent resistivity ρ_a and the impedance phase Φ by

$$\rho_a = \mu_0 \omega |c|^2 \tag{2.127}$$

and

$$c = |c| e^{i(\Phi - \pi/2)} \quad . \tag{2.128}$$

Therefore the 1D code by Parker and Booker (1996) is able to calculate a model from either apparent resistivities or phases or both. This can be used for a consistency check of measured data and give helpful guidance for the selection - or rejection - of apparent resistivity and/or phase values at certain frequencies. An example is given in Spratt et al. (2005).

2.9.4 *Forward modelling and inversion*

Once the MT data are processed, analysed, decomposed (removal of distortion effects and rotation into strike direction) and the D^+ or ρ^+ consistency check has been performed (to reject bad data points), the data set is ready for the modelling process. Forward modelling and inversion are used to produce a 1D, 2D or 3D model based on the measured data to determine the subsurface conductivity structure. These models help to relate the resistivity structure to geology and other geophysical models to define the current state of the subsurface and potentially provide an indication of Earth processes and Earth history.

The procedure of generating synthetic data responses for a given conductivity structure is called FORWARD MODELLING. The conductivity model (in 1D, 2D or 3D) will be discretised into cells that form the model mesh. Based on this discretised form of the model, the basic equations of MT (including appropriate boundary conditions) will be solved. The exact formulation of the equation system depends on the approximation used (e.g., finite difference (FD), finite element (FE) and integral equation (IE) methods), but generally the equation system is solved for one of the fields (electric or magnetic) everywhere in the mesh. Since the electric and the magnetic fields are related to each other by Maxwell's Equations, the calculated field can be used to determine the other one (also everywhere in the mesh). Knowing the electric and magnetic fields, it is easy to estimate the impedance (or resistivity and phase or tipper) values at the observation locations. The derived synthetic response will be compared with the measured data, and their difference is usually presented by an RMS misfit. Finding a model representing the observed data reasonably well by forward modelling is a time consuming trial-and-error process, where the input model has to be changed continuously by hand. The automatic optimisation of the model between the different forward solutions is known as the INVERSION process. The applied changes to the forward models are driven by the minimisation of the misfit between the observed data and that predicted from the model.

Forward modelling codes for MT data are available for 1D, 2D and 3D cases, whereas in the inversion case mainly 1D and 2D codes are available for standard applications (e.g., REBOCC, Siripunvaraporn and Egbert (2000); OCCAM 1D and 2D, Constable et al. (1987); RLM2DI, Rodi and Mackie (2001), of which an updated version is implemented in Geosystem's commercial software WinGLink®). Although the number of 3D inversion codes has grown in recent years, only one code (Siripunvaraporn et al., 2005) has become freely available. However, Siripunvaraporn et al.'s (2005) inversion requires a huge amount of computer memory, so that an application to a larger data set on a normal PC is impossible.

The 2D code used within this thesis is the one by Rodi and Mackie (2001) implemented in WinGLink® from Geosystem. The forward part of the code is described by Mackie et al. (1988). It is based on a finite difference approximation of the Maxwell Equations and uses a rectangular mesh to discretise the model. The inversion part of the code (Rodi and Mackie, 2001) is based on a nonlinear conjugate gradients scheme to minimise a regularised objective function (Tikhonov regularisation (Tikhonov and Arsenin, 1977)).

The 3D forward modelling and inversion approach - as well as more details on inversion schema - will be discussed in Part III of this thesis.

2D modelling and inversion of 3D structures

Although real MT data are often measured over more or less dominant 3D structures, the standard analysis and modelling approach is still to work in 2D. When using such a questionable approach, one should be aware of the problems and limitations. Therefore a few studies dealing with the use of 2D approaches in the presence of 3D geology are briefly mentioned here.

For example de Lugão and Kriegshäuser (1997) calculated synthetic 2D and 3D data for two different 3D structures - first a resistive pipe (mineral deposit) and then a conductive struc-

ture (geothermal target). The comparison of these responses showed that for the resistive feature the TE responses of the 2D and 3D data agree better, whereas for the conductive case the TM responses match better. They also used the 3D responses for separate 2D inversion of the TE and TM modes. The result of the comparison of the responses was confirmed; for the resistive target the 2D inversion of the 3D TE mode yielded models closer to the original model, with better agreement between the synthetic input and the modelled MT data, but in the conductive case the TM model gave the better 2D model. Therefore de Lugão and Kriegshäuser (1997) concluded that in a case of a resistive, 3D target a 2D TE inversion is more suitable and TM should be chosen for a conductive target.

Other authors (e.g., Garcia et al. (1999), Ledo et al. (2002) and Ledo (2005)) also point out the problems and limitations of using 2D approaches, modelling and inversion for 3D data. Garcia et al. (1999) inverted the Kayabe dataset (a geothermal target in Hokkaido, Japan) and found that the resulting 2D model contains questionable conductivity structures that might be artefacts resulting from the 2D algorithm trying to match 3D effects.

Ledo et al. (2002) designed a synthetic model that contains the two major problems associated with 2D interpretation of 3D data: the presence of structures with different strike directions and the effects of a finite body length. In addition to these 3D effects, they applied galvanic distortion to their synthetic data as well. They found that it is important to always remove the small-scale galvanic distortion, no matter if the regional structure is 2D or 3D, before applying 2D modelling. Although the data were 3D, they were able to retrieve the first-order structure with 2D techniques. Ledo et al. (2002) conclude that the effects of finite strike are not significant if the profile crosses a 3D conductive structure that has a strike extent larger than about half a skin depth. In this case, both a TM-only and a combined TE and TM mode 2D inversion image the conductive structure reasonably well, although the TM-only inversion does not resolve the 2D structure below the conductor well. In the case where the conductor is laterally off the profile, it is possible that 'phantom' structures will be imaged, if the end of the structure is not more than a skin depth away (Jones, 1983b; Wannamaker et al., 1984).

One should always keep in mind that a 2D interpretation of 3D data is only an approximation, of which the validity is not always obvious. In complex geological regimes, 3D modelling and interpretation of MT data cannot be avoided.

3

SOUTHERN AFRICA

This chapter provides an overview and background information about the area of interest - southern Africa. The magnetotelluric experiment (SAMTEX) is briefly described as well as previous geophysical work, together with an overview of the geology. This knowledge will be of interest for the chapters dealing with the interpretation of the SAMTEX data (see Chapter 4 and Chapter 5).

3.1 GEOLOGY OF SOUTHERN AFRICA

The geological structures and tectonic processes which formed southern Africa are discussed briefly, but the geological features of interest for this thesis will be discussed in more detail: namely the Limpopo belt, the Zimbabwe Craton, the Magondi belt, the Ghanzi-Chobe belt, the Okavango giant mafic dyke swarm and the Makgadikgadi Pans. Figure 3.1 shows a chart of the geological time scales including the regional, southern African nomenclature for certain eras.

Continental fragments formed before 2.5 Ga ago are known as Archaean cratons. These cratons can be found world wide (Kusky and Polat (1999) categorised 35 cratons on all continents, e.g., in Canada, USA, Scandinavia, Australia and southern Africa) and two of them - the Kaapvaal craton (formed and stabilised between 3.7 and 2.7 Ga (de Wit et al., 1992)) and the Zimbabwe craton (3.5 Ga to 2.6 Ga (Kusky, 1998; Horstwood et al., 1999)) - form the core of the southern African continent and are known together as the Kalahari craton. The crust of these earliest continental fragments in southern Africa is predominantly a variable mixture of plutonic rocks with calcalkaline-like chemistry and supracrustal rocks, such as sediments and volcanic rocks, which are often overprinted by greenschist facies metamorphism. These granites and greenstones make up the granite-greenstone terrains of the southern African Archaean cratons (de Wit et al., 1992). Figure 3.2 shows a rough outline of the Kaapvaal and the Zimbabwe cratons including their surrounding mobile belts and the granite-greenstone belts of the Kaapvaal craton (digital terrane boundaries courtesy of Susan J. Webb, University of the Witwatersrand, Johannesburg, South Africa, and based on known geology in South Africa and Zimbabwe, and primarily on interpretation of potential field data in Namibia and Botswana, where thick Kalahari sands cover basement; Webb, 2009).

Since the Kaapvaal craton is known for its enormous concentration of accessible minerals, this region has probably been more extensively investigated than any other Archaean craton. The at least one billion year accretionary period of the Kaapvaal craton is subdivided by de Wit et al. (1992) into two periods. The first period is the initial separation of the continental lithosphere of the craton from the mantle, which took place through plate-tectonic-like

	Eon	Era	Period	Epoch	Age (Ma)	Regional
	Phanerozoic	Cenozoic	Neogene (23.0 - 0)	Holocene	0.0117 - 0	
				Pleistocene	1.81 - 0.0117	
				Pliocene	5.33 - 1.81	
				Miocene	23.0 - 5.33	
			Palaeogene (65.5 - 23.0)	Oligoncene	33.9 - 23.0	
				Eocene	55.8 - 33.9	
				Palaeocene	65.5 - 55.8	
		Mesozoic	Cretaceous (146 - 65.5)	Upper	99.6 - 65.5	Karoo
				Lower	146 - 99.6	
			Jurassic (200 - 146)	Upper	161 - 146	
				Middle	176 - 161	
				Lower	200 - 176	
			Triassic (251 - 200)	Upper	229 - 200	
				Middle	246 - 229	
				Lower	251 - 246	
		Paleozoic	Permian (299 - 251)	Lopingian	260 - 251	
				Guadalupian	271 - 260	
				Cisuralian	299 - 271	
			Carboniferous (359 -299)	Pennsylvanian	318 - 299	
				Mississippian	359 - 318	
			Devonian (416 - 359)	Upper	385 -359	
				Middle	398 - 385	
				Lower	416 -398	
			Silurian (444 - 416)	Pridoli	419 - 416	
				Ludlow	423 - 419	
				Wenlock	429 - 423	
				Llandovery	444 - 429	
			Ordovician (488 - 444)	Upper	461 - 444	Namibian
				Middle	472 - 461	
				Lower	488 - 472	
			Cambrian (542 - 488)	Furongian	499 - 488	
				Series 3	510 - 499	
				Series 2	521 - 510	
				Terreneuvian	542 -521	
Precambrian	Proterozoic	Neo-	Ediacaran		635 - 542	
			Cryogenian		850 - 635	
			Tonian		1000 - 850	
		Meso-	Stebian		1200 - 1000	Mokolian
			Ectasian		1400 - 1200	
			Calymmian		1600 - 1400	
		Palaeo-	Stratherian		1800 - 1600	
			Ososirian		2050 - 1800	
			Rhyacian		2300 - 2050	Vaalian
			Siderian		2500 - 2300	
	Archaean	Neoarchaean			2800 - 2500	Randian
		Mesoarchaean			3200 - 2800	Swazian
		Paleoarchaean			3600 - 3200	
		Eoarchaean			4000 - 3600	
	Hadian (informal)				> 4000	

Figure 3.1: Geological time scale and regional southern African stratigraphy based on the international commission on stratigraphy (ICS)'s international stratigraphic chart and time scale generator (www.stratigraphy.org).

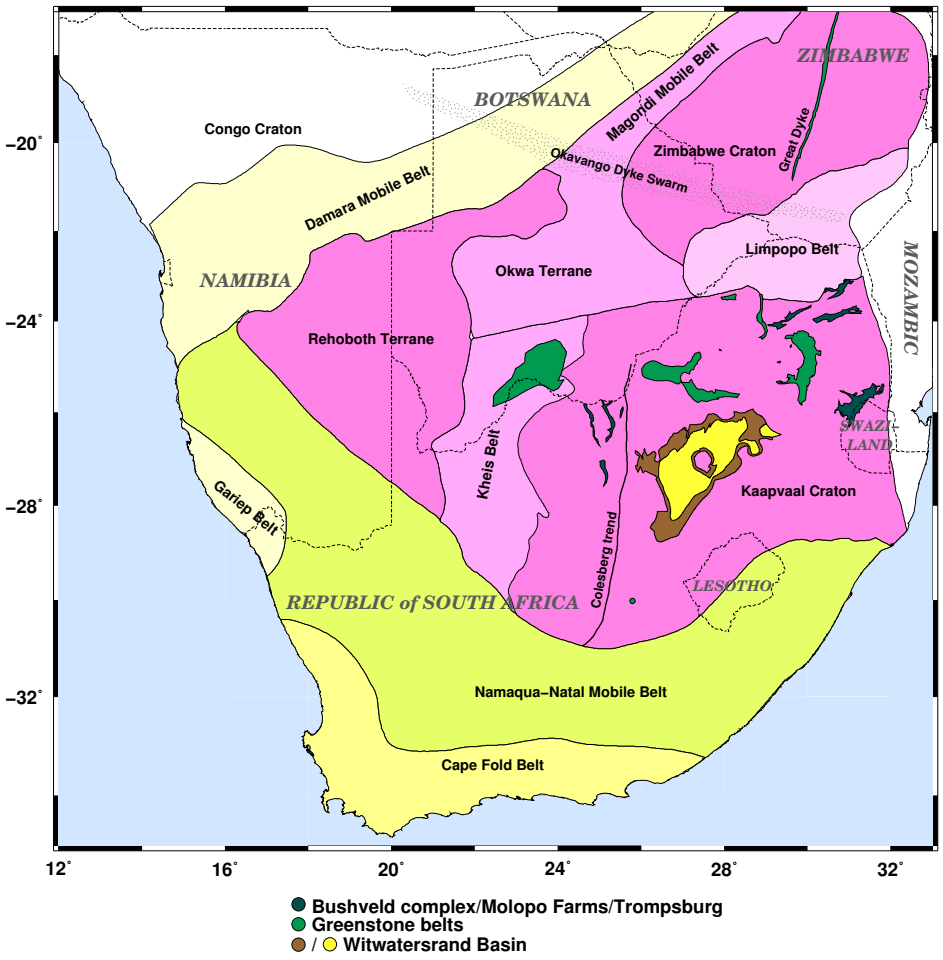

Figure 3.2: Rough outline of the geological provinces and main structures of southern Africa (digital terrane boundaries courtesy of Susan J. Webb, University of the Witwatersrand, Johannesburg, South Africa, and based on known geology in South Africa and Zimbabwe, and primarily on interpretation of potential field data in Namibia and Botswana, where thick Kalahari sands cover basement; Webb, 2009). The Ghanzi-Chobe belt and the Damara orogenic belt are not differentiated and are only outlined as one belt (Damara mobile belt).

processes that are interpreted to be comparable to those forming modern-day ocean basins, but in the mid-Archaean most likely occurred in shallower water depths (de Wit et al., 1992). The second period was dominated by intra-continental and continental-margin processes, where continental growth occurred mainly through a combination of tectonic accretion of crustal fragments and subduction-related igneous processes (similar to that found today along the margin of the Pacific). Evidence for the intra-continental and continental-margin processes is the continental-shelf terrane of the central Limpopo belt that is located between the granite-greenstone terranes of the Kaapvaal and the Zimbabwe cratons (de Wit et al., 1992). Note that the accretionary scenario involving plate-tectonic-like processes is disputed, e.g., Hamilton (1998) and Bleeker (2003) are in favour of sagduction and mantle plumes being the dominant processes during the Archaean.

The Kaapvaal and the Zimbabwe cratons collided at about 2.7 - 2.6 Ga, and the collision formed the Limpopo belt in between (van Reenen et al., 1987). These three Archaean regions are often referred to together as the Kalahari craton (or Proto-Kalahari craton as proposed by Jacobs et al. (2008), who define the Kalahari craton as the Archaean Proto-Kalahari craton plus the Palaeoproterozoic Magondi belt, Rehoboth and Okwa terranes), which is bounded to the northwest by the Palaeoproterozoic Kheis belt, Okwa terrane and the Magondi belt. To the northwest of these belts are the Ghanzi-Chobe belt (northeast Botswana) and the Damara belt (Namibia and northwest Botswana). The latter belt stabilised after the Damara orogen, that records the Gondwanan assembly of the Congo-Kalahari-Rio de la Plata cratons. First, at about 750 - 600 Ma, the Congo craton and the Rio de la Plata craton (today in South America) collided and accreted, and later (about 550 Ma) suturing of the Congo and the Kalahari cratons completed the Gondwanan assembly of southern Africa (Prave, 1996).

The Laurentia-Kalahari collision that began at about 1.15 Ga will not be discussed here because it involved mainly the Namaqua-Natal belt and the southern margin of the Kaapvaal craton (in South Africa) which are not related to the area of interest in this thesis.

Figure 3.3 shows a more detailed map of the subsurface Precambrian geology of Botswana, including the location of some drill sites where rock samples were taken for age determination. The MT data discussed later are from the northeastern part of Botswana, crossing the Limpopo belt and the Zimbabwe craton in Botswana, as well as the Magondi and Ghanzi-Chobe belts. Other features that are important in the area of interest are the Okavango dyke swarm (about 179 Ma, but also a few Proterozoic dykes; see Jourdan et al., 2004) which cuts across the craton and the belts in a 110° E of N angle, and the area of today's Makgadikgadi salt pans in east Botswana that are correlated with a near-surface brine aquifer.

More detailed descriptions of the geological structures and the tectonic framework in southern Africa can be found in many publications, e.g., van Reenen et al. (1987), Roering et al. (1992), van Reenen et al. (1992), de Wit et al. (1992), Singletary et al. (2003) and McCourt et al. (2004).

3.1.1 *The Limpopo Belt*

The Limpopo belt is a zone of Archaean high-grade metamorphic and igneous rocks situated between the Kaapvaal and the Zimbabwe cratons, where a major tectonic-metamorphic event occurred at about 2.7 Ga (van Reenen et al., 1987). The Limpopo belt is subdivided into several zones, each of which has a distinctive geological signature and that can be considered as individual terranes in a tectonic sense (van Reenen et al., 1992). Figure 3.4 shows the subdivision of the belt into the Northern Marginal Zone, the Central Zone and the Southern Marginal Zone. Major shear zones separate these zones from each other and from the surrounding cratons.

The Northern Marginal Zone, a high-grade granite-greenstone terrane, is separated from the low-grade granite-greenstone terrane of the Zimbabwe craton by a southwards-dipping shear zone (van Reenen et al., 1992; Roering et al., 1992; de Wit et al., 1992). On the southern boundary a southerly-dipping shear zone (Tuli-Sabi/Triangle shear zone) divides the Northern Marginal Zone from the shelf-type supracrustal sequence of the Central Zone.

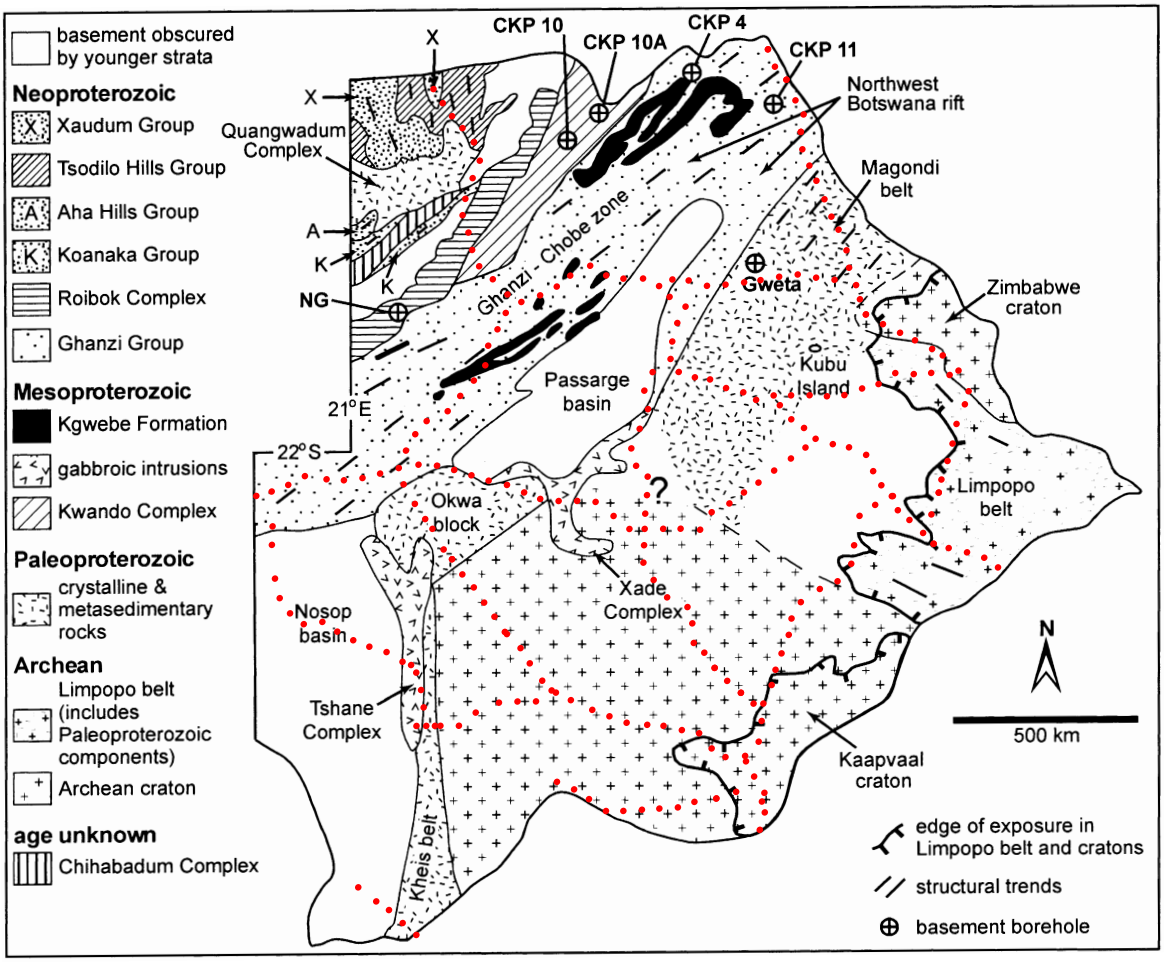

Figure 3.3: Subsurface Precambrian geology of Botswana. Taken from Singletary et al. (2003) (based on Carney et al., 1994; Key and Mothibi, 1999; Key and Ayres, 2000). The red dots indicate the MT site locations in Botswana.

The Palala shear zone separates the Central Zone from the shield-type granite-greenstone terrane of the Southern Marginal Zone (van Reenen et al., 1992; de Wit et al., 1992). The northwards-dipping, ductile Hout River shear zone is the terrane boundary between the Southern Marginal Zone and the granite-greenstone terrane of the Kaapvaal craton (van Reenen et al., 1992). The Northern Marginal Zone appears to have been thrust northwards onto the Zimbabwe craton (Stuart and Zengeni, 1987), while the Southern Marginal Zone was thrust southwards onto the Kaapvaal craton (van Reenen et al., 1987).

Barton and van Reenen (1992) found that geochronology data sets (Rb-Sr, Pb-Pb and U-Pb isotopic ages) from the Limpopo belt suggest that high-grade metamorphism and tectonism in the Northern Marginal Zone and the Zimbabwe craton (2.6 - 2.55 Ga) occurred about 100 million years more recently than in the Central and Southern Marginal Zones and the adjacent Kaapvaal craton (2.7 - 2.65 Ga). The term LIMPOPO OROGENY refers to the older high-grade metamorphic and tectonic events affecting the Archaean rocks of the Central and South Marginal Zones and its influence on the Kaapvaal craton (Barton and van Reenen, 1992).

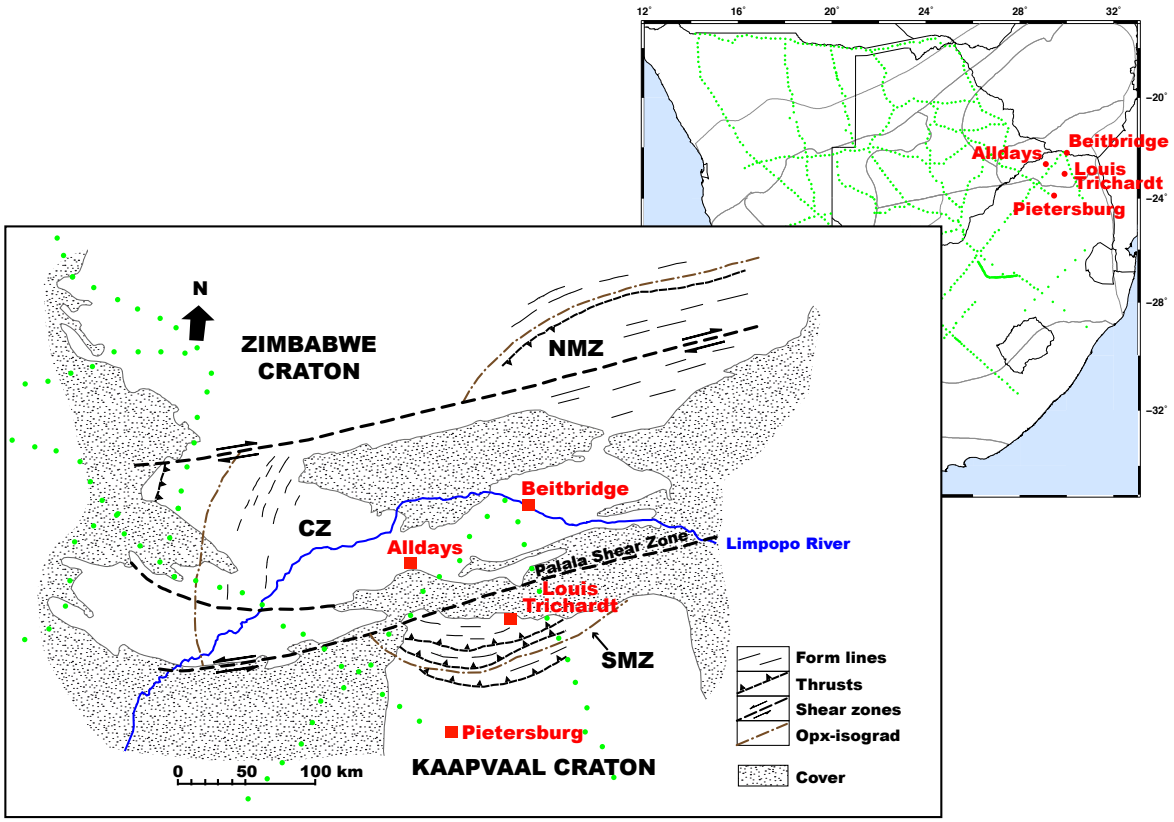

Figure 3.4: The Limpopo belt is subdivided into the Northern Marginal Zone (NMZ), the Central Zone (CZ) and the Southern Marginal Zone (SMZ). These zones are separated from each other and from the adjacent cratons by major shear zones. Redrawn and modified from van Reenen et al. (1987). The green dots indicate the MT sites in that area.

The evolution of the Limpopo belt is described by van Reenen et al. (1987) as follows. The granite-greenstone terrane and the Southern Marginal Zone remained relatively stable in a low heat-flow regime from 3.5 Ga until about 2.7 Ga. Then the tectonic setting of the Archaean crust changed abruptly, crustal thickening occurred as direct result of a continent collision in a similar manner to that of the Himalaya. A crustal thickness of at least 65 km in the high-grade area at about 2.7 Ga was estimated by van Reenen et al. (1987). Isotherms and isograds in the area of crustal thickening were initially disrupted, but readjusted with time. High-grade metamorphism was distributed over larger areas in the Limpopo belt and the thickened crust responded by uplift, as evident from the presence of shear zones and thrusting and associated decompression textures. The granulitic terrane exposed today was driven upward from deeper crustal levels and spread out radially over the nonthickened crust adjacent to the suture (van Reenen et al., 1987). At 2.675 $\pm$ 0.05 Ga, an east-west transcurrent shearing, that displaced the Central Zone ~ 100 km westwards relative to the Marginal Zones (Roering et al., 1992) and a southward thrusting documents the final collision of the Zimbabwe craton with the Kaapvaal craton causing backthrusting along the southern edge of the Limpopo belt (de Wit et al., 1992).

3.1.2 *The Zimbabwe Craton*

The Zimbabwe craton is mainly located in Zimbabwe, but, as Figures 3.3 and 3.5 show, the southwestern part of the craton extends into Botswana. The full extent of the Zimbabwe craton in Botswana is unknown, as the western boundary is obscured beneath Phanerozoic cover rocks and the southern boundary is ill defined (McCourt et al., 2004).

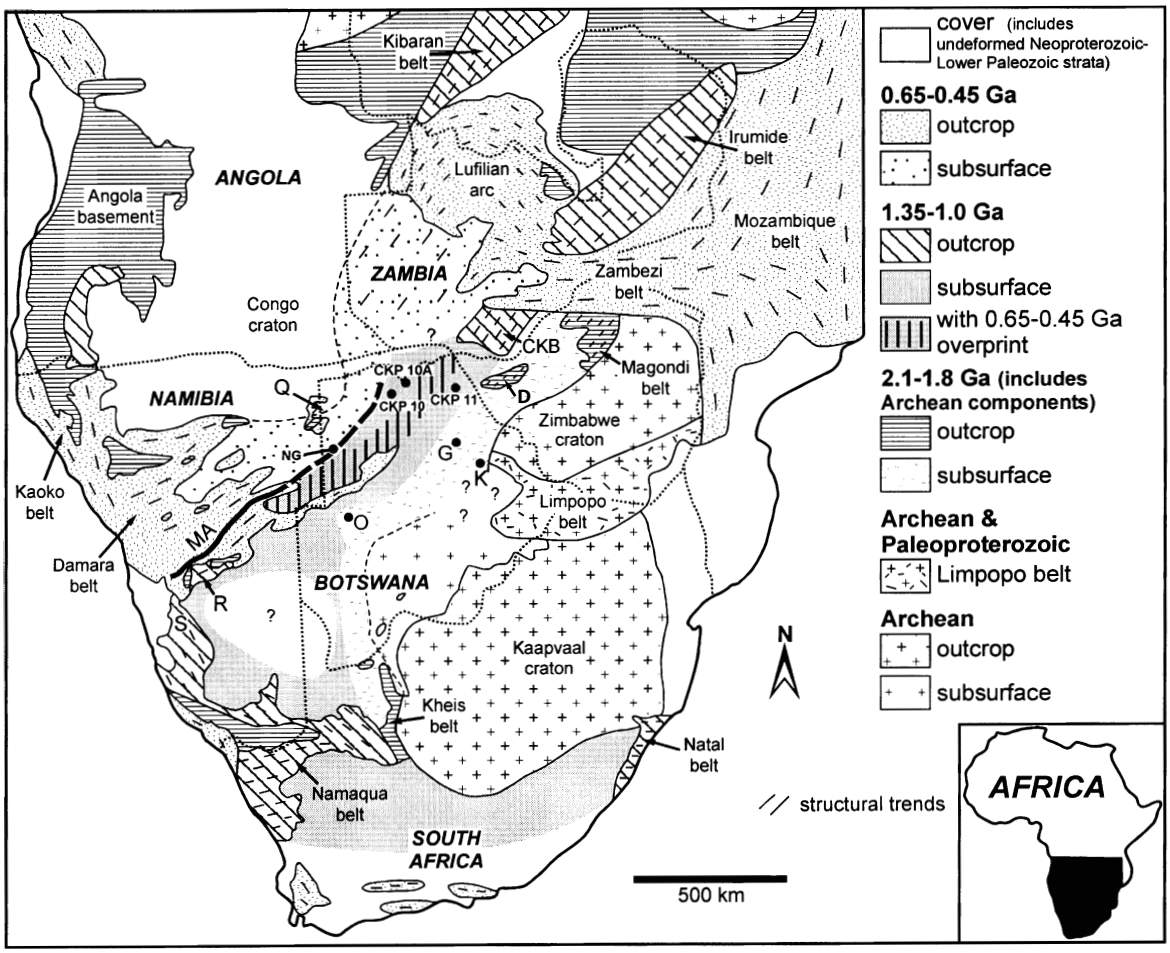

Figure 3.5: Precambrian tectonic framework of southern Africa, showing inferred subsurface extents of Proterozoic belts. Approximate extent of Neoproterozoic - Early Paleozoic overprinting in the buried Mesoproterozoic (1.35 - 1.0 Ga) orogen in Botswana is based on deformation recorded in the Northwest Botswana rift. Locations of the boreholes Gweta (G), NG and CKP 10, 10A and 11 are also shown. CKB - Choma-Kalomo block, D - Dete Inlier, K - Kubu Island, MA - Matchless Amphibolite and its inferred subsurface extent (dashed) in northwestern Botswana, O - Okwa Inlier, Q - Quangwadum Valley, R - Rehoboth Inlier in Damara belt, S - Sinclair Sequence. Taken from Singletary et al. (2003).

The Zimbabwe (formerly Rhodesian) craton is composed of a number of distinct terranes (Figure 3.6). The oldest rocks in the Zimbabwe craton include tonalitic to granodioritic,

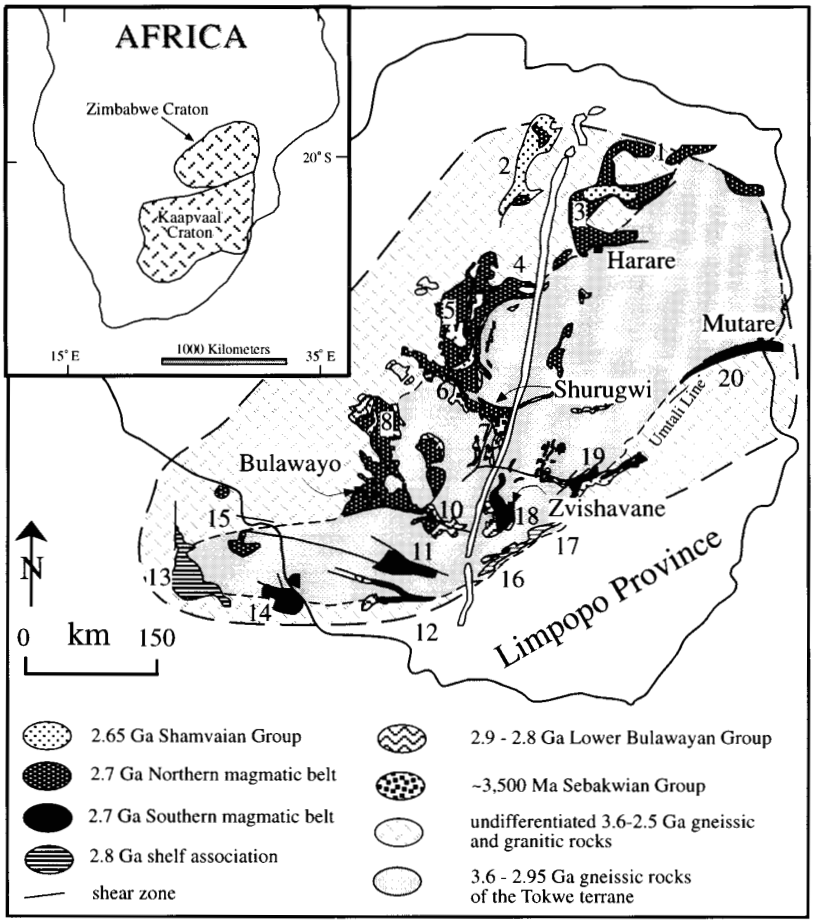

Figure 3.6: Map of the Zimbabwe craton showing the distribution of the old gneissic Tokwe terrane, northern and southern magmatic belts and shelf type associations. Numbers correspond with individual greenstone belts: 1 - Mount Darwin, 2 - Chipuriro, 3 - Harare, 4 - Chegutu, 5 - Midlands, 6 - Gweru-Mvuma, 7 - Shurugwi, 8 - Bubi, 9 - Bulawayo, 10 - Filabusi, 11 - Gwanda, 12 - Antelope-Lower Gwanda, 13 - Matsitama, 14 - Tati, 15 - Vumba, 16 - Mweza, 17 - Buhwa, 18 - Belingwe, 19 - Masvingo, 20 - Mutare. Taken from Kusky (1998).

locally migmatitic, gneissic rocks with U-Pb and Pb-Pb ages between 3.5 Ga and 2.95 Ga (Kusky, 1998; Horstwood et al., 1999). The ancient core of the Zimbabwe craton, which was established as a coherent block by 2.95 Ga and consists of greenstone belts and older gneissic rocks, is called the Tokwe terrane. At many places the Tokwe terrane is unconformably overlain by a heterogeneous mix of volcanic and sedimentary rocks regionally known as Lower Greenstones or Lower Bulawayan Group (Wilson, 1979; Kusky, 1998). The Belingwe belt consists of mafic, ultramafic, intermediate and felsic volcanic rocks (the later two have U-Pb ages of 2.8 - 2.9 Ga), pyroclastic deposits and a wide variety of sedimentary rocks (Bickle and Nisbet, 1993; Wilson et al., 1995; Kusky, 1998). The Lower Bulawayan Group rocks (2.79 - 2.81 Ga) are also well developed in the Midlands, Filabusi, Antelope-Lower Gwanda, Shangani, Bubi and Gweru-Mvuma greenstone belts (Kusky, 1998). On the southern boundary of the Zimbabwe craton the Buhwa and Mweza greenstone belts contain up to 4 km thick sequences of shelf-facies shallow-water sedimentary rocks, which include quartz-rich sandstone, shale and iron formation in the western shelf succession, whereas the eastern deeper-water basinal facies consist of strongly deformed shale, mafic-ultramafic lava,

chert, iron formation and possible metacarbonate rocks (Fedo and Eriksson, 1996; Kusky, 1998). Similar shelf facies rocks extend along the southeastern margin of the Tokwe terrane into Botswana. Aldiss (1991) found a 10 - 20 km thick structurally imbricated succession of interlayered quartzite, iron formation, marble, metacarbonate and quartzfeldspathic gneiss in the Matsitama belt (Number 13 in Figure 3.6).

Kusky (1998) describes the accretion of the Zimbabwe craton as follows. From 3.6 - 2.95 Ga a series of tectonomagmatic events formed the Tokwe terrane, a result of complex deformation of the 3.5 Ga Sebakwian greenstone belts and intervening gneissic rocks. Several smaller terranes, perhaps arcs or microcontinents, were joined and acting as a coherent unit by 2.95 Ga. Younger volcanic and sedimentary rocks were deposited on the Tokwe terrane at 2.9 Ga and show large lateral variations in stratigraphic thickness and volcanic and sedimentary rock types, which suggest that the Tokwe terrane formed a widespread graben at 2.9 Ga in which the Lower Greenstones were deposited. At the same time several kilometres of shallow water sandstone, shale and carbonate were deposited in the passive margin sequences along the southeastern margin of Tokwe terrane. Rifting occurred along the line from the Mutare belt through the Buhwa-Mweza greenstone belts to the Matsitama belt in Botswana forming an ocean basin called the SEA OF UMTALI. This ocean closed at 2.7 Ga forming the southern greenstone belts which exhibit stratigraphic, structural and geochemical characteristics consistent with thick oceanic crust. The last Archaean tectonic event affecting the Zimbabwe craton is related to the collision of the Zimbabwe craton at 2.58 Ga with and during the assembly of the Limpopo belt and the Kaapvaal craton (Kusky, 1998).

The tectonic model outlined by Kusky (1998) describes the stabilization of the craton and the formation of the continental lithospheric mantle roots. Dirks and Jelsma (1998) state that the rapid, efficient cooling, and thus the stabilization of the craton, is a result of the establishment of an equilibrium geotherm in the continental crust that originated from stacking hot and relatively thick crustal fragments up to an isostatically stable thickness of ~ 35 km, and the formation of large volumes of crustally derived granitic melts. The tectonic mechanism of outward growth and accretion provides a framework for the successive underplating of depleted slabs of oceanic lithosphere. These underplated slabs of depleted oceanic lithosphere would be cold and compositionally buoyant compared to the formation of the cratonic lithospheric mantle roots (Kusky, 1998).

3.1.3 *The Magondi Belt*

In Botswana the 2.0 - 1.8 Ga old Magondi orogenic belt lies completely beneath Phanerozoic cover. Due to the Karoo (300 - 100 Ma) and younger deposits in the Kalahari, the western margin of the Zimbabwe craton, as well as the interpretation of the nature and boundaries of the Proterozoic terranes west of the craton, are obscure (Majaule et al., 2001). In western Zimbabwe, the Zimbabwe craton is bordered to the northwest by the Palaeoproterozoic Magondi belt (Majaule et al., 2001; Leyshon and Tennick, 1988; Treloar, 1988), as one can see on Figure 3.5. A second outcrop of the Magondi mobile belt (the Dete Inlier, D in Figure 3.5) dating 2.1 - 1.8 Ga can be found further southeast close to political border of Botswana and Zimbabwe, on the Zimbabwean side. Treloar (1988) describes the Magondi belt in Zimbabwe as a product of early Proterozoic basinal sedimentation followed by deformation

and associated metamorphism on the northwestern margin of the Zimbabwe craton. The deformation and metamorphism is of early to mid-Proterozoic age, and the rocks are essentially unaffected by the subsequent Pan-African deformation and metamorphism (Treloar, 1988; Treloar and Kramers, 1989).

The north-trending, Palaeoproterozoic Kheis Belt adjoins the Kaapvaal craton to its west. These two Palaeoproterozoic terranes, i.e., the Magondi and Kheis belts, exposed on either side of the Archaean Kalahari craton (i.e., consisting of the Limpopo belt and the Zimbabwe and Kaapvaal cratons), might be part of a single, major Palaeoproterozoic orogenic belt present along the western margin of the Archaean Kalahari craton (e.g. Aldiss and Carney, 1992; Carney et al., 1994; Majaule et al., 2001). The northwestern and southern extent of the Kheis-Magondi belt is delimited by Mesoproterozoic terranes: the Choma-Kalomo block (Hanson et al., 1988, location: CKB in Figure 3.5) in southern Zambia and the Namaqua belt in South Africa and Namibia (e.g., Thomas et al., 1994). The Okwa Inlier (O in Figure 3.5) appears to expose a part of the central segment of the Kheis-Magondi belt and therefore helps to constrain the overall form and extent of this partly buried orogen (Aldiss and Carney, 1992; Carney et al., 1994; Majaule et al., 2001). On the other hand McCourt et al. (2001) state that the minimum age of the Magondi orogen, from new U-Pb (SHRIMP - Sensitive High Resolution Ion MircoProbe) data, is 70 million years older than the maximum age of deformation and metamorphism in the Kheis Belt. Therefore McCourt et al. (2001) suggest that models linking the two fold and thrust belts as coeval components of the same Palaeoproterozoic orogen are no longer valid.

Majaule et al. (2001) state that the inferred pre-Karoo geology under the ubiquitous cover in northeast Botswana primarily relies on air photography, satellite imagery and regional aeromagnetic and gravity surveys, which all indicate a northeast-trending structure. Prominent brittle fractures trending northeast occur within the cover rocks, as well as northeast-trending structures in the underlying basement. These structures are considered to reflect the subsurface continuation of the Magondi belt from Zambia/Zimbabwe into Botswana (Majaule et al., 2001).

On the southwestern edge of Sua Pan, the easternmost of the Makgadikgadi Pans (near Gweta, Figures 3.3 and 3.5, more details below), isolated basement exposures form islands. The main exposures are at Kubu (K in Figure 3.5) and Khumkago (20 km south of Kubu) Islands. Majaule et al. (2001) dated the exposed granites at Kubu Island mainly at about 2.0 Ga, but one zircon grain was dated at 2.68 Ga. They interpreted their results as an indication that Kubu Island lies within the region affected by Palaeoproterozoic orogenesis in the Magondi belt, and that Archaean crustal components were involved in the petrogenesis. Similar granites were found at Khumkago island, therefore Majaule et al. (2001) suggest that the Zimbabwe craton margin and/or the Archaean elements of the western Limpopo belt extend this far west in the subsurface and were overprinted in the region by the Magondi orogenesis. The SADC (Southern Africa Development Community) published a map in 1997 of regional areomagnetic data that clearly shows that the Magondi anomalies bend to the south (see Figure 3.10), defining an arcuate trend that joins with the Limpopo belt. Together with the similarity in timing of the Palaeoproterozoic orogensis in the Kheis-Magondi belt and parts of the Limpopo belt, the spatial trend of the Kheis-Magondi and Limpopo belts suggests that a buried triple junction exists between the Kheis-Magondi and Limpopo belts. The location and geometry of the triple junction depend, in part, on the age and the extent

of the Limpopo belt, both of which remain unclear, but Kubu island is likely to be located near the buried triple junction. (Majaule et al., 2001)

3.1.4 *The Ghanzi-Chobe Belt*

Knowledge of the Ghanzi-Chobe belt is very limited, due to the lack of exposure caused by a cover of Cenozoic superficial deposits, called the Kalahari group, which overlie more than 90% of the Ghanzi-Chobe belt (Modie, 1996). The Ghanzi-Chobe belt is Meso- to Neoproterozoic in age and is a northeast-trending, approximately 500 km long by 100 km wide, elongated volcano-sedimentary basin in northern Botswana (its extent deduced from regional areomagnetic and gravimetric surveys (Reeves, 1985)). To the northwest it is bounded by the complex Damara orogenic belt, that is widely developed in Namibia, and to the southeast by the Magondi belt. Unfortunately, most of the work done on the Ghanzi-Chobe belt is documented in unpublished reports and theses (e.g., US Steel, Anglo American Botswana, Geological Survey Botswana), but Modie (1996) summarises them as follows. There are great similarities between the sequences in the Ghanzi-Chobe belt and its correlatives in Namibia, which implies that these volcano-sedimentary basins developed along the entire length of the northwest margin of the Kalahari craton, thus forming a basement to the rocks of the Damara orogen. The Ghanzi-Chobe belt has undergone a two-phase mode of sedimentary basin development represented by the Kgwebe Formation (see Figure 3.3; start of the accumulation of the sequence dated at 1106 ± 2 Ma) and the Ghanzi Group (see Figure 3.3). The Kgwebe Formation - the first phase - was initiated by extensional tectonics and rifting with subsequent bimodal volcanism and clastic sedimentation in small lake environments. The second phase - the Ghanzi Group - indicates a major basin development stage with renewed extension resulting in an expansion of the depositional zone. A marine basin evolved with a shallow shelf environment dominated by storm and fair-weather conditions. A mix of clastic-carbonate lagoons and possible progradational deltas is indicated within the intermediate sequence. The final development of the sedimentary succession was marked by increased sediment supply and the deposition of a progradational shoreline facies, implying a major period of uplift in the source area, presumably related to the initial stage of the Damaran deformation. Finally, Modie (1996) suggests that the Ghanzi-Chobe belt represents a failed intra-continental rift basin that developed as part of an extensive, but segmented, linear rift system extending from south central Namibia.

Samples taken from research drill cores at CKP 4 and CKP 11 (see Figure 3.3 for locations) were dated at about 1.1 Ga and are therefore considered to belong to the Ghanzi-Chobe belt (Kampunzu et al., 2000; Singletary et al., 2003).

3.1.5 *The Okavango giant mafic dyke swarm*

The Okavango giant dyke swarm is part of the large scale Karoo tectonomagmatic framework in southern Africa (Figure 3.7). The focus of the description here is on the Okavango dyke swarm, but nevertheless some of the other magmatic features, of which the locations can be found in Figure 3.7, will be described in course of the explanation as well.

Continental flood basalts consist of vast quantities of lava, sills and giant dyke swarms that are associated with continental break-up. The commonly radiating geometry of dyke

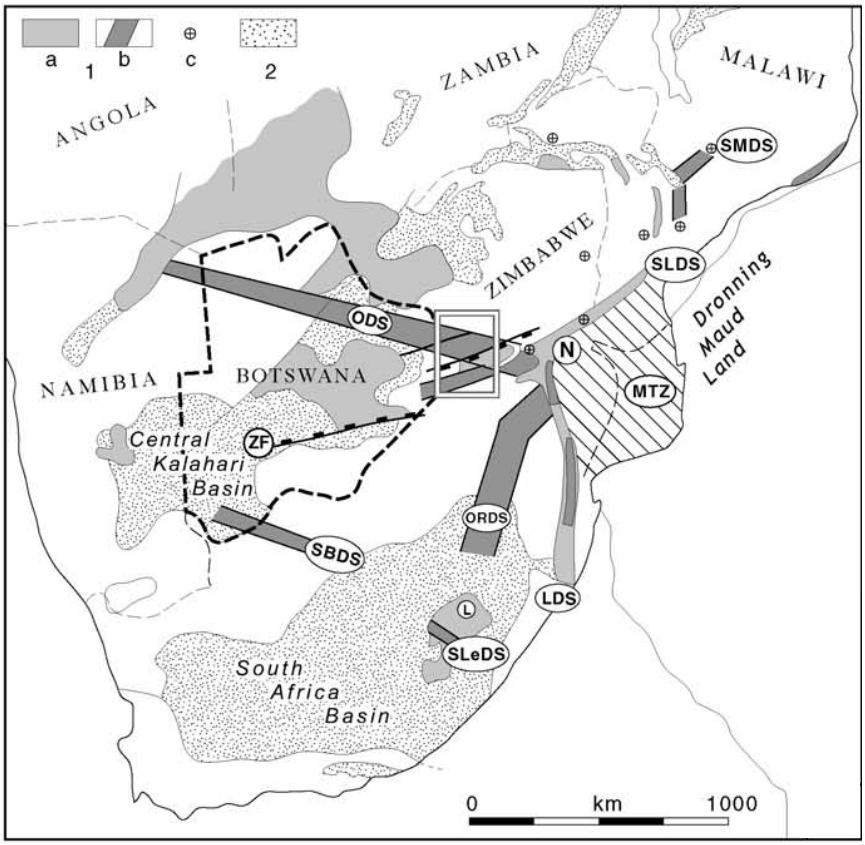

Figure 3.7: Karoo tectonomagmatic framework of southern Africa, showing (1) magmatic complexes with (1a) flood basalt, (1b) dykes and sills, and (1c) eruptive centres and (2) Karoo sedimentary basins in southern Africa. L, Lesotho; N, Nuanetsi; LDS, ODS, ORDS, SBDS, SLDS, SLeDS, SMDS, Lebombo, Okavango, Olifants River, South Botswana, Sabi-Limpopo, South Lesotho, South Malawi, dyke swarms, respectively. Taken from Le Gall et al. (2005).

swarms in these provinces is interpreted to be the result of the stress regime that affected the lithosphere during the initial stage of continental break-up or as the result of plume impact at the base of the lithosphere (Jourdan et al., 2006). Structures in the basement may also control dyke orientation (Jourdan et al., 2006). The Okavango dyke swarm, together with the Save-Limpopo and the Olifants River dyke swarms, form the so-called NUANETSI TRIPLE JUNCTION that is not a structure of Jurassic origin alone, but reflects weakened lithospheric pathways (pre-existing ancient basement structures) that have controlled the dyke orientation over hundreds of millions of years. (Jourdan et al., 2006)

The 110°-trending (Jourdan et al. (2006): 109°±12° E of N) giant Okavango dyke swarm (also called the northern Botswana dyke swarm) extends over a 1500 km strike length through Archaean basement terranes and Permo-Jurassic sedimentary sequences. The dykes are mainly coarse-grained dolerites (Elburg and Goldberg, 2000; Aubourg et al., 2008), which are hosted by granites, gneiss and amphibolites in the Francistown area (Aubourg et al., 2008). $^{40}Ar/^{39}Ar$ age determinations by Elburg and Goldberg (2000) and Le Gall et al. (2002) show that the dykes are about 178.4 ± 1.1 Ma to 179.3 ± 1.2 Ma in age, but they also identify one dyke in the swarm as Proterozoic in age. Jourdan et al. (2004) broadened the

range of emplacement ages of the Karoo dykes to between 178.4 ± 1.1 Ma to 180.9 ± 1.3 Ma, with a probability peak at 179 Ma. They also identified eight Proterozoic dykes and three Proterozoic sills with ages of $850 - 1700$ Ma. Jourdan et al. (2004) suggest, based on the relationships between the age and geochemical composition, that the Okavango dyke swarm includes at least 10% of Proterozoic dykes located in the central part of the Jurassic swarm. Therefore they conclude that the Nuanesti triple junction is an inherited Proterozoic structure that was reactivated during Jurassic times.

Le Gall et al. (2005) studied the dyke swarm and the geometry and distribution of individual dykes within the swarm in more detail. They mapped the dyke swarm in detail along the river bed of the Shashe River near Francistown, which cuts at a high angle through the densest zone of the Okavango dyke swarm and also considered maps from aerial photographs. Although the latter maps do not distinguish between the two chronologically unrelated dyke populations (Proterozoic and Karoo in age), Le Gall et al. (2005) assume that the statistical analysis is not biased, because of the estimated high percentage of about 87% Karoo dykes in the Okavango swarm. They found that about 70% of the dykes are within 10° of parallelism with the 110° E of N trend of the swarm envelop. The Karoo dyke length ranges from 1 to 18 km, and about 91% of the dykes are vertical, the other 9% are within 30°of vertical. Le Gall et al. (2005) constrained the width of the dykes by accurate, but incomplete, field measurements and by ground magnetic records, which supply a complete spatial data set but no certainties on the age of the mapped dykes. They estimate the accuracy of the field measurements to be with in 0.5 m, and note that the sampling interval of the ground magnetic signal is 5 - 10 m and therefore that dykes narrower than 5 m are likely to not be detected, which also might cause an error of several metres in estimating dyke width. The resulting range of dyke widths is from 0.2 to 69 m based on the field measurements, and 11 to 69 m from the magnetic data. The arithmetic mean dyke width is about 17 m based on the magnetic measurements and about 16 m from the field measurements. The low frequency of narrow dykes (< 0.5 m) compared to the thickest dykes (16 - 70 m) is a real geological feature, which still remains to be explained in terms of either mechanical conditions of emplacement, pre-dyke fracture work or nature of magma (Le Gall et al., 2005).

Le Gall et al. (2005) also investigated the gradual westerly narrowing of the high density zone of the Okavango dyke swarm from 60 km in the Francistown area to 53 km and 45 km in the Maun (about 400 km northwest) and Ngami (about 200 km further northwest) areas respectively. Table 3.1 summarises the total width of the swarm, the number of aeromagnetic anomalies, the dyke spacing, the cumulative dyke width and the crustal dilatation for these three areas. It is suggested that the dyke-driven extension decreases abruptly westwards from 12.2% in the Francistown area to 2.6% in the Maun and Ngamiland areas, based on the assumption that the parameters measured at the Shashe river bed, e.g., the ratio of Proterozoic/Karoo dykes ($\sim 1/6$) and the average Karoo dyke thickness (17 m), remain constant along-strike. Le Gall et al. (2005) suggest that such a change in lateral distribution of dykes, coupled with the lack of map-scaled deflection of the swarm trend around magma chambers at depth, can be explained by the Karoo mafic dykes propagating laterally westwards, away from the Nuanetsi source region, instead of being injected vertically from deep-seated linear magmatic ridges. The model of lateral flow of Karoo magma is also supported by the anisotropy of magnetic susceptibility data that show a transition from predominantly vertical (near the Nuametsi source region) to horizontal magma flow with increasing distance from the Nuanetsi focal point (Tshoso, 2003; Le Gall et al., 2005; Aubourg et al., 2008).

Table 3.1: Along-strike variations of the width and dyke-induced extension in the high dyke density zone of the ~1500 km long Okavango dyke swarm. Measurement sections are at Francistown, about 400 km northwest at Maun and another 200 km further northwest at Ngamiland. Numbers for Francistown are for the Shashe transect with the extrapolated values for the entire swarm in brackets. Taken from Le Gall et al. (2005).

	NGAMILAND	MAUN	FRANCISTOWN
Total width of the swarm (km)	45	53	52 (60)
Number of anomalies in (high resolution) aeromagnetic data (Tshoso, 2003)	31	37	162 (195)
Dyke spacing (km)	1.5	1.5	0.3 (0.3)
Cumulative dyke width (m)	1160	1384	6315 (7295)
Crustal dilatation (%)	2.6	2.6	12.2 (12.2)

Similar anisotropy of magnetic susceptibility (AMS) was found at the Mackenzie dyke swarm of the Canadian Shield (Ernst and Baragar, 1992). Unlike the Okavango dyke swarm, the Mackenzie swarm is fan-shaped and a plume model is used to explain the observed magnetic susceptibility and other petrological data for the latter (Ernst and Baragar, 1992; Baragar et al., 1996).

3.1.6 *The Makgadikgadi Pans Complex*

The Makgadikgadi Pans Complex is a large and unusual surface feature (> 8 400 km^2) in northeastern Botswana (Figure 3.8). It occupies a basin that is the lowest point in a drainage system extending from Botswana into Namibia, Angola and Zimbabwe. The pans are the remnants of a once-great Pleistocene lake that is estimated to have covered 34 000 km^2 at its maximum extent, with a water volume of 500 to 1 000 km^3 (Grove, 1969). Such a lake would have required a substantial inflow, but also an evaporation rate considerably less than today's. The major source of water for the lake was probably the Okavango River prior to its division into a series of swamps (i.e., Okavango delta). Other potential sources of inflow might have been the westward flowing rivers that currently feed the Sua Pan and the now-dry Okwa River that once flowed northwards from the central Kalahari. Since there is no identified outlet for Lake Makgadikgadi, it is assumed that a static state was reached where the inflow balanced the evaporation. Thus the lake became increasingly saline with time, providing a source for the extensive brine aquifer beneath that area and today's salt pans. Figure 3.8 shows the present day extent of the Makgadikgadi Pan Complex, as well as the Okavango Swamps and the major river systems in Botswana (Baillieul, 1979).

3.2 THE SAMTEX PROJECT

The Southern African MagnetoTelluric EXperiment (SAMTEX) was established in 2003 to understand the early Earth tectonic evolution of South Africa and to compare it with other Archaean regions of the world, for example, the Slave and Superior cratons in Canada. The project consortium is a multi-national, multi-institutional academic-government-industry collaboration.

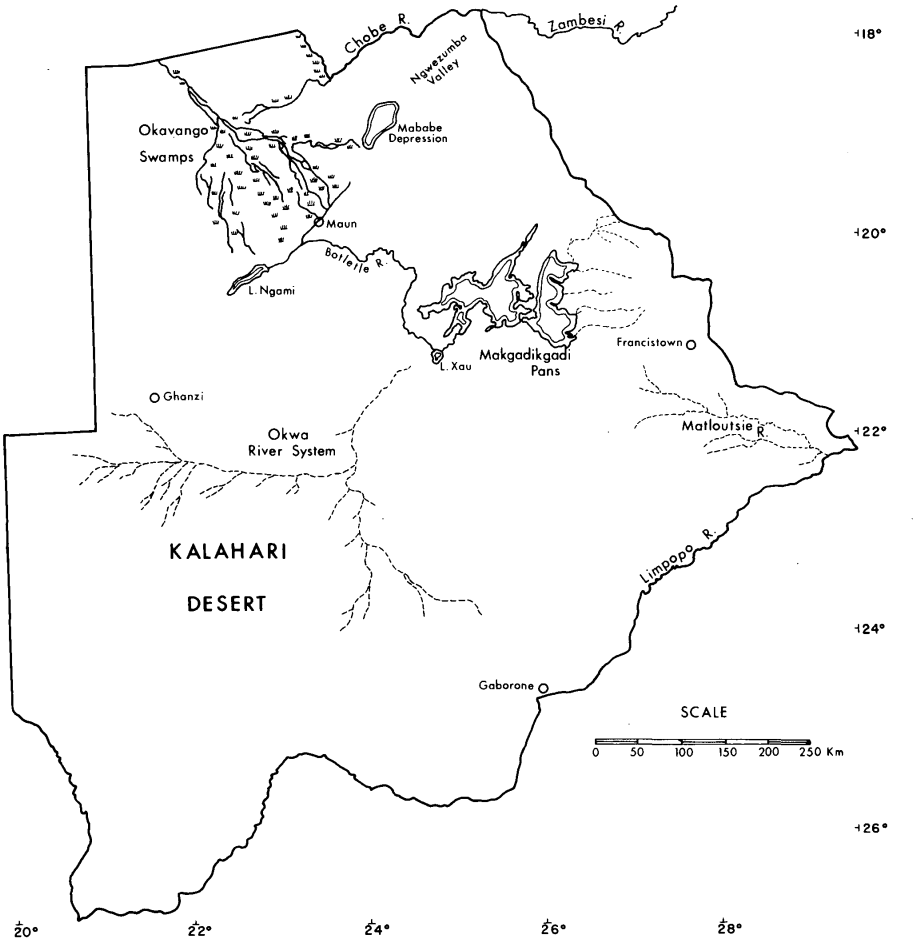

Figure 3.8: Map showing the location of the Makgadikgadi Pan Complex in relation to the Okavango Swamps and the major river systems in Botswana. Taken from Baillieul (1979).

The scientific interest in the tectonic processes taking place during the earliest stages of Earth evolution is founded in the question as to whether the modern plate tectonic paradigm is valid for the Archaean era or not. There is much debate as to how far back the plate tectonic paradigm can be extrapolated in the interpretation of the cryptic rock records. Some argue that it can validly be applied early in Earth's history (e.g., de Wit et al., 1992), whereas others think that processes such as sagduction and mantle plumes dominated during the Archaean (Hamilton, 1998; Bleeker, 2003). Allied to this question is the uncertainty about the formation process of the cratonic lithosphere (Archaean-age) and the limited fundamental information (e.g., geochemical, petrological and geophysical, as the methodologies are limited themselves but also not all Archaean craton areas have been studied in the same detail, using all available methodologies) about the sub-continental lithospheric mantle. Geophysical imaging can provide physical and geometrical information about the current state of fossil lithospheric structures to address this knowledge gap. Primarily only passive seismology has been used over Archaean cratonic areas. However the work done on the Slave craton (Jones et al., 2001; Jones and Ferguson, 2001; Jones et al., 2003; Davis et al., 2003) has demonstrated that MT measurements can provide significant additional constrains on lithospheric formation processes.

As part of the Kaapvaal project, the South African Seismic Experiment (SASE) recorded broadband seismic data at 82 sites. These sites were located in a NNE-SSW area about 1800 km long by 600 km wide. This array covers the Cape Fold Belt, the Namaqua-Natal mobile belt and the centre of the Kaapvaal craton in South Africa, across the Limpopo Belt and onto the Zimbabwe craton in Zimbabwe and Botswana (see Figure 3.9 for site locations, grey stars). The original SAMTEX proposal was to collect MT data along four profiles that were coincident with the SASE coverage to allow for comparison and possibly joint interpretation (or even joint inversion) of the two data sets. In reality, MT data were collected in South Africa in 2003/2004 (SAMTEX phase I) along the 'main profile' (KAP03 in Figure 3.9) that extends along the long axis of the SASE array and on additional crossing profiles. In 2004/2005 more MT data acquisition was undertaken and the area of coverage was expanded outwards into Namibia and Botswana. After two additional field seasons in 2005/2006 (phase III) and 2008 (phase IV), the coverage of Botswana and northern Namibia is now very good, but is a little bit more sparse in southern Namibia and South Africa. There was no data acquisition in Zimbabwe due to political/safety issues. There is now a total of 679 occupied sites on 31 profiles (& 2 mini-arrays) (see Figure 3.9 for site locations). Broadband MT (BBMT) data were recorded at 662 of these sites and long-periodic data at 109 sites. The sites are roughly at 20 km intervals and cover about 14 000 profile-km. There are also 22 audio-magnetotelluric (AMT) sites in northern Namibia, which were recorded in two mini-arrays. Hence, SAMTEX is probably the world's largest-ever land-based MT project.

To date, three papers have been published and one PhD thesis written on the SAMTEX project. Jones et al. (2009) provides an overview of the SAMTEX project, from the original idea to what SAMTEX finally became, including a comparison of the spatial distribution of resistivity and velocity anomalies across southern Africa. A correlation between high velocity regions and resistive areas can be found, whereas low velocity regions are related to more conductive areas. Hamilton et al. (2006) studied the electrical anisotropy of the South African lithosphere in comparison with the published (Silver et al., 2001) seismic anisotropy determined from shear-wave splitting analysis (using the SASE data set). The work is more extensively discussed in Hamilton (2008). A relationship between seismic and electrical anisotropy was only found for asthenospheric depths. They suggest that the source regions of the anisotropy are different and therefore they proposed a model which explains both the shear wave splitting and the MT results. Their model has an anisotropic, heterogeneous lithosphere in the cratonic region and more coherent structure and anisotropy in the lithosphere of the mobile belts. The asthenosphere is anisotropic, with a very strong anisotropic region below the thicker cratonic keel, which explains the correlation between the shear wave splitting direction in the seismic data and the plate motion direction.

Muller et al. (2009) found significant lateral heterogeneity in the electrical resistivity structure of the lithosphere along a 2D profile from the western Kaapvaal Craton across the Rehoboth Terrane and the Ghanzi-Chobe/Damara-Belts (KIM03 and KIM04 in Figure 3.9). The latter two terranes are areas where the lithosphere has not been imaged previously. They determine the most resistive (i.e., coldest) lithospheric thickness of the Eastern Kimberley Block of the Kaapvaal Craton to be 220 ± 20 km. The lower resistivity portions of the profile across the Western Kimberley Block, the Rehoboth Terrane and the Ghanzi-Chobe/Damara Belts correspond with, on average, ~ 30 km, ~ 40 km and ~ 60 km thinner

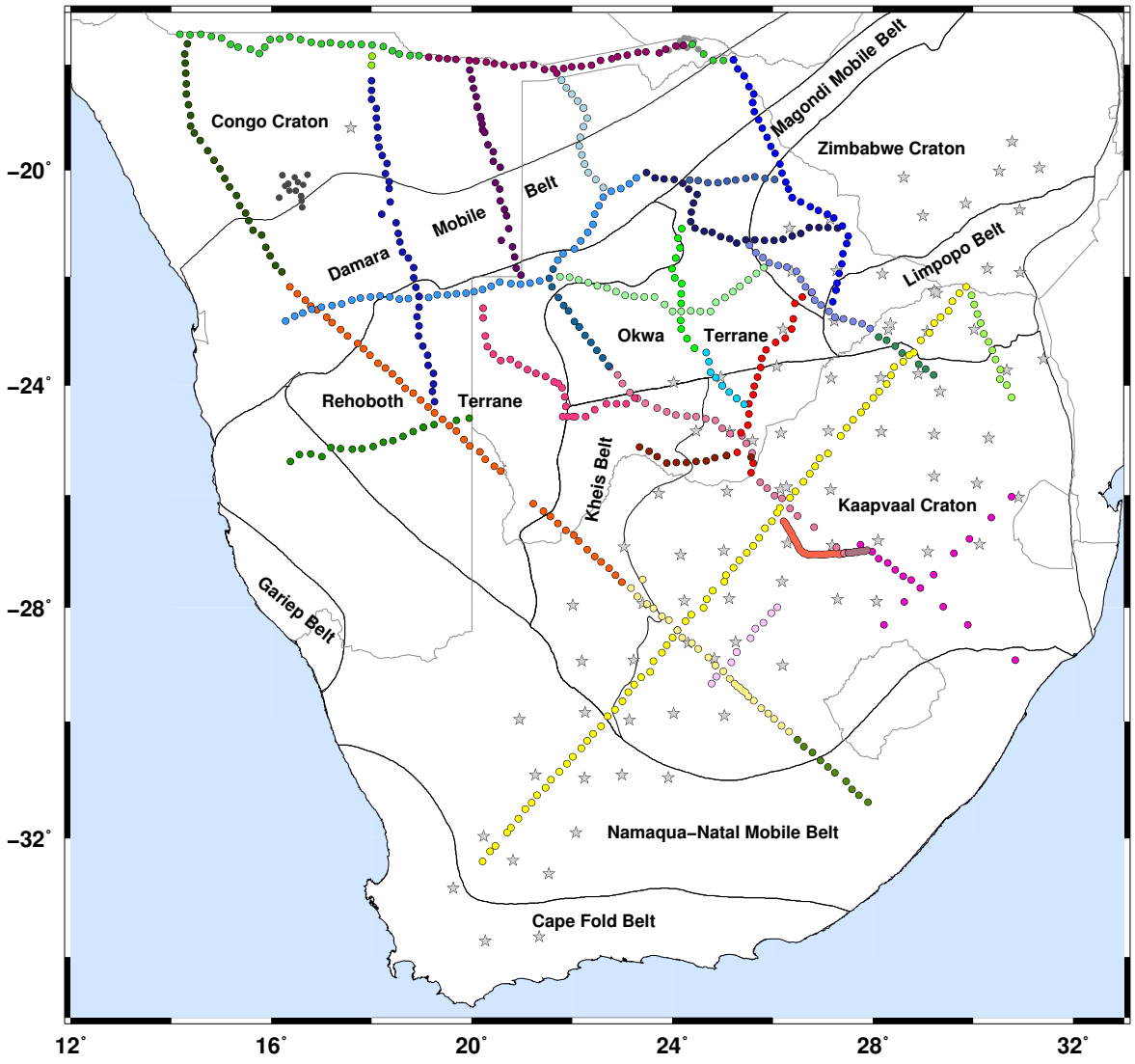

Figure 3.9: Overview of all SAMTEX site locations (coloured dots - colour coding for different profiles) in comparison to the SASE seismic stations (grey stars). (Digital terrane boundaries courtesy of Susan J. Webb, University of the Witwatersrand, Johannesburg, South Africa, and based on known geology in South Africa and Zimbabwe, and primarily on interpretation of potential field data in Namibia and Botswana, where thick Kalahari sands cover basement; Webb, 2009)

lithosphere, respectively. Muller et al. (2009) argue that a limited lithospheric depth extent into the diamond stability field is able to explain the absence of diamondiferous kimberlites in the Rehoboth Terrane and the Western Kimberley Block.

3.3 PREVIOUS GEOPHYSICAL WORK IN SOUTHERN AFRICA

Several deep structural studies in the Karoo basin using Schlumberger soundings, were carried out in the period 1966 to 1980 (van Zijl, 2006). For most of these soundings with a maximum current electrode separation of 40 km, the very conductive carbon and pyrite-rich Whitehill Formation acted as an electrical basement. In 1967, a deep Schlumberger electrical sounding, with centre point being close to the town of Pofadder and a maximum current electrode separation of 270 km, was used to investigate the Namaqualand Granite-Gneiss Complex, a structure of about 500 km by 150 km in extent (van Zijl, 1969). A second ultra-deep Schlumberger sounding was undertaken in 1969 with a maximum current electrode spacing of 600 km, located mainly on the Kaapvaal craton with the centre located near the village of Dealesville (van Zijl et al., 1970). The main results of the comparison of these two deep soundings are, first, both support a dehydrated lower crust and second, the transverse resistance (product of resistivity and layer thickness) of the lowermost crust is about 100% larger at Pofadder compared to Deaesville, probably due to a second period of metamorphism in the Namaqualand Granite-Gneiss Complex (van Zijl, 1969; van Zijl et al., 1970).

The 100% difference in conductivity of the lower crust of the Archaean Kaapvaal craton and the 1 Ga old Namaqualand Granite-Gneiss Complex aroused interest. In 1971 Gough (1973) investigated the contrast in electrical conductivity in the crust and upper mantle between the Kaapvaal craton and the Namaqualand Metamorphic mobile belt using an array of 24 three-component magnetometers to record the variation of the horizontal and vertical magnetic fields. He discovered an east-west elongated conductive body beneath the Cape-Karoo basin, which was thought to be located in the lower crust or upper mantle. In 1977 de Beer and Gough (1980) deployed a second array with 53 magnetometers as a southern extension to the earlier survey (south of 30° S) with the aim of locating the edge of the conductive region. They identified three anomalies related to currents flowing in conductive structures: two continental edge structures off the south-east and west coasts and an intra-continental conductive strip in lower crustal or uppermost mantle depth, which runs east-west from coast to coast - the Southern Cape Conductive Belt. Surface heat flow measurements above the Conductive Belt and the Namaqua-Natal Belt exclude a thermal source for the high conductivity anomaly. Furthermore, the high electrical conductivity zone and a static magnetic anomaly - the Beattie anomaly - are spatially correlated, and both were explained by an accumulation of oceanic lithospheric rocks outside the cratonic margin (de Beer and Gough, 1980).

Figure 3.10 shows a regional magnetic anomaly map of southern Africa. The Beattie anomaly is the extensive red, long wavelength feature within the Namaqua-Natal belt (NN) and on the geolocial boundary between this belt and the Cape fold belt (CFB).

In 1971/1972 another magnetometer array study discovered a zone of concentrated induced electric currents at crustal depths crossing Namibia, Botswana and Zimbabwe (de Beer et al., 1975, 1976). The results of electrical sounding studies by van Zijl and de Beer (1983) confirmed the existence of a prominent conductive structure. Figure 3.11 shows the maps

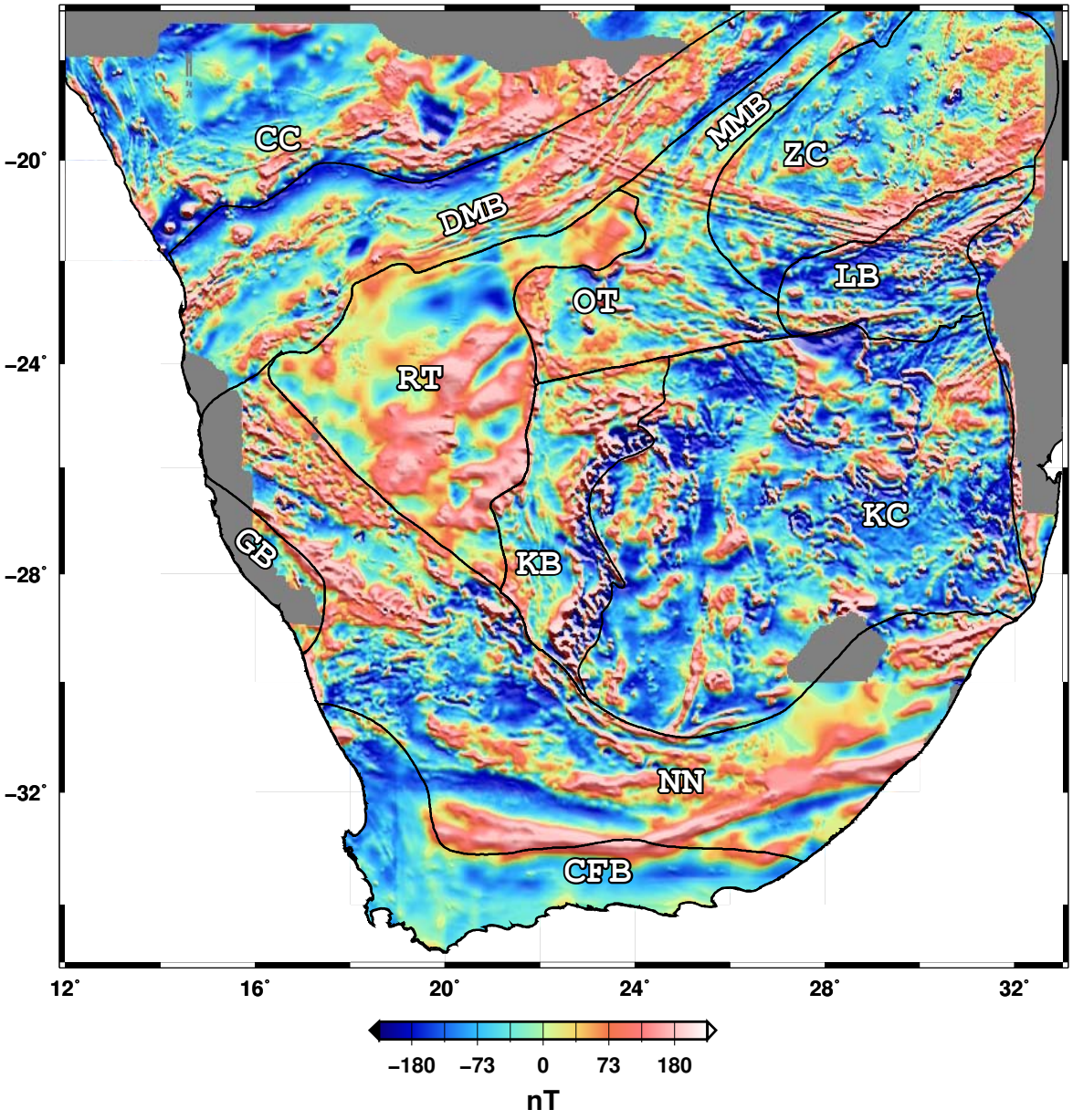

Figure 3.10: Regional magnetic anomaly map of southern Africa with the rough outline of the geological provinces shown (digital terrane boundaries courtesy of Susan J. Webb, University of the Witwatersrand, Johannesburg, South Africa, and based on known geology in South Africa and Zimbabwe, and primarily on interpretation of potential field data in Namibia and Botswana, where thick Kalahari sands cover basement; Webb, 2009): CC - Congo craton, DMB - Damara mobile belt (representing the Ghanzi-Chobe belt and the Damara orogenic belt as one), MMB: Magondi mobile belt, ZC: Zimbabwe craton, LB: Limpopo belt, OT: Okwa terrane, RT: Rehoboth terrane, GB: Gariep belt, NN: Namaqua-Natal belt, KB: Kheis belt, KC: Kaapvaal craton, CFB: Cape fold belt (see Figure 3.2). Magnetic data courtesy of the Council for Geoscience, Pretoria, South Africa.

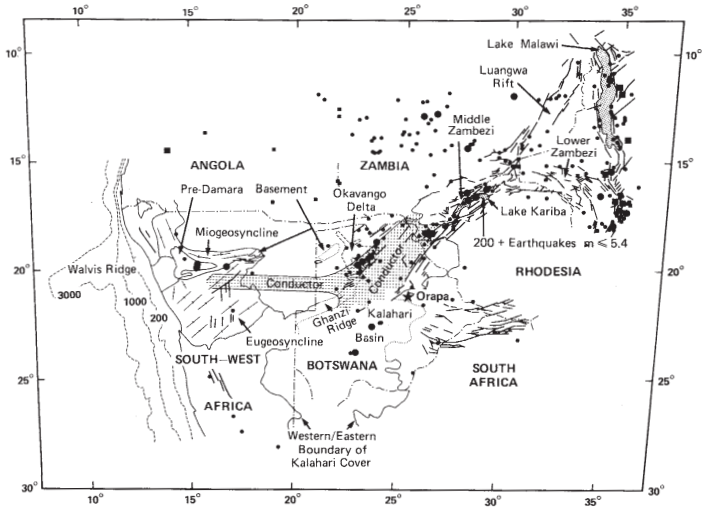

(a) The conductor in relation to seismicity and tectonics of southern central Africa (small dots, $2 \leqslant m \leqslant 4$; large dots $m > 4$, small squares, intensity $\leqslant 3$, large squares > 3). Faults are indicated by lines. Map taken from de Beer et al. (1975).

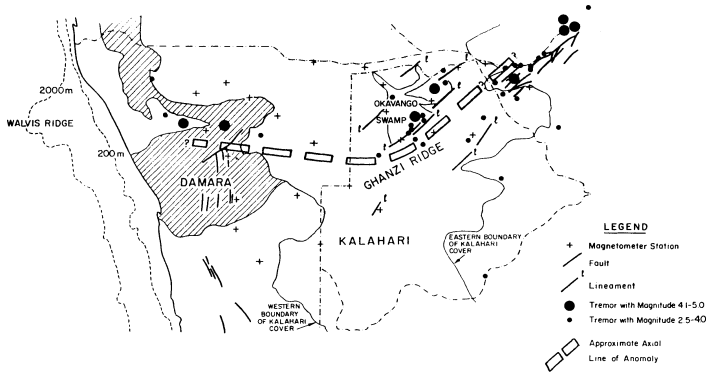

(b) The main tectonic features of the area are shown, as well as approximate axial line of the conductivity anomaly. Map taken from de Beer et al. (1976).

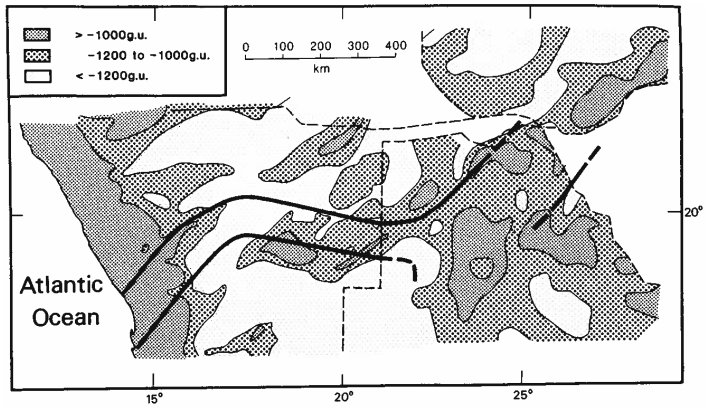

(c) Outline of conductive zone deduced from magnetovariational studies and Schlumberger soundings in relation to a simplified Bourguer anomaly map of southern Africa. Map taken from van Zijl and de Beer (1983).

Figure 3.11: These maps show the location of a crustal conductor found by magnetovariational studies and Schlumberger soundings.

from de Beer et al. (1975, 1976) and van Zijl and de Beer (1983), in which they indicated the location of the conductive zone.

An MT study over the Kheis-Namaqua front boundary was undertaken in combination with the recording of reflection seismic, gravity and magnetic data, in order to gain a better understanding of the crustal structure and history of the Namaqua metamorphic province in South Africa. The work was a very limited crustal study with only seven MT sites recorded in 1994 and 1995. Full results of the combined data sets can be found in Stettler et al. (1998) and Stettler et al. (1999), but the main findings are that the Kheis terrane possesses a resistive basement, which is overlied by the Namaqua Foreland and Front Zone that probably have been placed there by intrusion and thrusting, whereas the Kheis terrane itself was emplaced onto the Kaapvaal craton by continent collision.

In 1998 and 1999 MT data at 107 sites were collected across the Damara Belt in Namibia by staff of the GeoForschungsZentrum (GFZ) in Potsdam, Germany. The data set consists of an approximately 200 km long profile with a site spacing of 4 to 12 km and a local 3D array of 60 sites with a site spacing of 500 m to 2 km. The work was a crustal study of two parts: 1. the regional scale results show three distinctive zones in the Damara belt: very resistive upper crust, which is typical for the granites and metasediments in the Damara belt, two subvertical conductors in upper to mid-crustal levels, which correlate with major tectonic zone boundaries and a highly conductive middle to lower crust in the southern part of the profile (Ritter et al., 2003); 2. a focused study of the Waterberg Fault/Omaruru Lineament, which showed great complexity in the shear zone and as such is comparable with models from other fault zones (e.g., San Andreas Fault): a conductive ring structure in the shallow crust, crustal-scale electric anisotropy and an elongated conductor running subparallel to the Waterberg Fault/Omaruru Lineament (Weckmann et al., 2003). More details can be found in Weckmann (2002), Ritter et al. (2003) and Weckmann et al. (2003).

The most recent MT work done in South Africa outside the SAMTEX project forms part of the Inkaba yeAfrica project. This 5-year project started in 2004 and is a joint German and South African research initiative, which aims at surveying a cone-shaped sector of the Earth from core to space (Bohannon, 2004; de Wit and Horsfield, 2006). In 2004, high-resolution MT data were recorded at 82 sites on a profile across the Beattie magnetic anomaly onto the Cape fold belt with an average site spacing of 2 km, as part of the Inkaba yeAfrica theme MARGINS OF AFRICA. In 2005 the profile was extended southwards to the coast. Weckmann et al. (2007) present the results of the first part of this data set. The 2D conductivity model at the scale of the whole crust shows a highly conductive anomaly in the 5 - 10 km depth range, which correlates with the Beattie magnetic anomaly, although it remains unclear if both anomalies have the same source. Another highly conductive feature is a shallow, regionally continuous subhorizontal band, that correlates with the Whitehill Formation, a 50 - 70 m thick pyritic-carbonaceous marker horizon found in nearby deep boreholes (Branch et al., 2007; Weckmann et al., 2007).

Numerous papers present the results of the South African Seismic Experiment (SASE). For example, crustal studies using receiver function analysis show that the crust of the Kaapvaal and the Zimbabwe cratons is typically 35 - 40 km thick and is characterized by a strong velocity contrast across a relatively sharp Moho, i.e., a Moho transition zone of less than 2 km (Nguuri et al., 2001; James et al., 2003; Nair et al., 2006). Deep-seismic reflection

profiles across the central Kaapvaal craton confirm a Moho depth of 36 - 41 km (de Wit and Tinker, 2001). The post-Archaean terranes and underlying Archaean regions affected by large-scale Proterozoic events (Bushveld complex and Magondi belt) have relatively thick crust of 45 - 50 km and a complex Moho (Nguuri et al., 2001; Nair et al., 2006).

Lithospheric studies using the SASE data suggest that the lithosphere beneath the cratonic regions of southern Africa is about 150 - 200 km thick (e.g., Priestley et al. (2006): 175 ± 25 km, Li and Burke (2006): 180 - 200 km in the central and northern Kaapvaal craton, James et al. (2001): 250 - 300 km in the southern Kaapvaal and parts of the Zimbabwe cratons, Saltzer (2002): 150 - 200 km), in comparison with, e.g., the Namaqua-Natal mobile belt which has a lithospheric thickness of only about 80 km (Li and Burke, 2006).

Saltzer (2002) found that the surface wave velocities in the upper mantle beneath southern Africa are faster than the global average, and that the mantle anisotropy is slightly greater than the global average anisotropy, whereas the shear wave splitting results (Vinnik et al., 1995; Silver et al., 2001) suggest less anisotropy than determined from surface wave analysis. Saltzer (2002) explains these differences with a model in which the local anisotropy axis remains close to horizontal, but varies in azimuth as a function of depth. Fouch et al. (2004) and Silver et al. (2004) interpret the lateral changes of the mantle anisotropy as evidence of lithospheric mantle deformational events. They state that the seismic anisotropy beneath the Archaean continental regions was not created during the initial continental formation, but instead during subsequent significant mantle-deformation events that record the Precambrian history of compression of orogens and collisions.

As mentioned earlier, most of Botswana's geology is unknown due to the Quaternary Kalahari sand cover. The little that is known is based on isolated exposures, borehole information and interpolation between the exposed geology of eastern Botswana, Namibia, South Africa and Zimbabwe. From the 1950's onwards, geophysical exploration in Botswana was directed towards the discovery of groundwater, using mostly electrical resistivity techniques (Hutchins and Reeves, 1980). During the late 1960's other geophysical methods were introduced for mineral exploration, first by the government and later by exploration companies. The first geophysical studies of regional significance were a seismic and gravity survey in the central Kalahari and a subsequent airborne magnetic survey in southern Botswana. In 1970 the Botswana Geological Survey commenced a regional geophysical programme. Hutchins and Reeves (1980) provide an overview of this program which included a seismicity study, gravity, seismic and areomagnetic surveys.

Reeves (1972) studied the earthquake epicentres in Botswana (September 1955 to August 1971) and recognised two distinct spatial populations, one is clustered in the Okavango Delta in northwest Botswana and assigned to tectonic activity along a northeast trending fault, and the second is broadly scattered over the central Kalahari and was found to parallel closely the linear features of the Makgadikgadi Salt pans, the Okavango lineaments and the Ghanzi Ridge (Hutchins and Reeves, 1980). Microseismic activity of the Okavango Delta was monitored for three month in 1974 and found to be greatest along the southeastern margin of the delta (associated with fault structures), relatively low in the centre of the delta and non-existent in the region of the Okavango River to the northwest.

A gravity survey surround the Ngamiland district followed in 1970 - 1971, as well as a seismic refraction survey in 1972 - 1973 to support the postulated existence of faults around the delta, which are associated with the seismic activity, and to determine the depth to bedrock (between 140 m to 300 m within the delta) from the seismic lines (Hutchins and Reeves, 1980). In 1972 and 1973 the gravity survey was extended to nationwide coverage consisting of 1854 gravity stations - mainly observations at 10 km intervals along roads, tracks and exploration cut-lines, except for 300 stations that were established by helicopter in the otherwise inaccessible central and southwestern region of Botswana. In 1998 - 1999 another gravity survey was undertaken to fill existing gaps in the earlier survey in northern Botswana (Yawsangratt, 2002). Figure 3.12 shows a regional Bourguer gravity map of southern Africa.

In October 1975 an aeromagnetic survey with 150 000 profile-km was flown in Botswana. Two major features were discovered by this aeromagnetic survey: the magnetically prominent Okavango dyke swarm and the Zoetfontein fault, which Hutchins and Reeves (1980) consider delimits the Kaapvaal craton's northern edge (see also Figure 3.10, the Zoetfontein fault (the extension of the Palala Shear Zone, see Figure 3.4) is indicated by the red magnetic anomaly coincident with the straight boundary between the Kaapvaal craton and the Okwa terrane).

One can be certain that a lot more unpublished geophysical work has been done in southern Africa for mineral exploration. These data are filed away by the mining industry and might never be made available for scientific research. But all geophysical investigations in Botswana to date haven been limited to crustal depths and the SAMTEX results, therefore, add new information about deeper structures and the unknown lithospheric extents of the geological terranes.

Other useful information can be obtained from geochemical, petrological and geothermal data. Figure 3.13 shows the locations of kimberlites and whether they are diamondiferous (red), non-diamondiferous (green) or unspecified (yellow). Clifford (1966) was the first to propose a relationship between old cratonic areas, which remained stable through younger periods of tectonism, and the presence of diamonds. Clifford's (1966) rule was revised by Griffin et al. (2004), who studied the kimberlite distribution of the North American Plate. They found the thinner edges of cratons to be more prospective than the thicker centres. Therefore diamondiferous kimberlites can be used as an indication of the thinner lithospheric edges of cratons. Note that the anomalous diamondiferous kimberlite (Figure 3.13 at 20.008 E / -26.746 S) in the Rietfontein cluster, in the southern part of the Rehoboth terrane, is now known to be a BICYCLE DIAMOND, i.e., the diamond(s) did not originate from that kimberlite pipe.

Kimberlites and other rock samples are studied in laboratories to gain information of the age and the temperature-pressure conditions of the source region and to derive chemical tomography sections which contain information about the mantle composition versus depth. Chemical tomographic sections beneath Archaean cratons show typically depleted, variably metasomatized lithospheric mantle extending to depths of between 150 - 250 km (Begg et al., 2009). Beneath this depleted layer, a zone of intense, melt-related metasomatism follows, which is defined as the lithosphere-asthenosphere boundary (O'Reilly and Griffin, 2006, and references therein). It remains unclear if that interpretation is appropriate, since

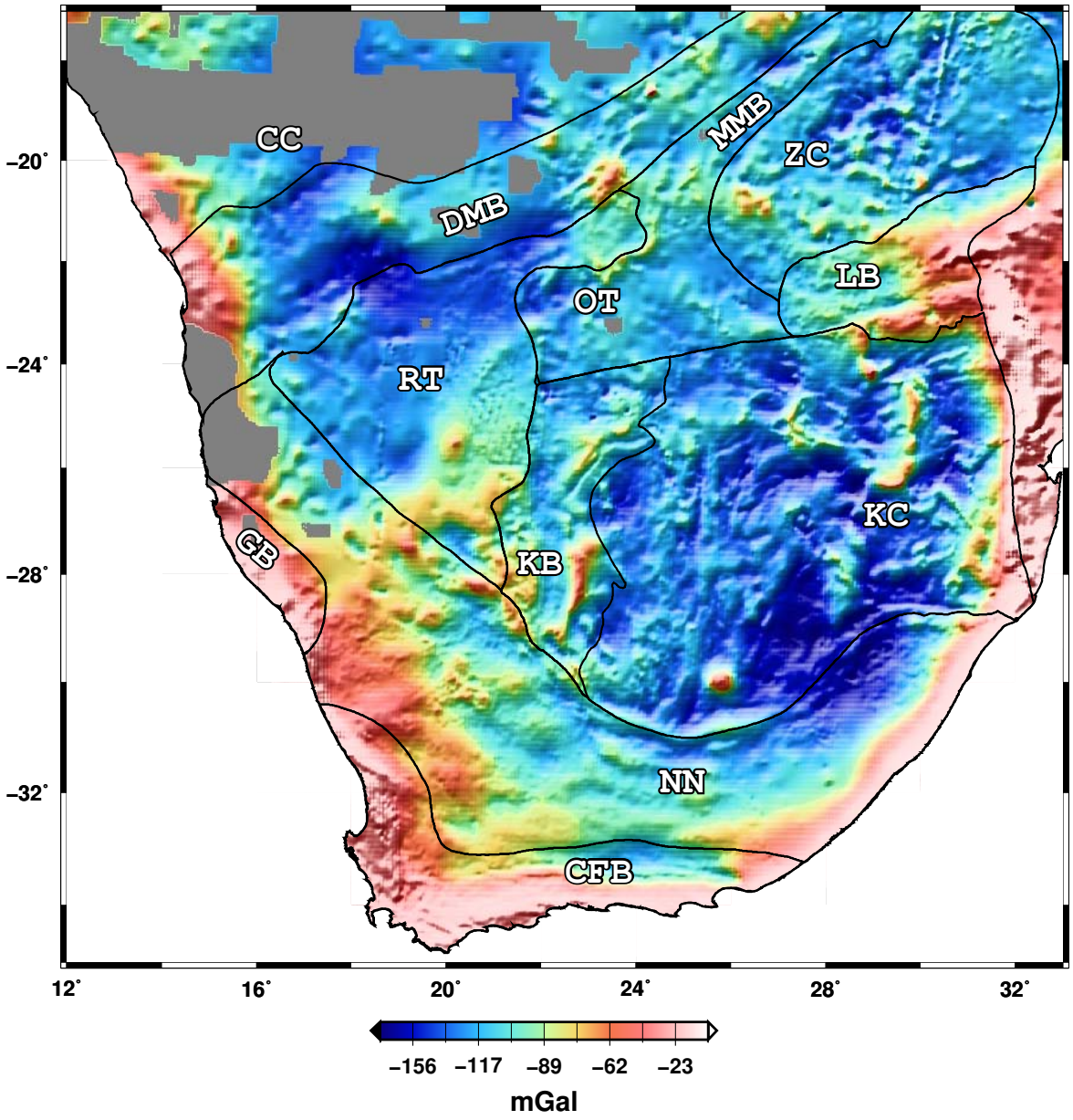

Figure 3.12: Bourguer gravity map of southern Africa, in mGal, with the rough outline of the geological provinces (digital terrane boundaries courtesy of Susan J. Webb, University of the Witwatersrand, Johannesburg, South Africa, and based on known geology in South Africa and Zimbabwe, and primarily on interpretation of potential field data in Namibia and Botswana, where thick Kalahari sands cover basement; Webb, 2009): CC - Congo craton, DMB - Damara mobile belt (presenting the Ghanzi-Chobe belt and the Damara orogenic belt as one), MMB: Magondi mobile belt, ZC: Zimbabwe craton, LB: Limpopo belt, OT: Okwa terrane, RT: Rehoboth terrane, GB: Gariep belt, NN: Namaqua-Natal belt, KB: Kheis belt, KC: Kaapvaal craton, CFB: Cape fold belt (see Figure 3.2). Gravity data courtesy of the Council for Geoscience, Pretoria, South Africa.

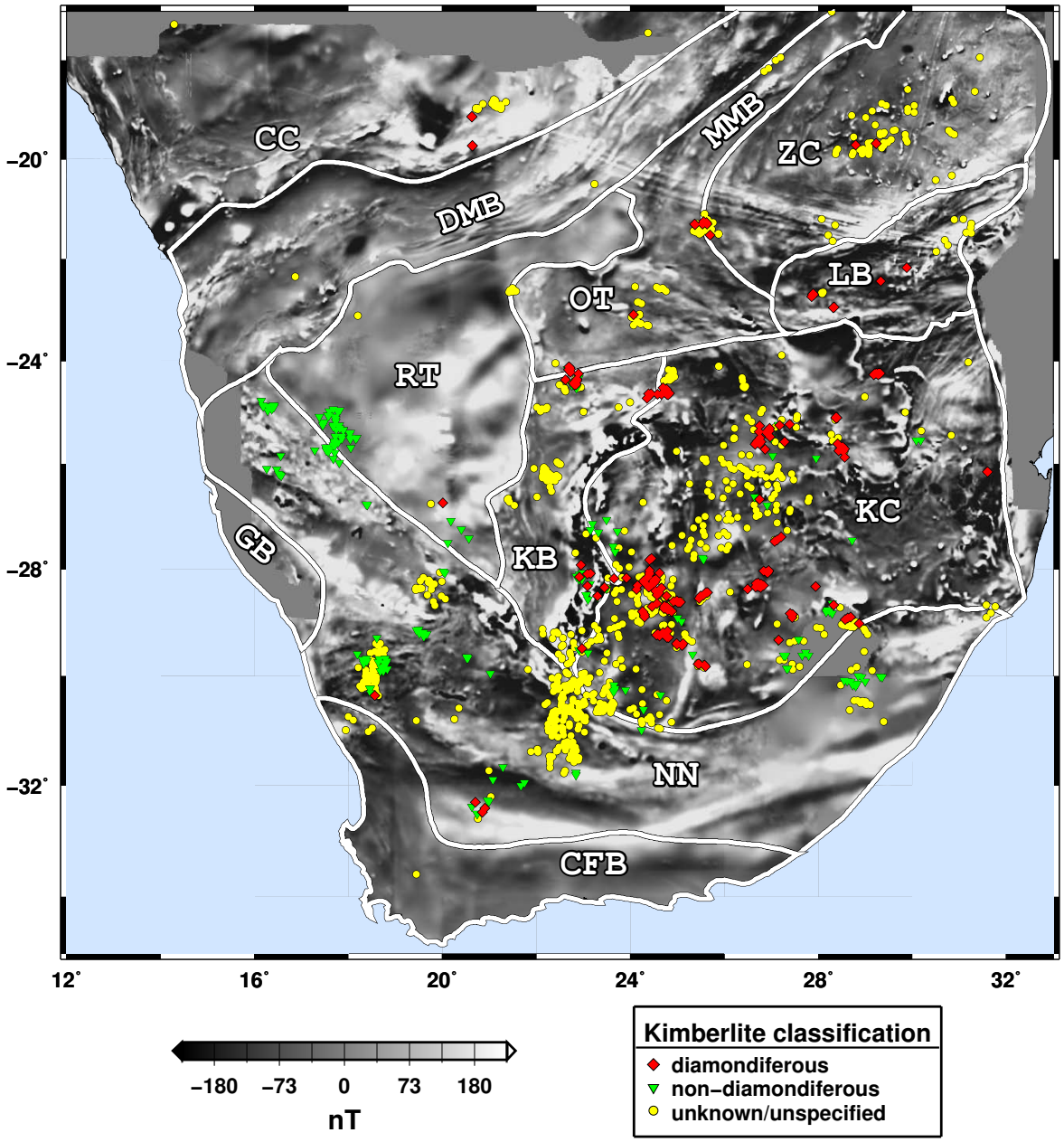

Figure 3.13: The regional magnetic map from Figure 3.10 in greyscale provides the background map for the Kimberlite database (South African Council for Geoscience unpublished numerical database, Jelsma et al. (2004), Faure (2006)). (Geological provinces (digital terrane boundaries courtesy of Susan J. Webb, University of the Witwatersrand, Johannesburg, South Africa, and based on known geology in South Africa and Zimbabwe, and primarily on interpretation of potential field data in Namibia and Botswana, where thick Kalahari sands cover basement; Webb, 2009): CC - Congo craton, DMB - Damara mobile belt (presenting the Ghanzi-Chobe belt and the Damara orogenic belt as one), MMB: Magondi mobile belt, ZC: Zimbabwe craton, LB: Limpopo belt, OT: Okwa terrane, RT: Rehoboth terrane, GB: Gariep belt, NN: Namaqua-Natal belt, KB: Kheis belt, KC: Kaapvaal craton, CFB: Cape fold belt. (Magnetic data courtesy of the Council for Geoscience, Pretoria, South Africa.)

there is no evidence from xenolith or geophysical data of a fertile, convecting mantle, i.e., the asthenosphere below the melt-metasomatized zone. It is also possible that simply a depth level is present where mantle-derived melts have accumulated, metasomatizing the surrounding lithospheric mantle. Therefore the lithosphere-asthenosphere boundary based on chemical tomography sections should be understood as minimum thickness of the depleted lithospheric mantle at the time of the kimberlite eruption, without any constraint on the maximum thickness (Begg et al., 2009). Griffin et al. (2004) and Begg et al. (2009) show chemical tomography sections for some southern African areas. Their base of the depleted lithospheric mantle beneath the Namaqua-Natal Belt is at least at 150 km depth. Sections from southern and central Botswana show slightly deeper bases of the depleted lithosphere (about 180 - 200 km). Another interesting finding is that kimberlites of different ages (Group II 143 - 117 Ma and Group I 108 - 74 Ma) that were intruded across the southwestern boundary of the Kaapvaal craton, sampling the same volume of lithosphere during two different time windows, showed very different depths to the base of the depleted lithospheric mantle (> 200 km and 160 - 170 km respectively). Heating and chemical refertilisation by the infiltration of asthenosphere-derived melts is assumed to be the cause of the thinning of the depleted lithosphere by about 40 km (Griffin et al., 2004; Kobussen et al., 2008).

Geothermal studies show that the Kaapvaal craton is characterized by a low surface heat flow ($\sim 45\,mW/m^2$) and the occurrence of diamondiferous kimberlites, whereas the younger surrounding mobile belts have relatively high heat flow values ($\sim 80\,mW/m^2$) and barren kimberlites (for more heat flow information see Jones, 1998). Geotherms calculated from heat flow data (reflecting the current present-day geotherm) yield similar information as that provided by thermobarometry of the upper-mantle obtained from kimberlite xenoliths (recording the mantle geotherm and lithospheric thickness at the time of kimberlite eruption): the cratons have deep, cool and chemically reduced lithospheric roots (de Wit et al., 1992).

Tsunogae et al. (1992) calculated crustal, metamorphic pressure-temperature (P - T) profiles in the eastern and western parts of the Limpopo Belt. They found very similar P - T profiles for the northern marginal zone and the southern marginal zone, which implies that both zones may have shared a similar metamorphic evolution, whereas the central zone indicated higher P - T conditions (i.e., higher pressure and higher temperature). The difference in the P - T profiles can possibly be related to differential movement along the triangle shear zone, so that the northern marginal zone may have slipped along the shear zone against the central zone during uplift. The P - T conditions of the central zone also suggest that it is of deeper crustal origin than the northern marginal zone. (Tsunogae et al., 1992)

Part II

INTERPRETATION OF THE 2D ZIM PROFILE

4

DATA IMAGING AND ANALYSIS

This chapter discusses and illustrates many of the data imaging, analysis and preliminary interpretation approaches that can be used before any forward modelling or inversion tool is applied. Looking at the raw data can provide information about the structures that might be expected from subsequent modelling and inversion.

The methods used to derive preliminary information are: estimation of the maximum investigation depths for both modes (TE and TM) independently; plotting of the raw data in the form of Niblett-Bostick resistivity maps; and phase tensor maps for selected depths. Strike analysis is a further procedure that aims to determine a common strike direction for the whole profile (at all frequencies and at all sites) to facilitate 2D modelling and inversion. In general, the strike angle can vary with depth and/or along the profile. If it is not possible to find a common strike angle within acceptable error bounds for the whole data set, the profile should be divided into parts and each part should be modelled/inverted separately.

Finally, the special case of two areas of sites located above the Okavango dyke swarm will be discussed. Both groups of sites indicate a strike angle similar to the dyke swarm orientation, but they present a very different appearance in the Niblett-Bostick resistivity maps. A quantitative comparison of the sounding curves is useful to examine whether possible static shifts might be a plausible reason for the differences in resistivity and 1D anisotropy forward modelling is also applied to fit the data of an example site.

The area of interest is located in northeastern Botswana. The major geological structures situated in that region have been discussed in detail in the previous chapter (see Section 3.1). Figure 4.1 (a) shows a map of the topography and bathymetry of southern Africa including all SAMTEX site locations. Highlighted in red are the sites of the so-call ZIM-line, which will be the subject of the 2D modelling and inversion of Chapter 5. The blue dots indicate the sites of other profiles which will be included in the imaging and analysis presented in this chapter. The topography in the area of interest is very flat and therefore can be neglected in further analysis and modelling. Figure 4.1 (b) shows an enlarged map of the sites in the area of interest including their names for further reference.

4.1 DATA IMAGING

Apparent resistivity and phase values are calculated after processing the data and estimating the impedance tensor for each frequency. Pseudo sections are plotted to gain a first impression of the frequency-dependent data set of resistivity and phase values; the investigation depth can be estimated using, e.g., the Niblett-Bostick approach (see Equation 2.67 in Section 2.6.1) and phase tensor (see Section 2.9.2) maps can be drawn. Vertical magnetic

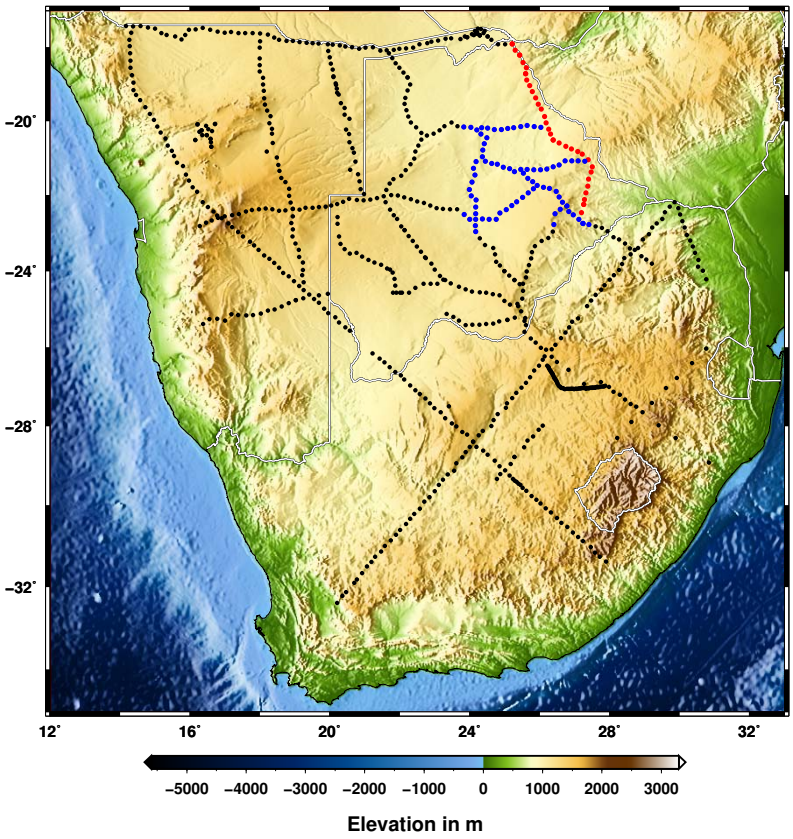

(a) Topography and bathymetry map

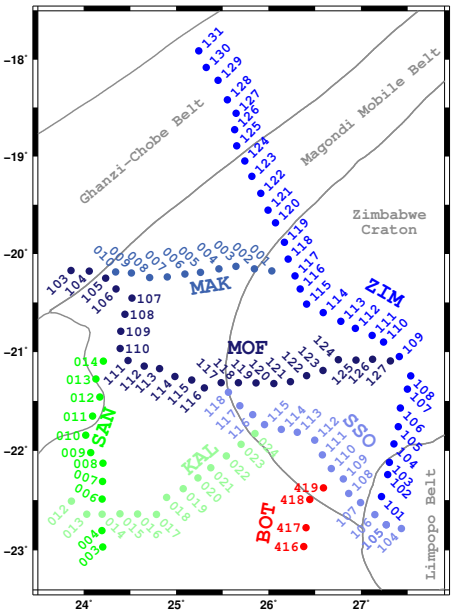

(b) Map of site names and locations

Figure 4.1: Topography and bathymetry map of southern Africa and a map of site locations and their names. (a) The ETOPO1 data set - freely available at: www.ngdc.noaa.gov/mgg/global/global.html - was used to produce the elevation background map. The MT site locations of the ZIM line are highlighted with red dots, and blue dots indicate other sites of interest. All the other SAMTEX sites are represented by black dots. (b) Map of site names and locations of the focused area. Each profile is represented by a different colour (colour coding identical to Figure 3.9) and the three-letter-profilename is given in the same colour. Each site name is composed of the profile name followed by the three digit site number (e.g., ZIM103, SAN009)

transfer function data were not available for the ZIM line and most of the other MT sites in northeastern Botswana for logistical reasons (solid surface rocks not enable burying the vertical coils and also some faulty coils reduced the number of available coils to less than required for recording all three magnetic field components at all sites).

4.1.1 *Pseudo sections*

Pseudo sections are interpolated and contoured images of apparent resistivity or phase values versus period, with period increasing downwards as a proxy for depth. Figure 4.2 shows one apparent resistivity and one phase pseudo section each for the TE and TM mode data of the ZIM line. High resistivity values are represented by blue (cold) colours, whereas red (warm) colours indicate low resistivity values. Since phase values smaller than 45° correspond with increasing resistivity values, these are represented by blue colours and the red colours are chosen for phase values larger than 45° (decreasing resistivities). The black inverted triangles indicate the site locations of the ZIM line. Although these images might be distorted due to the representation of distances versus period instead of true depth, some major features can already be recognised. There are two large resistors and one near surface conductor. The resistor on the south shows relatively sharp vertical boundaries, which are roughly located at site ZIM106 and between sites ZIM114 and ZIM115. The other resistor is located beneath sites ZIM124 to ZIM131 (and might continue northwards in extension of the profile), but its boundaries are not as sharp as for the first resistor. A near surface conductor is located in between these two resistors (roughly from ZIM115 to ZIM121) and is related to periods shorter than 1 s, but the phase values at about 100 - 1000 s of both modes indicate that there might be a second conductor beneath. In the TE mode the conductor is located beneath ZIM122/ZIM123, whereas in the TM mode the conductor is a bit more fuzzy and is located further south (beneath ZIM121/ZIM122). It is also worth noting that the data set contains changes of resistivity values of at least three orders of magnitude over very short (lateral) distances (see Figure 4.3). The effect of the rapid changes in resistivity on the investigation depths at neighbouring sites will be shown in the next section.

4.1.2 *Niblett-Bostick investigation depths and resistivity maps*

The Niblett-Bostick approach to estimate penetration depths and the related resistivity values at this depth was described in Section 2.6.1. Since the investigation depth is frequency-dependent but also related to the apparent resistivity, which varies strongly in the ZIM line data set as shown in the pseudo sections, the maximum investigation depths will vary along the profile. Figure 4.4 shows the depth estimates for all frequencies at all sites for both modes. Each dot represents a data point and the colour gives an idea of the frequency it is related to (red - short periods, blue - long periods). Beneath each site two of these columns of dots are plotted: the one on the left is for the TE mode data and the one on the right (with a grey bar in the background) is for the TM mode. The plot of Figure 4.4 illustrates how variable the maximum penetration depths are; the data from some sites cannot be associated with depths greater than the base of the crust, whereas data at other sites seem to have penetration depths deep into the upper mantle. One can also see that at neighbouring sites up to two orders of magnitude difference in period is required for the same penetration depth, and for some sites (e.g., ZIM106, ZIM121) a difference is apparent between the penetration depths of the two modes. The penetration depth plot also makes obvious how skewed the pseudo section must be in some parts of the profile. Therefore

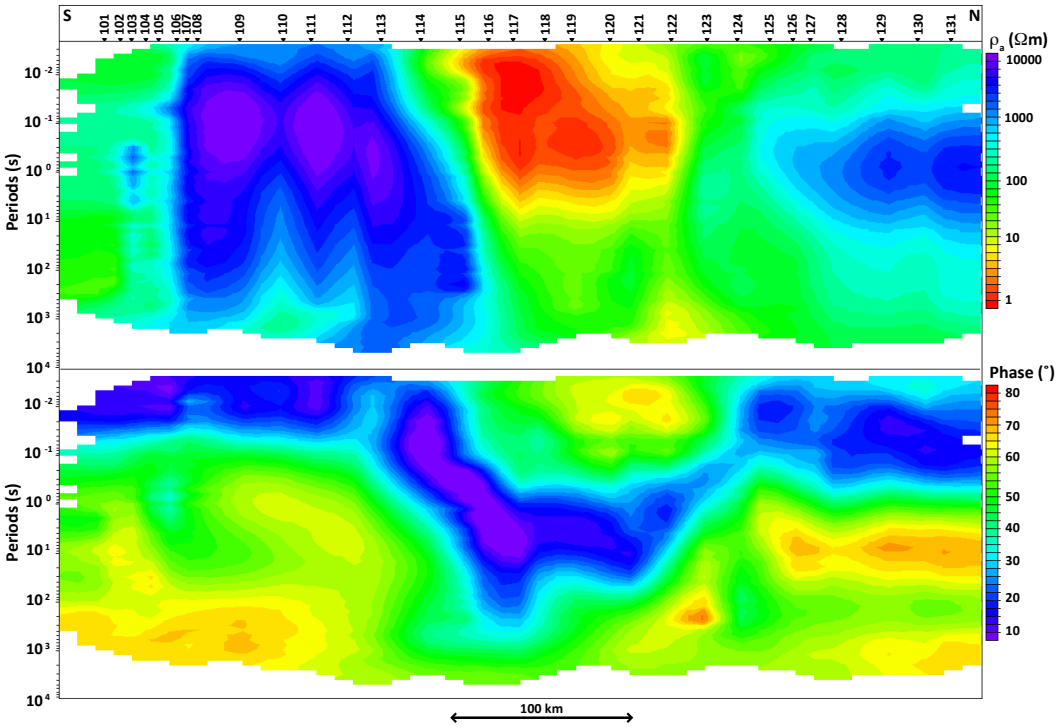

(a) Resistivity (top) and phase (bottom) pseudo sections of the TE mode

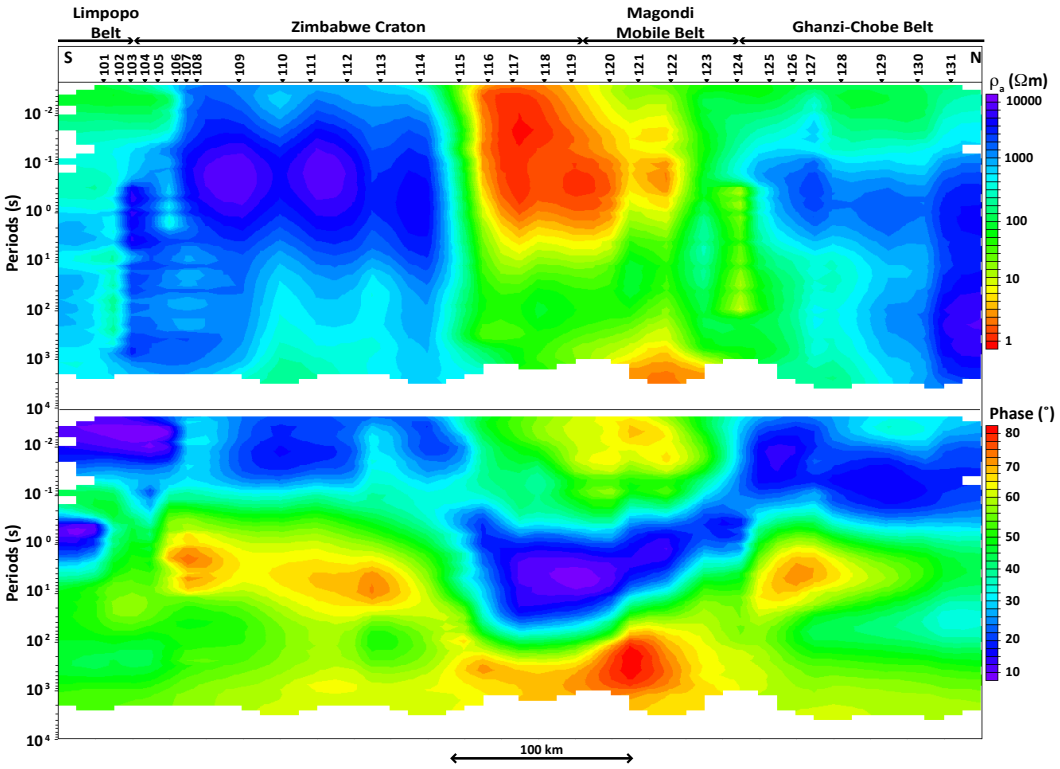

(b) Resistivity (top) and phase (bottom) pseudo sections of the TM mode

Figure 4.2: Pseudo sections of the ZIM line: TE mode (a) and TM mode (b). Pseudo sections are shown for apparent resistivity (top) and phase (bottom). The inverse triangles indicate the site locations. (The grid was generated using WinGlink® software from Geosystem applying the following settings: grid increment in the x-driection of 10 km, number of period intervals per decade 10, interpolation radius 3, spline weight 0 and smoothing factor 4.)

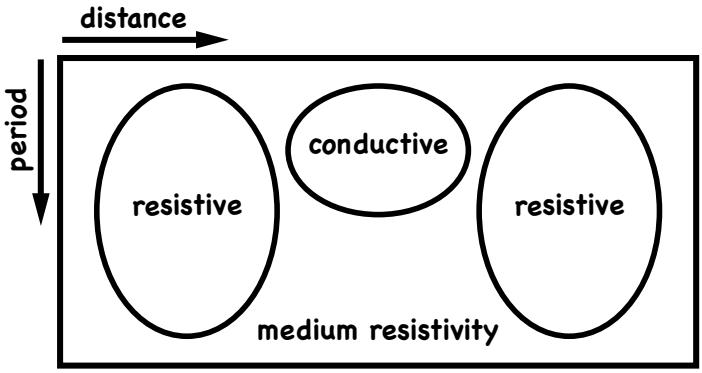

Figure 4.3: Sketch illustrating the strong lateral resistivity contrasts found in the ZIM line data. A conductor is located between two very resistive areas causing resistivity changes of at least three orders of magnitude over very short lateral distances.

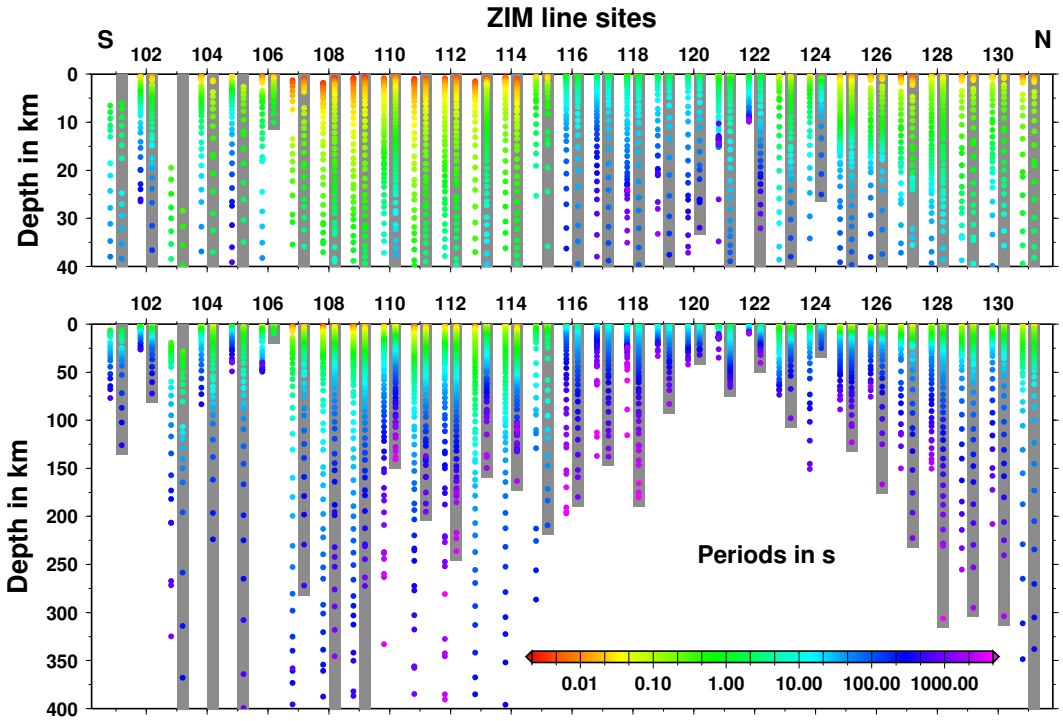

Figure 4.4: Niblett-Bostick penetration depths for all sites on the ZIM line. Each coloured circle represents a measurement at a certain period and depth with the colour indicating the period. The penetration depths are plotted separately for TE mode (left column of dots beneath each site) and TM mode (right column with grey bar in the background). The upper figure examines the depth range 0 - 40 km and the lower figure the range 0 - 400 km.

viewing resistivities at a certain depth is more appropriate than using plots versus frequency. Niblett-Bostick resistivity maps show (Niblett-Bostick estimated) resistivity values for a chosen depth. Figures 4.5 and 4.6 show maps for crustal (10 km) and lithospheric mantle (70 km) depths. Each circle shows a site that has data associated with the chosen depth. The colour of the symbol shows the resistivity value and its size is related to the period that is required to penetrate to the respective depth. As Figure 4.4 shows, there are differences in penetration depths between the two modes. Therefore two maps, one for each mode, are plotted in Figures 4.5 and 4.6.

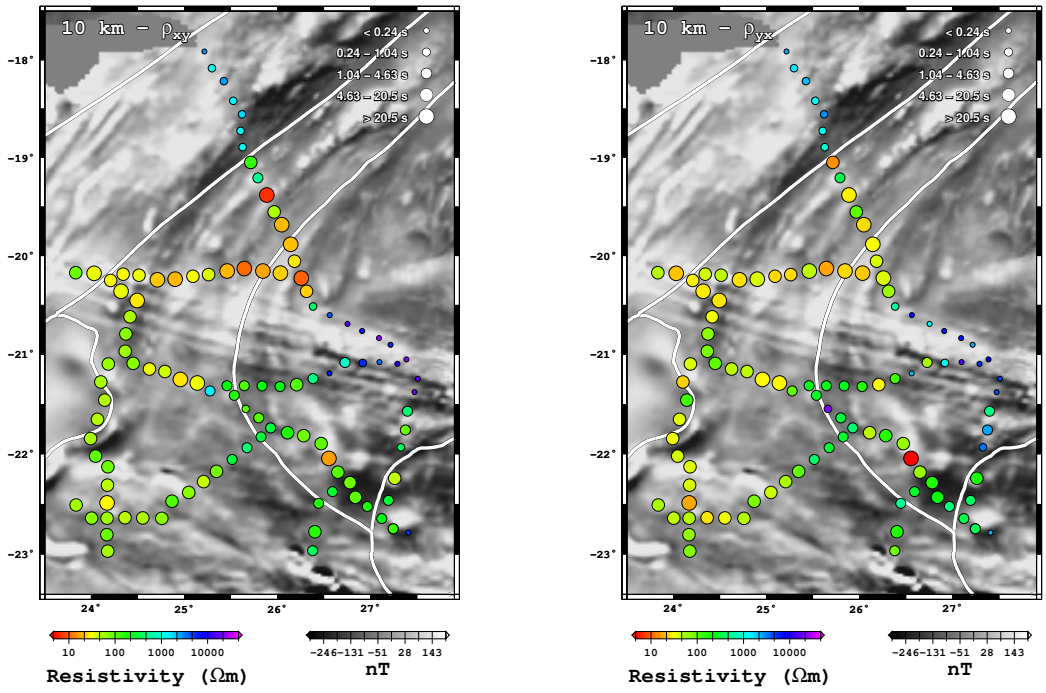

(a) Niblett-Bostick resistivities ρ_{xy}

(b) Niblett-Bostick resistivities ρ_{yx}

Figure 4.5: Niblett-Bostick resistivities (a) ρ_{xy} and (b) ρ_{yx} at 10 km depth. While the colour of the circles represents the Niblett-Bostick resistivity value at that depth, the size of the symbol indicates the period that is required to penetrate to this depth.

Again it is clear that very different periods are required at different sites to obtain the same penetration depth (different sizes of circles in Figures 4.5 and 4.6 are related to the period). Shorter periods are coincident with higher resistivities, expected from the definition of the depth estimation. In addition to the two sets of Niblett-Bostick resistivity maps presented here, more maps for different crustal and lithospheric depths can be found in Appendix B.1.

For crustal depths, four different zones can be identified (see Figure 4.7). There is a resistive area of about 1000 Ωm at the northern end of the ZIM line which seems to coincide with the Ghanzi-Chobe belt as outlined in magnetic field data. A second resistive area (1000 Ωm and more) can be found in the middle to southern part of the ZIM line and on the eastern part of the MOF line. These sites associated with the second resistive area are located on

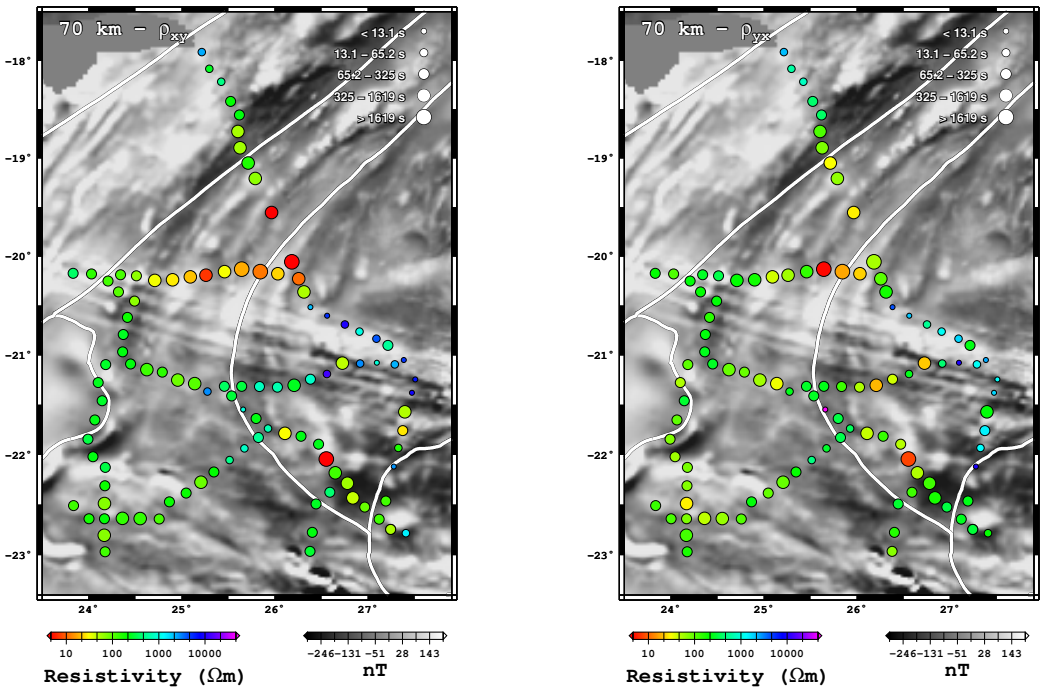

(a) Niblett-Bostick resistivities ρ_{xy}

(b) Niblett-Bostick resistivities ρ_{yx}

Figure 4.6: Niblett-Bostick resistivities (a) ρ_{xy} and (b) ρ_{yx} at 70 km depth. While the colour of the circles represents the Niblett-Bostick resistivity value at that depth, the size of the symbol indicates the period that is required to penetrate to this depth.

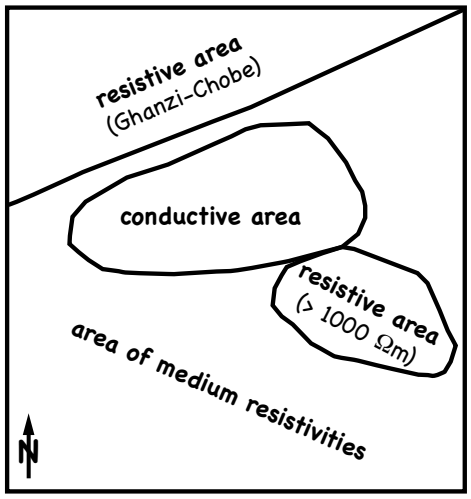

Figure 4.7: Sketch in plan view outlining four distinct areas found in the crustal resistivity distribution of Figure 4.5. There is a resistive area in the north that is coincident with the Ghanzi-Chobe belt, the boundary of which is defined in magnetic field data. A second very resistive area is located further to the southeast. In between these two resistive areas is located a conductor that extends to the west. The other areas are characterised by medium resistivity values.

top of the Okavango dyke swarm, which can be clearly seen on the grey scale magnetic map shown in the background. Between these two resistors is located a conductor that extends to the west. The sites to the west and southwest of the very high resistive area show intermediate resistivity values of about 100 Ωm to 500 Ωm. It is worth noting that, although the one highly resistive area in the southeast coincides well with the location of the dyke swarm, none of the sites above the swarm in the west show such high resistivity values (they are about two to three orders of magnitude smaller).

With increasing depth, nearly all sites show intermediate resistivity values (Figure 4.6) except for the few sites located on top of the crustal conductor, which still appear conductive (known as 'bleeding down' of the conductive layer, see e.g., Jones, 1999). For greater depths, not all sites contribute resistivity information, especially the ones located above the conductor (see Figure 4.4).

4.1.3 *Phase tensor profile and maps*

The phase tensor was introduced in Section 2.9.2 and its parameters are graphically illustrated by an ellipse (see Figure 2.14). It is a data imaging tool that does not suffer from electric field galvanic distortion. Figures 4.8 and 4.9 show phase tensor profiles of the ZIM line data, where the axes of the ellipses are normalised by Φ_{max} and the colour represents Φ_{min} (Figure 4.8) and the skew angle β (Figure 4.9) respectively. For each frequency, a phase tensor ellipse is plotted at the estimated Niblett-Bostick depth (average depth of the two modes). The top graph shows the depths range from surface to 40 km to account for the higher frequency density and therefore higher phase tensor density, at shallower depths, whereas the bottom graph covers the depth range from 40 km to 250 km. Once again the different penetration depths of the sites is clear.

The shapes of the ellipses give an idea of the dimensionality of the subsurface. A 1D structure can be assumed when the phase tensor is circular, as is nearly the case for some of the phase tensors, e.g., from sites ZIM108, ZIM110 and ZIM111. The orientation of the major axis of the ellipse in the non-1D case represents the strike direction (with a 90° ambiguity applicable). In the case of these section views, the angle shown with respect to the vertical direction represents the strike angle with respect to north in the horizontal plane.

The colour coding of Figure 4.8 represents the values of the minor axis Φ_{min} of the ellipses. Analogous to the pseudo sections, the red/warm colours are related to high phase values and therefore to decreasing resistivity. Low Φ_{min} values, represented by blue/cold colours, indicate an increasing resistivity. The dominant features of the frequency based pseudo sections (Figure 4.2) appear very different when compared to the phase tensor representation in depth. The near surface conductor, which was a major feature in the pseudo sections and showed large phase values for the first one to one and a half decades, does not appear similarly in the phase tensor profile. The large Φ_{min} values still exist in the phase tensor data set, but they are all related to very shallow depths so that they are not visible when plotted using a crustal depth scale. Figure 4.8 (b) shows an inset figure for the top 200 m for sites ZIM119 to ZIM122, in which these large Φ_{min} values are clear. At the same time the near-surface low-phase-value areas in the pseudo sections, that extend over nearly the same period range to the left and right of the high-phase anomaly and seem to bend around it, are seen to correspond with an upper- to mid-crustal layer of more or less

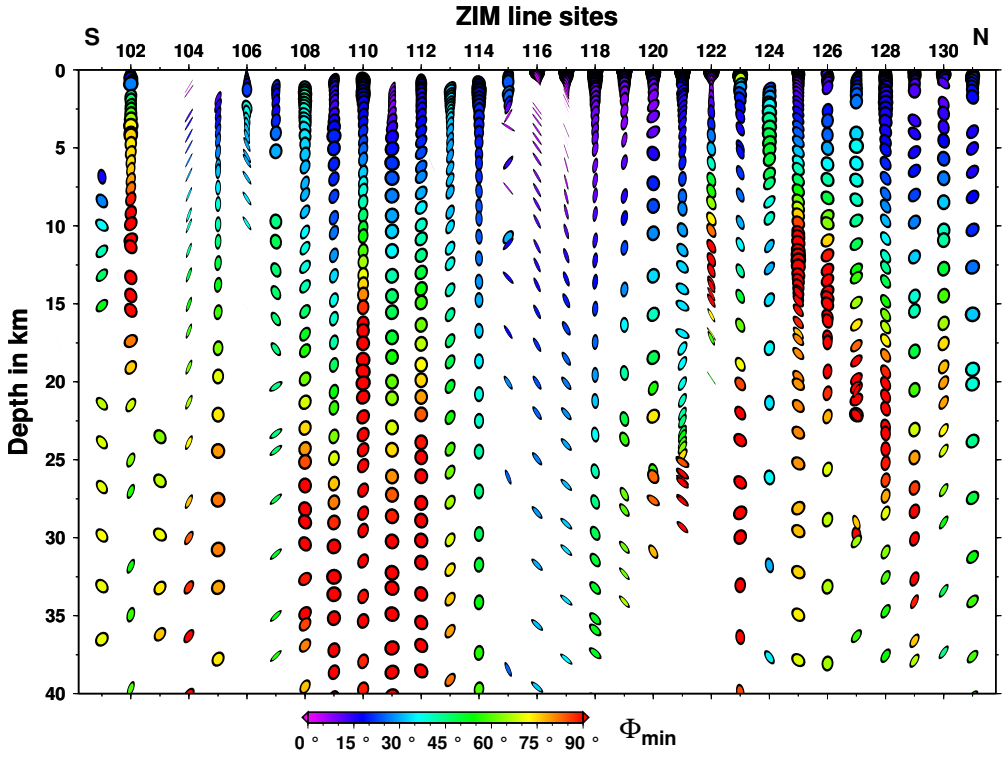

(a) Phase tensor profile of 0 - 40 km depth

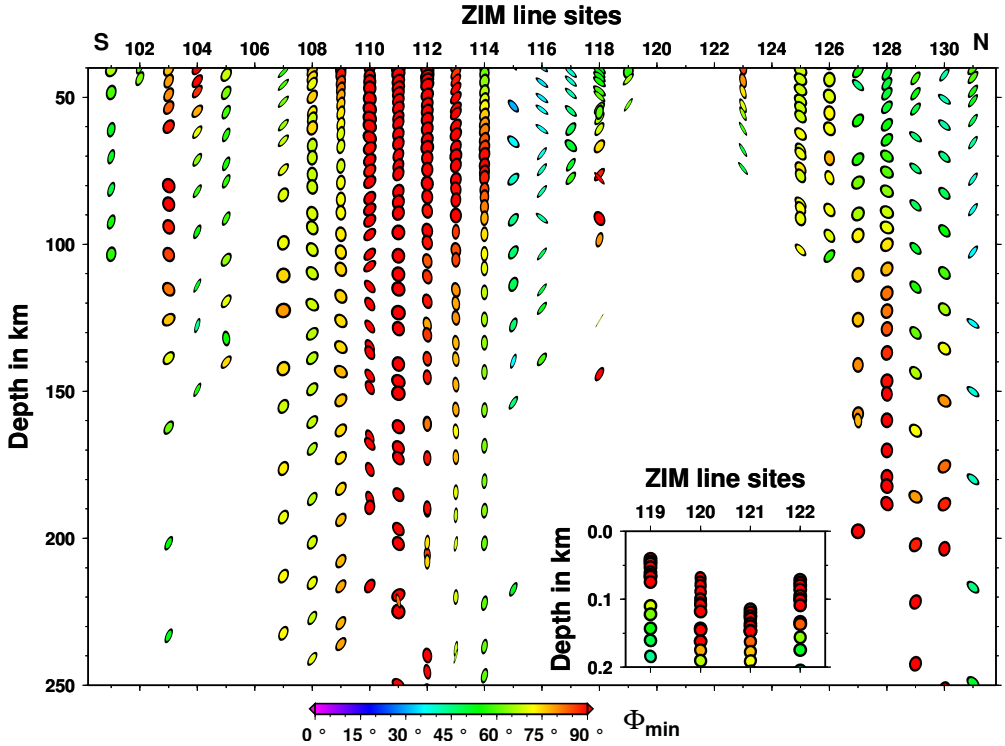

(b) Phase tensor profile of 40 - 250 km depth (inset figure: 0 - 200 m depth

Figure 4.8: ZIM line phase tensor sections for depths ranges (a) 0 - 40 km and (b) 40 - 250 km with an inset figure showing the phase tensors for the top 200 m for sites ZIM119 to ZIM122. The axes of the ellipses are normalised by Φ_{max} and the colours represent Φ_{min}. Vertical ellipse orientation represents the phase tensor direction with respect to north. The depth estimates are calculated using the Niblett-Bostick approach (average depth of the two modes).

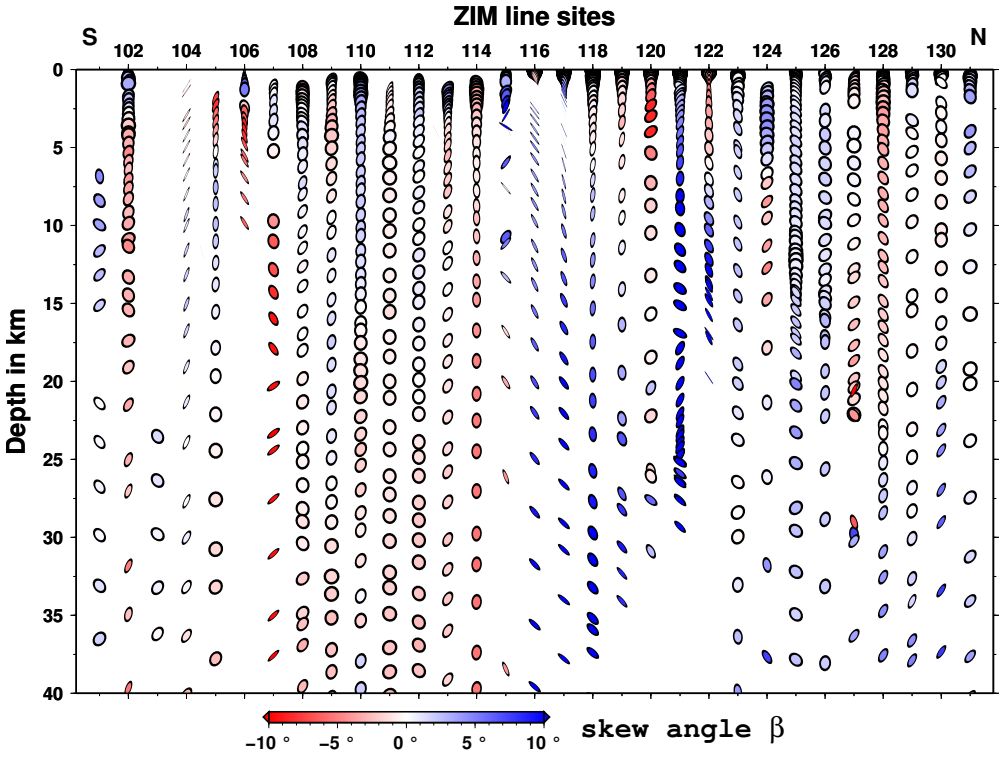

(a) Phase tensor profile of 0 - 40 km depth

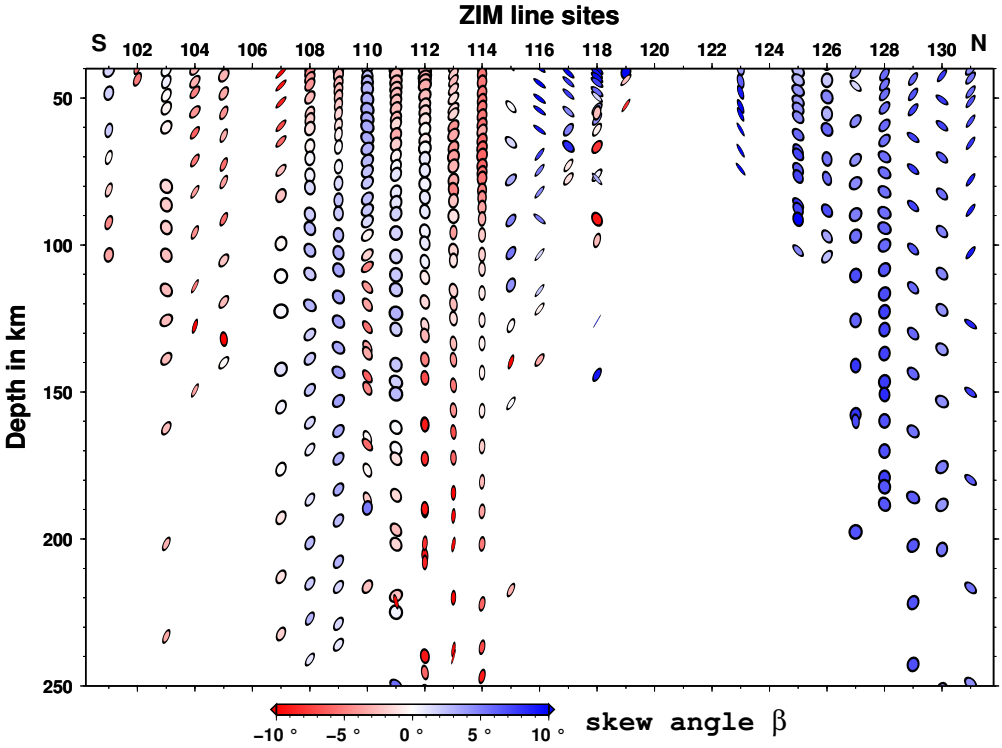

(b) Phase tensor profile of 40 - 250 km depth

Figure 4.9: ZIM line phase tensor profiles of depths ranges (a) 0 - 40 km and (b) 40 - 250 km. The axes of the ellipses are normalised by Φ_{max} and the colours represent the skew angle β. Vertical ellipse orientation represents the phase tensor direction with respect to north. The depth estimates are calculated by the Niblett-Bostick approach (average depth of the two modes).

constant thickness of a few kilometres in the phase tensor plot. Beneath sites ZIM120 to ZIM129, a decrease in resistivity in the mid- to lower-crust is apparent, while some of these sites indicate an increase of resistivity or a constant resistivity for the upper lithosphere. Another decrease in resistivity apparent in the pseudo section data below sites ZIM108 to ZIM114 also starts in the mid- to lower-crust, but remains present for more or less the whole lithosphere.

In Figure 4.9, the colour of the phase tensor ellipses is related to the skew angle β, which provides some information about the possible dimensionality of the data set. In an ideal, noise-free, 1D or isotropic 2D case, the phase tensor is symmetric and the skew angle is equal to zero ($\beta = 0$). Since the skew angle is a measure of the phase tensor's asymmetry produced by 3D structure, a large skew angle indicates a 3D resistivity distribution. It is worth remembering that a small skew angle of only a few degrees is a necessary but not sufficient requirement for a 1D or 2D structure (see Section 2.9.2 and references therein). For the phase tensor profile of the ZIM line one can see that most of the sites and frequencies have a very small skew angle (light red to white to light blue colours indicate a skew angle of a maximum $\pm 2°$). Phase tensor ellipses with a skew angle of $\pm 5°$ or more are seldom. ZIM121 is the only site that shows large β values for nearly all depths. Some other sites (ZIM116 to ZIM119 and ZIM123 to ZIM 131) have large skew angles for greater depths (lower crust and lithosphere respectively). For these areas a 3D resistivity distribution should be expected. Since the majority of the phase tensor ellipses are potentially 1D or 2D, a 2D modelling and inversion approach is valid for this profile.

Analogous to the Niblett-Bostick resistivity maps, phase tensor maps can also be plotted. Figures 4.10 and 4.11 show two representative depths, one for the crust (10 km) and one for the lithospheric mantle (70 km). More phase tensor maps at various crustal and lithospheric mantle depths can be found in Appendix B.2.

For each depth there are two maps where the phase tensor is coloured by (a) the skew angle β and (b) Φ_{min} respectively. At crustal depths, nearly all phase tensors have a small skew angle (smaller than $\pm 2°$), which indicates a potential 2D environment. Also for greater depths the majority of the sites show a small increase in skew angle. Some areas with high β values, indicating a 3D structure, are near proposed boundaries of geological units, in vicinity of the dykes and, as mentioned earlier, at lithospheric depths at the northern end of the ZIM line. The Φ_{min} values are very low for the very shallow crust, indicating increasing resistivities especially in areas that are coincident with the cover of Kalahari sands and, further to the west, where the sands are thicker, the low Φ_{min} values can be seen to greater depth, before they reach a level of about $45°$ at most of the sites. It also becomes obvious that the most eastern profile, the ZIM line, is quite different from the rest of the sites. Whereas all the other sites show a smooth, gradual change in Φ_{min} values from site to site, there are many abrupt changes between neighbouring sites along the ZIM line.

Continuous indications of decreasing resistivities from the mid- to lower-crust downwards though the whole lithosphere (as seen for sites ZIM108 to ZIM114 in Figure 4.8) can be found on the depths maps in the area around the dyke swarm. The other zone of low Φ_{min} values that is located in the mid- to lower-crust seems to be coincident with the proposed boundary between the Magondi and Ghanzi-Chobe mobile belts.

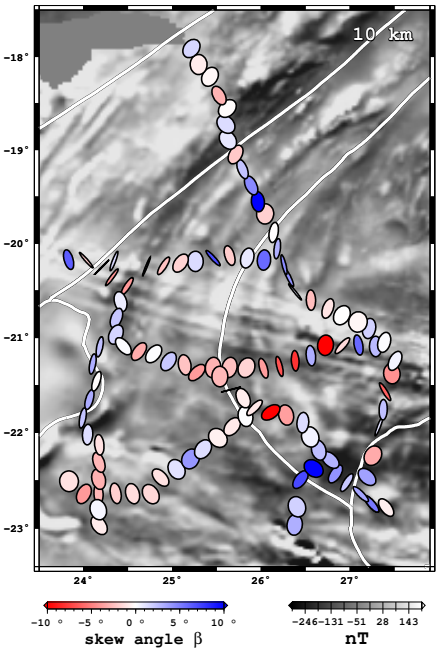

(a) Phase tensor ellipses coloured by skew angle β

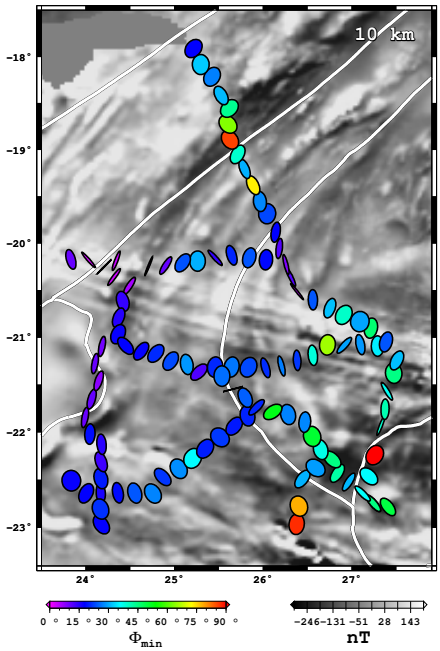

(b) Phase tensor ellipses coloured by Φ_{min}

Figure 4.10: Phase tensor maps at 10 km depth. The phase tensors are represented by ellipses (axes normalised by Φ_{max}) at each site. The colour of the ellipses indicates (a) the skew angle β and (b) Φ_{min} respectively.

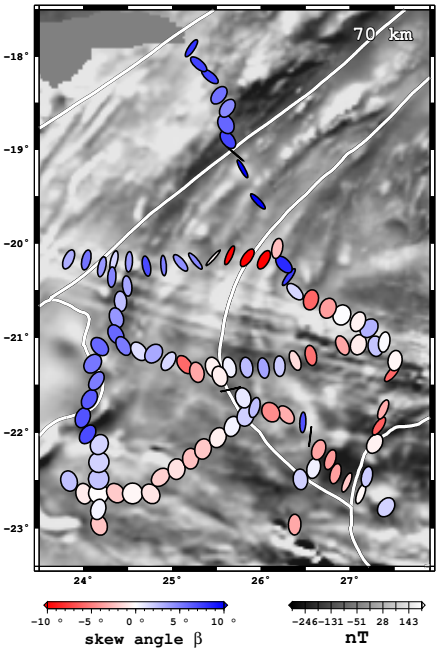

(a) Phase tensor ellipses coloured by skew angle β

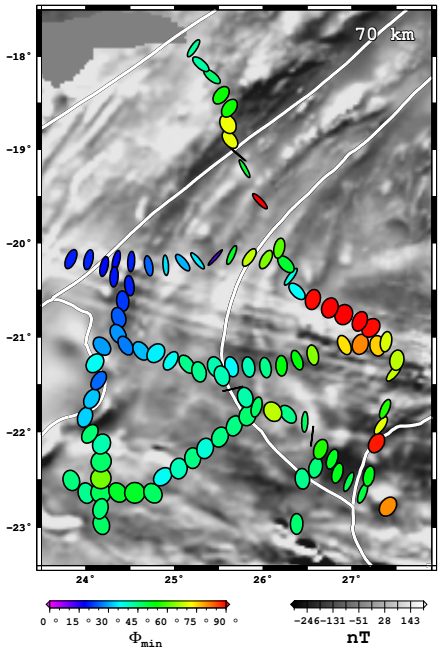

(b) Phase tensor ellipses coloured by Φ_{min}

Figure 4.11: Phase tensor maps at 70 km depth. The phase tensors are represented by ellipses (axes normalised by Φ_{max}) at each site. The colour of the ellipses indicates (a) the skew angle β and (b) Φ_{min} respectively.

4.2 STRIKE ANGLE ANALYSIS

Defining a common strike direction for all sites and frequencies is essential for 2D modelling and inversion. The program STRIKE by McNeice and Jones (2001) based on the Groom-Bailey decomposition (Bailey and Groom, 1987; Groom, 1988; Groom and Bailey, 1989) was introduced in Section 2.9.2. STRIKE facilitates the finding of a strike angle and decomposes the data to 2D responses. One can choose the number of sites and a frequency bandwidth (together with a maximum and minimum frequency) to select the data that are decomposed and fitted to Groom and Bailey distortion models jointly. The latest version of STRIKE (v6.0) has a new option that allows selection of the frequencies by defining the minimum and maximum depths of interest and a depth bandwidth. The Niblett-Bostick depth estimation (based on the average depths of both modes) is used to find the frequencies that fall into the requested depth range. The approach allows, even for data sets such as the ZIM line, a multi-site strike analysis to be performed without the risk of trying to match data from completely different depths. Figure 4.12 shows the results of a single-site strike analysis for (c) a crustal depth range of 5 - 35 km and (d) a lithospheric depth range of 50 - 150 km. The orientation of the arrows represents the strike direction (with a 90° ambiguity applicable), the colour of the arrows indicates the average phase difference and its length is a measure of the RMS misfit of the distortion model to the data (the longer the arrow, the smaller the average RMS value and therefore the better the goodness-of-fit). The histograms above for (a) crustal and (b) lithospheric depths show that the majority of sites have an average RMS misfit below 1.5 with a peak at about 0.7 for the crust. No clear peak can be found for the lithosphere. A phase difference of less than 10° (blue to turquoise colours) indicates a 1D structure. Large phase differences (> 35°) mean that a strongly 2D (or 3D) environment is present (orange to red colours). The intermediate values represented by green to yellow colours indicate weak two-dimensionality. Very short arrows are observed where no adequate distortion model was found to decompose the data to a 2D response. Therefore these sites are most likely associated with a 3D structure or optimistically small error estimates (Chave and Jones, 1997). For crustal depths (Figure 4.12 (c)) such high-RMS-error sites are mainly located where the dyke swarm and the boundary between the Zimbabwe craton and the Magondi mobile belt converge as well as the southern half of the Magondi mobile belt (possible lateral correlation with the extent of the Makgadikgadi salt pan complex). Another point to notice at crustal depths is the coincidence of the orientation of the dyke swarm with the strike direction (or its 90° ambiguity) at the sites located above.

At lithospheric depths (Figure 4.12 (d)) for nearly all ZIM line sites north of the dyke swarm the preferred strike direction is very consistent, although the average RMS values are increased compared to the crust. The higher RMS values at lithospheric depths north of the dyke swarm are the main cause of the change in the RMS distribution from (a) crustal to (b) lithospheric depth.

Figure 4.13 shows a comparison of the average RMS misfit and the average of the absolute phase difference (see Figure 4.12) to the average of the absolute phase tensor skew angle β (see Figures 4.10 and 4.11) for all sites and both (a) crustal (5 - 35 km) and (b) lithospheric mantle (50 - 150 km) depths ranges. All three parameters are indicators for dimensionality as described above. For crustal depth (a), there is a good correlation between the small RMS misfit values (i.e., good fit to the distortion model), the small phase differences (i.e., 1D or 2D structure) and the small phase tensor skew angles (potentially 1D or 2D structure).

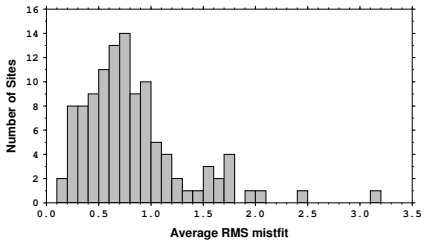

(a) Average RMS misfit for crustal depths.

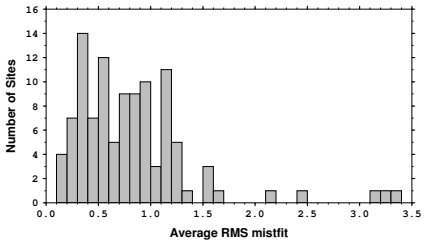

(b) Average RMS misfit for lithospheric depths.

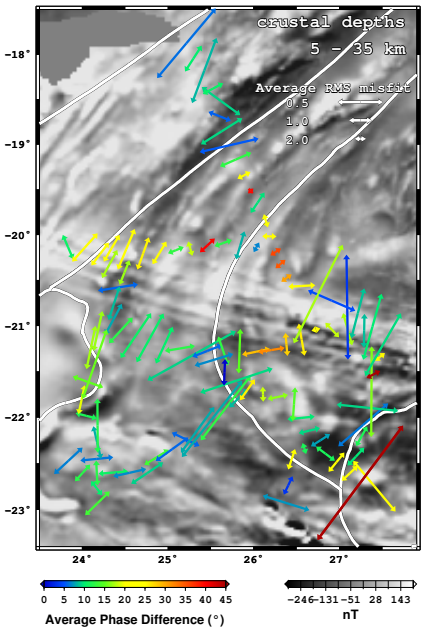

(c) Single-site strike directions for crustal depths.

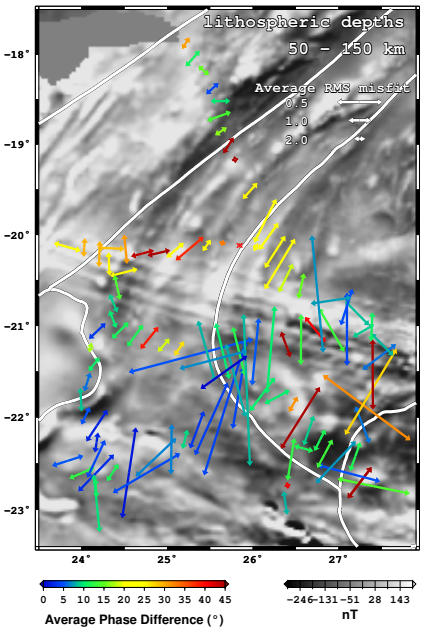

(d) Single-site strike directions for lithospheric depths.

Figure 4.12: Figure showing on top histograms of the average RMS misfit and on the bottom the single site strike directions over (a and c) crustal (5 - 35 km) and (b and d) lithospheric (50 - 150 km) depths ranges. The colour coding indicates the average of the absolute phase difference in the two orthogonal directions, whereas the length of the arrows is related to the average RMS misfit (the longer the arrow the smaller the average RMS value and therefore the better the goodness-of-fit). Note that the strike directions plotted are the directions resulting from the program STRIKE, but there is a 90° ambiguity in strike direction.

Only a few sites show large phase tensor skew angles indicating a 3D environment. These sites also have larger RMS misfit values and tend to larger phase differences. Therefore these sites are probably sensing 3D structures. At lithospheric mantle depths (b) a similar distribution can be found with an additional group of sites that show large phase tensor skew angles and mainly large phase differences but small RMS misfit values. These sites are probably above a 3D structure that can be compensated by a distortion model that leads to a good fit to the data and therefore to a small RSM misfit value. All three criteria for both depths ranges support the assumption of a 2D structure beneath the majority of sites and therefore justify a 2D modelling and inversion approach to interpret the data.

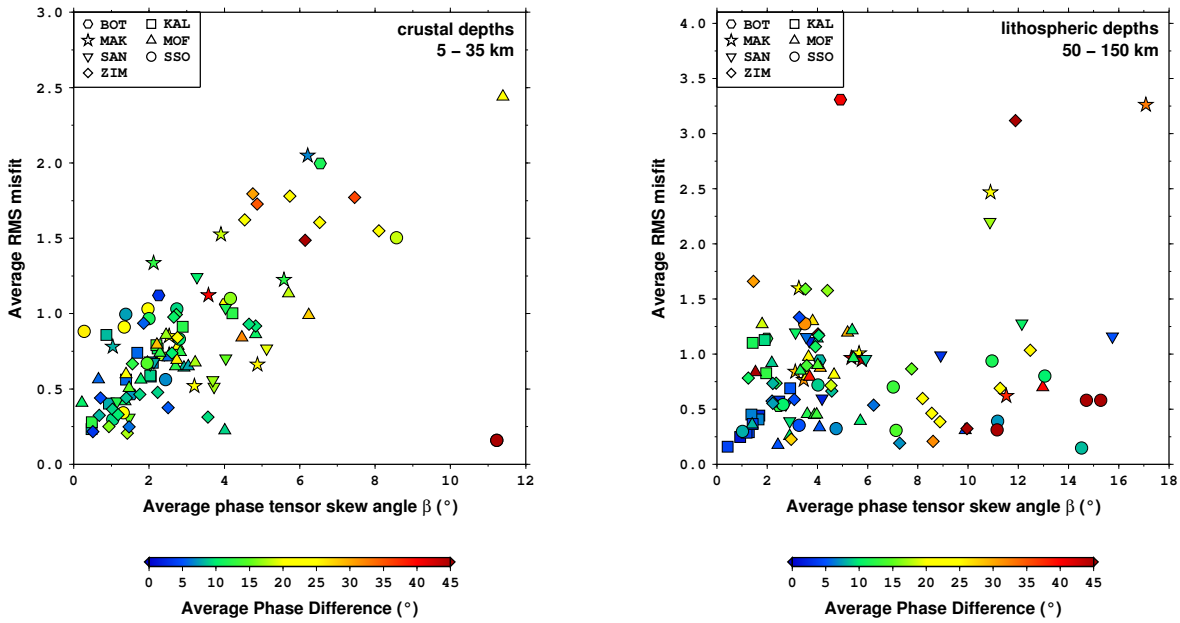

(a) Comparison for crustal depths.

(b) Comparison for lithospheric depths.

Figure 4.13: Figure showing a comparison of the average RMS misfit, the average of the absolute phase difference and the average of the absolute phase tensor skew angel β over (a) crustal (5 - 35 km) and (b) lithospheric (50 - 150 km) depths ranges. The colour coding indicates the average of the absolute phase difference in the two orthogonal directions. A small phase difference indicates a possible 1D or 2D environment, whereas large phase tensor skew angles represent a 3D structure. The smaller the RMS misfit the better the goodness-of-if of the distortion model to the data. Each symbol represents one site and the shape of the symbol indicates to which profile the site belongs.

The RMS values and strike directions for the individual sites shown in Figure 4.12 are not only based on a simple rotation of the data but also on the decomposition of the data set with the aim of removing possible galvanic distortion effects. The Groom-Bailey decomposition is based on determining the twist and shear angle for the chosen data band (and the anisotropy factor for each individual frequency) to generate the distortion matrix. Figures 4.14 and 4.15 show these two variables representing (parts of) the distortion models for the individual sites at crustal and lithospheric depths.

The observed twist angles fall mostly within the range of $\pm 10°$ for crustal (Figure 4.14 (a)) and $\pm 15°$ for lithospheric depths (Figure 4.14 (b)). The majority of the sites have a consistently low twist value for the crust (c) as well as for the lithosphere (d), and the few sites with higher angles are scattered. High twist angles are absent in the areas of uniform, conductive Kalahari sand cover.

The shear angles shown in Figure 4.15 predominantly are within the range of $\pm 10°$ for crustal depths (a). For the lithosphere (b) the shear angles are spread out over the physically possible range of $\pm 45°$. As the map of the crustal shear shows (c), high shear angles are absent in the western part coincident with the Kalahari sand cover. The distribution of sites with high shear is scattered for the crust, but for the lithosphere clusters of similar high shear are suggested. In general the majority of the high shear angles are located on

the Zimbabwe craton or close to terrane boundaries. North of the dyke swarm at both lithospheric mantle and crustal depths, high positive shear values are dominant, whereas sites at the boundary between the Ghanzi-Chobe and Magondi mobile belts have moderate to high negative shear value. Another reason why the lithospheric shear angles near the dyke swarm are relatively high is that for longer periods the dykes become small compared to the skin depths and will act as additional galvanic scatterer. It is worth noting that these distortion models are based on twist and shear, but neglect any static shifts (the gain and anisotropy terms in the distortion matrix, see Section 2.9.2).

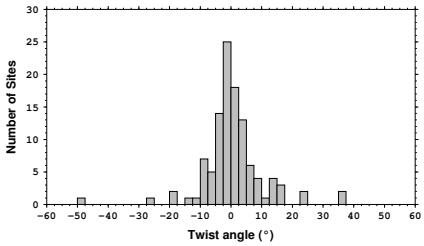

(a) Twist angles for crustal depths.

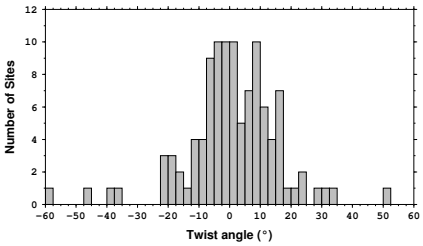

(b) Twist angles for lithospheric depths.

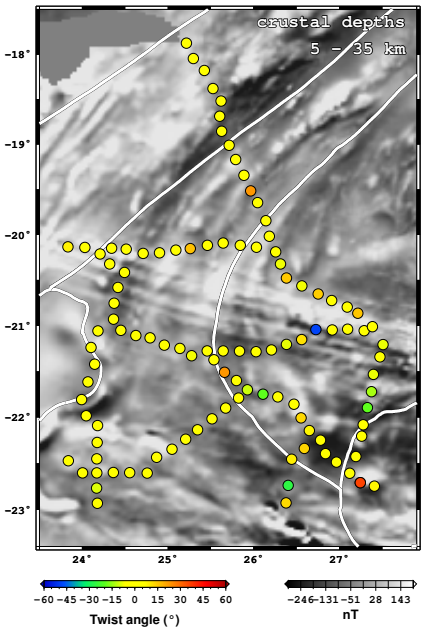

(c) Twist angles of individual sites for crustal depths.

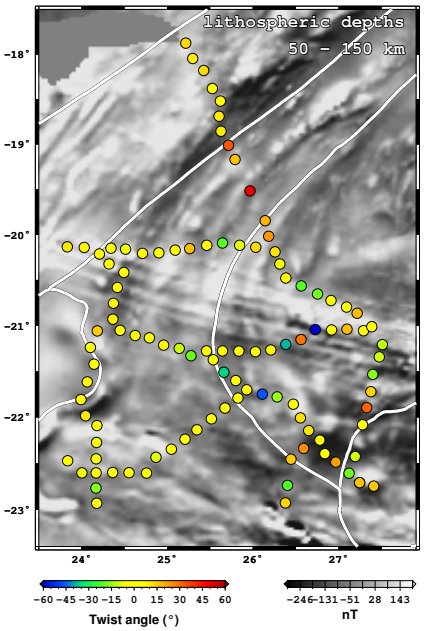

(d) Twist angles of individual sites for lithospheric depths.

Figure 4.14: Figure showing on top histograms of the twist angles over (a) crustal (5 - 35 km) and (b) lithospheric (50 - 150 km) depths ranges. Below are maps representing the twist angles for the individual sites for (c) crustal and (d) lithospheric depths.

Figure 4.16 shows plots of the most conductive direction for the crust (a) and lithospheric mantle (b), which is a way of avoiding the 90° ambiguity in the strike direction. As it was shown in Figure 2.6 for a simple fault structure, on the side of the resistive quarter space

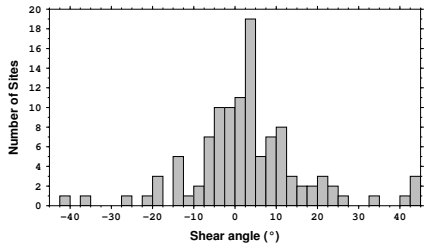

(a) Shear angles for crustal depths.

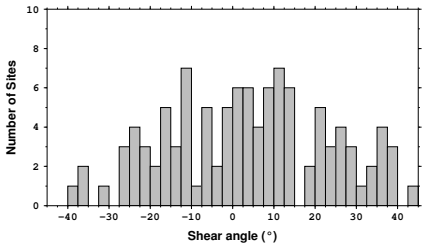

(b) Shear angles for lithospheric depths.

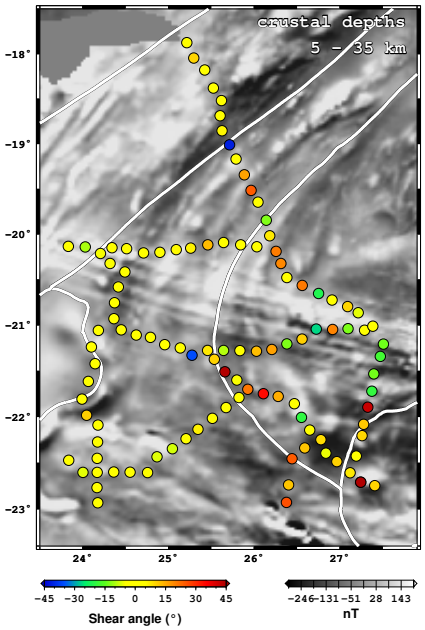

(c) Shear angles of individual sites for crustal depths.

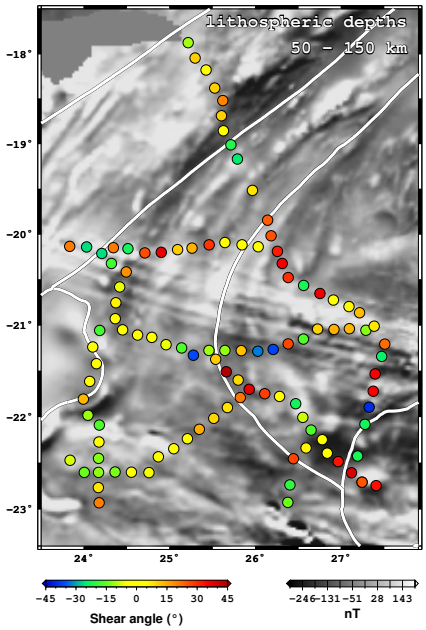

(d) Shear angles of individual sites for lithospheric depths.

Figure 4.15: Figure showing on top histograms of the shear angles over (a) crustal (5 - 35 km) and (b) lithospheric (50 - 150 km) depths ranges. Below are maps representing the shear angles for the individual sites for (c) crustal and (d) lithospheric depths.

the TE mode is more conductive than the TM mode, whereas on the conductive side of the fault the TM mode is more conductive than the TE. Therefore plotting the most conductive direction will result in plotting the TE mode on the resistive side of a fault or a terrane boundary and the TM mode on the conductive side. Since the TE mode is defined as having the electric field parallel to the strike direction of the fault, the most conductive direction on the resistive side will be parallel to it. On the other hand, the TM mode is defined as having the electric field direction perpendicular to the fault direction and therefore the most conductive direction on the conductive side is also perpendicular to it. Hence at a fault or a terrane boundary a 90° flip in the most conductive direction will occur. Since the resistivity values could be affected by static shifts, the most conductive direction of the true structure based on the apparent resistivity curves could be misleading. As the phases are unaffected by static shift, it is preferred to use the maximum phase instead of the minimum resistivity to define the most conductive direction. Maximum phases are used to determine the most conductive directions plotted in Figure 4.16.

Figure 4.16 shows some of these 90° flips in most conductive direction in the crust (a) as well as in the lithosphere (b). Since these directions represent a band of frequencies, phase cross-overs within the band cannot be excluded, and therefore the colour of the arrow at each site indicates the percentage of the frequencies in the band that show the plotted direction as most conductive. A blue arrow (100%) means all frequencies have a consistent most conductive direction, whereas red (50%) indicates sites where half of the frequencies have a most conductive direction in the plotted orientation, but the other half is in favour of the perpendicular direction as the most conductive. Most of these undecided cases are located at places where the 90° flip occurs. Looking at the northern end of the ZIM line, the sites inside the Ghanzi-Chobe belt seem to be more or less parallel to the proposed terrane boundary with the Magondi belt, whereas sites on the Magondi belt show a perpendicular most conductive direction. If the flip is related to the terrane boundary between these two belts, two things can be stated. First, the Magondi mobile belt is more conductive than the Ghanzi-Chobe mobile belt (which agrees with, e.g., the pseudo sections (Figures 4.2) and Niblett-Bostick resistivity maps (Figures 4.5 and 4.6)) and second, the proposed terrane boundary is probably drawn too far south since the flip happens somewhere around ZIM128 (and not ZIM124) at crustal as well as lithospheric depths.

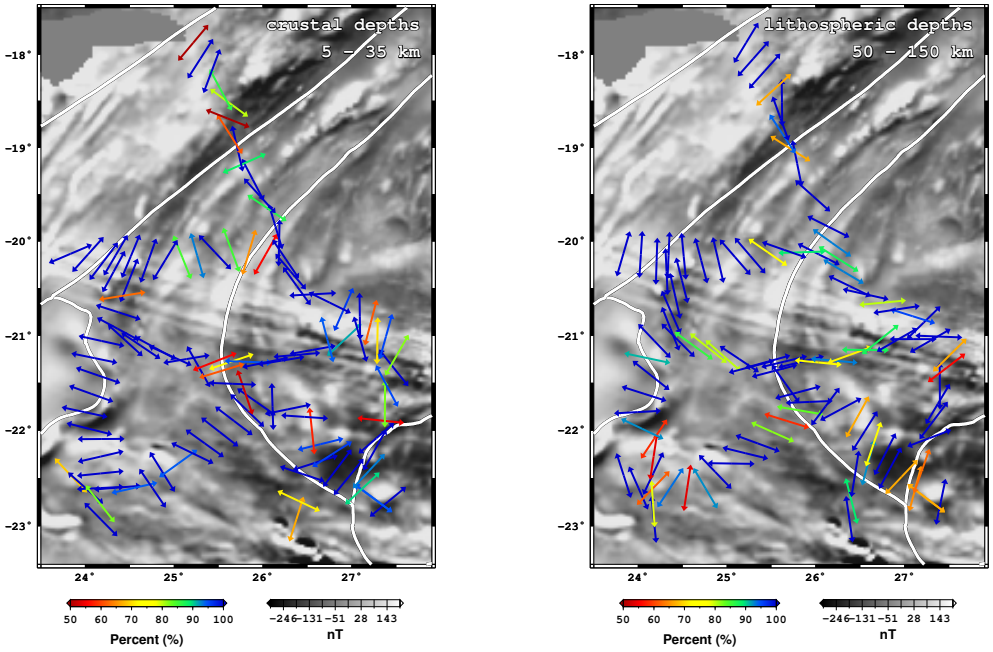

(a) Most conductive directions for crustal depths.

(b) Most conductive directions for lithospheric depths.

Figure 4.16: Figure showing the most conductive directions (defined using maximum phase) over (a) crustal (5 - 35 km) and (b) lithospheric (50 - 150 km) depths ranges. The colour coding indicates the percentage of the frequencies in the depth range on which this direction is based for each individual site. Blue (100%) means all frequencies in this depths range show the same most conductive direction whereas red (50%) represents sites where the direction plotted is only based on half of the frequencies, while the other half is in favour of the perpendicular direction as most conductive.

Another eye-catching flip in the crust can be seen at the western sites above, and south of, the dyke swarm. All sites above the dyke swarm show a most conductive direction perpendicular to the dyke orientation, whereas all the sites south of the swarm have most conductive directions parallel to it. Although it is not as sharp as for the crust, the flip still is present in the lithosphere. The sites above the dyke swarm in the east indicate also a most conductive direction perpendicular to the dyke swarm orientations, but this orientations is not as dominant as for the western sites.

While no flip can be identified at the terrane boundary between the Zimbabwe craton and the Magondi mobile belt on the ZIM line, there are two 90° changes in the most conductive direction in the south which could indicate the southwestern boundary of the Zimbabwe craton. One is located at the proposed boundary of the Zimbabwe craton, where the most conductive direction at the sites of the KAL line is oriented parallel to the outlined boundary and the SSO line sites show directions perpendicular to it. If that is the correct terrane boundary for the craton, then the most conductive direction would suggest that the craton would be more conductive than the neighbouring mobile belt. The other location is a little further to the westsouthwest, just east of the crossing of the SAN and KAL lines. The sites of the SAN line (sites SAN003 to SAN008) indicate being on the more conductive site, whereas the KAL sites (sites KAL017/018/019 to KAL024) show a most conductive direction that would place them on the more resistive side of the boundary. If the Zimbabwe craton would extend that far, (as far as KAL017/018/019) the KAL sites would be located on the craton and the shift in terrane boundary would agree with the expectation of a resistive craton. Another supportive argument for the shifted boundary is the fact that in Gope (near KAL018/019) diamondiferous kimberlites were found (mining is supposed to start in 2012 (Read and Janse, 2009)), and diamondiferous kimberlites are known to appear on the edges of cratons (Jones et al., 2009).

Although the results shown represent the most preferred distortion model and strike direction for each site, that does not imply that any other strike direction will cause an unacceptably high RMS value. Therefore the decomposition was run for fixed strike angles from 0° to 90° in 1° intervals to see the effect on the resulting RMS misfit. Table 4.1 shows a list of strike angles that provide a good fit of the distortion model to the data (RMS < 1.0) and acceptable fits (RMS < 2.0) for all ZIM line sites. Three different frequency ranges were used to analyse the RMS values for all strike angles; one each related to crustal (5 - 35 km) and lithospheric depths (50 - 150 km) and one containing all available frequencies for each site. At some sites, the strike angle ranges are different for the crust, the lithosphere and the whole frequency range, which indicates that while a strike analysis simply carried out over all frequencies might give a good RMS fit, the determined strike direction does not necessarily conform with either the crustal or the lithospheric directions. The problem of the variation in preferred strike direction for different depth bands becomes more obvious looking at Figure 4.17, which illustrates the RMS misfit versus strike angle for all three depth ranges for two sites. The dots represent the individual RMS values at each frequency (in the chosen range) for all strike angles, whereas the colour of the symbol indicates, which period it is related to (hotter colours = higher frequencies/shorter periods). Site ZIM107 shows a clear minimum in RMS for all frequencies in the crustal depths band and in the band over all frequencies, whereas for lithospheric depths all strike angles have low RMS values. The vertical red line indicates the strike direction one would obtain performing a normal strike analysis for the same frequency range (the exact value is given in the top

Table 4.1: For all ZIM line sites the ranges of strike angles that provide a good fit of the distortion model to the data, i.e., average RMS misfit < 1.0 (or an acceptable fit, i.e., average RMS misfit < 2.0) were determined for crustal depths (5 km - 35 km), lithospheric depths (50 km - 150 km) and the whole frequency range using an error floor for 3.5%. (∗ indicates that no strike angles are found with an average RMS < 1.0 (< 2.0). ‡ indicates that no frequencies are available in this depths range.)

	STRIKE RANGES OF AVERAGE RMS MISFIT < 1.0 (< 2.0)		
SITE	CRUST	LITHOSPHERE	ALL FREQUENCIES
101	38° - 50° (0° - 90°)	-25° - 30° (0° - 90°)	∗ (2° - 45°)
102	27° - 32° (0° - 90°)	‡	∗ (0° - 90°)
103	0° - 90°	-53° - 21° (0° - 90°)	27° - 42° (0° - 90°)
104	0° - 90°	0° - 90°	∗ (18° - 37°)
105	0° - 90°	0° - 90°	∗ (-6° - 31°)
106	∗ (56° - 71°)	0° - 90°	∗ (∗)
107	∗ (43° - 61°)	0° - 90°	∗ (45° - 57°)
108	8° - 54° (0° - 90°)	0° - 90°	∗ (0° - 90°)
109	-2° - 33° (0° - 90°)	-14° - 17° (0° - 90°)	∗ (0° - 90°)
110	-9° - 39° (0° - 90°)	23° - 66° (0° - 90°)	∗ (0° - 90°)
111	0° - 90°	0° - 90°	0° - 90°
112	0° - 90°	-46° - 24° (0° - 90°)	∗ (0° - 90°)
113	0° - 90°	0° - 90°	15° - 42° (0° - 90°)
114	-10° - 3° (-27° - 20°)	3° - 24° (0° - 90°)	∗ (-9° - 20°)
115	∗ (47° - 62°)	-2° - 36° (0° - 90°)	∗ (∗)
116	∗ (26° - 64°)	0° - 90°	∗ (50° - 65°)
117	∗ (43° - 69°)	76° - 90° (62° - 96°)	∗ (69° - 78°)
118	∗ (-11° - 17°)	16° - 48° (0° - 90°)	∗ (∗)
119	∗ (-37° - 14°)	-7° - 52° (0° - 90°)	∗ (0° - 90°)
120	-16° - 39° (0° - 90°)	‡	0° - 90°
121	∗ (∗)	∗ (∗)	∗ (∗)
122	∗ (43° - 78°)	‡	∗ (58° - 99°)
123	56° - 75° (-61° - 10°)	∗ (∗)	∗ (65° - 72°)
124	0° - 90°	∗ (-67° - 15°)	0° - 90°
125	44° - 72° (0° - 90°)	∗ (36° - 83°)	∗ (30° - 85°)
126	3° - 57° (0° - 90°)	61° - 92° (0° - 90°)	∗ (0° - 90°)
127	13° - 60° (0° - 90°)	∗ (0° - 90°)	29° - 42° (0° - 90°)
128	59° - 64° (-58° - 5°)	∗ (0° - 90°)	∗ (45° - 86°)
129	-7° - 46° (0° - 90°)	∗ (24° - 62°)	∗ (23° - 50°)
130	13° - 45° (0° - 90°)	∗ (0° - 90°)	∗ (20° - 56°)
131	0° - 90°	∗ (23° - 38°)	∗ (33° - 43°)

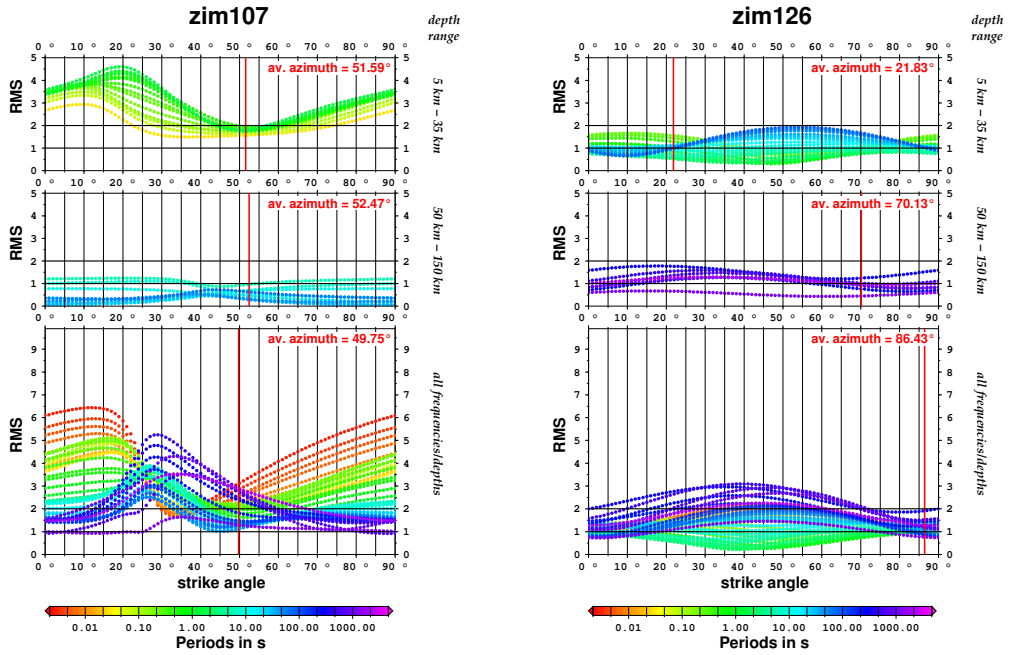

Figure 4.17: Figure showing the different RMS values for strike angles from 0° - 90° for the sites ZIM107 and ZIM126. The RMS values for the whole azimuth range are plotted for three different depth/frequency ranges: crustal depth (5-35 km), lithospheric depth (50-150 km) and over the whole frequency range. The colour coding is related to the frequencies. The red line indicates the strike direction one would obtain performing a normal strike analysis for the same frequency/depth range.

right corner as average azimuth). In the case of ZIM107 all three average azimuth values agree reasonably well, but that is not always the case, as ZIM126 shows. Unlike ZIM107, there is no clear RMS minimum apparent in any of the depth/frequency bands and all strike angles result in acceptably small RMS values. The individual strike analysis for each frequency band shows a huge difference between the average crustal angle of about 22° and the lithospheric angle of about 70°. The strike direction obtained for all frequencies is about 86°, again different, and roughly an average or mix of crustal and lithospheric azimuths (taking into account the 90° ambiguity). Therefore one should be careful with just applying one overall strike analysis, because it could be misleading. Similar plots for all ZIM line sites are compiled in Appendix B.3.

Multi-site, multi-frequency strike analysis was undertaken for numerous groups of different sites and period (or depth) bands. The sketch in Figure 4.18 (a) summarises the resulting strike directions for different groups of sites for the crust and lithospheric mantle. The group of sites (ZIM107 to ZIM114) above the dyke swarm shows a strike direction of about 20° E of N, but since there is the 90° ambiguity and the dyke swarm orientation is about 110° E of N the latter direction was chosen. Both groups of sites to the north and to the south of the dyke swarm showed varying strike direction (the range is given in parenthesis). Nevertheless an overall crustal strike direction of 55° E of N was chosen because it was a dominant direction for the crustal depths at all sites (except for the dyke swarm sites) and it is also the direction of the terrane boundary of the Ghanzi-Chobe and Magondi mobile belts based on the magnetic data. Figure 4.18 (b) shows the chosen strike directions for the crust, where the length of the arrow is related to the RMS misfit (the longer the better the

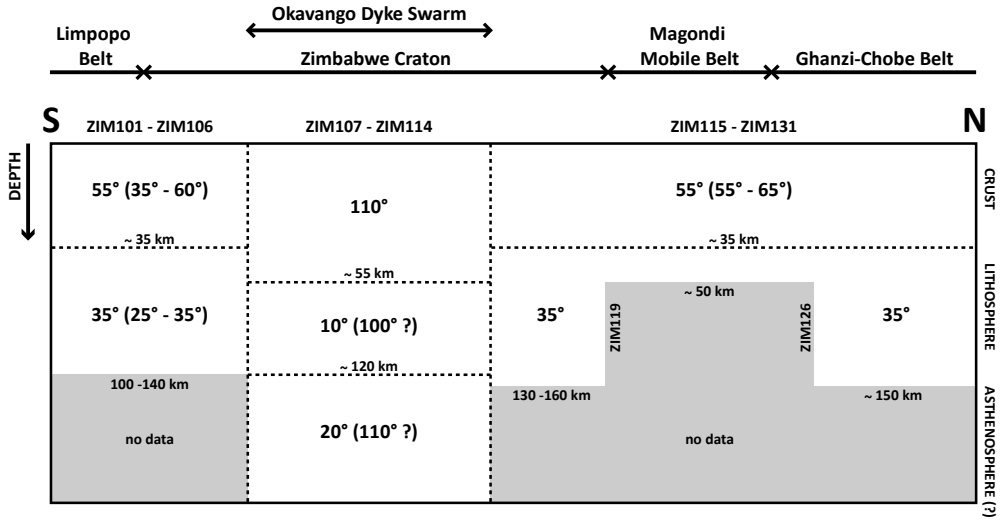

(a) Strike direction profile of the ZIM line.

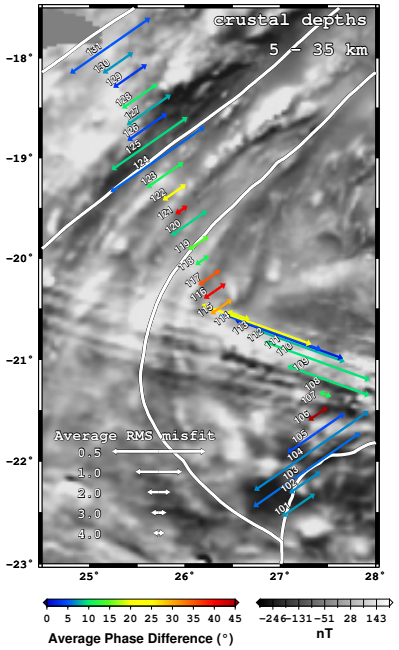

(b) Chosen strike direction for crustal depths.

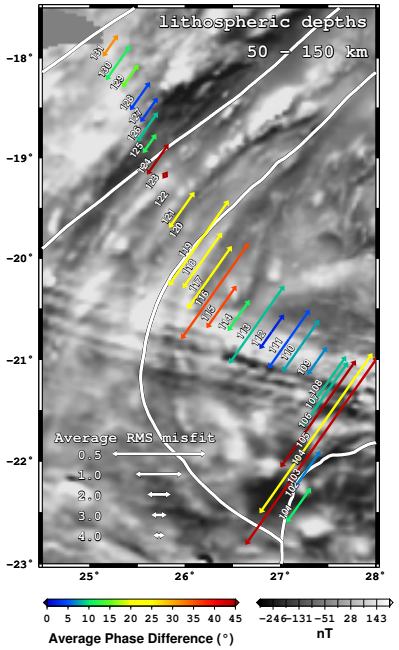

(c) Chosen strike direction for lithospheric depths.

Figure 4.18: Figure showing (a) a sketch of the different strike angles for different depths and areas of the ZIM profile. The values in parenthesis are the ranges of possible strike directions depending on the grouping of sites and frequencies, whereas the angle before is the one chosen as the final strike angle for that part of the profile. Below are the chosen strike directions plotted for (b) crustal (5 - 35 km) and (c) lithospheric (50 - 150 km) depths ranges. The colour coding indicates the average of the absolute phase difference in the two orthogonal directions, whereas the length of the arrows is related to the average RMS misfits (the larger the arrow the smaller the average RMS value and therefore the better the goodness-of-fit).

goodness-of-fit) for that site, having enforced the chosen strike direction, and the colour represents the phase difference.

As the sketch (a) shows, there is an area with a lack of information in the lithospheric mantle between ZIM119 and ZIM126 due to the small maximum penetration depth at these sites. For the sites north and south of the dyke swarm a strike direction of 35° E of N dominates, whereas the dyke swarm sites prefer a strike angle close to 10° E of N (and deeper again of 20° E of N), that may or may not be related to the dyke swarm direction. Including the dyke sites in a large group of sites for the strike analysis, the 35° E of N remains the dominant angle. Figure 4.18 (c) shows the chosen strike direction for the lithospheric mantle with its RMS values (arrow length) and phase differences (colour) for each site. None of the dyke sites indicates a poor fit to the enforced strike direction of 35° E of N.

Since 2D modelling requires one single strike direction, the lithospheric mantle direction (35° E of N) was chosen for the inversion of the whole data set. Firstly, because the major interest lies in the lithospheric structures and the depth to the electrical lithosphere-asthenosphere boundary and secondly, because the data set has an approximately 20 km site spacing and is undersampled with respect to providing a detailed image of the crust. While for the results shown in Figure 4.18, where each depth band was decomposed and rotated separately, for the inversion, a consistent data set is required with one distortion model suitable for all frequencies of each site. Table 4.2 lists the results of a single-site strike analysis using one band over all frequencies and an enforced strike direction of 35° E of N. For each site the twist and shear angles of the distortion model are listed as well as the overall, the crustal and the lithospheric average, minimum and maximum phase differences. The last column gives the average RMS values for the crust, lithospheric mantle and all frequencies. The information in Table 4.2 allows one to distinguish if a large overall value (in twist, shear, phase difference and/or RMS) is representative for the whole site or only for crustal or lithospheric mantle depths. Note that the crustal depth range (5 - 35 km) does not start at the surface and there is also a gap between the crustal and the lithospheric depth range (50 - 150 km).

Only a few sites indicate strong distortion effects: ZIM105, ZIM108, ZIM113 and ZIM114, which are all very close to the dyke swarm, and ZIM124. Figure 4.19 shows a comparison of the true north data from site ZIM114 (a) with the responses obtained after a simple rotation into strike direction (b) and after decomposition into strike direction (c). The original and the rotated data show very large diagonal element resistivity values, which may indicate a 3D environment. The decomposition procedure tries to fit the data to a distortion model that results in the required zero-value diagonal elements (10^{-11} Ωm to 10^{-14} Ωm can be considered as zero, and the phase values become meaningless) to make it suitable for a 2D inversion. ZIM114 shows clearly the need for decomposition, rather than rotation, to prepare data for 2D inversion and interpretation.

Also several very large phase differences are listed in Table 4.2; e.g., ZIM101, ZIM102 and ZIM116 have a large overall maximum phase difference whereas neither the crustal nor the lithospheric values are of similar size. At site ZIM101, the TE phases for periods < 0.9 s (not deep enough to fall into the crustal depth range) are out of quadrant. For ZIM102 a large scatter of phase values can be found for periods > 800 s (below the crustal depth range). For ZIM116 the period range of 1 - 4 s (between the crustal and lithospheric depth

Table 4.2: Table listing the constrained distortion decomposition values for a geological strike direction of 35° E of N. Shear and twist angles are a measure of the strength of galvanic distortion, whereas the phase difference can be used as an indicator of dimensionality. The goodness-of-fit of the distortion model to the observed data is related to a low average RMS misfit. The distortion models were estimated for each individual site over a single frequency band containing all frequencies available. The average, minimum and maximum phase difference values as well as the average RMS misfit are given for the whole frequency band, but also values for parts of the frequency band related to crustal (5 - 35 km) and lithospheric (50 - 150 km) depths ranges (all frequencies/crustal depths/lithospheric depths). (‡ indicates that no frequencies are available in this depth range.)

			ABSOLUTE PHASE DIFFERENCE			AVERAGE
SITE	SHEAR	TWIST	AVERAGE	MINIMUM	MAXIMUM	RMS MISFIT
101	-5.9	-6.4	18.2 / 9.1 / 16.9	0.1 / 2.7 / 0.1	110.7 / 15.4 / 24.6	1.56 / 1.09 / 1.70
102	11.8	5.7	11.9 / 10.8 / ‡	0.6 / 6.3 / ‡	106.7 / 19.6 / ‡	1.18 / 1.08 / ‡
103	3.6	-6.7	11.2 / 5.7 / 7.3	2.7 / 3.0 / 2.7	21.4 / 8.3 / 12.6	0.88 / 0.64 / 0.97
104	5.2	-0.1	23.6 / 21.9 / 20.5	5.2 / 12.3 / 7.8	50.8 / 48.2 / 31.6	1.68 / 2.28 / 1.32
105	24.2	4.4	10.1 / 2.3 / 15.1	0.1 / 0.2 / 4.4	37.7 / 6.6 / 20.9	2.09 / 1.77 / 1.74
106	-8.3	5.8	71.7 / 57.3 / 190.1	1.0 / 41.1 / 96.3	242.8 / 92.9 / 242.8	5.01 / 5.92 / 6.78
107	-9.8	-7.4	17.8 / 23.5 / 21.8	0.3 / 3.3 / 0.6	42.9 / 40.1 / 41.3	2.58 / 2.59 / 2.53
108	-18.3	-8.7	9.6 / 8.7 / 7.6	0.7 / 1.0 / 0.9	21.8 / 16.1 / 14.4	1.04 / 0.91 / 0.91
109	-9.1	2.0	8.3 / 6.6 / 6.4	0.0 / 0.2 / 0.3	15.7 / 11.6 / 10.7	1.41 / 1.34 / 1.52
110	-12.3	14.9	6.1 / 6.8 / 7.4	0.1 / 0.2 / 2.6	11.2 / 11.2 / 9.9	1.15 / 1.17 / 1.04
111	-9.5	0.7	4.5 / 1.0 / 4.7	0.0 / 0.0 / 0.6	17.1 / 2.2 / 8.2	0.79 / 0.55 / 0.84
112	-2.6	1.9	3.7 / 4.4 / 2.1	0.1 / 0.2 / 0.1	10.5 / 9.7 / 5.7	1.40 / 0.81 / 1.27
113	-27.8	12.9	9.5 / 11.1 / 11.2	0.0 / 9.1 / 0.1	19.3 / 15.2 / 18.3	0.91 / 0.49 / 0.42
114	-24.9	-28.2	16.8 / 23.9 / 11.2	4.2 / 18.5 / 6.5	34.6 / 32.7 / 16.9	2.93 / 3.68 / 1.21
115	9.4	11.9	18.6 / 22.0 / 22.7	0.1 / 5.6 / 12.7	38.6 / 29.6 / 31.2	2.48 / 2.52 / 1.88
116	11.7	3.9	16.7 / 17.1 / 37.2	0.0 / 10.5 / 26.2	82.4 / 28.2 / 43.1	3.21 / 3.46 / 3.68
117	10.2	4.5	10.8 / 14.3 / 26.1	0.0 / 3.8 / 6.3	46.2 / 31.4 / 38.2	3.63 / 3.66 / 5.57
118	6.3	6.3	8.8 / 8.8 / 20.8	0.0 / 1.3 / 4.6	44.8 / 15.5 / 41.1	3.19 / 2.97 / 5.53
119	3.8	1.1	5.7 / 9.6 / 23.7	0.0 / 0.9 / 21.2	26.1 / 20.6 / 26.1	1.79 / 2.56 / 4.21
120	1.2	0.2	4.6 / 9.7 / ‡	0.0 / 0.6 / ‡	36.8 / 36.8 / ‡	0.95 / 1.31 / ‡
121	13.6	18.2	14.9 / 30.1 / 13.9	0.1 / 1.3 / 3.5	43.1 / 43.1 / 22.0	5.12 / 4.51 / 5.36
122	8.8	2.4	4.3 / 8.7 / ‡	0.0 / 2.2 / ‡	11.7 / 11.7 / ‡	2.71 / 3.62 / ‡
123	-8.2	-0.6	9.7 / 6.1 / 33.9	0.1 / 3.8 / 15.8	56.7 / 7.8 / 56.7	3.20 / 2.32 / 7.07
124	-36.9	39.8	21.0 / 10.1 / 38.2	0.5 / 1.3 / 19.7	72.9 / 18.6 / 72.9	0.57 / 0.43 / 2.04
125	-1.5	3.6	8.4 / 7.3 / 7.8	0.3 / 0.6 / 0.3	47.2 / 14.8 / 16.9	1.79 / 1.59 / 2.83
126	-1.4	3.9	5.0 / 5.4 / 5.3	0.1 / 0.1 / 1.6	16.1 / 10.1 / 16.1	1.46 / 0.92 / 2.43
127	2.7	3.4	8.1 / 9.1 / 5.8	0.1 / 1.3 / 2.8	20.2 / 16.3 / 11.6	0.95 / 0.54 / 1.51
128	4.0	-1.6	5.5 / 8.3 / 6.0	0.0 / 0.9 / 1.8	17.6 / 15.0 / 14.3	2.16 / 2.13 / 1.91
129	-1.3	6.5	9.3 / 7.4 / 15.0	0.6 / 5.5 / 8.2	22.1 / 17.3 / 22.0	1.54 / 1.03 / 2.04
130	5.6	1.9	8.3 / 9.1 / 11.8	0.1 / 0.2 / 6.2	23.2 / 22.8 / 20.7	1.38 / 1.39 / 1.80
131	-7.5	9.8	13.3 / 6.0 / 32.9	0.9 / 0.9 / 29.8	35.2 / 14.6 / 35.2	1.92 / 1.37 / 1.86

ranges) contains TE phases out of quadrant. ZIM123 and ZIM124 have large overall, but also lithospheric, maximum phase differences as well, which are related to TE phase and TM phase respectively being out of quadrant at long periods (> 300 s and > 100 s respectively). One relatively extreme site is ZIM106 where the TM mode is out of quadrant over decades > 2 s. Although a large maximum phase difference seems to be a good indication of data with phases out of quadrant, one should be aware that if both modes are out of quadrant and close to each other the phase difference will remain small although both are out of quadrant. All data points with phases out of quadrant have to be removed before the 2D inversion, e.g., using a D^+ consistency scheme for guidance.

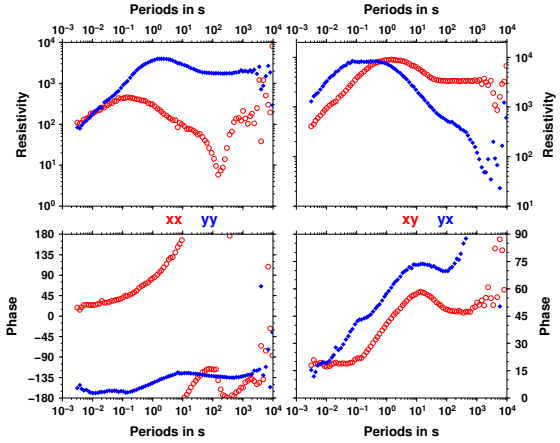

(a) Original ZIM114 data (true north)

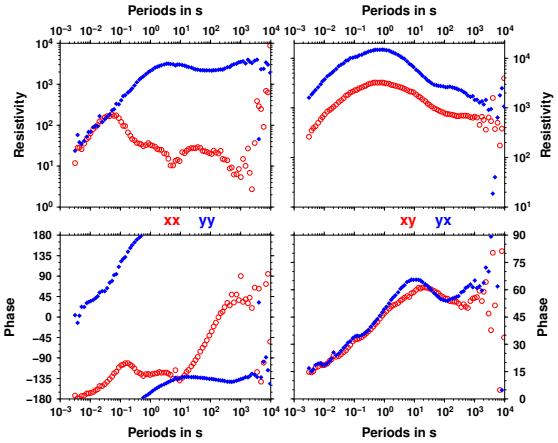

(b) ZIM114 data rotated into strike direction

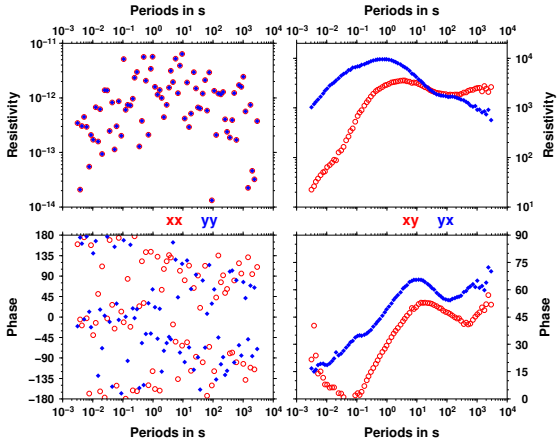

(c) ZIM114 data decomposed into strike direction

Figure 4.19: Figure (a) shows the original data of ZIM114 orientated in the direction of true north, while (b) shows the same data rotated and (c) decomposed (using the program STRIKE) into the strike direction of 35° E of N. Note the different scale of the y-axis of the resistivity plot of the diagonal elements in (c) (compared to the same panel in (a) and (b)).

4.3 SITES ABOVE THE OKAVANGO DYKE SWARM

Two groups of MT sites are located above the Okavango dyke swarm. The eastern area is around Francistown and includes sites of the ZIM line and of the MOF line; the western group is located southeast of the Okavango delta and is close to Maun consisting of sites from the MAK and MOF profiles. These two towns are used as names for the groups of sites and Table 4.3 lists the names of all sites included in each group. Figure 4.20 (a) shows a map of these sites and areas.

Although strike analysis of sites from both areas indicates a dominant direction parallel (or perpendicular) to the dyke orientation, the Niblett-Bostick resistivity maps (Figures 4.5 and 4.6) showed very different resistivity values for these two groups of sites. The difference in

Table 4.3: Table listing the names of the sites associated with either the Maun area or the Francistown area. See Figure 4.20 for a location map of these areas.

MAUN AREA			FRANCISTOWN AREA			
MAK008	MAK009	MAK010	MOF123	MOF124	MOF125	MOF126
MOF103	MOF104	MOF105	MOF127	ZIM107	ZIM108	ZIM109
MOF106	MOF107	MOF108	ZIM110	ZIM111	ZIM112	ZIM113
MOF109			ZIM114			

resistivity values between the two groups seems to be a regional effect, and therefore static shifts are not a very likely cause. Static shift is rather a local-effect that causes the up or down shifting of the resistivity curve at individual sites. Since static shifts only affect the level of the resistivity curve, but not its shape nor the phase curve, it is easy to test the static shift hypothesis. Figure 4.20 shows the XY (b) and YX (c) resistivity and phase curves for the data decomposed into the strike direction of the dyke swarm (110° E of N). All curves for the sites from the Francistown area are quite similar, whereas the cluster of curves from the Maun area is also consistent but significantly different from the Francistown group. The shapes of these two clusters of resistivity curves are very different, as the shapes of the phase curves are also not matching. Therefore a simple static shift cannot account for the different resistivity values shown in the Niblett-Bostick resistivity maps of the two areas. The Francistown sites are characterised by at least two decades wide envelopes of the XY and YX resistivity curve clusters and the phase curves are only broadly similar. The Francistown sites are clearly affected by intra- and inter-site static effects. Figure 4.21 shows the response curves of each individual site of both groups. Whereas the Maun sites (a) are 1D for the first decades and all have a similar shape across the entire frequency band, there is a lot scatter in the resistivity level of the Francistown sites (b) between neighbouring sites as well as between the two modes for each site. Figure 4.22 shows phase difference curves of the D^+ smoothed data for both groups of sites. It shows clearly that the Maun sites have phase differences far below 10° at periods < 10 s (or rather depths < approx. 5 km) and therefore are 1D in this part of the data. The Francistown sites on the other hand show no period ranges where phase differences are less than 10° for more than a quarter of a

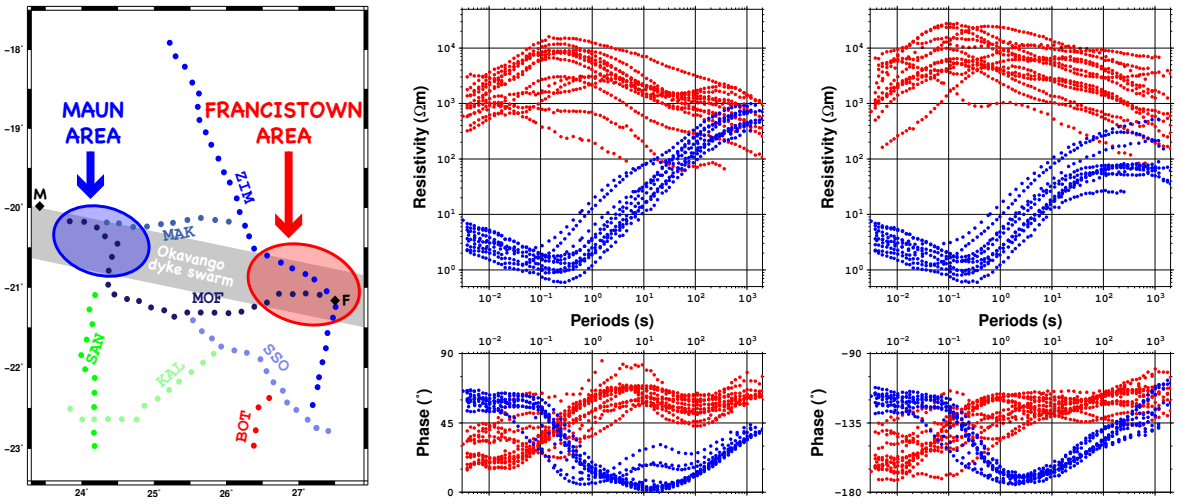

(a) Location map of Maun and Francistown areas

(b) Resistivity and phase curves - XY component

(c) Resistivity and phase curves - YX component

Figure 4.20: Resistivity and phase curves of sites from two different areas above the Okavango dyke swarm. On the left (a) is a map of the site locations relative to the dyke swarm and the ellipses indicate which sites are includes in which area: Maun area or Francistown area. (The names of the sites included in each area can be found in Table 4.3). The towns of Maun and Francistown are represented by the black diamonds labelled with M and F, respectively. The same colour coding by area is used in the two adjacent figures, where the resistivity (top) and phase (bottom) curves are plotted for all selected sites. The XY components are shown in (b) and the YX components in (c) (after decomposition into the common strike direction of 110° E of N, which is the orientation of the Okavango dyke swarm).

decade in period, if at all (expect MOF126 and ZIM111). Most of the time the phase split is between 10° and 20° (sometimes even higher) and reduces where phase crossings appear (see Figures 4.21 and 4.22). Whereas none of Maun area sites exhibit D^+ inconsistencies, several sites of the Francistown area do (MOF123: in the YX mode for periods < 0.01 s and in the XY mode at about 10 s, MOF124: XY for > 0.3 s, MOF125: YX for 0.025 - 1 s and 3 - 30 s, ZIM108: YX for < 0.01 s, ZIM109: YX for < 0.1 s, ZIM113: XY for 0.2 - 18 s).

Figure 4.19 showed the original data for ZIM114, which is an example of the high diagonal element resistivity values of the Francistown area that indicates a 3D environment. Although the values are related to a different strike direction, the distortion model values for twist and shear in Table 4.2 are relatively high for some of the Francistown sites (ZIM108, ZIM110, ZIM113 and ZIM114) compared to the rest of the ZIM line sites, which also suggests a more complicated near-surface structure than a simple 1D or 2D case.

The Okavango dyke swarm consists of Karoo-aged dolerite dykes (Elburg and Goldberg, 2000; Aubourg et al., 2008). Based on deep electrical soundings investigating the Karoo Supergroup in South Africa, van Zijl (2006) estimates that the dolerites have an average resistivity of 30000 Ωm, as determined exclusively from soundings close to or at the sites of deep boreholes, where the distribution and thickness of the dolerites and hosting sediments were known. The dyke swarm is therefore a resistive structure that should enhance the resistivities observed in that area. Hence, the conductive Maun area is the anomalous region

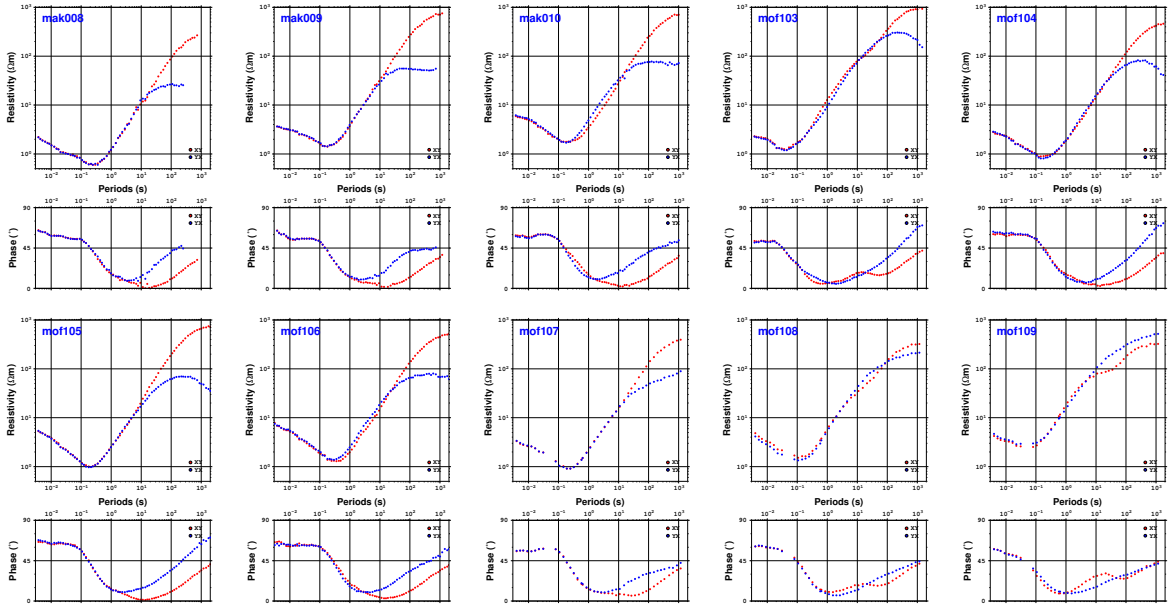

(a) Resistivity and phase curves - Maun sites

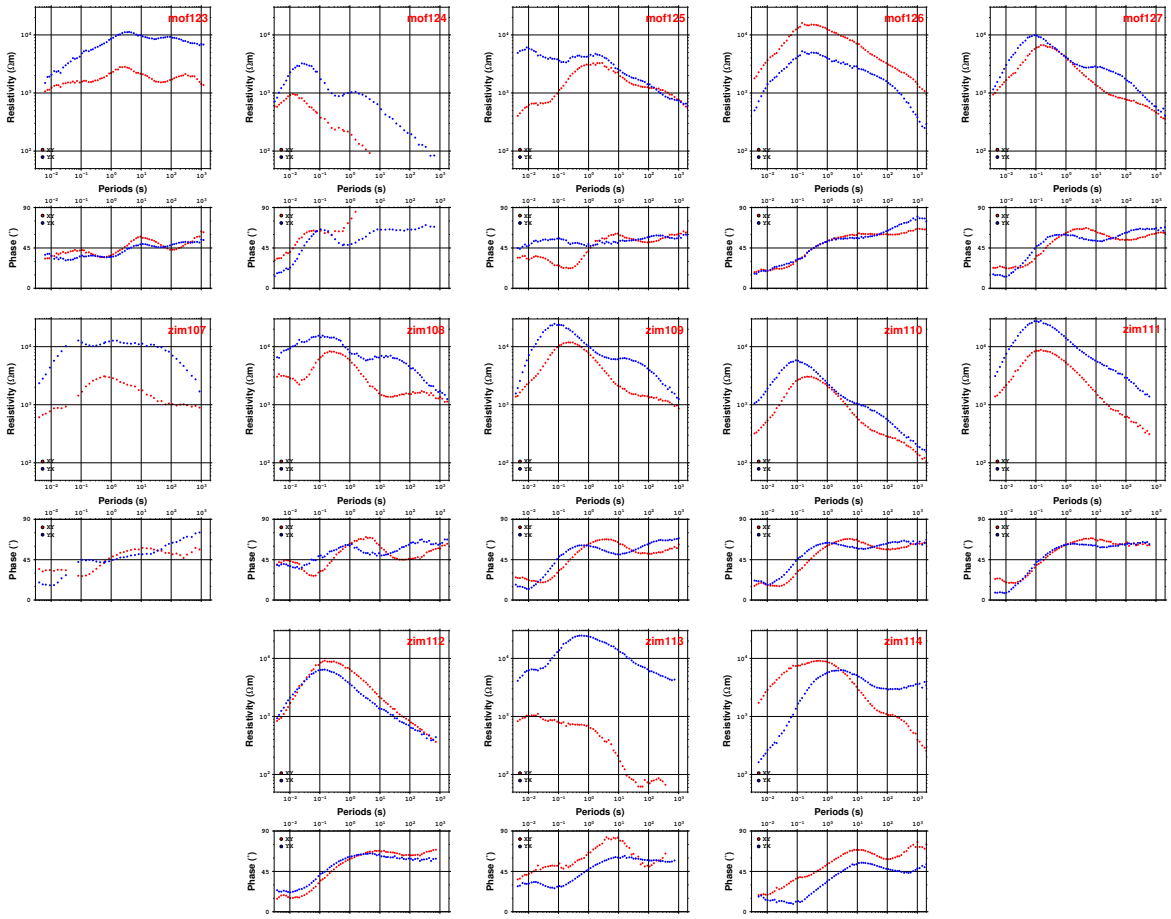

(b) Resistivity and phase curves - Francistown sites

Figure 4.21: Resistivity and phase curves for the Maun (a) and Francistown (b) sites. The Maun sites show 1D responses for the first decades, whereas the Francistown sites obviously suffer from static shifts.

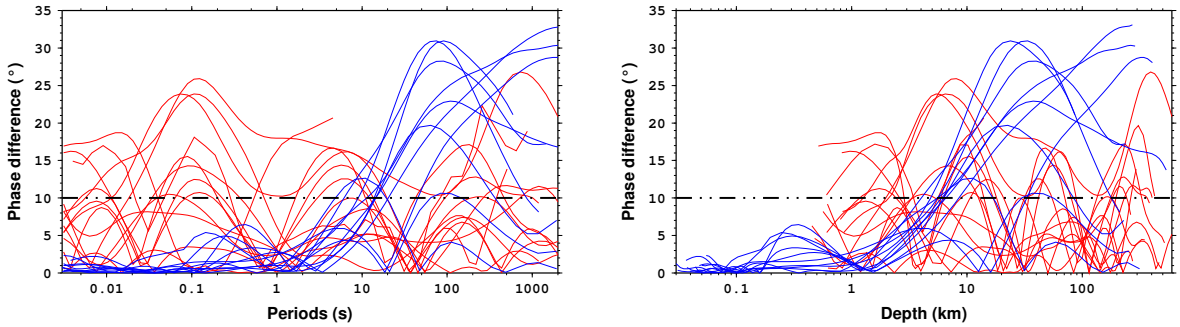

(a) Phase difference vs. periods

(b) Phase difference vs. depth (in log scale)

Figure 4.22: Phase difference curves of the D^+ smoothed data versus periods (a) and depth (b), decomposed to 110°, for the Maun and Francistown sites. The black dashed line indicates a phase difference of 10°, which is assumed to be the maximum difference for a largely 1D environment.

of the two and the open question is why is a resistive structure missing in the Maun area? In the following, the Maun area data are investigated further to address this question.

Taking into account that the individual dykes are on average about 17 m wide (see Section 3.1.5), they are more of an anisotropic feature than a 2D structure on the scale of the MT soundings. Therefore the 1D anisotropic forward modelling code by Pek and Santos (2002) was used to fit the data of one example site (MOF107) of the Maun group. Since the data were decomposed into the dyke swarm direction, the x-axis of the coordinate system of the site (and therefore the XY mode data) is parallel to the dyke direction and the y-axis (and YX mode data) is perpendicular to it. Figure 4.23 shows a sketch of the dyke direction and the orientation of the XY and YX modes for the decomposed data. If the anisotropic direction (i.e., the orientation of the foliation strike) is parallel to the dyke swarm, and therefore also parallel to the XY mode, then the XY mode data should be more conductive than the YX mode data (a). If, on the other hand, the anisotropy is perpendicular to the dyke swarm, then the YX mode becomes the more conductive mode (b). The sketch already gives the suggestion that the structure causing the split in the data of site MOF107 cannot be the dyke swarm, as the more conductive mode in the observed data is the YX mode (suggesting an anisotropic direction perpendicular to the dyke swarm direction, see Figure 4.24).

For a single site investigation 1D anisotropic modelling is more flexible than a 2D isotropic approach as it allows anisotropy and/or fault-like structures of different layers to be orientated in more than just one direction. Therefore Pek and Santos' (2002) code is used to fit the data of MOF 107. Figure 4.24 shows a sketch (a) of the 1D anisotropic model that fits the data of this site. The model is an isotropic layered Earth with an anisotropic layer from about 10 km to about 125 km. The anisotropic strike direction was assumed to be parallel (b) and perpendicular (c) to the dyke swarm. As expected, an anisotropic strike angle of 110° E of N fits the data but the modes are flipped, whereas the anisotropic strike direction of 20° E of N matches the data correctly. The depth extent of the anisotropic layer, but even more the anisotropic strike direction, exclude the dyke swarm as the possible cause of the mode split.

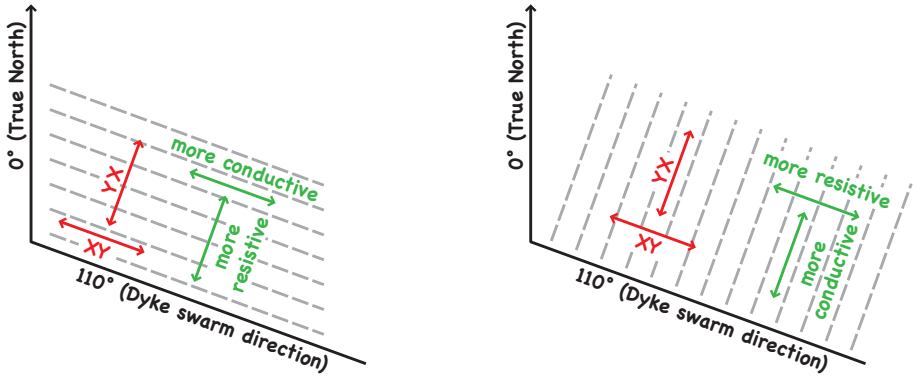

(a) Structure/anisotropy parallel to the dyke swarm direction

(b) Structure/anisotropy perpendicular to the dyke swarm direction

Figure 4.23: Sketch in plan view of structure or anisotropy (a) parallel and (b) perpendicular to the orientation of the dyke swarm. As the data are decomposed into the direction of the dyke swarm, the XY mode data are parallel and the YX mode data are perpendicular (red arrows) to the dyke swarm direction (110° E of N). The grey dashed lines indicate the orientation of the structure or anisotropy and the green arrows indicated the more conductive and more resistive directions. For the structure/anisotropy parallel to the dyke swarm orientation, the XY mode is the more conductive direction (a), whereas for the perpendicular direction the YX mode data are more conductive (b).

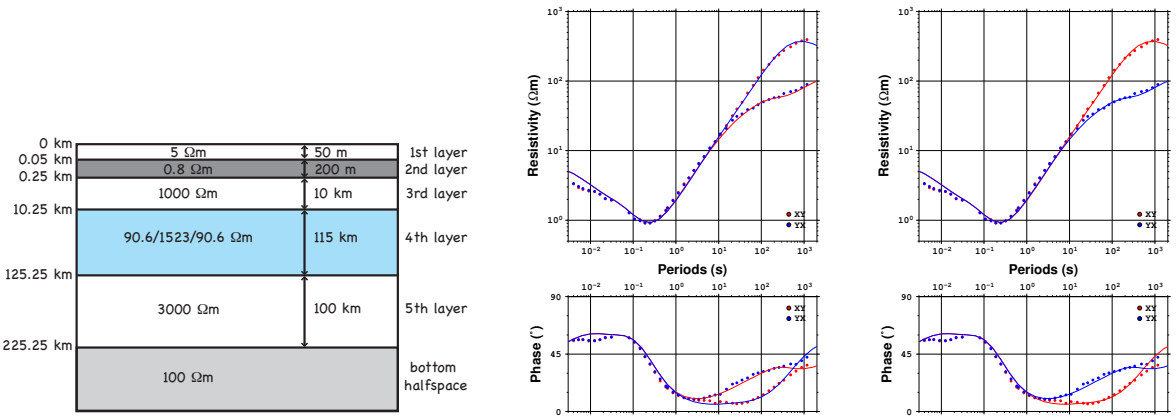

(a) Sketch of the 1D anisotropic model

(b) Anisotropic strike direction: 110° E of N

(c) Anisotropic strike direction: 20° E of N

Figure 4.24: Forward 1D anisotropic modelling of site MOF107 using Pek and Santos' (2002) code. The decomposed (to 110° E of N) data of MOF107 are represented by the symbols, the solid lines are the 1D forward modelling results. The model that fits the data is shown in (a). It is a 1D layered earth, where the third layer is anisotropic. If the anisotropic strike direction is set to be 110° E of N (along the dyke swarm direction) the modes between observed and modelled data are flipped (b). An anisotropic strike direction of 20° E of N (perpendicular to the dyke swarm direction) fits the data well (with the correct mode modelled to be the more conductive).

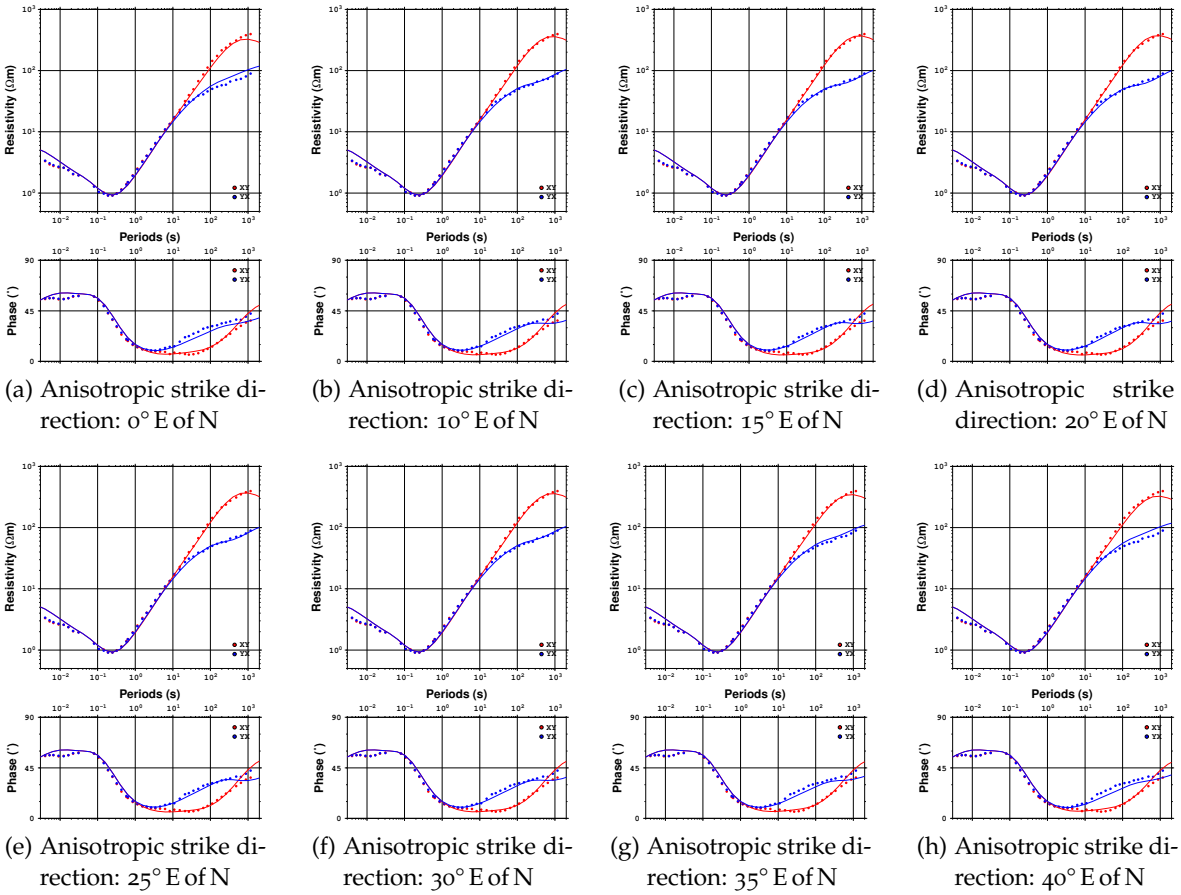

(a) Anisotropic strike direction: 0° E of N

(b) Anisotropic strike direction: 10° E of N

(c) Anisotropic strike direction: 15° E of N

(d) Anisotropic strike direction: 20° E of N

(e) Anisotropic strike direction: 25° E of N

(f) Anisotropic strike direction: 30° E of N

(g) Anisotropic strike direction: 35° E of N

(h) Anisotropic strike direction: 40° E of N

Figure 4.25: Forward 1D anisotropic modelling using Pek and Santos' (2002) code to constrain the anisotropic strike direction. The decomposed (to 110° E of N) data of MOF107 are represented by the symbols. The solid lines show the synthetic 1D anisotropic data obtained from the model sketched in Figure 4.24 (a) by choosing different anisotropic strike directions (specified beneath each plot).

Figure 4.25 shows various models testing anisotropic strike angles for the model shown in Figure 4.24 to estimate a range of acceptable strike directions. Anisotropic strike angles of 0° E of N and 40° E of N already show recognisable deviations from the observed data. An angle of 35° E of N, which is the angle identified for the Magondi Mobile Belt on the ZIM line (at lithospheric depth), also does not fit the data as well as angles of 10° - 30° E of N. The location of the Maun area is in a part of the Magondi Mobile Belt where the orientation of the belt rotates to a more north-south direction than observed in the vicinity of the ZIM line, which conforms with the orientation of the large negative magnetic anomaly found in that region (see Figure 3.10). Therefore, an angle of slightly less then 35° E of N seems reasonable.

To obtain constraints on the depth to the top of the anisotropic layer, the thickness of the third layer (just above the anisotropic layer) is varied, and the resistivity is changed to conserve the conductance of that layer. Figure 4.26 shows the results of the 1D forward modelling for layer thicknesses of 1 km (10000 Ωm), 2 km (5000 Ωm), 5 km (2000 Ωm), 10 km (1000 Ωm), 15 km (666.67 Ωm), 20 km (500 Ωm), 50 km (200 Ωm) and 100 km (100 Ωm), keeping all the other model parameters unchanged (anisotropic strike direction is 20° E of N). The period of the mode split, especially, gives a strong indication that the top of the

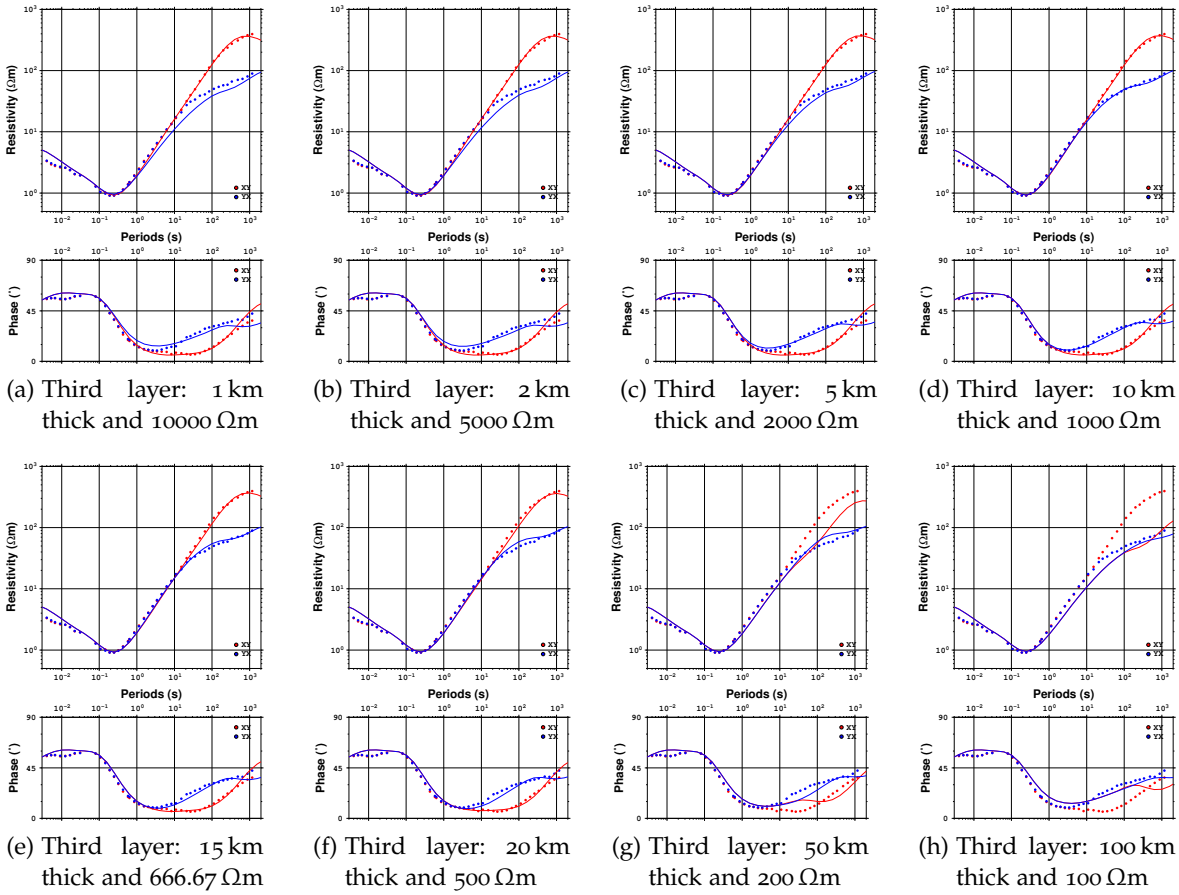

(a) Third layer: 1 km thick and 10000 Ωm

(b) Third layer: 2 km thick and 5000 Ωm

(c) Third layer: 5 km thick and 2000 Ωm

(d) Third layer: 10 km thick and 1000 Ωm

(e) Third layer: 15 km thick and 666.67 Ωm

(f) Third layer: 20 km thick and 500 Ωm

(g) Third layer: 50 km thick and 200 Ωm

(h) Third layer: 100 km thick and 100 Ωm

Figure 4.26: Forward 1D anisotropic modelling using Pek and Santos' (2002) code to constrain the top of the anisotropic layer. The decomposed (to 110° E of N) data of MOF107 are represented by the symbols. The solid lines show the synthetic 1D anisotropic data obtained from the model sketched in Figure 4.24 (a) by variation of the thickness and resistivity (equivalent conductances) of the layer above the anisotropic layer (thickness and resistivity of third layer are specified beneath each plot).

anisotropic layer is at about 10 - 15 km. An estimation the thickness of the anisotropic layer is more difficult. Assuming that in the anisotropic layer the background resistivity and the anomalous resistivity contribute equally to the principal anisotropic resistivities, then the background resistivity of the anisotropic layer is equal to the resistivity of the layer beneath (the fifth layer). Modifying the thicknesses of both the anisotropic layer and the layer beneath it (keeping their combined thickness the same) gives a suggestion of the minimum depth extent of the anisotropy. Figure 4.27 shows the results of the thickness test. Whereas the minimum thickness of the anisotropic layer seems to be about 100-115 km, a maximum thickness cannot be identified. Even extending the anisotropic layer to 215 km (the combined thickness of layers four and five) does not show a significant mismatch between observed and modelled data (Figure 4.27 (h)).

As a final test, the third layer, which has an isotropic resistivity of 1000 Ωm and a depth extent from 250 m to about 10 km (Figure 4.28 (a)), is replaced by an anisotropic layer to investigate whether the dykes have any effect on the data ((b) and (c)). The anisotropic strike direction has been set to 110° E of N and the anisotropic dip angle and slant an-

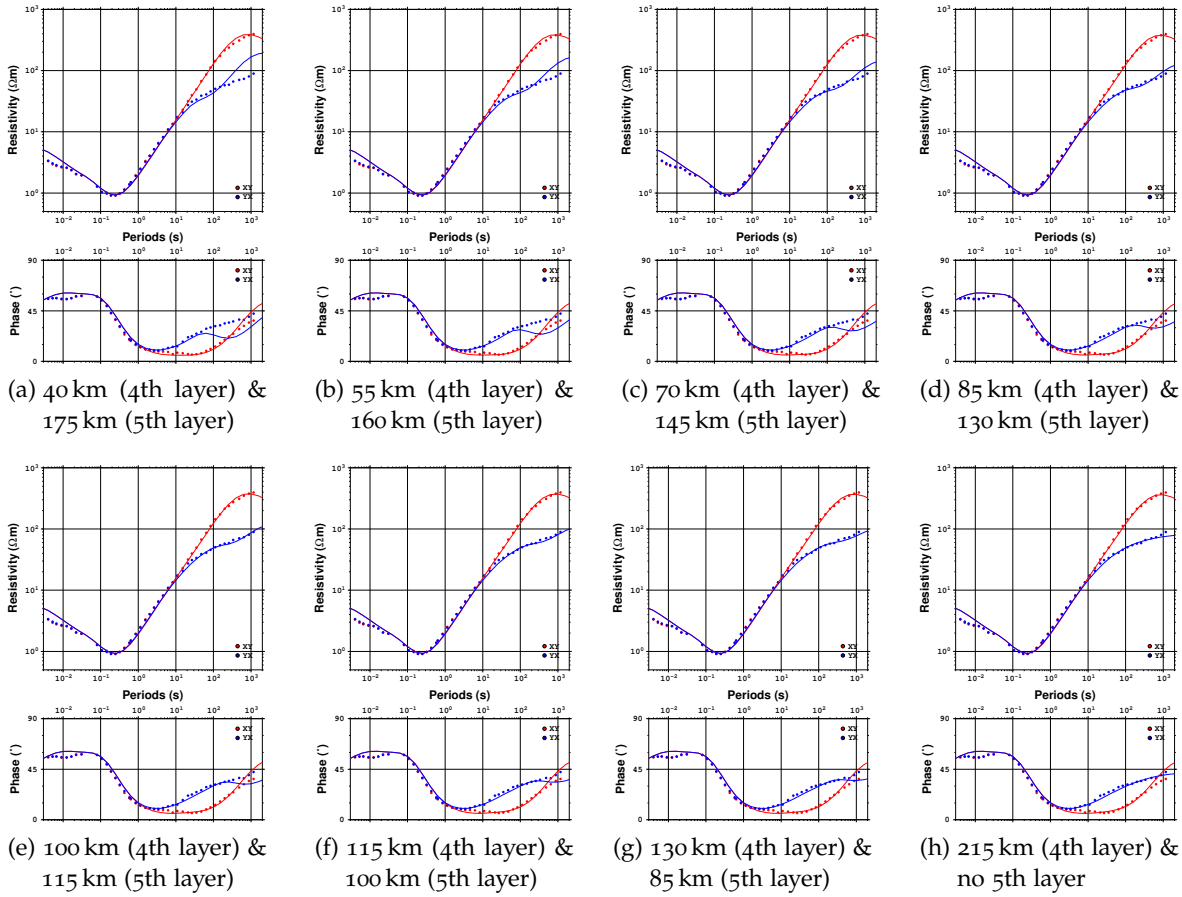

(a) 40 km (4th layer) & 175 km (5th layer)

(b) 55 km (4th layer) & 160 km (5th layer)

(c) 70 km (4th layer) & 145 km (5th layer)

(d) 85 km (4th layer) & 130 km (5th layer)

(e) 100 km (4th layer) & 115 km (5th layer)

(f) 115 km (4th layer) & 100 km (5th layer)

(g) 130 km (4th layer) & 85 km (5th layer)

(h) 215 km (4th layer) & no 5th layer

Figure 4.27: Forward 1D anisotropic modelling using Pek and Santos' (2002) code to constrain the thickness of the anisotropic layer. The decomposed (to 110° E of N) data of MOF107 are represented by the symbols. The solid lines show the synthetic 1D anisotropic data obtained from the model sketched in Figure 4.24 (a) by variation of the thicknesses of the anisotropic layer and the layer below it (thicknesses of fourth and fifth layers are specified beneath each plot).

gle were set to zero as the dykes are described by Le Gall et al. (2005) as vertical (see Section 3.1.5). The principal anisotropic resistivities have been calculated using Equations 2.86 and 2.89 based on a 1000 Ωm background resistivity and 30000 Ωm resistivity for the dykes. Assuming a 2.6% spatial dilatation of the dykes yields principal resistivities of 1025.8 Ωm/1754 Ωm/1025.8 Ωm for the anisotropic layer. Such an anisotropic layer causes a nearly unrecognisable change to the response curves (b). As such a small number of dykes only enhances the anisotropic resistivities by a small amount, the number of dykes was increased to the 12.2% dilatation found in the Francistown area (1133.7 Ωm/4538 Ωm/1133.7 Ωm, (b)). Even if the number of dykes is comparable to the Francistown area, the dyke signature still cannot be identified in the MT data. The small number of dykes in the Maun area is therefore not the only reason why the dykes do not appear in the Maun data set. The screening effect of the very conductive near-surface layers also contributes to hiding the signal of the dykes.

As the 1D anisotropic model is fit by using one single anisotropic layer, the data can be equally well fit by a 2D model. Figure 4.29 (a) shows a sketch of the 2D model, which has a

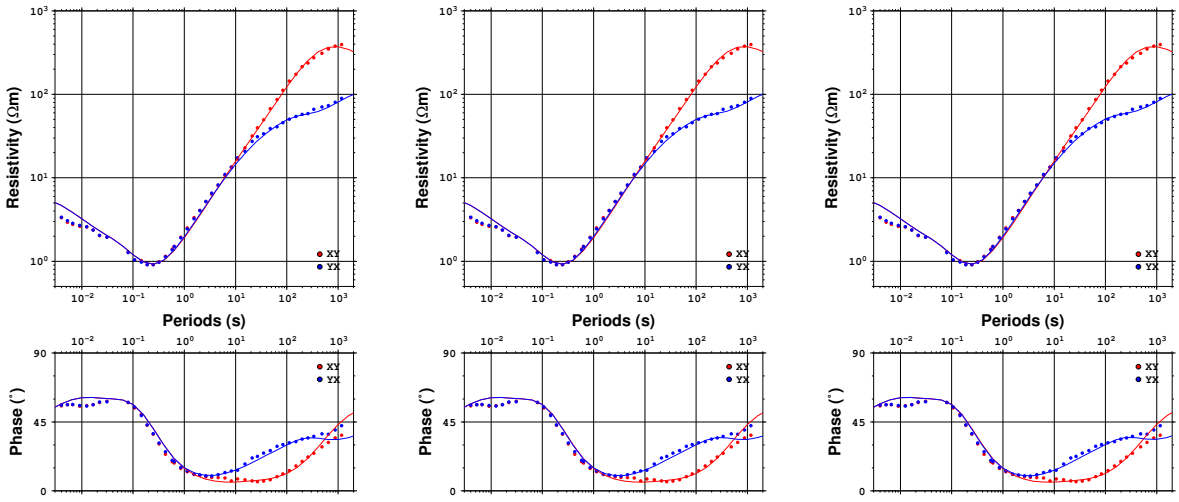

(a) Third layer: isotropic (1000 Ωm)

(b) Third layer: anisotropic (1025.8 Ωm/1754 Ωm/1025.8 Ωm)

(c) Third layer: anisotropic (1133.7 Ωm/4538 Ωm/1133.7 Ωm)

Figure 4.28: Forward 1D anisotropic modelling using Pek and Santos' (2002) code to try to identify a response of the dyke swarm in the data. The decomposed (to 110° E of N) data of MOF107 are represented by the symbols, the solid lines are the 1D forward modelling results. The isotropic third layer (a) has been replaced by an anisotropic layer with strike direction of 110° E of N. Based on a 1000 Ωm background resistivity and 30000 Ωm for the dykes the anisotropic principal resistivities have been calculated (see Equations 2.86 and 2.89) to simulate the 2.6% dilatation of dykes as observed for the Maun area (b) and 12.2% dilatation as present in the Francistown area (c).

fault-like structure to replace the anisotropic layer. The 2D forward modelling responses have been calculated using WinGLink® from Geosystem (Mackie et al., 1988; Rodi and Mackie, 2001). Unfortunately the minimum resistivity value that one can specify in the code is 1 Ωm and therefore the resistivity of the second layer (0.8 Ωm) cannot be set accurately. The solid line in Figure 4.29 (b) shows the responses obtained from WinGLink®. The phase curves fit well and the shape of the resistivity curves is very similar to the curves in the observed data. To compensate for the upwards static shift of the resistivity curves caused by using the wrong resistivity value for the second layer, both resistivity curves are multiplied by a factor 0.8 (dashed lines in (b)). For a two quarterspace model one would expect a change in most conductive direction above the contact. Due to the covering layers in this model such a change in most conductive direction is shifted several tens of kilometres to the conductive side of the contact (where no data is available). The 2D fault model must therefore be considered as an equivalent model to the 1D anisotropic model. Without any additional information one cannot distinguish between them.

It also was made a effort to trial and error model the Francistown sites, but none of these sites could be fitted by 1D anisotropic forward modelling with a similar simple model. (Even no model was found that only fits the phase curves.) The Francistown sites are probably distorted or affected by 3D structures and require a 1D anisotropic model consisting of different anisotropic layers with different anisotropic directions (and maybe dip and slant), which requires a large number of parameter settings and therefore the trial and error approach to find a model becomes an unreasonable time effort.

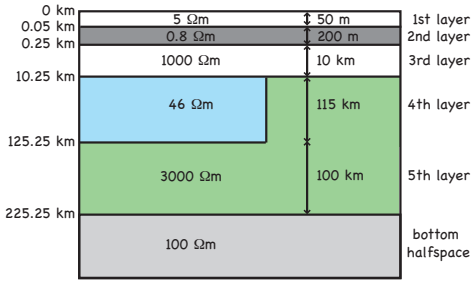

(a) Sketch of the 2D fault model

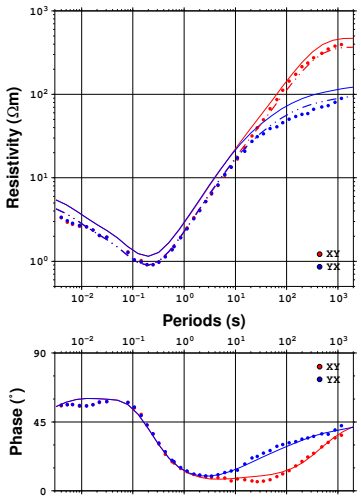

(b) Comparison of observed and modelled response curves

Figure 4.29: Forward 2D modelling of site MOF107 using the isotropic code of Rodi and Mackie (2001) as implemented in WinGLink® from Geosystem (forward routine from Mackie et al. (1988)). The decomposed (to 110° E of N) data of MOF107 are represented by the symbols, the solid lines are the 2D forward modelling results. The model that fits the data is shown in (a), where the strike direction of the fault structure in the third layer is 20° E of N. The minimum resistivity one can specify within WinGLink® is 1 Ωm (and therefore larger than the required 0.8 Ωm). Using 1 Ωm results in response curves that are shown as solid lines in (b). The phase curves match the data well, but the resistivity curves are shifted upwards. The dashed lines show the resistivity curves multiplied by 0.8 to account for the shift due to the wrong resistivity value of the second layer.

In conclusion, the Maun sites show a 1D background model with an anisotropic or a fault-like structure perpendicular to the dyke swarm direction, and therefore excludes the dykes as the cause of the mode splitting observed in the data. The depth to the top of anisotropic layer (or the fault structure) is about 10 - 15 km. The orientation of the Magondi Belt on geological maps (e.g., Figure 3.5) and the regional magnetic map (Figure 3.10) is consistent with the acceptable range of the anisotropic (or fault) strike direction (10° - 30° E of N). The minimum thickness of the anisotropic (or fault-structure) layer is about 100 - 115 km, a maximum thickness cannot be estimated. Therefore the layer is clearly a mid- to lower-crustal structure that extends into the lithospheric mantle (at least down to about 120 - 125 km depth). Such a depth extent suggests a crust-mantle coupling and anisotropy due to, e.g., graphite rather than hydrogen diffusion. (Although one cannot exclude that the anisotropy has two different causes for the crustal and lithospheric mantle depths.) The resistive dykes are not resolved in the MT data at the Maun sites, firstly because the 2.6% dilatation of the dykes enhances the resistivity of that layer by an insignificant amount and secondly, the very conductive near-surface layers have a screening effect.

5

2D INVERSION OF THE ZIM LINE

This chapter describes the 2D inversion of the ZIM line data and shows resistivity models obtained from the inversions using different parameter settings and data subsets. The results are compared to other available information in the area (see Chapter 3, where the geology and previous geophysical work are reviewed) and a geological interpretation of the modelled resistivity structures is discussed.

The 2D inversion code applied to the data is the smooth model inversion routine of the software package WinGLink® by Geosystem, which assumes isotropic resistivity cells in the mesh. This routine was developed by Rodi and Mackie (2001) and is based on a finite difference formulation to compute the regularised solution of the 2D MT inverse problem. The inverse algorithm employs a nonlinear conjugate gradient (NLCG) scheme to minimise an objective function that penalises data residuals and second spatial derivatives with respect to the resistivity structure (Rodi and Mackie, 2001). The different inversion parameters used for the inversions are given in the first section, followed by the 2D inversion results and interpretation of a crustal data subset from the northern part of the profile, and finally of the whole data set.

5.1 INVERSION PARAMETERS

Many different parameters need to be defined in the inversion code. All inversion results shown in the sections below are based on the following settings (unless stated differently):

- data range: minimum period 0.001 s and seven decades
- invert for observed station data
- using data errors, if available, otherwise the errors of the resistivity values were set to 10% and the errors in the phases to 5%
- error floor: 5% for TM phase, 25% for TE phase and 50% for the resistivities of both modes for the first inversion run. Successively the error floors of the TE phase, of the TM resistivity and finally of the TE resistivity were reduced: error floor of the final inversion run: 5% for phases and 10% for apparent resistivity values
- vertical magnetic transfer function data were not available for the ZIM line

All the starting models for all the inversion results shown were 100 Ωm for the crustal data subset of the northern part of the profile (see Section 5.2) and for the whole data set (see Section 5.3) were 100 Ωm for the top ~400 km with a fixed bottom halfspace of 10 Ωm below (clamping τ of 10^{10}). The inversion scheme of the standard Laplacian regularisation and

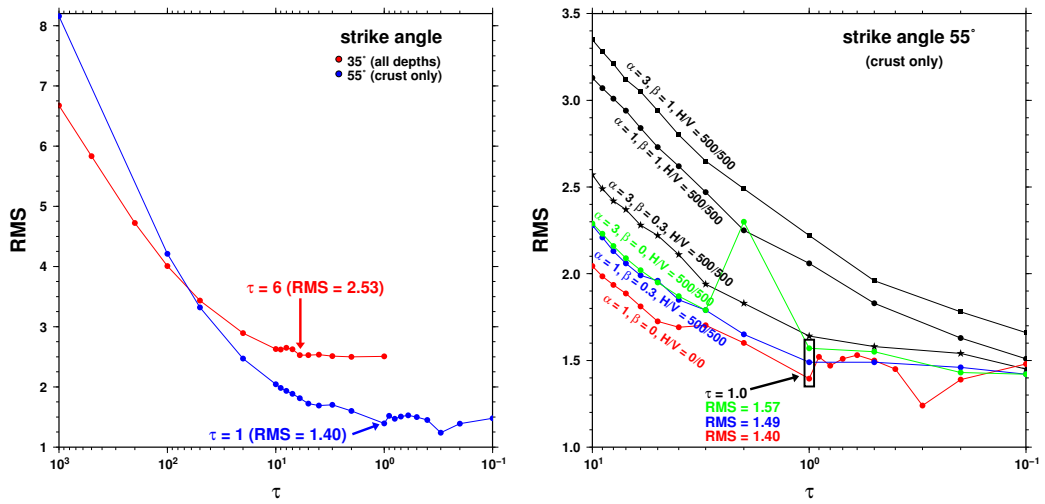

(a) RMS vs. τ trade-off curves - standard settings: $\alpha = 1$, $\beta = 0$.

(b) RMS vs. τ trade-off curves - crustal northern part of the profile

Figure 5.1: RMS versus τ trade-off curves for the whole data set with a strike angle of 35° E of N and for the crustal data set on the northern part of the profile with a strike angle of 55° E of N, using standard settings for the weighting parameters (a) and for the crustal data set using different weighting parameters (b). The marked τ value of 6 for the whole data set and 1 for the crustal data set, are chosen for the 2D inversion of the profile and its subset. In addition to the standard settings of the weighting parameters (red line in (b)), the crustal subset was also inverted using two other settings (blue and green lines in (b)).

minimising the gradient of the model were used to calculated the models. The regularisation parameter τ (also called smoothing operator) controls the trade-off between fitting the data and the model smoothness. A larger τ causes a smoother model at the expense of a higher RMS misfit. Therefore a few inversion runs were necessary to determine the optimal regularisation parameter for the chosen mesh and the data set (or subset). Since the resistivity data can be affected by static shift, which would enhance the RMS value, test runs were set up to fit the phases only. Figure 5.1 (a) shows the resulting trade-off curves of RMS versus τ values for the inversion of the whole data set (red) and for a data subset at crust levels at the northern end of the profile (blue). For the crustal data subset different weighting parameters (α, β and H/V) were also tested and the resulting trade-off curves are shown in Figure 5.1 (b). The parameter α is the factor to multiply the horizontal derivatives (default is $\alpha = 1$, larger values increase the horizontal smoothness), β is the exponent in the weighting function (default is $\beta = 0$, which means no weighting is applied to the regularisation term). Additional parameter H and V specify the minimum block dimension in the horizontal and vertical directions to be used in computing the weighting function (see WinGLink® manual for more details). For the whole data set with a strike angle of 35° E of N $\tau = 6$ and for the crustal, northern part of the profile with a strike direction of 55° E of N $\tau = 1$ are the chosen regularisation parameters for all subsequent inversions. (See Section 4.2 for more details about the chosen strike directions.) The weighting function parameters used for inversion of the crustal data set are $\alpha = 1$, $\beta = 0$ and H/V =0/0 (red line), $\alpha = 1$, $\beta = 0.3$ and H/V =500/500 (blue line) and $\alpha = 3$, $\beta = 0$ and H/V =500/500 (green line).

5.2 CRUSTAL, NORTHERN PART OF THE ZIM LINE - CRUSTAL STRIKE DIRECTION

5.2.1 *2D inversion results*

A separate 2D inversion of a data subset from the northern part of the ZIM profile was undertaken to investigate the crustal structures imaged when using the appropriate strike direction (i.e., 55° E of N), in order to subsequently differentiate between true crustal structures and artificial structures in the inversion model of the whole profile (see Section 5.3) caused by enforcing the lithospheric strike direction of 35° E of N to the crustal, northern part of the data.

The data of sites ZIM118 to ZIM131 were decomposed according to a fixed strike direction of 55° E of N using STRIKE (McNeice and Jones, 2001). The Niblett-Bostick penetration depths were estimated for both modes independently and all data points with penetration depths greater than 40 km were rejected (Figures C.1 and C.2 in Appendix C.1 show the response curves). The data set obtained was imported into WinGLink® and where necessary a D^+ consistency assessment was used to eliminate inconsistent data points before the inversion. The inversion strategy described in Section 5.1 was used (i.e., TM phase first, then TE phase, TM resistivity and finally TE resistivity). Inversions of the individual modes only, starting with inverting for phase only and then adding the resistivity values, were also undertaken. Figure 5.2 shows the inversion results of (a) TE only, (b) TM only and (c) joint TE and TM inversions using three different parameter settings, namely the settings that relate to the three lowest RMS vs. τ trade-off curves shown in Figure 5.1 (i.e., the red, blue and green curves; the colour coding is the same in Figures 5.1 and 5.2).

Comparing the inversion results using the three different weighting function settings shows that the final average RMS of the inversions is similar for all three models and also the RMS values for individual sites, plotted on top of the models in Figure 5.2, show hardly any differences for the three settings. The resistivity structures obtained from TE only, TM only and joint TE and TM inversion, however, clearly exhibit differences, which is a well known issue (e.g., Unsworth et al., 1999; Ritter et al., 2003) that is caused by the different sensitivities of the two modes. While the TM mode is sensitive to charges at boundaries, the anomalies in the TE mode are inductive in nature, i.e., it is sensitive to the current flows (e.g., Wannamaker et al., 1984; Berdichevsky et al., 1998). Wannamaker et al. (1984) state that the apparent resistivity identified as TE by conventional means over and around a confined 3D conductive body suffers a widespread depression (due to current gathering) that is increasingly pronounced towards longer periods. The interpretation of such a 3D response using 1D or 2D TE modelling routines would infer erroneously low resistivities at depths below the true inhomogeneity (Wannamaker et al., 1984). Such an effect is apparent in the TE mode inversion results in Figure 5.2 (a), which show a mid- to lower-crustal conductor that extends clearly deeper than it does for the TM mode inversion (b) or the joint TE/TM inversion (c). Berdichevsky et al. (1998) studied the advantages and disadvantages of the individual modes using synthetic data generated for different geological scenarios. They found the TM mode to be more sensitive to the near-surface structures, while the TE mode may be more sensitive to deeper structures. They also noticed that the TM mode is more accurate if a conductive 3D structure is interpreted by a 2D approximation (similar to the observations of Jones (1983b) and Wannamaker et al. (1984)), whereas in the case of a resistive 3D body, the TE mode may be more accurate. Therefore the information that can

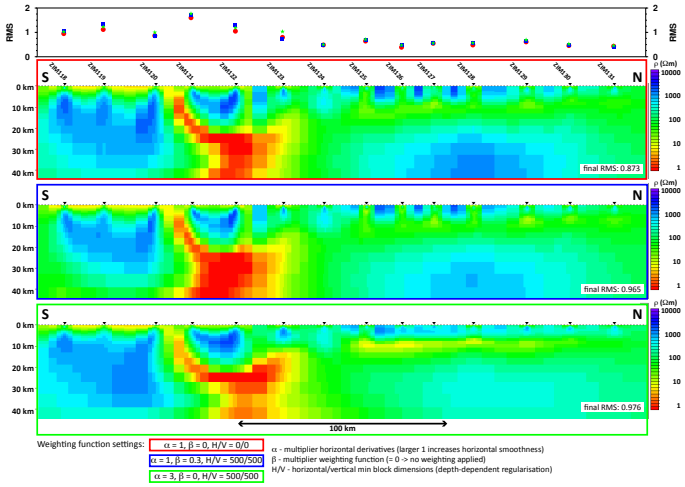

(a) TE only inversion (vertical exaggeration = 1.0)

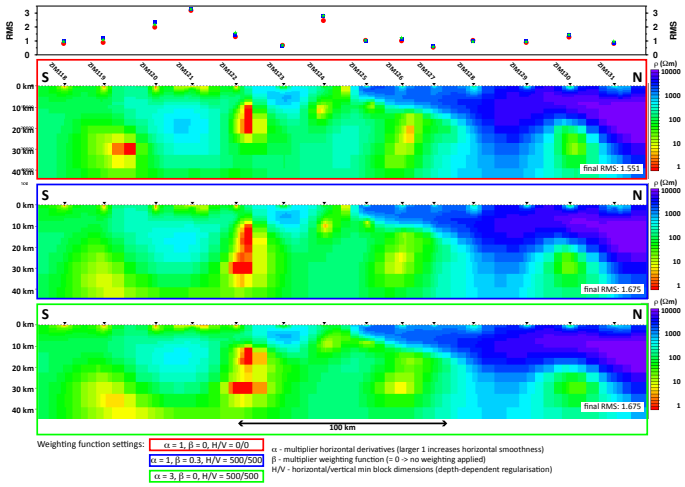

(b) TM only inversion (vertical exaggeration = 1.0)

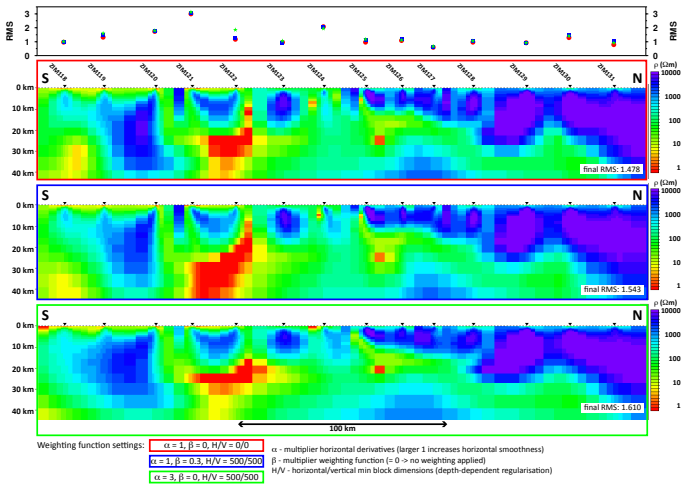

(c) Joint TE and TM inversion (vertical exaggeration = 1.0)

Figure 5.2: Figures showing the inversion results of the crustal, northern part of the ZIM line. Panel (a) shows the results if only the TE mode data are used for the inversion, whereas in (b) only the TM mode data are taken into account during the inversion. The results of a joint TE and TM mode data inversion are shown in (c). For each of these inversions three models resulting from the use of different weighting function parameters are shown, where the colour coding of the border of each model is identical to the one used for the crustal trade-off curves in Figure 5.1 (b).

be obtained from the individual TE and TM modes seem to complement one another, and, as expected, the joint TE/TM inversion Figure 5.2 (c) exhibits some features from each of the inversions of the individual modes ((a) and (b)).

To test if some of the key structures are supported by the data, the joint TE and TM inversion model was manually edited and used as starting model for a new inversion sequence using the option to find the model closest to the starting model. Figures C.3 to C.7 in Appendix C.1 show five different manually edited starting models and the final inversion results obtained for the joint TE and TM mode inversion using the three different weighting function settings. The different starting models are (i) a model where all the conductive structures have been removed (see Figure C.3), (ii) a model containing only the main conductive features and all resistive structures have been removed (see Figure C.4), (iii) a model with smoothed shapes of the main conductive and resistive structures and where smaller features as well as deeper structures have been removed (see Figure C.5) and (iv) finally two models with the main conductive and resistive structures defined by tear zones with slightly different shapes of the tear zones (see Figures C.6 and C.7).

All the inversion results of the different manually edited starting models suggest that the northwards dipping resistor beneath sites ZIM125 to ZIM131 is a data-supported structure, including the upwelling at the base of the resistor beneath site ZIM130. Although the shape of the conductors beneath sites ZIM121 to ZIM123 and beneath site ZIM125 varies from model to model, the existence of these conductors is a persistent feature. The two upper crustal resistors beneath sites ZIM121/ZIM122 and ZIM123 remain disconnected and the vertical resistive structure beneath ZIM119/ZIM120 is a distinctive block with sharp boundaries in the resistivity model. Finally, a thin near-surface conductor can be found beneath ZIM118 to ZIM122 which appears discontinuous due to the sparse lateral sampling provided by a site spacing of about 20 km, but imposing the conductor in the model as a continuous feature is accepted by the inversion as well (see e.g., the enlarged parts in Figure C.4). These tests suggest that the inversion results shown in Figure 5.2 represent the data well (Figures C.1 and C.2 show the synthetic data of the three inversion models in comparison to the observed data). Inversions allowing for static shifts were tested as well, but did not produce any significant changes in the models.

As the differences between the three results obtained using different weighting function settings is small, the top model (i.e., the one with the standard settings marked by the red border) is taken for interpretation in Section 5.2.2 below.

5.2.2 *Interpretation*

The known geology and results from previous geophysical investigations of the ZIM line area were discussed in Chapter 3, but the relevant constraints for the interpretation of the crustal northern part of the profile are summarised in the following: The Makgadikgadi Pans (see Section 3.1.6) are associated with a near-surface brine aquifer and Figure 5.3 shows the locations of the ZIM line sites with respect to the surface extent of the salt pans on a satellite image from Google Earth. It is very likely that the data of sites ZIM118 to ZIM120/ZIM121 are affected by the brine aquifer, which causes the low resistivities observed. Figure 5.4 (a) shows a sketch of the a priori information with respect to the site locations. The possible extent of the brine aquifer is indicated by the orange line. The black

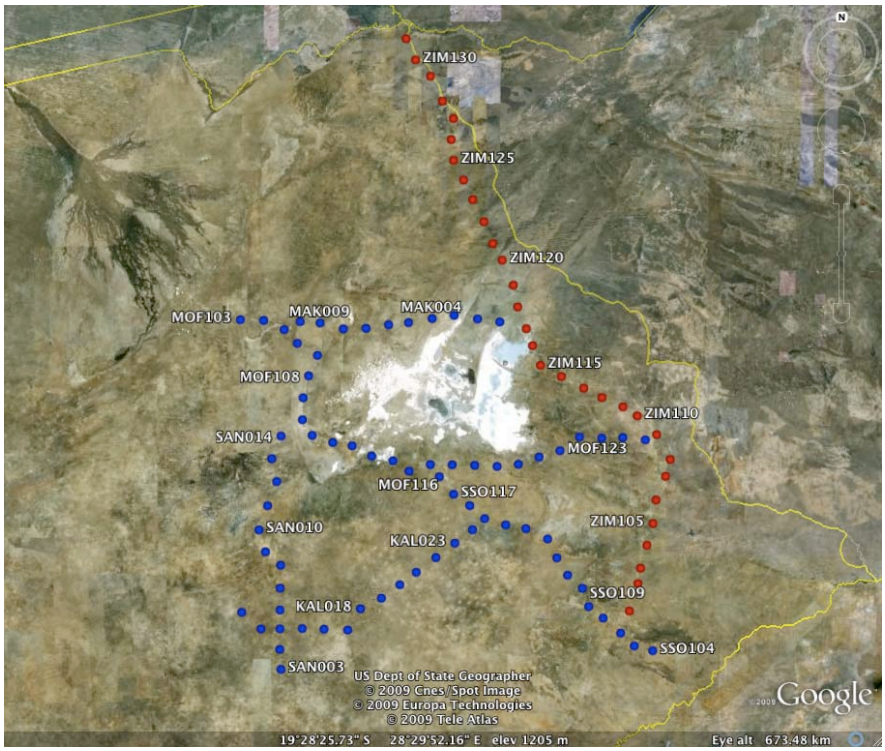

(a) Google Earth image of the Makgadikgadi Pans

(b) Enlarged Google Earth image of the northeastern part of the Makgadikgadi Pans

Figure 5.3: Google Earth images of site locations with respect to the Makgadikgadi Pan Complex. The ZIM line (red) and its neighbouring profiles (blue) are shown in (a), where the white lake-like area surrounded by the profiles ZIM, MAK and MOF is the surface extent of the salt pan complex. The enlarged image (b) shows the proximity of the ZIM sites to the pan complex. The northeast-trending riverbed-like extension suggests that a near-surface brine aquifer in this area could affect the MT data at sites as far north as ZIM120/ZIM121.

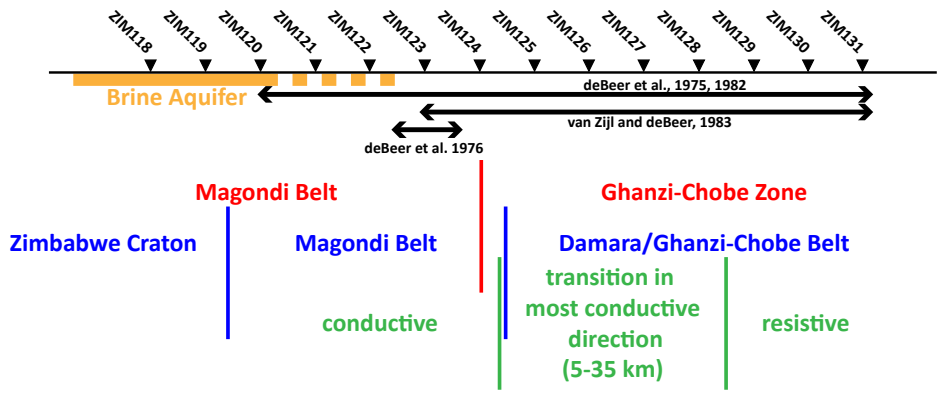

(a) A priori information with respect to ZIM north sites

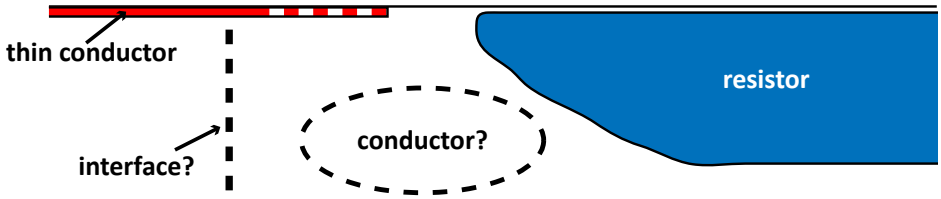

(b) Sketch of a possible subsurface resistivity structure based on the a priori information

Figure 5.4: Figure showing the a priori information (a) and a possible subsurface resistivity structure based on them (b). In orange is the possible extent of the brine aquifer, which is related to the Makgadikgadi salt pan complex (see Figure 5.3). The black arrows indicate the location of the crustal conductor (20 - 45 km depth) mapped by de Beer et al. (1975, 1976, 1982) and van Zijl and de Beer (1983) using electrical sounding and magnetometer array data (see Figure 3.11). The location of the geological terranes as they are proposed on the geological map of Singletary et al. (2003, and references therein, also see Figure 3.3) are indicated in red and based on the aeromagnetic data in blue. In green is shown the zone of transition in the most conductive strike direction, which indicates a dipping resistor at the northern end of the profile (see Section 4.2 and Figure 4.16).

arrows outline the locations of the crustal conductor mapped by de Beer et al. (1975, 1976, 1982) and van Zijl and de Beer (1983) using electrical sounding and magnetometer array data (see Figure 3.11). Originally the conductor was thought to be a upper lithospheric mantle feature (de Beer et al., 1975, 1976), but de Beer et al. (1982) and van Zijl and de Beer (1983) revised the depth extent to the mid- to lower-crust (20 - 45 km depth). The locations of the boundary between the Magondi Belt and the Ghanzi-Chobe Zone, as proposed on the geological map of Singletary et al. (2003, and references therein, also see Figure 3.3), is sketched in red, whereas the blue geological terrane outline is based on the aeromagnetic data (see e.g., Figure 3.10). Finally, the transition in the most conductive strike direction, which indicates a resistor at the northern end of the profile (as discussed in Section 4.2, see also Figure 4.16) is represented in green. As the flip in the most conductive direction is a rather smooth transition (where not all frequencies in the crustal depth band agree in the most conductive direction) than an abrupt change from one site to the next, an increasing thickness of the resistor towards the north and therefore a dipping interface could be expected. Figure 5.4 (b) shows a sketch of the probable resistivity structure based on the a priori information shown in (a). The Ghanzi-Chobe belt is expected to be a resistive feature and the boundary to the Magondi Belt is most likely dipping northwards with increasing thickness of the Ghanzi-Chobe belt from ZIM124/ZIM125 to about ZIM128/ZIM129. The

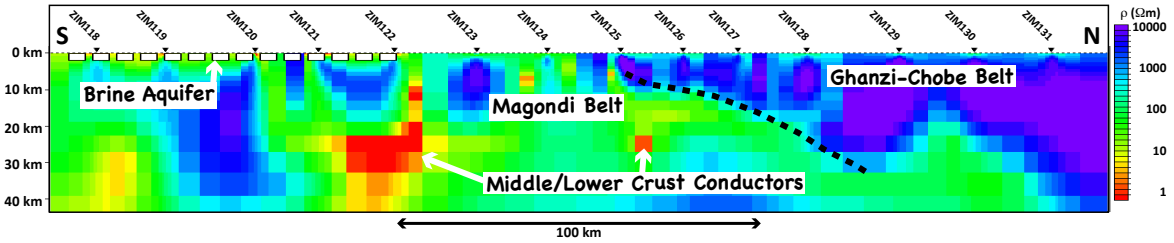

Figure 5.5: This figure shows the 'red' 2D inversion model (vertical exaggeration = 1.0) from Figure 5.2 (c) with geological interpretation. The black dashed line indicates the northward dipping boundary between the resistive Ghanzi-Chobe Belt to the north and the Magondi Belt to the south. Two major mid- to lower-crustal conductors are identified. The brine aquifer is indicated by the approximately 600 m thick conductive (about 1 - 5 Ωm) layer beneath the southern sites (white dashed line).

brine aquifer causes a thin near-surface conductor beneath sites ZIM118 to ZIM120 (maybe as far as ZIM121/ZIM122) and there is possibly an interface between the Zimbabwe Craton and the Magondi Belt somewhere between ZIM119 and ZIM120. Finally, there are (one or maybe several) mid- to lower-crustal conductors likely, the exact locations in lateral position of which are unclear. Comparing the sketch of the possible subsurface resistivity structure with the 2D inversion result for the MT data of the crustal northern part of the ZIM line (see Figure 5.5), a good agreement is found. The northwards dipping very resistive structure is identified as the Ghanzi-Chobe belt, with the Magondi Belt to its south. A clear boundary between the Magondi Belt and the Zimbabwe Craton cannot be identified in the model. The thin (about 600 m thick) conductive (about 1 - 5 Ωm) near-surface layer is related to the brine aquifer, and the two mid- to lower-crustal conductors have been found in the lateral range suggested by de Beer et al. (1975, 1976) and van Zijl and de Beer (1983). The depth of the conductor beneath sites ZIM121/122 in the 2D inversion model (see Figure 5.5) matches the depth of 20 - 45 km proposed by de Beer et al. (1982) and van Zijl and de Beer (1983) for their conductor. They associated the conductor with a zone of crustal weakness and a serpentinised lower crust. Ritter et al. (2003) studied the conductive zone using MT data from a cross-section in Namibia. They argue that the improved knowledge and theory about crustal conductivity suggests that shear zones are a more plausible explanation, as they often have anomalous conductivity due to higher contents of fluid, fault gouge, sulphide or graphite. In the case of the ZIM line, no additional information about the presence of fluids, sulphides or graphites is available, but if de Beer et al. (1975, 1976, 1982) and van Zijl and de Beer (1983) are correct in their mapping of the conductor, then the conductor investigated by Ritter et al. (2003) and the one found in the ZIM data are connected (or at least associated). Therefore it seems reasonable to follow Ritter et al.'s (2003) arguments about the cause of the conductor. Ritter et al. (2003) cannot exclude fluids as a cause of the conductive anomaly because no supporting field evidence for hydrothermal alteration is available, whereas graphite-bearing marble units are present in the area. Laboratory measurements show that interconnected graphite flakes or graphite grain boundary coatings can significantly enhance electrical conductivity (e.g., Nover et al., 1998). Ritter et al. (2003) suggest that regardless of what the conductive material in the rocks is, it must be reasonably well-interconnected over a distance of kilometres to cause the observed anomalies, and that interconnectivity is best accomplished by movement along discrete fault zones. Sulphides must also be considered as a possible cause as base metal sulphide ores are known in the Damara Belt (e.g., Kamona et al., 1999; Chetty and Frimmel,

2000). In summary, the origin of the lower-crustal conductor found in the ZIM data remains uncertain, but a graphite and/or sulphide origin is favoured.

5.3 WHOLE ZIM LINE - LITHOSPHERIC STRIKE DIRECTION

5.3.1 *2D inversion results*

The complete ZIM line data set was decomposed according to a fixed strike direction of 35° E of N using STRIKE (McNeice and Jones, 2001) and afterwards it was imported into WinGLink® and, where necessary, D^+ consistency checks were used as guidance to manually eliminate inconsistent data points before inversion. Figures C.8 and C.9 in Appendix C.2 show the full data set and indicate which data points of each response curve are used for the inversion. During the inversion process sites ZIM102, ZIM103, ZIM104, ZIM107, ZIM113 and ZIM115 were excluded as they could not be fit well by the model responses and their individual site RMS values were greater than 15. As the testing of different weighting function parameters (α, β, H/V) for the inversion of the crustal part of the ZIM line showed no major differences in the resulting inversion model, default values (i.e., $\alpha = 1$, $\beta = 0$, $H = 0$ and $V = 0$) are used to inverted the whole data set. The same inversion strategy as for the crustal part in Section 5.2 and as described in Section 5.1 was applied (i.e., TM phase first, then TE phase, TM resistivity and finally TE resistivity).

Figure 5.6 shows the final 2D isotropic smooth inversion model for the whole ZIM line. For each site the individual TE only, TM only and joint TE/TM RMS values are plotted on top of the model, clearly showing that for nearly all sites it is more difficult to fit the TE mode data than the TM mode data. It is also apparent that the data of the northern sites are better fit than the data of the southern sites. In addition to the quality of data fit, the model constraints depend also on the data distribution with respect to the 2D section. As discussed in Section 4.1.2 and shown in Figure 4.4, the penetration depth varies not only from site to site but also between the two modes. The vertical lines beneath each site in Figure 5.6 indicate the maximum Niblett-Bostick penetration depth of the TE (black) and TM (white) modes, respectively. Unfortunately the area inbetween the two deeper resistors in the north (R4 in Figure 5.6) and south (R5) of the profile is not sensed by the sites above it, but only by those sites to the side, and therefore raises the question if they are connected or not. Another interesting question is whether the upper resistors and the lower resistors are connected or not, and if the connection that is apparent beneath ZIM131 is real or an artefact. (The existence of the two conductors beneath ZIM121-123 and ZIM125 are not questioned as they conform with the conductors found in the focused inversion of the northern crustal part of the profile, see Section 5.2).

To test the presence of the (relatively more) conductive zones between the resistors, in a lateral but also vertical direction, the final 2D inversion model was manipulated by drawing resistive connections between them. Four different manipulated models were designed (see Appendix C.2): (i) the two deeper resistors (R4 and R5 in Figure 5.6) are drawn to be one continuous resistor with a connection to the shallower resistor (R2 in Figure 5.6) beneath ZIM117 to ZIM120 (the model is called CONNECTED1, see Figure C.10 (a)), (ii) the two deeper resistors (R4 and R5) are continuous but are separated from the shallower (R2) one (called CONNECTED2, see Figure C.10 (b)), (iii) the upper and lower resistors in the south (R1-R4) and the north (R3-R5) are connected but there is no lateral connection

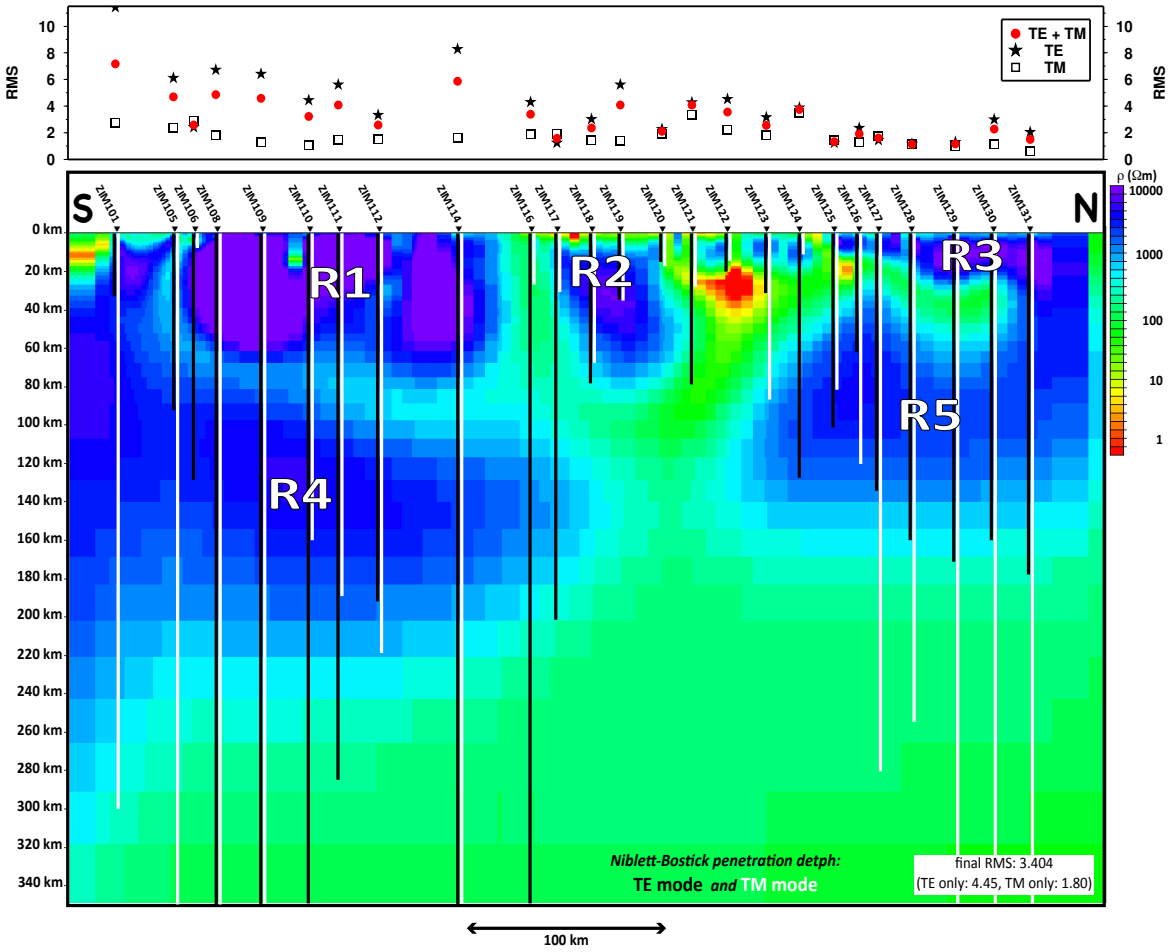

Figure 5.6: Final 2D smooth inversion model of the ZIM line (vertical exaggeration = 1.0). The triangles indicate the locations of the sites used and the black and white lines beneath each site represent the Niblett-Bostick penetration depths of the TE (black) and TM (white) mode data, respectively. The RMS values of the TE, the TM and joint TE/TM modes with respect to the final model at each individual site is shown on top.

between northern and southern ones (called CONNECTED3, see Figure C.11 (a)) and (iv) the connection between the upper (R3) and lower (R5) resistors beneath ZIM131 is disconnected (called DISCONNECTED, see Figure C.11 (b)). For these four scenarios, forward responses were calculated and compared to the observed data and the responses of the final 2D inversion model in Figure 5.6 (Figures C.12 to C.14 in Appendix C.2 show the comparison of the response curves). The responses of two example sites, ZIM118 and ZIM131, are shown in Figure 5.7. The black symbols represent the observed data and the red line is the model response of the final 2D inversion result shown in Figure 5.6. In Figure 5.7 (a) and (b) are the responses of the models CONNECTED1 (blue dashed lines) and CONNECTED2 (green dashed lines). One cannot distinguish between the red and the green lines, which both fit the observed data equally well, i.e., the enforced changed of connecting the resistors R4 and R5 can neither be verified nor falsified by the observed data. At longer periods the blue curves differ from the red and green curves and also from the observed data. Therefore the additional connection to the shallower resistor (R2) beneath ZIM118 to ZIM120 is not consistent with the observed data. (The conclusion that the shallower resistor R2 must be

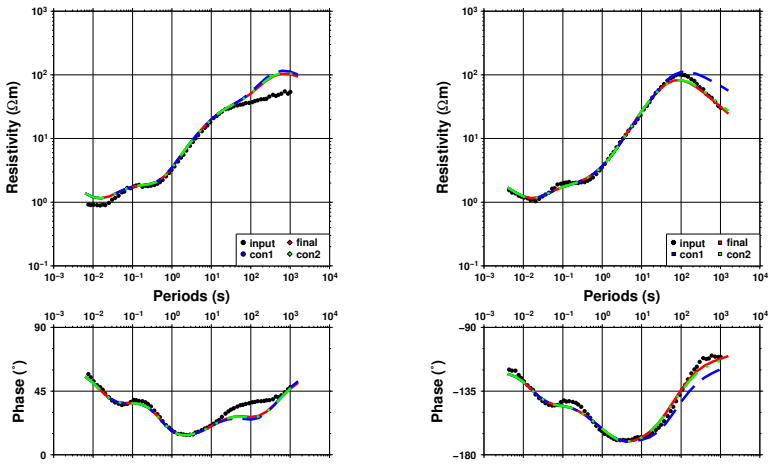

(a) ZIM118/XY component

(b) ZIM118/YX component

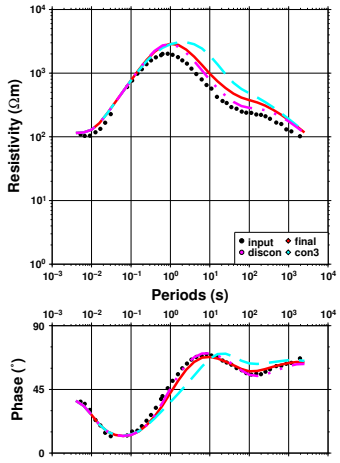

(c) ZIM130/XY component

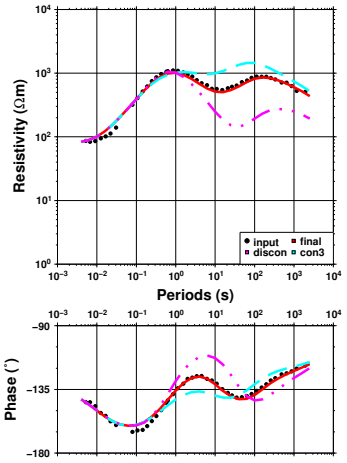

(d) ZIM130/YX component

Figure 5.7: Figure showing example response curves from the forward modelling tests using modified versions of the 2D inversion model of Figure 5.6. The black dots represent the observed data, the red line is the response curve of the final 2D inversion model and the other coloured curves are the forward responses of the different modified models shown in Appendix C.2 (con1 - CONNECTED1, Figure C.10 (a); con2 - CONNECTED2, Figure C.10 (b); con3 - CONNECTED3, Figure C.11 (a) and discon - DISCONNECTED, Figure C.11 (b)).

separate from the deeper ones (R4 and R5), but that no statement can be made about the connectivity between the resistors R4 and R5, is also supported by the responses of the other sites in that area; see Figures C.12 to C.14). Figure 5.7 (c) and (d) show the response curves of ZIM131, where the response curves of models CONNECTED3 (turquoise lines) and DISCONNECTED (pink lines) are shown. Although the XY resistivity data are not well fit by any of the curves, the phases and the YX resistivity show clearly that neither the complete connection of the upper (R3) and lower (R5) resistors, nor their absolute disconnection, are consistent with the observed data at ZIM131. The other northern sites confirm the findings at ZIM131, and in addition the southern sites of the profile also show that the connection of the upper (R1) and lower (R4) resistors in the south are not consistent with the observed data (see Figures C.12 to C.14). Therefore the vertical connectivity (or

the lack of it) of the different resistors in the final inversion model are constrained by and consistent with the observed data, but in the area of very limited penetration depth beneath sites ZIM118 to ZIM123, the data do not provide any constraints on the lateral connectivity of the resistors in the south (R4) and north (R5).

Different approaches allowing for static shift estimation, or using a limited resistivity range, during the inversion were also applied to the data set, but could not contribute any additional (or different) information.

5.3.2 *Interpretation*

Figure 5.8 shows the 2D resistivity model of the ZIM profile with respect to the surface extent of the geological terranes, the magnetic anomaly due the Okavango Dyke Swarm

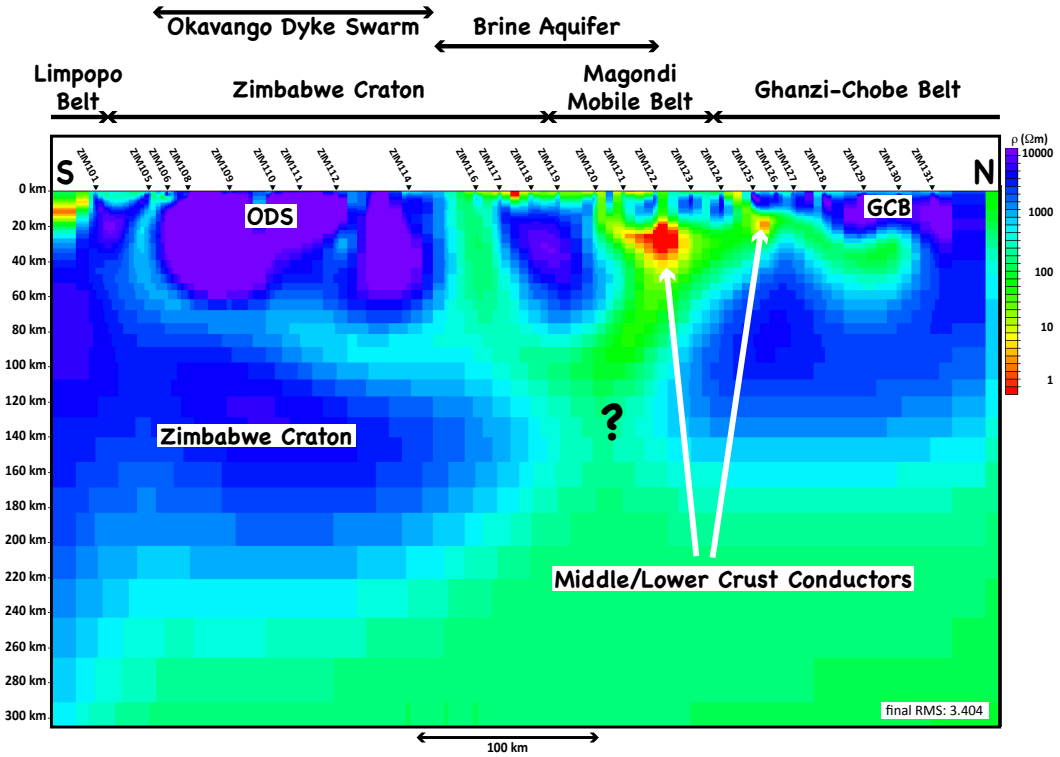

Figure 5.8: The 2D smooth inversion model (vertical exaggeration = 1.0) from Figure 5.6 in relation to the known surface extent of geological terranes. The arrows above the image of the resistivity structure show the crustal extents of the Limpopo Belt, Zimbabwe Craton, Magondi Mobile Belt and Ghanzi-Chobe Belt (GCB) with respect to MT sites of the ZIM line, adapted from the geological terrane boundaries drawn based on potential field data (see e.g., Figure 3.9). The extent of the Okavango Dyke Swarm (ODS), known from magnetic data, is indicated, as well as an estimated extent of the brine aquifer related to the Makgadikgadi salt pan complex. The dominant resistivity features related to the main geological terranes are labelled and the question mark indicates the area of missing data coverage. Two dominant mid- to lower-crustal conductors are also apparent (compare with inversion results from the northern crustal part of the profile, Figure 5.5).

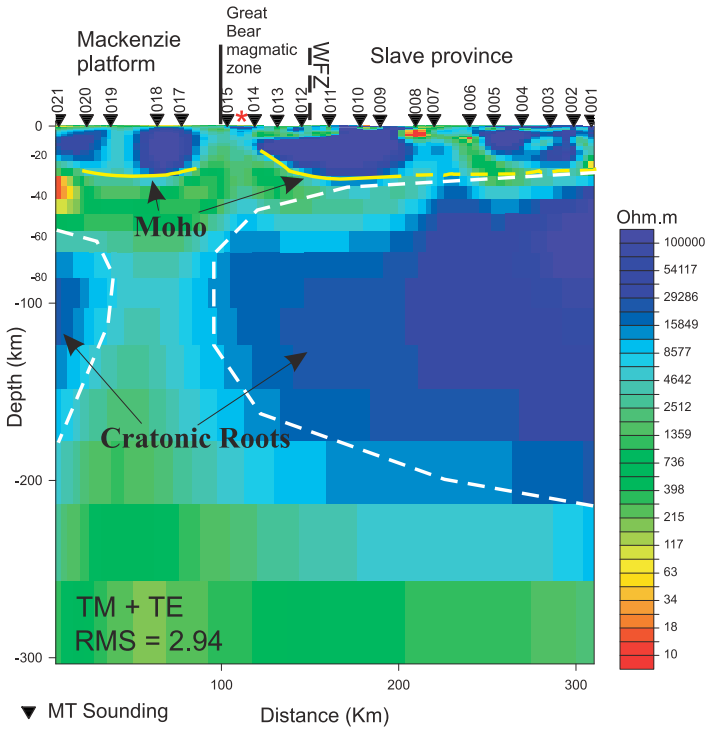

Figure 5.9: 2D inversion model of the Wopmay lithospheric mantle in the Northwest Territories, Canada (taken from Spratt et al. (2009)). The yellow line marks the crust-mantle boundary and the white dashed lines indicate the cratonic roots beneath both the Slave and the Bear provinces. (WFZ - Wopmay fault zone.)

and the estimated extent of the brine aquifer related to the Makgadikgadi salt pan complex. The crustal structures of the northern end of the model show a very strong correlation with the models obtained in Section 5.2, where this area was inverted separately using its appropriate strike direction of 55° E of N. Therefore, enforcing the lithospheric strike direction of 35° E of N for the whole data set has not caused any artefacts in the resistivity structure of the crust in the northern part of the profile. The mid- to lower-crustal conductors, and the dipping crustal resistor of the Ghanzi-Chobe Belt (GCB, in Figure 5.8), remain dominant crustal features in the model of the whole ZIM profile. Another dominant crustal feature is the extremely high resistivity area that has a lateral extent that matches the location of the Okavango Dyke Swarm (ODS, in Figure 5.8).

Most parts of the lithospheric mantle are resistive, but its thickness and resistivity vary along the profile. The Zimbabwe Craton (on the southern end of the profile) is characterised by very thick and very resistive lithosphere, whereas the lithosphere beneath the Ghanzi-Chobe Belt is significantly thinner and less resistive. The more conductive part of the lithospheric mantle, beneath the Magondi Mobile Belt (sites ZIM117 to ZIM123), is unfortunately located in an area of poor data coverage. The higher conductivities of the Magondi Belt could nevertheless represent a real structure similar to that found by Spratt et al. (2009) in the upper Wopmay lithospheric mantle in the Northwest Territories, Canada (see Figure 5.9). They find very high resistivities down to about 210 km depth that shallow to about 150 km depth beneath the western edge of the Slave craton (similar to the southern part of the ZIM profile where the western edge of the Zimbabwe craton is

imaged). At depths of about 100 km in the Northwest Territories data there is a distinct decrease in the overall present resistivity located between the Great Bear magmatic zone and the Phanerozoic platform compared to the neighbouring resistive mantle (Spratt et al., 2009). Such a lower resistivity lithospheric mantle might be apparent beneath the Magondi Mobile Belt surrounded by the resistive Archaean Zimbabwe Craton and the Meso- to Neoproterozoic Ghanzi-Chobe Belt. Interpretation of moderately resistive (some hundreds of Ωm) mantle is fraught with difficulty. None of the proposed mechanisms for reducing resistivity is without serious problems. In the case of the Wopmay lithospheric mantle, Spratt et al. (2009) suggest an explanation based on ten Grotenhuis et al.'s (2004) work predicting that upper mantle shear zones have a 1.5 - 2 orders of magnitude higher conductivity than less-deformed regions in the lithosphere. ten Grotenhuis et al. (2004) found a systematic, inverse linear relationship between the electrical conductivity of mantle olivine and its grain size on a micrometer scale. Whereas a change of size for grains larger 1 cm has no effect on the electrical conductivity, a significant increase in grain size (for grains smaller than 1 cm) is predicted to lower the conductivity by up to two orders of magnitude. Assuming a stable mantle grain size of > 1 cm (Spratt et al., 2009, and references therein) a reduction of grain size to 100 µm would be required to obtain resistivity changes of the order found beneath the Wopmay orogen (Spratt et al., 2009) (and maybe also beneath the Magondi belt), possibly suggesting the presence of a mantle shear zone in this region.

The 2D forward model of site MOF107 (see Figure 4.29) shows a strike direction consistent with the orientation of the Magondi Mobile Belt in that area. The top of the fault structure in this 2D model is located at 10 - 15 km depth and it extends at least down to 120 - 125 km depth (see Section 4.3). The resistivity on one side of the fault is about 50 Ωm and 3000 Ωm on the other side. This scenario is similar to the resistivities of the Magondi Mobile Belt and Ghanzi-Chobe Belt as shown in the 2D inversion model of the ZIM line (Figure 5.8). The Ghanzi-Chobe Belt (a few 1000 Ωm) is more resistive than the Magondi Mobile Belt (about 100 Ωm). If the 2D forward model of site MOF107 represents the same terrane boundary (but a few hundred kilometres further southwest), this is supporting the suggestion of a conductive lithospheric mantle beneath the Magondi Mobile Belt. Also the depths extent of the resistivity contrast is similar in both models. While the 2D inversion model of the ZIM line shows a conductive layer beneath, the 2D forward model of MOF107 requires a layer of a similar resistivity as the resistive side of the boundary (the Ghanzi-Chobe Belt). The location of MOF107 is in a geological very complex area and it is possible that a resistive, cratonic root of the Zimbabwe craton is underlying the mobile belts in that region. The bottom of the resistive layer in the 2D forward model is at about 220 km depth, which seems to match the thickness of the resistive lithospheric mantle of the Zimbabwe craton.

Figure 5.10 shows a comparison of the geological map by Singletary et al. (2003) (left column) and the regional magnetic field anomaly map (right column) with the resistivities of the 2D inversion model. The average resistivity values (calculated as mean of the logarithmic resistivity values) beneath each ZIM site were extracted from the 2D inversion model at three depth ranges: near-surface (0 - 1 km), crustal depths (5 - 35 km) and lithospheric depths (50 - 150 km). The near-surface resistivities exhibit the conductor that is associated with the brine aquifer of the Makgadikgadi Pan Complex. The conductor is spatially located in the Gweta and Kubu Island area on the geological map (a). No correlation between the magnetic anomaly map and the near-surface resistivities is apparent (b). At crustal depths (5 - 35 km), the high resistivities found at the southern end of the ZIM line fall

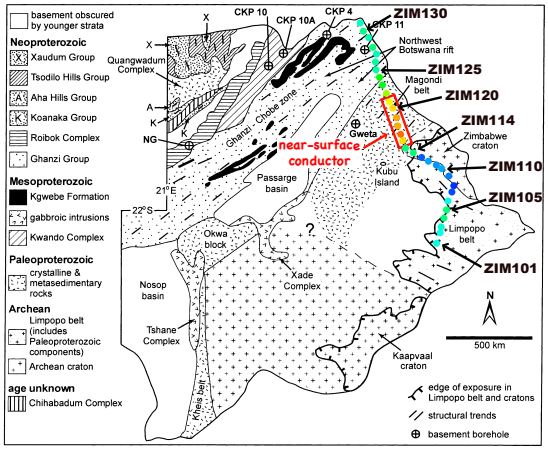

(a) Geology map; average resistivities at 0 - 1 km

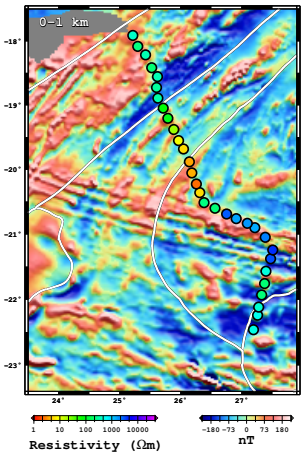

(b) Magnetic map; average resistivities at 0 - 1 km

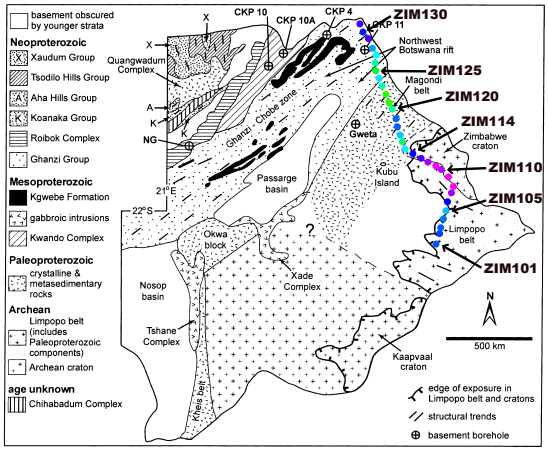

(c) Geology map; average resistivities at 5 - 35 km

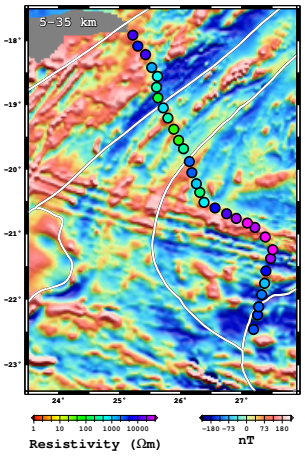

(d) Magnetic map; average resistivities at 5 - 35 km

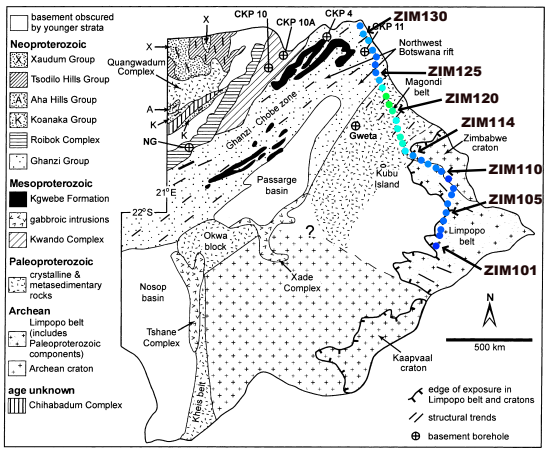

(e) Geology map; average resistivities at 50 - 150 km

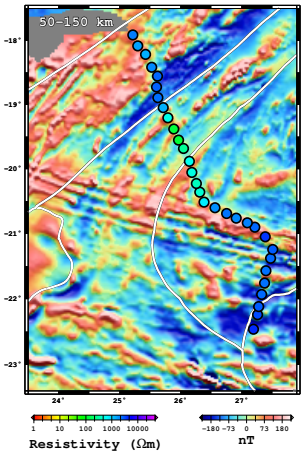

(f) Magnetic map; average resistivities at 50 - 150 km

Figure 5.10: Figures showing the average resistivity values of the 2D inversion model beneath each site of the ZIM line for three different depth ranges, namely 0 - 1 km, 5 - 35 km and 50 - 150 km. Background map on the left is the subsurface Precambrian geology map (see Figure 3.3, taken from Singletary et al. (2003)) and the regional magnetic anomaly map on the right (see Figure 3.10, magnetic data courtesy of the Council for Geoscience, Pretoria, South Africa). Note the colour scale of the circles indicating the resistivity values at each site is the same for all six panels.

into the Archaean Zimbabwe Craton and the Limpopo Belt on the geological map (c), whereas the extremely resistive part (purple colour) matches the magnetic anomaly of the Okavango dyke swarm (d). The resistive northern end is located in the Ghanzi-Chobe Belt (c), but not all sites in the belt at crustal depths are highly resistive. At lithospheric mantle depths (50 - 150 km) the resistive northern and southern ends of the profile correlate with the Ghanzi-Chobe Belt and the Zimbabwe Craton (and Limpopo Belt), respectively (e). The more conductive zone (green) matches the lateral extent of the Magondi Mobile Belt (although, the resistivity values are not very well constrained due to the lack of penetration depth in that area). No correlation between the magnetic anomalies and the resistivity structure at lithospheric depths can be found (f), which is not surprising as the magnetics are sampling shallower targets at temperatures above the Curie isotherm. Figure 5.11 shows a similar comparison of the resistivity values with the Bouguer gravity map. No correlation can be identified for these two data sets.

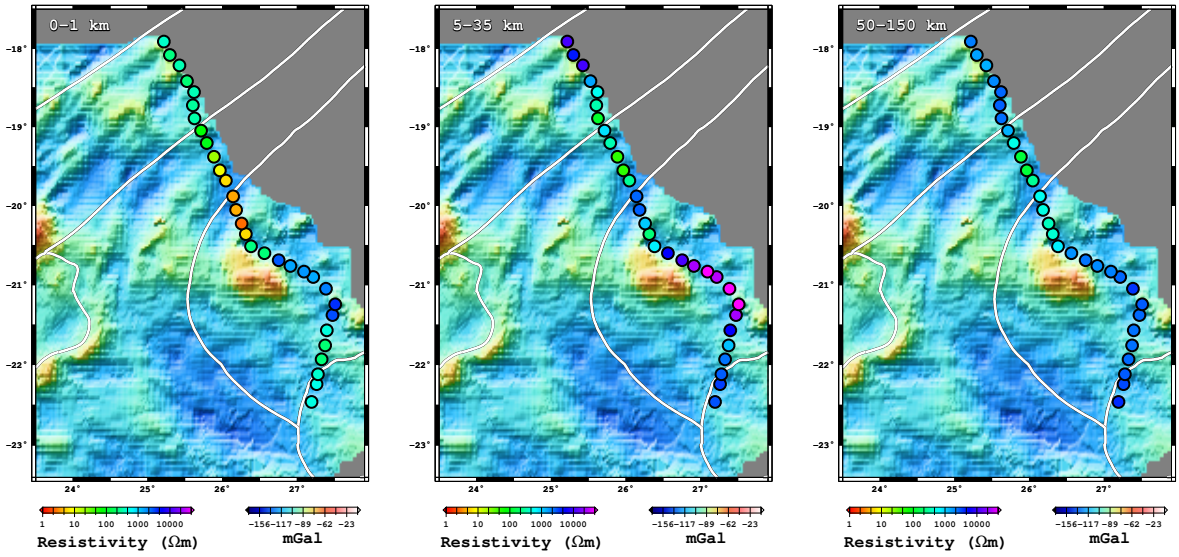

(a) Average resistivities at 0 - 1 km

(b) Average resistivities at 5 - 35 km

(c) Average resistivities at 50 - 150 km

Figure 5.11: Figures showing the average resistivity values of the 2D inversion model beneath each site of the ZIM line for three different depth ranges, namely 0 - 1 km, 5 - 35 km and 50 - 150 km. The background map is the Bouguer gravity map (see Figure 3.12, gravity data courtesy of the Council for Geoscience, Pretoria, South Africa).

As the MT method is able to constrain the thickness of resistive features well, due to its sensitivity to the onset of high conductivities below, (Jones, 1999), a reliable estimate of the lithospheric thickness can be made. Curves of average (i.e., mean logarithmic) and maximum resistivity versus depth for each terrane (shown in Figure 5.12 (c)), calculated within areas defined in Figure 5.12 (a) and (b), illustrate differences in the bulk or average resistivity characteristics for each terrane traversed on the ZIM and the KIM-NAM profiles. Muller et al. (2009) published the model (a) of the KIM-NAM profile (the straight profile with NW-SE orientation traversing the Damara and Ghanzi-Chobe belts, the Rehoboth Ter-

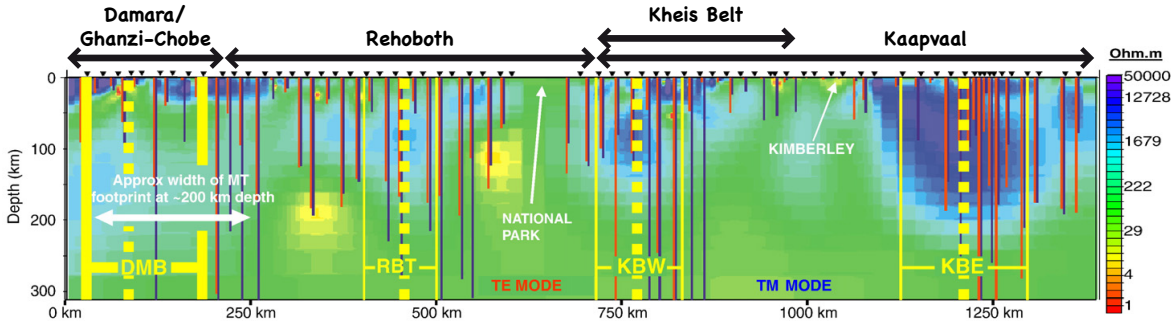

(a) KIM-NAM resistivity model taken from Muller et al. (2009).

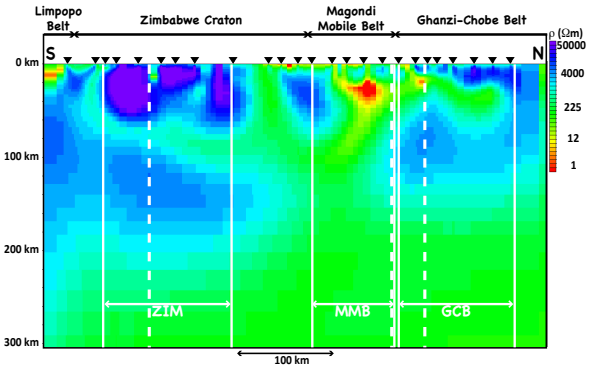

(b) ZIM line resistivity model using the same colour scale as Muller et al. (2009) for the KIM-NAM model in (a).

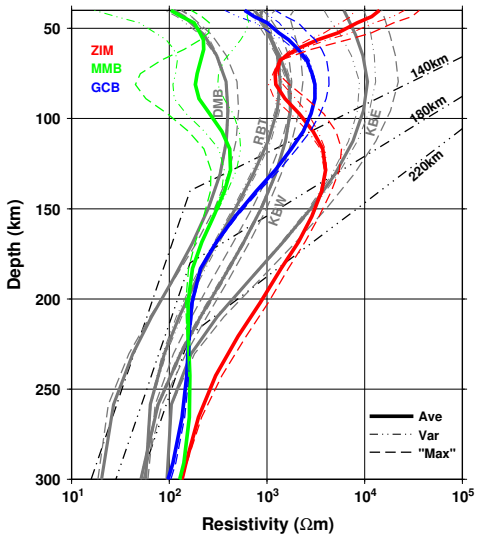

(c) Electrical resistivity versus depth profiles for different geological terranes, modified from Muller et al. (2009).

Figure 5.12: Electrical resistivity models for (a) the profile KIM-NAM (taken from Muller et al., 2009) and (b) the ZIM line using the same resistivity colour scale as for the KIM-NAM profile in (a). Representative resistivity-depth profiles for the different geological terranes are shown in (c). In (a) the estimation of the depth of penetration (Niblett-Bostick) achieved at each individual site for both the TE (red) and the TM (blue) modes are overlain on the model obtained for 25° E of N strike azimuth, the surface extent of the geological terranes is shown above and the solid vertical yellow lines define the zones used in each terrane to compute the average resistivity profiles presented in (c). The dotted yellow lines indicate the position of the 'maximum' resistivity profiles in (c). The white solid and dotted lines in (b) define the zones used to compute the average resistivity profiles and the position of the 'maximum' resistivity profiles for the three terranes transversed by the ZIM profile. In (c) profiles of average resistivity, variance and 'maximum' resistivity are shown as indicated by the key. The profiles published by Muller et al. (2009) are shown in grey and are overlain by the coloured ones from the ZIM model in (b). The average (and variance) profiles are computed from the 2D sections within the spatial areas defined in (a) and (b). Predicted resistivity-depth profiles for hypothetical mantle geotherms for different lithosphere thicknesses are shown (black dotted and dashed lines), based on laboratory electrical conductivity versus temperature and pressure measurements for dry olivine and pyroxene (Constable et al., 1992; Xu and Shankland, 1999; Xu et al., 2000). The inflection point in the theoretical curves corresponds with the intersection of the conductive mantle geotherm with the adiabat. (Abbreviations used are as follows: Damara/Ghanzi-Chobe (DMB, for the KIM-NAM line), Rehoboth (RBT), Western Kimberley Block (KBW), Eastern Kimberley Block (KBE), Zimbabwe Craton (ZIM), Magondi (MMB) (profile unconstrained below 80 - 100 km due to limited penetration depth in this area) and Ghanzi-Chobe (GCB, for ZIM line).)

rane and the Kaapvaal Craton, see Figure 3.9) and determined the lithospheric thicknesses of the Kaapvaal Craton (Eastern Block ~ 220 km, KBE, Western Block ~ 190 km, KBW), the Rehoboth Terrane (~ 180 km, RBT) and the Damara/Ghanzi-Chobe Belt (~ 160 km, DMB) using the resistivity versus depth profiles shown in grey in Figure 5.12 (c) and constraints from xenolith data. In comparison the resistivity curves of the three ZIM line terranes (defined in (b)), namely Zimbabwe Craton (ZIM), Magondi Mobile Belt (MMB) and Ghanzi-Chobe Belt (GCB), are plotted as coloured curves. (Note that the resistivity curve of the Magondi Mobile Belt (MMB, green) is unconstrained below 80 - 100 km due to the limited penetration depth in that area.) None of the three ZIM line resistivity curves match any of the KIM-NAM resistivity versus depth profiles. Unfortunately, the KIM-NAM and ZIM profiles do not intersect, therefore a static shift of absolute resistivity values between the two models cannot be excluded. However, the average resistivities for the ZIM line terranes show clear relative differences between one another, e.g., at about 100 km depth the Zimbabwe Craton is, at ~ 3000 Ωm, nearly one order of magnitude more resistive than the Ghanzi-Chobe Belt which has an average resistivity of ~ 500 Ωm. As the electrical resistivity of mantle minerals decreases strongly with increasing temperature (Constable et al., 1992; Xu and Shankland, 1999; Xu et al., 2000), hotter geotherms, which are associated with thinner lithosphere, result in lower bulk resistivities (see Figure 5.12 (c) where hypothetical mantle geotherms for several different lithospheric thicknesses are shown). Electrical resistivity is significantly more sensitive to temperature than it is to compositional variation in the mantle (Maumus et al., 2005; Jones et al., 2009), and therefore the observed differences in the bulk resistivities of each terrane are more readily accounted for by variations in the temperature of the lithosphere, i.e., the lithospheric geotherm. On both the KIM-NAM and the ZIM profile, the cratons, namely the Eastern Kimberley Block of the Kaapvaal Craton and the Zimbabwe Craton, are associated with the coolest geotherm and therefore the thickest lithosphere. Hotter geotherms (and thinner lithosphere) are associated with the mobile belts (GCB, MMB (no constraints below 80 - 100 km), DMB). All resistivity versus depth profiles fail systematically to match the very high resistivities predicted in the upper mantle for dry cratonic lithosphere above 120 km depth. The failure could be caused by different reasons: (i) the MT method is sensitive to the thickness of resistive layers but has a relative low sensitivity to their absolute resistivity, particularly when a more conductive layer such as the crust is located above (see, e. g., Jones, 1999), (ii) the regularisation (smoothing) inherent in the 2D smooth inversion algorithm used and the averaging to compute the depth profiles (although the variance, which is affected by the regularization, at lithospheric depths is very small), and (iii) the temperature-based model used does not account for possible properties that systematically affect the electric conductivity, for example the presence of hydrogen in the mantle (Karato, 1990, 2006), partial melts or enhanced conductivities due to very small grain sizes in shear zones (ten Grotenhuis et al., 2004).

As the 2D inversion model and the resistivity-depth profiles derived from them are smooth, the transition from the lithosphere into the more conductive mantle asthenosphere below is not sharply defined. Relative lithosphere thickness variations between each terrane of the same profile can be determined from the observed systematic changes in bulk resistivity. The theoretical curves in Figure 5.12 (c) provide a useful reference frame and indicate that an order of magnitude difference in electrical resistivity in the depth range of 100 - 150 km can be accounted for by a ~ 40 km lithospheric thickness change. Based on that observation Muller et al. (2009) conclude that with respect to the Eastern Kimberley Block, the Western Kimberley Block is associated with ~ 30 km thinner lithosphere, the Rehoboth Terrane with

~40 km thinner lithosphere, and the Damara/Ghanzi-Chobe Belt with ~60 km thinner lithosphere. Similar relative differences for the lithospheric thickness can be defined for the Ghanzi-Chobe Belt with respect to the Zimbabwe Craton (about one order of magnitude change in bulk resistivity) which indicates that the Ghanzi-Chobe Belt has a lithosphere about ~40 km thinner than that of the Zimbabwe Craton. The vague indication that the lithosphere beneath the Magondi Mobile Belt might be about ~60 km thinner has to be treated with caution as there is no data resolution for depths below 80 - 100 km at the sites directly above it, and poor resolution from neighbouring sites. (Muller et al. (2009) suggest that the absolute depth to the base of the lithosphere can most reasonably be estimated as close to ~220 km for the Eastern Kimberley Block, which results in absolute depths to the lithosphere of 190 km, 180 km and 160 km for the Western Kimberley Block, the Rehoboth Terrane and the Damara/Ghanzi-Chobe Belt respectively.) In the case of the Ghanzi-Chobe Belt (GCB) resistivity-depth profile presented here, an inflection point at about 180 km most likely marks the intersection of the conductive geotherm with the mantle adiabat, which, by definition, represents the thermal thickness of the lithosphere. The inflection point indicates that the lithosphere of the Ghanzi-Chobe Belt is possibly 20 km thicker than about 1000 km further southwest (160 km by Muller et al. (2009)). Therefore the absolute thickness of the lithosphere beneath the western extent of the Zimbabwe Craton is deduced to be about 220 km and hence is of similar thickness as the Eastern Kimberley Block of the Kaapvaal Craton in the study by Muller et al. (2009). Note that both 2D inversion models of the KIM-NAM and the ZIM profile have vertical cell dimensions of about 20 km at a depth of 200 km. Therefore the depth of the lithosphere-asthenosphere boundary cannot be identified to a precision of better than about $\pm$ 20 km.

Despite the very large distance between the KIM-NAM and the ZIM profiles there are similarities between the GCB (this study) and the Damara/Ghanzi-Chobe Belt by Muller et al. (2009). Both profiles show a very resistive crust and, although the Ghanzi-Chobe Belt is Meso- to Neoproterozoic and not Archaean, the lithospheric mantle resistivity is enhance compared to the neighbouring belts. Resistive lithospheric mantle was also observed beneath the Proterozioc Nipigon Embayment in Canada, which has been interpreted as a failed rift (Ian Ferguson, University Manitoba, Canada, pers. com.). Modie (1996) also suggests that the Ghanzi-Chobe belt represents a failed intra-continental rift basin, which could be the reason for the enhanced lithospheric mantle resistivities.

The resistivity-depth profiles of the Zimbabwe Craton and the unconstrained Magondi Mobile Belt show a strong decrease in bulk resistivity at depths of about 60 - 100(120) km, which is not apparent in any of the resistivity versus depth profiles of the KIM-NAM terranes nor the Ghanzi-Chobe Belt. Inspecting the KIM-NAM and ZIM models in Figure 5.12 (a) and (b), respectively, such a conductive zone does seem to exist in the Damara/Ghanzi-Chobe (DMB) and the Ghanzi-Chobe Belt (GCB) in lower crustal/upper mantle depths above 50 km (and therefore is cut-off in the resistivity versus depth profiles in Figure 5.12 (c)). Figure 5.13 shows the average resistivity-depth profiles of Figure 5.12 (c) including the crustal depth range. The full depth range reveals a conductive zone in nearly all the resistivity-depth profiles in mid- to lower-crustal depths that is already indicated in the 2D inversion models in Figure 5.12. Ignoring the poorly constrained lithospheric mantle part of the Magondi resistivity-depth curve, the only resistivity-depth profile that shows the conductor below 50 km is the ZIM profile. That raises the question, what is different about the Zimbabwe Craton relative to all the other terranes? The most obvious difference is the Okavango dyke

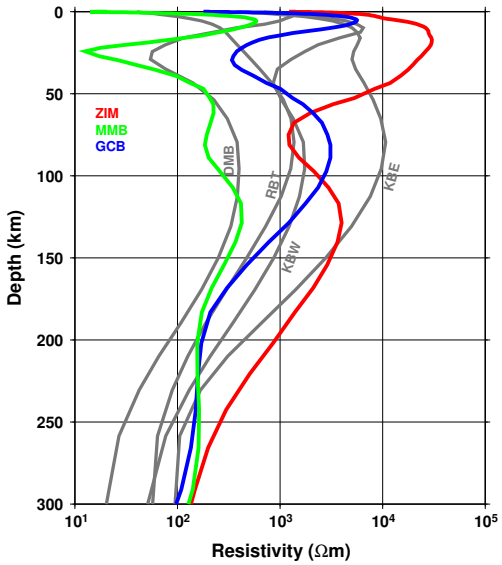

Figure 5.13: Average resistivity-depth profiles from SAMTEX data. This figure shows the average resistivity-depth curves from Figure 5.12 but also includes the crustal depths.

Table 5.1: Table listing the resistivity values of the top layer and the related principal resistivities of the anisotropic block of the models shown in Figure 5.14. Based on the background resistivity of the top layer, ρ_b, and the assumption that the dykes have a dilatation of 12.2% and a resistivity of about 30000 Ωm, the principal resistivities, ρ_x, ρ_y and ρ_z, of the anisotropic block are calculated using Equations 2.86 and 2.89.

MODEL	ρ_b	$\rho_x/\rho_y/\rho_z$
A	100 Ωm	113.8 Ωm / 3747.8 Ωm / 113.8 Ωm
B	200 Ωm	227.6 Ωm / 3835.6 Ωm / 227.6 Ωm
C	500 Ωm	568.2 Ωm / 4099 Ωm / 568.2 Ωm
D	1000 Ωm	1133.7 Ωm / 4538 Ωm / 1133.7 Ωm
E	2000 Ωm	2257 Ωm / 5416 Ωm / 2257 Ωm
F	5000 Ωm	5565.9 Ωm / 8050 Ωm / 5565.9 Ωm

swarm at crustal depths. To examine the possible effect of the dyke swarm, synthetic data, accounting for the dyke swarm by using an anisotropic layer, were generated and then inverted isotropically. As discussed in Section 4.3, the very limited width of the dykes makes them more of an anisotropic feature than a normal 2D structure at the MT scale. The Karoo-aged dolerites of the dyke swarm are assumed to have a resistivity of 30000 Ωm (van Zijl, 2006), the dilatation of the dykes in that area is estimated to be 12.2% (Le Gall et al., 2005) and Equations 2.86 and 2.89 are used to calculate the principal anisotropic resistivities for various background resistivities, which are listed in Table 5.1. Figure 5.14 shows three classes of models used to calculate forward responses: a reference model, which contains only the layered background model but no dykes ((a), the model is called NODYKES), a model where an anisotropic block in the top layer simulates the dykes ((b), TOPLAYER) and a model where the anisotropic dykes extend through both crustal layers ((c), CRUST). The 2D forward anisotropy code by Pek and Verner (1997) was used to calculated the synthetic data sets, which were then decomposed using STRIKE (McNeice and Jones, 2001) and

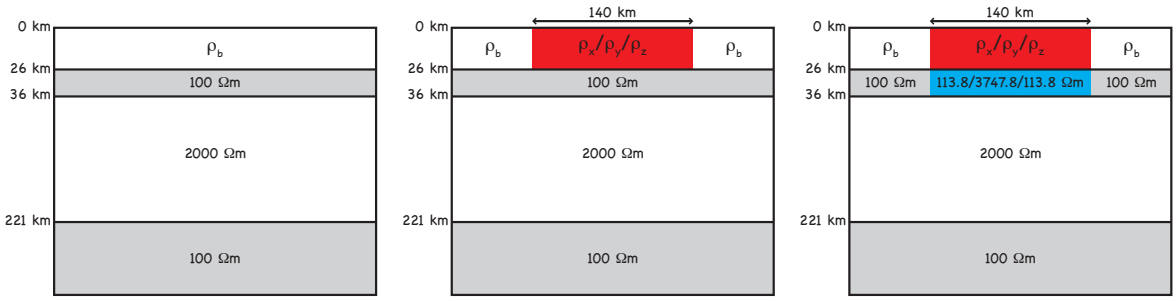

(a) Model: NODYKES (b) Model: TOPLAYER (c) Model: CRUST

Figure 5.14: Figure showing sketches of the three model classes tested: NODYKES (a), which is the background model of the two other classes, TOPLAYER (b), where dykes, and therefore anisotropy, are only present in the top layer, and CRUST (c), where the anisotropic dykes extend through both crustal layers. Different resistivity settings for the top layer of the three model classes are listed in Table 5.1.

finally inverted using the same inversion strategy as for the ZIM line data using WinGLink® (Rodi and Mackie, 2001).

The WinGlink® 2D inversion results are shown for 3 example models in Figure 5.15 (and for all models in Figures C.15 to C.17 in Appendix C.2). It is obvious that the presence of the dykes (or an anisotropic layer) causes the lower crustal conductor to deflect downward, when an isotropic inversion is applied, and allows it to appear as an upper lithospheric mantle structure. Although the meshing is relatively coarse at depths close to 200 km, and therefore an accurate estimate in kilometres cannot be made, it is apparent that the lithosphere-asthenosphere boundary might also be affected by the presence of the dyke swarm. The boundary seems to be slightly deeper than the case without the dykes and the resistivity of the lithospheric mantle seems slightly enhanced. The models with the dykes in the top layer only exhibit a 'drop-like' or undulating resistivity structure at the boundary between the anisotropic layer and the mid- to lower-crustal conductor. The smoother downwards deflection that appears if the dykes are present in both crustal layers is more similar to the 2D inversion result of the ZIM line and might therefore be an indication that the dykes extend into the mid- to lower-crust. Introducing a tear zone into the model, where the anisotropic block is located, does not improve the inversion result (see Figure C.18 in Appendix C.2). Resistivity-depth profiles have been extracted from all models, averaging over the lateral extent of the anisotropic block, and are plotted in Figure 5.16 sorted by model classes (NODYKES (a), TOPLAYER (b) and CRUST (c)). In the absence of the anisotropic layer, the conductor appears as mid- to lower-crustal structure (a) as it does for all SAMTEX resistivity-depth profiles in Figure 5.13, except for the ZIM profile. Although none of these simple synthetic models is able to reproduce the exact shape of the ZIM line resistivity-depth profile, the downward shift of the conductor due to the dykes is obvious. Also, changes in the depth of the inflection point of the resistivity-depth profiles associated with the thermal thickness of the lithosphere, towards greater depths, can be identified. The test of 2D isotropic inversion of the anisotropic dyke model data strongly suggests that the appearance of the conductor below 50 km in the ZIM resistivity-depth profile and the deflected conductor in the 2D inversion model are artefacts, and that the conductor is in reality located in the mid- to lower-crust, as is observed in all other resistivity-depth profiles.

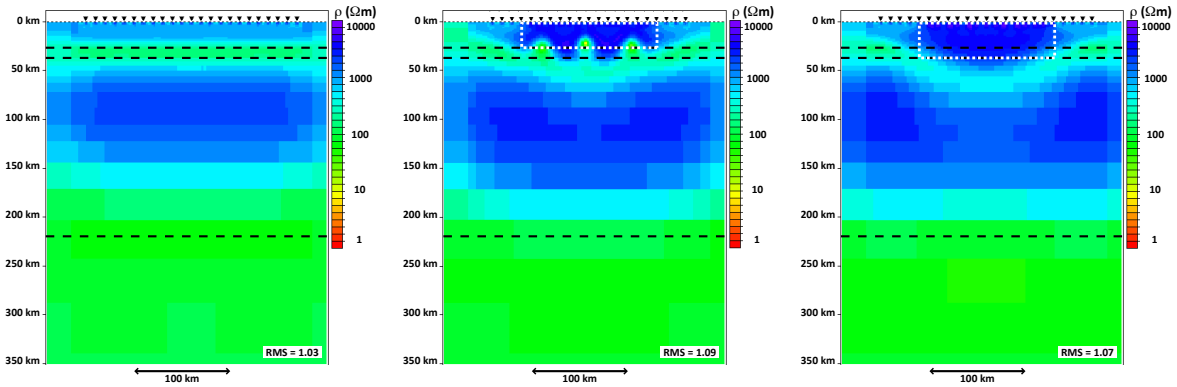

(a) Model: NODYKES D (b) Model: TOPLAYER D (c) Model: CRUST D

Figure 5.15: Figures showing the 2D isotropic inversion results of synthetic 2D anisotropic data (generated using Pek and Verner's (1997) code) simulating dykes of 30000 Ωm in the crust. The white dashed line outlines the area of the anisotropic block representing the dykes and the layered background is illustrated by black dashed lines (for more details on the exact models see Figure 5.14 and Table 5.1). Panel (a) shows, as reference, the NODYKES D model (1000 Ωm top layer). In (b) the example of model TOPLAYER D is shown and in (c) model CRUST D. Figures C.15 to C.17 in Appendix C.2 show the results of all 18 test models.

Schwarz (1990) reviewed the nature of lower-crustal conductors. As the porosity in rocks decreases with increasing depth, the hydrostatic pore volume should be reduced exponentially, leaving a residual isolated pore volume of highly saline fluids (Schwarz, 1990). Therefore a continuously increasing electrical resistivity with depth, with a change from electrolytic conduction in pore space to solid state electrical conduction in minerals, is expected, but MT studies showed more conductive resistivities than expected (e.g., Shankland and Ander, 1983). Candidates for lowering the electrical resistivity of the continental crust are fluids (free water with a high ionic content), free carbon (graphite) and other conducting minerals, such as magnetic oxides or sulphides, or partial melting (Schwarz, 1990). If a zone of high electrical conductivity correlates with high seismic reflectivity in the lower-crust, then the existence of fluids (especially in the deep, ductile crust) is the most likely cause (e.g., Jones, 1987). However, there are no seismic reflection constraints available in the ZIM line area. Shankland and Ander (1983) found that free water of 0.01 - 0.1 vol% kept in fracture porosity would be sufficient to account for the observed lower resistivities. Schwarz (1990) notes that large interconnected fluid systems are required, and an effective pore pressure near zero is demanded over a geological time scale (at least several millions of years), which is highly unlikely as such a lithostatic fluid system would have unrealistically small hydraulic permeabilities.

If interconnected graphite flakes or graphite grain coatings are present, the electrical resistivity decreases by several orders of magnitude (Nover et al., 1998), which accounts for large-scale resistivity anomalies in the continental crust in some settings (Duba and Shankland, 1982). Other conducting minerals such as found in hydrothermal ore deposits originate in the uppermost crust at temperatures below 400°C and pressures of less than 2 kbar (Schwarz, 1990), and therefore are not very likely to be the cause of a lower crustal conductor of such a large spatial scale (other than the more localised conductors within the Magondi Mobile Belt).

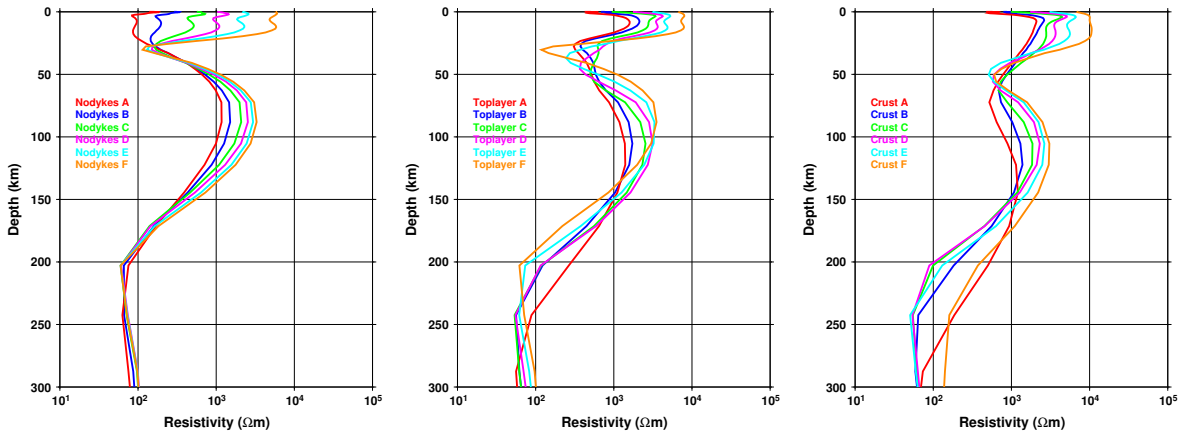

(a) Average resistivity-depth profiles of NODYKES models

(b) Average resistivity-depth profiles of TOPLAYER models

(c) Average resistivity-depth profiles of CRUST models

Figure 5.16: Resistivity-depth profiles through the inversion models in Figure 5.15 (and Figures C.15 to C.17 in Appendix C.2), averaged over the lateral extent of the anisotropic block simulating the dykes. Panel (a) shows the resistivity-depth profiles of the NODYKES A - F models, while (b) shows the profiles of the TOPLAYER A - F models and (c) of the CRUST A - F models. The models, described in Figure 5.14 and Table 5.1, were used to generate synthetic anisotropic data sets using Pek and Verner's (1997) code and these data were then decomposed and modelled using 2D isotropic inversion (results are shown Figures 5.15, C.15 to C.17).

Melt or partial melt also can reduce the electrical resistivities, but for melt to occur in crustal depths, very high temperatures of above 700°C are required, which may only be found in tectonically active zones (Schwarz, 1990). To account for large scale conductors the melts must also be connected over large distances, which seems very unlikely for the Archaean and Proterozoic terranes of and around the Zimbabwe Craton.

No final conclusion regarding the cause of such a lower crustal conductor can be made in the case of the ZIM line, as additional information is required to support or rule out the different hypotheses, but graphite might be the explanation to favour.

In conclusion, the lithospheric mantle of the Ghanzi-Chobe Belt and the Zimbabwe Craton is highly resistive, but due to a lack of data coverage at depth, no information is available to constrain whether these resistors are connected or not. The inflection point of the Ghanzi-Chobe Belt resistivity-depth profile suggests a depth of about 180 km to the thermal lithosphere-astenosphere boundary. A lithospheric thickness of about 220 km is therefore estimated for the Zimbabwe Craton based on a 40 km relative difference in thickness between the Ghanzi-Chobe Belt and the Zimbabwe Craton. The synthetic model study has shown that the 220 km thickness might be overestimated, as the isotropic inversion in the presence of the anisotropic dyke swarm not only images the mid- to lower-crustal conductor at greater depths, but might also increase the thickness of the resistor related to the lithospheric mantle of the Zimbabwe Craton. The Letlhakane and Orapa kimberlite pipes are about 150 - 200 km to the west of the ZIM line. Stiefenhofer et al. (1997) and Griffin et al. (2003) found that the pressure-temperature data of the kimberlite xenoliths from these pipes show a ~41 mW/m^2 lithospheric geotherm at the time of pipe emplacement (at about 93 Ma, Stiefenhofer et al. (1997)), which is similar to the geotherm found at the Eastern Kimberley

Block and corresponds to a thermal thickness of the lithosphere (defined by the intersect of the geotherm with the mantle adiabat) of about 220 km (Muller et al., 2009, and references therein). Xenoliths are only available from a maximum depth of about 200 - 205 km. Fertile lherzolites dominate in abundance above 120 km depth. Between 120 - 190 km depth, depleted harzburgites, with evidence of metasomatism, increase in abundance and below a very sharp transition at 190 km depth, sheared melt-metasomatised xenoliths dominate, with abundances of 80 - 100% (Griffin et al., 2003). Sheared melt-metasomatism is often taken as indication of proximity to the base of the lithosphere. Kennedy et al. (2002) propose that sheared melt-metasomatised xenoliths are a result of transitory, high-strain-rate deformation in a zone of noncoaxial strain localised at the base of the lithosphere. As it remains unclear as to which geological terrane the pipes of Orapa and Letlhakane are associate with (the Zimbabwe Craton or the Magondi Mobile Belt), it may not be appropriate to use the geothermal information from the Letlhakane and Orapa pipes to support the lithospheric thickness of about 220 km suggested by the MT 2D inversion result for the Zimbabwe Craton.

Using 2D modelling of magnetic data, Dailey et al. (2009) estimated the depth extent of the Okavango Dyke Swarm in the ZIM line area. They derived a broad range for the maximum possible extent - between 4 - 30 km - but favour an extent of about 14 - 18 km. The synthetic 2D anisotropy test described above supports a depth extent through most of the crust, which is not inconsistent with the maximum depth range estimated from the magnetic data.

Part III

3D FORWARD MODELLING AND INVERSION

6

THE FORWARD SOLVER

This chapter discusses the 3D finite-element forward solver, which is the driving engine of the inversion algorithm (Chapter 8). The basics of the forward code will be explained in detail to provide the background knowledge needed when discussing the inversion program later. Although the forward solver does not take full advantage of the flexibility and power of the finite-element method (i.e., it only uses rectilinear meshes and not unstructured ones), the code is an appropriate choice: the forward solver provides good results (see Chapter 7) and was selected for this thesis work because of the full access to the source code and to the support of Colin Farquharson (MUN, St. John's, Newfoundland, Canada), who is the programmer of the forward solver.

Three-dimensional forward modelling of MT data is essential for understanding the physics of the MT problem, inverting MT data (since each inversion code is based on a forward algorithm), verification of hypothetical 3D resistivity models and for feasibility studies. In the 1970's, several methods for computing the fields of 3D resistivity models (or conductivity models) of the subsurface were developed (e.g., Jones and Pascoe (1972), Raiche (1974), Hohmann (1975), Weidelt (1975)). Since then, these methods have been improved and refined (see Avdeev (2005) for a recent review) and the recent advances in computing facilities and iterative solvers allow the computation of larger and more complicated numerical problems.

There are three categories of methods for solving the 3D numerical problem: integral equation (e.g., Wannamaker (1991), Xiong (1992), Avdeev et al. (2002)), finite difference (e.g., Mackie et al. (1994), Sasaki (1999), Siripunvaraporn et al. (2005)) and finite element (e.g., Mitsuhata and Uchida (2004), Nam et al. (2007)). Integral-equation methods are appropriate for models with a localised, anomalous region (such as mineral deposits) embedded in a simple background. Only the anomalous region requires discretisation, and therefore fewer unknowns are involved and smaller systems of equations must be solved than required for the other methods. In earlier years, with limited computer resources, integral-equation methods were the most practical option, but increasing computer speed and memory have promoted the use of finite-difference methods. These finite-difference methods have the advantage that they are more suitable for more complicated and generalised models. Due to the requirement of discretisation of the whole 3D mesh, however, many more unknowns are involved than for the integral-equation methods, and therefore a much larger system of equations must be solved. Finite-difference methods, compared to finite-element methods, are relatively straight-forward to implement on a rectilinear grid, which is the simplest 3D mesh. Recently the interest in finite-element methods has increased because they are better suited to unstructured meshes than the finite-difference methods. Unstructured grids allow a better representation of surface topography and realistic subsurface interfaces than

do rectilinear grids. Finite-element methods also allow a transition to larger cells in the padding/boundary regions of the mesh without significant increase in aspect ratios of the cells, and therefore enable an efficient discretisation of a volume without the numerical solution problems that can be caused by large aspect ratios.

First applications of the finite-element method to the 3D EM problem are described by Reddy et al. (1977), Pridmore et al. (1981), Livelybrooks (1993) and Mogi (1996). They all used a rectilinear mesh and nodal elements, i.e., the electric field is expressed as a linear combination of scalar basis functions, which are each associated with a particular cell vertex. By construction, nodal basis functions automatically satisfy the requirement of continuity of the tangential electric field between cells of different conductivities, but violates the boundary condition of continuity of normal current density and divergence-free electric fields within each cell (see Section 6.1 for more details). To avoid the problems with nodal elements, vector finite elements, or edge elements, were developed (see e.g., Jin (2002), and references therein, for more details). For the edge-element approach the electric field is approximated by a linear combination of vector basis functions, which are each associated with a particular edge and, by construction, the approximate electric field is divergence-free within a cell (i.e., a cell does not contain a source of current or charge) and its tangential component is continuous from one cell to the next (see Section 6.1 for more details). Vector basis functions with these properties (i.e., divergence-free within a cell and continuity of tangential component between cells) can be constructed for general hexahedral and tetrahedral meshes (e.g., Jin, 2002). In 3D EM modelling, edge elements are used for rectilinear meshes (Sugeng, 1998), structured meshes of hexahedral (i.e., distorted brick) elements (Nam et al., 2007) and unstructured grids of tetrahedral elements (Börner et al., 2008; Liu et al., 2008). Lee et al. (1991) and Zyserman and Santos (2000) used higher-order vector elements on tetrahedral elements and rectilinear meshes, respectively, where the variation in perpendicular direction to the edge is controlled by the higher-order function. Some authors also decompose the electric field into vector and scalar potentials: Everett and Schultz (1996), Badea et al. (2001) and Stalnaker et al. (2006) use nodal elements to approximate both potentials, whereas Yoshimura and Oshiman (2002) neglect the scalar potential as a gauge condition (after Hano, 1991) and use edge elements to approximate the vector potential. Mitsuhata and Uchida (2004) use edge and nodal elements to approximate the vector and scalar potentials, respectively, of the decomposed magnetic field.

The edge finite element code presented here uses a standard edge-element electric field approach including the application of the divergence correction after Smith (1996) and is described by Farquharson and Miensopust (subm).

6.1 NODAL- AND EDGE-ELEMENT BASIS FUNCTIONS

Both the nodal- and the edge-element formulations have been introduced above and since both will be used in the forward code, their basis functions will be discussed in more detail. Figure 6.1 shows sketches for (a) the nodal-element approach and (b) the edge-element formulation. The grey surface in the mesh sketch shows the spatial location of the faces with the basis function arrows. One can see the decrease in all directions from unity at the shared vertex to zero at all other vertices for the nodal element (Figure 6.1 (a)). By construction, every component is continuous from one cell to the next, but there are not necessarily divergence-free conditions within the cell. In the case of the edge-element formulation, the

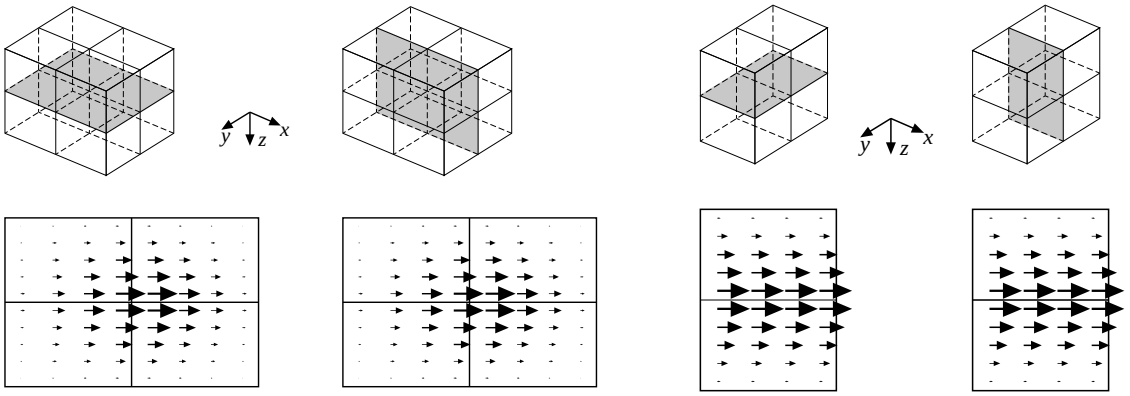

(a) Basis functions of nodal elements

(b) Basis functions of edge elements

Figure 6.1: Sketch of (a) nodal- and (b) edge-element basis functions. The nodal-element basis functions are equal to unity at the shared vertex, decrease linearly in each direction and are zero at all other vertices, whereas the edge-element basis functions are equal to unity along the shared edge, are invariant in the direction of the shared edge and decrease linearly in the two directions perpendicular to the shared edge. (Taken from Farquharson and Miensopust (subm).)

basis functions are equal to unity along the shared edge and consistent in the direction of the edge, while in the two perpendicular directions to the shared edge, the linear decrease to zero at all the other edges is clear (Figure 6.1 (b)). For the edge-element formulation, both the conditions of the continuity of the tangential component from one cell to the next and zero divergence within the cells are fulfilled by construction. Therefore, the edge elements are used for the determination of the approximate electric field (see Section 6.2), whereas the nodal elements are applied to the divergence correction (see Section 6.3).

As an example, for the edge-element formulation, the basis function $\underline{v}_j$ of the jth edge is the one shared by the four cells as sketched in Figure 6.2. Assuming that this edge is orientated in x-direction, the associated basis function is given by

$$\underline{v}_j = \begin{cases} C_{m-1,n-1}(y - y_{m-1})(z - z_{n-1})\,\underline{\hat{x}}, & y \in Y_m, z \in Z_n, \\ C_{m,n-1}(y_{m+1} - y)(z - z_{n-1})\,\underline{\hat{x}}, & y \in Y_{m+1}, z \in Z_n, \\ C_{m-1,n}(y - y_{m-1})(z_{n+1} - z)\,\underline{\hat{x}}, & y \in Y_m, z \in Z_{n+1}, \\ C_{m,n}(y_{m+1} - y)(z_{n+1} - z)\,\underline{\hat{x}}, & y \in Y_{m+1}, z \in Z_{n+1}, \\ 0, & \text{otherwise}, \end{cases} \tag{6.1}$$

where $Y_m = [y_{m-1}, y_m[$, $Z_m = [z_{m-1}, z_m[$, $C_{m,n} = 1/[(y_{m+1} - y_m)(z_{n+1} - z_n)]$, and $\underline{\hat{x}}$ is the unit vector in x-direction. Equation 6.1 is only valid for $x_l \leqslant x < x_{l+1}$, and for all other values of x this particular basis function is zero. Basis functions for the y- and z-directed edges are defined in a similar manner. For an example cell, all edge basis functions, their curl operations and the multiplication of the curl basis functions (as required for the determination of the approximate electric field; see Equation 6.10) are formulated as shown in Appendix D.1.

A nodal-element basis functions u_k associated with the kth node that has coordinates (x_l, y_m, z_n) is given by

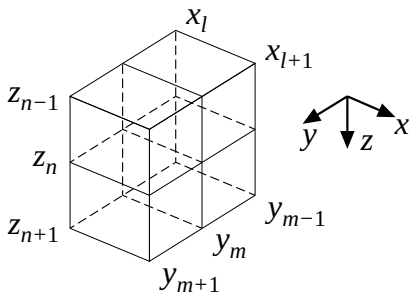

Figure 6.2: Sketch of the jth edge shared by four cells. The x-directed edge ($x_l \leqslant x < x_{l+1}$) at y_m and z_n is shared by four cells and the coordinate labels are those used in Equations 6.1. (Taken from Farquharson and Miensopust (subm).)

$$u_k = \begin{cases} C_{l-1,m-1,n-1}(x-x_{l-1})(y-y_{m-1})(z-z_{n-1}), & x \in X_l, y \in Y_m, z \in Z_n, \\ C_{l,m-1,n-1}(x_{l+1}-x)(y-y_{m-1})(z-z_{n-1}), & x \in X_{l+1}, y \in Y_m, z \in Z_n, \\ C_{l-1,m,n-1}(x-x_{l-1})(y_{m+1}-y)(z-z_{n-1}), & x \in X_l, y \in Y_{m+1}, z \in Z_n, \\ C_{l,m,n-1}(x_{l+1}-x)(y_{m+1}-y)(z-z_{n-1}), & x \in X_{l+1}, y \in Y_{m+1}, z \in Z_n, \\ C_{l-1,m-1,n}(x-x_{l-1})(y-y_{m-1})(z_{n+1}-z), & x \in X_l, y \in Y_m, z \in Z_{n+1}, \\ C_{l,m-1,n}(x_{l+1}-x)(y-y_{m-1})(z_{n+1}-z), & x \in X_{l+1}, y \in Y_m, z \in Z_{n+1}, \\ C_{l-1,m,n}(x-x_{l-1})(y_{m+1}-y)(z_{n+1}-z), & x \in X_l, y \in Y_{m+1}, z \in Z_{n+1}, \\ C_{l,m,n}(x_{l+1}-x)(y_{m+1}-y)(z_{n+1}-z), & x \in X_{l+1}, y \in Y_{m+1}, z \in Z_{n+1}, \\ 0, & \text{otherwise}, \end{cases} \tag{6.2}$$

where $X_l = [x_{l-1}, x_l[$, $Y_m = [y_{m-1}, y_m[$, $Z_m = [z_{m-1}, z_m[$ and $C_{l,m,n} = 1/[(x_{l+1} - x_l)(y_{m+1} - y_m)(z_{n+1} - z_n)]$. All nodal basis functions and their gradients for an example cell (as required to determine the correction potential; see Equation 6.24) can be found in Appendix D.2.

Several publications deal with the advantages and disadvantages of nodal- versus edge-element formulations (e.g.,Mur (1993) ,Webb (1993), Mur (1994, 1998)). The major points are:

- For nodal elements all components are automatically continuous, which is a disadvantage because in electromagnetism often the discontinuity of a field component is needed (e.g., the normal component of the electric field changes abruptly across an interface between two media of different resistivity). Edge elements on the other hand ensure continuity of tangential field components across an interface between different media, but at the same time allow jumps of the normal field components across such interfaces.
- Boundary conditions in EM have often the form of a specification of the tangential components only. Implementation of this kind of boundary conditions is straightforward with edge elements, but requires a transformation into a linear relationship between the Cartesian coordinates for nodal elements.
- Most types of edge elements have zero divergence and therefore can only be applied to solve problems where the solution is a priori known to be divergence-free. For the

MT case (unlike e.g., controlled-source EM) the source-free assumption is valid and therefore edge elements can be applied.

- Edge elements are computationally much more expensive (e.g., in storage requirements and computation time) than nodal elements because they involve many more unknowns (e.g., for a rectilinear mesh with 10 x 10 x 10 cells there are 11 x 11 x 11 = 1331 nodes but 3 x (10 x 11 x 11) = 3630 edges).

6.2 THE EDGE FINITE-ELEMENT FORWARD PROBLEM

The forward code that will be used as engine for the inversion code (Chapter 8) is an edge finite element code by Colin Farquharson (pers. com.). It is implemented for an $e^{-i\omega t}$ time dependence and a simple rectilinear mesh. The partial differential equation to be solved is (analogous to Equation 2.34) given by

$$\begin{aligned} \nabla \times \nabla \times \underline{E} &= \nabla \times i\omega \underline{B} = i\omega\mu_0\sigma\underline{E} \\ \Rightarrow \nabla \times \nabla \times \underline{E} - i\omega\mu_0\sigma\underline{E} &= 0 \quad , \end{aligned} \tag{6.3}$$

where $\underline{E}$ is the electric field, ω is the angular frequency, μ_0 is the free space magnetic permeability and σ is the electric conductivity. (Note that σ is used in the equations to simplify matters, but the numerical formulation uses $\log(\sigma)$ instead, as it offers a more linearised solution and automatic positivity constraints on the conductivity for the inversion part of the code.) There is no explicit source term in Equation 6.3 as boundary conditions are used to implement the effects of the plane-wave source, which is generally assumed as the source for modelling MT data. Inhomogeneous Dirichlet boundary conditions are used, i.e., specifically, the tangential component of the electric field on the boundary of the solution domain is set up equal to the MT electric field in a homogeneous halfspace.

A rectilinear mesh and a Cartesian coordinate system with axes normal to the planes of the cells are used to discretise and describe the Earth's subsurface and the air above. Based on the assumption of uniform conductivity within each cell, the approximate electric field $\tilde{\underline{E}}$ throughout the mesh is explicitly specified for a particular frequency as

$$\tilde{\underline{E}} = \sum_{j=1}^{N} \tilde{E}_j \underline{\nu}_j \quad , \tag{6.4}$$

where $\underline{\nu}_j$ is the edge-element vector basis function (see Equation 6.1) associated with the jth cell edge in a mesh containing a total number of N edges. The complex coefficient $\tilde{E}_j$ corresponds to the component of the approximate electric field on and aligned with the jth edge. Substituting the electric field in Equation 6.3 with the approximate electric field (Equation 6.4) yields

$$\sum_{j=1}^{N} \tilde{E}_j \left\{ \nabla \times \nabla \times \underline{\nu}_j - i\omega\mu_0\sigma\underline{\nu}_j \right\} - \underline{R} = 0 \quad , \tag{6.5}$$

where the error, or residual, of using an approximate electric field is represented by $\underline{R}$. The Galerkin method is used to derive an edge finite-element solution to Equation 6.5.

Galerkin's method belongs to the family of weighted residual methods, which seek the solution by weighting the residual of the differential equation (Jin, 2002). Therefore a set of weighting functions $\underline{w}_i$ $(i = 1, ..., M)$ are considered. Taking the scalar product of the weighting functions with Equation 6.5 and integrating over the whole 3D volume V gives

$$\sum_{j=1}^{N} \tilde{E}_j \left\{ \int_V \underline{w}_i \cdot \nabla \times \nabla \times \underline{v}_j \, dv - i\omega\mu_0 \int_V \sigma \underline{w}_i \cdot \underline{v}_j \, dv \right\} - \int_V \underline{w}_i \cdot \underline{R} \, dv = 0 \quad . \tag{6.6}$$

The best approximation for a solution will be the one that reduces the average (over all points of V) of the weighted residual to the least value. Therefore Galerkin's method enforces the condition

$$R_i = \int_V \underline{w}_i \cdot \underline{R} \, dv = 0 \quad , \tag{6.7}$$

where R_i is the weighted residual integral corresponding to the chosen weighting function $\underline{w}_i$. In Galerkin's method, the weighting functions are selected to be the same as those used for the expansion of the approximate solution (Jin, 2002), i.e., the basis functions are used as weighting functions. Therefore the system of equations to solve is given by

$$\sum_{j=1}^{N} \tilde{E}_j \left\{ \int_V \underline{v}_i \cdot \nabla \times \nabla \times \underline{v}_j \, dv - i\omega\mu_0 \int_V \sigma \underline{v}_i \cdot \underline{v}_j \, dv \right\} = 0 , \qquad i = 1, ..., N. \tag{6.8}$$

Because of the linear spatial dependence of the edge-element basis functions, the first integral on the left-hand side of Equation 6.8 is zero. Considering the real electric field rather than the basis function $\underline{v}_j$, the integral would not necessary be zero because of the deficiency of such a linear dependence for the electric field (Jin, 2002). Therefore integration by parts is applied to the first integral considering only the pth cell (where the basis functions are non-zero)

$$\int_{V_p} \underline{v}_i \cdot \nabla \times \nabla \times \underline{v}_j \, dv = \int_{V_p} (\nabla \times \underline{v}_i) \cdot (\nabla \times \underline{v}_i) \, dv - \int_{S_p} (\underline{v}_i \times \nabla \times \underline{v}_j) \cdot \hat{\underline{n}} \, ds , \tag{6.9}$$

where S_p is the whole surface of the pth cell and $\hat{\underline{n}}$ is the unit outward normal to the surface. The first integral on the right-hand side of Equations 6.9 involves only first-order derivatives and is therefore non-zero. The contribution to the second integral is zero if the basis function $\underline{v}_i$ is normal to the face, and therefore $\underline{v}_i \times \nabla \times \underline{v}_j$ is purely tangential. For the other cases, where the $\underline{v}_i$ is tangential to the face, the normal component of $\underline{v}_i \times \nabla \times \underline{v}_j$ depends on $\underline{v}_i$ and the tangential component $\nabla \times \underline{v}_j$. By construction, $\underline{v}_i$ is continuous from one cell to its neighbour and, thinking in terms of electric fields rather than basis functions, the integrand would involve $\nabla \times \underline{E} = i\omega\mu_0 \underline{H}$ instead of $\nabla \times \underline{v}_j$. Therefore the tangential component of $\underline{H}$ would be continuous from cell p to its neighbour, and for this face, the normal component of $\underline{v}_i \times \underline{H}$ would be continuous from cell p to its neighbour too. Hence, the contribution to the surface integral from this face of cell p would be cancelled by the contribution of the same face for the neighbouring cell to the corresponding surface integral. Based on this argument the surface integral can be neglected and Equation 6.8 can be written as

$$\sum_{j=1}^{N} \tilde{E}_j \left\{ \int_V (\nabla \times \underline{\nu}_i) \cdot (\nabla \times \underline{\nu}_j) \, dv - i\omega\mu_0 \int_V \sigma \underline{\nu}_i \cdot \underline{\nu}_j \, dv \right\} = 0 , \qquad i = 1, ..., N. \tag{6.10}$$

Since the boundary conditions are such that the tangential component of the electric field is specified on the boundaries of the mesh, the weighting functions with non-zero tangential components on the boundary need not be included. This means that the contributions to the surface integral in Equation 6.9 vanish for cell faces on the boundaries of the mesh.

The system of equations in Equation 6.10 can be expressed as a matrix equation of the form $\underline{\underline{A}}\,\underline{x} = \underline{b}$, separating real $\underline{\tilde{E}}^R$ and imaginary $\underline{\tilde{E}}^I$ parts of the electric field

$$\begin{pmatrix} \underline{\underline{C}} & \underline{\underline{S}} \\ -\underline{\underline{S}} & \underline{\underline{C}} \end{pmatrix} \begin{pmatrix} \underline{\tilde{E}}^R \\ \underline{\tilde{E}}^I \end{pmatrix} = \begin{pmatrix} 0 \\ 0 \end{pmatrix} \quad , \tag{6.11}$$

where $C_{ij} = \int_V (\nabla \times \nu_i) \cdot (\nabla \times \nu_j) \, dv$ and $S_{ij} = \omega\mu_0 \int_V \sigma \nu_i \cdot \nu_j \, dv$ for $i, j = 1, ..., N$. The integration for C_{ij} and S_{ij} can be performed to give formulae that depend only on i, j, and the dimensions and conductivities of the cells for the given form of basis functions (Equation 6.1).

The matrix equation is manipulated in the following way to accommodate the Dirichlet boundary conditions for the electric field. All elements on a row of the matrix in Equation 6.11 that correspond to a weighting function associated with an edge located at the boundary of the mesh are set to zero, except for the main diagonal element, which is set to one. The related element of the right-hand side vector (Equation 6.11) is set equal to the value of the relevant component of the electric field on the boundary of the mesh. Homogeneous halfspace conditions are assumed for the Earth surrounding the discretised model domain, and therefore the values of the tangential electric field on the boundary of the mesh are those of the electric field generated in a homogeneous halfspace for the plane-wave source of MT. Iterative solvers in SPARSKIT (Saad, 1990) - such as BCGSTAB (stabilised bi-conjugate gradient), GMRES (generalised minimum residual), TFQMR (transpose-free quasi-minimum residual) and DQGMRES (direct versions of quasi generalised minimum residual) - with incomplete LU decomposition as preconditioner are applied to solve the matrix equation system (Equation 6.11). GMRES is the preferred choice, as it gives steady, reliable convergence (see Chapter 7). Throughout the iterative solution of Equation 6.11, a divergence correction, which is described below (Section 6.3), is applied at regular intervals. Once the approximate electric field is determined, the magnetic field can be obtained by applying Faraday's Law (Equation 2.10: $\nabla \times \underline{E} = i\omega\mu_0 \underline{H}$) to Equation 6.4

$$\underline{\tilde{H}} = -\frac{i}{\omega\mu_0} \sum_{j=1}^{N} \tilde{E}_j \nabla \times \underline{\nu}_j \quad , \tag{6.12}$$

where $\nabla \times \underline{\nu}_j$ are straight-forward to determine for the given spatial distribution of $\underline{\nu}_j$ (Equation 6.1). The MT transfer functions are calculated from the electric and magnetic field approximations, for the two different polarisations, by

$$\begin{pmatrix} Z_{xx} & Z_{xy} \\ Z_{yx} & Z_{yy} \end{pmatrix} = \begin{pmatrix} E_{x1} & E_{x2} \\ E_{y1} & E_{y2} \end{pmatrix} \begin{pmatrix} H_{x1} & H_{x2} \\ H_{y1} & H_{y2} \end{pmatrix}^{-1} \quad , \tag{6.13}$$

where the indices 1 and 2 indicate the two polarisations. For one polarisation, the magnetic field at the top of the mesh is pointing in the x-direction and for the other polarisation the magnetic field is pointing in the y-direction.

6.3 DIVERGENCE CORRECTION

For a standard edge-element electric field solution for the MT case using a rectilinear mesh, the iterative solution of the system of equations was found to converge slowly. The normal component of the current density across interfaces between cells of different conductivities, and across interfaces between cells which are of the same conductivity but in close proximity to conductivity changes, are definitely not continuous for early iterations and improve only slowly (Farquharson and Miensopust, subm). This observation is similar to that shown by Smith (1996) for a staggered-grid finite-difference solution to the electric field equation for plane-wave sources of the MT case. He found the convergence rate of the iterative solver slowed considerably at low frequencies and ascribed this to the decreasing significance of the conductivity term in the electric field equation (Equation 6.3) as frequencies decrease. The decreasing significance of the conductivity term implicitly diminishes the divergence-free current density requirement of the finite-difference approximation of the electric field and therefore Smith (1996) introduced a divergence correction term that significantly improved the convergence rate of his finite-difference solution. Similar correction terms are also used by Mackie et al. (1994), Sasaki (2001) and Siripunvaraporn et al. (2002) in their finite-difference algorithms for modelling MT data, and Uyeshima and Schultz (2000) for computing the response of a spherical Earth model.

In terms of the edge finite-element implementation presented here, the conductivity terms of the electric field equation are the elements of the submatrix $\underline{\underline{S}}$ in Equation 6.11. If the significance of $\underline{\underline{S}}$ is small, $\tilde{\underline{E}} + \nabla\phi$, for any scalar function of position ϕ, can provide an adequate solution of the matrix equation, and therefore an approximate solution of the partial differential equation. However, such an electric field would not satisfy the conservation of charges

$$\nabla \cdot \underline{J} = 0 \quad . \tag{6.14}$$

Equation 6.14 requires within a cell, in which the conductivity is constant,

$$\nabla \cdot \underline{E} = 0 \quad , \tag{6.15}$$

whereas on an interface between cells, Equation 6.14 explicitly requires that the normal component of the current density be continuous

$$\underline{\hat{n}} \cdot (\sigma_p \underline{E}_p)|_{S_{pq}} = \underline{\hat{n}} \cdot (\sigma_q \underline{E}_q)|_{S_{pq}} \quad , \tag{6.16}$$

where σ_p and σ_q are the conductivities in cell p and q respectively, $\underline{E}_p$ and $\underline{E}_q$ are the electric fields in those cells and S_{pq} is the interface between cells p and q. Equation 6.16 specifies by how much the normal electric field should be discontinuous between regions of different conductivities. The electric-field partial differential equation, and therefore the matrix equation (Equation 6.11), contains the information about the discontinuity in the normal electric field, but only implicitly and via the conductivity term. Iterative solution procedures struggle due to the disappearance, numerically, of the normal electric field discontinuity information from the matrix equation.

In general, edge elements are capable of modelling appropriate discontinuity in the normal electric field component between two cells of different conductivities, but there is no explicit information about the necessary jump built into the edge elements (unlike the continuity of the tangential field). The information about the discontinuity in the normal electric field would come from the differential equation, but at the low frequencies of the MT method this information (the conductivity term) vanishes from the discretised partial differential equations, and it is beneficial if the information about the discontinuity in the normal electric field comes from elsewhere. Following Smith's (1996) correction procedure, an approximate electric field that exists at some point in the iterative solution of Equation 6.11 and the divergence of the corresponding current density ($\nabla \cdot \underline{\tilde{J}}$, where $\underline{\tilde{J}}$ is the current density corresponding to the approximate electric field) are considered. The divergence of the current density will be non-zero where the jump in the normal component of the approximate electric field between cells of different conductivities is incorrect, or where there is a discontinuity between cells of the same conductivity. Physically, these erroneous jumps can be thought of as excessive (or deficient) charge densities on the cell faces. Calculating the static potential arising from these spurious charges and subtracting its gradient from the approximate electric field removes (to some extent) the part causing the violation of the charge conservation. As demonstrated by Smith (1996), applying such a correction at various points during the iterative solution of a finite-difference approximation to the electric field partial differential equation significantly improved the convergence rate.

The implementation of the static divergence correction requires the solution of the inhomogeneous partial differential equation for the static potential ϕ

$$\nabla \cdot (\sigma \nabla \phi) = -\nabla \cdot \underline{\tilde{J}} \quad , \tag{6.17}$$

where $\underline{\tilde{J}}$ is the current density of the approximate electric field $\underline{\tilde{E}}$. Within each cell the right-hand side of Equation 6.17 is zero, because the basis functions are divergence-free and the conductivity is constant within a cell. However, the approximate current density may be discontinuous across interfaces between cells. Therefore the term on the right-hand side of Equation 6.17 is non-zero on cell faces. The preceding inhomogeneous partial differential equation (see Equation 6.17) for the static potential is therefore replaced with the system

$$\nabla \cdot (\sigma \nabla \phi) = 0 \quad , \tag{6.18}$$

within cell p and

$$\underline{\hat{n}} \cdot (\sigma_p \nabla \phi_p - \sigma_q \nabla \phi_q)|_{S_{pq}} = \underline{\hat{n}} \cdot (\sigma_p \underline{\tilde{E}}_p - \sigma_q \underline{\tilde{E}}_q)|_{S_{pq}} \quad , \tag{6.19}$$

at the interface between cells p and q. The boundary condition is that the potential, ϕ, is zero on the boundaries of the mesh.

The standard nodal-element approach is used here to solve Equation 6.18 with the modifications necessary to incorporate Equation 6.19. The approximate potential, $\tilde{\phi}$, is given by

$$\tilde{\phi} = \sum_{k=1}^{N_n} \tilde{\phi}_k \, u_k \quad , \tag{6.20}$$

where u_k is the nodal element basis function (see Equation 6.2) associated with the kth node, N_n is the total number of nodes in the mesh and $\tilde{\phi}_k$ is the approximate potential at the kth node. As for the electric field equation, the Galerkin method is applied to obtain the approximate potentials by substituting Equation 6.20 into Equation 6.18 and multiplying by the basis function u_h as a weighting function. Integration over the whole domain, requiring that the residual is orthogonal to the basis functions, yields

$$\sum_{k=1}^{N_n} \tilde{\phi}_k \int_V u_h \nabla \cdot (\sigma \nabla u_k) \, dv = 0 \, , \qquad h = 1, ..., N_n \quad . \tag{6.21}$$

The integral on the left-hand side is zero for the given linear spatial dependence of the basis functions, but it would be non-zero if the potentials were used rather than the basis function u_k. Therefore integration by parts over the pth cell is applied

$$\int_{V_p} u_h \nabla \cdot (\sigma_p \, \nabla u_k) \, dv = -\int_{V_p} \sigma_p \, \nabla u_h \cdot \nabla u_k \, dv + \int_{S_p} \sigma_p \, u_h \, \nabla u_k \cdot \underline{\hat{n}} \, ds \quad , \tag{6.22}$$

where σ_p is the conductivity of the pth cell. For typical occurrences of potential differential equations, for example in DC resistivity, the contribution from the surface integral in Equation 6.22 will be cancelled by the contribution for the same face coming from the cell that shares the face. However in the situation here, Equation 6.19 means that there will be a non-zero difference between the contributions coming from the two cells that share a face, and that the difference will depend on the discontinuity of the approximate current density. The surface integral in Equation 6.22 can therefore be replaced by

$$\int_{S_p} \sigma_p \, u_h \, \nabla u_k \cdot \underline{\hat{n}} \, ds = \int_{S_p} \sigma_p \, u_h \, \tilde{E}_k \, \underline{v}_k \cdot \underline{\hat{n}} \, ds \quad , \tag{6.23}$$

where $\underline{v}_k$ is the basis function with the same spatial variation as ∇u_k. Using Equations 6.22 and 6.23, Equation 6.21 becomes

$$\sum_{k=1}^{N_n} \tilde{\phi}_k \int_V \sigma \nabla u_h \cdot \nabla u_k \, dv = \sum_{j=1}^{N} \tilde{E}_j \int_S \sigma \, u_h \, \underline{v}_j \cdot \underline{\hat{n}} \, ds \, , \qquad h = 1, ..., N_n \quad , \tag{6.24}$$

or in matrix form

$$\underline{\underline{D}}\,\underline{p} = \underline{t} \quad , \tag{6.25}$$

where $D_{hk} = \int_V \sigma \nabla u_h \cdot \nabla u_k \, dv$, $p_k = \tilde{\phi}_k$ and $t_h = \sum_{j=1}^{N} \tilde{E}_j \int_S \sigma u_h \underline{v}_j \cdot \underline{\hat{n}} \, ds$ for $h, k = 1, ..., N_n$ and S indicates all cell surfaces. Given the specific form of the basis functions (Equation 6.2), the formulae for D_{hk} and t_h can readily be derived in dependence of h, k, and the cell dimension and conductivity. Homogeneous Dirichlet boundary conditions are assumed for the potential, which are implemented in the same way as the electric field boundary conditions. That is, the elements on each row of the matrix for a weighting function corresponding to a node on the mesh boundary are set to zero, except for the diagonal element, which is set to one and the corresponding element of the right-hand side vector $\underline{t}$ is set to zero. Equation 6.25 is solved using the bi-conjugate gradient routine (BCGSTAB) from SPARSKIT (Saad, 1990) with incomplete LU decomposition as the preconditioner using $lfil = 10$ and a maximum of 1000 iterations. Since the coefficients of the approximate electric field, $\tilde{E}_j$, are complex valued, the above matrix equation (see Equation 6.25) is solved twice, once using the real part of $\tilde{E}_j$ in $\underline{t}$ and once using the imaginary part, while the matrix $\underline{\underline{D}}$ remains the same for both cases. The gradient of the computed approximate potential is added to the current approximated electric field

$$\underline{\tilde{E}} \leftarrow \underline{\tilde{E}} + \nabla \tilde{\phi} \quad . \tag{6.26}$$

After applying the correction to the approximate electric field, the corrected field is fed back into the iterative solution of the electric field system of equations (Equation 6.11). This correction process is repeated frequently during the solution of the electric field system.

7

HOW TO PROVE THE 3D FORWARD SOLVER?

Since there is no useful 3D analytic solution as reference to determine if a 3D forward algorithm is working properly, comparative studies are essential. (Groom and Bailey (1991) describe a partially analytic solution for a small hemisphere embedded in an otherwise 1D or 2D structure, but it is impractical to design a hemisphere using a rectilinear mesh.) Zhdanov et al. (1997) compared modelling results from various 3D forward codes as part of the COMPARISON OF MODELLING METHODS FOR ELECTROMAGNETIC INDUCTION (COMMEMI) project. Siripunvaraporn et al. (2002) investigated the accuracy of 3D MT finite-difference modelling in dependence on an E- or H-field formulation of the governing equations. A review of modelling and inversion schemes based on integral equation (IE), finite differences (FD) and finite elements (FE) was given by Avdeev (2005) and recently Han et al. (2009) compared the FE code by Nam et al. (2007) with the three widely used FD codes by Mackie et al. (1994), Sasaki (1999) and Siripunvaraporn et al. (2005).

The forward algorithm is the engine of an inversion code. Therefore it is necessary to investigate the reliability of the used forward code (described in Chapter 6). There are different strategies to test the forward algorithm, the ones being presented in this chapter are the comparison with 2D results as well as with 3D responses calculated by other people and/or codes.

To calculate the responses of the different 3D models various 3D meshes are set up. The number of unknowns in the electric-field and correction-potential computations are equal to the number of edges and nodes, respectively, in the mesh. All meshes include layers in the air, where the conductivity of the cells is set to 10^{-8} S/m (i.e., a non-zero value small enough to be considered as approximately zero). The number of airlayers varies from mesh to mesh and depends on the longest period used and on the trade-off between an adequately small increasing factor of the airlayers' thicknesses and the minimum number of airlayers required to ensure a sufficient distance between the top boundary of the mesh, where the magnetic dipole sources are located, and the air-Earth interface. In the ideal case the top boundary of the mesh should be at infinity because a plane wave source is assumed. As this cannot be implemented, the top boundary should at least be far enough away from the air-Earth interface that any magnetic field generated by induced currents in the ground has decayed to zero at the top boundary of the mesh. This is to enforce that the magnetic field on this boundary is equal to only the plane wave source field without any contribution from a secondary magnetic field, and therefore one would like the top boundary to be at least one skin depth away from the Earth's surface at the longest period, but even that is hard to attain given the resistivity of the air. Increasing the thickness of the airlayers with increasing distance above the Earth's surface avoids having to use a large number of layers to provide an adequate distance between the top boundary of the mesh and the Earth's

surface. On the other hand, the ratios by which the airlayer thicknesses increase should not be too large (less than a factor of two increase would be adequate), otherwise the numerical solution is slowed down. Finally the increase between the thicknesses of the top layer in the Earth (which depends on the shortest period used and the resistivities in the ground) and the first airlayer should not be too abrupt (preferentially they have the same thickness). Taking all the points above into consideration, one ends up with slightly different numbers of airlayers for different examples.

7.1 2D VERSUS 3D

7.1.1 *Extension of a 3D body to approach a 2D structure*

Jones (1983b) showed that the difference between data from a profile over a 3D structure (e.g., a dyke of finite length l) and the 2D response across the same dyke, but of infinite length, is dependent on the dimensionless ratio of length l to skin depth δ, where δ is the skin depth at a specific frequency in the host medium. If this ratio is far greater than 1, then the 2D and 3D results should show approximately the same TM response curves (TM mode data is sensitive to charges at boundaries, whereas TE is not), whereas if l/δ is smaller than 1, i.e., either the length l is too short or the frequency is too low, this assumption will not be valid. Therefore a 2D versus 3D comparison will give a good correlation for a certain range of high frequencies, whereas at lower frequencies this conformity cannot be expected. Note that the dimensionless ratio l/δ depends on the resistivity of the host medium but not on the resistivity of the 3D structure (e.g., the dyke resistivity). Table 7.1 shows the l/δ ratios related to a body with length $l = 50$ km for different periods (0.1 s to 1000 s) and different host medium resistivities (1 Ωm to 1000 Ωm) as well as ratios for a 100 Ωm host medium but different body length ($l = 10$ km to 100 km). These values suggest for a 50 km body that the 2D and 3D responses would be identical (within acceptable bounds) down to 100 s, possibly even down to 1000 s, for a 1 Ωm host medium, whereas in a 1000 Ωm host a correlation could only be expected for periods shorter than 1 s (possibly 10 s). One can also see that for the 100 Ωm host medium the shorter the body the smaller the period up to which the 3D response would be identical to the 2D solution. In the case of the 100 Ωm host, the 10 km body might result in 3D responses equal to the 2D results for periods $\leqslant 1$ s, whereas for a 100 km body length periods $\leqslant 100$ s result in comparable 2D and 3D responses.

Table 7.1: Ratios l/δ for different periods (0.1 s to 1000 s) and host medium resistivities (1 Ωm to 1000 Ωm) calculated for an assumed body length $l = 50$ km (left) as well as for different body length ($l = 10$ km to 100 km) in a 100 Ωm host medium (right).

	length l = 50 km				100 Ωm host medium			
	1 Ωm	10 Ωm	100 Ωm	1000 Ωm	10 km	20 km	50 km	100 km
0.1 s	316	100	31.6	10	6.32	12.6	31.6	63.2
1 s	100	31.6	10	3.16	2	4	10	20
10 s	31.6	10	3.16	1	0.63	1.26	3.16	6.32
100 s	10	3.16	1	0.32	0.2	0.4	1	2
1000 s	3.16	1	0.32	0.1	0.06	0.13	0.32	0.63

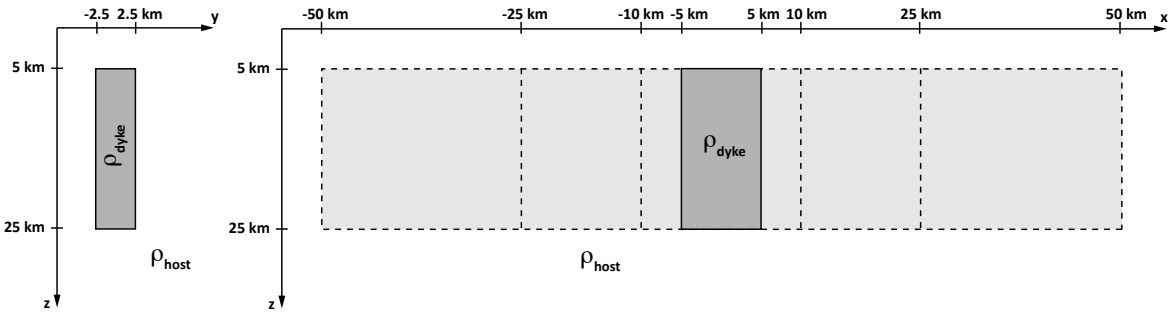

Figure 7.1: Sketch of the dyke model. The dyke is 5 km wide and 20 km thick. Its length extent (in x-direction) varies from 10 km, 20 km, 50 km to 100 km for the 3D model (and is infinite for the 2D model). Responses were calculated for a dyke resistivity of 1000 Ωm and a host medium resistivity of 100 Ωm.

The chosen model for this comparison is a dyke structure along the x-axis (see Figure 7.1). The dyke is located 5 km below the surface and is embedded in a homogeneous halfspace of 100 Ωm. The width of the dyke structure is 5 km and its thickness is 20 km. For the 3D modelling the length of the dyke was varied from 10 km, 20 km, 50 km to 100 km and its resistivity is 1000 Ωm. To calculate the 2D reference data set, which was assumed to be absolute correct, the 2D code from Rodi and Mackie (2001) (implemented in Geosystem's software WinGLink®) was used. Figure 7.2 shows the mesh, which was used to calculate the 3D responses for all four different dyke lengths at a site located directly in the mesh centre (at x = 0 km, y = 0 km). The total number of mesh cells is 71 x 71 x 47 (including 15 airlayers) and the mesh extent is 300 km x 300 km x 200 km. The numbers of edges and nodes, and hence the unknowns in the electric-field and correction-potential computations, are 734 400 and 248 832, respectively. Figure 7.3 shows the comparison of the 3D responses of the different dyke lengths (coloured symbols) and the 2D curves (solid black line) for (a) the xy and (b) the yx components. The results are obtained after 5000 iterations applying the divergence correction after Smith (1996) (see Section 6.3) every 50 iterations. The solver for these runs was the GMRES routine from SPARSKIT (Saad, 1990) with the size of the Krylov subspace set to 40 (just less than the number of iterations between each divergence correction to avoid the subspace acquiring and storing information from both, before and after a correction, which would happen if the subspace were larger than the number of iterations between the corrections). As expected the 3D response of the 100 km dyke matches the 2D curves well. The 3D responses of the other dyke lengths only agree with the 2D results for shorter periods. The shorter the dyke the shorter the periods where the 3D response starts to differ from the 2D curves. In general the effect on the yx (quasi-TM) component is stronger as expected but it is also visible in the xy (quasi-TE) component. As predicted from the table, the 10 km dyke shows a good agreement only up to $\leqslant 1$ s, for the 20 km dyke up to about 1 s and for 50 km up to $\leqslant 10$ s. The disadvantage of this comparison is that there is only a good constraint on the off-diagonal components (xy and yx), but no comparison for the diagonal values (xx and yy) is possible.

7.1.2 *Rotate 2D data to gain 3D responses*

Another approach to compare 2D and 3D results is taking advantage of the inverse of a standard procedure known from strike analysis; rotating the data into strike direction.

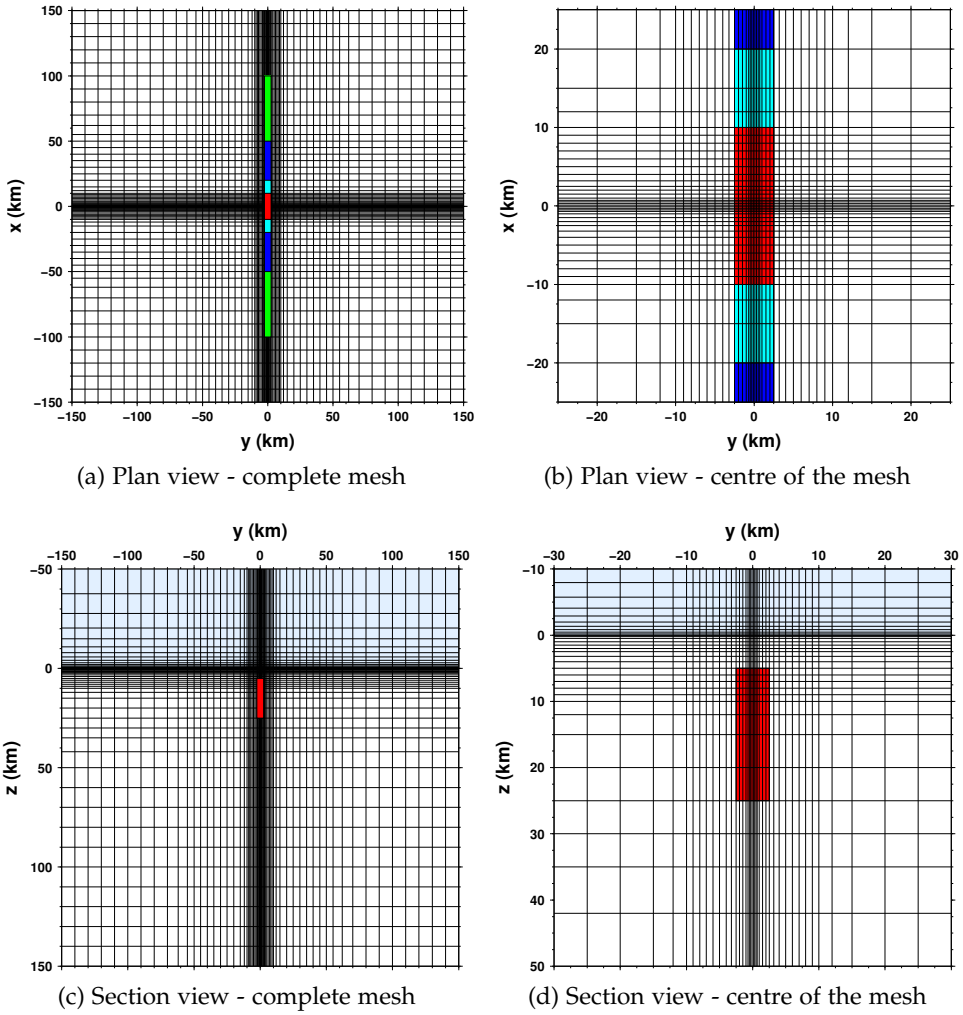

(a) Plan view - complete mesh

(b) Plan view - centre of the mesh

(c) Section view - complete mesh

(d) Section view - centre of the mesh

Figure 7.2: Figures showing the 3D mesh design for the 2D versus 3D extended dyke model in plan view ((a) and (b)) and in section view ((c) and (d)). The mesh consists of 71 x 71 x 47 cells with a centre cell width of 200 m. The coloured rectangulars show the different extensions of the 1000 Ωm dyke (red - 10 km, turquoise - 20 km, blue - 50 km and green - 100 km) and the lightblue layer indicates the airlayers.

Instead of rotating (or decomposing) a 3D impedance tensor into the strike direction to gain a 2D response, for this approach a originally 2D response will be rotated out of strike direction to make it a tensor with non-zero diagonal elements. This allows, unlike the comparison described above, to gain constraints on the off-diagonal and diagonal elements.

Figure 7.4 shows the 3D model and mesh used for this comparison. The mesh consists of 70 x 70 x 43 cells (including 13 airlayers; number of edges is 654 123 and number of nodes is 221 804), has an extent of 300 km x 300 km x 200 km and the lateral centre cell size is 750 m x 750 m. The red polygon shows the dyke-like structure with a strike direction of 45° west of north and the blue circles in Figure 7.4 (b) indicate the site locations. The 1 Ωm, 900 m wide dyke is embedded in a 100 Ωm homogeneous halfspace and its depth extent is from 250 - 1400 m below surface. The 3D responses are calculated using the forward code described in Chapter 6 with the GMRES solver set up for a total number of iterations of 5000, where the divergence correction (Smith, 1996, see Section 6.3) is applied every 50 iterations

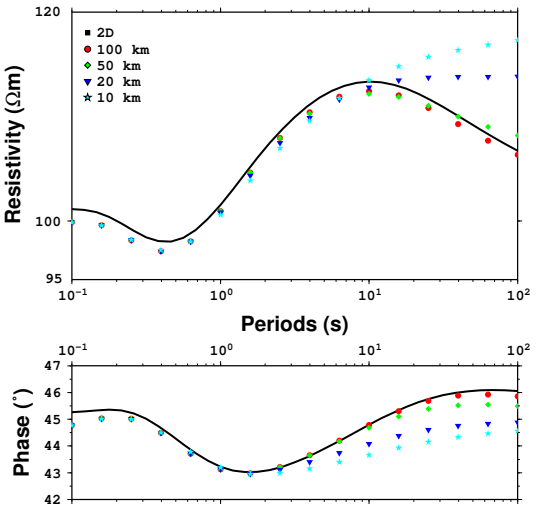

(a) Resistivity and phase curves of the xy component (quasi-TE mode)

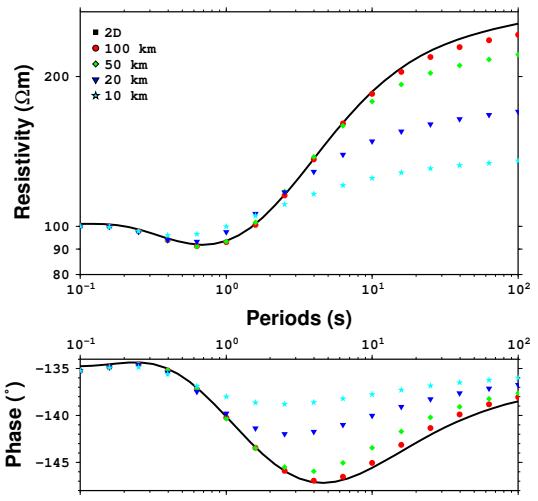

(b) Resistivity and phase curves of the yx component (quasi-TM mode)

Figure 7.3: Resistivity and phase curves of the extended dyke model. The solid black line represents the 2D solution, whereas the coloured symbols show the 3D responses for different dyke lengths (turquoise - 10 km, blue - 20 km, green - 50 km, red - 100 km) for the xy/quasi-TE (a) and the yx/quasi-TM (b) component. Please note that the resistivity axis in panel (a) is enlarged compared to panel (b), and therefore the mismatch at short periods looks worse than it actually is (e.g., the resistivity value at 0.1 s of the 2D solution is 101.01 Ωm compared to 99.85 Ωm for the 10 km dyke, 99.86 Ωm for the 20 km dyke, 99.88 Ωm for the 50 km and the 100 km dykes).

and the Krylov subspace size is 40. To simulate the same structure using a 2D forward algorithm, the code of Rodi and Mackie (2001) (implemented in Geosystem's software WinGLink®) was used to calculated the 2D responses, which afterwards were rotated by 45°.

Figure 7.5 shows all four components of the 3D (red stars) and rotated 2D (blue squares) responses at site 1 (a), site 3 (b) and site 5 (c) (responses curves and comparison for all seven sites can be found in Appendix E.1). The 3D and rotated 2D resistivity and phase curves match very well, not only for the off-diagonal (xy and yx) but also for the diagonal elements (xx and yy). Small differences at site 1 (and 2, see Figure E.2) are most likely related to the rather blocky realisation of the 45° dyke in the 3D model. In general the results show clearly that all four components are determined correctly using the forward solver described in Chapter 6.

7.2 COMPARISON OF RESPONSES FROM DIFFERENT 3D CODES

To investigate the accuracy of the 3D forward solver the retrieved responses can also be compared to results calculated by other 3D codes. In the following the comparison with the published results of two commonly used COMMEMI models by Zhdanov et al. (1997) will first be shown - namely the results of the 3D-1A and the 3D-2A models - and then the results of the Dublin Test Model 1 (DTM1), which is available on MTnet (*http://www.dias.ie/mtnet/dublin_intro.html*).

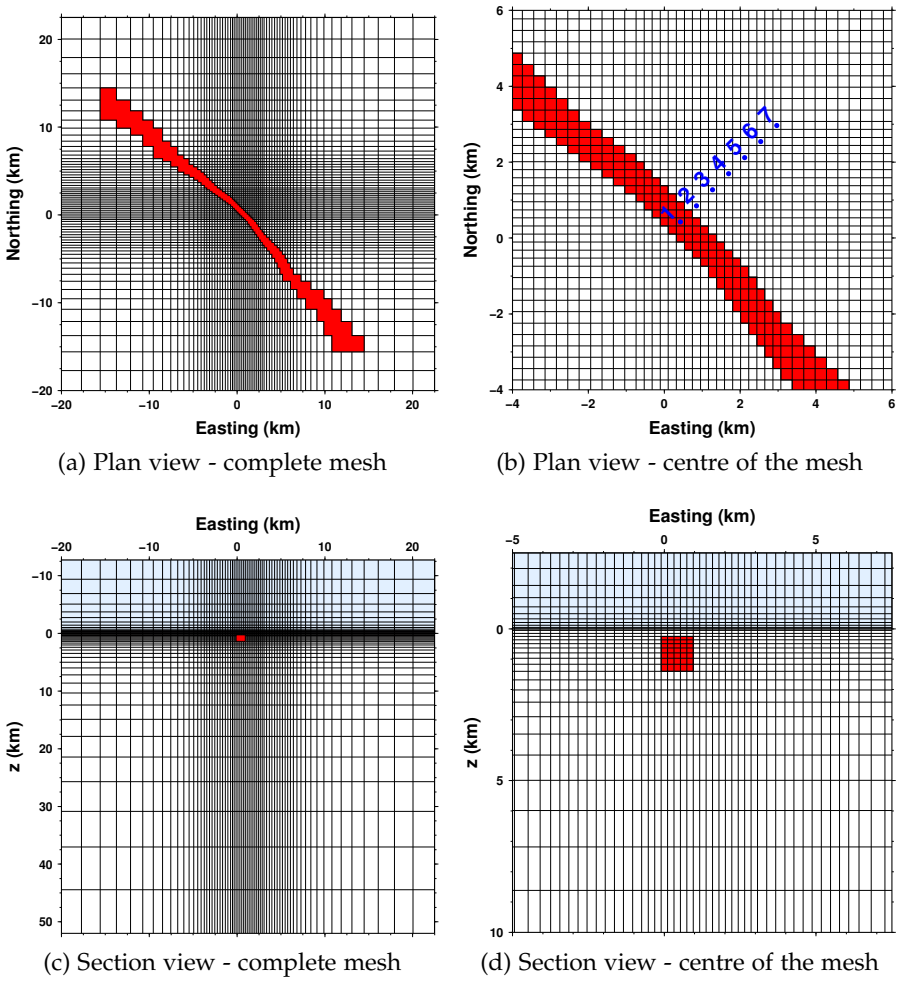

(a) Plan view - complete mesh

(b) Plan view - centre of the mesh

(c) Section view - complete mesh

(d) Section view - centre of the mesh

Figure 7.4: Figures showing the 3D mesh design for the 2D rotated versus 3D dyke model in plan view (a) and (b) and in section view (c) and (d). The mesh consists of 70 x 70 x 43 cells with a centre cell width of 750 m. The red area shows the location of the 1 Ωm dyke embedded in a 100 Ωm homogeneous halfspace, the lightblue layer indicates the airlayers and the blue circles in (b) show the site locations.

7.2.1 *COMMEMI models*

The COMPARISON OF MODELLING METHODS FOR ELECTROMAGNETIC INDUCTION (COMMEMI) project was initiated in 1983 by a working group of the International Association of Geomagnetism and Aeronomy (IAGA) and coordinated by the IZMIRAN, Russia. Zhdanov et al. (1997) summarized the results of intensive 2D and 3D code testing and comparison of results. The 3D models known as COMMEMI 3D-1A and 3D-2A will be described in the following and the forward results from the code introduced in Chapter 6 will be compared to the COMMEMI responses. Results of COMMEMI 3D-2A were also published by Wannamaker (1991), Mackie et al. (1993), Mackie et al. (1994), Siripunvaraporn et al. (2002) and Nam et al. (2007).

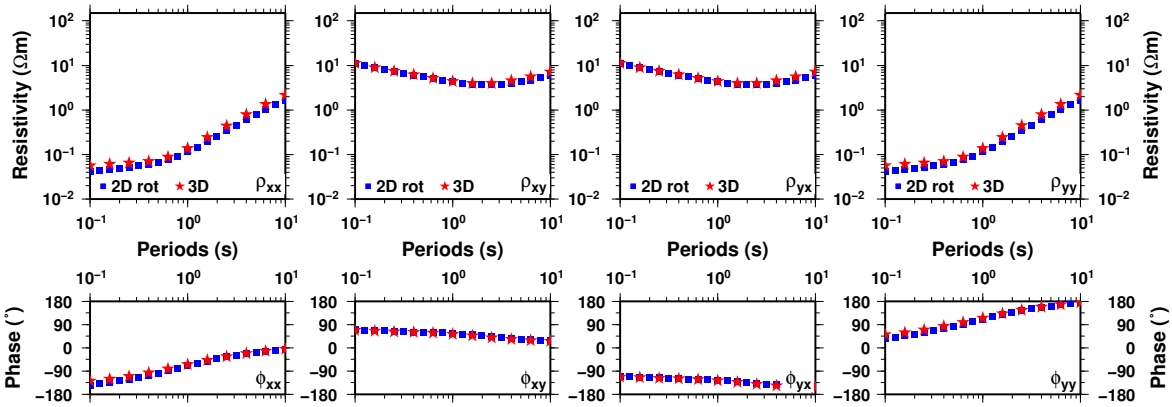

(a) Site 1

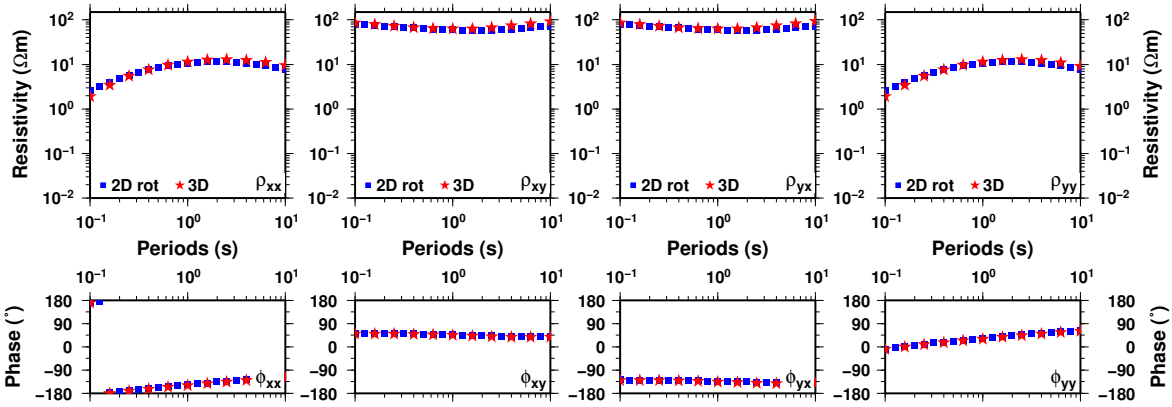

(b) Site 3

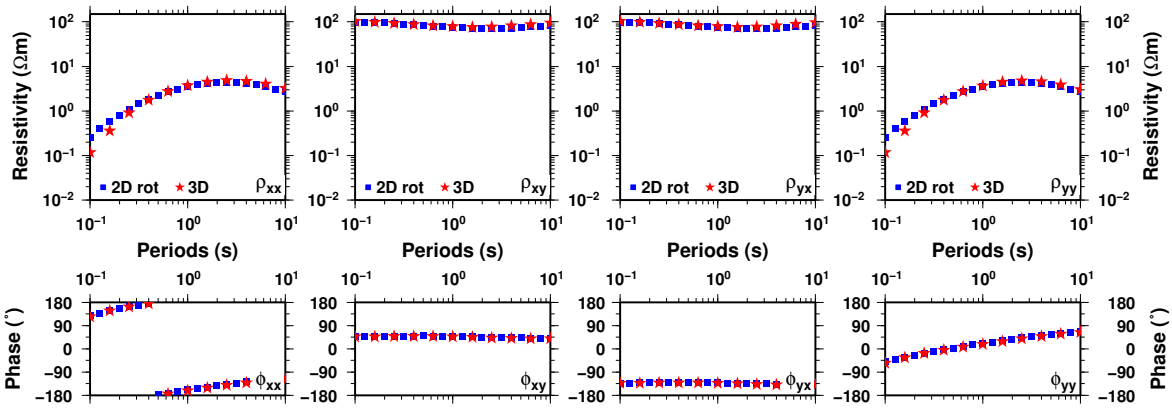

(c) Site 5

Figure 7.5: Resistivity and phase curves for all four components calculated at sites 1 (a), 3 (b) and 5 (c). The blue squares represent the rotated 2D responses and the red stars are the 3D responses. (Similar plots for all seven sites can be found in Appendix E.1.)

COMMEMI 3D-1A

The COMMEMI 3D-1A model is a geometrically simple model with a relative high resistivity contrast: a 0.5 Ωm cube embedded in a 100 Ωm homogeneous halfspace. Figure 7.6 shows the specifications of COMMEMI 3D-1A: a cube with a 1:2 lateral edge ratio (plan view: Figure 7.6 (a) and section view: Figure 7.6 (b)). The COMMEMI data set for this model consists of resistivity values (ρ_{xy} and ρ_{yx} only) for 2 periods (0.1 s and 10 s) at 13 sites. The different site locations are listed in Table 7.2.

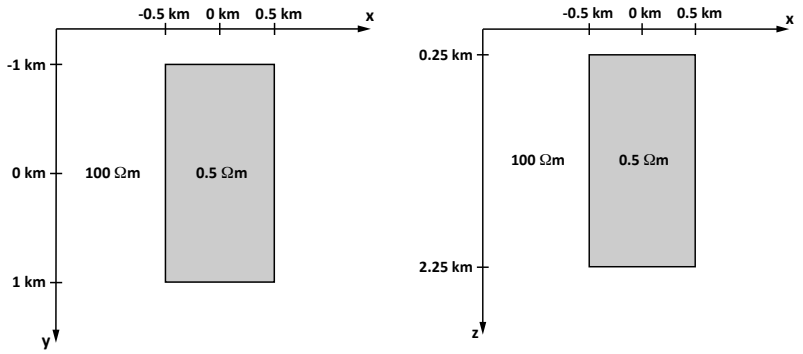

(a) COMMEMI 3D-1A - plan view (b) COMMEMI 3D-1A - section view

Figure 7.6: Sketch of the COMMEMI 3D-1A model: (a) shows a plan view and (b) the section view.

Table 7.2: Table of the different site locations of the COMMEMI 3D-1A model.

x (km)	0	0	0	0	0	0	0	0.25	0.5	0.75	1	1.5	2
y (km)	0	0.5	0.75	1	1.25	1.5	2	0	0	0	0	0	0

The responses for the COMMEMI 3D-1A model were calculated using three different meshes. The cells' thicknesses remained unchanged whereas the lateral widths were varied from 250 m x 250 m (coarse mesh) to 100 m x 100 m (fine mesh) to 50 m x 50 m (very fine mesh). The mesh dimensions are 46 x 46 x 39 cells (259 111 edges and 88 360 nodes), 70 x 70 x 39 cells (594 199 edges and 201 640 nodes) and 96 x 96 x 39 cells (1 111 911 edges and 376 360 nodes) for the coarse, the fine and the very fine mesh, respectively (9 airlayers are included), whereas all three meshes have the same extent of about 65 km x 65 km x 60 km. Figures E.4, E.5 and E.6 in Appendix E.2 show the different mesh layouts as plan and section views. Beside different meshes also different settings for the divergence correction were tested. Figure 7.7 (and 7.11) show some results for the fine mesh but the same plots for the coarse and very fine meshes can be found in the Appendix E.2. Each of these figures shows the results at 0.1 s in the top four graphs and at 10 s in the bottom four. Within the block of four the two on the left show the resistivity curves for ρ_{xy} and on the right for ρ_{yx}. The top two graphs are the results from the profile along the y axis and on the bottom for

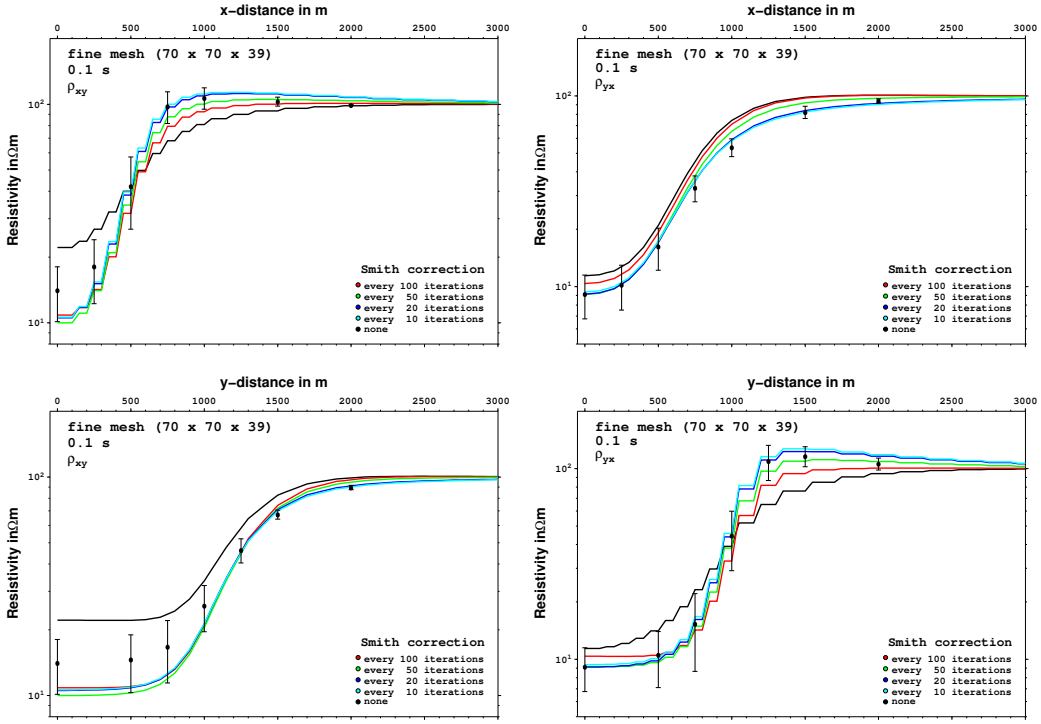

(a) Responses at 0.1 s

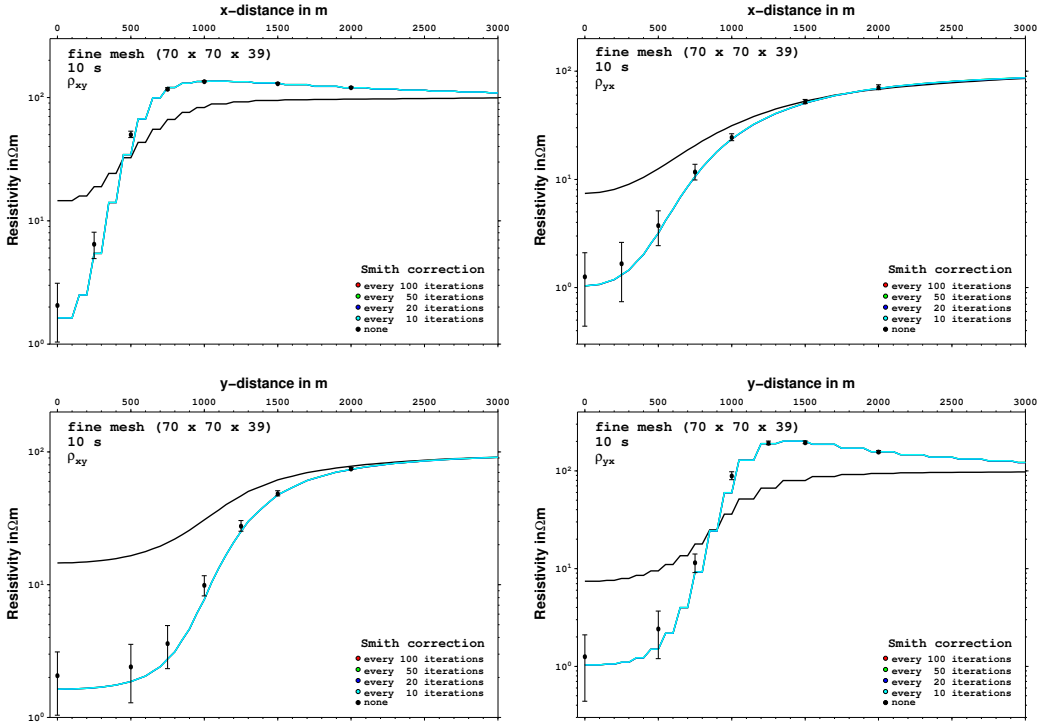

(b) Responses at 10 s

Figure 7.7: Figure showing the response curves at 0.1 s (a) and 10 s (b) obtained from the COMMEMI 3D-1A model using a fine mesh (70 x 70 x 39 cells) and applying the divergence correction every 10, 20, 50 and 100 iterations. The black line shows the response curve calculated without the divergence correction and the symbols with error bars represent the mean value and the standard deviation of the published results from Zhdanov et al. (1997).

the profile along the x axis. The black symbols with error bars represent the mean value and the standard deviation of the range of values that comprised the COMMEMI comparison and that are published by Zhdanov et al. (1997).

Figure 7.7 shows the comparison of applying the divergence correction every 10 (turquoise), 20 (blue), 50 (green) or 100 (red) iterations or not at all (black). The size of the Krylov subspace was set to be just less than the number of iterations between each divergence correction (i.e., 8, 16, 40 and 80, respectively) and for the run without correction the subspace had a size of 100. The improvement of the results (here after a total of 1000 iterations) can be seen, once the correction is applied. While the results with correction cannot be distinguished at 10 s, at 0.1 s there is a difference between the individual curves. This behaviour is apparent for all three meshes (see Appendix E.2). Figure 7.8 shows the convergence curves for the polarisation with y-directed source magnetic field of those runs whose results are shown in Figure 7.7 (fine mesh). Plotted is the preconditioned residual norm (ILU-preconditioning with zero fill-in of the sparse matrix), which is a measure of the convergence provided during the iterative procedure by the SPARSKIT solver (Saad, 1990). (Convergence curves for all three meshes are shown in Figure E.10 in Appendix E.2.) These curves show that the convergence is significantly quicker when the divergence correction is applied, and that the convergence tends to be somewhat quicker if the divergence correction is applied more frequently. It was found that a relative tolerance of the residual norm of 10^{-15} or less could easily be reached in 1000 iterations, if the divergence correction is applied. The run without divergence correction has not really reached a sufficiently small tolerance after 1000 iterations, which is consistent with the poor match between the corresponding apparent resistivities and the COMMEMI values (Figure 7.7).

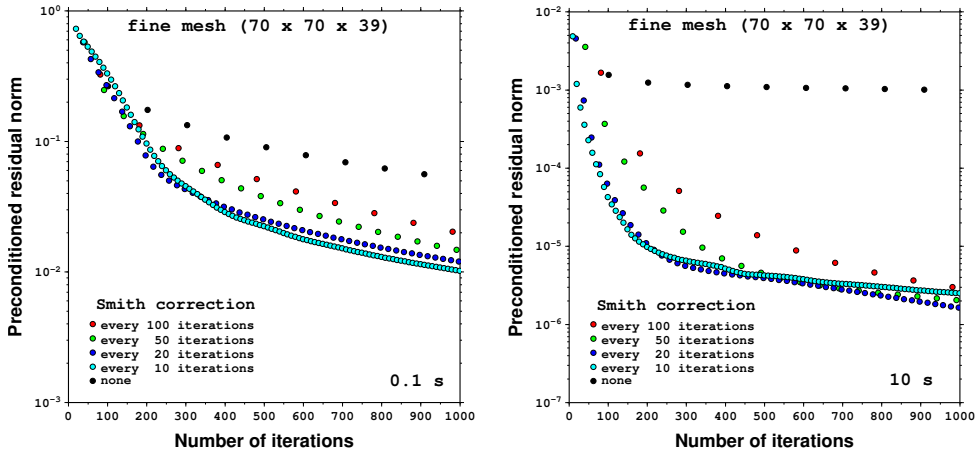

(a) Fine mesh convergence curve at 0.1 s (b) Fine mesh convergence curve at 10 s

Figure 7.8: Figure showing the convergence curves for the fine mesh. These curves belong to the calculation of responses curves at (a) 0.1 s and (b) 10 s for the COMMEMI 3D-1A model.

The effect of the divergence correction on the electric field is illustrated in Figure 7.9 (for 0.1 s and a y-directed source magnetic field). All panels show the horizontal component of

the electric field in the upper-most horizontal plane of cells that has cells in the conductive body. The horizontal field component is plotted at each cell centre, therefore the displayed electric field is at 275 m depth, which is 25 m beneath the top of the conductive prism. Panels (a) to (f) show the real ((a) to (c)) and imaginary parts ((d) to (f)) of the horizontal electric field for the run without divergence correction, whereas (g) to (l) correspond to the run where the divergence correction was applied every 20 iterations (real part (g) to (i) and imaginary part (j) to (l)). The left column shows the field after 40 iterations (one correction has occurred in generation of the field in (g) and (j)), the middle column after 500 iterations and the right one shows the final field after 1000 iterations. Considering the fields after 40 iterations, there is a hint of decreased strength in the conductive body of the imaginary part (Figure 7.9 (a)) of the run without correction, but not in the corresponding real part (Figure 7.9 (d)). The electric field of the same stage in the run with the divergence correction applied every 20 iterations shows both, the strength of this electric field is decreased within the conductive body and channelling of the electric field from the surrounding halfspace into the body is evident. The intermediate field in panels (g) and (j) differ from the final electric field ((i) and (l)), but it is considerably closer to the final field than the intermediate field at the same stage computed without divergence correction ((a) and (d)). It is also apparent that the resulting electric field after 500 iterations ((h) and (k)) is basically identical with the final one ((j) and (l)), if the correction is applied. Without divergence correction even 1000 iterations are insufficient to gain the correct electric field, which is again consistent with the poor match between the corresponding apparent resistivities and the COMMEMI values (Figure 7.7).

Figure 7.10 shows the divergence correction potential and the electric field given by its gradient for the first application of the correction for the run in which the divergence correction was applied every 20 iterations (at 0.1 s and for a y-directed source magnetic field). That is the one correction that has been applied to calculate the electric field after 40 iterations shown in Figure 7.9 (g) and (j). Figure 7.10 (a) and (b) illustrate the potential for the real and imaginary computations at the same depth as the field in Figure 7.9 (275 m). Panels (c) and (d) show the horizontal components of the gradient of the potential. The figure shows that the correction potential is generated by sources located over the two faces of the conductive body that are normal to the x-direction, that is normal to the predominant direction of the electric field. The source of the potential is the discontinuity of the normal component of the current density for the corresponding intermediate electric field (see for example the intermediate electric field in Figure 7.9 (a) and (d)). Similar figures of the electric field, the correction potential and its gradient for both source magnetic field directions and both frequencies (0.1 s and 10 s) can be found in Appendix E.2 (Figures E.11 to E.18).

For the COMMEMI 3D-1A model, applying the correction every 20 iterations seems to be a good choice (but it is model dependent and can therefore vary). Figure 7.11 shows the responses of the COMMEMI 3D-1A model after 100, 200, 400, 600, 800, 1000 and 5000 iterations (applying the divergence correction every 20 iterations). Once again the results at 10 s are not distinguishable (except 100 iterations), but 0.1 s shows variations in the curves. It is obvious the 100 and 200 iterations are too few, but 400 iterations and more already give reasonable results. Making the results a little more accurate through the cost of more iterations results in longer computation time. Keeping this in mind, the difference between 1000 iterations and 5000 iterations is not considered to be worth the extra time.

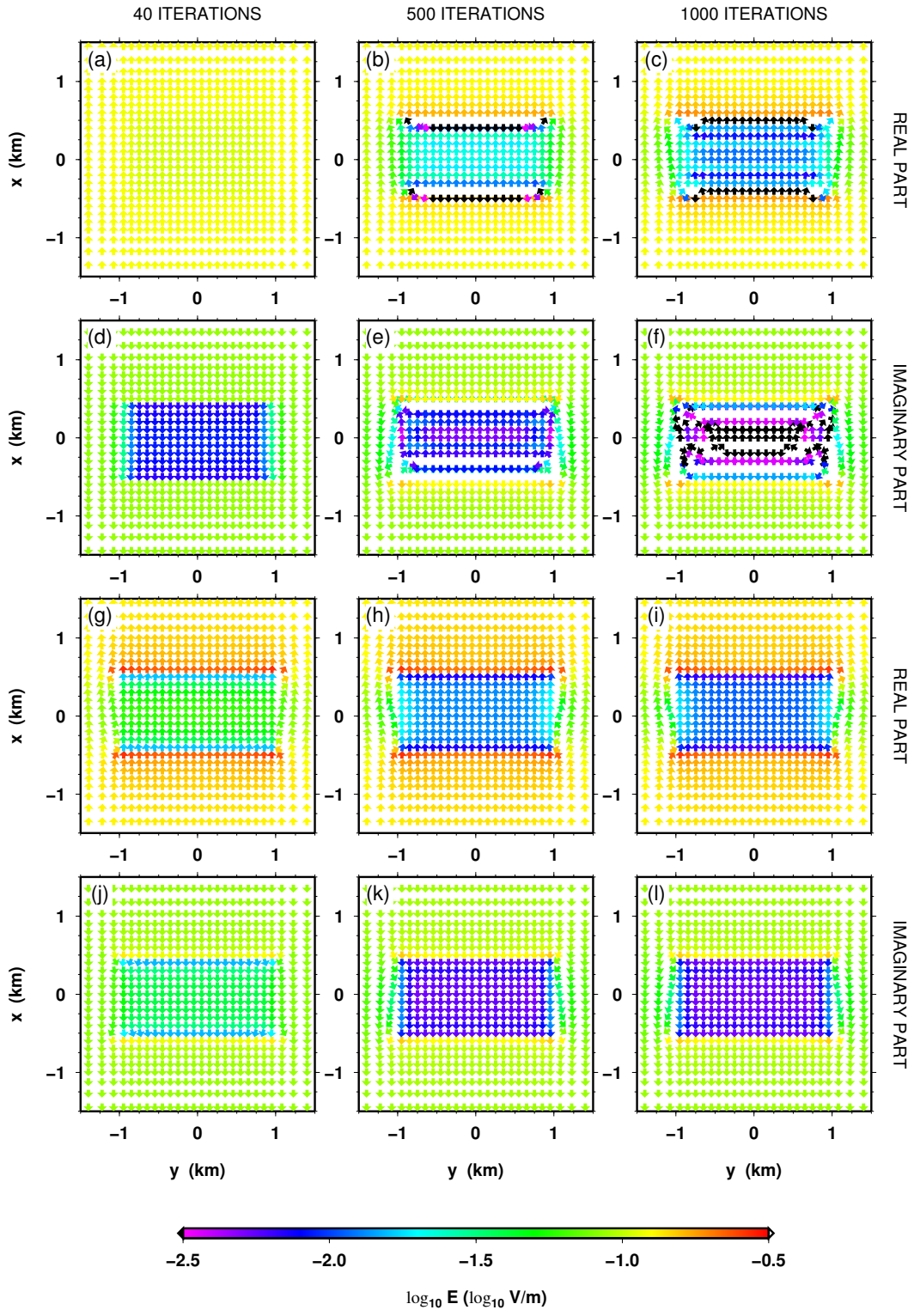

Figure 7.9: Horizontal components of the electric field at 0.1 s at a depth of 275 m (y-directed source magnetic field). Panels (a) to (c) show the real and (d) to (f) the imaginary parts of the electric fields for the run without divergence correction, whereas (g) to (i) are the real and (j) to (l) the imaginary parts of the electric fields for the run in which the divergence correction is applied every 20 iterations. The panels on the left show intermediate electric fields after 40 iterations, the middle ones are after 500 iterations and on the right are the final electric fields after 1000 iterations.

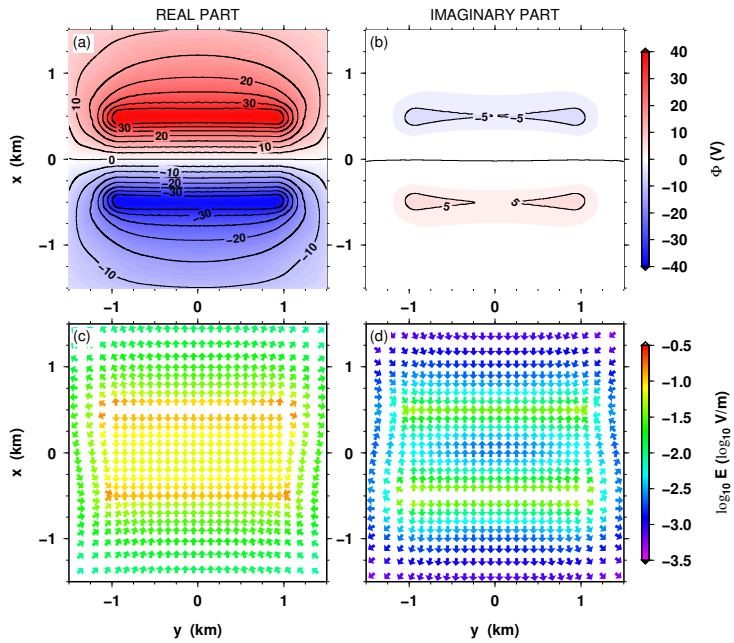

Figure 7.10: Divergence correction potential and its gradient at 0.1 s for a y-directed source magnetic field). Panel (a) shows the real and (b) the imaginary parts of the divergence correction potential applied after 20 iterations in the run whose intermediate electric field is shown in Figure 7.9 ((g) and (j)). The real (c) and imaginary (d) parts of the horizontal correction electric field are given by the gradient of the correction potential. The potentials and fields are shown at a depth of 275 m.

Figure 7.12 summarises the results of all three meshes for the parameters identified as optimal (1000 iterations with the correction being applied every 20 iterations). The solid lines are the curves from the coarse (blue), fine (green) and very fine (red) mesh obtained from the calculation with correction, whereas the dashed lines (same colour coding) show for comparison the curves obtained without correction. While at the short period (0.1 s) a finer mesh can improve the results even without divergence correction, the correction is essential for the longer period (10 s). Or, looking at it the other way, where very small cells were required the application of the correction can compensate somewhat so that larger cells give reasonable results, which would result in smaller meshes and directly related shorter computation time.

COMMEMI 3D-2A

The second COMMEMI model is more complicated. It is based on a three-layered Earth with two rectangular blocks in the top layer. The top layer (surface down to 10 km) is 10 Ωm, in 10 km to 30 km depth is a 100 Ωm layer and underneath is a 0.1 Ωm halfspace assumed. The two blocks of 1 Ωm and 100 Ωm, respectively, are 20 km wide, 40 km long and extend over the whole thickness of the top layer. Figure 7.13 shows the plan and section views of the COMMEMI 3D-2A model. Tabel 7.3 lists the site locations from Zhdanov et al. (1997), where resistivity values (no phase values available) at the periods 100 s and 1000 s have been calculated.

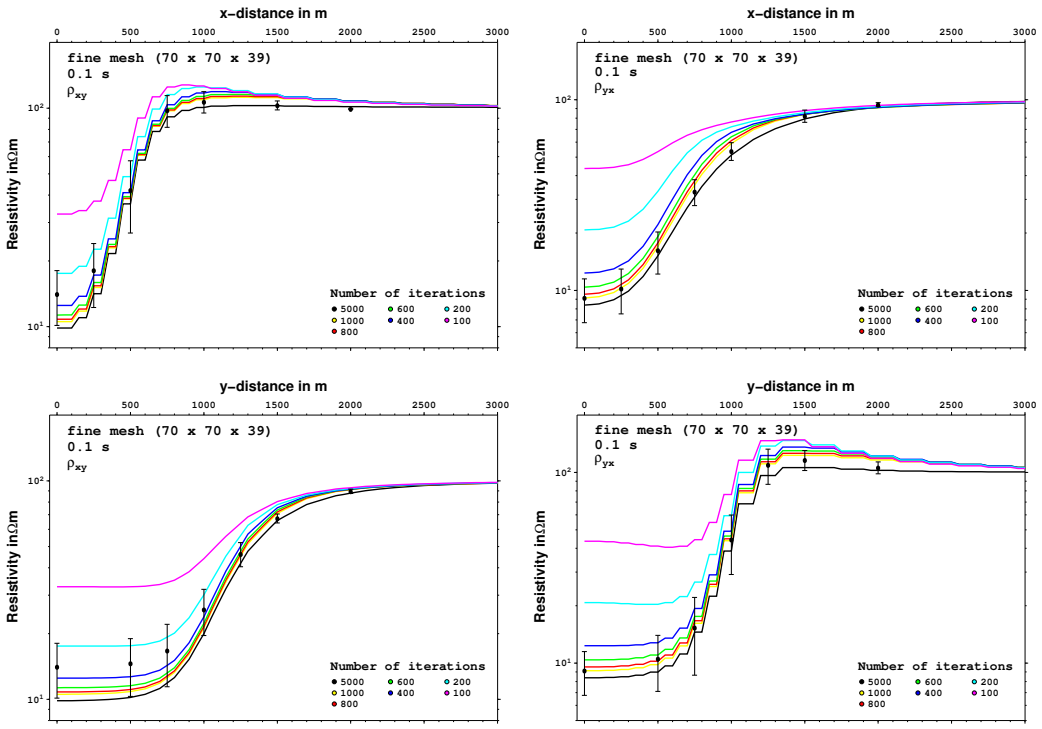

(a) Responses at 0.1 s

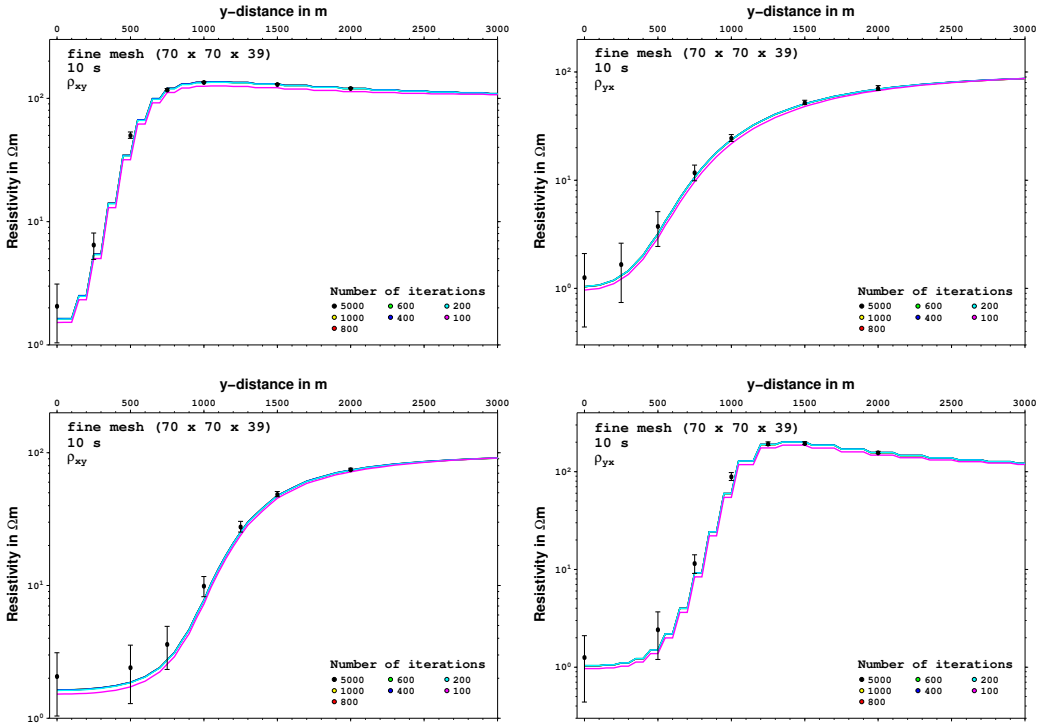

(b) Responses at 10 s

Figure 7.11: Figure showing the response curves at 0.1 s (a) and 10 s (b) obtained from the COMMEMI 3D-1A model after 100, 200, 400, 600, 800, 1000 and 5000 iterations using a fine mesh (70 x 70 x 39 cells). The black symbols with error bars represent the mean value and the standard deviation of the published results from Zhdanov et al. (1997).

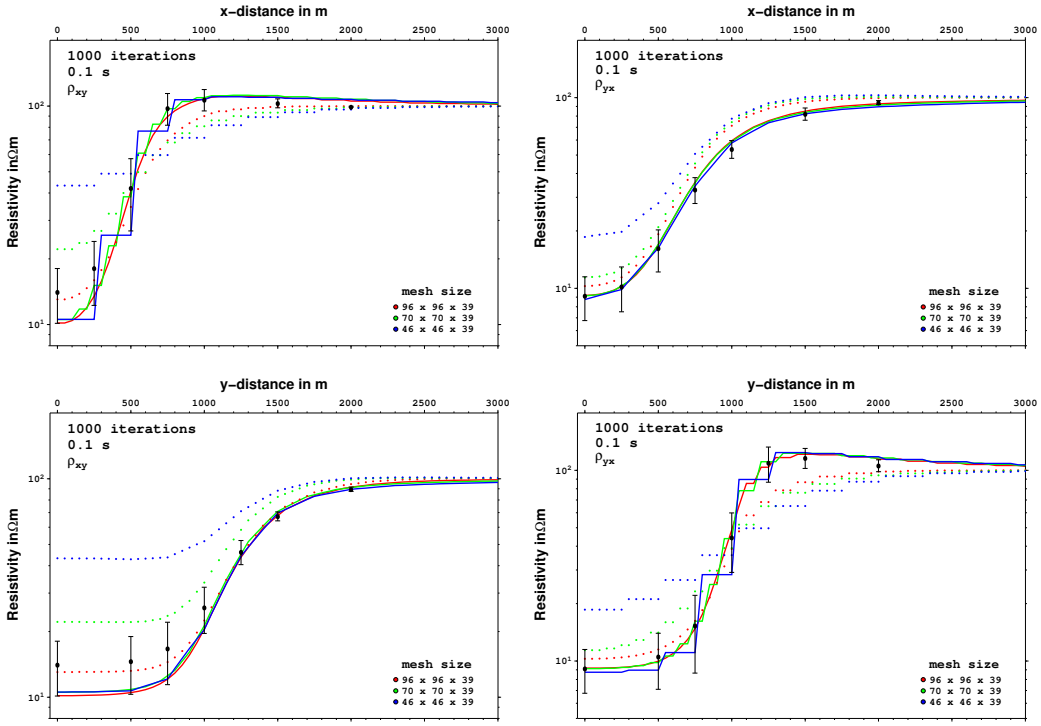

(a) Responses at 0.1 s

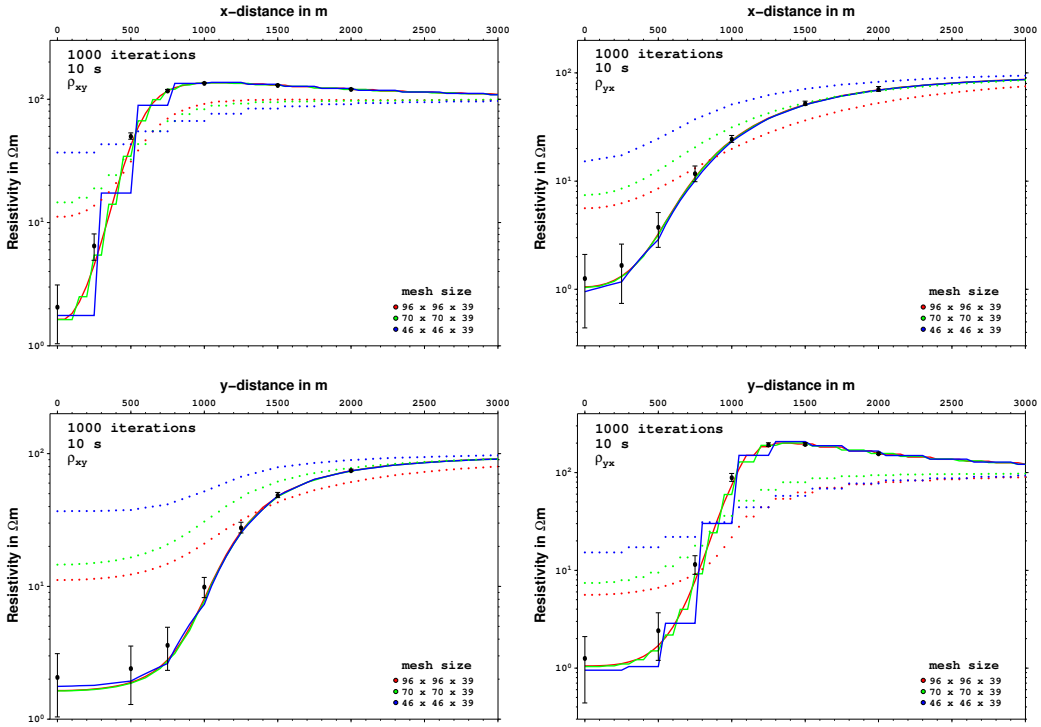

(b) Responses at 10 s

Figure 7.12: Figure showing the response curves at 0.1 s (a) and 10 s (b) obtained from the COMMEMI 3D-1A model using three different meshes: coarse mesh (blue), fine mesh (green) and very fine mesh (red). The solid lines are the responses curves after 1000 iterations applying the divergence correction every 20 iterations. For comparison the dashed lines represent the curves after 1000 iterations without any correction being applied. The symbols with error bars represent the mean value and the standard deviation of the published results from Zhdanov et al. (1997).

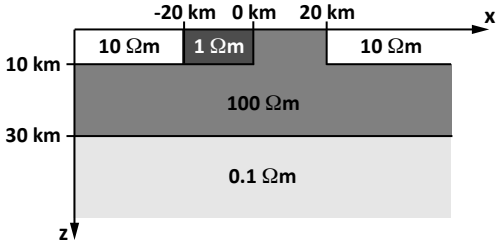

(a) COMMEMI 3D-2A - section view

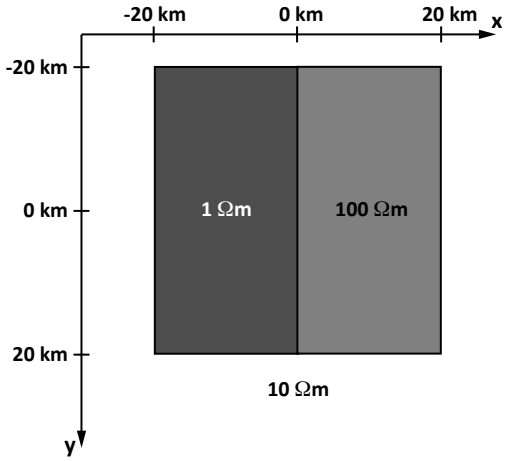

(b) COMMEMI 3D-2A - plan view

Figure 7.13: Sketch of the COMMEMI 3D-2A model: (a) shows the section view and (b) the plan view of the 3D-2A model.

Table 7.3: Table of the different site locations of the COMMEMI 3D-2A model.

x (km)	0	±5	±15	±20	±25	±40	±70
y (km)	0	0	0	0	0	0	0

To calculate the forward responses a mesh of 70 x 70 x 43 cells (including 15 airlayers; 654 123 edges and 221 804 nodes) was used, which has a total mesh extent of about 210 km x 210 km x 200 km and the lateral size of the centre cells is 1 km x 1 km. Figure E.23 in Appendix E.3 shows the mesh design as plan and section views. The divergence correction was applied every 400 iterations using a Krylov subspace 396 (just less than the number of iterations between each divergence correction). As the COMMEMI 3D-2A is based on a layered background model, the chosen homogeneous halfspace boundary conditions of the forward solver might not be ideal. Therefore faked 1D boundary conditions were implemented for testing (i.e., 1D boundary conditions are not generally available in the forward solver code, but are included hard-wired specifically for the 3D-2A example; there is an analytical formula for the fields in a homogeneous halfspace whereas a layered Earth requires a numerical solution which requires additional programming). Figure 7.14 shows the xy and yx component data at 100 s for the homogeneous halfspace and 1D boundary conditions in comparison. Solid lines are the forward responses after 6000 (blue), 40000 (green) and 80000 iterations (red). Also plotted are the published results from Wannamaker (1991) (star), Mackie et al. (1993) (diamond) and Zhdanov et al. (1997) (square). Figure 7.15 shows the responses at 1000 s in the same way.

It can be seen that homogeneous halfspace boundaries cause shifted and skewed response curves for the 3D-2A model due to the layered background. Compared to 6000 iterations the resistivity curves improve to a reasonable fit after 40000 iterations, but the phases remain strongly affected. At 1000 s not even 80000 iterations can improve the fit of the phases. Using 1D boundary conditions solves the problem and resistivity and phase curves fit well already after 40000 iterations at 100 s and after 6000 iterations at 1000 s. Many more iterations are

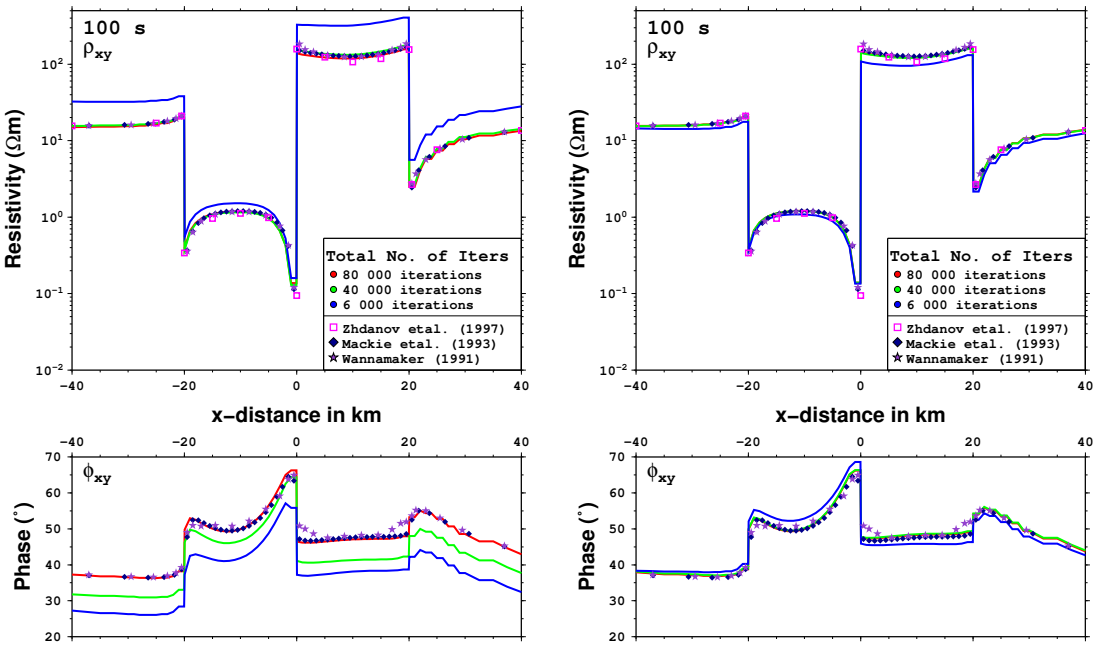

(a) Hom. halfspace boundaries - xy component

(b) 1D boundaries - xy component

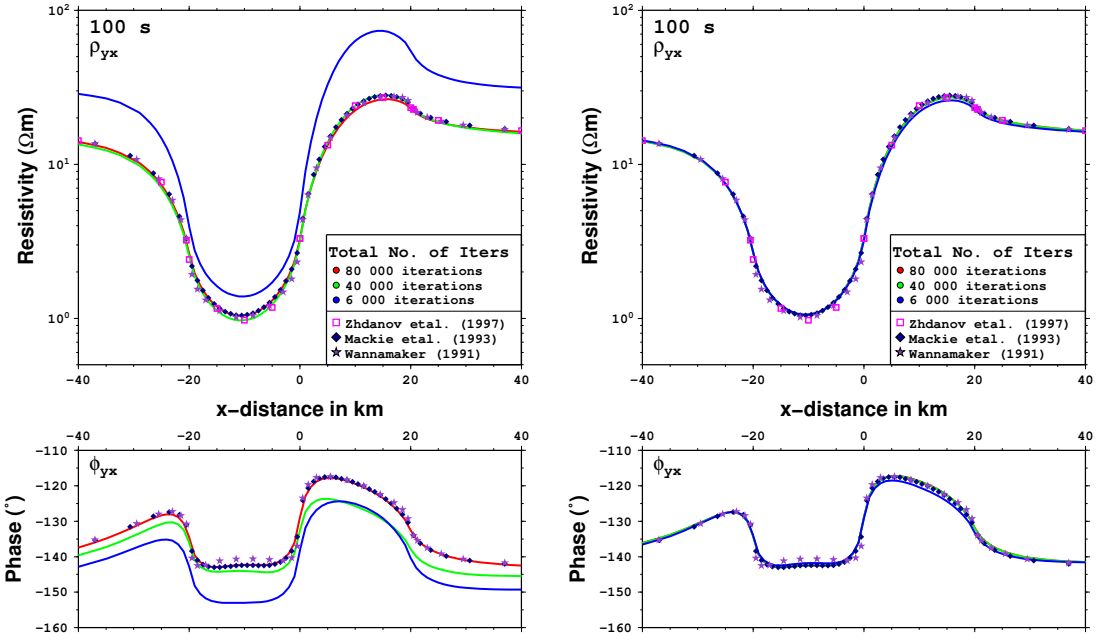

(c) Hom. halfspace boundaries - yx component

(d) 1D boundaries - yx component

Figure 7.14: COMMEMI 3D-2A responses curves at 100 s: The xy component is shown in (a) for homogeneous halfspace boundaries and in (b) using 1D boundaries, whereas the yx response curves for homogeneous halfspace boundaries (c) and 1D boundaries (d) are shown below. For comparison symbols are plotted representing the results from Wannamaker (1991), Mackie et al. (1993) and Zhdanov et al. (1997) (no phase values).

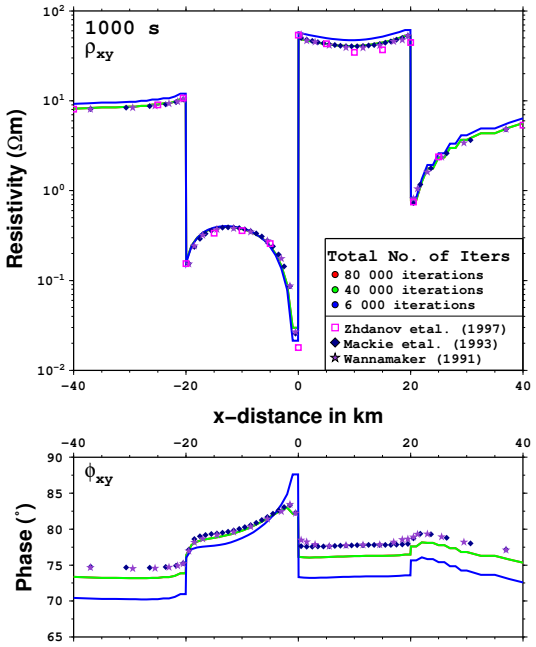

(a) Hom. halfspace boundaries - xy component

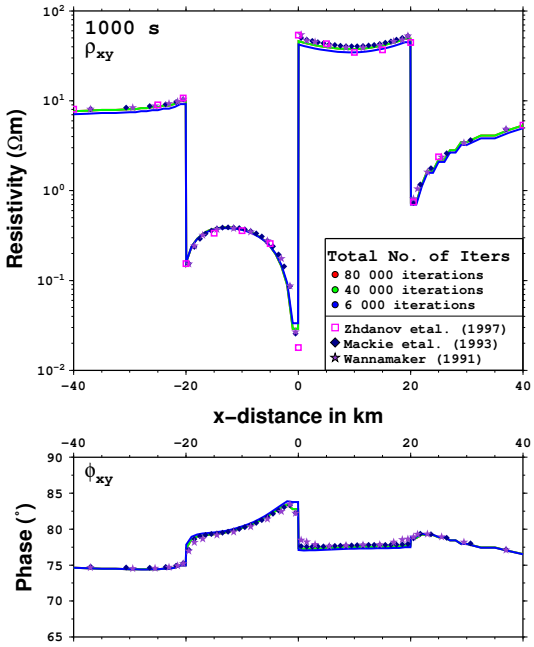

(b) 1D boundaries - xy component

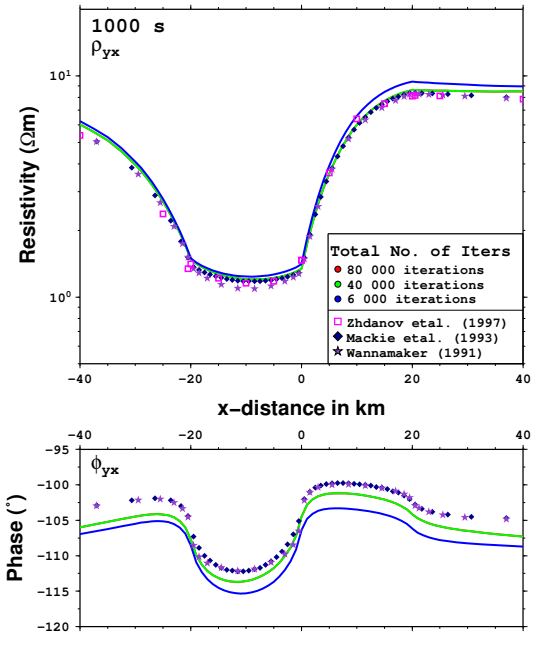

(c) Hom. halfspace boundaries - yx component

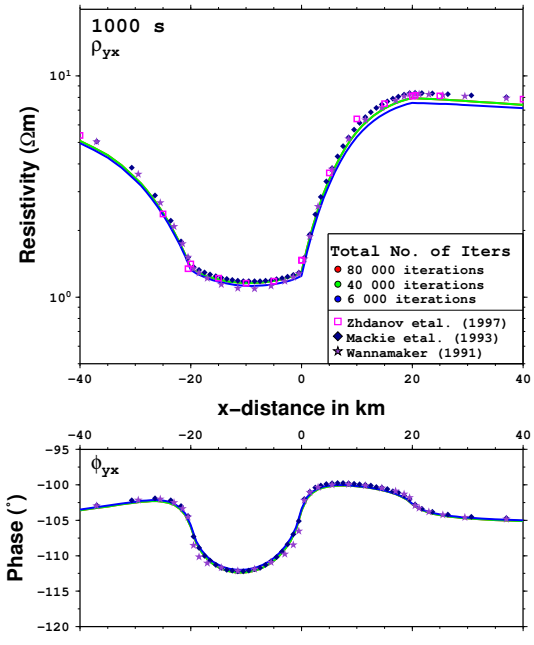

(d) 1D boundaries - yx component

Figure 7.15: COMMEMI 3D-2A responses curves at 1000 s: The xy component is shown in (a) for homogeneous halfspace boundaries and in (b) using 1D boundaries, whereas the yx response curves for homogeneous halfspace boundaries (c) and 1D boundaries (d) are shown below. For comparison symbols are plotted representing the results from Wannamaker (1991), Mackie et al. (1993) and Zhdanov et al. (1997) (no phase values).

required to compute reasonable responses for the 3D-2A model than for the 3D-1A model, although the numbers of cells in the mesh are similar. This illustrates the more challenging nature of the 3D-2A model. For the sake of completeness, the corresponding plots of the horizontal electric field, the correction potential and its gradient are shown in Appendix E.3.

7.2.2 *The Dublin Test Model 1 - DTM1*

The Dublin Test Model 1 was designed for the MT 3D inversion workshop at the Dublin Institute of Advanced Studies in March 2008. This model was sent to a number of code writers and users, who performed 3D forward modelling to obtain responses at 59 sites. A few sets of these responses are available on MTnet and can be used for comparison.

Figure 7.16 shows one plan view and two section views of the DTM1. It consists of three blocks embedded in a 100 Ωm homogeneous halfspace. The first body is 5 km wide, 40 km

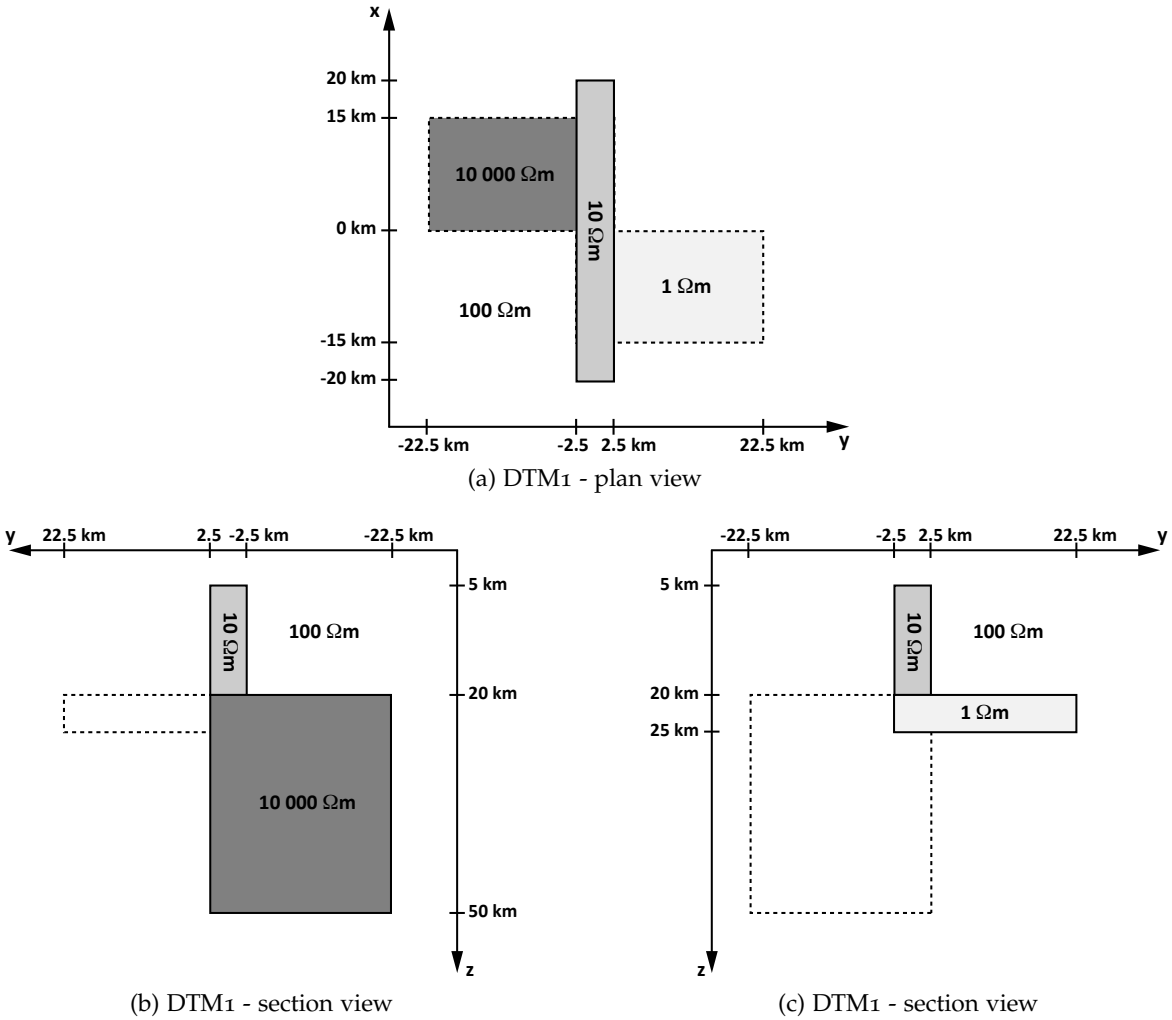

(a) DTM1 - plan view

(b) DTM1 - section view

(c) DTM1 - section view

Figure 7.16: Sketch of the Dublin Test Model 1 (DTM1): (a) shows the plan view, (b) shows a section view of the y-z-plane through the high resistive body (10 000 Ωm) and (c) is a section view of the y-z-plane through the conductive block (1 Ωm).

long and 15 km thick. Its resistivity is 10 Ωm. Underneath the first block two others are located with resistivities of 1 Ωm and 10 000 Ωm, respectively. Both have a lateral extent of 15 km by 25 km. The resistor is 30 km thick, whereas the thickness of the conductor is only 5 km. In total 59 sites are located on three profiles parallel to the y-axis (at x = 15 km (Profile N), 0 km (Profile C) and -15 km (Profile S)) and one profile along the y-axis (Profile V). Table 7.4 lists the exact locations of all sites.

Table 7.4: Table of the different site locations of the Dublin Test Model 1 (DTM1) on three profiles parallel to the y-axis (Profiles N, C and S) and one profile along the y-axis (Profile V).

Profile N	x (km)	15	15	15	15	15	15	15	15
	y (km)	± 2.5	± 7.5	± 12.5	± 17.5	± 22.5	± 27.5	± 32.5	± 37.5
Profile C	x (km)	0	0	0	0	0	0	0	0
	y (km)	± 2.5	± 7.5	± 12.5	± 17.5	± 22.5	± 27.5	± 32.5	± 37.5
Profile S	x (km)	-15	-15	-15	-15	-15	-15	-15	-15
	y (km)	± 2.5	± 7.5	± 12.5	± 17.5	± 22.5	± 27.5	± 32.5	± 37.5
Profile V	x (km)	0	± 5	± 10	± 15	± 20	± 25		
	y (km)	0	0	0	0	0	0		

The mesh used for the forward modelling is shown in the Appendix E.4 (Figure E.44). It consists of 91 x 60 x 57 cells (including 15 airlayers; 962 002 edges and 325 496 nodes) with a lateral extent of 1 km x 1 km for the centre cells. Figures 7.17 and 7.18 show the forward results (black symbols) at 100 s and 1000 s, respectively, after 1000 iterations applying the divergence correction every 20 iterations (with a size of 16 for the Krylov subspace). For comparison, results were calculated using the following codes: RLM3D (as implemented in WinGlink®, Mackie et al., 1994) , wsinv3dmt (Siripunvaraporn et al., 2005) and MT3Dinv (from GIF, University of British Columbia, Canada). Also results from Nuree Han and Tae Jong Lee using the code by Nam et al. (2007) and from Randy Mackie using his code (Mackie et al., 1994) are used for comparison. These five data sets (21 logarithmic equidistant periods in the range of 0.1 s to 10 000 s for all 59 sites) are available on MTnet for download and are plotted here with different coloured symbols.

Figures E.45 to E.52 in Appendix E.4 show the results for all four profiles at 100 s and 1000 s. All of them show a very good agreement between the forward results using the code described in Chapter 6 and all the other responses - for resistivities as well as phases and also for off-diagonal as well as diagonal elements. Figures E.53 to E.56 show the corresponding horizontal components of the electric field at 5.5 km (through the 10 Ωm block) and 26.4 km (through the two bottom blocks) and Figures E.57 to E.64 show the divergence correction potential and its gradient at 5.5 km and 26.4 km and at 100 s and 1000 s for the first application of the correction.

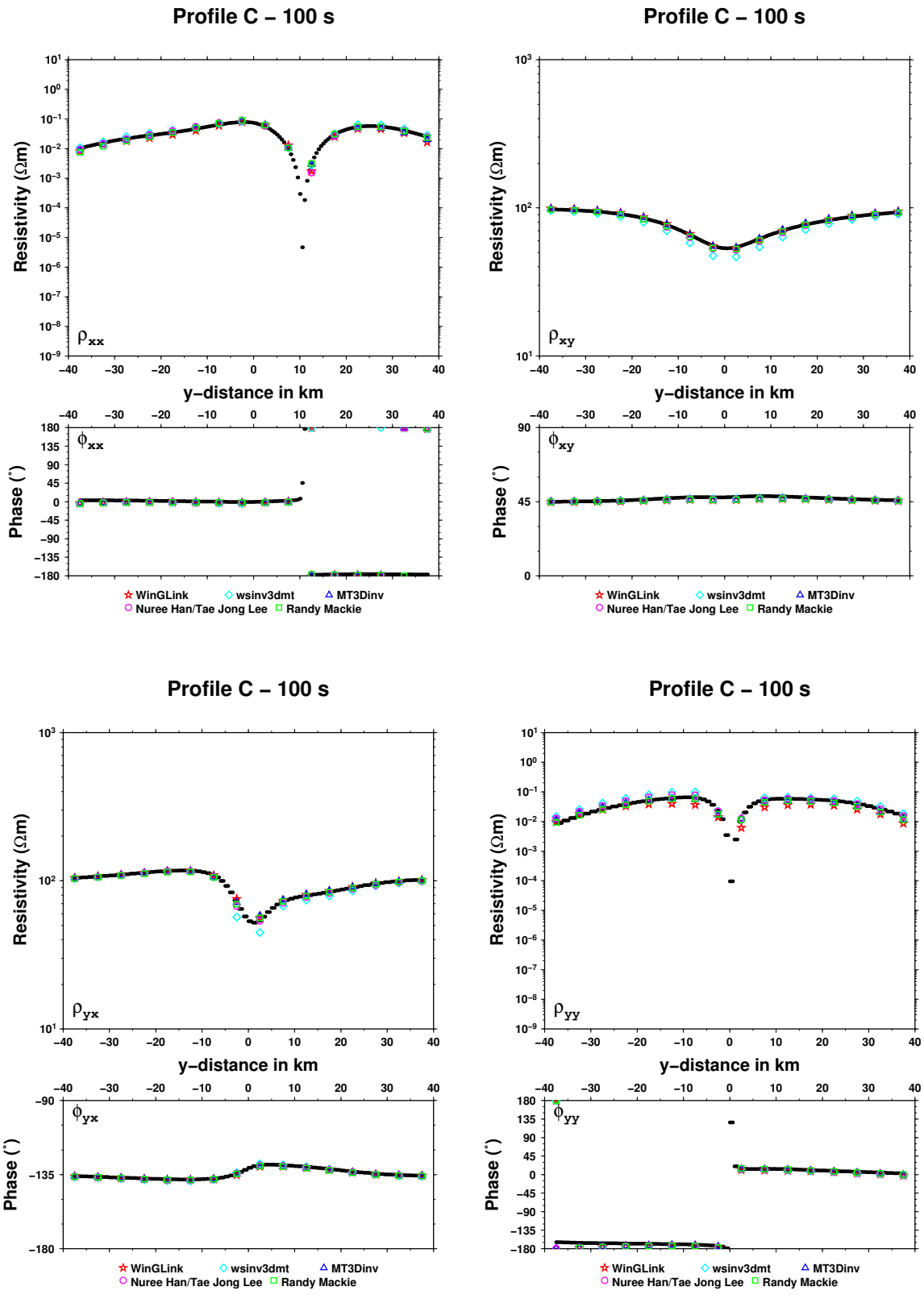

Figure 7.17: Figure showing the responses curves (black symbols) of Profile C at 100 s calculated for the Dublin Test Model 1 (DTM1) (see Figure 7.16). Each panel, one each for xx, xy, yx and yy components, shows the apparent resistivity curves on top and the phase curves below. The colour symbols are results from other codes/users (see legend), which are available as reference data sets on MTnet.

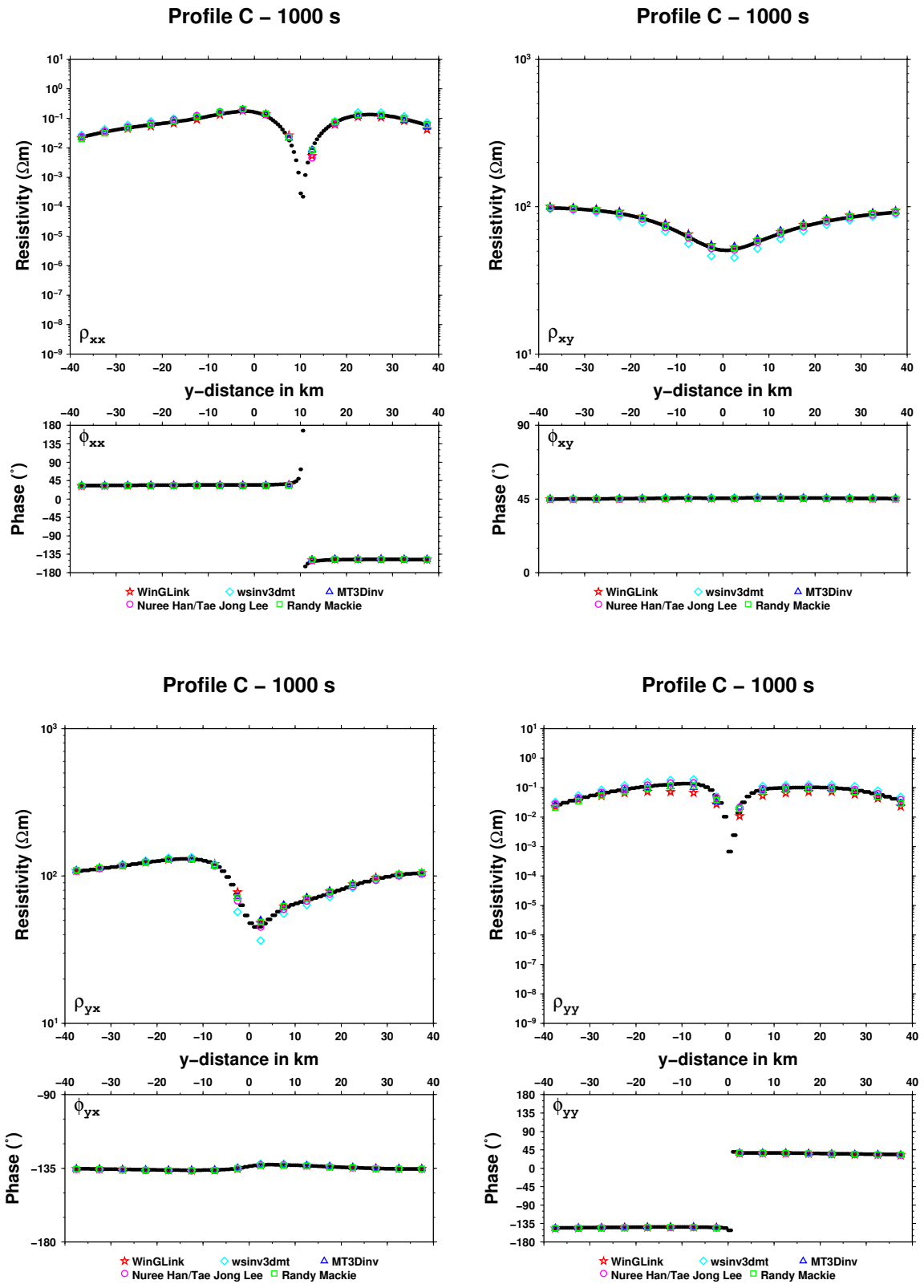

Figure 7.18: Figure showing the responses curves (black symbols) of Profile C at 1000 s calculated for the Dublin Test Model 1 (DTM1) (see Figure 7.16). Each panel, one each for xx, xy, yx and yy components, shows the apparent resistivity curves on top and the phase curves below. The colour symbols are results from other codes/users (see legend), which are available as reference data sets on MTnet.

7.3 SUMMARY OF THE FORWARD MODELLING TESTS

All five forward tests discussed in this chapter were proved successful. They showed in very different ways that the used forward algorithm calculates reliable resistivity and phase curves for all four components. Only using the COMMEMI 3D-2A model showed a limitation of the forward routine, which is caused by the assumption of homogeneous halfspace boundary conditions. Using faked 1D boundaries showed the forward solver itself is working fine. Keeping the boundary problem related to the very challenging 3D-2A model in mind, one can be confident that the forward algorithm is working reliably and it can therefore be considered suitable as the engine for the inversion code, which will be described in Chapter 8.

8

THE INVERSION ALGORITHM

This chapter describes the 3D MT inversion code that is based on the finite-element forward solver described in Chapter 6 and tested in Chapter 7. The inversion code uses a Gauss-Newton method and allows the simultaneous inversion for the resistivity structure and distortion parameters. It also tries to avoid noise propagation from one impedance element into the others due to rotation during data processing. In the following the inversion code will be called MCMT3DID (i.e., Marion and Colin's MT 3D Inversion code including Distortion).

There have been quite a few recent efforts to develop 3D MT inversion algorithms. The inversion codes are based on forward algorithms using finite-difference (FD) (e.g., Mackie and Madden, 1993; Newman and Alumbaugh, 2000; Farquharson et al., 2002; Sasaki, 2004; Siripunvaraporn et al., 2005; Han et al., 2008), finite-element (FE) (e.g., MCMT3DID) and integral-equation approaches (IE) (e.g., Avdeeva, 2008; Avdeev and Avdeeva, 2009). The 3D MT inverse problem is far from being solved, but these codes using different inversion schemes showed that one can recover the conductivity structure of simple synthetic test models reasonably well. The major issues of making MT 3D inversion a routinely used procedure are the long computation time and the requirement of fast workstations with large memories, preferable even huge clusters for parallel computation. The timewise most expensive part is the construction of the sensitivity matrix. To avoid this time consuming procedure different schemes were developed that use approximations of the sensitivity matrix. Smith and Booker (1991) developed a rapid relaxation inversion scheme, where approximate 1D sensitivities are used. Farquharson and Oldenburg (1999) approximate the sensitivities by calculating them for a homogeneous or layered halfspace. Another approach is based on quasi-linear approximations of the Green's function (Zhdanov and Fang, 1996; Zhdanov et al., 2000). However, such approximate methods have their limitations (e.g., work best for small resistivity contrasts, and the accuracy of the inversion is questionable) and they are therefore of value but cannot replace methods based on the full solution of the EM induction equations (Siripunvaraporn et al., 2005). Mackie and Madden (1993) use a conjugate gradient (CG) method and Newman and Alumbaugh (2000) and Rodi and Mackie (2001) (also Mackie et al., 2001) apply a non-linear conjugate gradient (NLCG) method that avoids both the explicit computation and storage of a full sensitivity matrix. This approach can be more practical in terms of computation time (Rodi and Mackie, 2001). The 3D inversion codes by Sasaki (2004) and Siripunvaraporn et al. (2005) are based on a Gauss-Newton-type (GN) approach in model- and data-space, respectively, and the inversion code by Avdeeva (2008) and Avdeev and Avdeeva (2009) uses the limited-memory quasi-Newton method. Some of these codes are written using the message passing interface (MPI) protocol or similar to make them run on PC-clusters or massively parallel systems in order to reduce the computation time.

8.1 MOTIVATION AND MAIN IDEA OF MCMT3DID

MT field data often suffer from distortion effects caused by small-scale, near-surface conductivity inhomogeneities (see Section 2.7). Therefore in 2D different strategies were developed to analysis and remove these distortion effects (see Section 2.9.2). In 2D de Groot-Hedlin (1991) was the first to integrate the static shift into the inversion and later de Groot-Hedlin (1995) also inverted for the full electric galvanic distortion matrix simultaneously to find the smoothest model. Sasaki (2004) extended de Groot-Hedlin's (1991) concept of inverting for static shift parameters into three dimensions. Based on Sasaki's (2004) code work on three-dimensional inversion of static shifted MT data has been published by Sasaki and Meju (2006) and Han et al. (2008), where only special limited cases of distortion or Earth structure have been investigated. Inspired by de Groot-Hedlin's (1995) simultaneous inversion for the full galvanic distortion matrix and the resistivity structure in 2D, the 3D inversion code presented here is written to accommodate galvanic distortion parameters during inversion; first just as constant values based on a priori information and second as inversion parameters. As only the electric galvanic distortion is considered the additional parameters are namely one frequency independent, real 2 x 2 matrix per MT site (see Section 2.7).

The second new aspect of MCMT3DID is the rotation of the synthetic data instead of the field data to avoid noise propagation from one impedance element into the others. In 2D the rotation of the impedance data into strike direction is essential (although the following approach for the 3D code can of course also be applied to 2D codes, but such a 2D code is not available yet) as the 2D inversion is based on the assumption that the impedance can be decoupled as TE and TM mode (see Section 2.6.2). Rotation into strike direction is not necessary for 3D inversion, but it is required that all impedance data are in the same coordinate system for inversion. MT data are recorded in individual coordinate systems at each site (e.g., magnetic north or any arbitrary orientation caused by local conditions), but normally the whole data set of all MT sites is rotated into a common coordinate system, e.g., true north. The rotation produces a mixing of the impedance elements and, in the case of noisy data, especially if one component is more strongly affected than the others, can cause degradation of data. Figure 8.1 shows a synthetic data example where Gaussian noise is added to a response curve and then both data sets (i.e., the original responses and the noisy responses) are rotated by 45°. Especially the xy phase shows loss of data quality at intermediate periods, but also the diagonal elements show resistivity values orders of magnitude too high. Therefore the applied strategy in MCMT3DID is to read in the MT data using the individual coordinate system for each site. Additionally a rotation angle has to be specified for each site with respect to the general modelling coordinate system. Instead of rotating the input data, which can be affected by noise, the noise-free synthetic data from the forward modelling will be rotated for each individual site by the specified angle before the comparison between input data and forward results is undertaken.

8.2 INVERSION STRATEGY

One important part of inverse numerical modelling is to determine the measure of the misfit. The sum of the data misfit and measures of model complexity is often called an objective function (or a penalty function). A procedure is used that attempts to minimise the objective function and therefore to provide a solution to the inverse problem.

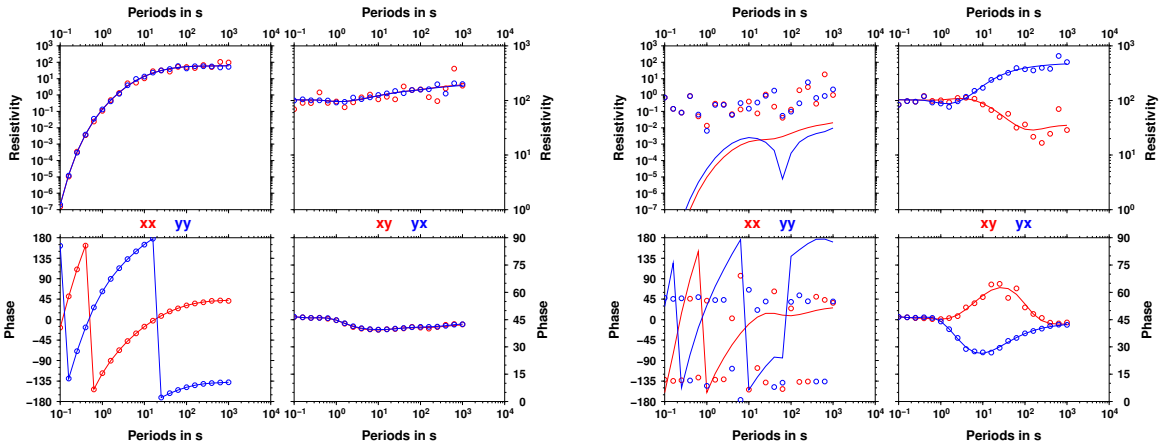

(a) Original synthetic data with and without noise

(b) Rotated noisy and noise-free synthetic data

Figure 8.1: A synthetic data example showing the noise propagation due to rotation of the impedance tensor. The solid lines represent the noise-free and the open circles the noisy synthetic data. Panel (a) shows both data sets before and (b) after rotation by 45°. The noisy data is generated by adding Gaussian noise to the response curve: 20% to the xx and xy component, 5% to yx and 10% to yy to simulate a distorted E_x field component. To accommodate the fact the longer periods are stronger effected by noise, for periods > 10 s a scaling factor ($\log_{10}$(period)) was multiplied to the percentage.

8.2.1 *Measures of data misfit and model complexity*

Considering the elements of a vector $\underline{x}$ to be the misfit between the observed and predicted data or the parameters describing the model structure, there are various functions that can be used to measure the 'size' of the vector. If $x_i, i = 1, ..., n$ are the elements of the vector, a general size of the vector is given by

$$\phi(x) = \sum_{i=1}^{n} f(x_i) \quad . \tag{8.1}$$

This general expression becomes the L_2 norm of the vector if $f(x) = x^2$,

$$||\underline{x}||_2^2 = \sum_{i=1}^{n} x_i^2 \quad , \tag{8.2}$$

or the more general form of the L_p norm

$$||\underline{x}||_p^p = \sum_{i=1}^{n} |x_i|^p \quad , \tag{8.3}$$

where $0 < p < \infty$. The L_1 norm and L_2 norm are common measures for data misfit and model complexity, however Farquharson and Oldenburg (1998) and Farquharson (2008) demonstrated the advantages of using two other measures: one considered the 'most robust' by Huber (1964) and one proposed by Ekblom (1973, 1987) (which are the two

measures used in the MCMT3DID code). Portniaguine and Zhdanov (1999) developed a technique called focussing inversion images, where they use different measures of model complexity as stabilizer functionals to calculate the objective function. They compared different measures, such as the maximum smoothness stabilizer (the standard L_2 norm; $f(x) = x^2$), the variational stabilizing functions ($f(x) = (x^2 + \beta^2)^{1/4}$), the minimum support functional ($f(x) = x/(x^2 + \beta^2)^{1/2}$, where x is not the difference vector, but the model vector) and the minimum gradient support functional ($f(x) = x/(x^2 + \beta^2)^{1/2}$, where x is again the difference vector). Portniaguine and Zhdanov (1999) find the minimum gradient support functional to be very helpful to generate clearer, more focused and more resolved images of geological structures.

The Huber measure

The measure by Huber (1964) is based on the function $f(x)$ to be

$$f(x_i) = \begin{cases} x_i^2 & \text{if } |x_i| \leqslant c \\ 2c|x_i| - c^2 & \text{if } |x_i| > c \end{cases} , \tag{8.4}$$

where c is a positive constant. If the absolute value of the largest element in vector $\underline{\mathbf{x}}$ is smaller than the constant c the Huber measure becomes identical to a L_2 norm, otherwise the constant will separate the elements of the vector into those that are considered large and those that are considered small. Due to this separation the large values only have a smaller influence on the measure than they would using a normal L_2 norm. The Huber measure is also linked to a probability density function for x_j that is Gaussian in the centre and exponential in the tails (Huber, 1964).

The Ekblom measure

Ekblom (1973, 1987) proposed a perturbed version of the L_p norm

$$f(x_i) = \left(x_i^2 + \varepsilon^2\right)^{p/2} , \tag{8.5}$$

where ε is some positive number. Farquharson and Oldenburg (1998) and Farquharson (2008) consider this measure as more numerically attractive than a normal L_p norm, because the derivative at $x_i = 0$ exists when $p = 1$.

Using the Huber and Ekblom measure allows for more flexibility in the code. The default parameters for both measures are set to apply the standard L_2 norm for both model complexity and data misfit, but if desired a L_1 norm can be used to generate blocky models and a robust data misfit. Roughly Gaussian data would justify the straight L_2 norm whereas for a more uniform distribution the Huber norm may perform better. The user has to decide which norm is appropriate for the used data set and chosen mesh (as for all other inversion parameters).

8.2.2 *The objective function*

A commonly used approach is the minimisation of a combination of data misfit and model complexity (e.g., Farquharson et al., 2002; Farquharson and Oldenburg, 2004; Han et al., 2008; Avdeev and Avdeeva, 2009). Such a objective function Φ is of the form

$$\Phi = \phi_d + \beta\ \phi_m \quad , \tag{8.6}$$

where ϕ_d is a measure of data misfit, ϕ_m is representing the model roughness and β is the trade-off parameter (or regularisation parameter) that balances, or 'regularises', the effects of the two terms. This kind of objective function is often also called Tikhonov regularised penalty function. In the case of the MCMT3DID code the objective function also contains a term for the measure of distortion complexity, which is needed if the distortion values become inversion parameters. Therefore the full objective function Φ is given by

$$\Phi = \phi_d + \beta_m(\alpha_s\ \phi_s + \underline{\alpha_x}\ \underline{\phi_x}) + \beta_c\ \phi_c \quad , \tag{8.7}$$

where ϕ_d is the measure of data misfit, ϕ_s is the measure of the closeness to a reference model, $\underline{\phi_x}$ is the measure of the amount of structure in the Earth, and ϕ_c, which is new to this code, is the measure of the closeness to reference distortion values. The trade-off parameters are given by α_s, $\underline{\alpha_x}$, β_m and β_c, where the α values internally trade-off the contributions of the different measures of model complexity and the β values trade-off the model complexity and distortion complexity against the data misfit. The model structure terms ϕ_s and $\underline{\phi_x}$ are calculated using the Ekblom measure. Therefore the closeness to reference model can be written as

$$\phi_s = \sum_i \left([W_s^i(m^i - m_{ref}^i)]^2 + \varepsilon^2 \right)^{p/2} \quad , \tag{8.8}$$

where W_s^i are the elements of a diagonal matrix $\underline{\underline{W}}_s$, m^i and m_{ref}^i are the ith elements of the vectors describing the model and the reference model, respectively. The Ekblom constants are set to the following default values: $\varepsilon = 0.0001$ and $p = 2$ (individual modification of ε and p values optional in code). The model roughness term $\underline{\phi_x}$ is a vector containing the information of changes in 13 different directions. Each of these elements, ϕ_x^k, has its own trade-off parameter (in $\underline{\alpha_x}$) and can be written as

$$\phi_x^k = \sum_i \left([W_x^{k,i}(m^i - m_{ref}^i)]^2 + \varepsilon^2 \right)^{p/2} \quad , \tag{8.9}$$

where $W_x^{k,i}$ is the ith element of the matrix $\underline{\underline{W}}_x^k$, which is one of the 13 direction matrices. $\underline{\underline{W}}_x^1$, $\underline{\underline{W}}_x^2$ and $\underline{\underline{W}}_x^3$ are the first order difference matrices in the x-, y- and z-directions of the mesh, $\underline{\underline{W}}_x^4$ to $\underline{\underline{W}}_x^9$ represent the diagonal directions in the xy-, xz- and yz planes and $\underline{\underline{W}}_x^{10}$ to $\underline{\underline{W}}_x^{14}$ are through the vertices of a cell (see Figure 8.2).

The data misfit ϕ_d is calculated using the Huber measure, where $\phi_d = \sum_i \phi_d^i$ with

$$\phi_d^i = \begin{cases} [W_d^i(d_{pred}^i - d_{obs}^i)]^2 & \text{if } |W_d^i(d_{pred}^i - d_{obs}^i)| \leqslant h \\ 2h|W_d^i(d_{pred}^i - d_{obs}^i)| - h^2 & \text{if } |W_d^i(d_{pred}^i - d_{obs}^i)| > h \end{cases} \quad , \tag{8.10}$$

where h is the chosen positive Huber constant (default value in the code is $h = 1000$, different value optional), d_{obs}^i and d_{pred}^i are the observed and predicted ith data values,

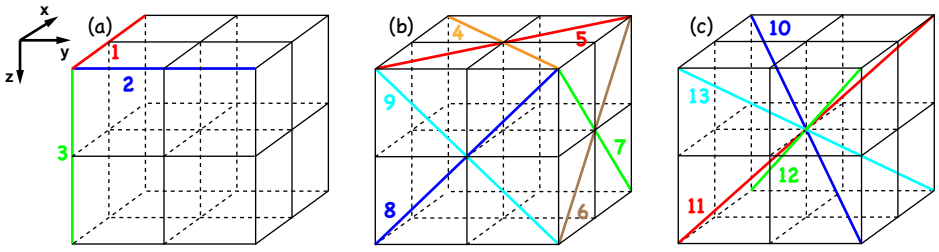

Figure 8.2: Figures showing the directions in space of the finite-difference matrices $\underline{\underline{W}}_x^k$, where $k = 1, ..., 13$. The x-, y- and z-directions are shown in (a), the directions in the xy-, xz, and yz-planes are in (b) and (c) shows the directions through the vertices of the cell, where the numbers represent the indices k of the matrices.

respectively, and W_d^i is the ith element of the diagonal weighting matrix, whose values are reciprocals of the measurement uncertainties.
The distortion complexity, $\phi_c = \sum_i \phi_c^i$, is calculated analogously using the Huber measure

$$\phi_c^i = \begin{cases} [W_c^i(c_{pred}^i - c_{obs}^i)]^2 & \text{if } |W_c^i(c_{pred}^i - c_{obs}^i)| \leqslant h \\ 2h|W_c^i(c_{pred}^i - c_{obs}^i)| - h^2 & \text{if } |W_c^i(c_{pred}^i - c_{obs}^i)| > h \end{cases}, \tag{8.11}$$

where h is the chosen positive Huber constant (default $h = 1000$, different value optional and note that h can be specified independently for the calculation of ϕ_d and ϕ_c). The observed and predicted ith distortion parameter is given by c_{obs}^i and c_{pred}^i, while W_c^i is the ith element of the diagonal weighting matrix, which are set to one by default, but can be set individually to any other value. Note that this measure of distortion complexity is comparing distortion matrix elements, it is not penalising individual gain, anisotropy, twist and shear values.

8.2.3 *Gauss-Newton method*

As the objective function (see Equation 8.7) is basically a sum-of-squares function, a Gauss-Newton (GN) algorithm can be applied to solve the non-linear least squares problem. The Gauss-Newton method can be seen as a modification of Newton's method for finding the minimum of a function, i.e., in this case finding the model and/or distortion parameters that minimize the objective function. The Newton method is based on a second order Taylor expansion to approximate the hyper-surface that corresponds to the objective function by a parabolic bowl, and therefore requires the full knowledge of the Hessian matrix (i.e., matrix of second order partial derivatives). The second order derivatives are computationally challenging, and therefore the Gauss-Newton method is used where the Hessian matrix is approximated by the transpose of the Jacobian matrix (i.e., matrix of first order partial derivatives times a factor of 2) times the Jacobian matrix. The resulting linear system of Gauss-Newton equations is solved using an iterative solver. The applied solver is the conjugate gradient solver from SPARSKIT (Saad, 1990). The solution of the linear system of Gauss-Netwon equations is the update to the model and/or distortion matrices, which leads to a reduced value of the objective function. The new objective function is approximated by the appropriate Gauss-Newton approximation of a parabolic bowl, the new Gauss-Netwon equation system is set up and solved to determine the new update to the model/distortion matrices. This sequence is repeated as an iterative procedure.

In the simple case of an inversion for conductivity structure only, the objective function (Equation 8.7) is reduced to

$$\Phi = \phi_d + \beta_m \left(\alpha_s \ \phi_s + \underline{\alpha}_x \ \underline{\phi}_x\right) \quad . \tag{8.12}$$

To simplify matters in the following the L_2-norm will be used to express the different measures of misfit and model complexity, as the Huber and the Ekblom measures involve a straight-forward modification (see Appendix F.1) of the equations obtained from the L_2-norm (Farquharson and Oldenburg, 1998). Therefore Equation 8.12 can be written as

$$\begin{aligned} \Phi \ &= \ \|\underline{\underline{W}}_d(\underline{d}_{pred} - \underline{d}_{obs})\|^2 + \beta_m \alpha_s \ \|\underline{\underline{W}}_s(\underline{m} - \underline{m}_{ref})\|^2 \\ &\quad + \beta_m \sum_k \alpha_k \ \|\underline{\underline{W}}_k(\underline{m} - \underline{m}_{ref})\|^2 \quad . \end{aligned} \tag{8.13}$$

At the $(n+1)$th iteration, the predicted data can be approximated by the linear Taylor series

$$\underline{d}_{pred} = \underline{d}^{n+1} \approx \underline{d}^n + \underline{\underline{J}}_m \ \delta\underline{m} \quad , \tag{8.14}$$

where $\delta\underline{m} = \underline{m}^{n+1} - \underline{m}^n$ and $\underline{\underline{J}}_m$ is the Jacobian matrix of sensitivities with respect to the model parameter

$$J_{m_{ij}} = \left.\frac{\partial d_i}{\partial m_j}\right|_{\underline{m}^n} \quad . \tag{8.15}$$

Substituting Equation 8.14 into the objective function in Equation 8.13 yields

$$\begin{aligned} \Phi^{n+1} \approx \ & \|\underline{\underline{W}}_d \underbrace{(\underline{d}_{pred} - \underline{d}_{obs})}_{\underline{d}^n + \underline{\underline{J}}_m \delta\underline{m} - \underline{d}_{obs}}\|^2 \ + \ \beta_m \alpha_s \ \|\underline{\underline{W}}_s \underbrace{(\underline{m}^{n+1} - \underline{m}_{ref})}_{\delta\underline{m} + \underline{m}^n - \underline{m}_{ref}}\|^2 \\ & + \ \beta_m \textstyle\sum_k \alpha_k \ \|\underline{\underline{W}}_k \underbrace{(\underline{m}^{n+1} - \underline{m}_{ref})}_{\delta\underline{m} + \underline{m}^n - \underline{m}_{ref}}\|^2 \end{aligned} \quad , \tag{8.16}$$

where $\underline{\underline{W}}_k$ are the 13 finite-difference matrices (see Equation 8.9 and Figure 8.2). Differentiating Equation 8.16 with respect to the elements of $\delta\underline{m}$ and equating the resulting derivatives to zero gives the following linear equation system

$$\begin{aligned} 0 \ &= \ \underline{\underline{J}}_m^T \ \underline{\underline{W}}_d^T \ \underline{\underline{W}}_d(\underline{d}^n + \underline{\underline{J}}_m \ \delta\underline{m} - \underline{d}_{obs}) + \beta_m \alpha_s \ \underline{\underline{W}}_s^T \ \underline{\underline{W}}_s(\delta\underline{m} + \underline{m}^n - \underline{m}_{ref}) \\ &+ \ \beta_m \sum_k \alpha_k \ \underline{\underline{W}}_k^T \ \underline{\underline{W}}_k(\delta\underline{m} + \underline{m}^n - \underline{m}_{ref}) \end{aligned} \tag{8.17}$$

$$\Rightarrow \quad \underbrace{\left[\underline{\underline{J}}_m^T \, \underline{\underline{W}}_d^T \, \underline{\underline{W}}_d \, \underline{\underline{J}}_m + \beta_m \alpha_s \, \underline{\underline{W}}_s^T \, \underline{\underline{W}}_s + \beta_m \sum_k \alpha_k \, \underline{\underline{W}}_k^T \, \underline{\underline{W}}_k\right]}_{\underline{\underline{A}}_m} \underbrace{\delta \underline{m}}_{\underline{x}_m} \tag{8.18}$$

$$= \underbrace{-\underline{\underline{J}}_m^T \, \underline{\underline{W}}_d^T \, \underline{\underline{W}}_d \, (\underline{d}^n - \underline{d}_{obs}) - \left[\beta_m \alpha_s \, \underline{\underline{W}}_s^T \, \underline{\underline{W}}_s + \beta_m \sum_k \alpha_k \, \underline{\underline{W}}_k^T \, \underline{\underline{W}}_k\right] (\underline{m}^n - \underline{m}_{ref})}_{\underline{b}_m}$$

This symmetric, linear system of Gauss-Newton equations ($\underline{\underline{A}}_m \, \underline{x}_m = \underline{b}_m$) is solved using the conjugate gradient (CG) method and an incomplete LU preconditioner (ILU) (SPARSKIT; Saad, 1990). The inverse of $\underline{\underline{A}}_m$ is not explicitly created, but the CG solver comprises products of matrix $\underline{\underline{A}}_m$ with vectors. These products require products of the Jacobian matrix, $\underline{\underline{J}}_m$, its transpose, $\underline{\underline{J}}_m^T$, and the various weighting matrices $\underline{\underline{W}}$ with vectors. The latter are trivial operations, but the products involving the Jacobian or its transpose are done by solving pseudo-forward problems, i.e., the system of equations to solve is given by $\underline{\underline{J}}_m \, \underline{u} = \underline{v}$ and $\underline{\underline{J}}_m^T \, \underline{v} = \underline{u}$, respectively (see e.g., Mackie and Madden, 1993; Rodi and Mackie, 2001).

If an inversion for only distortion parameters is required, the objective function (Equation 8.7) reduces to

$$\Phi = \phi_d + \beta_c \, \phi_c = \|\underline{\underline{W}}_d(\underline{d}_{pred} - \underline{d}_{obs})\|^2 + \beta_c \, \|\underline{\underline{W}}_c(\underline{c}_{pred} - \underline{c}_{obs})\|^2 \quad , \tag{8.19}$$

where L_2-norms are used to approximate the measures of data misfit and distortion complexity in Equation 8.19, and the subsequent description for clarity (the contributions of using non-L_2 norms can be taken into account in a straight-forward manner, see Appendix F.1; Farquharson and Oldenburg, 1998). Analogous to the above, the predicted data can be approximated by the linear Taylor series at the $(n+1)$th iterations as

$$\underline{d}_{pred} = \underline{d}^{n+1} \approx \underline{d}^n + \underline{\underline{J}}_c \, \delta \underline{c} \quad , \tag{8.20}$$

where $\delta \underline{c} = \underline{c}^{n+1} - \underline{c}^n$ and $\underline{\underline{J}}_c$ is the Jacobian matrix of sensitivities with respect to the distortion parameters

$$J_{c_{ij}} = \left.\frac{\partial d_i}{\partial c_j}\right|_{\underline{c}^n} \quad . \tag{8.21}$$

Substituting Equation 8.20 into the objective function in Equation 8.19 yields

$$\Phi^{n+1} \approx \|\underline{\underline{W}}_d(\underline{d}_n + \underline{\underline{J}}_c \, \delta \underline{c} - \underline{d}_{obs})\|^2 + \beta_c \, \|\underline{\underline{W}}_c(\delta \underline{c} + \underline{c}_n - \underline{c}_{obs})\|^2 \quad . \tag{8.22}$$

Differentiating Equation 8.22 with respect to the elements of $\delta \underline{c}$ and equating the resulting derivatives to zero yields

$$0 \quad = \quad \underline{\underline{J}}_c^T \, \underline{\underline{W}}_d^T \, \underline{\underline{W}}_d(\underline{d}^n + \underline{\underline{J}}_c \, \delta \underline{c} - \underline{d}_{obs}) + \beta_c \, \underline{\underline{W}}_c^T \, \underline{\underline{W}}_c(\delta \underline{c} + \underline{c}^n - \underline{c}_{ref}) \tag{8.23}$$

$$\Rightarrow \quad \underbrace{\left[\underline{\underline{J}}_c^T \, \underline{\underline{W}}_d^T \, \underline{\underline{W}}_d \, \underline{\underline{J}}_c + \beta_c \, \underline{\underline{W}}_c^T \, \underline{\underline{W}}_c\right]}_{\underline{\underline{A}}_c} \underbrace{\delta \underline{c}}_{\underline{x}_c}$$

$$= \underbrace{-\underline{\underline{J}}_c^T \, \underline{\underline{W}}_d^T \, \underline{\underline{W}}_d \, (\underline{d}^n - \underline{d}_{obs}) - \beta_c \, \underline{\underline{W}}_c^T \, \underline{\underline{W}}_c \, (\underline{c}^n - \underline{c}_{ref})}_{\underline{b}_c} \tag{8.24}$$

The system of symmetric and linear Gauss-Newton equations ($\underline{\underline{A}}_c \, \underline{x}_c = \underline{b}_c$) is solved with a CG solver using a ILU preconditioning (SPARSKIT; Saad, 1990). In this case the product of $\underline{\underline{A}}_c$ with vectors involved by the CG solver are trivial operations and do not require an iterative solution of a pseudo-forward problem (as it is required for the solution of Equation 8.18).

Slightly more complicated is the case of simultaneous inversion for the model structure and the distortion parameters. In this case the full objective function (Equation 8.7) has to be taken into account. To simplify matters once again the L_2-norm is used to express the measures of data misfit, model and distortion complexity instead of using the Huber and the Ekblom measures. The contribution of using the non-L_2-norms can be taken into account in a straight-forward manner (see Appendix F.1; Farquharson and Oldenburg, 1998).

The full objective function is given by

$$\begin{aligned} \Phi \quad = \quad & \|\underline{\underline{W}}_d(\underline{d}_{pred} - \underline{d}_{obs})\|^2 + \beta_m \alpha_s \, \|\underline{\underline{W}}_s(\underline{m} - \underline{m}_{ref})\|^2 \\ & + \beta_m \sum_k \alpha_k \, \|\underline{\underline{W}}_k(\underline{m} - \underline{m}_{ref})\|^2 + \beta_c \, \|\underline{\underline{W}}_c(\underline{c}_{pred} - \underline{c}_{obs})\|^2 \quad . \end{aligned} \tag{8.25}$$

At the $(n+1)$th iteration, the linear Taylor approximation describes the predicted data as

$$\underline{d}_{pred} = \underline{d}^{n+1} \approx \underline{d}^n + \underline{\underline{J}}_g \, \delta \underline{g} \quad , \tag{8.26}$$

where

$$\delta \underline{g} = \begin{pmatrix} \delta \underline{m} \\ \cdots\cdots \\ \delta \underline{c} \end{pmatrix} = \underline{g}^{n+1} - \underline{g}^n = \begin{pmatrix} \underline{m}^{n+1} - \underline{m}^n \\ \cdots\cdots\cdots\cdots \\ \underline{c}^{n+1} - \underline{c}^n \end{pmatrix} \tag{8.27}$$

is the vector of changes in the inversion parameters (at the top the model and at the bottom the distortion parameters) and

$$\underline{\underline{J}}_g = \begin{pmatrix} \underline{\underline{J}}_m & \vdots & \underline{\underline{J}}_c \end{pmatrix} \tag{8.28}$$

is the Jacobian matrix of sensitivities with respect to the model and distortion parameters

$$J_{g_{ij}} = \left.\frac{\partial d_i}{\partial g_j}\right|_{\underline{g}^n} = \begin{cases} \left.\frac{\partial d_i}{\partial m_j}\right|_{\underline{m}^n} & \text{if } g_{ij} \text{ is related to a model parameter} \\ \left.\frac{\partial d_i}{\partial c_j}\right|_{\underline{c}^n} & \text{if } g_{ij} \text{ is related to a distortion parameter} \end{cases} \quad . \tag{8.29}$$

Substituting Equation 8.26 into the objective function in Equation 8.25 yields

$$\begin{aligned}\Phi^{n+1} &\approx \|\underline{\underline{W}}_d(\underline{d}^n + \underline{\underline{J}}_g\,\delta\underline{g} - \underline{d}_{obs})\|^2 + \beta_m\alpha_s\,\|\underline{\underline{V}}_s(\delta\underline{g} + \underline{g}^n - \underline{g}_{ref})\|^2 \\ &+ \beta_m \sum_k \alpha_k\,\|\underline{\underline{V}}_k(\delta\underline{g} + \underline{g}^n - \underline{g}_{ref})\|^2 + \beta_c\,\|\underline{\underline{V}}_c(\delta\underline{g} + \underline{g}_n - \underline{g}_{ref})\|^2 \quad , \end{aligned} \tag{8.30}$$

where

$$\underline{\underline{V}}_s = \begin{pmatrix} \underline{\underline{W}}_s & 0 \\ 0 & 0 \end{pmatrix},\ \underline{\underline{V}}_k = \begin{pmatrix} \underline{\underline{W}}_k & 0 \\ 0 & 0 \end{pmatrix} \text{ and } \underline{\underline{V}}_c = \begin{pmatrix} 0 & 0 \\ 0 & \underline{\underline{W}}_c \end{pmatrix} \quad .$$

Differentiating Equation 8.30 with respect to the elements of $\delta\underline{g}$ and equating the resulting derivatives to zero yields

$$\begin{aligned} 0 &= \underline{\underline{J}}_g^T\,\underline{\underline{W}}_d^T\,\underline{\underline{W}}_d(\underline{d}^n + \underline{\underline{J}}_g\,\delta\underline{g} - \underline{d}_{obs}) + \beta_m\alpha_s\,\underline{\underline{V}}_s^T\,\underline{\underline{V}}_s(\delta\underline{g} + \underline{g}^n - \underline{g}_{ref}) \\ &+ \beta_m \sum_k \alpha_k\,\underline{\underline{V}}_k^T\,\underline{\underline{V}}_k(\delta\underline{g} + \underline{g}^n - \underline{g}_{ref}) + \beta_c\,\underline{\underline{V}}_c^T\,\underline{\underline{V}}_c(\delta\underline{g} + \underline{g}^n - \underline{g}_{ref}) \end{aligned} \tag{8.31}$$

$$\begin{aligned} \Rightarrow \quad & \underbrace{\begin{bmatrix} \underline{\underline{J}}_g^T\,\underline{\underline{W}}_d^T\,\underline{\underline{W}}_d\,\underline{\underline{J}}_g + \beta_m\alpha_s\,\underline{\underline{V}}_s^T\,\underline{\underline{V}}_s \\ +\beta_m\sum_k \alpha_k\,\underline{\underline{V}}_k^T\,\underline{\underline{V}}_k + \beta_c\,\underline{\underline{V}}_c^T\,\underline{\underline{V}}_c \end{bmatrix}}_{\underline{\underline{A}}_g} \underbrace{\delta\underline{g}}_{\underline{x}_g} \\ = \quad & \underbrace{-\underline{\underline{J}}_g^T\,\underline{\underline{W}}_d^T\,\underline{\underline{W}}_d\,(\underline{d}^n - \underline{d}_{obs}) - \begin{bmatrix} \beta_m\alpha_s\,\underline{\underline{V}}_s^T\,\underline{\underline{V}}_s \\ +\beta_m\sum_k \alpha_k\,\underline{\underline{V}}_k^T\,\underline{\underline{V}}_k \\ +\beta_c\,\underline{\underline{V}}_c^T\,\underline{\underline{V}}_c \end{bmatrix}\left(\underline{g}^n - \underline{g}_{ref}\right)}_{\underline{b}_g} \end{aligned} \tag{8.32}$$

The right hand side, $\underline{b}_g$, is simply a merged vector made of $\underline{b}_m$ and $\underline{b}_c$, because $\underline{\underline{V}}_s$ and $\underline{\underline{V}}_k$ only contribute if the element of $\underline{b}_g$ is a model parameter and if it is a distortion parameter then only $\underline{\underline{V}}_c$ contributes. Also

$$\underline{\underline{J}}_b^T = \begin{pmatrix} \underline{\underline{J}}_m^T \\ \cdots\cdots \\ \underline{\underline{J}}_c^T \end{pmatrix} \quad , \tag{8.33}$$

which also separates the contribution with respect to model and distortion parameters. However, the matrix $\underline{\underline{A}}_b$ cannot simply be separated into a top and a bottom part related to model and distortion parameters, respectively, although parts of the matrix are identical to $\underline{\underline{A}}_m$ and $\underline{\underline{A}}_c$, i.e.,

$$\underline{\underline{A}}_b = \begin{pmatrix} \underline{\underline{A}}_m & \underline{\underline{M}}_1 \\ \underline{\underline{M}}_2 & \underline{\underline{A}}_c \end{pmatrix} \quad , \tag{8.34}$$

where $\underline{\underline{M}}_1 = \underline{\underline{J}}_m^T \underline{\underline{W}}_d^T \underline{\underline{W}}_d \underline{\underline{J}}_c$ and $\underline{\underline{M}}_2 = \underline{\underline{J}}_c^T \underline{\underline{W}}_d^T \underline{\underline{W}}_d \underline{\underline{J}}_m$ are mixed terms. A CG solver using a ILU preconditioning (SPARSKIT; Saad, 1990) is applied to solve the symmetric and linear system of Gauss-Newton equations ($\underline{\underline{A}}_g \underline{x}_g = \underline{b}_g$). Analogous to Equation 8.18 the CG solver requires products of the matrix $\underline{\underline{A}}_g$ with vectors that involve products of the Jacobian, $\underline{\underline{J}}_m$, and its transpose, $\underline{\underline{J}}_m^T$, with vectors. These products are calculated by solving the pseudo-forward problem of a system of equations given by $\underline{\underline{J}}_m \underline{u} = \underline{v}$ and $\underline{\underline{J}}_m^T \underline{v} = \underline{u}$, respectively (see e.g., Mackie and Madden, 1993; Rodi and Mackie, 2001).

8.3 CALCULATION OF JACOBIAN MATRICES

To check if the calculation of the Jacobian matrices is done correctly within the inversion code the calculated Jacobian is compared to the so-called brute-force Jacobian.

8.3.1 *Jacobian matrix with respect to the resistivity structure*

The Jacobian matrix with respect to the resistivity structure can be brute-force computed by changing the conductivity value of an individual cell (one at a time) and calculating the forward responses for the modified model. The original model, m^{org}, and the related responses, d^{org}, will be subtracted from the modified model, m^{mod}, and its responses, d^{mod}. Therefore each individual element of the brute-force Jacobian matrix can be determined as

$$J^{bf}_{m_{ij}} \approx \frac{d_i^{mod} - d_i^{org}}{m_j^{mod} - m_j^{org}} \quad , \tag{8.35}$$

where the effect of the change in the jth model parameter on the ith data value is calculated. The brute-force Jacobian ($\underline{\underline{J}}^{bf}_m$) is compared to the Jacobian matrix calculated within the inversion code. The Jacobian matrix elements are the derivatives of the synthetic data, $\underline{\underline{D}}$, with respect to the conductivity structure (note that to simplify matters σ is used in the equations but the numerical formulation uses $\log(\sigma)$)

$$J_{ij} = \frac{\partial}{\partial \sigma_j} D_i \quad . \tag{8.36}$$

In the simplest case the required data is an undistorted and unrotated set of impedances values, $\underline{\underline{Z}}$, where

$$\frac{\partial}{\partial \sigma} \underline{\underline{D}} = \frac{\partial}{\partial \sigma} \underline{\underline{Z}} \quad . \tag{8.37}$$

If the impedance data is distorted then $\underline{\underline{D}} = \underline{\underline{C}}\,\underline{\underline{Z}}$, where $\underline{\underline{C}}$ is the distortion matrix, and the derivative is given by

$$\frac{\partial}{\partial \sigma} \underline{\underline{D}} = \frac{\partial}{\partial \sigma} \underline{\underline{C}}\,\underline{\underline{Z}} = \underline{\underline{C}} \frac{\partial}{\partial \sigma} \underline{\underline{Z}} \quad , \tag{8.38}$$

because the distortion matrix is, by definition, independent of the conductivity model. During the inversion process the Jacobian is required in two matrix-vector multiplications;

once in a subroutine determining $\underline{\underline{J}}_m \underline{u} = \underline{v}$ and once calculating the inverse operation, i.e., $\underline{\underline{J}}_m^T \underline{v} = \underline{u}$. These matrix-vector multiplications are determined by solving pseudo-forward problems iteratively (Mackie and Madden, 1993; Rodi and Mackie, 2001).

To compare the Jacobian matrix elements of $\underline{\underline{J}}_m$ and $\underline{\underline{J}}_m^T$ to the brute-force values of $\underline{\underline{J}}_m^{bf}$, one feeds the iterative solver of the pseudo-forward problem with a vector $\underline{u}$ (or $\underline{v}$ respectively) that is set to zero except for one element that is set to one. Repeating this process for each vector element the full Jacobian matrix (or its transpose) is calculated. Unfortunately the comparison in Figures 8.3 and 8.4 shows that the iterative solution does not match the brute-force Jacobian in a satisfying way (i.e., the resulting values are incorrect). Several debugger and memory checking software (e.g., gdb, valgrind, absoft) have been applied to the code. None of them found a memory or numerical problem with the coding. It seems to be a formulation/equation problem. The comparison in Figures 8.3 and 8.4 shows the true matrix elements as well as the absolute values. They indicate a good tendency for many values, but a closer look reveals quite significant differences. Unfortunately no pattern (in neither figure) is obvious that could give an indication of the cause of the problem. Also trying to calculate the derivatives of the electric field components (instead of the impedance data) with respect to the resistivity structure has not revealed any helpful information.

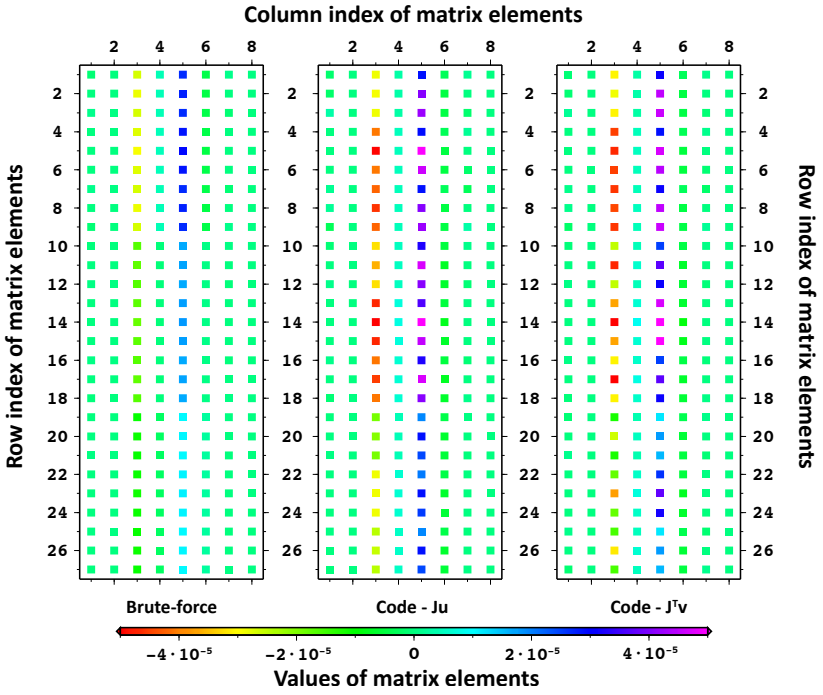

Figure 8.3: Figure showing the comparison of the brute-force with the calculated J_m values for a homogeneous halfspace model using the subroutines to determine $\underline{\underline{J}}\underline{u}$ and $\underline{\underline{J}}^T\underline{v}$ respectively. Data values are in impedance.

Therefore, to be able to show some preliminary inversion results, the code is modified in the following way: For a small area the brute-force Jacobian is calculated and written to a file. This file is read into the inversion code and every time the calculation of $\underline{\underline{J}}_m \underline{u} = \underline{v}$

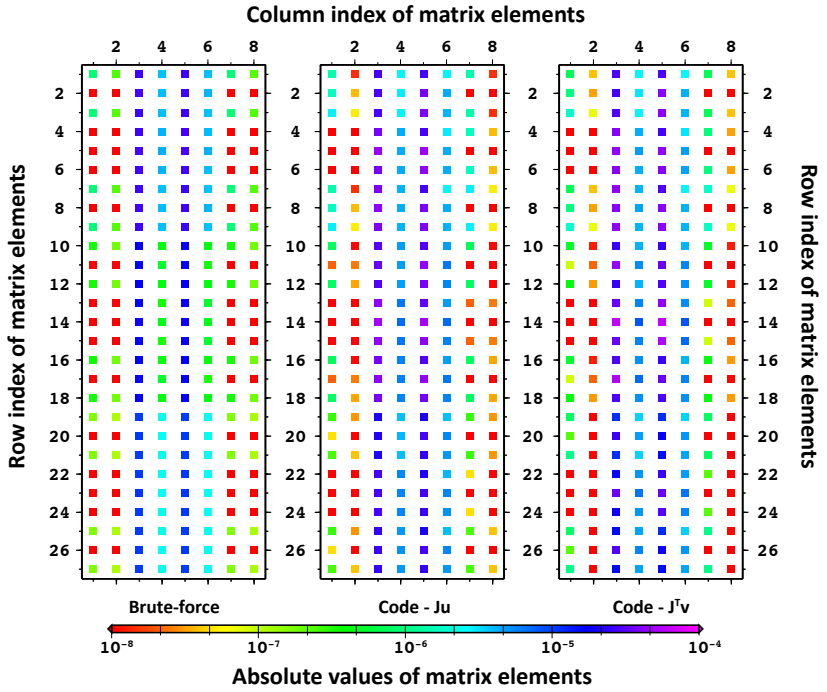

Figure 8.4: Figure showing the comparison of the brute-force with the calculated J_m absolute values for a homogeneous halfspace model using the subroutines to determine $\underline{\underline{J}}\underline{u}$ and $\underline{\underline{J}}^T\underline{v}$ respectively. Data values are in impedance.

or $\underline{\underline{J}}^T_m \underline{v} = \underline{u}$ is required, the hard-wired, brute-force Jacobian is used to execute a simple multiplication with the vector, instead of using the iterative solver. The disadvantage of this procedure is that calculating the brute-force Jacobian is very time consuming and therefore it is impracticable to redo the calculation every time the model has changed. The Jacobian of the starting model will be used throughout the whole inversion, which seems to be a reasonable approach as the perfect inversion result is not the aim but to demonstrate the functionality of the code.

Using a homogeneous halfspace or 1D Jacobian (as, e.g., Smith and Booker (1991) and Farquharson and Oldenburg (1999) applied) to approximate the Jacobian instead of calculating the brute-force values is not possible. The comparison of brute-force and calculated Jacobian matrix elements shown in Figures 8.3 and 8.4 is based on a homogeneous halfspace resistivity model and shows that calculation even for such a simple model is not working properly.

8.3.2 *Jacobian matrix with respect to the distortion parameters*

Analogous to the Jacobian with respect to the resistivity parameters the Jacobian with respect to the distortion parameters, $\underline{\underline{J}}_c$, can be checked by comparison with the brute-force values. One distortion parameter is modified at a time to calculate the forward responses. The fraction of the differences between the modified and original distortion parameters and their response values gives the values of each of the brute-force Jacobian matrix elements

$$J^{bf}_{c_{ij}} \approx \frac{d_i^{mod} - d_i^{org}}{c_j^{mod} - c_j^{org}} \quad , \tag{8.39}$$

where the effect of the change in the jth distortion parameter on the ith data value is calculated. If distortion is present the data matrix, $\underline{\underline{D}}$, is given by

$$\underline{\underline{D}} = \underline{\underline{C}}\underline{\underline{Z}} \quad , \tag{8.40}$$

or in components

$$\begin{aligned} \begin{pmatrix} D_{xx} & D_{xy} \\ D_{yx} & D_{yy} \end{pmatrix} &= \begin{pmatrix} C_{11} & C_{12} \\ C_{21} & C_{22} \end{pmatrix} \begin{pmatrix} Z_{xx} & Z_{xy} \\ Z_{yx} & Z_{yy} \end{pmatrix} \\ &= \begin{pmatrix} C_{11}Z_{xx} + C_{12}Z_{yx} & C_{11}Z_{xy} + C_{12}Z_{yy} \\ C_{21}Z_{xx} + C_{22}Z_{yx} & C_{21}Z_{xy} + C_{22}Z_{yy} \end{pmatrix} \quad , \end{aligned} \tag{8.41}$$

where $\underline{\underline{C}}$ is the known distortion matrix and $\underline{\underline{Z}}$ is the known matrix of impedance values from the forward solution related to the given conductivity structure. As $\underline{\underline{Z}}$ is independent of the distortion parameters, its elements only act as factors on the $\underline{\underline{C}}$ matrix. Therefore the derivative with respect to the distortion parameters is easy to calculate, e.g.,

$$\frac{\partial D_{xx}}{\partial C_{11}} = \frac{\partial}{\partial C_{11}}(C_{11}\, Z_{xx} + C_{12}\, Z_{yx}) = Z_{xx} \quad . \tag{8.42}$$

Appendix F.3 lists the derivatives of all data matrix elements with respect to all distortion matrix elements and also the calculations of the derivatives for the case where data are not in impedances but in resistivity and phase values. Other than for the Jacobian with respect to the resistivity, where an iterative solution was required due to the dependence of the matrix elements on the resistivity, the Jacobian with respect to distortion can be set up directly as the matrix values are independent of the distortion values themselves.

The comparison of the brute-force Jacobian and the set-up one in the code is done using two different resistivity structures; first an homogeneous halfspace of 100 Ωm and second two blocks embedded in a 100 Ωm homogeneous halfspace. The latter model is sketched in Figure 8.5.

Figures 8.6 and 8.7
show the true values and the absolute values of the Jacobian matrix elements, respectively. In both cases the agreement of the brute-force values and the values from the code is very good for both resistivity structures (same comparison but for data values in resistivity and phase instead of impedance is shown in Appendix F, Figures F.1 and F.2). Therefore the subroutine generating the Jacobian with respect to the distortion parameters is verified, and one can be confident in the calculated values.

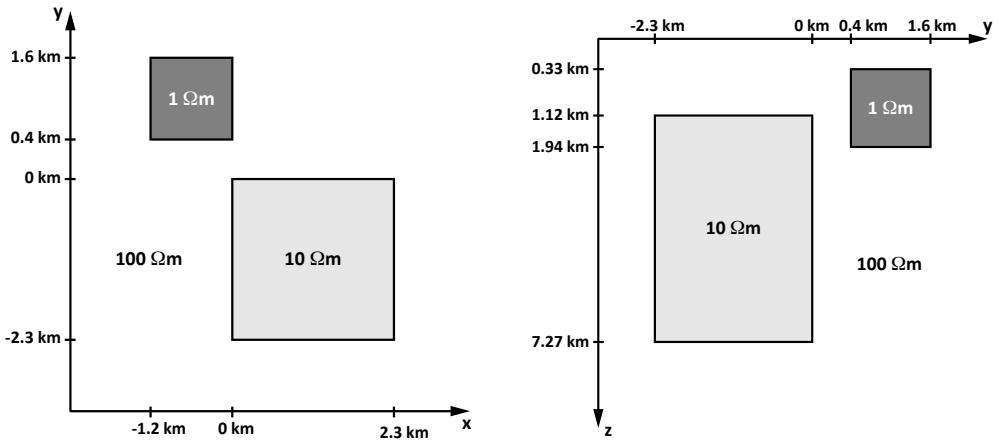

(a) 3D model for J_c test - plan view (b) 3D model for J_c test - section view

Figure 8.5: Sketch of the 3D model used for the J_c test: (a) shows the plan view and (b) the section view.

8.3.3 *Jacobian matrix with respect to the resistivity structure and to the distortion parameters*

As Equations 8.28 and 8.33 show, the Jacobian with respect to the resistivity structure and the distortion parameter is just a matrix that is merged using the individual Jacobian matrices with respect to either parameter set. Therefore, no additional subroutine is required to deal with the Jacobian with respect to both parameter sets, as the existing ones for $\underline{\underline{J}}_m$, $\underline{\underline{J}}_m^T$ and $\underline{\underline{J}}_c$ are adequate to perform all necessary calculations. Even the mixed terms in the $\underline{\underline{A}}_g$ matrix (see Equation 8.34), can be determined using the subroutines calculating the matrix-vector products of a vector with one of the Jacobians (i.e., $\underline{\underline{J}}_m$, $\underline{\underline{J}}_m^T$, $\underline{\underline{J}}_c$ or $\underline{\underline{J}}_c^T$).

8.4 ROTATION OF THE SYNTHETIC DATA

To rotate the noise-free synthetic data instead of the noisy (and distorted) observed data, the individual rotation angle for each site is required as input information. The rotation needs to be taken into account at two parts of the inversion code. First, if the difference between observed and synthetic/predicted data is required to calculate the data misfit, and second, when the Jacobian matrix elements are calculated.

To calculate the difference between the observed data, $\underline{\underline{D}}_{obs}$, and the synthetic forward data, $\underline{\underline{Z}}_{pred}$, both data sets need to be in the same coordinate system, therefore the predicted data is rotated into the coordinate system used by the observed data,

$$\underline{\underline{D}}_{pred} = \underline{\underline{R}}(\theta)\, \underline{\underline{Z}}_{pred} \underline{\underline{R}}^T(\theta) \quad , \tag{8.43}$$

where θ is the individual rotation angle for each site and $\underline{\underline{R}}$ is the rotation matrix given by

$$\underline{\underline{\mathbf{R}}}(\theta) = \begin{pmatrix} \cos\theta & \sin\theta \\ -\sin\theta & \cos\theta \end{pmatrix} \quad \text{and} \quad \underline{\underline{\mathbf{R}}}^T(\theta) = \begin{pmatrix} \cos\theta & -\sin\theta \\ \sin\theta & \cos\theta \end{pmatrix} . \tag{8.44}$$

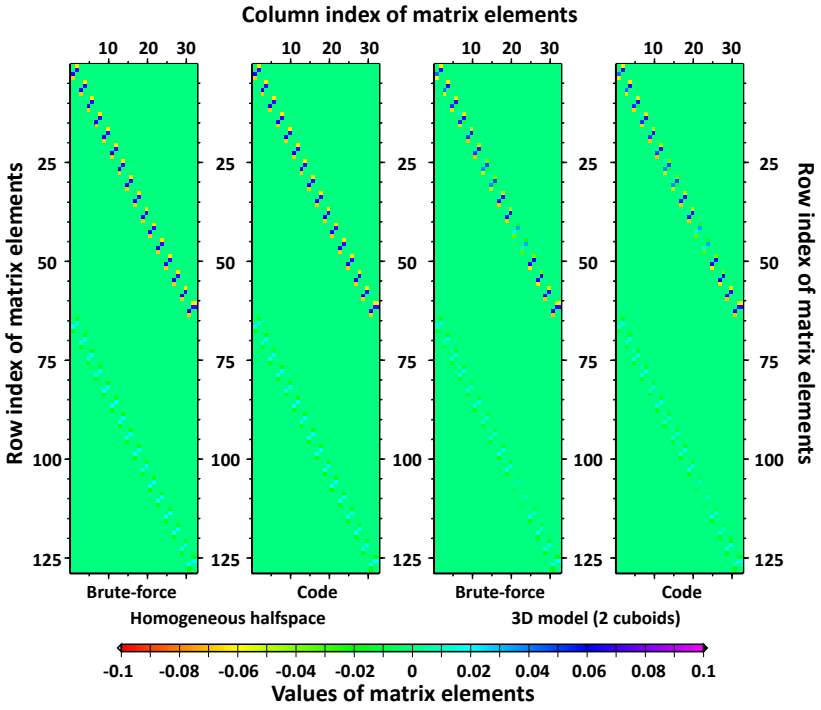

Figure 8.6: Figure showing the comparison of the brute-force with the calculated J_c values for a homogeneous halfspace model (left) and a 3D model as shown in Figure 8.5 (right). Data values are in impedance.

In the case where also the distortion parameters need to be taken into account the predicted data is calculated by

$$\underline{\underline{D}}_{\text{pred}} = \underline{\underline{R}}(\theta)\ \underline{\underline{C}}\ \underline{\underline{Z}}_{\text{pred}}\underline{\underline{R}}^{T}(\theta) \quad . \tag{8.45}$$

Based on these additional matrices and their multiplication with the actual forward impedance, $\underline{\underline{Z}}_{\text{pred}}$, also the calculation of the derivatives is affected. In the case of distortion-free but rotated data the elements of the Jacobian matrix with respect to the resistivity structure are given by

$$\frac{\partial}{\partial\sigma}\ \underline{\underline{D}}_{\text{pred}} = \frac{\partial}{\partial\sigma}\ \underline{\underline{R}}\ \underline{\underline{Z}}_{\text{pred}}\ \underline{\underline{R}}^{T} = \underline{\underline{R}}\ \frac{\partial \underline{\underline{Z}}_{\text{pred}}}{\partial\sigma}\ \underline{\underline{R}}^{T} \quad . \tag{8.46}$$

If the data is distorted and rotated the derivatives with respect to the resistivity structure can be written as

$$\frac{\partial}{\partial\sigma}\ \underline{\underline{D}}_{\text{pred}} = \frac{\partial}{\partial\sigma}\ \underline{\underline{R}}\ \underline{\underline{C}}\ \underline{\underline{Z}}_{\text{pred}}\ \underline{\underline{R}}^{T} = \underline{\underline{R}}\ \underline{\underline{C}}\ \frac{\partial \underline{\underline{Z}}_{\text{pred}}}{\partial\sigma}\ \underline{\underline{R}}^{T} \quad , \tag{8.47}$$

and additionally the derivatives with respect to the distortion parameters is required, which is given by

$$\frac{\partial}{\partial C}\ \underline{\underline{D}}_{\text{pred}} = \frac{\partial}{\partial C}\ \underline{\underline{R}}\ \underline{\underline{C}}\ \underline{\underline{Z}}_{\text{pred}}\ \underline{\underline{R}}^{T} = \underline{\underline{R}}\ \frac{\partial \underline{\underline{C}}\ \underline{\underline{Z}}_{\text{pred}}}{\partial C}\ \underline{\underline{R}}^{T} \quad , \tag{8.48}$$

where the determination of $\partial\underline{\underline{C}}\ \underline{\underline{Z}}/\partial C$ is given by Equation 8.42 (and the equations in Appendix F.3).

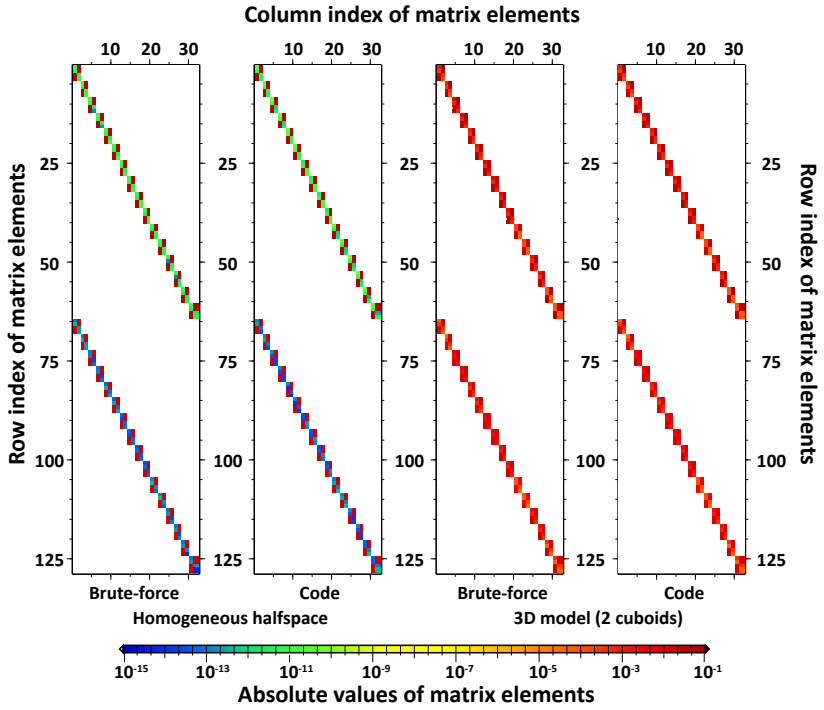

Figure 8.7: Figure showing the comparison of the brute-force with the calculated J_c absolute values for a homogeneous halfspace model (left) and a 3D model as shown in Figure 8.5 (right). Data values are in impedance. (Note white colour indicates absolute values less than 10^{-15}.)

9

TESTING OF THE 3D INVERSION CODE

This chapter shows the preliminary results of a test inversion using the 3D inversion code MCMT3DID (described in Chapter 8). As already mentioned in the previous chapter, there is still a coding problem in the part of the code that is calculating the Jacobian matrix with respect to the resistivity structure. The brute-force Jacobian matrix of the starting model is used instead, but as the calculation is expensive in computation time no updates of the Jacobian are derived for the subsequent iteration steps. Based on this approximation the inversion result cannot be expected to be perfect; it will be a rather fuzzy image of the structure, but it can give an impression if the overall inversion part of the code is performing well.

The COMMEMI 3D-1A model (Zhdanov et al., 1997) is used as the test model and the synthetic forward responses, used as observed data for the inversion, were calculated using the 3D forward routine of Mackie et al. (1994) (implemented in Geosystem's WinGLink® package). A sketch of the COMMEMI 3D-1A model can be found in Chapter 7 (Figure 7.6). Figure 9.1 shows the mesh used for the inversion. It consist of 38 x 37 x 26 cells (including 9 airlayers) with a lateral centre cell width of 200 m. An array of 48 sites (blue dots in Figure 9.1 (b)) was placed above and around the lateral extent of the conductive body and a full impedance data set (i.e., real and imaginary part of diagonal and off-diagonal elements) was calculated at three periods, namely 0.1 s, 1 s and 10 s. The black dashed line in Figure 9.1 (b) indicates the location of the profile, which is used later for data comparison.

For the inversion normally all cells in the subsurface would be active (i.e., the resistivity of the cells would be updated during the inversion process), whereas the cells in the airlayer are inactive (i.e., cannot be changed by the inversion algorithm). That means, the Jacobian matrix has a dimension of 1152 data values (48 sites · 8 response values · 3 frequencies) by 23902 active cells (38 x 37 x 17). For a brute-force calculation of the Jacobian matrix elements, 23902 active cells are too many, as that would require 23903 forward solutions (one for each cell plus one as reference to subtract from; see description of how the brute-force values are calculated in Section 8.3). Only the centre part of the mesh (15 x 20 x 12 cells) was therefore selected to be active, while the padding cells were all set to be inactive. Calculating the brute-force Jacobian matrix, J_{bf}, for 15 x 20 x 12 (=3600) active cells and three periods would require about 180 days on a single CPU (in fact the elements of the brute-force Jacobian were calculated in 72 individual parts and merged by hand). It is therefore impossible to update the brute-force Jacobian matrix for every iteration step during the inversion, but the brute-force Jacobian calculated for the starting model was kept for all iterations.

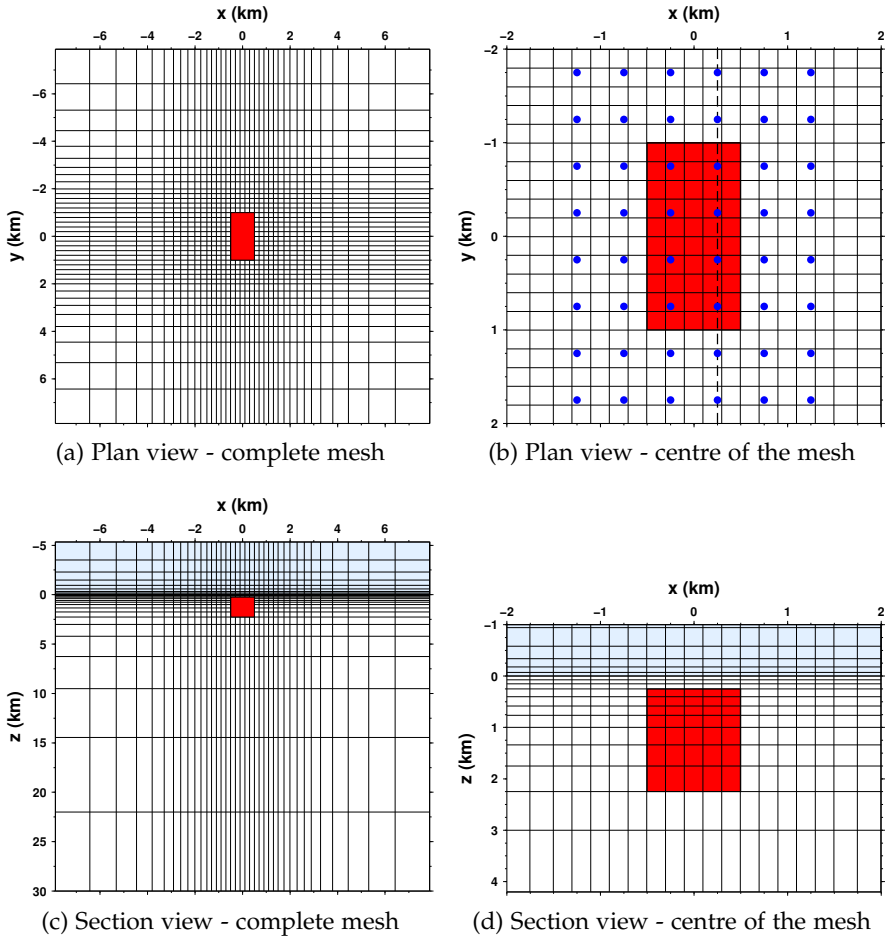

(a) Plan view - complete mesh

(b) Plan view - centre of the mesh

(c) Section view - complete mesh

(d) Section view - centre of the mesh

Figure 9.1: Figure showing the design of the inversion mesh. Panels (a) and (b) show the inversion mesh in plan view and (c) and (d) in section view. The red block indicates the location of the 0.5 Ωm block that is embedded in a 100 Ωm halfspace (COMMEMI 3D-1A model from Zhdanov et al. (1997)). The lightblue colour in (c) and (d) represents the airlayers. The blue dots in (b) show the location of the 48 sites and the black dashed line represents the location of the profile used for data comparison in Figures 9.5 to 9.7.

Figure 9.2 shows the depth slices of the COMMEMI 3D-1A model. The 12 depth layers show (in lateral and vertical direction) the active cells only. The conductive block extends from the third to tenth layer (250 m to 2250 m depth).

Figure 9.3 shows the same depth slices as in Figure 9.2, the resistivity structure is not representing the true model but the inversion result after five iterations. All eight impedance elements were taken into account for the inversion at all 48 sites and all three periods. The error of the impedance elements was chosen to be 5% of the complex absolute value of the XY component in XX and XY and 5% of the complex absolute value of the YX component in YX and YY. (Noise was not added to the synthetic data.) The starting and reference models were a 100 Ωm homogeneous halfspace, the forward solver was set to 1000 iterations applying the divergence correction (see Section 6.3) every 20 iterations (using a Krylov subspace of 16) and the trade-off parameter β_m was set to 10. The model trade-off parameter α_s was set to 10^{-6} and the values of $\underline{\alpha}_x$ were 1.0 for the differences in the main direction x, y and z and 0.0 for all other directions (see Section 8.2.2 for more details).

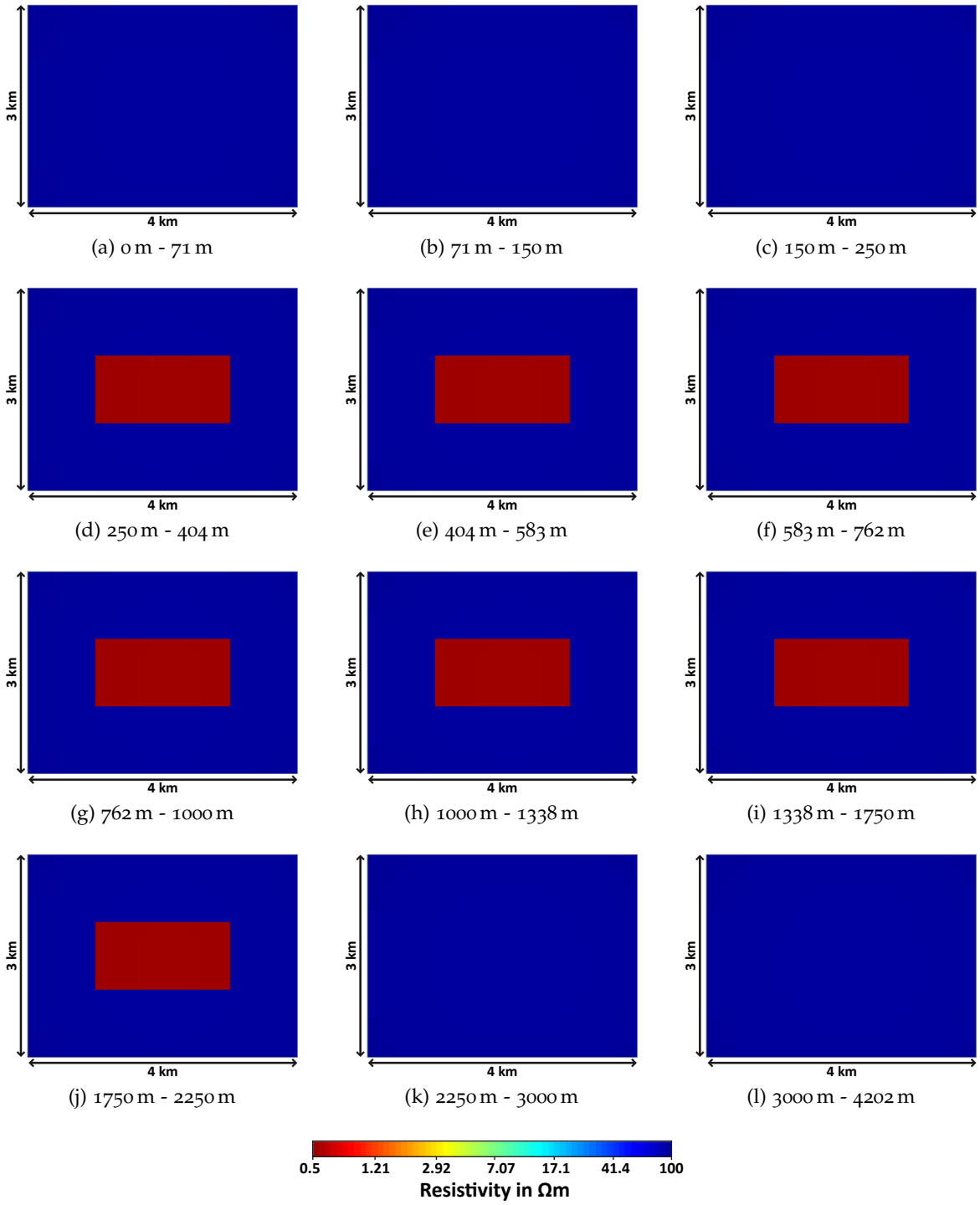

Figure 9.2: Figure showing depth slices of the true inversion model (depth range for each slice listed below the figures). The inversion test model is the COMMEMI 3D inversion model (Zhdanov et al., 1997) consisting of a 0.5 Ωm block in a homogeneous halfspace of 100 Ωm. The extracted depth slices shown represent the complete area of active cells.

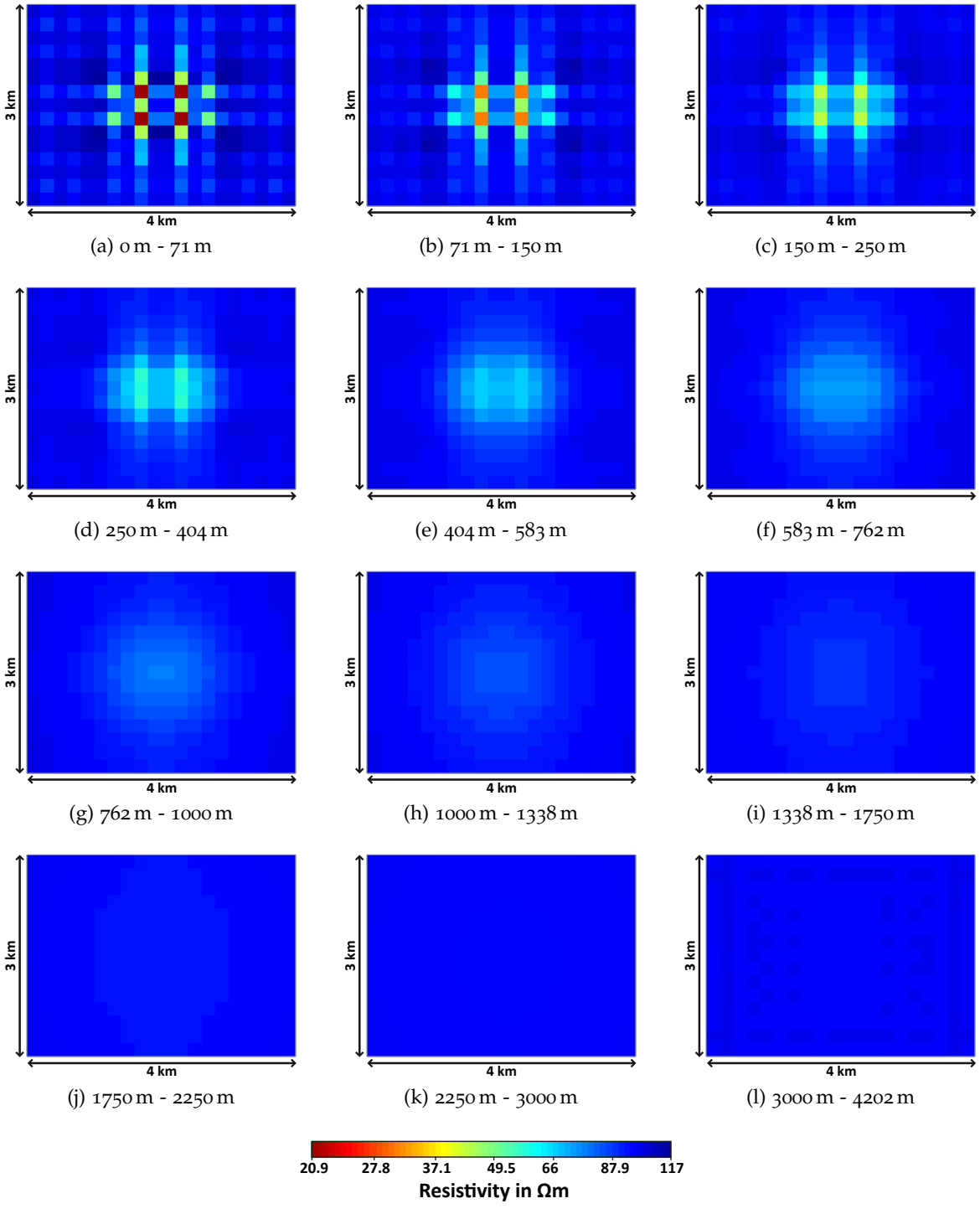

(a) 0 m - 71 m (b) 71 m - 150 m (c) 150 m - 250 m

(d) 250 m - 404 m (e) 404 m - 583 m (f) 583 m - 762 m

(g) 762 m - 1000 m (h) 1000 m - 1338 m (i) 1338 m - 1750 m

(j) 1750 m - 2250 m (k) 2250 m - 3000 m (l) 3000 m - 4202 m

Figure 9.3: Figure showing depth slices of the 3D inversion result after 5 iterations. The depth range is specified below each depth slice. (Undistorted impedance data is used and no extra weighting is applied.)

The model resulting from the inversion indicates the lateral location of the structure more or less in the correct place, the tendency of the structure being more conductive than the background is also correct. But neither the absolute resistivity values nor the depth extent of the structure is similar to the true structure. Instead strong near-surface scatter can be found in the top three layers. More periods than just one per decade, higher frequencies (sensing the resistivity above the conductor) and closer site spacing might reduce the near-surface scatter. It can also not be excluded that the scatter is enhanced due to the approximation using the brute-force Jacobian for all iteration steps, although the phenomenon of near-surface scatter is known from other 3D MT inversion codes as well (e.g., Siripunvaraporn et al., 2005; Avdeeva, 2008). Avdeeva (2008) states that the singularity of the gradient in the vicinity of the MT sites introduces erratic structures to the model, which complicate the solution of the 3D MT inverse problem, and, in particular, is a problem for Newton-type optimisation approaches. More direct constraints on the model conductivity values, especially for near-surface cells, are suggested as a solution by Siripunvaraporn et al. (2005) (called covariance matrix, as kind of low-pass filtering of the conductivities) and Avdeeva (2008) (suggesting a covariance matrix or a inverse Hessian matrix to smooth the gradients).

MCMT3DID has the option to introduce a covariance smoothing by adding extra weights for each individual cell of the reference model to the elements of matrix $\underline{\underline{W}}_s$. Figure 9.4 shows the inversion result after five iterations trying to inhibit the near-surface scatter by giving an extra weight of a factor 10000 to the top three layers, that means the cells are forced to stay close to the reference model (the larger the factor the stronger the constraint), which has a resistivity of 100 Ωm. All other inversion parameter settings remain unchanged. Clearly the top three layers show the correct homogeneous resistivity of 100 Ωm, but once again, the depth extent and the resistivity of the conductive body is not resolved well (note that different colour scales had to be used in Figures 9.2 to 9.4 to make the resistivity structures visible).

The inversion appears to work correctly, but the limitation of using the brute-force Jacobian matrix of the starting model is hindering the inversion process to reach a satisfying result and data fit. Figures 9.5 to 9.7 show a comparison of the input data (undistorted impedances, red circles) and the inversion result (blue triangles) at 0.1 s, 1 s and 10 s. The fit is poor and the responses curves of the inversion results stay close to how responses of a 100 Ωm homogeneous halfspace would look like.

In a next step of testing the same inversion parameter settings including the extra weighting for the top three layers were used to invert distorted impedance tensor data. To calculate the distorted data the impedance data of the previous inversion test were multiplied with individual distortion matrices for each site. The distortion matrices were randomly generated by using the Groom-Bailey decomposition approach (i.e., a random shear angle between $\pm 45°$ and a random twist angle between $\pm 60°$ were generated, the gain was set to 10 and the anisotropy to 1). Inverting the distorted impedance data for the resistivity structure only (as standard 3D inversion codes do) the resulting model and responses are identical to the result obtained from the inversion using undistorted data. The green diamonds in Figures 9.5 to 9.7 represent the distorted input impedance data set. The inversion result response curves are identical to the blue triangles plotted for the undistorted data inversion.

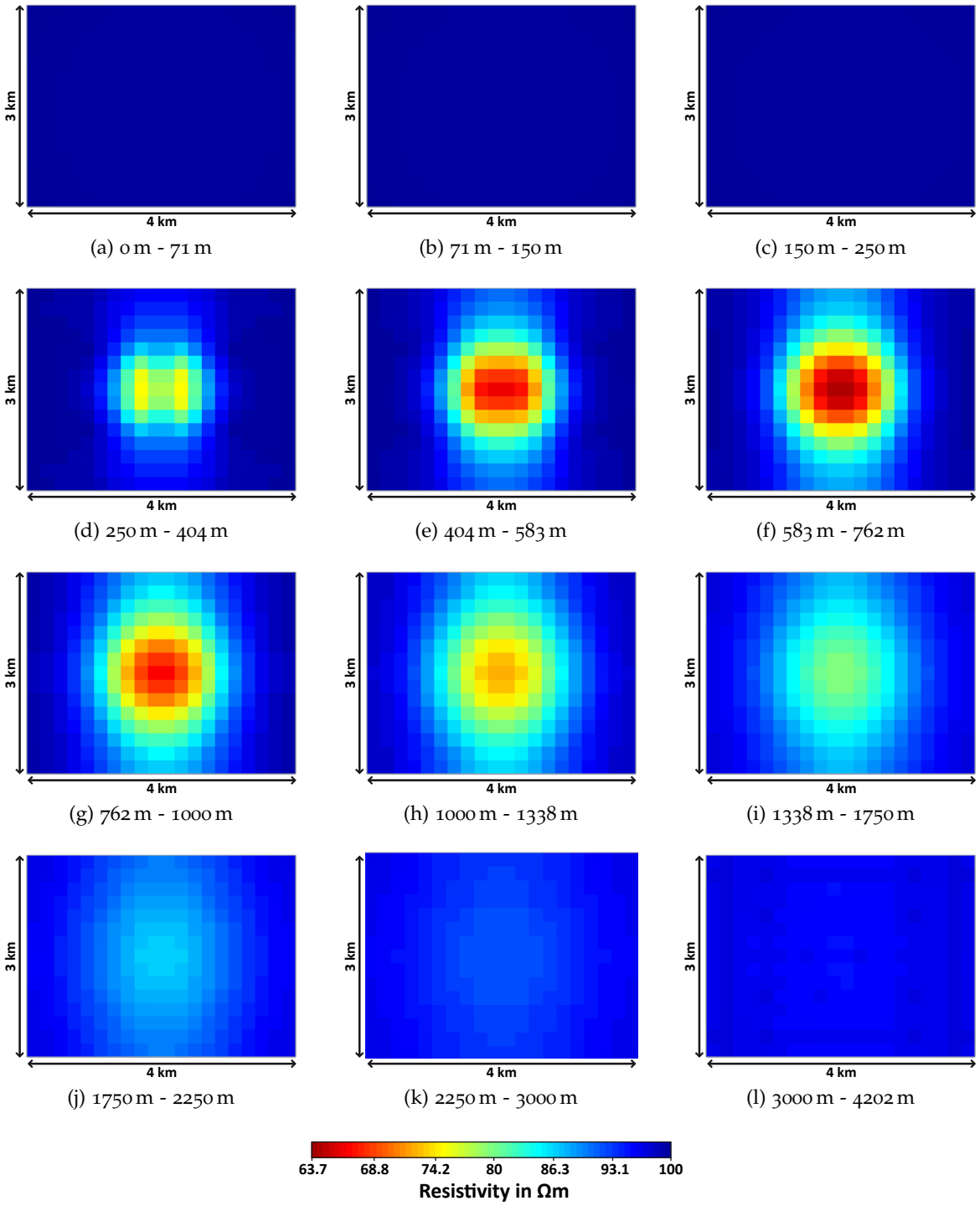

(a) 0 m - 71 m (b) 71 m - 150 m (c) 150 m - 250 m

(d) 250 m - 404 m (e) 404 m - 583 m (f) 583 m - 762 m

(g) 762 m - 1000 m (h) 1000 m - 1338 m (i) 1338 m - 1750 m

(j) 1750 m - 2250 m (k) 2250 m - 3000 m (l) 3000 m - 4202 m

Figure 9.4: Figure showing the 3D inversion results after 5 iterations using an extra weighting of a factor 10000 for the top three layers to avoid the near-surface scatter. The depth range is specified below each depth slice. (This inversion result is obtained for undistorted impedance data, although using distorted data results in an identical inversion model.)

Since there is no recognisable difference in the inversion (for resistivity structure only) result using distorted or undistorted data, it is impossible at the current form of the code to say whether or not the inclusion of the distortion parameter during the inversion would improve the results or not. Once again, the brute-force approximation of the Jacobian is the likely cause (although another coding problem in addition to the brute-force approximation can also not be excluded at the current testing level).

In conclusion, using the brute-force Jacobian of the starting model allows determining whether or not the inversion for the resistivity structure only is progressing correctly and changing the resistivity values in the correct direction. Although the inversion results are still far from the true structure, the fuzzy model found using extra weighting for the top three layers suggests a block that is more conductive than the background and has in lateral direction the correct location but the depth extent is not accurately found. Therefore the inversion (with respect to the resistivity structure) part of the program is considered as working fine, and resolving the true structure better is only hindered by the brute-force approximation of the Jacobian using the starting model. Unfortunately the inversion cannot progress far enough to be able to test whether or not the inclusion of the distortion parameters during the inversion process (or the internal rotation of the synthetic data into the local measurement coordinate system) would improve the result if distorted (and/or noisy) data are inverted.

Once the coding problem regarding the calculation of the Jacobian matrix is solved, more detailed tests are required. Beside testing different parameter settings (e.g., different α and β values), reducing the extra weighting of the top layers and running inversion for the different input data formats (i.e., impedance, resistivity and phase, tipper), the various aspects of the inclusion of the distortion parameters and their related inversion settings need to be tested. Especially the trade-off between model structure and distortion parameter requires thorough testing. Possible scenarios are to increase or decrease both trade-off parameters (β_m and β_c) every iteration step or increase one and at the same time decrease the other one. They also can be kept fixed, or one could try to fit the data by distortion only for the first iteration and then keep the resulting distortion values fixed and only invert for the resistivity structure for all remaining iteration steps (suggested by Laust Pedersen, University Uppsala, Sweden). A thorough testing is required to get a suggestion which might be the best choice for the trade-off parameter settings. Only then a careful assessment can be made on how useful the approach is to take the distortion parameters into account during the inversion and how much one relies on a priori information about the distortion parameter. The assessment of the internal rotation of the synthetic data into the local coordinate systems of each site also relies on a properly working inversion algorithm and has to be postponed as well.

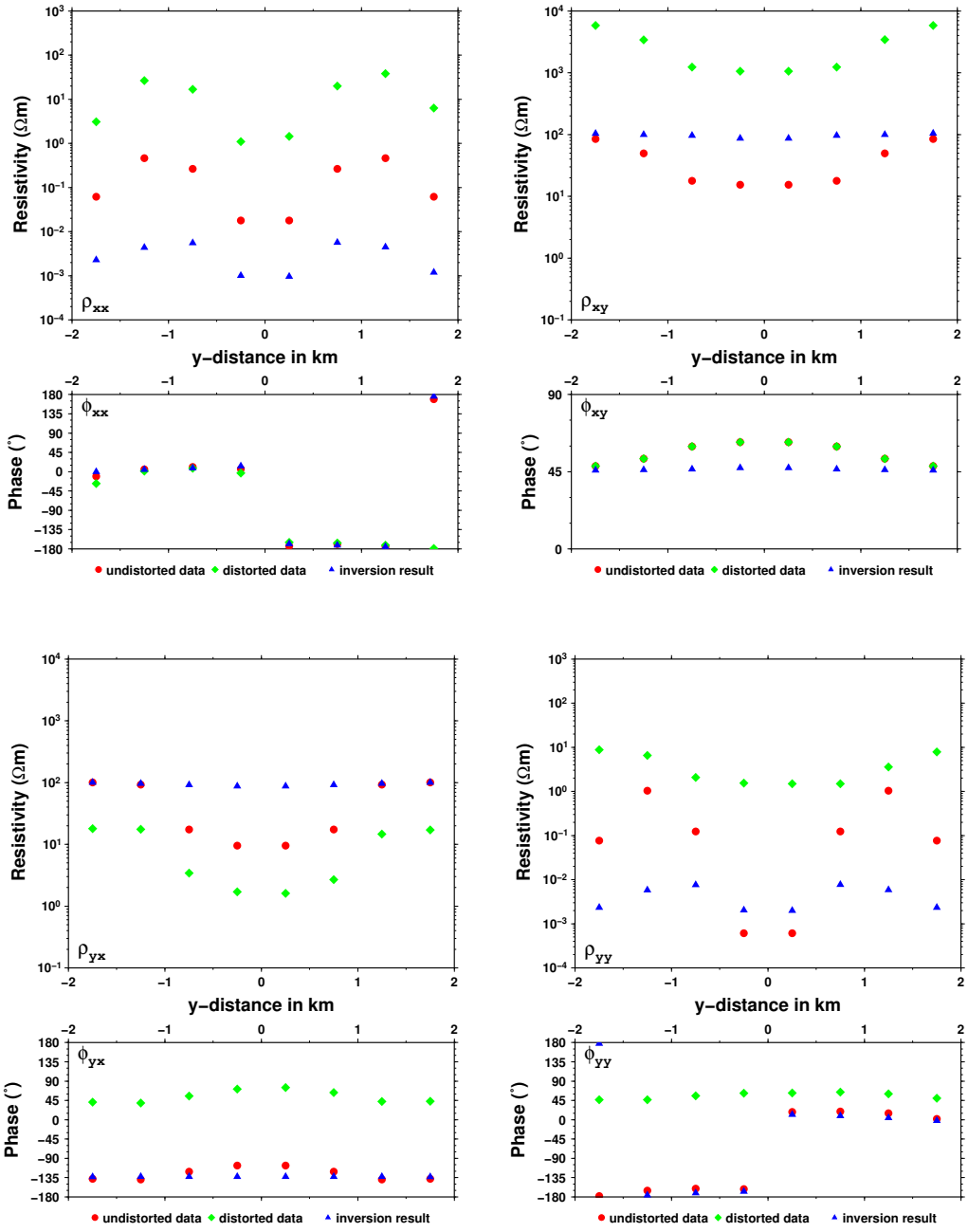

Figure 9.5: Figure showing a comparison of the undistorted (red circles), and distorted (green diamonds) input data with the forward synthetic response from the inversion (blue triangles) obtained after 5 iterations using the brute-force Jacobian approximation. The responses shown are at 0.1 s and along a y-directed profile (x = 250 m, black dashed line in Figure 9.1 (b)).

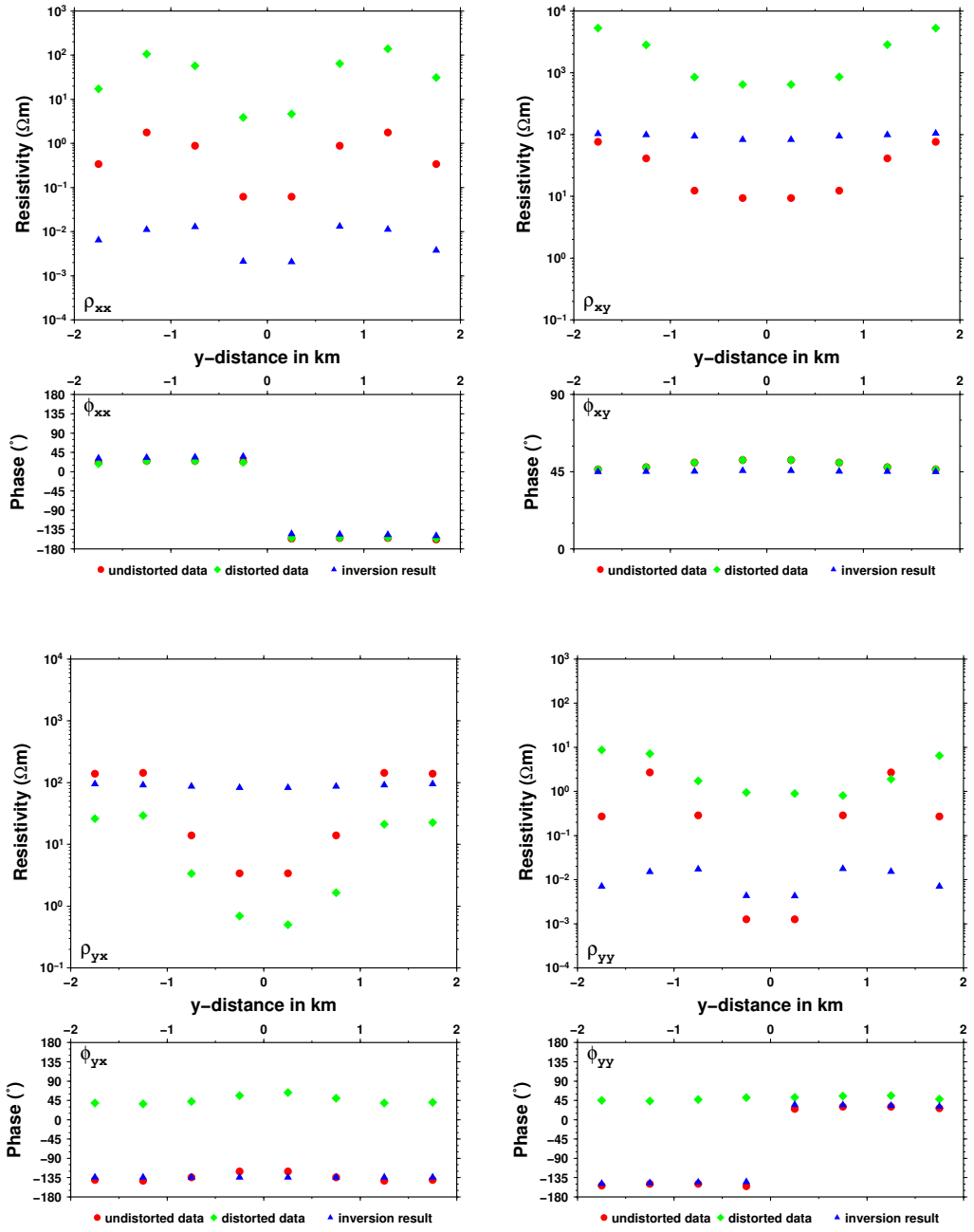

Figure 9.6: Figure showing a comparison of the undistorted (red circles), and distorted (green diamonds) input data with the forward synthetic response from the inversion (blue triangles) obtained after 5 iterations using the brute-force Jacobian approximation. The responses shown are at 1 s and along a y-directed profile (x = 250 m, black dashed line in Figure 9.1 (b)).

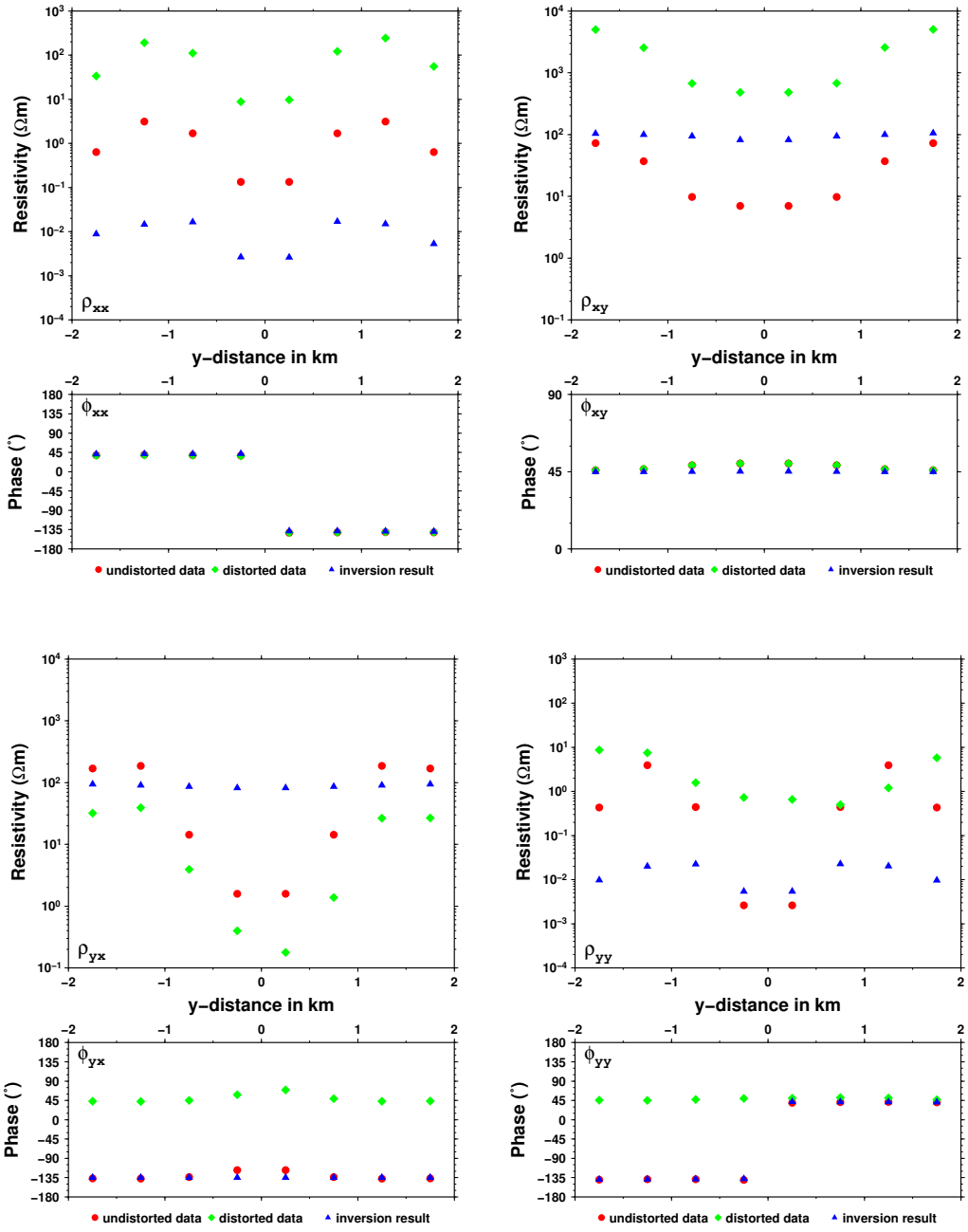

Figure 9.7: Figure showing a comparison of the undistorted (red circles), and distorted (green diamonds) input data with the forward synthetic response from the inversion (blue triangles) obtained after 5 iterations using the brute-force Jacobian approximation. The responses shown are at 10 s and along a y-directed profile (x = 250 m, black dashed line in Figure 9.1 (b)).

Part IV

CONCLUSION, BIBLIOGRAPHY AND APPENDICES

10

CONCLUSIONS AND OUTLOOK

The thesis work presented here consists of two parts, (i) processing, analysis, modelling and interpretation of a MT data set in northeastern Botswana (as part of SAMTEX) and (ii) developing a 3D MT inversion code that deals with electric galvanic distortion. As the topics of these two parts are so different, their summaries, conclusions and discussions of future work and possible improvements are outlined separately.

10.1 MODELLING AND INTERPRETATION OF THE ZIM LINE DATA

10.1.1 *Summary and conclusion*

During the SAMTEX project a broad region in South Africa, Botswana and Namibia has been investigated by deep-probing MT measurements. The area of interest for the thesis work presented here is located in northeastern Botswana and is associate with the geological terranes of the Limpopo Belt, the Zimbabwe Craton, the Magondi Mobile Belt and the Ghanzi-Chobe Belt. Other dominant features in the area are the giant mafic Okavango Dyke Swarm, which has a strong magnetic field signature, and the Makgadikgadi Pans, a huge salt pan complex that is most likely associated with a brine aquifer.

The data set from the ZIM line crossing the terranes mentioned above exhibits strong lateral variation in penetration depth. Neighbouring sites require periods with a difference of up to 3 decades to penetrate to a similar depth. Therefore standard strike analysis using the Groom-Bailey decomposition technique for one frequency, or a frequency range, is not appropriate - instead one depth or depth range is required. Strike analyses based on depth ranges showed that the strike angle varies along the profile and with depth. Data sensing the lithospheric mantle generally prefer a strike angle of 35° E of N, whereas the crustal depths showed two dominant directions - 110° E of N for sites located on top of the Okavango dyke swarm, and therefore consistent with its strike direction, and 55° E of N for all other sites.

Niblett-Bostick resistivity maps showed that the two groups (one close to Francistown and the other close to Maun) of sites located above the Okavango dyke swarm have different resistivities. As the dykes are known independently to be highly resistive, the rather conductive Niblett-Bostick resistivities at Maun were considered to be the anomalous ones. One-dimensional anisotropic forward modelling tests showed that the very conductive near-surface layers mask all possible effects of the dyke swarm and that a 2.6% dilatation of the dykes causes a nearly unrecognisable enhancement of the resistivity. The models also suggest that there is a structure - either anisotropic or fault-like - that is orientated perpendicular to the dyke swarm and extends from about 10 - 15 km depth deep

into the lithospheric mantle (to about 120 km or deeper). Such a depth extent suggests a crustal-mantle coupling and anisotropy due to, e.g., graphite rather than hydrogen diffusion.

Maps of the most conductive direction for crustal and lithospheric depth ranges indicate that the boundary of the Magondi Mobile Belt and the Ghanzi-Chobe Belt is located (about 60 - 80 km) further to the north (roughly at site ZIM128) than previously estimated based on potential field data. Additionally, the southwestern boundary of the Zimbabwe Craton is located further to the west (somewhere close to Gope; near KAL018/019) than the terrane outline from the potential field data suggests.

The crustal 2D inversion (using the appropriate strike direction of 55° E of N) for the northern part of the ZIM line shows an about 600 m thick conductive near-surface layer identified as the brine aquifer associated with the Makgadikgadi Pan Complex. The boundary between the resistive Ghanzi-Chobe Belt to the north and the more heterogeneous Magondi Mobile Belt to the south was found to be dipping northwards. A boundary between the Magondi Belt and the Zimbabwe Craton could not be identified, but two mid- to lower-crustal conductors within the Magondi Belt were found in the area and depth range suggested by de Beer et al. (1975, 1976) and van Zijl and de Beer (1983) (the top of the conductors is at about 20 km depth in the crustal 2D MT inversion model; located beneath ZIM121/ZIM122 and ZIM125). The cause of these conductors remains uncertain, but graphite and/or sulphide are favoured.

The whole ZIM profile was inverted using the lithospheric strike angle of 35° E of N. The crustal structures obtained from the focussed inversion appear unchanged, therefore artefacts resulting from enforcing the lithospheric strike angle on the crustal data are not evident. The Zimbabwe Craton and the Ghanzi-Chobe Belt show a resistive, thick lithospheric mantle. In the case of the Magondi Mobile Belt, the lithospheric mantle is poorly constrained in the 2D inversion model and it is therefore impossible to say with any certainty that a real structure is responsible for the higher conductivities observed there. Resistivity-depth profiles have been extracted from the 2D inversion model and compared with the KIM-NAM resistivity-depth profiles from Muller et al. (2009) and theoretical geotherms. Based on the inflection point (which defines the thermal lithospheric thickness) of the resistivity-depth profile of the Ghanzi-Chobe Belt, its depth to the lithosphere-asthenosphere boundary (LAB) is estimated at 180 ±20 km. The relative difference in thickness between the Ghanzi-Chobe Belt lithospheric mantle and that of the Zimbabwe Craton is about 40 km and therefore the depth to the LAB is estimated to be about 220 ±20 km for the Zimbabwe Craton. Geotherms of 41 mW/m^2 at the Orapa and Letlhakane kimberlite pipes (about 150 - 200 km east of the ZIM line) also suggest a lithospheric thickness of about 220 km at the time of the emplacement of the pipes (at about 93 Ma, Stiefenhofer et al. (1997) and references therein). Geochemical analysis of xenoliths from these pipes (from a maximum depth of 205 km, with no samples available from deeper depth) showed, at 190 km, a sharp increase to 80 - 100% in the abundance of xenoliths showing melt-related metasomatism. Above 190 km, fertile lherzolites and depleted harzburgites, both with some evidence of metasomatism, are the dominant rock types (Griffin et al., 2003). The melt-metasomatised classes all show shearing (Griffin et al., 2003), which is often taken as indicating proximity to the base of the lithosphere. Kennedy et al. (2002) propose that sheared melt-metasomatism is a result of transitory, high-strain-rate deformation in a zone of noncoaxial strain localised at the base of the lithosphere.

The Okavango dyke swarm is a highly resistive crustal structure, and since the average dyke width is about 17 m, the dyke swarm should be treated as anisotropic at the MT scale, rather than as a 2D structure. In the 2D inversion model, a conductor is imaged beneath the dyke swarm at about 60 - 70 km depth, whereas for the other terranes a conductor is apparent in mid- to lower-crustal depths. Tests with synthetic 2D anisotropic data showed that an isotropic 2D inversion of anisotropic data may cause the imaging of a crustal conductor incorrectly at lithospheric mantle depths. Additionally, the tests showed that the dykes may extend throughout most of the crust. Based on 2D modelling of magnetic data, Dailey et al. (2009) find that maximum depths of between 4 - 30 km for the dyke swarm can be accommodated by the magnetic data.

10.1.2 *Future work and possible improvements*

For the crustal study of the northern part of the ZIM line the site spacing of about 20 km is relative sparse and completely undersamples the top 10-20 km of the subsurface. Additional sites would therefore be useful to gain better constraints at the crustal scale. As there are only broadband MT sites on the ZIM line, it would be good to return to the sites above the Magondi Mobile Belt using long period MT systems (preferential during a period of greater sun spot activity) to achieve greater penetration depths, which could answer the question whether the Magondi lithospheric mantle is really more conductive than the lithospheric mantle beneath the Zimbabwe Craton and the Ghanzi-Chobe Belt, or whether there is possibly a connection between the resistive lithospheric mantle of the Zimbabwe Craton and the Ghanzi-Chobe Belt. A re-recording of some sites with the long period MT system would also give additional vertical magnetic field data, which are missing on the ZIM line for logistical reasons. The vertical magnetic field data will help to distinguish between anisotropy and 2D heterogeneity.

To gain a better overall understanding of the geological terranes and their structure it is also important to investigate neighbouring profiles using 2D modelling methods. Unfortunately only profiles to the west of the ZIM line are available (i.e., the KAL, MAK, MOF, SAN and SSO profiles), as everything to the east would be located in Zimbabwe, where, due to political/safety issues, no data were recorded. If the situation improves in Zimbabwe, it might be worthwhile to collect additional data there as well. Finally, a more equal distribution of the MT sites would be preferable in terms of potential 3D modelling and inversion, although that would be logistically very difficult.

Some of the areas with more dense 2D profiles, such as e.g., the area of the southwestern boundary of the Zimbabwe craton using sites of the KAL, MAK, MOF, SSO, SAN and ZIM profiles, could possibly be reduced to a 3D inversion data set. The main problem is the limited number of cells for 3D meshes (due to limited computation time and computer memory), which causes large cell widths to cover an area of several hundreds of kilometres. As only one site per mesh cells is allowed, along profile a number of sites need to be rejected. The resolution of such a large scale mesh is also not suitable to resolve crustal scale structures. The other issue of 3D inversion is the limited number of periods that can be taken into account and the requirement of using the same periods for all sites. An interpolation and/or averaging scheme is required to produce a data set of common periods. Three-dimensional inversion of individual 2D profiles might be a useful approach, as a structure placed beneath the profile using a 2D modelling and inversion approach

might be a 3D structure next to the profile, which a 3D inversion model might be able to reconstruct correctly.

10.2 DEVELOPMENT OF A 3D MT INVERSION CODE

10.2.1 *Summary and conclusion*

The 3D finite-element solver by Colin Farquharson (MUN, St. John's, Newfoundland, Canada) uses edge-element basis functions to calculate the solution for the electric field equation system for the MT case. As the significance of the conductivity term in the electric field equation decreases with decreasing frequencies, the divergence-free current density requirement implicitly diminishes. Therefore a divergence correction, after Smith (1996), is applied. A nodal-element basis function formulation is used to calculate the static potential related to the current density of the approximate electric field. The gradient of the approximated potential is added to the approximated electric field to correct the field. This correction scheme is applied frequently during the iterative solution of the electric field equation system and improves the convergence significantly.

Different tests using various 2D and 3D models and response sets for comparison, showed that the forward algorithm calculates reliable resistivities and therefore can be considered as providing a reasonable and robust basis for the 3D inversion code. Due to the uniform boundaries implemented in the code, there might be difficulties in calculating an accurate response for a model with a layered halfspace background.

The 3D inversion code presented here accommodates electric galvanic distortion parameters during inversion. The distortion parameters can either be treated as constant values (if e.g., a priori information is available) or as inversion parameters (i.e., simultaneous inversion for the resistivity structure and the distortion parameters). Additionally, the code has the option to rotate the noise-free synthetic data into the local measurement coordinate system of each site to avoid the rotation of the noisy observed data prior to modelling, and therefore tries to avoid degradation of the data due to the propagation of noise from one component into the others.

Typically, an objective function within an inversion code contains a measure of the data misfit, a measure of the model complexity and a trade-off parameter to balance these two terms. The 3D inversion code presented here also has a measure of closeness to a reference model and a measure of closeness to reference distortion values. The objective function is essentially a sum-of-squares function, and therefore a Gauss-Newton algorithm can be applied to solve the non-linear least square problem. The Gauss-Newton method approximates the Hessian matrix by the multiplication of the transpose Jacobian matrix and the Jacobian matrix. The approximation results in a linear system of Gauss-Newton equations that is solved using an iterative solver.

A normal inversion for the resistivity structure only requires first derivatives of the data with respect to the cell conductivities, which become the elements of the Jacobian matrix. Inverting for the resistivity structure and the distortion parameters requires a modification of the Jacobian matrix to account additionally for the first derivatives of the data with respect to the distortion parameters. Comparison of the Jacobian matrix with a so-called

brute-force Jacobian matrix computation approach (compute forward response of a model, change one model parameter and calculate the forward response again, then divide the difference of the forward responses by the difference of the model parameter) showed that the derivatives with respect to the distortion parameter are calculated correctly. But the comparison also revealed that there is still an unsolved coding problem in computing the Jacobian matrix elements with respect to the resistivity structure. Therefore the inversion results shown are calculated using the brute-force Jacobian of the starting model to replace the Jacobian with the resistivity structure for all iteration steps (note that normally the Jacobian would be recalculated each iteration using the updated model).

Including the rotation of the synthetic data requires only a simple matrix multiplication of the impedance tensor with a rotation matrix and its transpose. This rotation needs to be applied when the forward responses are calculated but also needs to be taken into account for the calculation of the elements of the Jacobian matrix.

The brute-force Jacobian approximation used suggests that the inversion with respect to the resistivity structure is working correctly (except for the calculation of the Jacobian itself). Unfortunately the resulting inversion models are fuzzy and not close to the true structure, which reveals the disadvantage of using the applied Jacobian approximation. Using undistorted compared to distorted data, the inversion results using the brute-force Jacobian approximation show indistinguishable inversion models. Testing of the distortion aspects of the code is therefore not possible at the current stage and has to be postponed until the coding problem for the calculation of the Jacobian with respect to the resistivity structure is identified and corrected.

10.2.2 *Future work and possible improvements*

Further testing is required to correct the coding problem for the calculation of the derivatives of the data with respect to the conductivity structure to avoid the current work-around using the brute-force Jacobian. A more thorough testing of the various parameter settings is also necessary, as well as test runs using synthetic data from different models, including the examination of the use of resistivity and phase data and tipper data. Once the inversion with respect to the resistivity structure is working reliably, a thorough investigation and testing of the distortion aspects of the code and the internal rotation into the local measurement coordinate systems must follow.

In general, there is the potential for further improvement and advancement in the inversion code. Applying a parallel programming protocol, such as, for example, MPI, the code could be used on clusters to save computational time and therefore it would become more feasible for application to real data sets or larger synthetic models.

In terms of distorted data, it would be interesting to extend the code to be able to invert for the phase tensor values instead of for impedance or resistivity and phase, as the phase tensor is distortion-free. Replacing the homogeneous halfspace boundary conditions by 1D, or possibly 2D, boundary conditions in the forward solver would make the code more suitable for synthetic models and real geology that require a layered background model (as seen for the COMMEMI 3D-2A model in Chapter 7).

The code, in its current form, uses a rectilinear discretised mesh and therefore does not take full advantage of the finite-element approach, where unstructured grids allow for a fine meshing where needed, and a reduced resolution, where not needed. Such a change would require the adoption of a good mesh generator and the adjustment of all basis functions and related operations executed in the code. In the case of using unstructured grids, it might be more beneficial to write a new code from scratch, that is designed from the beginning on for the use of these grids.

BIBLIOGRAPHY

Aldiss, D. T.(1991). *The Motloutse Complex and the Zimbabwe Craton/Limpopo Belt transition in Botswana*. Precambrian Research, 50, pages 89 – 109. (Cited on page 61.)

Aldiss, D. T. and Carney, J. N.(1992). *The geology and regional correlation of the Okwa Valley Inlier, western Botswana*. Precambrian Research, 56, pages 255 – 274. (Cited on page 62.)

Aubourg, C., Tshoso, G., le Gall, B., Bertrand, H., Tiercelin, J.-J., Kampunzu, A. B., Dyment, J. and Modisi, M.(2008). *Magma flow revealed by magnetic fabric in the Okavango giant dyke swarm, Karoo igneous province, northern Botswana*. Journal of Volcanology and Geothermal Research, 170, pages 247 – 261. (Cited on pages 64, 65, and 107.)

Avdeev, D. B.(2005). *Three-dimensional electromagnetic modelling and inversion from theory to application*. Surveys in Geophysics, 26, pages 767 – 799. (Cited on pages 143 and 155.)

Avdeev, D. B. and Avdeeva, A.(2009). *3D magnetotelluric inversion using a limited-memory quasi-Newton optimization*. Geophysics, 74(3), pages F45 – F57. doi:10.1190/1.3114023. (Cited on pages 179 and 182.)

Avdeev, D. B., Kuvshinov, A. V. and Pankratov, O. V.(2002). *Three-dimensional induction logging problems, Part I: An integral equation and model comparisons*. Geophysics, 67(2), pages 413 – 426. (Cited on page 143.)

Avdeeva, A.(2008). *Three-dimensional Magnetotelluric Inversion*. Dissertation, Department of Earth and Ocean Sciences, Faculty of Science, National University of Ireland, Galway, Ireland. (Cited on pages 179 and 201.)

Badea, E. A., Everett, M. E., Newman, G. A. and Biro, O.(2001). *Finite-element analysis of controlled-source electromagnetic induction using Coulomb-gauged potentials*. Geophysics, 66(3), pages 786 – 799. (Cited on page 144.)

Bahr, K.(1988). *Interpretation of the magnetotelluric impedance tensor: regional induction and local telluric distortion*. Journal of Geophysics, 62, pages 119–127. (Cited on page 43.)

Bailey, R. C.(1970). *Inversion of the geomagnetic induction problem*. Proceedings of the Royal Society of London, 315, pages 185 – 194. (Cited on page 22.)

Bailey, R. C. and Groom, R. W.(1987). *Decomposition of the magnetotelluric impedance tensor which is useful in the presence of channeling*. In: Expanded abstracts of the 57th annual international Society of Exploration Geophysicists meeting and exposition, volume 57, pages 154 – 156, Tulsa, OK. (Cited on pages 43 and 93.)

Baillieul, T. A.(1979). *Makgadikgadi Pans Complex of central Botswana: Summary*. Geological Society of America Bulletin, 90, pages 133 – 136. (Cited on pages 66 and 67.)

Baragar, W. R. A., Ernst, R. E., Hubert, L. and Peterson, T.(1996). *Longitudinal petrochemical variation in the Mackenzie Dyke Swarm, Northwestern Canadian Shield*. Journal of Petrology, 37(2), pages 317 – 359. (Cited on page 66.)

Barton, Jr., J. M. and van Reenen, D. D.(1992). *When was the Limpopo Orogeny?* Precambrian Research, 55, pages 7 – 16. (Cited on page 57.)

Becken, M., Ritter, O. and Burkhardt, H.(2008). *Mode separation of magnetotelluric responses in three-dimensional environments*. Geophysical Journal International, 172, pages 67 – 86. doi: 10.1111/j.1365-24X.2007.03612.x. (Cited on pages 30 and 43.)

Begg, G. C., Griffin, W. L., Natapov, L. M., O'Reilly, S. Y., Grand, S. P., O'Neill, C. J., Hronsky, J. M. A., Djomani, Y. P., Swain, C. J., Deen, T. and Bowden, P.(2009). *The lithospheric architecture of Africa: Seismic tomography, mantle petrology, and tectonic evolution*. Geosphere, 5(1), pages 23 – 50. doi: 10.1130/GES00179.1. (Cited on pages 75 and 78.)

Berdichevsky, M. N.(1960). *Principles of magnetotelluric profiling theory*. Applied Geophysics, (Prikl. Geofiz.), 28. (Cited on page 7.)

Berdichevsky, M. N. and Dmitriev, V. I.(1976a). *Basic principles of interpreation of magnetotelluric sounding curves*. In: A. Adam (ed), *Geoelectric and Geothermal Studies*, pages 165 – 221. KAPG Geophysical Monograph, Akadémiai Kiadó, Budapest. (Cited on page 36.)

Berdichevsky, M. N. and Dmitriev, V. I.(1976b). *Distortion of magnetic and electrical fields by near-surface lateral inhomogeneities*. Acta Geodaetica, Geophysica et Montanistica, Academy Sciences Hungary, 11, pages 447 – 483. (Cited on page 37.)

Berdichevsky, M. N., Bezruk, I. A. and Chinavera, O. M.(1973). *Magnetotelluric sounding with the use of mathematical filters*. Izv. Akad. Nauk. SSSR Fiz. Zeml., 3, pages 72 – 92. (in Russian). (Cited on page 35.)

Berdichevsky, M. N., Dmitriev, V. I. and Pozdnjakova, E. E.(1998). *On two-dimensional interpretation of magnetotelluric soundings*. Geophysical Journal International, 133(3), pages 585–606. (Cited on page 119.)

Bickle, M. J. and Nisbet, E. G.(1993). *The geology of the Belingwe greenstone belt*. Geological Society of Zimbabwe Special Publication, 2. (Cited on page 60.)

Bleeker, W.(2003). *The late Archean record: a puzzle in ca. 35 pieces*. Lithos, 71, pages 99 – 134. (Cited on pages 55 and 67.)

Bohannon, J.(2004). *Earth sciences seek niche apart from mining industry*. Science, 304, pages 380 – 381. (Cited on page 73.)

Börner, R.-U., Ernst, O. G. and Spitzer, K.(2008). *Fast 3-d simulation of transient electromagnetic fields by model reduction in the frequencey domain using Krylov subspace projection*. Geophysical Journal International, 173, pages 766 – 780. (Cited on page 144.)

Bostick, F. X.(1977). *A simple almost exact method of MT analysis*. Workshop on Electrical Methods in Geothermal Exploration, US. Geol. Surv. Contract No. 14080001-8-359. (Cited on page 24.)

Bostick, F. X. and Smith, H. W.(1962). *Investigation of large scale inhomogeneities in the Earth by the magnetotelluric method*. Proc. Inst. Radio Engineers, 50, pages 2339 – 2346. (Cited on page 7.)

Branch, T., Ritter, O., Weckmann, U., Sachsenhofer, R. F. and Schilling, F.(2007). *The Whitehill Formation - a high conductive marker horizon in the Karoo Basin*. South African Journal of Geology, 110, pages 465 – 476. doi:10.2113/gssajg.110.2-3.465. (Cited on page 73.)

Cagniard, L.(1953). *Basic theory of the magneto-telluric method of geophysical prospecting*. Geophysics, 18, pages 605 – 635. (Cited on pages 7, 8, and 13.)

Caldwell, T. G., Bibby, H. M. and Brown, C.(2004). *The magnetotelluric phase tensor*. Geophysical Journal International, 158, pages 457–469. (Cited on pages 43, 46, 47, 48, 49, and 50.)

Carmichael, R. S.(1989). *The magnetic properties of minerals and rocks*. In: R. S. Carmichael (ed), *C.R.C. Practical Handbook of Physical Properties of Rocks and Minerals*. C.R.C. Press Inc., Boca Raton, FL. (Cited on page 13.)

Carney, J. N., Aldiss, D. T. and Lock, N. P.(1994). *The geology of Botswana*. Bostwana J. Earth Sci., 1, pages 1 – 13. (Cited on pages 57 and 62.)

Chave, A. D. and Jones, A. G.(1997). *Electric and magnetic field galvanic distortion decomposition of BC87 data*. J. Geomag. Geoelectr., 49, pages 767 – 789. (Cited on pages 35 and 93.)

Chave, A. D. and Smith, J. T.(1994). *On electric and magnetic galvanic distortion tensor decompositions*. Journal of Geophysical Research (Solid Earth), 99(B3), pages 4669 – 4682. (Cited on pages 35, 36, and 37.)

Chave, A. D. and Thomson, D. J.(2004). *Bounded influence magnetotelluric response function estimation*. Geophysical Journal International, 157, pages 988–1006. (Cited on page 42.)

Chetty, D. and Frimmel, H. E.(2000). *The role of evaporites in the genesis of base metal sulphide mineralisation in the Northern Platform of the Pan-African Damara Belt, Namibia: geochemical and fluid inclusion evidence from carbonate wall rock alteration*. Mineralium Deposita, 35(4), pages 364 – 376. doi: 10.1007/s001260050247. (Cited on page 124.)

Clifford, T. N.(1966). *Tectono-metallogenic units and metallogenic provinces of Africa*. Earth and Planetary Science Letters, 1, pages 421 – 434. (Cited on page 75.)

Constable, S. C., Parker, R. L. and Constable, C. G.(1987). *Occam's inversion: A practical algorithm for generating smooth models from electromagnetic sounding data*. Geophysics, 52(3), pages 289 – 300. (Cited on page 51.)

Constable, S. C., Shankland, T. J. and Duba, A. G.(1992). *The electrical conductivity of an isotropic olivine mantle*. Journal of Geophysical Research, 97, pages 3397 – 3404. (Cited on pages 133 and 134.)

Dailey, M. K. M., Mortimer, D. J. and Atekwana, E. A.(2009). *Using 2d and 3d modelling to infer the depth of the Okavango Dyke Swarm*. AGU fall meeting, San Francisco, USA. (Cited on pages 140 and 211.)

Davis, W. J., Jones, A. G., Bleeker, W. and Grütter, H.(2003). *Lithospheric development in the Slave craton: a linked crustal and mantle perspective*. Lithos, 71, pages 575 – 589. (Cited on page 67.)

Dawson, T. W., Weaver, J. T. and Raval, U.(1982). *B-polarization induction in two generalised thin sheets at the surface of a conducting half-space*. Geophys. J. R. Astr. Soc., 69, pages 209 – 234. (Cited on page 25.)

de Beer, J. H. and Gough, D. I.(1980). *Conductive structures in southernmost Africa: a magnetometer array study*. Geophys. J. R. astr. Soc., 63, pages 479 – 495. (Cited on page 70.)

de Beer, J. H., Gough, D. I. and van Zijl, J. S. V.(1975). *An electrical conductivity anomaly and rifting in southern Africa*. Nature, 255, pages 678 – 680. (Cited on pages 2, 70, 72, 73, 123, 124, and 210.)

de Beer, J. H., van Zijl, J. S. V., Huyssen, R. M. J., Hugo, P. L. V., Joubert, S. J. and Meyer, R.(1976). *A magnetometer array study in South-West Africa, Botswana and Rhodesia*. Geophysical Journal Royal astr. Soc., 45, pages 1 – 17. (Cited on pages 2, 70, 72, 73, 123, 124, and 210.)

de Beer, J. H., Huyssen, R. M. J., Joubert, S. J. and van Zijl, J. S. V.(1982). *Magnetometer array studies and deep Schlumberger soundings in the Damara orogenic belt, South West Africa*. Geophys. J. R. astr. Soc., 70(1), pages 11 – 29. (Cited on pages 123 and 124.)

de Groot-Hedlin, C.(1991). *Short Note: Removal of static shift in two dimensions by regularized inversion*. Geophysics, 56(12), pages 2102 – 2106. (Cited on pages 43 and 180.)

de Groot-Hedlin, C.(1995). *Inversion for regional 2-D resistivity structure in the presence of galvanic scatterers*. Geophysical Journal International, 122, pages 877 – 888. (Cited on pages 43 and 180.)

de Lugão, P. P. and Kriegshäuser, B.(1997). *2-D inversion of magnetotelluric data over 3-D structures*. 67th Ann. Internat. Mtg. Soc. of Expl. Geophys. (Cited on pages 51 and 52.)

de Wit, M. and Horsfield, B.(2006). *Inkaba yeAfrica project surveys sector of Earth from core to space*. EOS, 87(11). (Cited on page 73.)

de Wit, M. and Tinker, J.(2001). *Crustal structures across the central Kaapvaal craton from deep-seismic reflection data*. South African Journal of Geology, 107, pages 185 – 206. (Cited on page 74.)

de Wit, M. J., Roering, C., Hart, R. J., Armstrong, R. A., Peberdy, E. and Hart, R. A.(1992). *Formation of an Archaean continent*. Nature, 357, pages 553 – 562. (Cited on pages 53, 55, 56, 57, 58, 67, and 78.)

Dirks, P. H. G. M. and Jelsma, H. A.(1998). *Horizontal accrection and stabilization of the Archean Zimbabwe Craton*. Geology, 26(1), pages 11 – 14. (Cited on page 61.)

Duba, A. G. and Shankland, T. J.(1982). *Free Carbon & electrical conductivity in the earth's mantle*. Geophysical Research Letters, 9(11), pages 1271–1274. (Cited on page 138.)

Egbert, G. D.(1997). *Robust multiple-station magnetotelluric data processing*. Geophysical Journal International, 130, pages 475–496. (Cited on page 42.)

Egbert, G. D. and Booker, J. R.(1986). *Robust estimation of geomagnetic transfer functions*. Geophys. J. R. Astro. Soc., 87, pages 173–194. (Cited on page 42.)

Ekblom, H.(1973). *Calculation of linear best* L_p*-approximations*. BIT Numerical Mathematics, 13(3), pages 292 – 300. (Cited on pages 181 and 182.)

Ekblom, H.(1987). *The* L_1*-estimate as limiting case of an* L_p*- or Huber-estimate*. In: Y. Dodge (ed), *Statistical Data Analysis Based on the* L_1*-Norm and Related Methods*, pages 109 – 116. Elsevier, Amsterdam. (Cited on pages 181 and 182.)

Elburg, M. and Goldberg, A.(2000). *Age and geochemistry of Karoo dolerite dykes from northeast Botswana*. Journal of African Earth Sciences, 31, pages 539 – 554. (Cited on pages 64 and 107.)

Ernst, R. E. and Baragar, W. R. A.(1992). *Evidence from magnetic fabric for the flow pattern of magma in the Mackenzie giant radiating dyke swarm*. Nature, 356, pages 511 – 513. doi:10.1038/356511a0. (Cited on page 66.)

Everett, M. E.(2005). *What do electromagnetic induction responses measure?* The Leading Edge, pages 154 – 157. (Cited on page 30.)

Everett, M. E. and Schultz, A.(1996). *Geomagnetic induction in a heterogeneous sphere: Azimuthally symmetric test computations and the response of an undulating 660-km discontinuity*. Journal of Geophysical Research, 101, pages 2765 – 2783. (Cited on page 144.)

Farquharson, C. G.(2008). *Constructing piecewise-constant models in multidimensional minimum-structure inversions*. Geophysics, 73(1). (Cited on pages 181 and 182.)

Farquharson, C. G. and Miensopust, M. P.(subm.). *Three-dimensional finite-element modelling of magnetotelluric data with a divergence correction*. Geophysical Journal International. (Cited on pages 144, 145, 146, and 150.)

Farquharson, C. G. and Oldenburg, D. W.(1998). *Non-linear inversion using general measures of data misfit and model structure*. Geophysical Journal International, 134, pages 213 – 227. (Cited on pages 181, 182, 185, 186, 187, and 339.)

Farquharson, C. G. and Oldenburg, D. W.(1999). *Approximate sensitivities for multidimensional electromagnetic inversion*. In: M. Oristaglio and B. Spies (ed), *Three-dimensional Electromagnetics*, number 7 in Geophysical Developments, pages 256 – 264. Soc. Expl. Geophys. (Cited on pages 179 and 191.)

Farquharson, C. G. and Oldenburg, D. W.(2004). *A comparison of automatic techniques for estimating the regularization parameter in non-linear inverse problems*. Geophysical Journal International, 156, pages 411 – 425. (Cited on page 182.)

Farquharson, C. G., Oldenburg, D. W., Haber, E. and Shekhtman, R.(2002). *An algorithm for the three-dimensional inversion of magnetotelluric data*. SEG Int'l Exposition and 72nd Annual Meeting, Salt Lake City, Utah. (Cited on pages 179 and 182.)

Faure, S.(2006). *World Kimberlites and Lamproites CONSOREM Database (version 2006 -1)*. Consortium de Recherche en Exploration Minérale, Université du Québec à Montréal. www.consorem.ca. (Cited on page 77.)

Fedo, C. M. and Eriksson, K. A.(1996). *Stratigraphic framework of the ~3.0 Ga Buhwa greenstone belt: A unique stable shelf succession in the Zimbabwe Archaean craton*. Precambrian Research, 77, pages 161 – 178. (Cited on page 61.)

Fouch, M. J., Silver, P. G., Bell, D. R. and Lee, J. N.(2004). *Small-scale variations in seismic anisotropy near Kimberley, South Africa*. Geophysical Journal International, 157, pages 764 – 774. (Cited on page 74.)

Gamble, T. D., Goubau, W. M. and Clarke, J.(1979). *Magnetotellurics with a remote magnetic reference*. Geophyiscs, 44(1), pages 53 – 68. (Cited on page 41.)

Garcia, X. and Jones, A. G.(2002a). *Atmospheric sources for audio-magnetotelluric (AMT) sounding*. Geophysics, 67(2), pages 448 – 458. (Cited on page 8.)

Garcia, X. and Jones, A. G.(2002b). *Decomposition of three-dimensional magnetotelluric data*. In: M. S. Zhdanov and P. E. Wannamaker (ed), *Three-Dimensional Electromagnetics*, volume 35 of Methods in Geochemistry and Geophysics, chapter 13, pages 235 – 250. Elsevier. ISBN 0-444-50429-X. (Cited on pages 35, 37, and 43.)

Garcia, X., Chave, A. D. and Jones, A. G.(1997). *Robust processing of magnetotelluric data from the auroral zone*. Journal of Geomagnetism and Geoelectricity, 49, pages 1451 – 1468. (Cited on page 9.)

Garcia, X., Ledo, J. and Queralt, P.(1999). *2D inversion of 3D magnetotelluric data: The Kayabe dataset*. Earth Planets Space, 51, pages 1135 – 1143. (Cited on page 52.)

Goubau, W. M., Gamble, T. D. and Clarke, J.(1978). *Magnetotelluric data analysis: removal of bias*. Geophysics, 43, pages 1157 – 1169. (Cited on page 41.)

Gough, D. I.(1973). *The geophysical significance of geomagnetic variation anomalies*. Physics of the Earth and Planetary Interiors, 7, pages 379 – 388. (Cited on page 70.)

Griffin, W. L., O'Reilly, S. Y., Natapov, L. M. and Ryan, C. G.(2003). *The evolution of lithospheric mantle beneath the Kalahari Craton and its margins*. Lithos, 71, pages 215 – 241. (Cited on pages 139, 140, and 210.)

Griffin, W. L., O'Reilly, S. Y., Doyle, B. J., Pearson, N. J., Coopersmith, H., Kivi, K., Malkovets, V. and Pokhilenko, N.(2004). *Lithosphere mapping beneath the North American plate*. Lithos, 77, pages 873 – 922. (Cited on pages 75 and 78.)

Groom, R. W.(1988). *The effects of inhomogeneities on magnetotellurics*. Dissertation, University Toronto, Canada. (Cited on pages 43, 44, and 93.)

Groom, R. W. and Bahr, K.(1992). *Corrections for near surface effects: Decomposition of the magnetotelluric impedance tensor and scaling corrections for regional resistivities: A tutorial*. Surveys in Geophysics, 13(4-5), pages 341–379. (Cited on page 37.)

Groom, R. W. and Bailey, R. C.(1989). *Decomposition of Magnetotelluric Impedance Tensors in the Presence of Local Three-Dimensional Galvanic Distortion*. Journal of Geophysical Research (Solid Earth), 94(B2), pages 1913–1925. (Cited on pages 43, 44, 45, and 93.)

Groom, R. W. and Bailey, R. C.(1991). *Analytic investigations of the effects of near-surface three-dimensional glavanic scatterers on MT tensor decompositions*. Geophysics, 56(4), pages 496 – 518. (Cited on page 155.)

Grove, A. T.(1969). *Landforms and climatic change in the Kalahari and Ngamiland*. Geographical Journal, 135, pages 191 – 212. (Cited on page 66.)

Hamilton, M. P.(2008). *Electrical and seismic anisotropy of the lithosphere with the focus on central southern Africa*. Dissertation, Faculty of Science, School of Geosciences, University of Witwatersrand, Johannesburg, South Africa. (Cited on page 68.)

Hamilton, M. P., Jones, A. G., Evans, R. L., Evans, S., Fourie, C. J. S., Garcia, X., Mountford, A., Spratt, J. E. and the SAMTEX Team(2006). *Electrical anisotropy of South African lithosphere compared with seismic anisotropy from shear-wave splitting analysis*. Physics of the Earth and Planetary Interiors, 158, pages 226 – 239. (Cited on page 68.)

Hamilton, W. B.(1998). *Archean magmatism and deformation were not products of plate tectonics*. Precambrian Research, 91, pages 143 – 179. (Cited on pages 55 and 67.)

Han, N., Nam, M. J., Kim, H. J., Lee, T. J., Song, Y. and Suh, J. H.(2008). *Efficient three-dimensional inversion of magnetotelluric data using approximate sensitivities*. Geophysical Journal International, 175, pages 477 – 485. doi: 10.1111/j.1365-246X.2008.03894.x. (Cited on pages 179, 180, and 182.)

Han, N., Nam, M. J., Kim, H. J., Song, Y. and Suh, J. H.(2009). *A comparison of accuracy and computation time of three-dimensional magnetotelluric modelling algorithms*. Journal of Geophysics and Engineering, 6, pages 136 – 145. doi: 10.1088/1742-2132/6/2/005. (Cited on page 155.)

Hano, M.(1991). *Finite element analysis of three-dimensional linear electromagnetic fields over the whole frequency range. Part I. Theory*. Electrical Engineering in Japan, 111, pages 570 – 576. (Cited on page 144.)

Hanson, R. E., Bruecker, H. K., Onstott, T. C., Wardlaw, M. S., Johns, C. C. and Hardcastle, K. C.(1988). *Reconnaissance geochronology, tectonothermal evolution, and regional significance of the Middle Proterozoic Choma-Kalomo block, southern Zambia*. Precambrian Research, 42, pages 39 – 61. (Cited on page 62.)

Heise, W., Caldwell, T. G., Bibby, H. M. and Brown, C.(2006). *Anisotropy and phase splits in magnetotellurics*. Physics of the Earth and Planetary Interiors, 158, pages 107–121. (Cited on pages 31, 32, 48, and 50.)

Hirth, G.(2006). *Protons lead the charge*. Nature, 443, pages 927–928. (Cited on page 30.)

Hirth, G., Evans, R. L. and Chave, A. D.(2000). *Comparison of continental and oceanic mantle electrical conductivity: Is the Archean lithosphere dry?* Geochemistry, Geophysics, Geosystems, 1. (Cited on page 30.)

Hohmann, G. W.(1975). *Three-dimensional induced polarisation and electromagnetic modeling*. Geophysics, 40, pages 309 – 324. (Cited on page 143.)

Horstwood, M. S. A., Nesbitt, R. W., Noble, S. R. and Wilson, J. F.(1999). *U-Pb zircon evidence for an extensive early Archean craton in Zimbabwe: A reassessment of the timing of craton formation, stabilization, and growth*. Geology, 27(8), pages 707 – 710. (Cited on pages 53 and 60.)

Huber, P. J.(1964). *Robust estimation of a location parameter*. Annals of Mathematical Statistics, 35, pages 73 – 101. (Cited on pages 181 and 182.)

Hutchins, D. G. and Reeves, C. V.(1980). *Review: Regional geophysical exploration of the Kalahari in Botswana*. Tectonophysics, 69, pages 201 – 220. (Cited on pages 74 and 75.)

Jacobs, J., Pisarevsky, S., Thomas, R. J. and Becker, T.(2008). *The Kalahari Craton during the assembly and dispersal of Rodinia*. Precambrian Research, 160, pages 142 – 158. (Cited on page 56.)

James, D. E., Fouch, M. J., VanDecar, J. C., van der Lee, S. and Kaapvaal Seismic Group(2001). *Tectospheric structure beneath southern Africa*. Geophysical Research Letters, 28(13), pages 2485 – 2488. (Cited on page 74.)

James, D. E., Niu, F. and Rokosky, J.(2003). *Crustal structure of the Kaapvaal craton and its significance for early crustal evolution*. LIthos, 71, pages 413 – 429. (Cited on page 73.)

Jelsma, H. A., de Wit, M. J., Thiart, C., Dirks, P. H., Viola, G., Basson, I. J. and Anckar, E.(2004). *Preferential distribution along transcontinental corridors of kimberlites and related rocks of Southern Africa*. South African Journal of Geology, 107, pages 301 – 324. (Cited on page 77.)

Ji, S., Rondenay, S., Mareschal, M. and Senechal, G.(1996). *Obliquity between seismic and electrical anisotropies as a potential indicator of movement sense for ductile shear zones in the upper Mantle*. Geology, 24(11), pages 1033–1036. (Cited on page 30.)

Jin, J.(2002). *The Finite Element Method in Electromagnetics*. Wiley-Interscience, John Wiley and Sons, Inc., second edition. ISBN 0-471-43818-9. (Cited on pages 144, 148, 281, and 285.)

Jiracek, G. R.(1990). *Near-surface and topographic distortions in electromagnetic induction*. Surveys in Geophysics, 11, pages 163–203. (Cited on pages 35, 36, and 37.)

Jones, A. G.(1977). *Geomagnetic induction studies in southern Scotland*. Dissertation, Faculty of Science, Universit of Edinburgh. (Cited on page 40.)

Jones, A. G.(1983a). *On the Equivalence of the "Niblett" and "Bostick" Transformations in the Magnetotelluric Method*. Journal of Geophysics, 53, pages 72 – 73. (Cited on page 24.)

Jones, A. G.(1983b). *The problem of current channelling: a critical review*. Geophysical Surveys, 6, pages 79 – 122. (Cited on pages 25, 26, 35, 52, 119, and 156.)

Jones, A. G.(1986). *Parkinson's pointers' potential perfidy!* Geophysical Journal of the Royal Astronomical Society, 87, pages 1215 – 1224. (Cited on page 20.)

Jones, A. G.(1987). *MT and Reflection: An Essential Combination*. Geophys. J. R. Astr. Soc., 89, pages 7 – 18. (Cited on page 138.)

Jones, A. G.(1992). *Electrical conductivity of the continental lower crust*. In: D. M. Fountain, R. J. Arculus, and R. W. Kay (ed), *Continental Lower Crust*, pages 81 – 143. Elsevier. (Cited on page 30.)

Jones, A. G.(1999). *Imaging the continental upper mantle using electromagnetic methods*. Lithos, 48, pages 57 – 80. (Cited on pages 88, 132, and 134.)

Jones, A. G.(2006). *Electromagnetic interrogation of the anisotropic Earth: Looking into the Earth with polarized spectacles*. Physics of the Earth and Planetary Interiors, 158, pages 281 – 291. (Cited on page 40.)

Jones, A. G. and Ferguson, I. J.(2001). *The electric Moho*. Nature, 409, pages 331 – 333. (Cited on page 67.)

Jones, A. G. and Groom, R. W.(1993). *Strike angle determination from the magnetotelluric tensor in the presence of noise and local distortion: rotate at your peril!* Geophysical Journal International, 113, pages 524 – 534. (Cited on page 45.)

Jones, A. G. and Jödicke, H.(1984). *Magnetotelluric transfer function estimation improvement by a coherence-based rejection technique*. 54th Ann. Mtg. Soc. of Expl. Geophys., Atlanta, Georgia. (Cited on page 42.)

Jones, A. G. and Spratt, J.(2002). *A simple method for deriving the uniform field MT responses in auroral zones*. Earth Planets Space, 54, pages 443 – 450. (Cited on pages 9 and 20.)

Jones, A. G., Chave, A. D., Egbert, G., Auld, D. and Bahr, K.(1989). *A Comparison of techniques for magnetotelluric response function estimation*. Journal of Geophysical Research (Solid Earth), 94(10), pages 14201 – 14213. (Cited on pages 40, 41, and 42.)

Jones, A. G., Ferguson, I. J., Chave, A. D., Evans, R. L. and McNeice, G. W.(2001). *Electric lithosphere of the Slave craton*. Geology, 29(5), pages 423 – 426. (Cited on page 67.)

Jones, A. G., Lezaeta, P., Ferguson, I. j., Chave, A. D., Evans, R. L., Garcia, X. and Spratt, J.(2003). *The electrical structure of the Slave craton*. Lithos, 71, pages 505 – 527. (Cited on pages 1 and 67.)

Jones, A. G., Evans, R. L., Muller, M. R., Hamilton, M. P., Miensopust, M. P., Garcia, X., Cole, P., Ngwisanyi, T., Hutchins, D., Fourie, C. J., Jelsma, H. A., Evans, S. F., Aravanis, T., Pettit, W., Webb, S. J., Wasborg, J. and The SAMTEX Team(2009). *Area selection for diamonds using magnetotellurics: Examples from southern Africa*. Lithos, 112S, pages 83 – 92. doi: 10.1016/j.lithos.2009.06.011. (Cited on pages 68, 99, and 134.)

Jones, F. W. and Pascoe, L. J.(1972). *The perturbation of alternating geomagnetic fields by three-dimensional conductivity inhomogeneities*. Geophys. J. R. astr. Soc., 27, pages 479 – 485. (Cited on page 143.)

Jones, F. W. and Price, A. T.(1970). *The perturbations of alternating geomagnetic fields by conductivity anomalies*. Geophys. J. R. astr. Soc., 20, pages 317 – 334. (Cited on pages 20 and 25.)

Jones, M. Q. W.(1998). *A Review of Heat Flow in Southern Africa and Thermal Structure of the Lithosphere*. In: South African Geophysical Review, volume 2, pages 115 – 122. South African Geophysical Association. (Cited on page 78.)

Jourdan, F., Féraud, G., Bertrand, H., Kampunzu, A. B., Tshoso, G., Le Gall, B., Tiercelin, J. J. and Capiez, P.(2004). *The Karoo triple junction questioned: evidence from Jurassic and Proterozoic* $^{40}Ar/^{39}Ar$ *ages and geochemistry of the giant Okavango dyke swarm (Botswana)*. Earth and Planetary Science Letters, 222, pages 989 – 1006. (Cited on pages 56, 64, and 65.)

Jourdan, F., Féraud, G., Bertrand, H., Watkeys, M. K., Kampunzu, A. B. and LeGall, B.(2006). *Basement control on dyke distribution in Large Igneous Provinces: Case study of the Karoo triple junction*. Earth and Planetary Science Letters, 241, pages 307 – 322. (Cited on page 64.)

Kalscheuer, T., Pedersen, L. B. and Siripunvaraporn, W.(2008). *Radiomagnetotelluric two-dimensional forward and inverse modelling accounting for displacement currents*. Geophysical Journal International, 175, pages 486 – 514. (Cited on page 12.)

Kamona, A. F., Lévêque, J., Friedrich, G. and Haack, U.(1999). *Lead isotopes of the carbonate-hosted Kabwe, Tsumeb, and Kipushi Pb-Zn-Cu sulphide deposits in relation to Pan African orogenesis in the Damaran-Lufilian Fold Belt of Central Africa*. Mineralium Deposita, 34(3), pages 273 – 283. doi: 10.1007/s001260050203. (Cited on page 124.)

Kampunzu, A. B., Armstrong, R. A., Modisi, M. P. and Mapeo, R. B. M.(2000). *Ion microprobe U-Pb ages on detrital zircon grains from the Ghanzi Group: implications for the identification of the Kibarab-age crust in northwest Botswana*. Journal of African Earth Sciences, 30, pages 579 – 587. (Cited on page 63.)

Kao, D. and Orr, D.(1982). *Magnetotelluric response of a uniformly stratified earth containing a magnetized layer*. Geophys. J. R. astr. Soc., 70, pages 339 – 347. (Cited on page 13.)

Karato, S.(1990). *The role of hydrogen in the electrical conductivity of the upper mantle*. Nature, 347, pages 272–273. (Cited on pages 9, 30, and 134.)

Karato, S.(2006). *Remote sensing of hydrogen in Earth's mantle, Water in Nominally Anhydrous Minerals*. Reviews in Mineralogy and Geochemistry, 62, pages 343 – 375. (Cited on page 134.)

Kariya, K. A. and Shankland, T. J.(1983). *Electrical conductivity of dry lower crustal rocks*. Geophysics, 48(1), pages 52 – 61. (Cited on page 9.)

Keller, G. V.(1987). *Rock and Mineral Properties*. In: M. N. Nabighian (ed), *Electromagnetic Methods in Applied Geophysics*, volume 1 - Theory, chapter 2. Society of Exploration Geophysicists, Tulsa, OK. (Cited on page 12.)

Kennedy, L. A., Russell, J. K. and Kopylova, M. G.(2002). *Mantle shear zones revisited: The connection between the cratons and mantle dynamics*. Geology, 30(5). (Cited on pages 140 and 210.)

Key, R. M. and Ayres, N.(2000). *The 1998 edition of the National Geological Map of Botswana*. J. Afr. Earth Sci, 30, pages 427 – 451. (Cited on page 57.)

Key, R. M. and Mothibi, D.(1999). *The national geological map of the Republic of Botswana*. Botswana Geological Survey (1:500,000). (Cited on page 57.)

Kobussen, A. F., Griffin, W. L., O'Reilly, S. Y. and Shee, S. R.(2008). *Ghosts of lithospheres past: Imaging an evolving lithospheric mantle in southern Africa*. Geology, 36(7), pages 515 – 518. doi: 10.1130/G24868A.1. (Cited on page 78.)

Kusky, T. M.(1998). *Tectonic setting and terrane accretion of the Archean Zimbabwe craton*. Geology, 26(2), pages 163 – 166. (Cited on pages 53, 60, and 61.)

Kusky, T. M. and Polat, A.(1999). *Growth of granite-greenstone terranes at convergent margins, and stabilization of Archean cratons*. Tectonophysics, 305, pages 43 – 73. (Cited on page 53.)

Larsen, J. C.(1977). *Removal of local surface conductivity effects from low frequency mantle response curves*. Acta Geodaet., Geophys. et Montanist. Acad. Sci. Hung., 12, pages 183 – 186. (Cited on page 43.)

Le Gall, B., Tshoso, G., Jourdan, F., Féraud, G., Bertrand, H., Tiercelin, J. J., Kampunzu, A. B., Modisi, M. P., Dyment, J. and Maia, M.(2002). $^{40}Ar/^{39}Ar$ *geochronology and structural data from the giant Okavango and related dyke swarms, Karoo igneous province, Botswana*. Earth and Planetary Science Letters, 202, pages 595 – 606. (Cited on page 64.)

Le Gall, B., Tshoso, G., Dyment, J., Kampunzun, A. B., Jourdan, F., Féraud, G., Bertrand, H., Aubourg, C. and Vétel, W.(2005). *The Okavango giant mafic dyke swarm (NE Botswana): its structural significance within the Karoo Large Igneous Province*. Journal of Structural Geology, 27, pages 2234 – 2255. (Cited on pages 64, 65, 66, 113, and 136.)

Ledo, J.(2005). *2-D versus 3-D magnetotelluric data interpretation*. Surveys in Geophysics, 26, pages 511 – 543. (Cited on page 52.)

Ledo, J., Queralt, P., Marti, A. and Jones, A. G.(2002). *Two-dimensional interpretation of three-dimensional magnetotelluric data: an example of limitations and resolution*. Geophysical Journal International, 150(1), pages 127–139. (Cited on page 52.)

Lee, J. F., Sun, D. K. and Cendes, Z. J.(1991). *Tangential vector finite elements for electromagnetic field computation*. IEEE Transactions on Magnetics, 27(5), pages 4032 – 4035. (Cited on page 144.)

Leyshon, P. R. and Tennick, F. P.(1988). *The Proterozoic Magondi mobile belt in Zimbabwe - a review*. South African Journal Geology, 91, pages 114 – 131. (Cited on page 61.)

Lezaeta, P., Chave, A., Jones, A. G. and Evans, R.(2007). *Source field effects in the auroral zone: Evidence from the Slave craton (NW Canada)*. Physics of the Earth and Planetary Interiors, 164, pages 21 – 35. (Cited on pages 8 and 9.)

Li, A. and Burke, K.(2006). *Upper mantle structure of southern Africa from Rayleigh wave tomography*. Journal of Geophysical Research, 111. (Cited on page 74.)

Liu, C., Ren, Z., Tan, J. and Yan, Y.(2008). *Three-dimensional magnetotellurics modeling using edge-based finite-element unstructured meshes*. Applied Geophysics, 5, pages 170 – 180. (Cited on page 144.)

Livelybrooks, D.(1993). *Program 3dfeem: a multidimensional electromagnetic finite element model*. Geophysical Journal International, 114, pages 443 – 458. (Cited on page 144.)

Mackie, R. L. and Madden, T. R.(1993). *Three-dimensional magnetotelluric inversion using conjugate gradients*. Geophysical Journal International, 115, pages 215 – 229. (Cited on pages 179, 186, 189, and 190.)

Mackie, R. L., Bennett, B. R. and Madden, T. R.(1988). *Long-period magnetotelluric measurements near the central California coast: A land-locked view of the conductivity structure under the Pazific Ocean*. Geophysical Journal International, 95, pages 181 – 194. (Cited on pages 51, 114, and 115.)

Mackie, R. L., Madden, T. R. and Wannamaker, P. E.(1993). *Three-dimensional magnetotelluric modeling using difference equations - Theory and comparisons to integral equation solutions*. Geophysics, 58(2), pages 215 – 226. (Cited on pages 160, 170, 171, and 172.)

Mackie, R. L., Smith, J. T. and Madden, T. R.(1994). *Three-dimensional electromagnetic modeling using finite difference equations: The magnetotelluric example*. Radio Science, 29, pages 923–935. (Cited on pages 143, 150, 155, 160, 174, and 197.)

Mackie, R. L., Rodi, W. and Watts, M. D.(2001). *3D magnetotelluric inversion for resource exploration*. Expanded Abstract, 71th Annual Meeting SEG. (Cited on page 179.)

Mackwell, S. J. and Kohlstedt, D. L.(1990). *Diffusion of Hydrogen in Olivine: Implications for Water in the Mantle*. Journal of Geophysical Research (Solid Earth), 95(B4), pages 5079–5088. (Cited on page 30.)

Madden, T. and Nelson, P.(1964). *A defense of Cagniard's magnetotelluric method*. Geophys. Lab. ONR proj. NR-371-401,MIT, Cambridge, Massachusetts. Reprinted 1986 in: K. Vozoff (ed), *Magnetotelluric Methods*, Tusla, OK: Society of Exploration Geophysicists, pages 89 - 95. (Cited on pages 7 and 8.)

Majaule, T., Hanson, R. E., Key, R. M., Singletary, S. J., Martin, M. W. and Bowring, S. A.(2001). *The Magondi Belt in northeast Botswana: regional relations and new geochronological data from the Sua Pan area*. Journal of African Earth Scienes, 32(2), pages 257 – 267. (Cited on pages 61, 62, and 63.)

Mareschal, M., Kellett, R. L., Kurtz, R. D., Ludden, J. N., Ji, S. and Bailey, R. C.(1995). *Archean cratonic roots, mantle shear zones and deep electrical anisotropy*. Nature, 375, pages 134–137. (Cited on page 30.)

Martí, A.(2006). *A Magnetotelluric Investigation of Geoelectrical Dimensionality and Study of the Central Betic Crustal Structure*. Dissertation, Department de Geodinmica i Geofsica, Universitat de Barcelona. (Cited on page 10.)

Martí, A., Queralt, P., Jones, A. G. and Ledo, J.(2005). *Research Note: Improving Bahr's invariant parameters using the WAL approach*. Geophysical Journal International, 163(1), pages 38–41. (Cited on page 43.)

Maumus, J., Bagdassarov, N. and Schmeling, H.(2005). *Electrical conductivity and partial melting of mafic rocks under pressure*. Geochimica et Cosmochimica Acta, 69(19), pages 4703–4718. (Cited on page 134.)

McCourt, S., Hilliard, P., Armstrong, R. A. and Munyanyiwa, H.(2001). *SHRIMP U-Pb zircon geochronology of the Hurungwe granite northwest Zimbabwe: Age constraints on the timing of the Magondi orogeny and implications for the correlation between the Kheis and Magondi Belts*. South African Journal of Geology, 104, pages 39 – 46. (Cited on page 62.)

McCourt, S., Kampunzu, A., Bagai, Z. and Armstrong, R.(2004). *The crustal architecture of Archaean terranes in Northeastern Botswana*. South African Journal of Geology, 107, pages 146 – 158. (Cited on pages 56 and 59.)

McNeice, G. W. and Jones, A. G.(2001). *Multisite, multifrequency tensor decomposition of magnetotelluric data*. Geophysics, 66(1), pages 158–173. (Cited on pages 45, 46, 93, 119, 125, and 136.)

Mitsuhata, Y. and Uchida, T.(2004). *3D magnetotelluric modeling using the T-Ω finite-element method*. Geophysics, 69(1), pages 108 – 119. (Cited on pages 143 and 144.)

Modie, B. N. J.(1996). *Depositional environments of the Meso- to Neoproterozoic Ghanzi-Chobe belt, northwest Botswana*. Journal of African Earth Sciences, 22(3), pages 255 – 268. (Cited on pages 63 and 135.)

Mogi, T.(1996). *Three-dimensional modeling of magnetotelluric data using finite element mehtod*. Journal of Applied Geophysics, 35, pages 185 – 189. (Cited on page 144.)

Muller, M. R., Jones, A. G., Evans, R. L., Grütter, H. S., Hatton, C., Garcia, X., Hamilton, M. P., Miensopust, M. P., Cole, P., Ngwisanyi, T., Hutchins, D., Fourie, C. J., Jelsma, H. A., Evans, S. F., Aravanis, T., Pettit, W., Webb, S. J., Wasborg, J. and The SAMTEX Team(2009). *Lithospheric structure, evolution and diamond prospectivity of the Rehoboth Terrane and the western Kaapvaal Craton, southern Africa: Constraints from broadband magnetotellurics*. Lithos, 112S, pages 93 – 105. doi: 10.1016/j.lithos.2009.06.023. (Cited on pages 1, 68, 70, 132, 133, 134, 135, 140, and 210.)

Mur, G.(1993). *The finite-element method of three-dimensional electromagnetic fields using edge and nodal elements*. IEEE Transactions on Antennas and Propagation, 41(7), pages 948 – 953. (Cited on page 146.)

Mur, G.(1994). *Edge elements, their advantages and their disadvantages*. IEEE Transactions on Magnetics, 30(5), pages 3552 – 3557. (Cited on page 146.)

Mur, G.(1998). *The fallacy of edge elements*. IEEE Transactions on Magnetics, 34(5), pages 3244 – 3247. (Cited on page 146.)

Nair, S. K., Gao, S. S., Liu, K. H. and Silver, P. G.(2006). *Southern African crustal evolution and composition: Constraints from receiver function studies*. Journal of Geophysical Research, 11. B02304, doi:10.1029/2005JB003802. (Cited on pages 73 and 74.)

Nam, M. J., Kim, H. J., Song, Y., Lee, T. J., Son, J.-S. and Suh, J. H.(2007). *3D magnetotelluric modelling including surface topography*. Geophysical Prospecting, 55, pages 277 – 287. (Cited on pages 143, 144, 155, 160, and 174.)

Neves, A. S.(1957). *The magnetotelluric method in two-dimensional structures*. Dissertation, Massachusetts Institute of Technology, Cambridge, Massachusetts. (Cited on page 7.)

Newman, G. A. and Alumbaugh, D. L.(2000). *Three-dimensional magnetotelluric inversion using non-linear conjugate gradients*. Geophysical Journal International, 140(2), pages 410–424. (Cited on page 179.)

Nguuri, T. K., Gore, J., James, D. E., Webb, S. J., Wright, C., Zengeni, T. G., Gwavava, O., Snoke, J. A. and Kaapvaal Seismic Group(2001). *Crustal structure beneath southern Africa and its implications for the formation and evolution of the Kaapvaal and Zimbabwe cratons*. Geophysical Research Letters, 28(13), pages 2501 – 2504. (Cited on pages 73 and 74.)

Niblett, E. R. and Sayn-Wittgenstein, C.(1960). *Variation of electrical conductivity with depth by the magneto-telluric method*. Geophysics, 25, pages 998 – 1008. (Cited on page 24.)

Nover, G., Heikamp, S., Meurer, H. J. and Freund, D.(1998). *In-situ electrical conductivity and permeability of mid-crustal rocks from the KTB drilling: consequences for high conductive layers in the earth crust*. Surveys in Geophysics, 19, pages 73 – 85. (Cited on pages 124 and 138.)

O'Reilly, S. Y. and Griffin, W. L.(2006). *Imaging chemical and thermal heterogeneity in the sub-continental lithospheric mantle: Geophysical implications*. Tectonophysics, 416, pages 289 – 309. doi: 10.1016/j.tecto.2005.11.014. (Cited on page 75.)

Palacky, G. J.(1987). *Resistivity characteristics of geologic targets*. In: M. N. Nabighian (ed), *Electromagnetic Methods in Applied Geophysics*, volume 1 - Theory, chapter 3, pages 53 – 129. Society of Exploration Geophysicists, Tusla, OK. (Cited on page 10.)

Parker, R. L.(1980). *The inverse problem of electromagnetic induction: existance and construction of solutions based on incomplete data.* Journal of Geophysical Research, 85, pages 4421 – 4425. (Cited on page 50.)

Parker, R. L.(1982). *The existence of a region inaccessible to magnetotelluric sounding*. Geophys. J. R. astr. Soc., 68, pages 165 – 170. (Cited on page 50.)

Parker, R. L. and Booker, J. R.(1996). *Optimal one-dimensional inversion and bounding of magnetotelluric apparent resistivity and phase measurements*. Physics of the Earth and Planetary Interiors, 98, pages 269 – 282. (Cited on page 50.)

Parker, R. L. and Whaler, K. A.(1981). *Numerical methods for establishing solutions to the inverse problem of electromagnetic induction*. Journal of Geophysical Research, 86, pages 9574 – 9584. (Cited on page 50.)

Parkinson, W. D.(1959). *Directions of rapid geomagnetic fluctuations*. Geophysical Journal of the Royal Astronomical Society, 2(1), pages 1 – 14. (Cited on page 20.)

Parkinson, W. D.(1962). *The influence of continents and oceans on geomagnetic variations*. Geophysical Journal of the Royal Astronomical Society, 6, pages 441 – 449. (Cited on page 20.)

Pek, J. and Santos, F. A. M.(2002). *Magnetotelluric impedances and parametric sensitivities for 1-D anisotropic layered media*. Computers & Geosciences, 28, pages 939 – 950. (Cited on pages 31, 32, 109, 110, 111, 112, 113, and 114.)

Pek, J. and Verner, T.(1997). *Finite-difference modelling of magnetotelluric fields in two-dimensional anisotropic media*. Geophysical Journal International, 128, pages 505 – 521. (Cited on pages 31, 136, 138, 139, 269, 277, 278, and 279.)

Pellerin, L. and Hohmann, G. W.(1990). *Transient electromagnetic inversion: A remedy for magnetotelluric static shifts*. Geophysics, 55(9), pages 1242 – 1250. (Cited on page 43.)

Portniaguine, O. and Zhdanov, M. S.(1999). *Focusing geophysical inversion images*. Geophysics, 64(3), pages 874 – 887. (Cited on page 182.)

Prave, A. R.(1996). *Tale of three cratons: Tectonostratigraphic anatomy of the Damara orogen in northwestern Namibia and the assembly of Gondwana*. Geology, 24(12), pages 1115 – 1118. (Cited on page 56.)

Price, A. T.(1962). *The theory of magnetotelluric methods when the source field is considered*. Journal of Geophysical Research, 67(5), pages 1907 – 1918. (Cited on pages 7 and 13.)

Price, A. T.(1973). *The theory of geomagnetic induction*. Physics of the Earth and Planetary Interiors, 7, pages 227 – 233. (Cited on pages 12, 13, and 26.)

Pridmore, D. F., Hohmann, G. W., Ward, S. H. and Sill, W. R.(1981). *An investigation of finite-element modeling for electrical and electromagnetic data in three dimensions*. Geophysics, 46, pages 1009 – 1024. (Cited on page 144.)

Priestley, K., McKenzie, D. and Debayle, E.(2006). *The state of the upper mantle beneath southern Africa*. Tectonophysics, 416, pages 101 – 112. (Cited on page 74.)

Raiche, A. P.(1974). *An integral equation approach to three-dimensional modelling*. Geophys. J. R. astr. Soc., 36, pages 363 – 376. (Cited on page 143.)

Read, G. H. and Janse, A. J. A. B.(2009). *Diamonds: Exploration, mines and marketing*. Lithos. doi:10.1016/j.lithos.2009.03.024. (Cited on page 99.)

Reddy, I. K., Rankin, D. and Phillips, D. J.(1977). *Three-dimensional modelling in magnetotelluric and magnetic variational soundings*. Geophys. J. R. astr. Soc., 51, pages 313 – 325. (Cited on page 144.)

Reeves, C. V.(1972). *Rifting in the Kalahari?* Nature, 237, pages 95 – 96. (Cited on page 74.)

Reeves, C. V.(1985). *The Kalahari Desert, central southern Africa: A case history of regional gravity and magnetic exploration*. In: W. J. Hinze (ed), *The utility of regional gravity and magnetic anomaly maps*, pages 144 – 153. (Cited on page 63.)

Ritter, O., Weckmann, U., Vietor, T. and Haak, V.(2003). *A magnetotelluric study of the Damara Belt in Namibia - 1. Regional scale conductivity anomalies*. Physics of the Earth and Planetary Interiors, 138, pages 71 – 90. (Cited on pages 73, 119, and 124.)

Rodi, W. and Mackie, R. L.(2001). *Nonlinear conjugate gradients algorithm for 2-D magnetotelluric inversion*. Geophysics, 66(1), pages 174 – 187. (Cited on pages 51, 114, 115, 117, 137, 157, 159, 179, 186, 189, 190, and 289.)

Roering, C., van Reenen, D. D., Smit, C. A., Barton, Jr., J. M., de Beer, J. H., de Wit, M. J., Stettler, E. H., van Schalkwyk, J. F., Stevens, G. and Pretorius, S.(1992). *Tectonic model for the evolution of the Limpopo Belt*. Precambrian Research, 55, pages 539 – 552. (Cited on pages 56 and 58.)

Saad, Y.(1990). *SPARSKIT: A basic tool kit for sparse matrix computations*. Report RIACS-90-20, Research Institute for Advanced Computer Science, NASA Ames Research Center. (Cited on pages 149, 153, 157, 164, 184, 186, 187, 189, and 293.)

Saltzer, R.(2002). *Upper mantle structure of the Kaapvaal craton from surface wave analysis - a second look*. Geophysical Research Letters, 29(6). doi:10.1029/2001GL013702. (Cited on page 74.)

Sasaki, Y.(1999). *Three-dimensional frequency-domain electromagnetic modeling using the finite-difference method*. Butsuri-Tansa, 52, pages 421 – 431. (in Japanese with English abstract). (Cited on pages 143 and 155.)

Sasaki, Y.(2001). *Full 3-D inversion of electromagnetic data on PC*. Journal of Applied Geophysics, 46, pages 45 – 54. (Cited on page 150.)

Sasaki, Y.(2004). *Three-dimensional inversion of static-shifted magnetotelluric data*. Earth Planets Space, 56, pages 239 – 248. (Cited on pages 179 and 180.)

Sasaki, Y. and Meju, M. A.(2006). *Three-dimensional joint inversion for magnetotelluric resistivity and static shift distributions in complex media*. Journal of Geophysical Research, 111. (Cited on page 180.)

Schmucker, U.(1970). *Anomalies of geomagnetic variations in the southwestern United States*. Bulli. Scripps Inst. Ocean, University of California, San Diego, California, 13. (Cited on page 18.)

Schmucker, U.(1973). *Regional induction studies: A review of methods and results*. Physics of the Earth and Planetary Interiors, 1973, pages 365 – 378. (Cited on page 18.)

Schmucker, U.(1987). *Substitute conductors for electromagnetic response estimates*. Pure and Applied Geophysics, 125, pages 341 – 367. (Cited on page 24.)

Schock, R. N., Duba, A. G. and Shankland, T. J.(1989). *Electrical conduction in olivine*. Journal of Geophysical Research, 94, pages 5829 – 5839. (Cited on page 30.)

Schön, J. H.(2004). *Physical properties of rocks: Fundamentals and principles of petrophysics*. In: K. Helbig and S. Treitel (ed), *Seismic Exploration*, volume 18. Elsevier, Amsterdam. (Cited on page 34.)

Schwarz, G.(1990). *Electrical conductivity of the earth's crust and upper mantle*. Surveys in Geophysics, 11, pages 133 – 161. (Cited on pages 137, 138, and 139.)

Shankland, T. J. and Ander, M. E.(1983). *Electrical conductivity, temperatures, and fluids in the lower crust*. Journal of Geophysical Research, 88(B11), pages 9475 – 9484. (Cited on page 138.)

Silver, P. G., Gao, S. S., Liu, K. H. and the Kaapvaal Seismic Group(2001). *Mantle deformation beneath southern Africa*. Geophysical Research Letters, 28(13), pages 2493 – 2496. (Cited on pages 68 and 74.)

Silver, P. G., Fouch, M. J., Gao, S. S., Schmitz, M. and Kaapvaal Seismic Group(2004). *Seismic anisotropy, mantle fabric, and the magmatic evolution of Precambrian southern Africa*. South African Journal of Geology, 107, pages 45 – 58. (Cited on page 74.)

Simpson, F. and Bahr, K.(2005). *Practical Magnetotellurics*. Cambrigde University Press. (Cited on pages 8, 13, 20, 21, 23, 27, 41, and 42.)

Sims, W. E., Bostick, F. X., Jr. and Smith, H. W.(1971). *The estimation of magnetotelluric impedance tensor elements from measured data*. Geophysics, 36(5), pages 938 – 942. (Cited on page 41.)

Singletary, S. J., Hanson, R. E., Martin, M. W., Crowley, J. L., Bowring, S. A., Key, R. M., Ramokate, L. V., Direng, B. B. and Michael A, K.(2003). *Geochronology of basement rocks in the Kalahari Desert, Botswana, and implications for regional Proterozoic tectonics*. Precambrian Research, 121, pages 47 – 71. (Cited on pages 56, 57, 59, 63, 123, 130, and 131.)

Siripunvaraporn, W. and Egbert, G.(2000). *An efficient data-subspace inversion method for 2-D magnetotelluric data*. Geophysics, 65(3), pages 791 – 803. (Cited on page 51.)

Siripunvaraporn, W., Egbert, G. and Lenbury, Y.(2002). *Numerical accuracy of magnetotelluric modeling: A comparison of finite difference approximations*. Earth Planets Space, 54, pages 721 – 725. (Cited on pages 150, 155, and 160.)

Siripunvaraporn, W., Egbert, G., Lenbury, Y. and Uyeshima, M.(2005). *Three-dimensional magnetotelluric inversion: data-space method*. Physics of the Earth and Planetary Interiors, 150, pages 3–14. (Cited on pages 51, 143, 155, 174, 179, and 201.)

Smith, J. T.(1996). *Conservative modeling of 3-d electromagnetic fields, Part II: Biconjugate gradient solution and an accelerator*. Geophysics, 61, pages 1319 – 1324. (Cited on pages 144, 150, 151, 157, 158, and 212.)

Smith, J. T.(1997). *Estimating galvanic-distortion magnetic fields in magnetotellurics*. Geophysical Journal International, 130, pages 65 – 72. (Cited on pages 35 and 36.)

Smith, J. T. and Booker, J. R.(1991). *Rapid inversion of two- and three-dimensional magnetotelluric data*. Journal of Geophysical Research, 96, pages 3905 – 3922. (Cited on pages 179 and 191.)

Spratt, J. E., Jones, A. G., Nelson, K. D., Unsworth, M. J. and INDEPTH MT Team(2005). *Crustal structure of the India-Asia collision zone, southern Tibet, from INDEPTH MT investigations*. Physics of the Earth and Planetary Interiors, 150, pages 227 – 237. (Cited on page 50.)

Spratt, J. E., Jones, A. G., Jackson, V. A., Collins, L. and Avdeeva, A.(2009). *Lithospheric geometry of the Wopmay orogen from a Slave craton to Bear Province magnetotelluric transect*. Journal of Geophysical Research, 114. (Cited on pages 1, 40, 46, 129, and 130.)

Srivastava, S. P.(1965). *Method of interpretation of magnetotelluric data when source field is considered*. Journal of Geophysical Research, 70, pages 945 – 954. (Cited on page 7.)

Stalnaker, J. L., Everett, M. E., Benavides, A. and Pierce, C. J.(2006). *Mutual induction and the effect of host conductivity on the EM induction response of buried targets using 3-D finite-element analysis*. IEEE Transactions on Geoscience and Remote Sensing, 44, pages 251 – 259. (Cited on page 144.)

Sternberg, B. K.(1993). *On: "Removal of static shift in two dimensions by regularized inversion" by Catherine deGroot-Hedlin*. Geophysics, 58, pages 598 – 599. (Cited on page 43.)

Sternberg, B. K., Washburne, J. C. and Pellerin, L.(1988). *Correction for the static shift in magnetotellurics using transient electromagnetic soundings*. Geophysics, 53(11), pages 1459 – 1468. (Cited on page 43.)

Stettler, E. H., Prinsloo, J. and Hauger, M. E.(1998). *A geophysical transect between Avondale on the Kheis tectonic province an Keimoes on the Namaqua metamorphic province, South Africa*. Southern African Geophysical Review, 2, pages 83 – 93. (Cited on page 73.)

Stettler, E. H., Prinsloo, J., Hauger, M. E. and du Toit, M. C.(1999). *A crustal geophysical model of the Kheis tectonic province, South Africa based on magnetotelluric, reflection seismic, gravity and magnetic data sets*. Southern African Geophysical Review, 3, pages 54 – 68. (Cited on page 73.)

Stiefenhofer, J., Viljoen, K. S. and Marsh, J. S.(1997). *Petrology and geochemistry of peridotite xenoliths from the Letlhakane kimberlites, Botswana*. Contrib Mineral Petrol, 127, pages 147 – 158. (Cited on pages 139 and 210.)

Stratton, J. A.(1941). *Electromagnetic theory*. McGraw-Hill Book Co. (Cited on page 15.)

Stuart, G. W. and Zengeni, T. G.(1987). *Seismic crustal structure of the Limpopo mobile belt, Zimbabwe*. Tectonophysics, 144, pages 323 – 335. (Cited on page 57.)

Sugeng, F.(1998). *Modelling the 3d tdem response using the 3d full-domain finite-element method based on the hexahedral edge-element technique*. Exploration Geophysics, 29, pages 615 – 619. (Cited on page 144.)

Swift, C. M.(1967). *A magnetotelluric investigation of an electrical conductivity anomaly in the Southwestern United States*. Dissertation, MIT, Cambridge, MA. (Cited on pages 7 and 43.)

Telford, W. M., Geldart, L. P. and Sheriff, R. E.(1990). *Applied Geophysics*. Cambridge University Press, second edition. (Cited on pages 11 and 12.)

ten Grotenhuis, S. M., Drury, M. R., Peach, C. J. and Spiers, C. J.(2004). *Electrical properties of fine-grained olivine: Evidence for grain boundary transport*. Journal of Geophysical Research, 109. (Cited on pages 130 and 134.)

Thomas, R. J., Agenbacht, A. L. D., Cornell, D. H. and Moore, J. M.(1994). *The Kibaran of southern Africa: Tectonic evolution and metallogeny*. Ore Geology Reviews, 9, pages 131 – 160. (Cited on page 62.)

Tikhonov, A. N.(1950). *The determination of the electrical properties of the deep layers of the Earth's crust*. Dokl. Acad. Nauk. SSR, 73, pages 295 – 297. (in Russian). (Cited on page 7.)

Tikhonov, A. N.(1965). *Mathematical basis of the theory of electromagnetic soundings*. USSR Comp. Math. Phys., 5, pages 201 – 211. (Cited on page 22.)

Tikhonov, A. N.(1986). *On determining electrical characteristics of the deep layers of the Earth's crust*. In: K. Vozoff (ed), *Magnetotelluric Methods*, pages 2 – 3. Tulsa: Society of Exploration Geophysicsts. (Cited on page 7.)

Tikhonov, A. N. and Arsenin, V. Y.(1977). *Solutions of ill-posed problems*. V. H. Winston and Sons. (Cited on page 51.)

Tikhonov, A. N. and Berdichevsky, M. N.(1966). *Experience in the use of magnetotelluric methods to study the geological structures of sedimentary basins*. Izv. Earth Phys., 2, pages 34 – 41. (Cited on page 7.)

Treloar, P. J.(1988). *The geological evolution of the Magondi mobile belt, Zimbabwe*. Precambrian Research, 38, pages 55 – 73. (Cited on pages 61 and 62.)

Treloar, P. J. and Kramers, J. D.(1989). *Metamorphism and geochronology of granulites and migmatitic granulites from the Magondi mobile belt, Zimbabwe*. Precambrian Research, 45, pages 277 – 289. (Cited on page 62.)

Tshoso, G.(2003). *Structure, chronologie et mode de mise en place du système de dykes géants de l'Okavango, Nord Botswana. Une approche pluridisclinaire*. Dissertation, Brest University. (Cited on pages 65 and 66.)

Tsunogae, T., Miyano, T. and Ridley, J.(1992). *Metamorphic P-T profiles from the Zimbabwe Craton to the Limpopo Belt, Zimbabwe*. Precambrian Research, 55, pages 259 – 277. (Cited on page 78.)

Unsworth, M., Egbert, G. and Booker, J.(1999). *High-resolution electromagnetic imaging of the San Andreas fault in Central California*. Journal of Geophysical Research, 104(B1), pages 1131 – 1150. (Cited on page 119.)

Utada, H. and Munekane, H.(2000). *On galvanic distortion of regional three-dimensional magnetotelluric impedances*. Geophysical Journal International, 140(2), pages 385–398. (Cited on page 43.)

Uyeshima, M. and Schultz, A.(2000). *Geoelectromagnetic induction in a heterogeneous sphere: a new three-dimensional forward solver using a conservative staggered-grid finite difference method*. Geophysical Journal International, 140, pages 636 – 650. (Cited on page 150.)

van Reenen, D. D., Barton, Jr., J. M., Roering, C., Smith, C. A. and van Schalkwyk, J. F.(1987). *Deep crustal response to continental collision: The Limpopo belt of southern Africa*. Geology, 15, pages 11 – 14. (Cited on pages 56, 57, and 58.)

van Reenen, D. D., Roering, C., Ashwal, L. D. and de Wit, M. J.(1992). *Regional geological setting of the Limpopo Belt*. Precambrian Research, 55, pages 1 – 5. (Cited on pages 56 and 57.)

van Zijl, J. S. V.(1969). *A deep Schlumberger sounding to investigate the electrical structure of the crust and upper mantle in South Africa*. Geophysics, 34(3), pages 450 – 462. (Cited on page 70.)

van Zijl, J. S. V.(2006). *A review of the resistivity structure of the Karoo Supergroup, South Africa, with emphasis on the dolerites: A study in anisotropy*. South African Journal of Geology, 109, pages 315 – 328. (Cited on pages 70, 107, and 136.)

van Zijl, J. S. V. and de Beer, J. H.(1983). *Electrical structure of the Damara orogen and its tectonic significance*. Spec. Publ. geol. Soc. S. Afr. (Cited on pages 2, 70, 72, 73, 123, 124, and 210.)

van Zijl, J. S. V., Hugo, P. L. V. and de Bellocq, J. H.(1970). *Ultra deep Schlumberger sounding and crustal conductivity structure in South Africa*. Geophyiscal Prospecting, 18, pages 615 – 634. (Cited on page 70.)

Vinnik, L. P., Green, R. W. E. and Nicolaysen, L. O.(1995). *Recent deformations of the deep continental root beneath southern Africa*. Nature, 375, pages 50 – 52. (Cited on page 74.)

Vozoff, K.(1991). *The magnetotelluric method*. In: M. N. Nabighian (ed), *Electromagnetic Methods in Applied Geophysics*, volume 2 - Application, chapter 8. Society Exploration Geophysicists, Tulsa, OK. (Cited on pages 8, 9, and 13.)

Wait, J. R.(1954). *On the relation between telluric currents and the earth's magnetic field*. Geophysics, 19, pages 281 – 289. (Cited on pages 7 and 8.)

Wannamaker, P. E.(1991). *Advances in three-dimensional magnetotelluric modeling using integral equations*. Geophysics, 56(11), pages 1716 – 1728. (Cited on pages 143, 160, 170, 171, and 172.)

Wannamaker, P. E.(2005). *Anisotropy versus heterogeneity in continental solid earth electromagnetic studies: fundamental response characteristics and implications for physicochemical state*. Surveys in Geophysics, 26, pages 733 – 765. (Cited on page 32.)

Wannamaker, P. E., Hohmann, G. W. and Ward, S. H.(1984). *Magnetotelluric responses of three-dimensional bodies in layered earths*. Geophysics, 49, pages 1517 – 1533. (Cited on pages 52 and 119.)

Ward, S. H. and Hohmann, G. W.(1987). *Electromagnetic theory for geophysical applications*. In: M. N. Nabighian (ed), *Electromagnetic Methods in Applied Geophysics*, volume 1 - Theory, chapter 4, pages 131 – 311. Society of Exploration Geophysicists, Tusla, OK. (Cited on page 15.)

Weaver, J. T., Agarwal, A. K. and Lilley, F. E. M.(2000). *Characterization of the magnetotelluric tensor in terms of its invariants*. Geophysical Journal International, 141(2), pages 321–336. (Cited on pages 19 and 43.)

Webb, J. P.(1993). *Edge elements and what they can do for you*. IEEE Transactions on magnetics, 29(2), pages 1460 – 1465. (Cited on page 146.)

Webb, S. J.(2009). *Southern African tectonics from potential field interpretation*. Dissertation, University of the Witswatersrand, Johannesburg, South Africa. (Cited on pages 53, 55, 69, 71, 76, and 77.)

Weckmann, U.(2002). *Entwicklung eines Verfahrens zur Abbildung krustaler Leitfähigkeitsstrukturen anhand von Magnetotellurikdaten aus Namibia*. Dissertation, Freie Universität Berlin, Germany. (in German). (Cited on page 73.)

Weckmann, U., Ritter, O. and Haak, V.(2003). *A magnetotelluric study of the Damara Belt in Namibia - 2. MT phases over 90°′, reveal the internal structure of the Waterberg Fault/Omaruru Lineament*. Physics of the Earth and Planetary Interiors, 138, pages 91 – 112. (Cited on page 73.)

Weckmann, U., Ritter, O., Jung, A., Branch, T. and de Wit, M.(2007). *Magnetotelluric measurements across the Beattie magnetic anomaly and the Southern Cape Conductive Belt, South Africa*. Geophysical Research Letters, 112. B05416, doi:10.1029/2005JB003975. (Cited on page 73.)

Weidelt, P.(1972). *The inverse problem of geomagnetic induction*. Zeitschrift für Geophysik, 38, pages 257 – 289. (Cited on pages 18 and 41.)

Weidelt, P.(1975). *Electromagnetic induction in three-dimensional structures*. Journal of Geophysics, 41, pages 85 – 109. (Cited on page 143.)

Wessel, P. and Smith, W. H. F.(1991). *Free software help map and display data*. EOS Transactions American Geophysical Union, 72, page 441. (Cited on page xxiv.)

Wessel, P. and Smith, W. H. F.(1998). *New, improved version of the Generic Mapping Tools released*. EOS Transactions American Geophysical Union, 79, page 579. (Cited on page xxiv.)

Wiese, H.(1962). *Geomagnetische Tiefentellurik. II. Die Streichrichtung der Untergrundstrukturen des elektrischen Widerstandes, erschlossen aus geomagnetischen Variationen*. Geofis. Pura Appl., 52, pages 83 – 103. written in German. (Cited on page 20.)

Wilson, J. F.(1979). *A preliminary reappraisal of the Rhodesian basement complex*. Geological Society of South Africa Special Publication, 5, pages 1 – 23. (Cited on page 60.)

Wilson, J. F., Nesbitt, R. W. and Fanning, C. M.(1995). *Zircon geochronology of Archean felsic sequences in the Zimbabwe craton: A revision of greenstone stratigraphy and a model for crustal growth*. In: M. P. Coward and A. C. Ries (ed), *Early Precambrian processes*, volume 95 of Geological Society London Special Publication, pages 109 – 126. (Cited on page 60.)

Xiong, Z.(1992). *Electromagnetic modeling of 3-D structures by the method of system iteration using integral equations*. Geophysics, 57(12), pages 1556 – 1561. (Cited on page 143.)

Xu, Y. S. and Shankland, T. J.(1999). *Electrical conductivity of orthopyroxene and its high pressure phases*. Geophysical Research Letters, 26, pages 2645 – 2648. (Cited on pages 133 and 134.)

Xu, Y. S., Shankland, T. J. and Duba, A. G.(2000). *Pressure effect on electrical conductivity of mantle olivine*. Physics of the Earth and Planetary Interiors, 118, pages 149–161. (Cited on pages 133 and 134.)

Yawsangratt, S.(2002). *A gravity study of northern Botswana: a new perspective and its implication for regional geology*. Master thesis, International Institute for Geo-Information Science and Earth Observation, Enschede, Netherlands. (Cited on page 75.)

Yoshimura, R. and Oshiman, N.(2002). *Edge-based finite element approach to the simulation of geoelectromagnetic induction in a 3-D sphere*. Geophysical Research Letters, 29, pages 1039 – 1045. (Cited on page 144.)

Yoshino, T., Matsuzaki, T., Yamashita, S. and Katsura, T.(2006). *Hydrous olivine unable to account for conductivity anomaly at the top of the asthenosphere*. Nature, 443, pages 973 – 976. (Cited on page 30.)

Yoshino, T., Manthilake, G., Matsuzaki, T. and Katsura, T.(2008). *Dry mantle transition zone inferred from the conductivity of wadsleyite and ringwoodite*. Nature, 451, pages 326 – 329. doi: 10.1038/nature06427. (Cited on page 30.)

Zhdanov, M. S. and Fang, S.(1996). *3D quasi-linear electromagnetic inversion*. Radio Science, 31, pages 741 – 754. (Cited on page 179.)

Zhdanov, M. S., Varentsov, I. M., Weaver, J. T., Golubev, N. G. and Krylov, V. A.(1997). *Methods for modelling electromagnetic fields: Results from COMMEMI - the international project on the comparison of modelling methods for electromagnetic induction*. Journal of Applied Geophysics, 37, pages 133 – 271. (Cited on pages 3, 155, 159, 160, 163, 164, 167, 168, 169, 170, 171, 172, 197, 198, 199, 293, 296, 297, 298, 306, 307, 308, 309, and 310.)

Zhdanov, M. S., Fang, S. and Hursan, G.(2000). *Electromagnetic inversion using quasi-linear approximation*. Geophysics, 65, pages 1501 –1513. (Cited on page 179.)

Zyserman, F. I. and Santos, J. E.(2000). *Parallel finite element algorithm with domain decomposition for three-dimensional magnetotelluric modelling*. Journal of Applied Geophysics, 44, pages 337 – 351. (Cited on page 144.)

A

LITTLE AUXILIARIES

A.1 CONVERSION FROM MAGNETOTELLURIC TENSOR (FIELD UNITS) TO IMPEDANCE TENSOR (SI UNITS)

The unit of the magnetotelluric tensor $\underline{\underline{M}}$ (also called impedance tensor in field units) is $\frac{mV}{km}/nT$, whereas the SI unit of the impedance tensor $\underline{\underline{Z}}$ is Ω. The following determination is in units not in parameters.
The magnetotelluric tensor is calculated from the E and B fields, therefore the (field) unit of its elements is given by

$$\frac{\frac{mV}{km}}{nT} = \frac{mV}{km \cdot nT} = \frac{0.001V}{1000m \cdot 10^{-9}T} \quad , \tag{A.1}$$

whereas the SI units of the impedance tensor are determined using the E and H fields. Because the relation between the magnetic flux density and the magnetic field is $B = \mu_0 H$, Equation A.1 needs to be multiplied by the vacuum permeability $\mu_0 = 4 \cdot \pi \, 10^{-7} \frac{Vs}{Am}$.

$$4 \cdot \pi \, 10^{-7} \frac{Vs}{Am} \cdot \frac{0.001 \, V}{1000 \, m \cdot 10^{-9} T} = \frac{4 \cdot \pi \, 10^{-7} \cdot 0.001}{1000 \cdot 10^{-9}} \frac{Vs \cdot V}{Am^2 \cdot T} \tag{A.2}$$

and because $T = \frac{Vs}{m^2}$ Equation A.2 becomes equal to

$$4 \cdot \pi \, \frac{10^{-10}}{10^{-6}} \frac{V^2 s m^2}{A m^2 V s} = 4 \cdot \pi \cdot 0.0001 \frac{V}{A} = \frac{4 \cdot \pi}{10000} \, \Omega \quad . \tag{A.3}$$

That means the value of the magnetotelluric tensor $\underline{\underline{M}}$ in field units needs to be multiplied by the factor $\frac{4 \cdot \pi}{10000}$ to convert it into an impedance tensor ($\underline{\underline{Z}}$) value in SI units.

A.2 COORDINATE ROTATION

Sometimes the local coordinate system of a site is not identical to the coordinate system required by processing routines, e.g., strike direction or coordinate system of the model mesh. In these cases the data of a site (observed or modelled data - preferable the later) needs to be rotated. A rotation of the coordinates affects the electrical and magnetic fields and therefore also the impedance matrix and the tipper vector. The rotation of the horizontal electrical field is giving by

$$\underline{\mathbf{E}}_{rot} = \underline{\underline{\mathbf{R}}} \, \underline{\mathbf{E}} \quad , \tag{A.4}$$

where $\underline{\mathbf{E}} = \begin{pmatrix} E_x \\ E_y \end{pmatrix}$ is the vector of the horizontal electric fields and $\underline{\underline{\mathbf{R}}} = \begin{pmatrix} \cos\theta & \sin\theta \\ -\sin\theta & \cos\theta \end{pmatrix}$ is the rotation matrix using the rotation angle θ (passive rotation, i.e., rotation of the co-

ordinate system, which results in clockwise rotation of the vector for a positive angle θ). Multiplying Equation A.4 by the transpose rotation matrix $\underline{\underline{\mathbf{R}}}^{\mathrm{T}}$ gives

$$\underline{\underline{\mathbf{R}}}^{\mathrm{T}}\,\underline{\mathbf{E}}_{\mathrm{rot}} = \underbrace{\underline{\underline{\mathbf{R}}}^{\mathrm{T}}\,\underline{\underline{\mathbf{R}}}}_{=\underline{\underline{\mathbf{I}}}}\,\underline{\mathbf{E}} \;\Rightarrow\; \underline{\mathbf{E}} = \underline{\underline{\mathbf{R}}}^{\mathrm{T}}\,\underline{\mathbf{E}}_{\mathrm{rot}} \quad , \tag{A.5}$$

where $\underline{\underline{\mathbf{I}}}$ is the identity matrix.

Doing analogous for the horizontal magnetic field vector $\underline{\mathbf{H}} = \begin{pmatrix} H_x \\ H_y \end{pmatrix}$ results in

$$\underline{\mathbf{H}} = \underline{\underline{\mathbf{R}}}^{\mathrm{T}}\,\underline{\mathbf{H}}_{\mathrm{rot}} \quad . \tag{A.6}$$

The relationship between the electric and magnetic fields and the impedance is given by (see Equation 2.52) $\underline{\mathbf{E}} = \underline{\underline{\mathbf{Z}}}\,\underline{\mathbf{H}}$ (therefore $\underline{\mathbf{E}}_{\mathrm{rot}} = \underline{\underline{\mathbf{Z}}}_{\mathrm{rot}}\,\underline{\mathbf{H}}_{\mathrm{rot}}$ should also be valid). Substitution of the fields using Equations A.5 and A.6 illustrate the necessary transformation that needs to be applied to $\underline{\underline{\mathbf{Z}}}$ to obtain $\underline{\underline{\mathbf{Z}}}_{\mathrm{rot}}$.

$$\begin{aligned} \underline{\mathbf{E}}_{\mathrm{rot}} &= \underbrace{\underline{\underline{\mathbf{R}}}\,\underline{\underline{\mathbf{Z}}}\,\underline{\underline{\mathbf{R}}}^{\mathrm{T}}}_{=}\;\underline{\mathbf{H}}_{\mathrm{rot}} \\ \underline{\mathbf{E}}_{\mathrm{rot}} &= \overbrace{\underline{\underline{\mathbf{Z}}}_{\mathrm{rot}}}\;\underline{\mathbf{H}}_{\mathrm{rot}} \end{aligned} \tag{A.7}$$

The tipper $\underline{\mathbf{T}}$ is expressed by $H_z = \underline{\mathbf{T}}\,\underline{\mathbf{H}}$, where H_z is the vertical magnetic field and $\underline{\mathbf{H}}$ is the vector of the horizontal magnetic fields. A rotation of the coordinate system around the z axis does not affect the vertical magnetic field, but the horizontal components (as shown in Equation A.6). Analogous to the rotated impedance matrix the rotated tipper vector can be calculated:

$$H_z = \underline{\mathbf{T}}\,\underline{\mathbf{H}} = \underline{\mathbf{T}}\,\underline{\underline{\mathbf{R}}}^{\mathrm{T}}\,\underline{\mathbf{H}}_{\mathrm{rot}} \;\Rightarrow\; \underline{\mathbf{T}}_{\mathrm{rot}} = \underline{\mathbf{T}}\,\underline{\underline{\mathbf{R}}}^{\mathrm{T}} \quad . \tag{A.8}$$

B

DATA IMAGING AND STRIKE ANALYSIS OF THE ZIM AREA

This appendix is a supplement to Chapter 4, which described the application of data imaging and analysis techniques, e.g., Niblett-Bostick resistivity maps, phase tensor maps and strike analysis to the ZIM line data (and near by sites). Since in Chapter 4 only a few representative figures were shown for completeness additional plots can be found in this appendix.

B.1 NIBLETT-BOSTICK RESISTIVITY MAPS FOR CRUSTAL AND LITHOSPHERIC DEPTHS

The Niblett-Bostick resistivity maps have been discussed in Section 4.1.2, where one representative depth each for the crust (Figure 4.5) and lithosphere (Figure 4.6) were shown. Figures B.1 to B.10 show similar plots for a number of different depths. For the crustal depths range the following investigation depths were selected: 5 km (Figure B.1), 10 km (Figure B.2), 20 km (Figure B.3) and 35 km (Figure B.4). The investigation depths of 50 km (Figure B.5), 70 km (Figure B.6), 100 km (Figure B.7) and 150 km (Figure B.8) are associated with lithospheric depths. At some sites the penetration depth is as large as 200 km (Figure B.9) or even 250 km (Figure B.10). These depths are most likely related to the lithosphere-asthenosphere boundary or the asthenosphere.

All Figures from B.1 to B.10 have the same set-up. The background is the regional magnetic map in grey scale (see Figure 3.10, magnetic data courtesy of the Council for Geoscience, Pretoria, South Africa). Each site is represented by a coloured circle, where the colour indicates the Niblett-Bostick resistivity value at this depth and the size of the symbol gives a suggestion of the period needed to penetrated to the chosen depth. The resistivity values for ρ_{xy} (a) and ρ_{yx} (b) are plotted on separated maps.

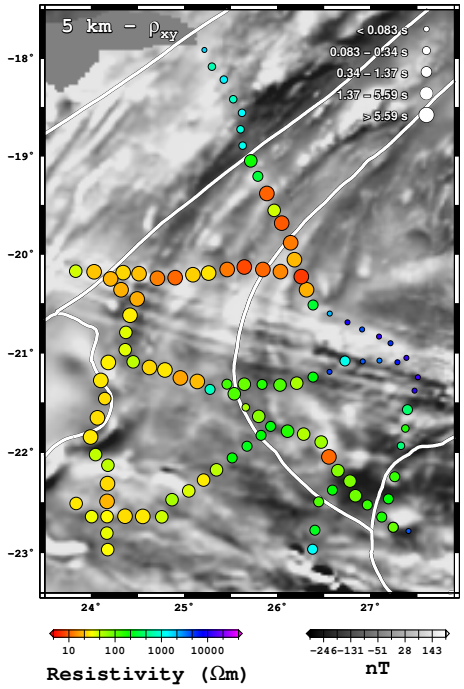

(a) Niblett-Bostick resistivities ρ_{xy}

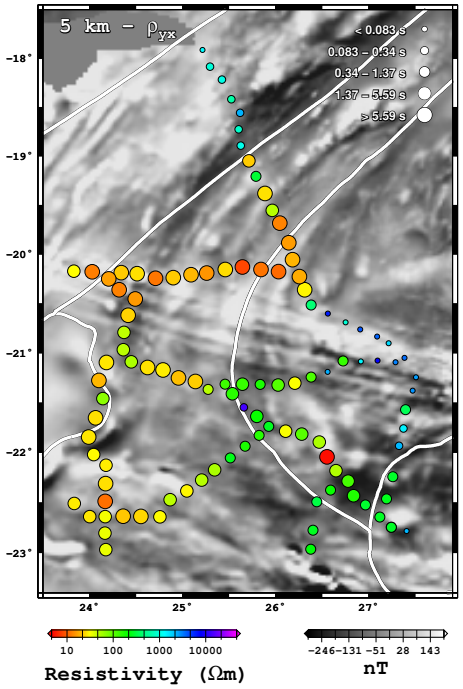

(b) Niblett-Bostick resistivities ρ_{yx}

Figure B.1: Niblett-Bostick resistivities ρ_{xy} (a) and ρ_{yx} (b) at 5 km depth. While the colour of the circles represents the Niblett-Bostick resistivity value at that depth, the size of the symbol indicates the period that is required to penetrate to this depth.

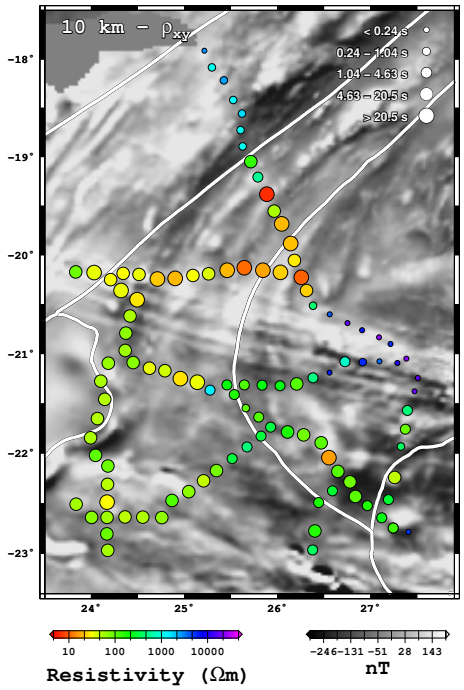

(a) Niblett-Bostick resistivities ρ_{xy}

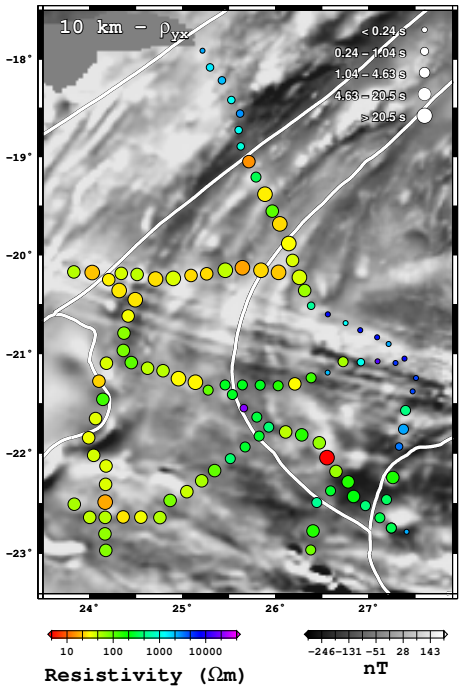

(b) Niblett-Bostick resistivities ρ_{yx}

Figure B.2: Niblett-Bostick resistivities ρ_{xy} (a) and ρ_{yx} (b) at 10 km depth. While the colour of the circles represents the Niblett-Bostick resistivity value at that depth, the size of the symbol indicates the period that is required to penetrate to this depth.

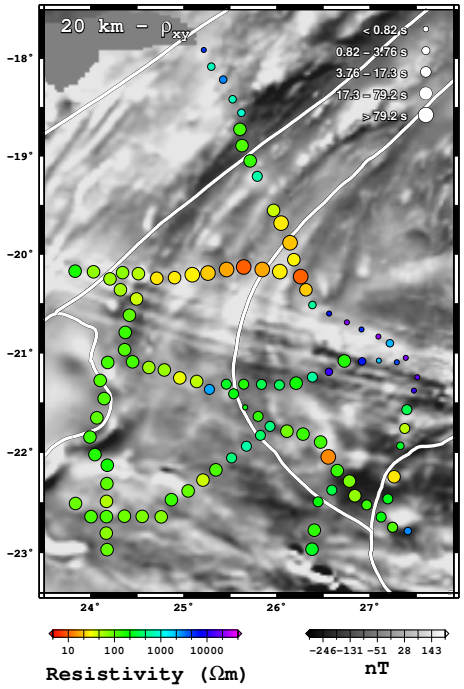

(a) Niblett-Bostick resistivities ρ_{xy}

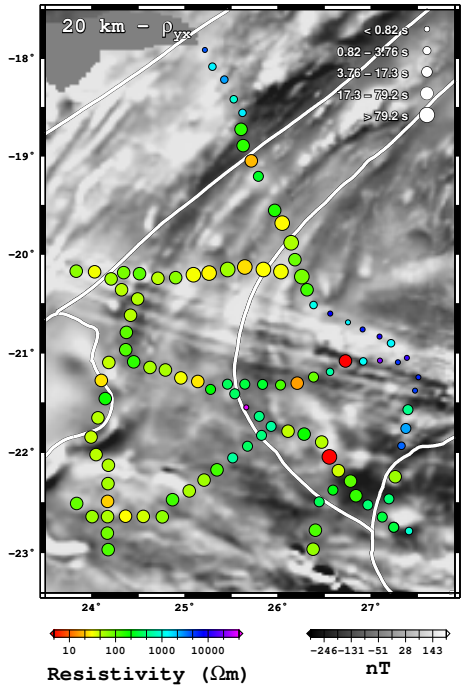

(b) Niblett-Bostick resistivities ρ_{yx}

Figure B.3: Niblett-Bostick resistivities ρ_{xy} (a) and ρ_{yx} (b) at 20 km depth. While the colour of the circles represents the Niblett-Bostick resistivity value at that depth, the size of the symbol indicates the period that is required to penetrate to this depth.

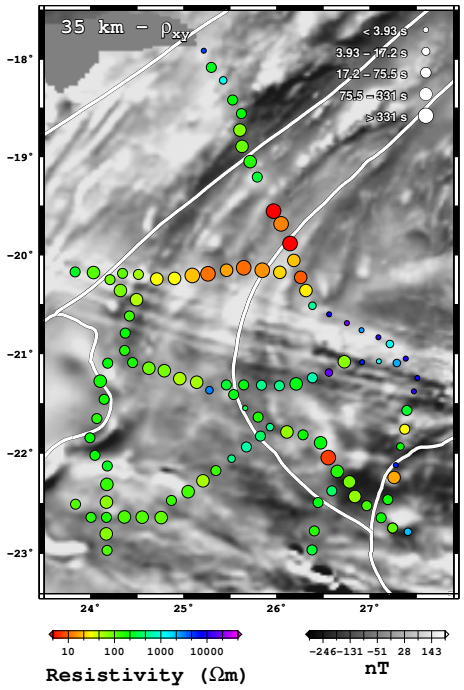

(a) Niblett-Bostick resistivities ρ_{xy}

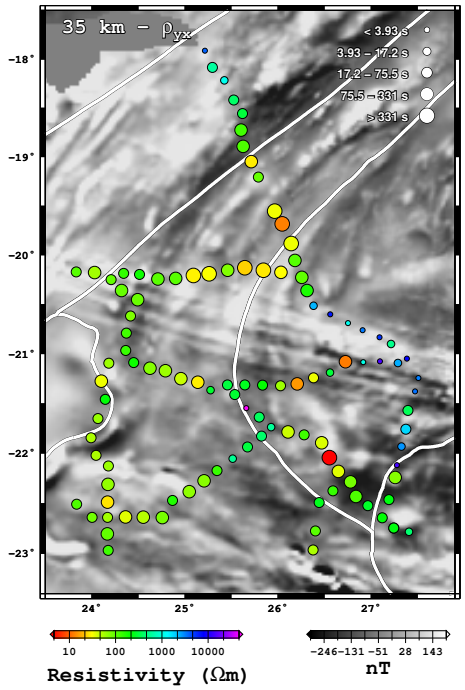

(b) Niblett-Bostick resistivities ρ_{yx}

Figure B.4: Niblett-Bostick resistivities ρ_{xy} (a) and ρ_{yx} (b) at 35 km depth. While the colour of the circles represents the Niblett-Bostick resistivity value at that depth, the size of the symbol indicates the period that is required to penetrate to this depth.

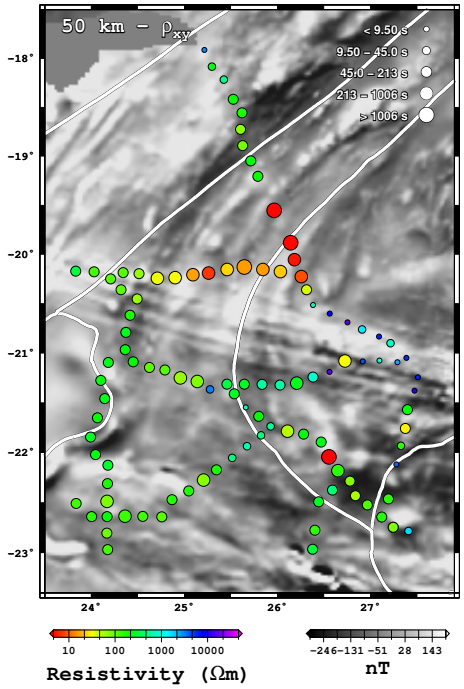

(a) Niblett-Bostick resistivities ρ_{xy}

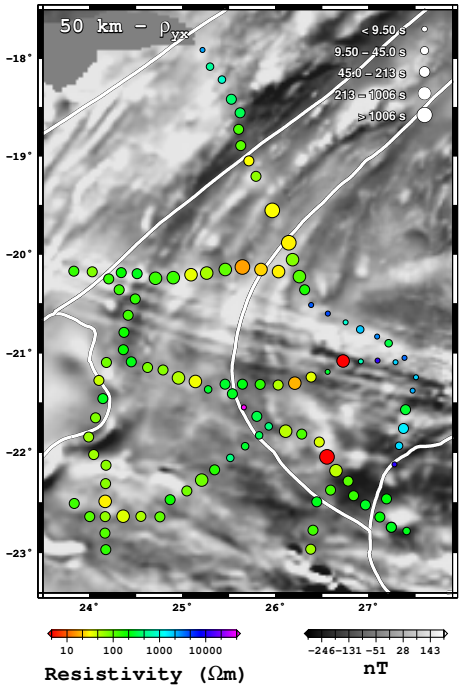

(b) Niblett-Bostick resistivities ρ_{yx}

Figure B.5: Niblett-Bostick resistivities ρ_{xy} (a) and ρ_{yx} (b) at 50 km depth. While the colour of the circles represents the Niblett-Bostick resistivity value at that depth, the size of the symbol indicates the period that is required to penetrate to this depth.

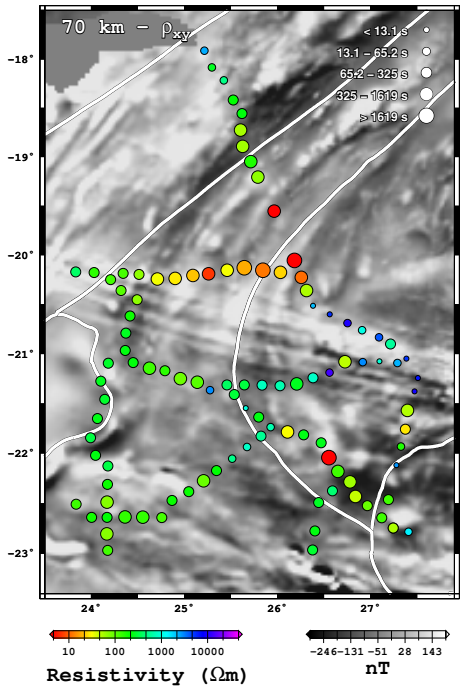

(a) Niblett-Bostick resistivities ρ_{xy}

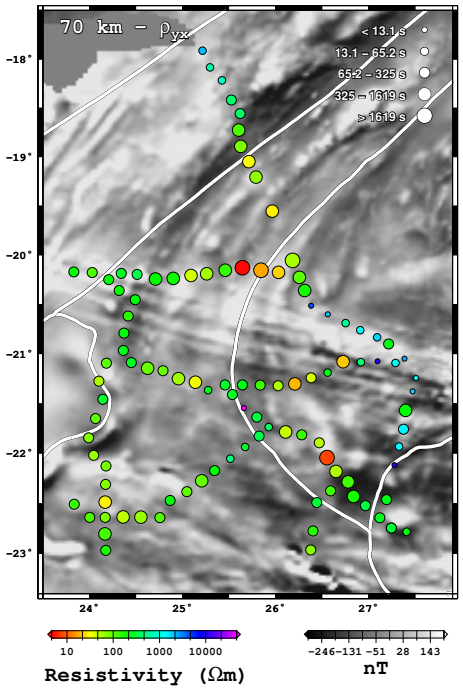

(b) Niblett-Bostick resistivities ρ_{yx}

Figure B.6: Niblett-Bostick resistivities ρ_{xy} (a) and ρ_{yx} (b) at 70 km depth. While the colour of the circles represents the Niblett-Bostick resistivity value at that depth, the size of the symbol indicates the period that is required to penetrate to this depth.

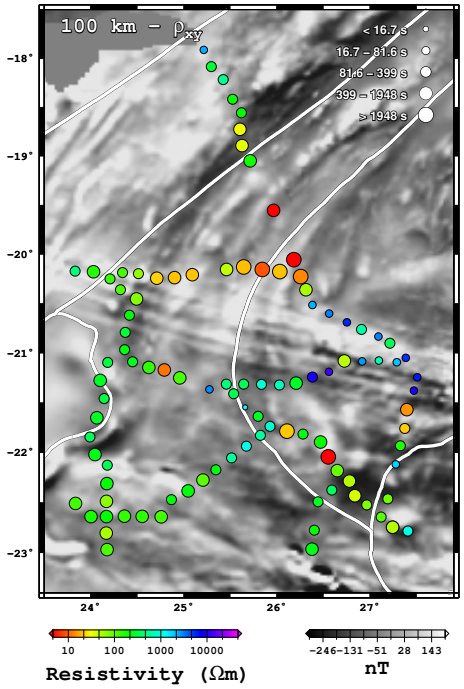

(a) Niblett-Bostick resistivities ρ_{xy}

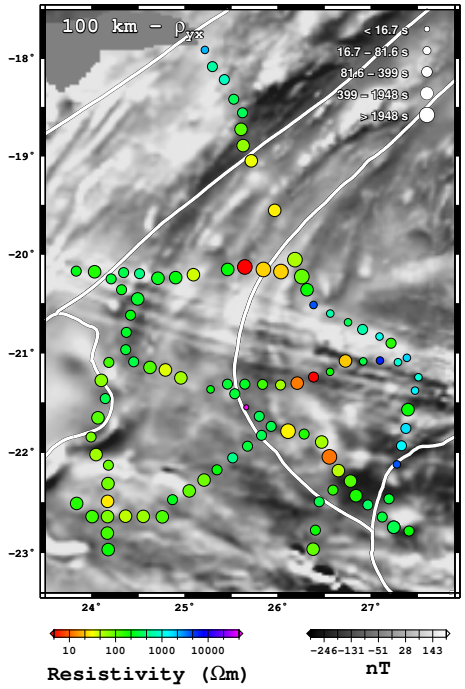

(b) Niblett-Bostick resistivities ρ_{yx}

Figure B.7: Niblett-Bostick resistivities ρ_{xy} (a) and ρ_{yx} (b) at 100 km depth. While the colour of the circles represents the Niblett-Bostick resistivity value at that depth, the size of the symbol indicates the period that is required to penetrate to this depth.

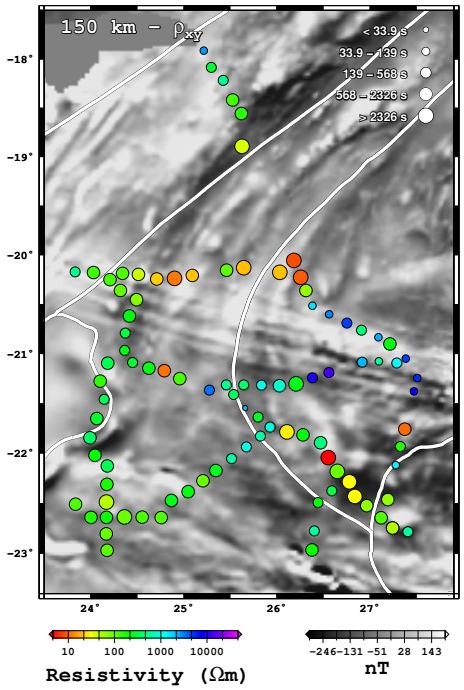

(a) Niblett-Bostick resistivities ρ_{xy}

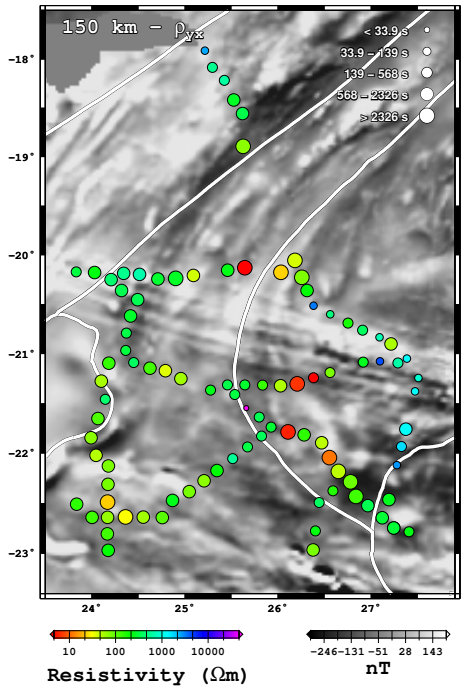

(b) Niblett-Bostick resistivities ρ_{yx}

Figure B.8: Niblett-Bostick resistivities ρ_{xy} (a) and ρ_{yx} (b) at 150 km depth. While the colour of the circles represents the Niblett-Bostick resistivity value at that depth, the size of the symbol indicates the period that is required to penetrate to this depth.

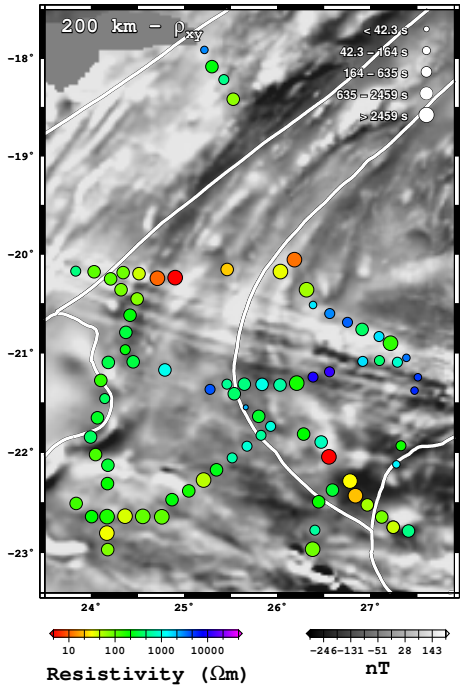

(a) Niblett-Bostick resistivities ρ_{xy}

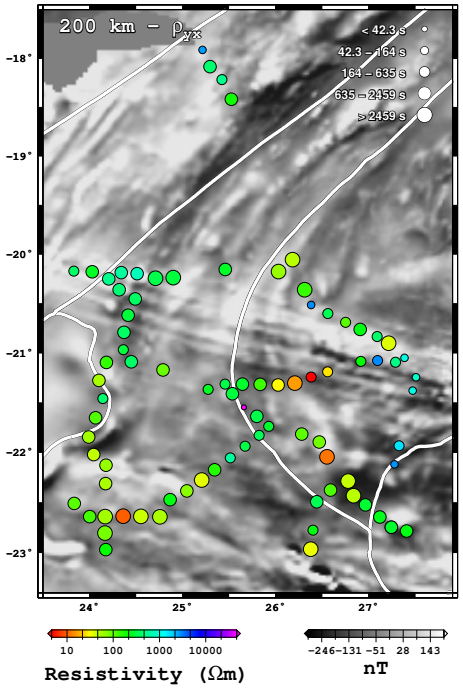

(b) Niblett-Bostick resistivities ρ_{yx}

Figure B.9: Niblett-Bostick resistivities ρ_{xy} (a) and ρ_{yx} (b) at 200 km depth. While the colour of the circles represents the Niblett-Bostick resistivity value at that depth, the size of the symbol indicates the period that is required to penetrate to this depth.

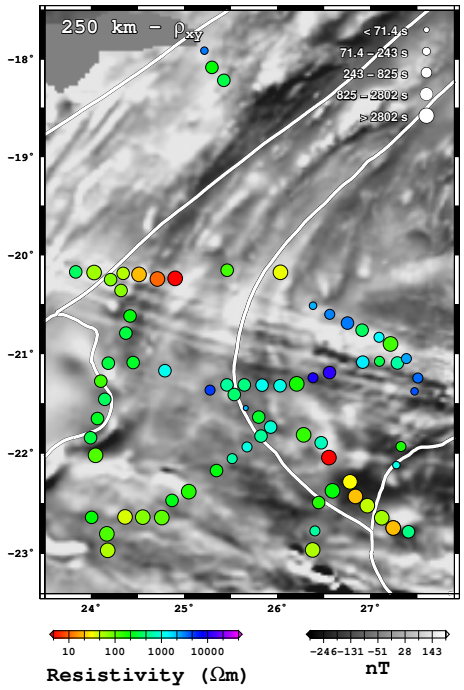

(a) Niblett-Bostick resistivities ρ_{xy}

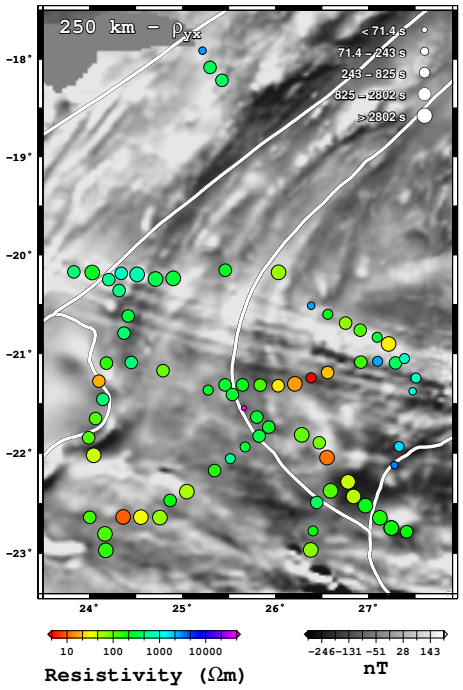

(b) Niblett-Bostick resistivities ρ_{yx}

Figure B.10: Niblett-Bostick resistivities ρ_{xy} (a) and ρ_{yx} (b) at 250 km depth. While the colour of the circles represents the Niblett-Bostick resistivity value at that depth, the size of the symbol indicates the period that is required to penetrate to this depth.

B.2 PHASE TENSOR MAPS FOR CRUSTAL AND LITHOSPHERIC DEPTHS

Phase tensor maps have been discussed in Section 4.1.3, but only representative plots for crustal (Figure 4.10) and lithospheric (Figure 4.11) depths were shown. Figures B.11 to B.20 show similar plots for a number of different depths: 5 km (Figure B.1), 10 km (Figure B.2), 20 km (Figure B.3) and 35 km (Figure B.4) all representing crustal depths and 50 km (Figure B.5), 70 km (Figure B.6), 100 km (Figure B.7) and 150 km (Figure B.8) are associated with lithospheric depths. At some sites the penetration depth is as large as 200 km (Figure B.9) or even 250 km (Figure B.10), which are most likely to reach down to the lithosphere-asthenosphere boundary or the asthenosphere.

The phase tensor ellipses are plotted with its axes being normalised by the major axis (Φ_{max}). The regional magnetic map (see Figure 3.10, magnetic data courtesy of the Council for Geoscience, Pretoria, South Africa) in grey scale is used as background and the colour of the ellipses is related to the skew angle β (a) and the minor axis Φ_{min} (b) respectively. A very small skew angle β is a possible indication of two-dimensionality in that area, whereas the large Φ_{min} for example indicates decreasing resistivities.

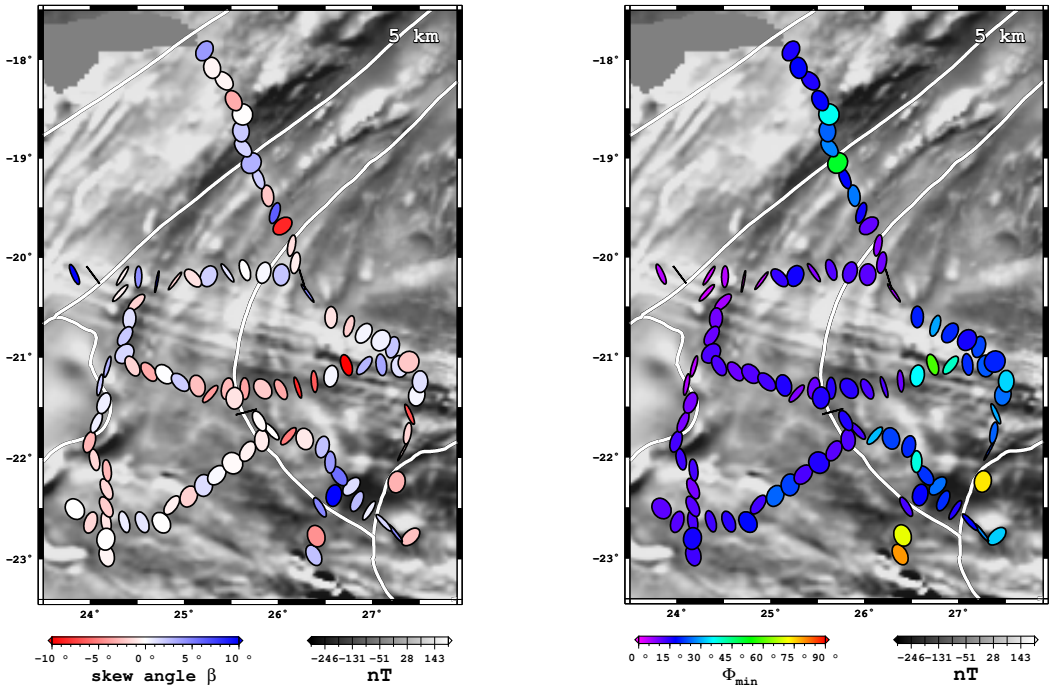

(a) Phase tensor ellipses coloured by skew angle β

(b) Phase tensor ellipses coloured by Φ_{min}

Figure B.11: Phase tensor maps at 5 km depth. The phase tensors are represented by ellipses (axes normalised by Φ_{max}) at each site. The colour of the ellipses indicates the skew angle β (a) and Φ_{min} (b) respectively.

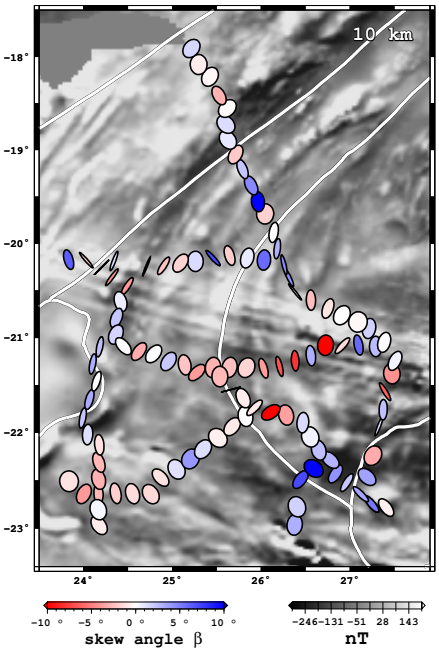

(a) Phase tensor ellipses coloured by skew angle β

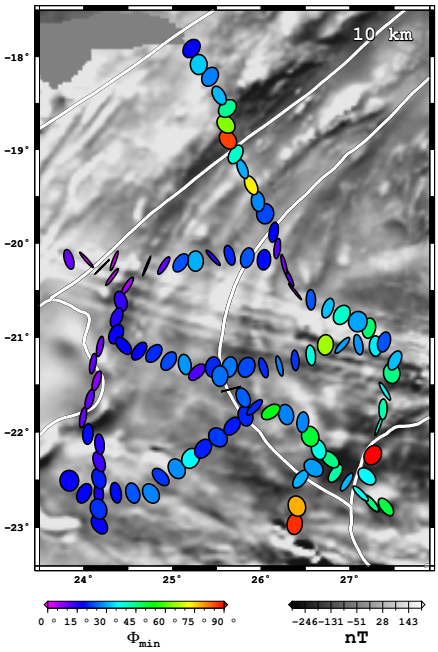

(b) Phase tensor ellipses coloured by Φ_{min}

Figure B.12: Phase tensor maps at 10 km depth. The phase tensors are represented by ellipses (axes normalised by Φ_{max}) at each site. The colour of the ellipses indicates the skew angle β (a) and Φ_{min} (b) respectively.

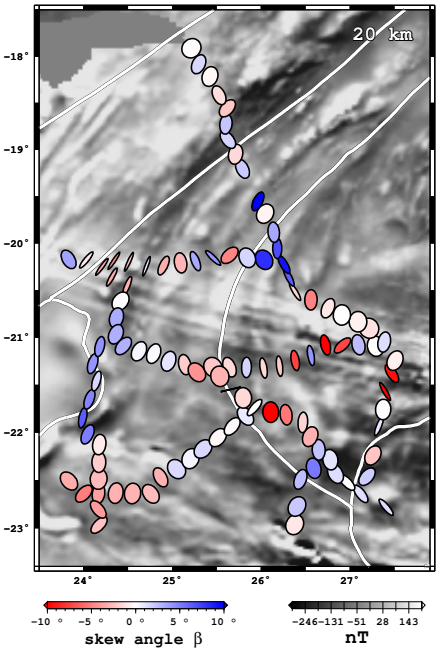

(a) Phase tensor ellipses coloured by skew angle β

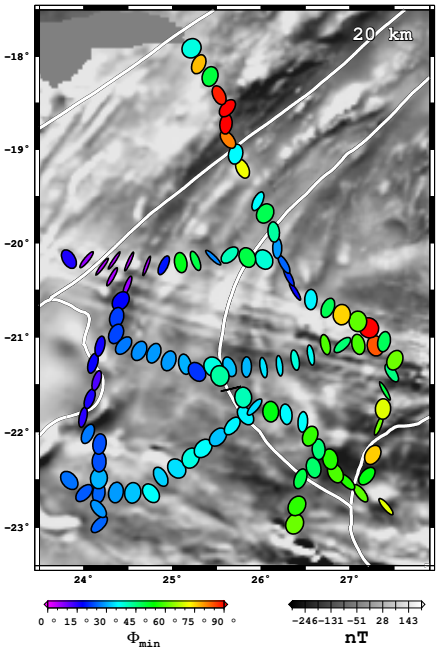

(b) Phase tensor ellipses coloured by Φ_{min}

Figure B.13: Phase tensor maps at 20 km depth. The phase tensors are represented by ellipses (axes normalised by Φ_{max}) at each site. The colour of the ellipses indicates the skew angle β (a) and Φ_{min} (b) respectively.

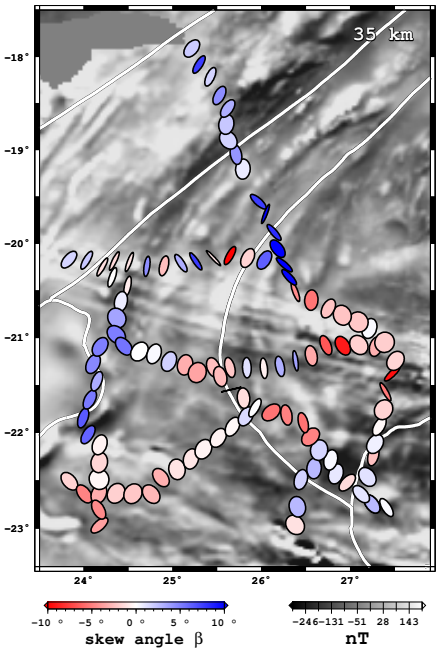

(a) Phase tensor ellipses coloured by skew angle β

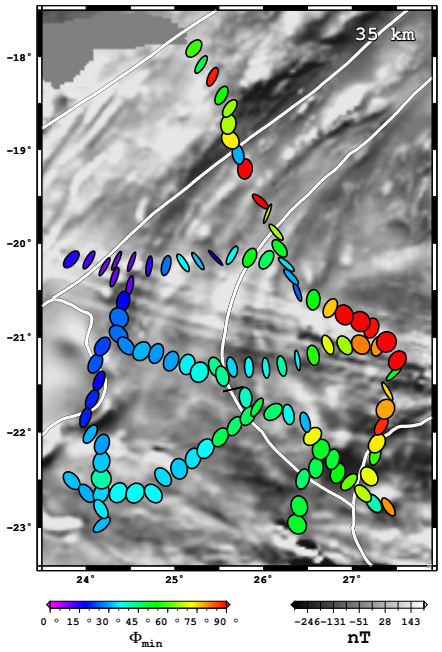

(b) Phase tensor ellipses coloured by Φ_{min}

Figure B.14: Phase tensor maps at 35 km depth. The phase tensors are represented by ellipses (axes normalised by Φ_{max}) at each site. The colour of the ellipses indicates the skew angle β (a) and Φ_{min} (b) respectively.

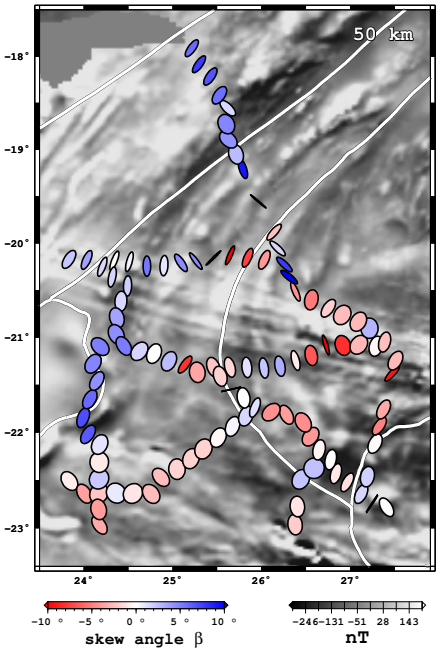

(a) Phase tensor ellipses coloured by skew angle β

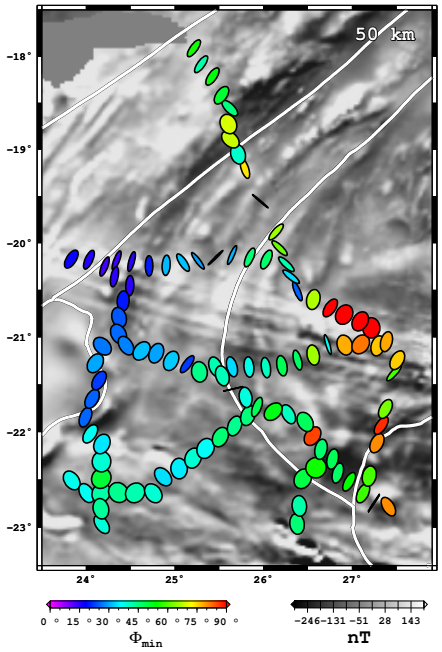

(b) Phase tensor ellipses coloured by Φ_{min}

Figure B.15: Phase tensor maps at 50 km depth. The phase tensors are represented by ellipses (axes normalised by Φ_{max}) at each site. The colour of the ellipses indicates the skew angle β (a) and Φ_{min} (b) respectively.

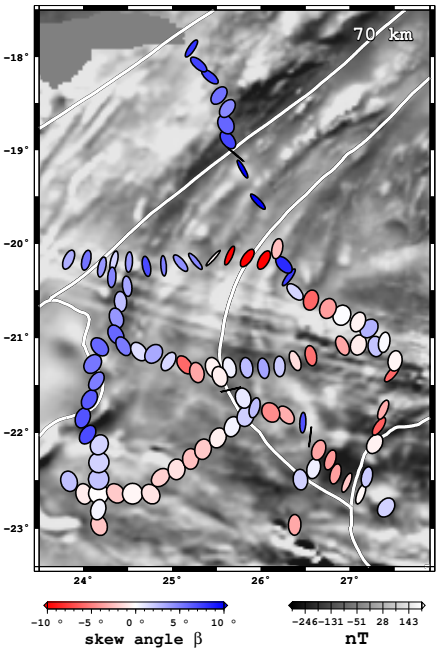

(a) Phase tensor ellipses coloured by skew angle β

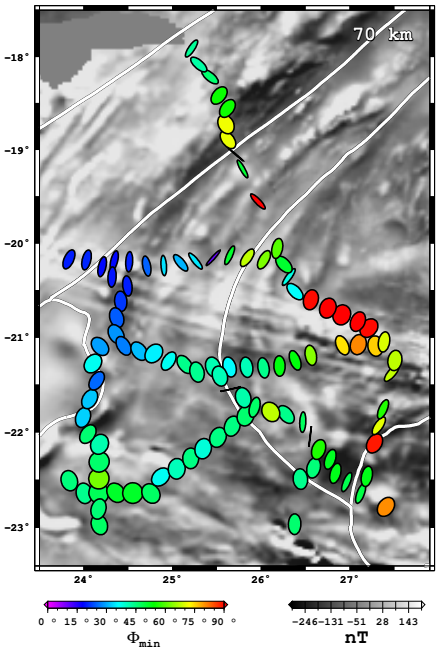

(b) Phase tensor ellipses coloured by Φ_{min}

Figure B.16: Phase tensor maps at 70 km depth. The phase tensors are represented by ellipses (axes normalised by Φ_{max}) at each site. The colour of the ellipses indicates the skew angle β (a) and Φ_{min} (b) respectively.

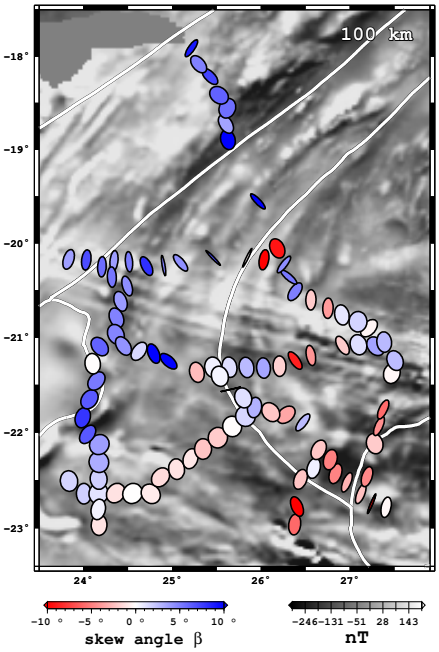

(a) Phase tensor ellipses coloured by skew angle β

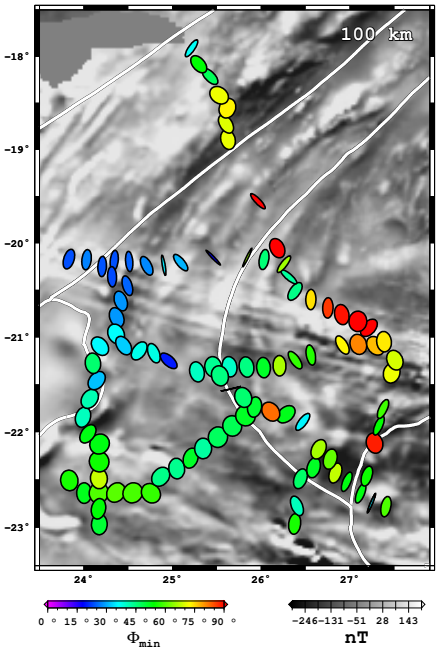

(b) Phase tensor ellipses coloured by Φ_{min}

Figure B.17: Phase tensor maps at 100 km depth. The phase tensors are represented by ellipses (axes normalised by Φ_{max}) at each site. The colour of the ellipses indicates the skew angle β (a) and Φ_{min} (b) respectively.

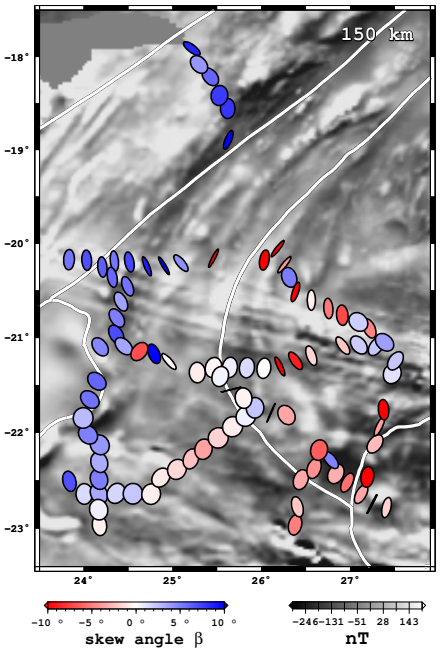

(a) Phase tensor ellipses coloured by skew angle β

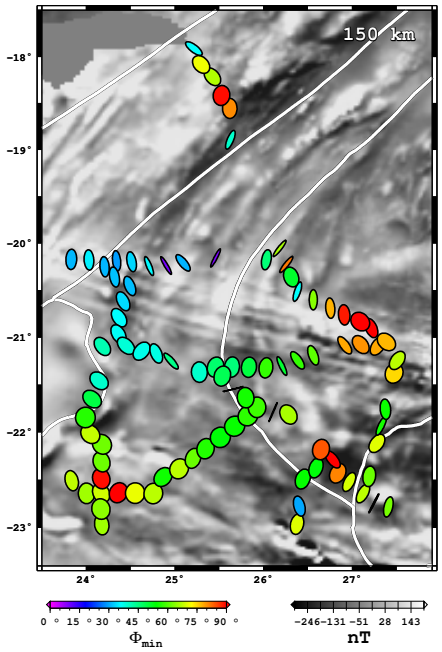

(b) Phase tensor ellipses coloured by Φ_{min}

Figure B.18: Phase tensor maps at 150 km depth. The phase tensors are represented by ellipses (axes normalised by Φ_{max}) at each site. The colour of the ellipses indicates the skew angle β (a) and Φ_{min} (b) respectively.

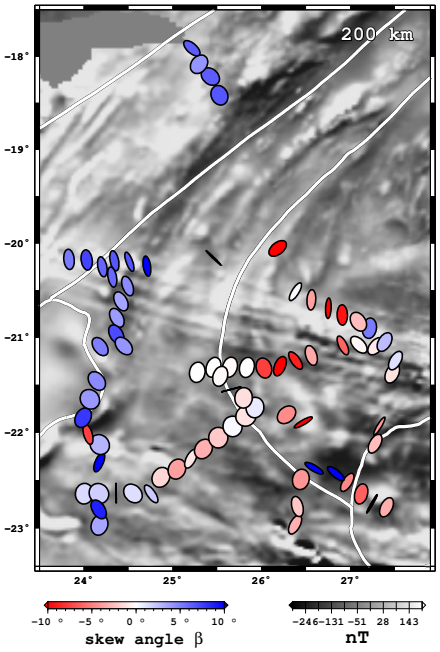

(a) Phase tensor ellipses coloured by skew angle β

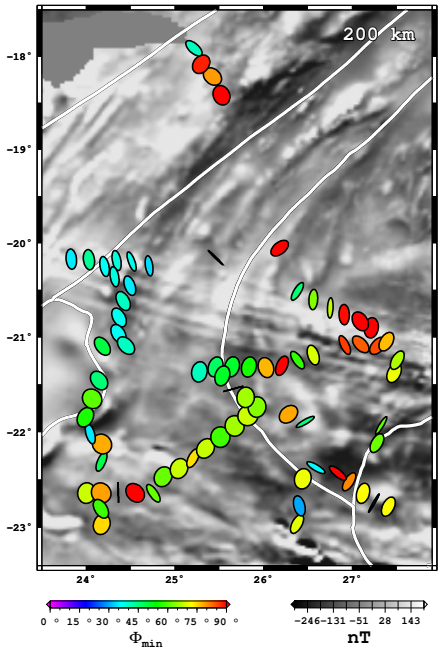

(b) Phase tensor ellipses coloured by Φ_{min}

Figure B.19: Phase tensor maps at 200 km depth. The phase tensors are represented by ellipses (axes normalised by Φ_{max}) at each site. The colour of the ellipses indicates the skew angle β (a) and Φ_{min} (b) respectively.

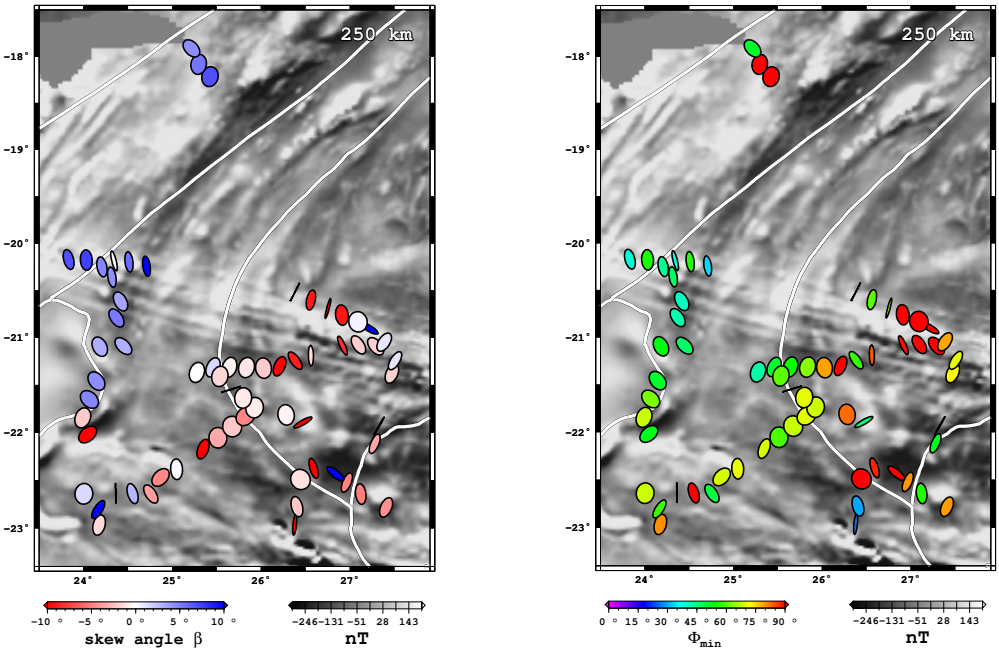

(a) Phase tensor ellipses coloured by skew angle β

(b) Phase tensor ellipses coloured by Φ_{min}

Figure B.20: Phase tensor maps at 250 km depth. The phase tensors are represented by ellipses (axes normalised by Φ_{max}) at each site. The colour of the ellipses indicates the skew angle β (a) and Φ_{min} (b) respectively.

B.3 ZIM LINE STRIKE ANALYSIS

As discussed in Section 4.2 the strike analysis is very much dependent on the chosen frequencies and sites. The following Figures B.21 to B.36 present for each site of the ZIM line the RMS values in dependence of the strike angle and the frequency band (selected via a depth range based on the Niblett-Bostick approach). For each site three frequency bands were selected; one band is related to crustal depths of 5 - 35 km, one represents the lithospheric depths from 50 to 150 km and the last band is over all existing frequencies. For each of the frequency bands the strike analysis and decomposition code STRIKE (see Section 2.9.2) was applied several times (in single site mode), each time enforcing a fixed strike angle from 0° to 90° in 1° intervals. For each frequency in the chosen range, the RMS is plotted versus the enforced strike angle, where the colour of the symbols represent the frequencies (red/warm colours are short periods and blue/cold colours are long periods). Additionally STRIKE was used to find a common strike angle over all frequencies in each band, which is represented as average strike by a red line. It is obvious that the average strike angles for the crust and the lithosphere independently are not necessarily close to the angle obtained over all frequencies. One can also see that (some or all bands of) some sites accept nearly all strike angles without a major increase in RMS value (e.g., ZIM103, ZIM111).

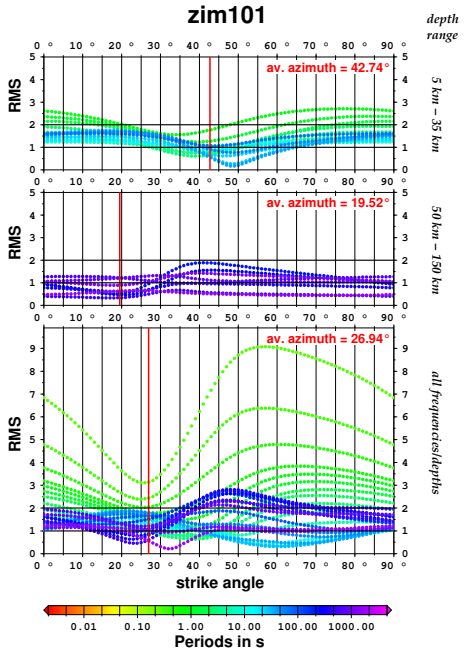

Figure B.21: Figure showing the different RMS values for strike angles from 0° - 90° for the site ZIM101. The RMS values for the whole azimuth range are plotted for three different depth/frequency ranges: crustal depth (5-35 km), lithospheric depth (50-150 km) and over the whole frequency range. The colour coding is related to the frequencies. The red line indicates the strike direction one would obtain performing a normal strike analysis for the same frequency/depth range.

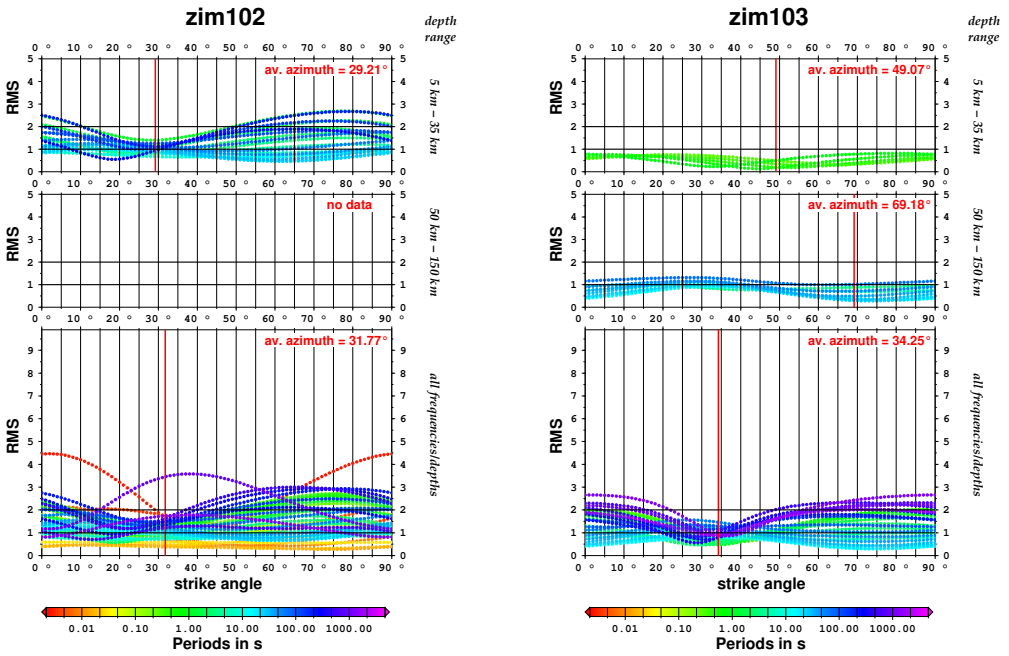

Figure B.22: Figure showing the different RMS values for strike angles from 0°-90° for the sites ZIM102 and ZIM103. The RMS values for the whole azimuth range are plotted for three different depth/frequency ranges: crustal depth (5-35 km), lithospheric depth (50-150 km) and over the whole frequency range. The colour coding is related to the frequencies. The red line indicates the strike direction one would obtain performing a normal strike analysis for the same frequency/depth range.

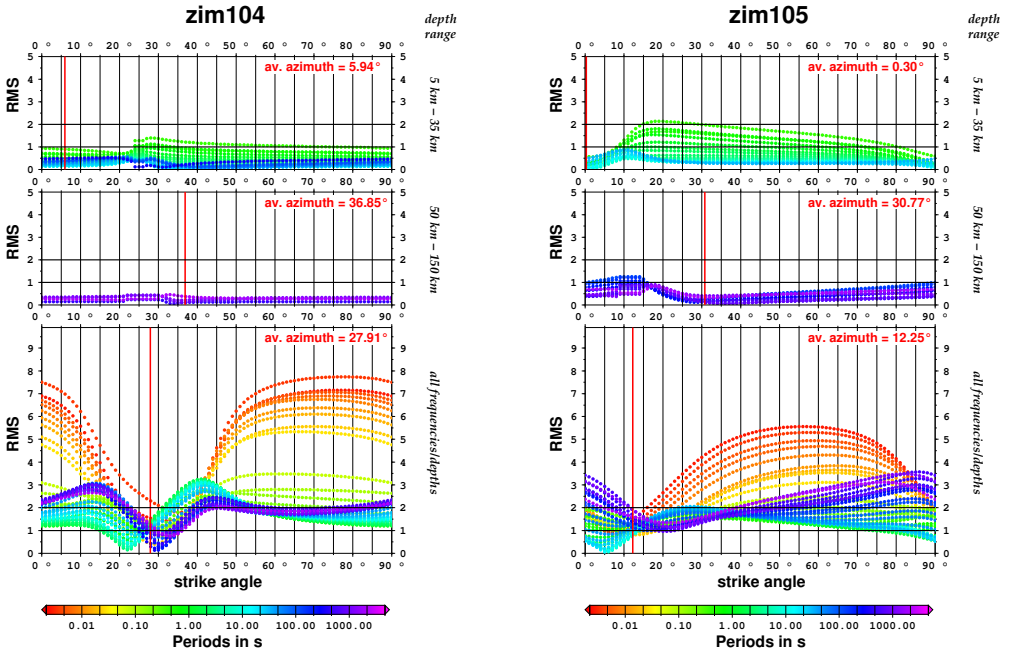

Figure B.23: Figure showing the different RMS values for strike angles from 0°-90° for the sites ZIM104 and ZIM105. The RMS values for the whole azimuth range are plotted for three different depth/frequency ranges: crustal depth (5-35 km), lithospheric depth (50-150 km) and over the whole frequency range. The colour coding is related to the frequencies. The red line indicates the strike direction one would obtain performing a normal strike analysis for the same frequency/depth range.

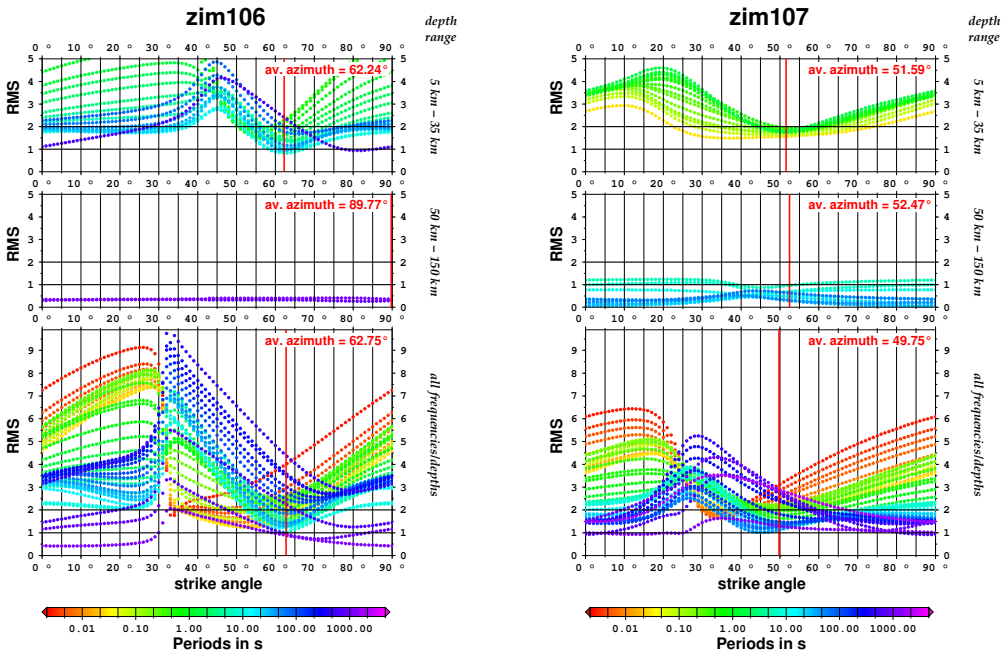

Figure B.24: Figure showing the different RMS values for strike angles from 0° - 90° for the sites ZIM106 and ZIM107. The RMS values for the whole azimuth range are plotted for three different depth/frequency ranges: crustal depth (5-35 km), lithospheric depth (50-150 km) and over the whole frequency range. The colour coding is related to the frequencies. The red line indicates the strike direction one would obtain performing a normal strike analysis for the same frequency/depth range.

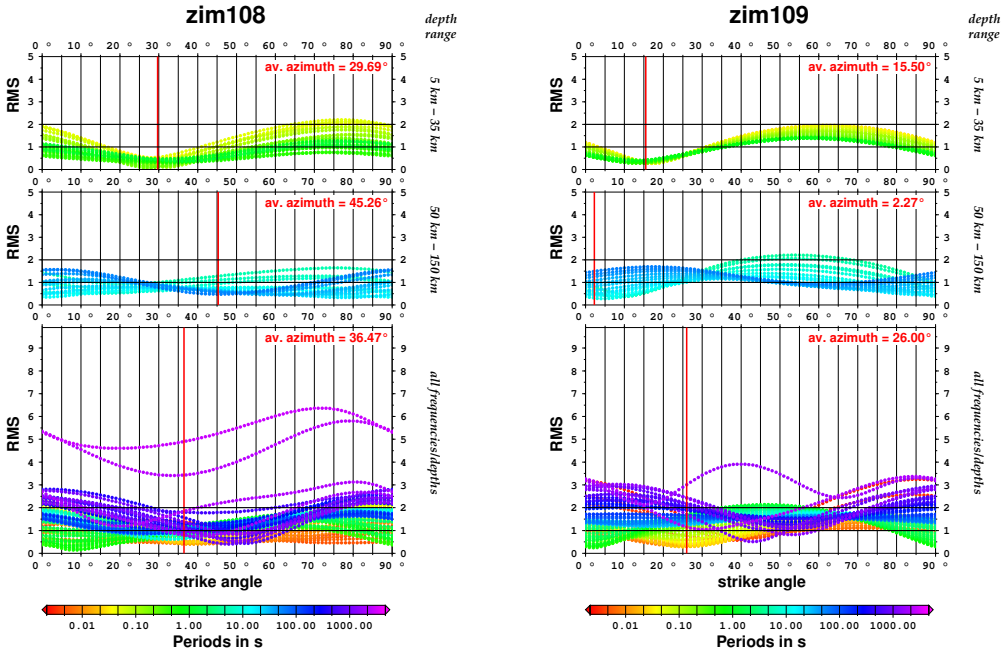

Figure B.25: Figure showing the different RMS values for strike angles from 0° - 90° for the sites ZIM108 and ZIM109. The RMS values for the whole azimuth range are plotted for three different depth/frequency ranges: crustal depth (5-35 km), lithospheric depth (50-150 km) and over the whole frequency range. The colour coding is related to the frequencies. The red line indicates the strike direction one would obtain performing a normal strike analysis for the same frequency/depth range.

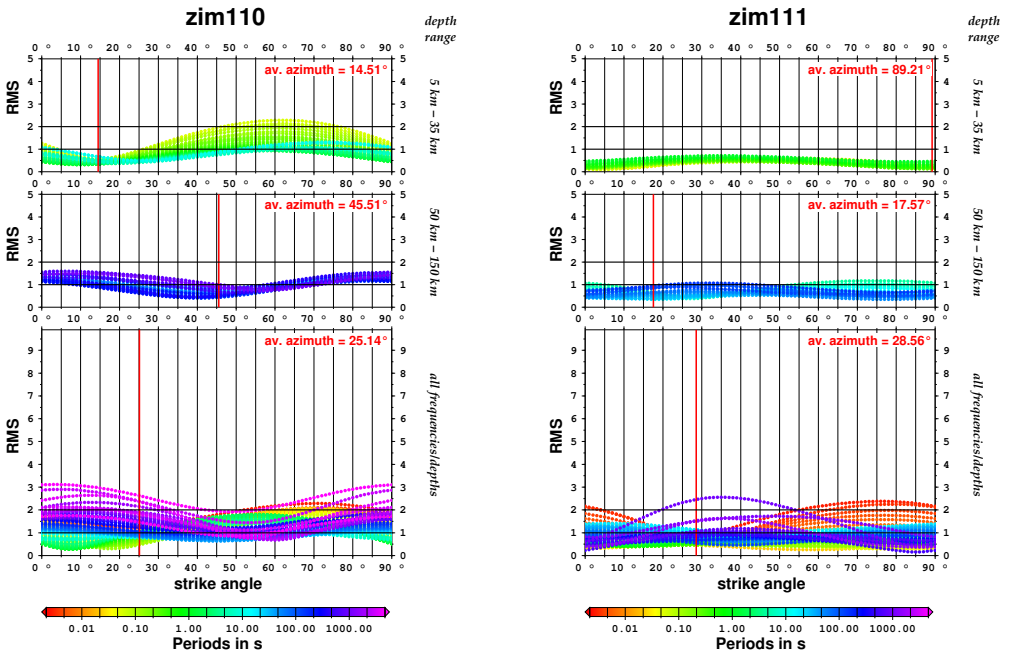

Figure B.26: Figure showing the different RMS values for strike angles from 0°-90° for the sites ZIM110 and ZIM111. The RMS values for the whole azimuth range are plotted for three different depth/frequency ranges: crustal depth (5-35 km), lithospheric depth (50-150 km) and over the whole frequency range. The colour coding is related to the frequencies. The red line indicates the strike direction one would obtain performing a normal strike analysis for the same frequency/depth range.

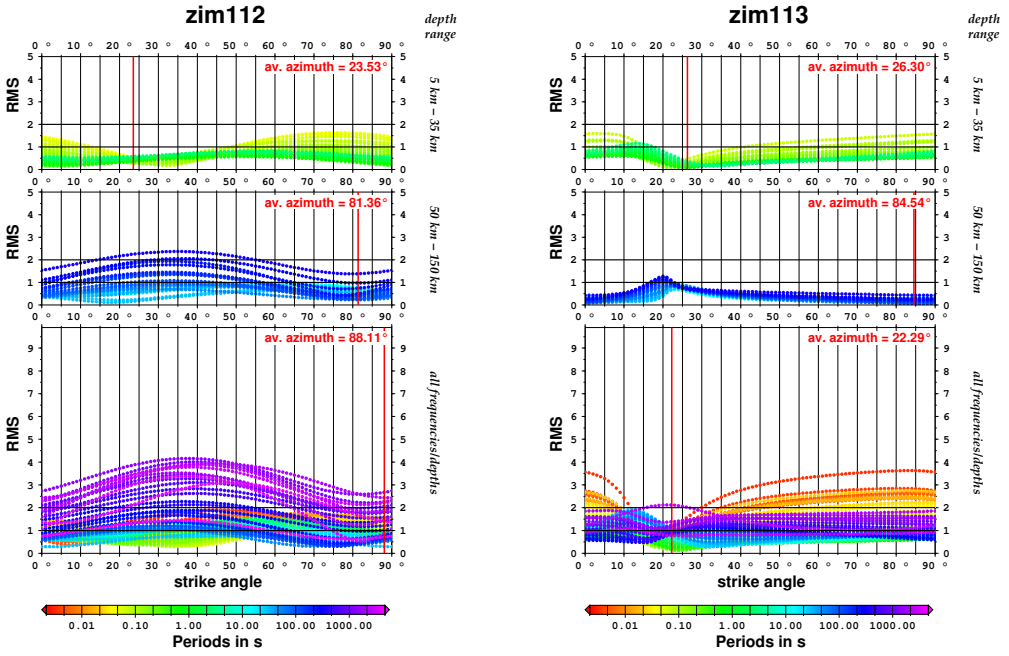

Figure B.27: Figure showing the different RMS values for strike angles from 0°-90° for the sites ZIM112 and ZIM113. The RMS values for the whole azimuth range are plotted for three different depth/frequency ranges: crustal depth (5-35 km), lithospheric depth (50-150 km) and over the whole frequency range. The colour coding is related to the frequencies. The red line indicates the strike direction one would obtain performing a normal strike analysis for the same frequency/depth range.

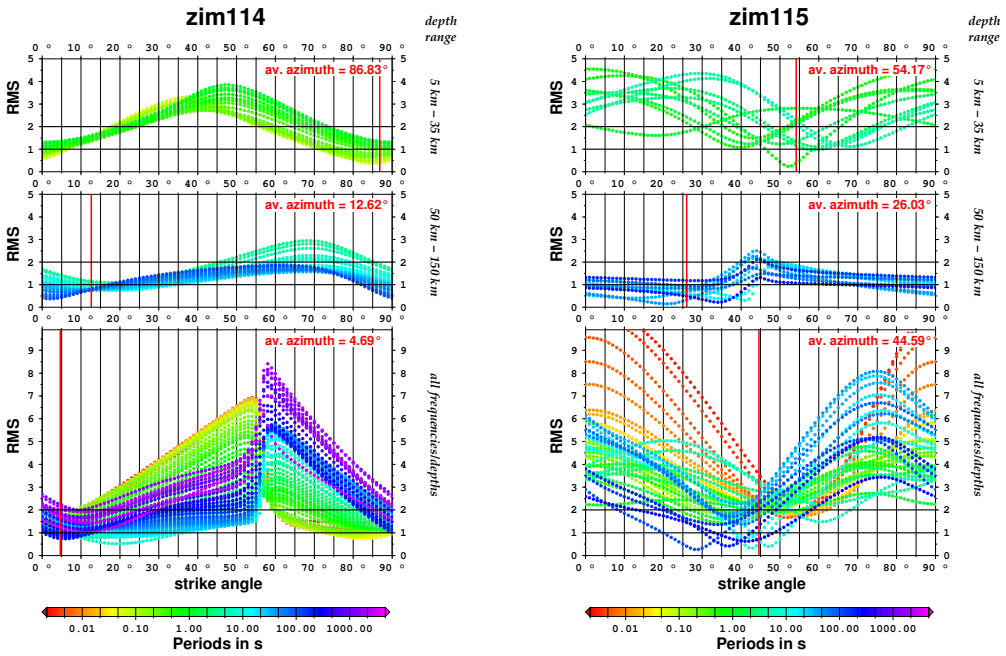

Figure B.28: Figure showing the different RMS values for strike angles from 0° - 90° for the sites ZIM114 and ZIM115. The RMS values for the whole azimuth range are plotted for three different depth/frequency ranges: crustal depth (5-35 km), lithospheric depth (50-150 km) and over the whole frequency range. The colour coding is related to the frequencies. The red line indicates the strike direction one would obtain performing a normal strike analysis for the same frequency/depth range.

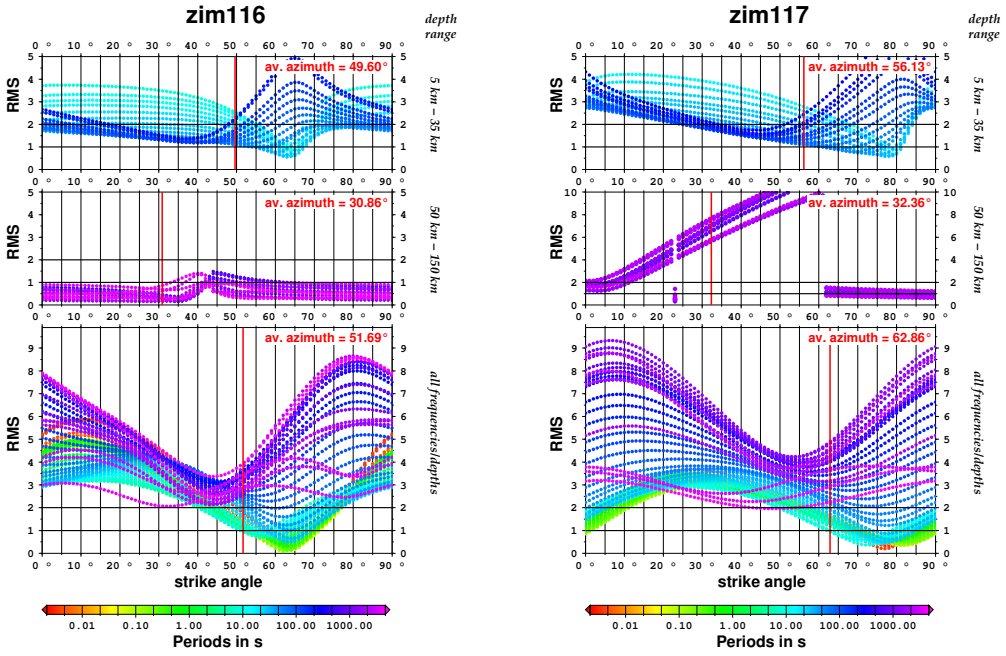

Figure B.29: Figure showing the different RMS values for strike angles from 0° - 90° for the sites ZIM116 and ZIM117. The RMS values for the whole azimuth range are plotted for three different depth/frequency ranges: crustal depth (5-35 km), lithospheric depth (50-150 km) and over the whole frequency range. The colour coding is related to the frequencies. The red line indicates the strike direction one would obtain performing a normal strike analysis for the same frequency/depth range.

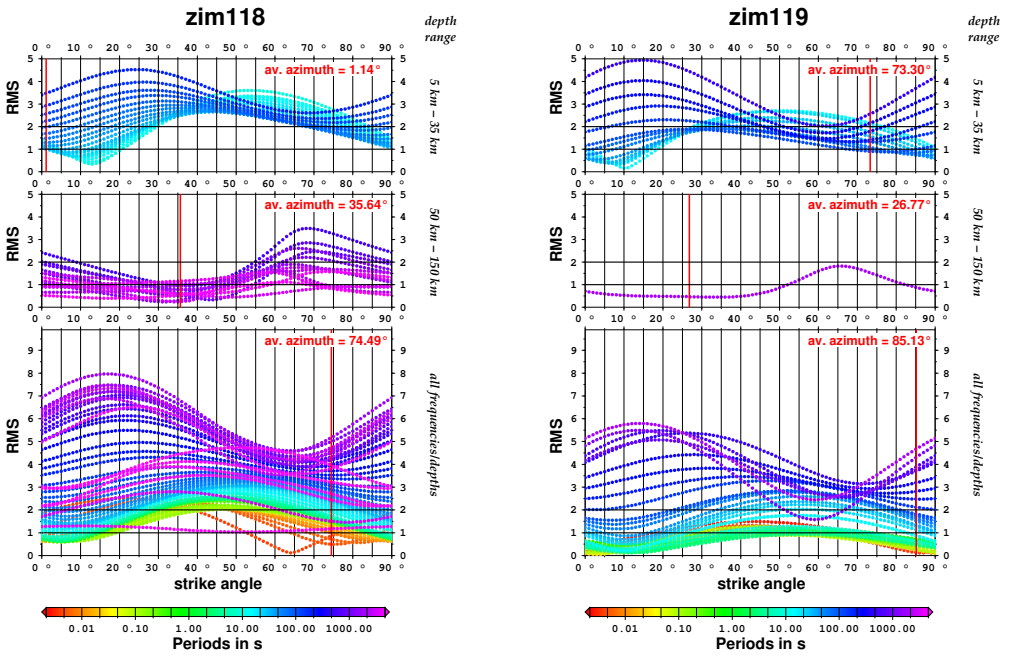

Figure B.30: Figure showing the different RMS values for strike angles from 0° - 90° for the sites ZIM118 and ZIM119. The RMS values for the whole azimuth range are plotted for three different depth/frequency ranges: crustal depth (5-35 km), lithospheric depth (50-150 km) and over the whole frequency range. The colour coding is related to the frequencies. The red line indicates the strike direction one would obtain performing a normal strike analysis for the same frequency/depth range.

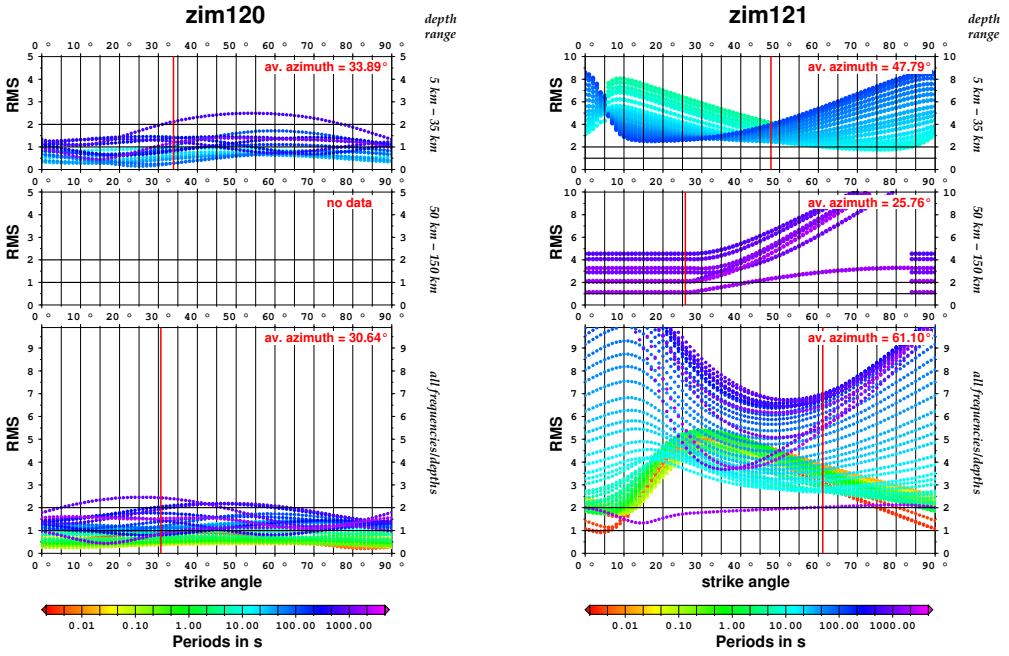

Figure B.31: Figure showing the different RMS values for strike angles from 0° - 90° for the sites ZIM120 and ZIM121. The RMS values for the whole azimuth range are plotted for three different depth/frequency ranges: crustal depth (5-35 km), lithospheric depth (50-150 km) and over the whole frequency range. The colour coding is related to the frequencies. The red line indicates the strike direction one would obtain performing a normal strike analysis for the same frequency/depth range.

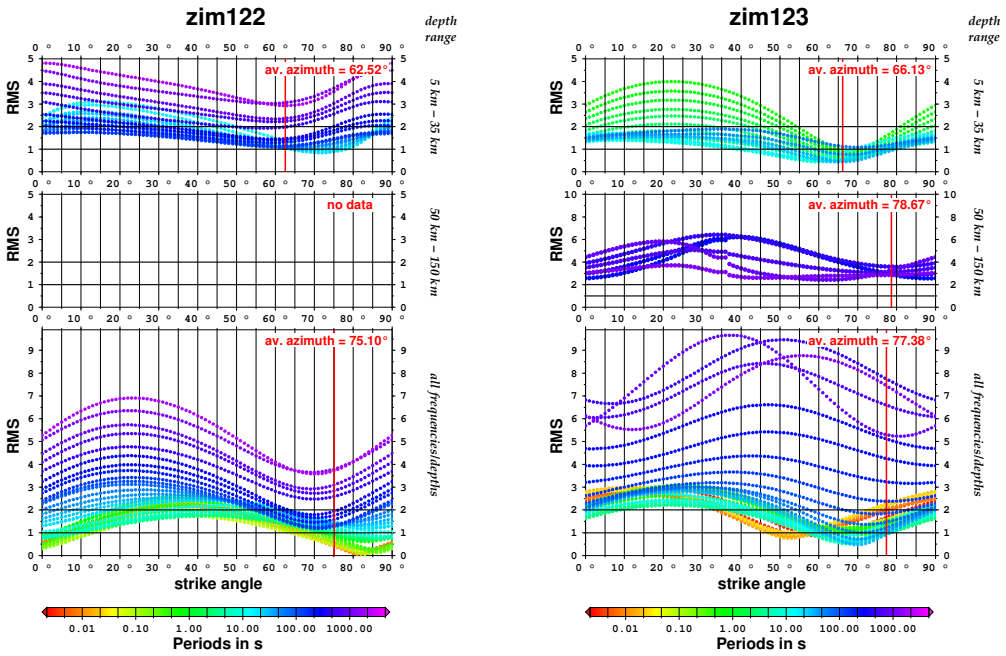

Figure B.32: Figure showing the different RMS values for strike angles from 0° - 90° for the sites ZIM122 and ZIM123. The RMS values for the whole azimuth range are plotted for three different depth/frequency ranges: crustal depth (5-35 km), lithospheric depth (50-150 km) and over the whole frequency range. The colour coding is related to the frequencies. The red line indicates the strike direction one would obtain performing a normal strike analysis for the same frequency/depth range.

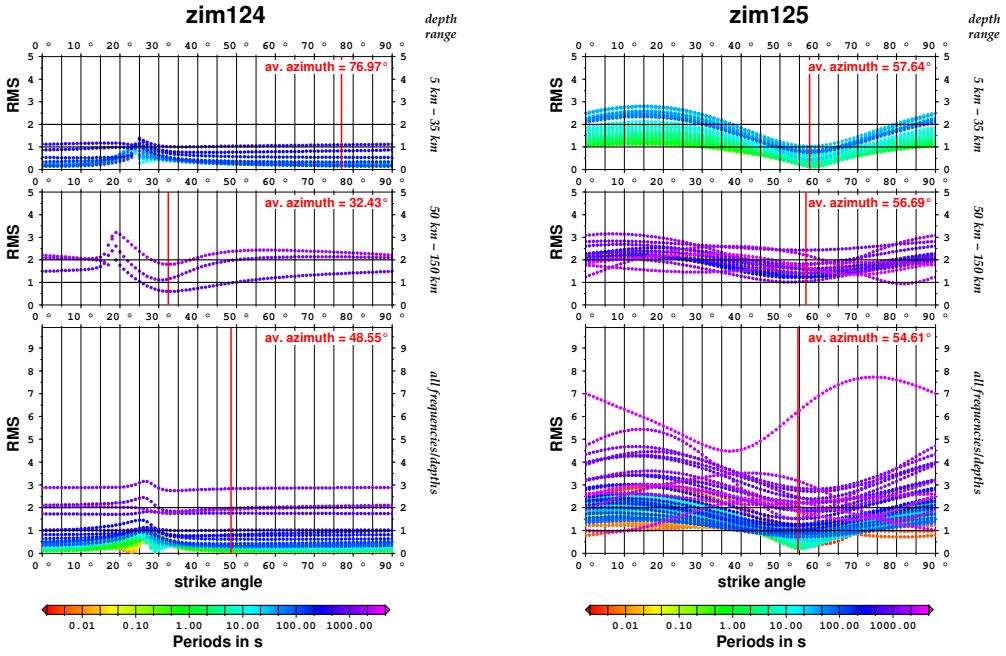

Figure B.33: Figure showing the different RMS values for strike angles from 0° - 90° for the sites ZIM124 and ZIM125. The RMS values for the whole azimuth range are plotted for three different depth/frequency ranges: crustal depth (5-35 km), lithospheric depth (50-150 km) and over the whole frequency range. The colour coding is related to the frequencies. The red line indicates the strike direction one would obtain performing a normal strike analysis for the same frequency/depth range.

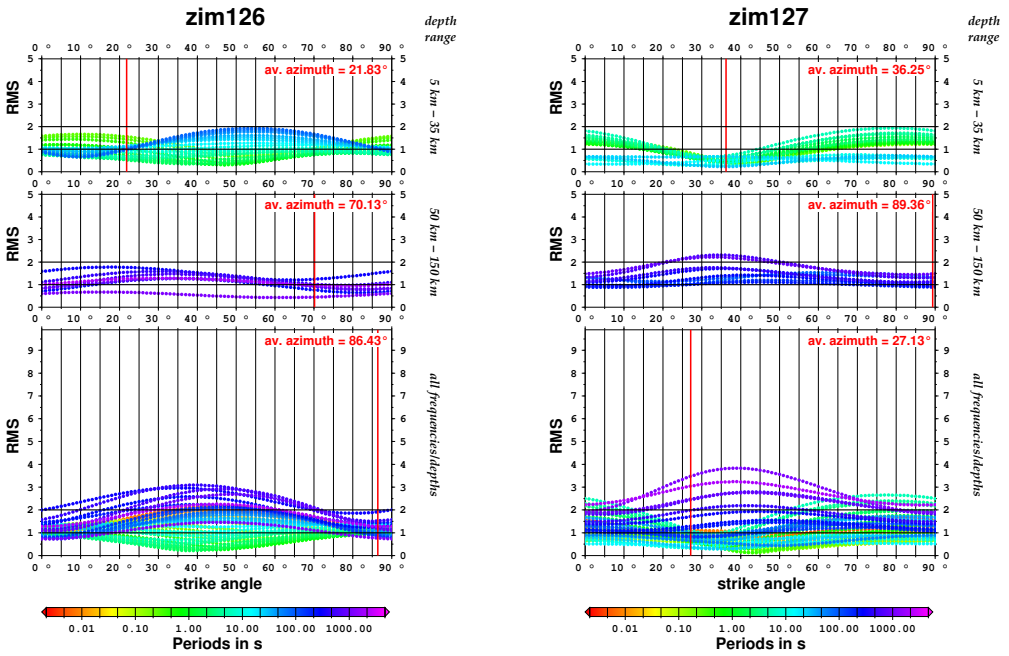

Figure B.34: Figure showing the different RMS values for strike angles from 0° - 90° for the sites ZIM126 and ZIM127. The RMS values for the whole azimuth range are plotted for three different depth/frequency ranges: crustal depth (5-35 km), lithospheric depth (50-150 km) and over the whole frequency range. The colour coding is related to the frequencies. The red line indicates the strike direction one would obtain performing a normal strike analysis for the same frequency/depth range.

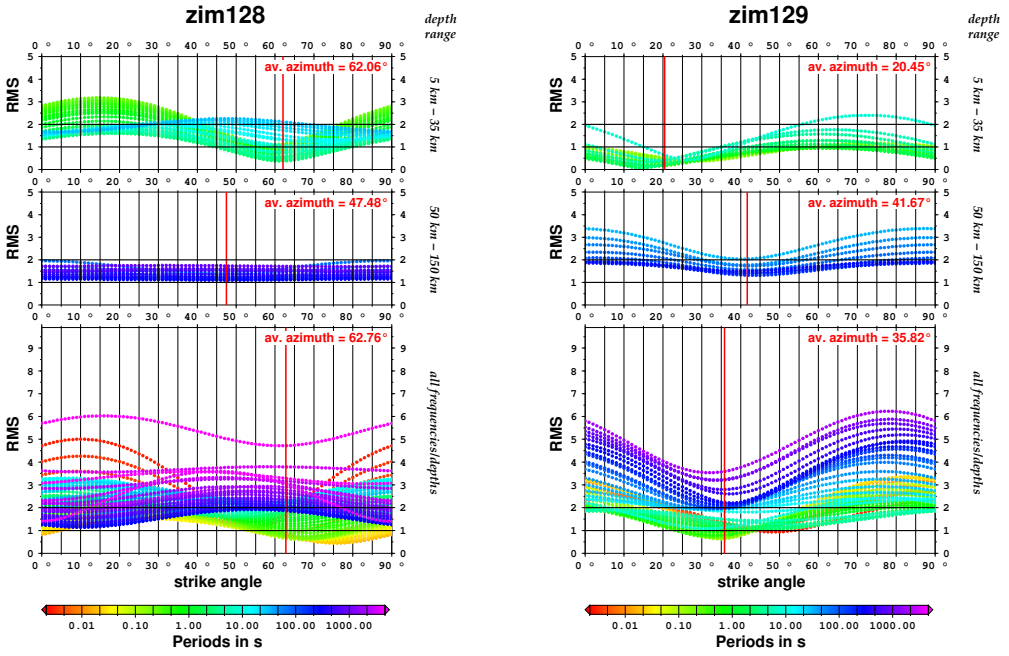

Figure B.35: Figure showing the different RMS values for strike angles from 0° - 90° for the sites ZIM128 and ZIM129. The RMS values for the whole azimuth range are plotted for three different depth/frequency ranges: crustal depth (5-35 km), lithospheric depth (50-150 km) and over the whole frequency range. The colour coding is related to the frequencies. The red line indicates the strike direction one would obtain performing a normal strike analysis for the same frequency/depth range.

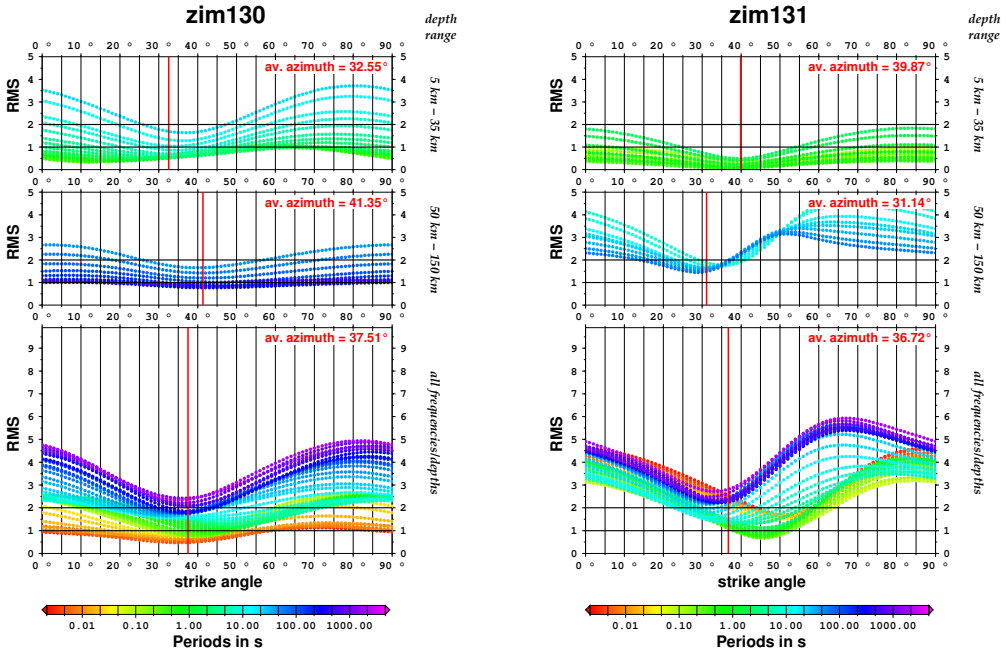

Figure B.36: Figure showing the different RMS values for strike angles from 0° - 90° for the sites ZIM130 and ZIM131. The RMS values for the whole azimuth range are plotted for three different depth/frequency ranges: crustal depth (5-35 km), lithospheric depth (50-150 km) and over the whole frequency range. The colour coding is related to the frequencies. The red line indicates the strike direction one would obtain performing a normal strike analysis for the same frequency/depth range.

C

ZIM LINE DATA, 2D INVERSION RESULTS AND MODELS

This appendix belongs to Chapter 5 and shows additional response curves and 2D resistivity models for the northern crustal part of the ZIM profile, the whole ZIM profile and the synthetic anisotropic models that complement the figures shown in Chapter 5.

C.1 CRUSTAL, NORTHERN PART OF THE ZIM LINE

In Section 5.2 the northern crustal part of the ZIM line was investigated using the appropriate strike direction of 55° E of N for this data set. The data set was reduced to sites ZIM118 to ZIM131 and to periods with Niblett-Bostick penetration depths of 40 km and less. The black dots in Figures C.1 and C.2 represent the used observed data. For the 2D inversion in WinGLink® three different weighting function settings were used (see Section 5.2 for more details) and the model responses resulting from these three inversions are shown in Figures C.1 and C.2 in comparison to the observed data (coloured lines).

To justify certain feature in the inversion model, five different manipulated version of the final inversion model were used to invert the data again trying to find the closest model to the starting model (the manipulated model). Figures C.3 to C.7 show in each case the manipulated starting model in (a) and below the obtained inversion models using the three different weighting function setting in (b), (c) and (d). Figure C.3 show the model where all conductors have been removed, while the model in Figure C.4 only contains the conductors, whereas the resistors have been removed. (The near-surface conductor associated with the brine aquifer is shown enlarged.) The model in Figure C.5 contains all major conductors and resistors but their shapes have been smoothed. Figures C.6 and C.7 are models where tear zones of different shapes are applied to a smoothed model of the major structures. In general, all the original observed structures recur in all these inversion test and therefore can be assumed to be reliable.

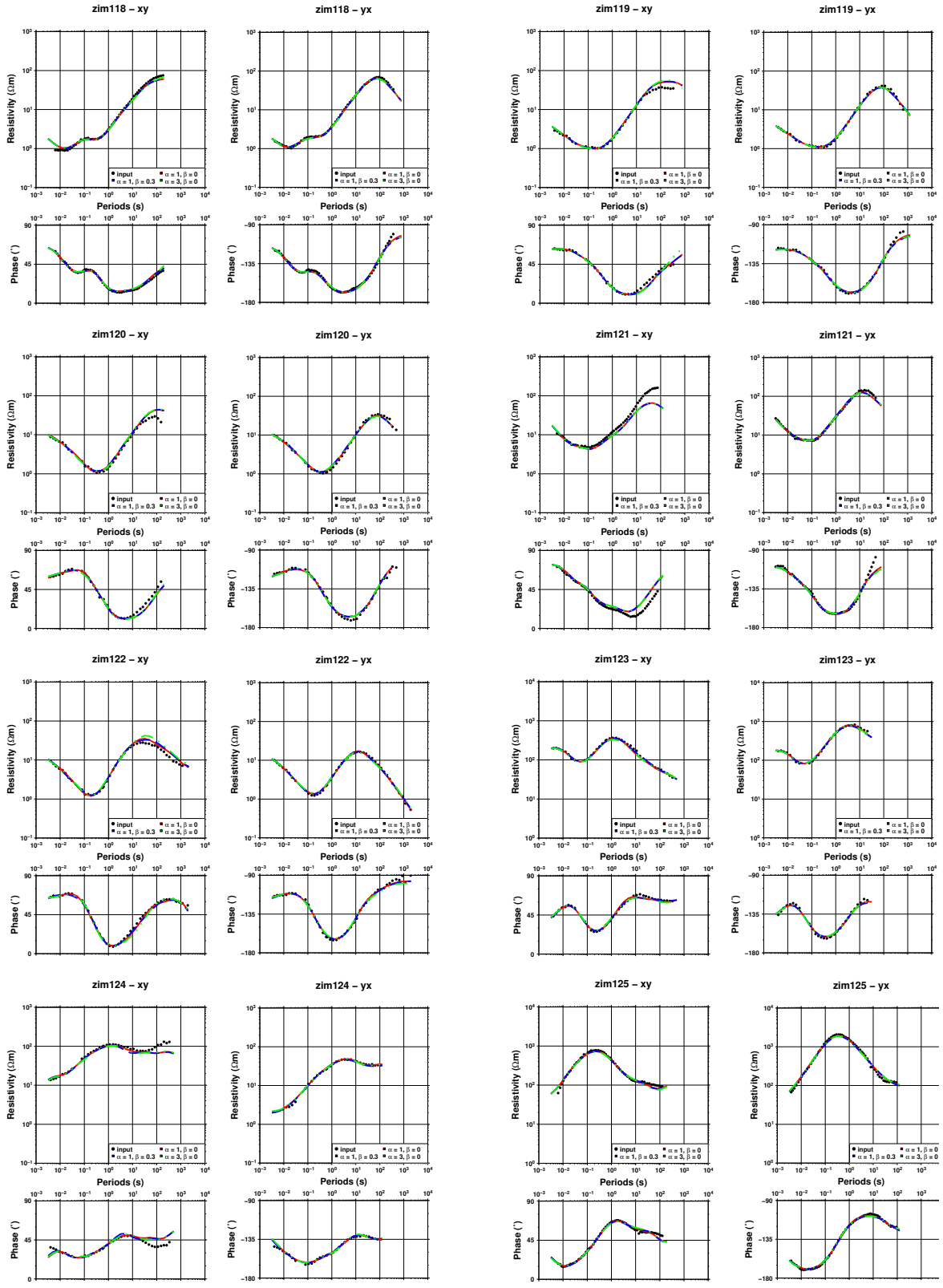

Figure C.1: This figure shows the responses curves of sites ZIM118 to ZIM125 of the crustal data set for a strike direction of 55° E of N. The resistivity curves are shown on top and below are the phase curves for each site. The symbols represent the observed data, and the coloured lines represent the response curves of the three inversion models obtained using different weighting function settings (see Figure 5.2; note colour coding is the same).

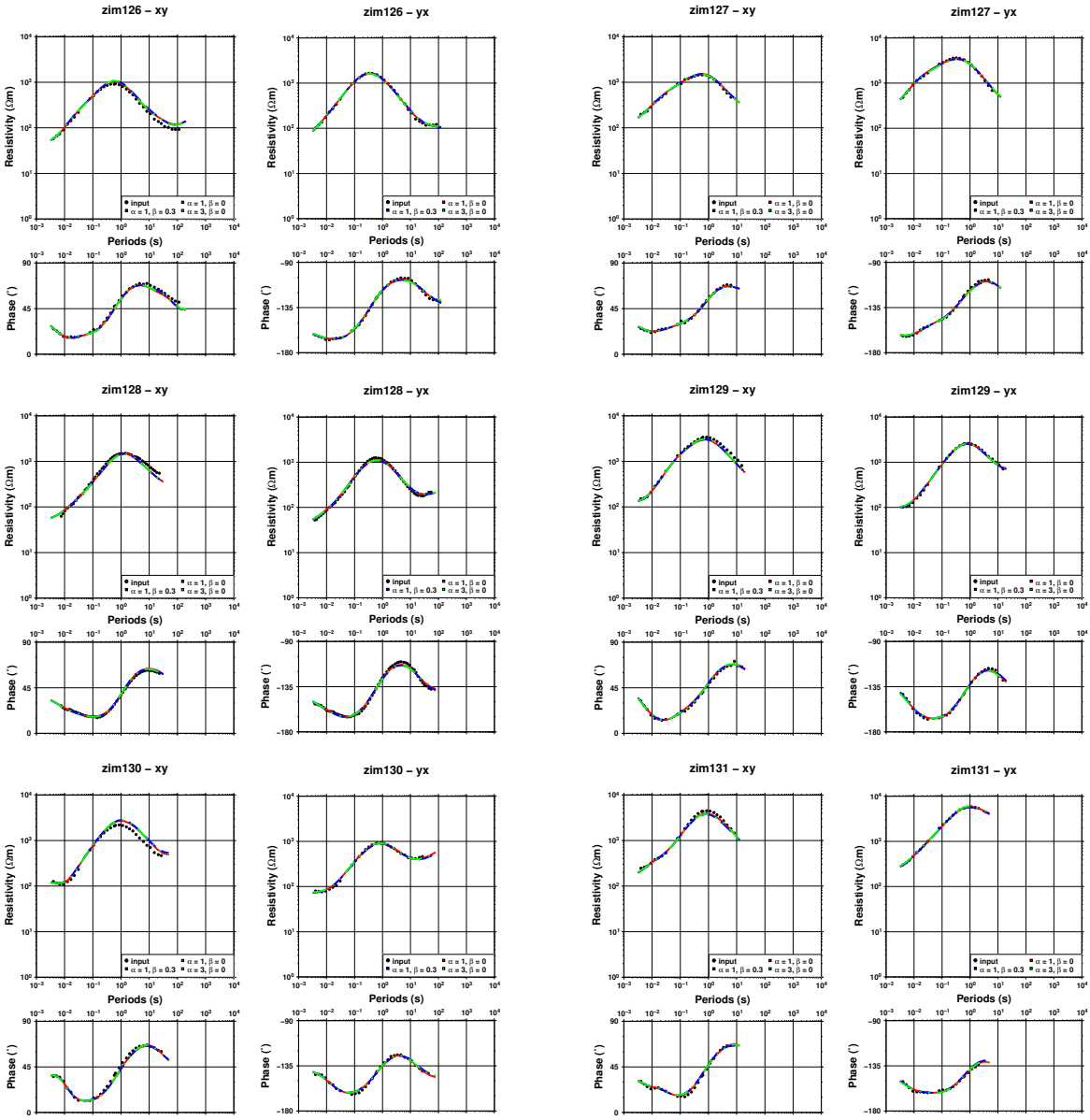

Figure C.2: This figure shows the responses curves of sites ZIM126 to ZIM131 of the crustal data set for a strike direction of 55° E of N. The resistivity curves are shown on top and below are the phase curves for each site. The symbols represent the observed data, and the coloured lines represent the response curves of the three inversion models obtained using different weighting function settings (see Figure 5.2; note colour coding is the same).

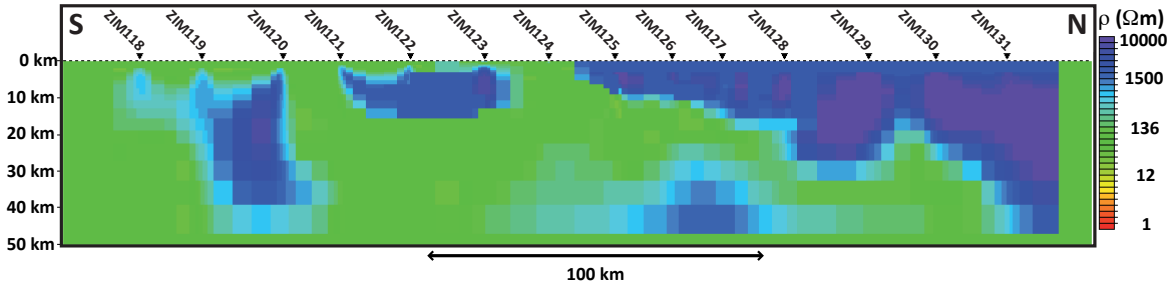

(a) Starting model

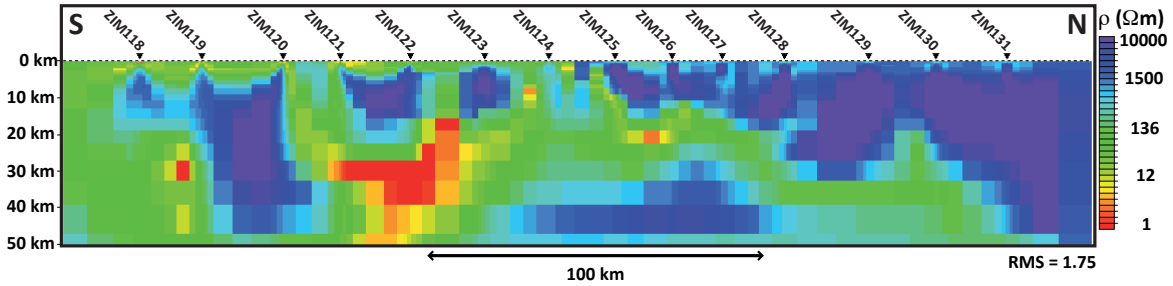

(b) Weighting function setting: $\alpha = 1$, $\beta = 0$, $H = 0$ and $V = 0$

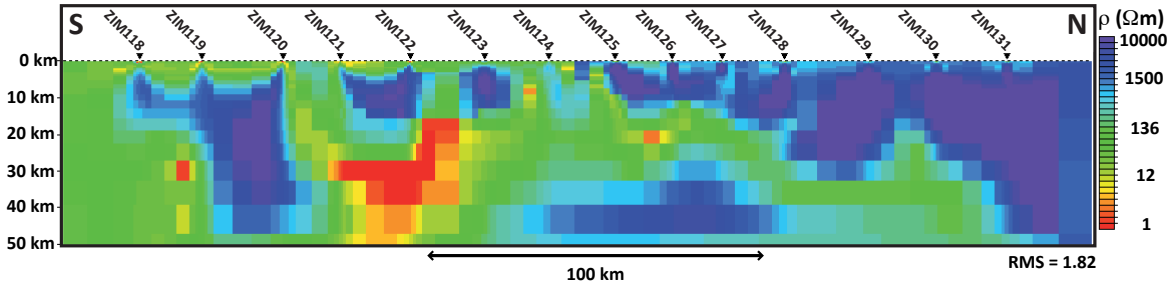

(c) Weighting function setting: $\alpha = 1$, $\beta = 0.3$, $H = 500$ and $V = 500$

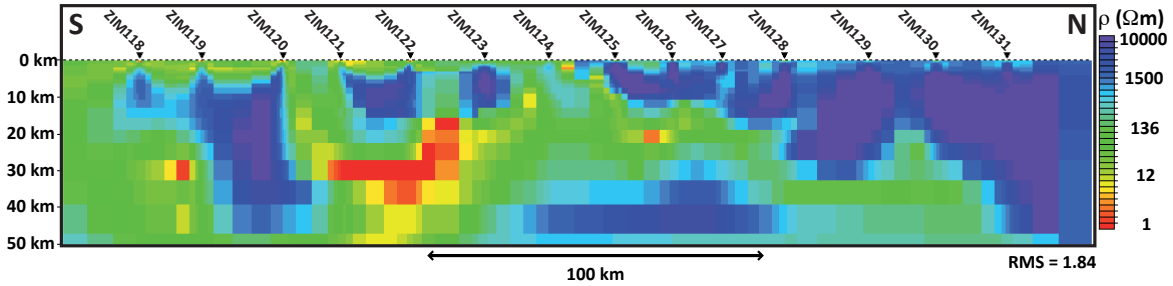

(d) Weighting function setting: $\alpha = 3$, $\beta = 0$, $H = 500$ and $V = 500$

Figure C.3: Results of inversion using the closest to starting model option. Panel (a) shows the starting model, where all conductors have been removed. The inversion results using different settings for the weighting function are shown in (b) to (d). For the inversions the smoothing operator was set to $\tau = 1$, and both TE mode and TM mode data were used.

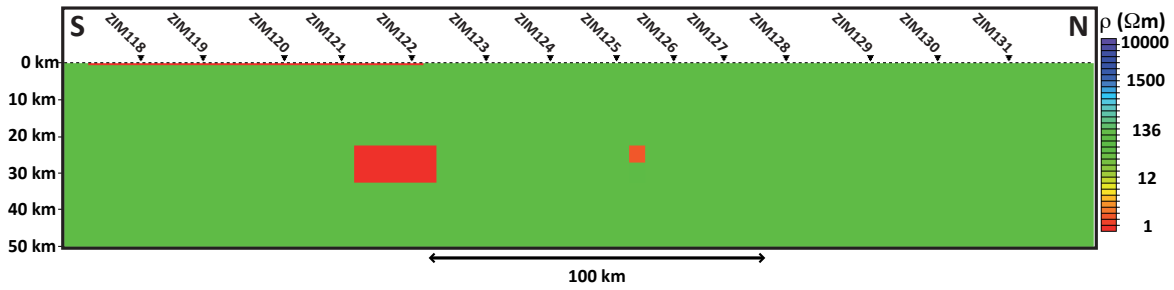

(a) Starting model

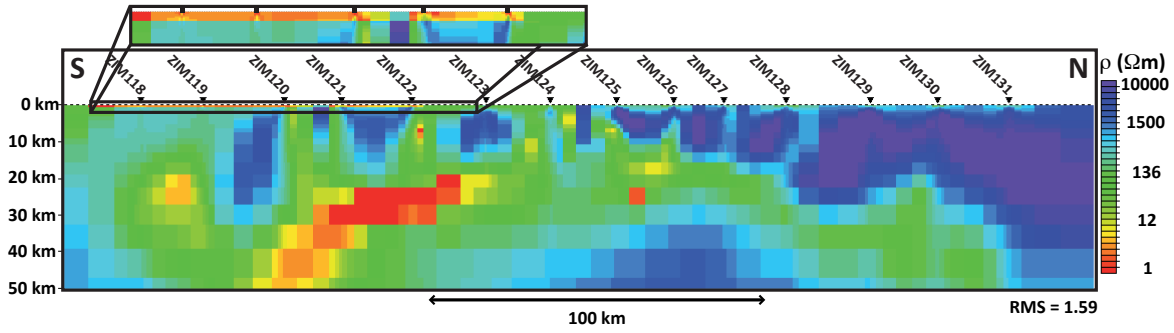

(b) Weighting function setting: $\alpha = 1$, $\beta = 0$, $H = 0$ and $V = 0$

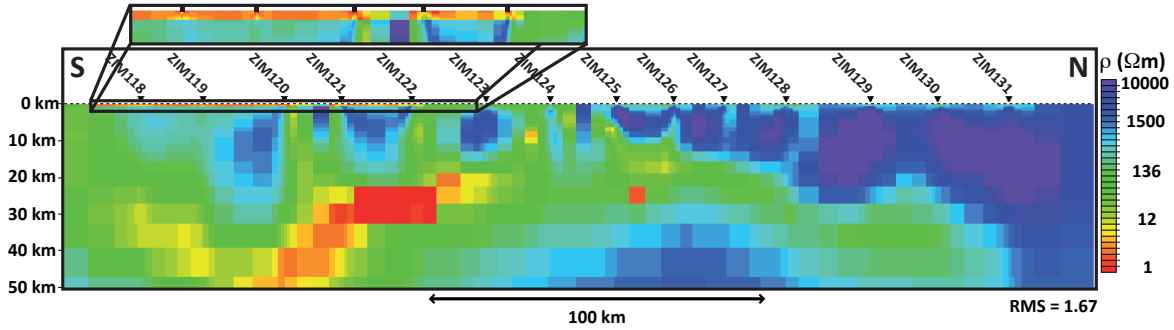

(c) Weighting function setting: $\alpha = 1$, $\beta = 0.3$, $H = 500$ and $V = 500$

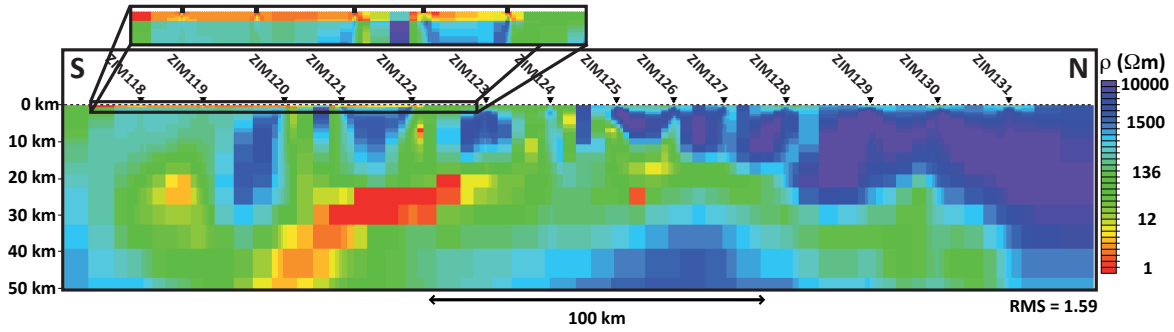

(d) Weighting function setting: $\alpha = 3$, $\beta = 0$, $H = 500$ and $V = 500$

Figure C.4: Results of inversion using the closest to starting model option. Panel (a) shows the starting model, where all resistors have been removed. The inversion results using different settings for the weighting function are shown in (b) to (d). For the inversions the smoothing operator was set to $\tau = 1$, and both TE mode and TM mode data were used. The enlarged part shows the near-surface conductor for each model, which is associated with the brine aquifer.

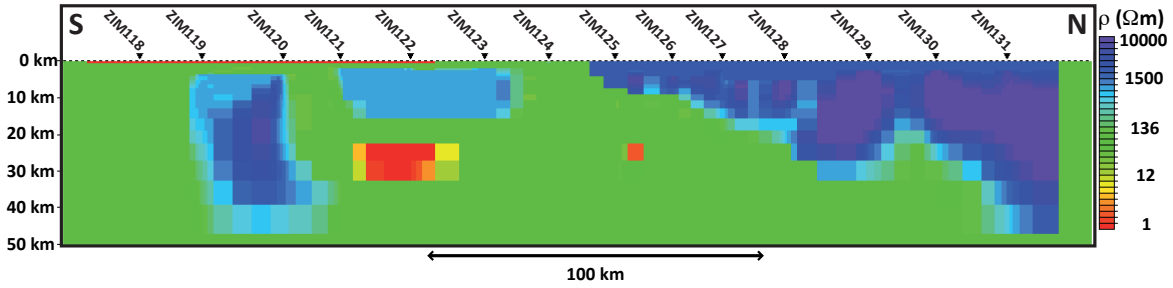

(a) Starting model

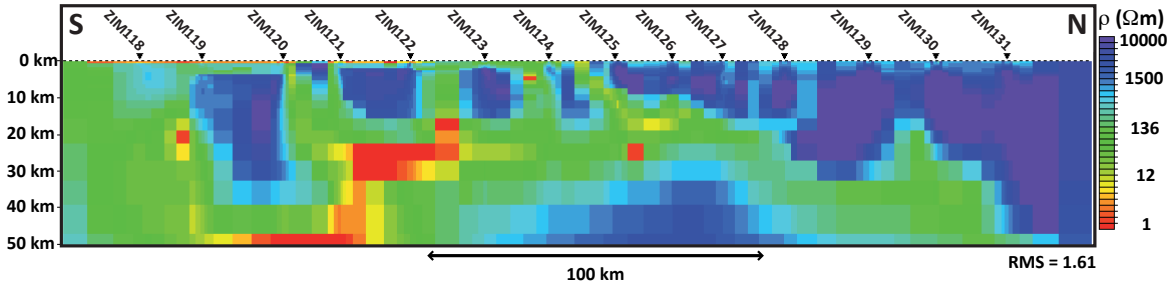

(b) Weighting function setting: $\alpha = 1$, $\beta = 0$, $H = 0$ and $V = 0$

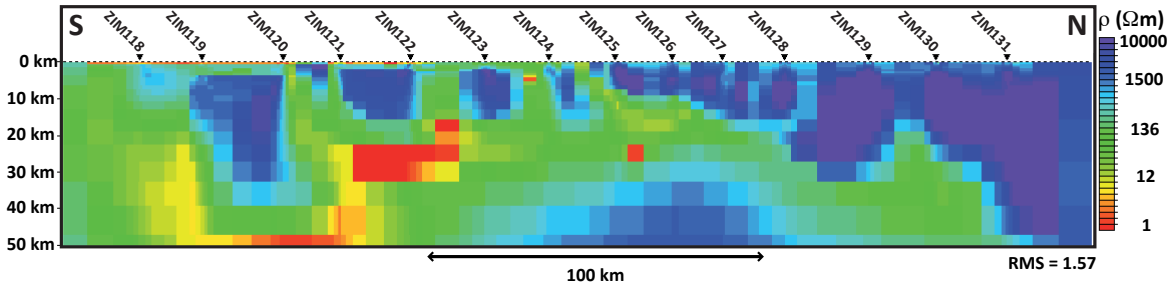

(c) Weighting function setting: $\alpha = 1$, $\beta = 0.3$, $H = 500$ and $V = 500$

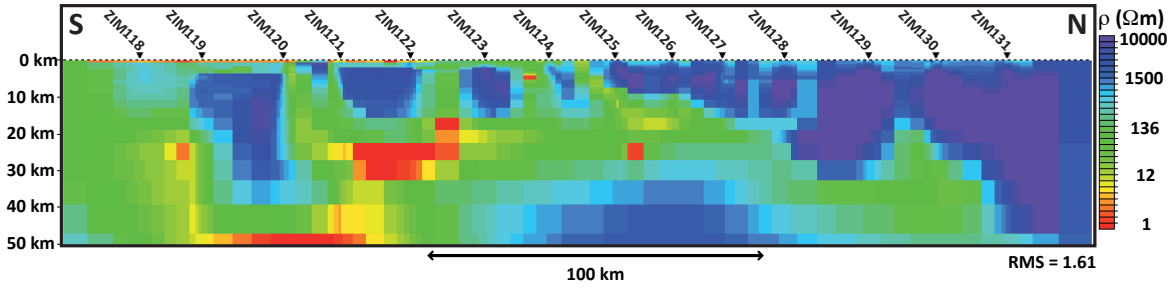

(d) Weighting function setting: $\alpha = 3$, $\beta = 0$, $H = 500$ and $V = 500$

Figure C.5: Results of inversion using the closest to starting model option. Panel (a) shows the starting model, which is a retoughed version of the model show in Figure 5.2. The inversion results using different settings for the weighting function are shown in (b) to (d). For the inversions the smoothing operator was set to $\tau = 1$, and both TE mode and TM mode data were used.

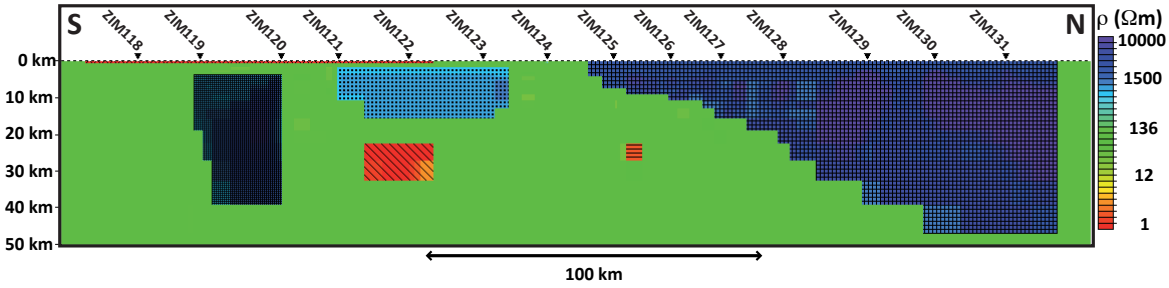

(a) Starting model

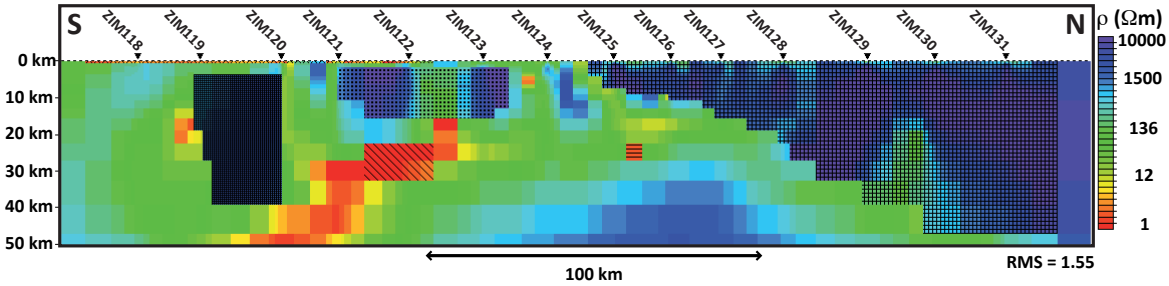

(b) Weighting function setting: $\alpha = 1$, $\beta = 0$, $H = 0$ and $V = 0$

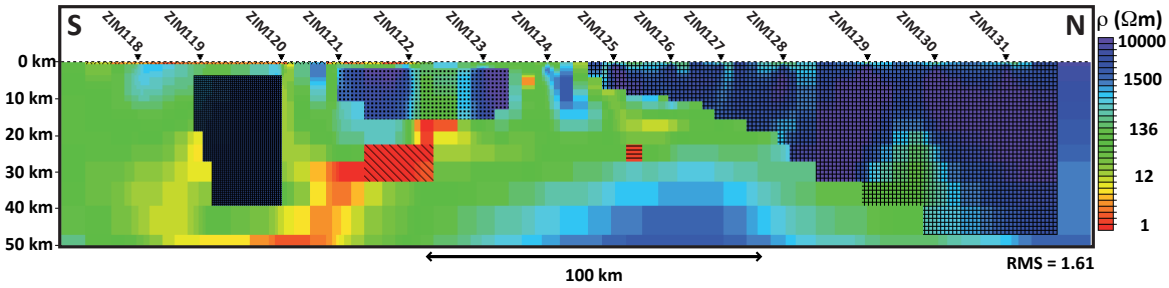

(c) Weighting function setting: $\alpha = 1$, $\beta = 0.3$, $H = 500$ and $V = 500$

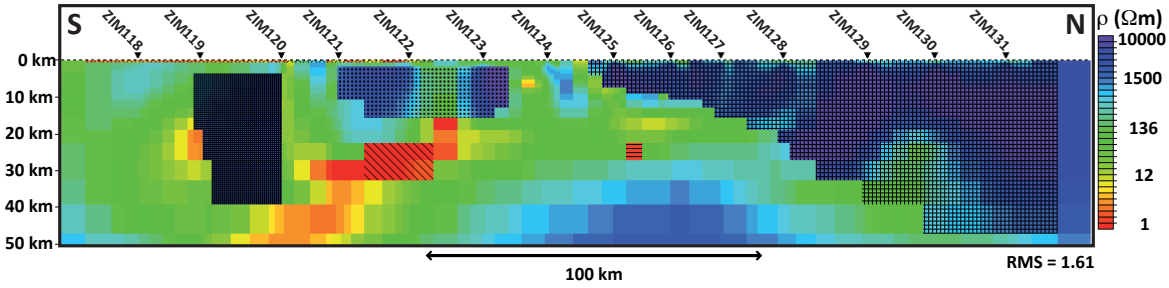

(d) Weighting function setting: $\alpha = 3$, $\beta = 0$, $H = 500$ and $V = 500$

Figure C.6: Results of inversion using the closest to starting model option. Panel (a) shows the starting model, where tear zones (indicated by the blocks of black pattern) have been introduced. The inversion results using different settings for the weighting function are shown in (b) to (d). For the inversions the smoothing operator was set to $\tau = 1$, and both TE mode and TM mode data were used.

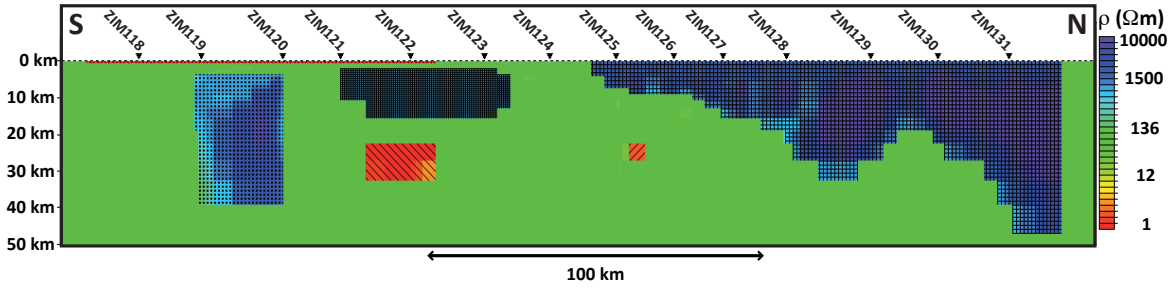

(a) Starting model

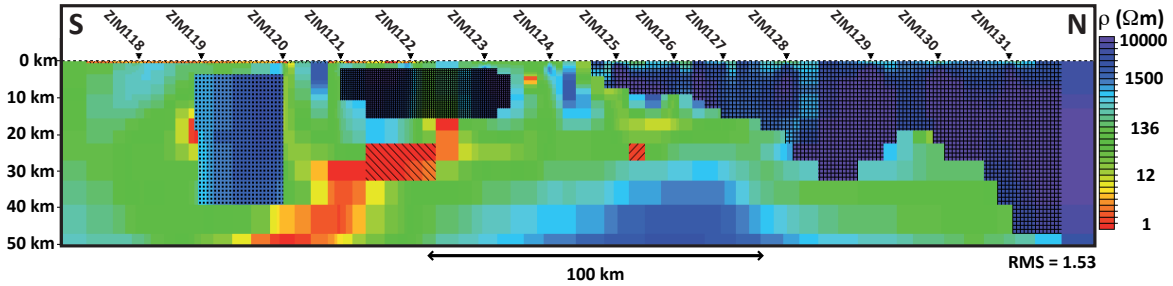

(b) Weighting function setting: $\alpha = 1$, $\beta = 0$, $H = 0$ and $V = 0$

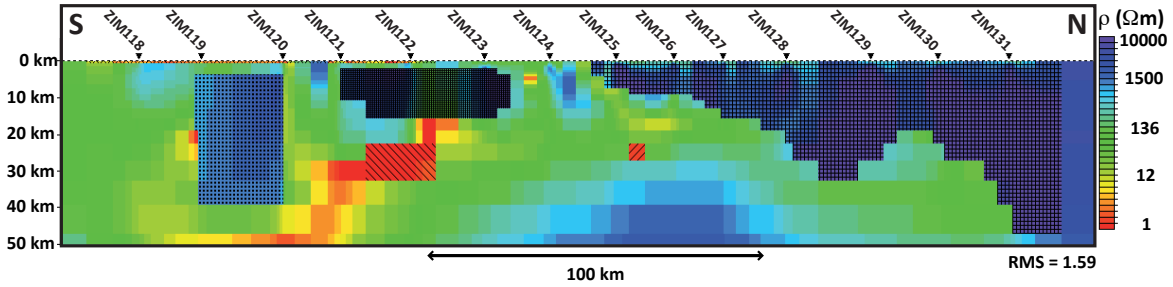

(c) Weighting function setting: $\alpha = 1$, $\beta = 0.3$, $H = 500$ and $V = 500$

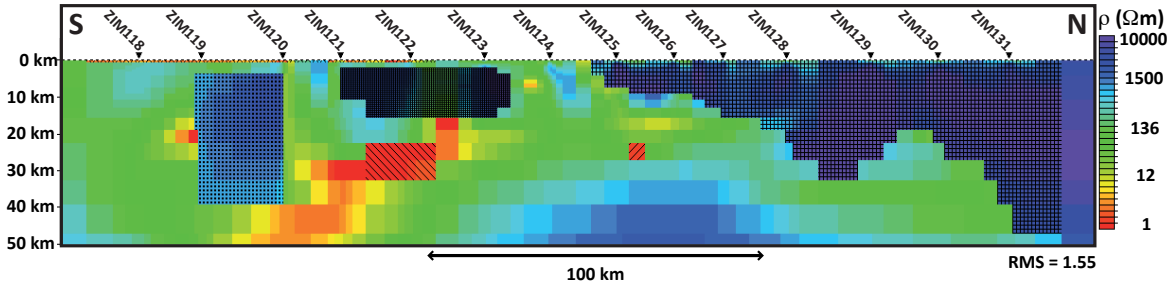

(d) Weighting function setting: $\alpha = 3$, $\beta = 0$, $H = 500$ and $V = 500$

Figure C.7: Results of inversion using the closest to starting model option. Panel (a) shows the starting model using tear zones (indicated by the blocks of black pattern). The inversion results using different settings for the weighting function are shown in (b) to (d). For the inversions the smoothing operator was set to $\tau = 1$, and both TE mode and TM mode data were used.

C.2 WHOLE ZIM LINE

In Section 5.3 the whole ZIM line data were inverted using the lithospheric strike angle of 35° E of N. Figures C.8 and C.9 show the complete data set of the ZIM line. The observed data are represented by the symbols. The red dots show the TE mode data and the blue diamonds the TM mode data that were taken into account during the inversion, while the black symbols show all other data points that have been rejected for the inversion guided by D+ smooth curves (via soundings menu in WinGLink®). During the process of the 2D inversion some sites had to be rejected completely because the responses could not be fit by the synthetic data and therefore caused very high RMS values (larger 15 for the individual sites). Therefore ZIM102, ZIM103, ZIM104, ZIM107, ZIM113 and ZIM115 do not have associated synthetic response curves from the final 2D inversion model. For all other sites represent the solid lines the synthetic data curves of the final model, where the black line shows the TE mode and the turquoise one is the TM mode.

To test the connectivity of the various resistors in the final 2D inversion model, resistive connections have been drawn into the model and the forward responses calculated for these model were compared to the observed data. Figure C.10 (a) shows the model were the lithospheric mantle resistors are connected with each other as well as with the crustal resistor beneath ZIM 117-ZIM120. A connection of only the two lithospheric resistors is shown in (b). Figure C.11 (a) enforces connections between the crustal resistors and the lithospheric ones beneath and in the model in (b) are the resistors beneath ZIM131 disconnected. Figures C.12, C.13 and C.14 show the observed data as symbols and the different forward responses curves of the four models are represented by coloured lines (only for the relevant sites).

Synthetic data calculated using the code by Pek and Verner (1997) for various models (see Figure 5.14 and Table 5.1 for details) were used to test the effects of applying an isotropic inversion code to anisotropic data, as it is most likely caused by the presence of the Okavango dyke swarm. It is apparent that the middle/lower crustal conductor is wrongly imaged as an upper mantle structure and that the lithospheric thickness might be affected as well (appears too resistive and too thick). Introducing a tear zone at the location of the anisotropic block does not help to avoid the wrong resistivity image (see Figure C.18).

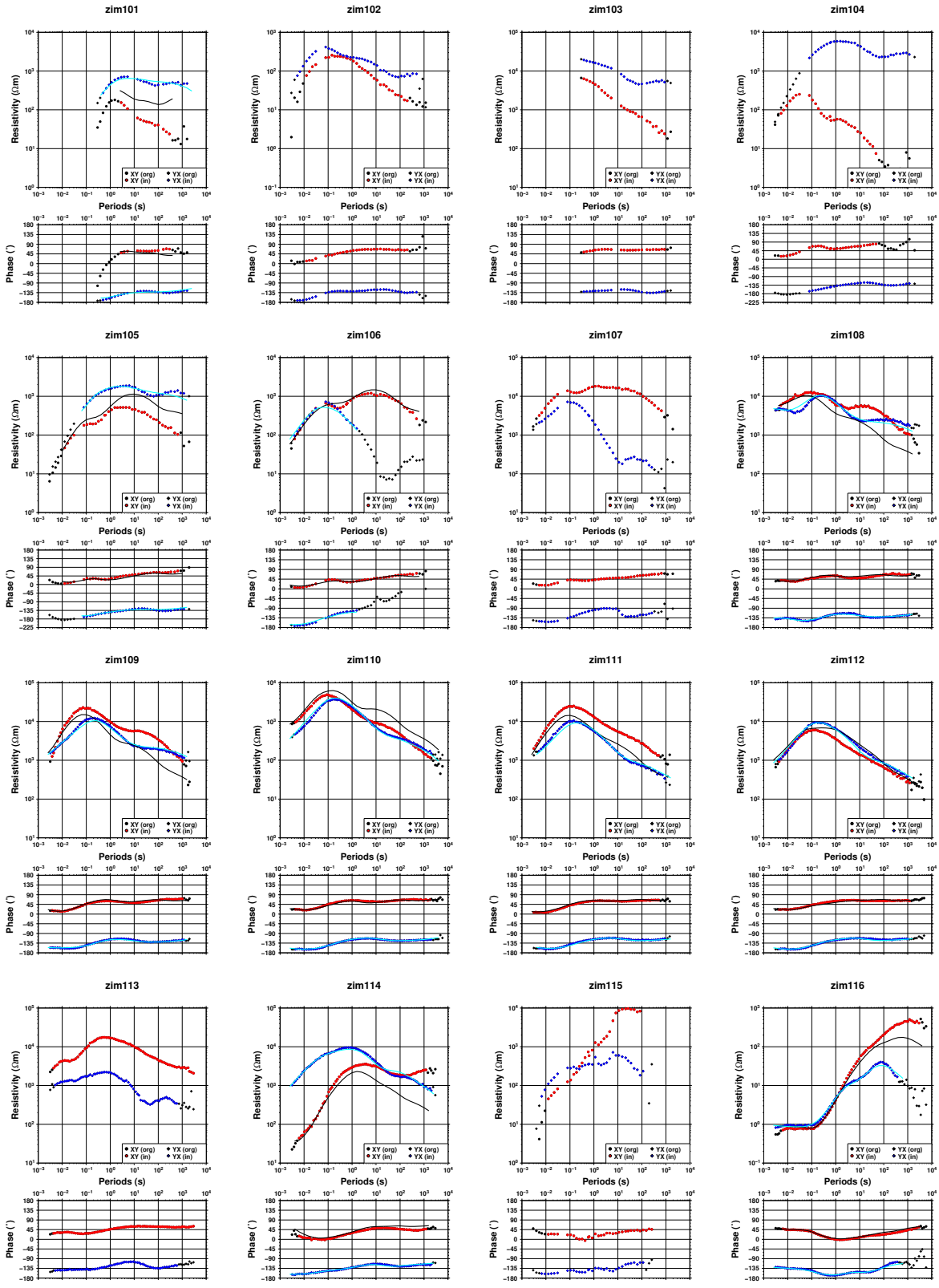

Figure C.8: This Figure shows the responses curves of sites ZIM101 to ZIM116 for a strike direction of 35° E of N. The resistivity curves are shown on top and below are the phase curves for each site. The symbols represent the observed data, where the red dots are the TE mode data and the blue diamonds are the TM mode data that are taken into account for the inversion, whereas the black symbols represent all other data points that have been rejected. The solid black line is the TE and the turquoise the TM response curve of the final 2D inversion model shown in Figure 5.6 (note some sites have been rejected during the inversion process and therefore don't have a final model response).

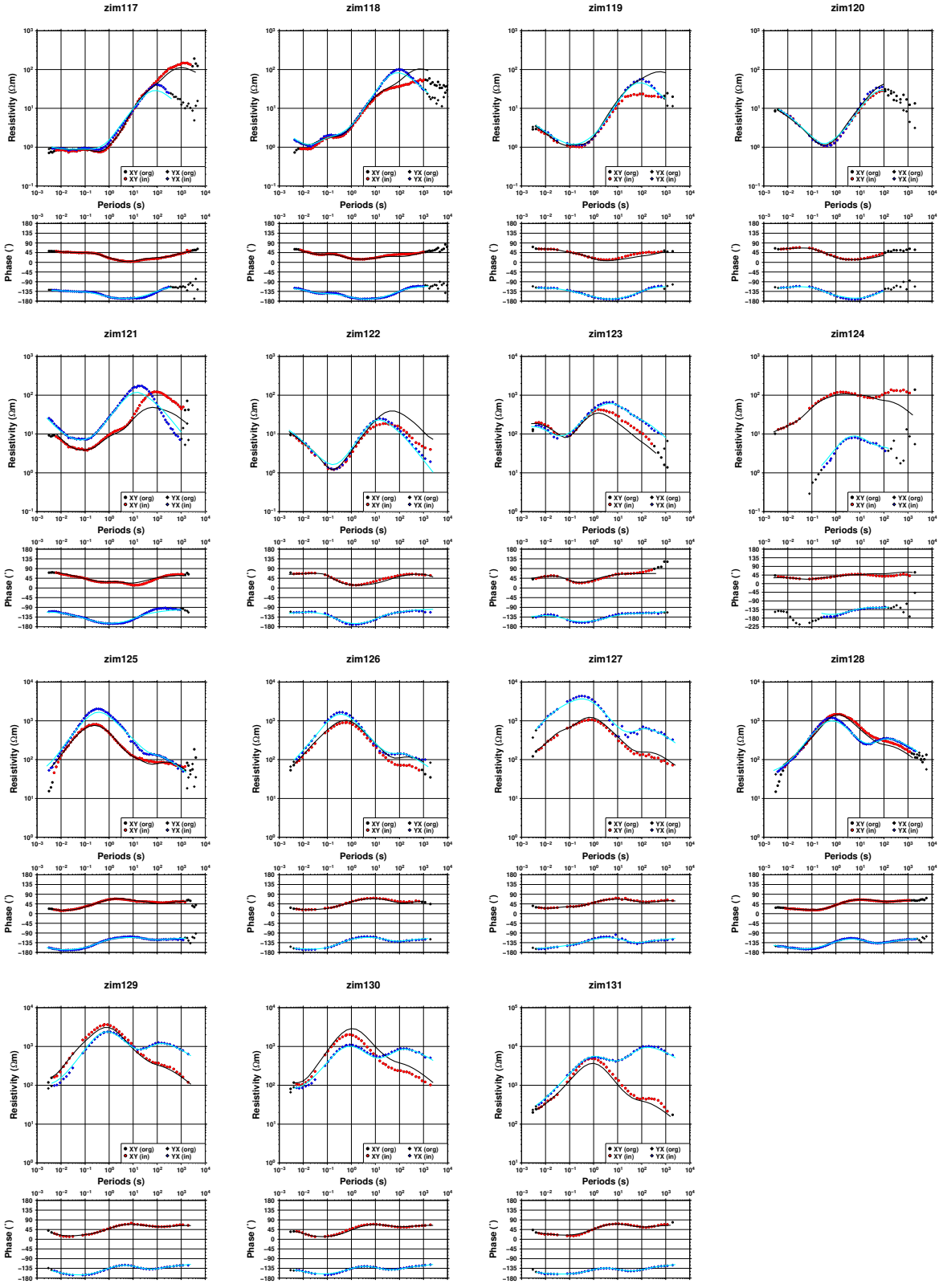

Figure C.9: This Figure shows the responses curves of sites ZIM117 to ZIM131 for a strike direction of 35° E of N. The resistivity curves are shown on top and below are the phase curves for each site. The symbols represent the observed data, where the red dots are the TE mode data and the blue diamonds are the TM mode data that are taken into account for the inversion, whereas the black symbols represent all other data points that have been rejected. The solid black line is the TE mode and the turquoise the TM mode response curve of the final 2D inversion model shown in Figure 5.6 (note some sites have been rejected during the inversion process and therefore do not have final model response curves).

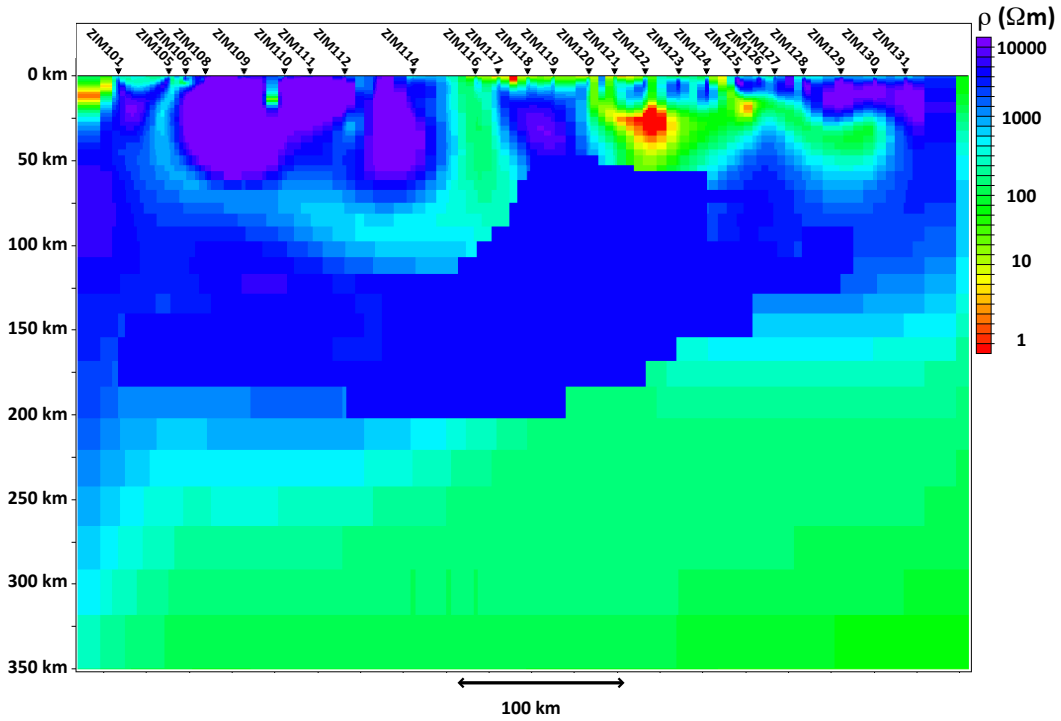

(a) Connection of both lithospheric resistors and the crustal resistor beneath ZIM117-ZIM120 (model called CONNECTED1; blue response curves in Figures C.12 to C.14)

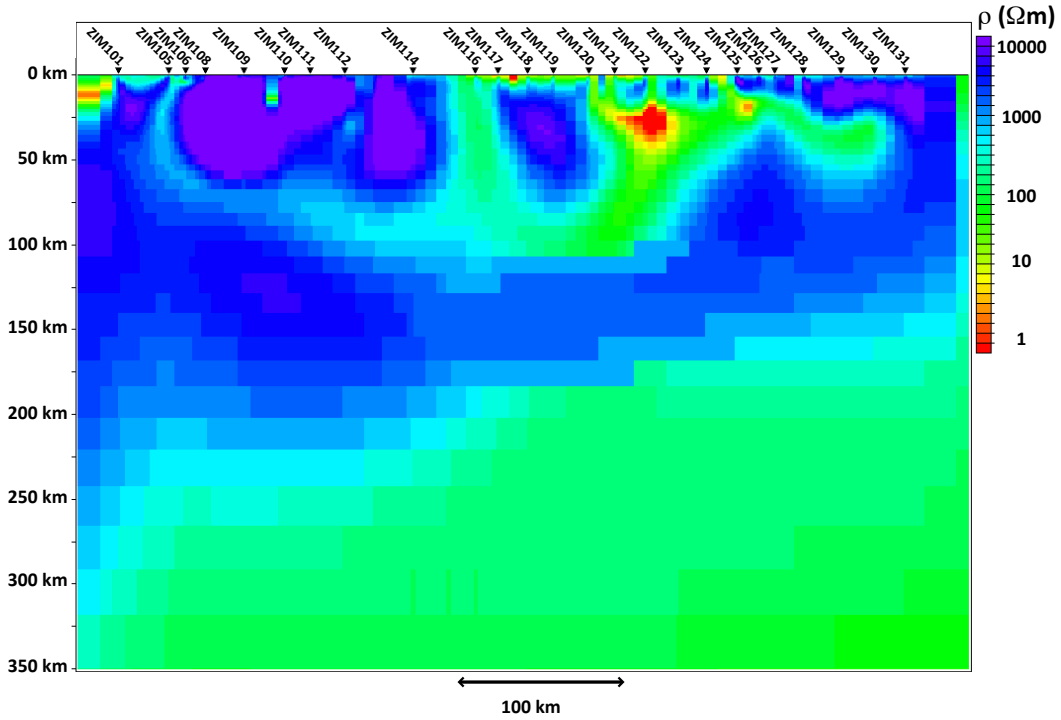

(b) Connection of both lithospheric resistors (model called CONNECTED2; green response curves in Figures C.12 to C.14)

Figure C.10: This figure shows manipulated versions of the final 2D inversion model (see Figure 5.6), which are used to prove or falsify hypotheses about connection or disconnection between the resistors in the model. The forward responses calculated for these models are shown in Figures C.12 to C.14, where they are compared to the observed data and the forward response curves from the final 2D inversion model.

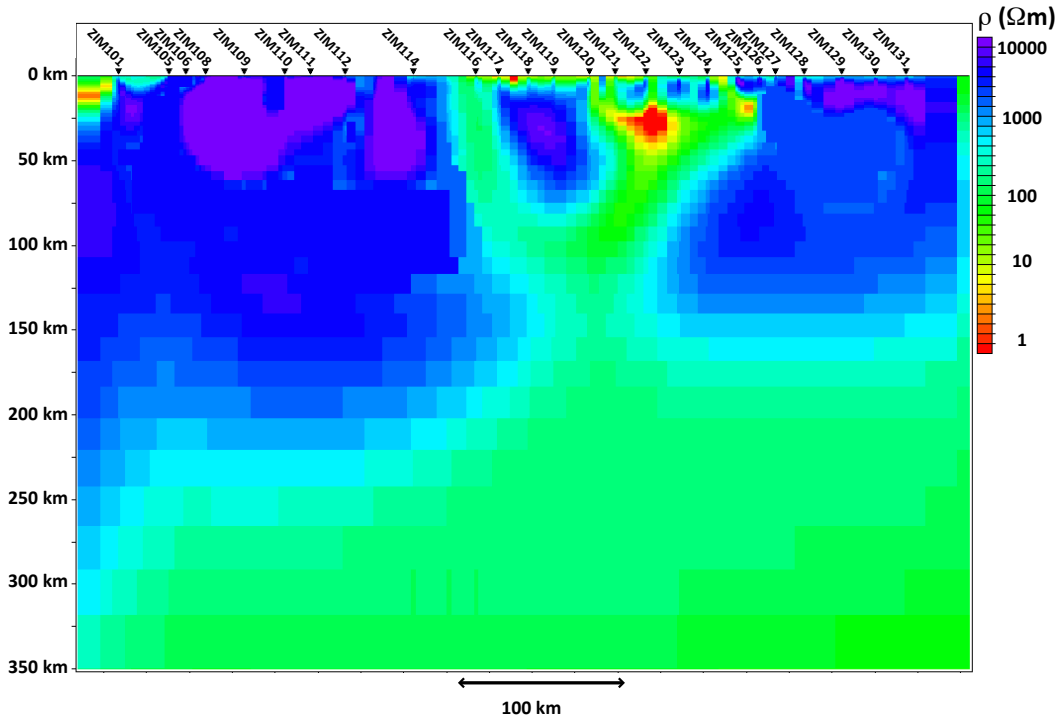

(a) Connection of the crustal and lithospheric resistors at the southern and at the northern end of the profile (model called CONNECTED3; turquoise response curves in Figures C.12 to C.14)

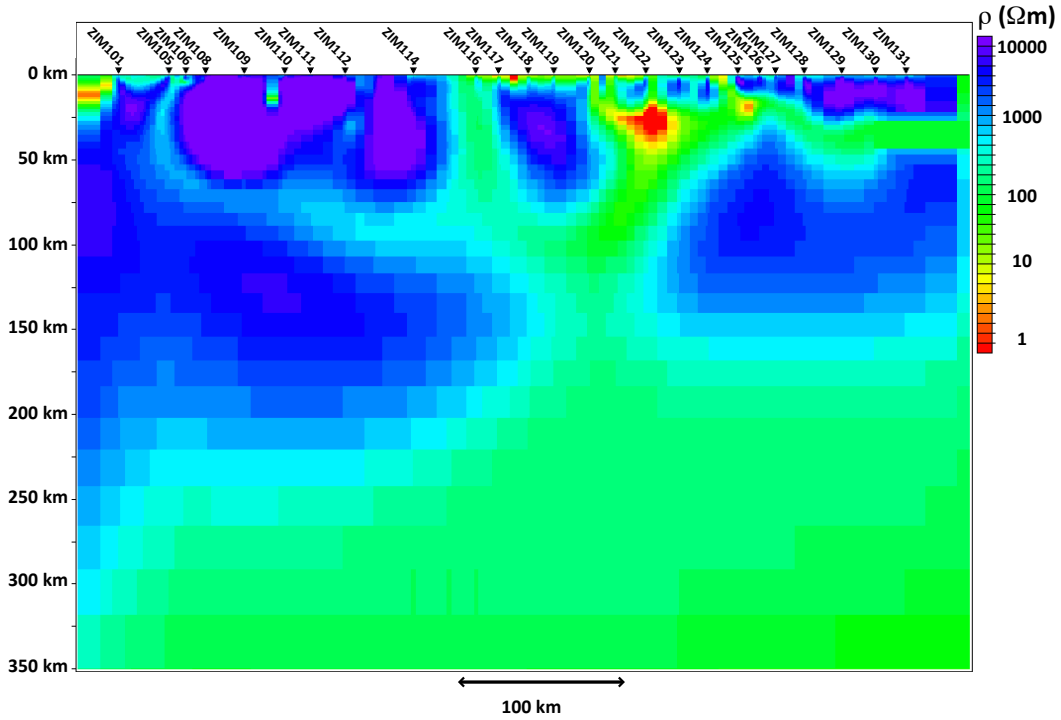

(b) Disconnection of the crustal and lithospheric resistors beneath ZIM130 / ZIM131 (model called DISCONNECTED; pink response curves in Figures C.12 to C.14)

Figure C.11: This figure shows manipulated versions of the final 2D inversion model (see Figure 5.6), which are used to prove or falsify hypotheses about connection or disconnection between the resistors in the model. The forward responses calculated for these models are shown in Figures C.12 to C.14, where they are compared to the observed data and the forward response curves from the final 2D inversion model.

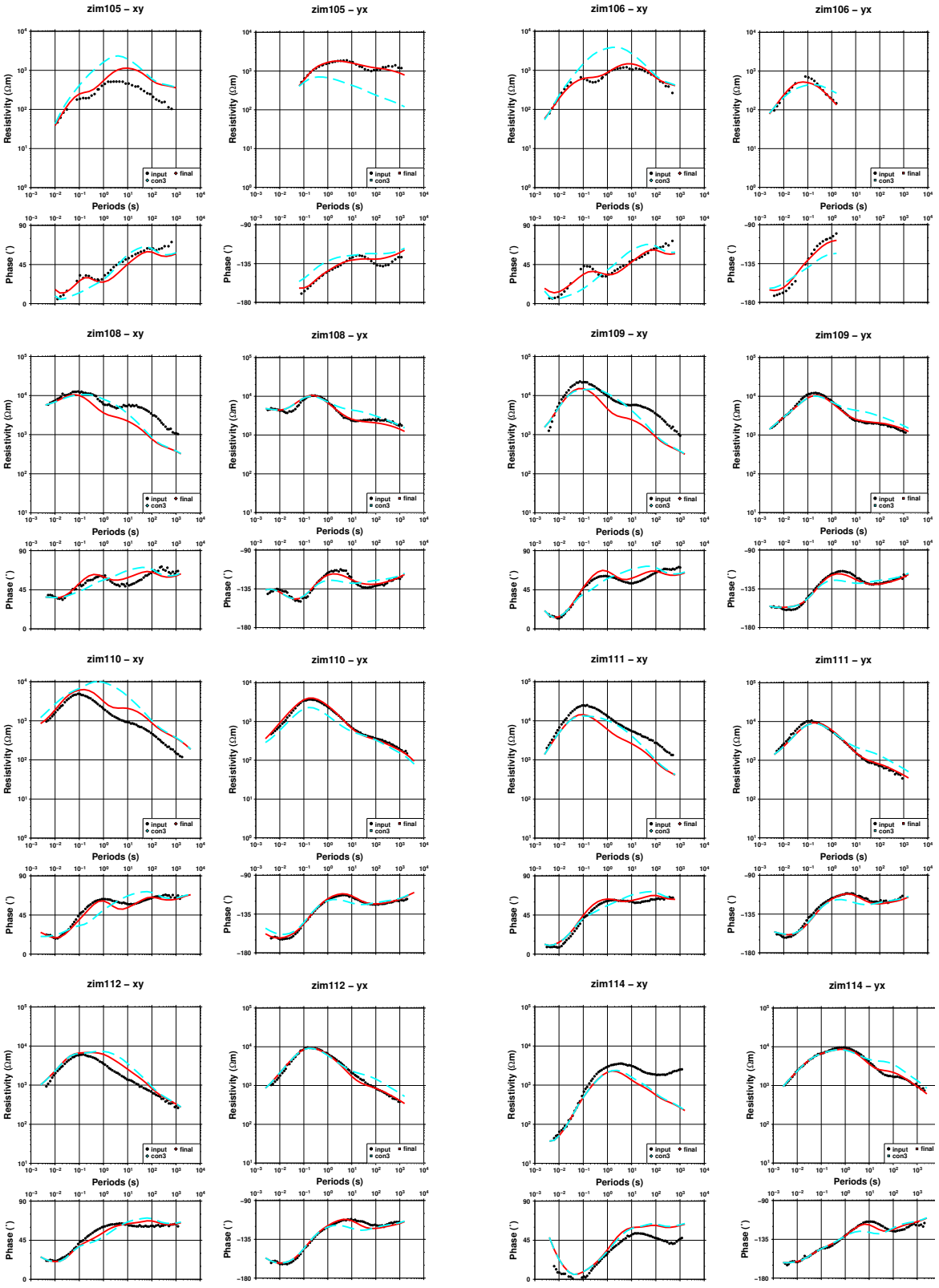

Figure C.12: This figure shows the comparison of the observed data (black dots) and the response curves of the final 2D inversion model (red line) with the response curves obtained from the modified models shown in Figures C.10 and C.11. For each of the models only the response curves of the relevant sites are plotted using the following colour coding: blue - CONNECTED1 (Figure C.10 (a)), green - CONNECTED2 (Figure C.10 (b)), turquoise - CONNECTED3 (Figure C.11 (a)) and pink - DISCONNECTED (Figure C.11 (b)).

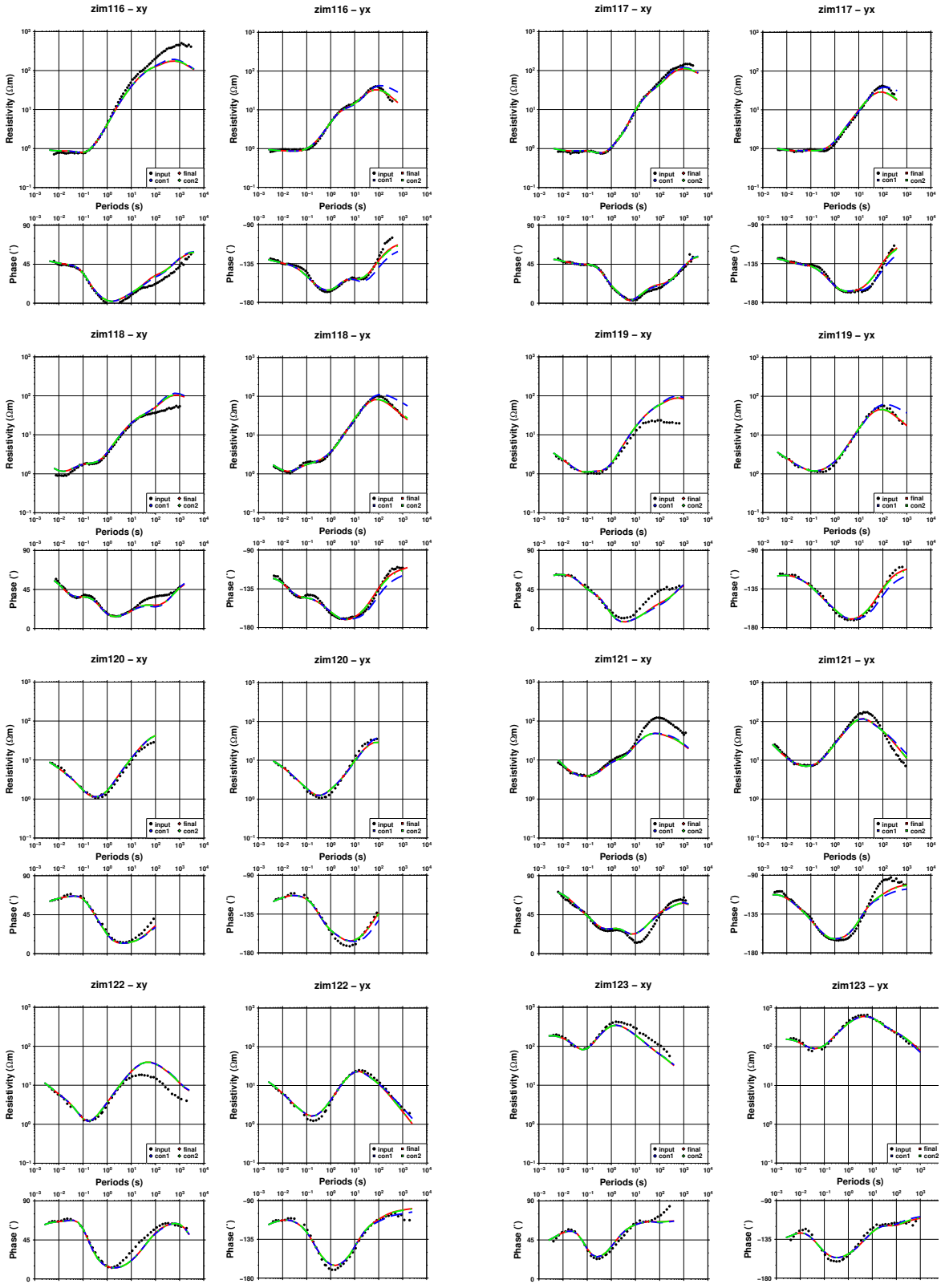

Figure C.13: This figure (Figure C.12 continued) shows the comparison of the observed data (black dots) and the response curves of the final 2D inversion model (red line) with the response curves obtained from the modified models shown in Figures C.10 and C.11. For each of the models only the response curves of the relevant sites are plotted using the following colour coding: blue - CONNECTED1 (Figure C.10 (a)), green - CONNECTED2 (Figure C.10 (b)), turquoise - CONNECTED3 (Figure C.11 (a)) and pink - DISCONNECTED (Figure C.11 (b)).

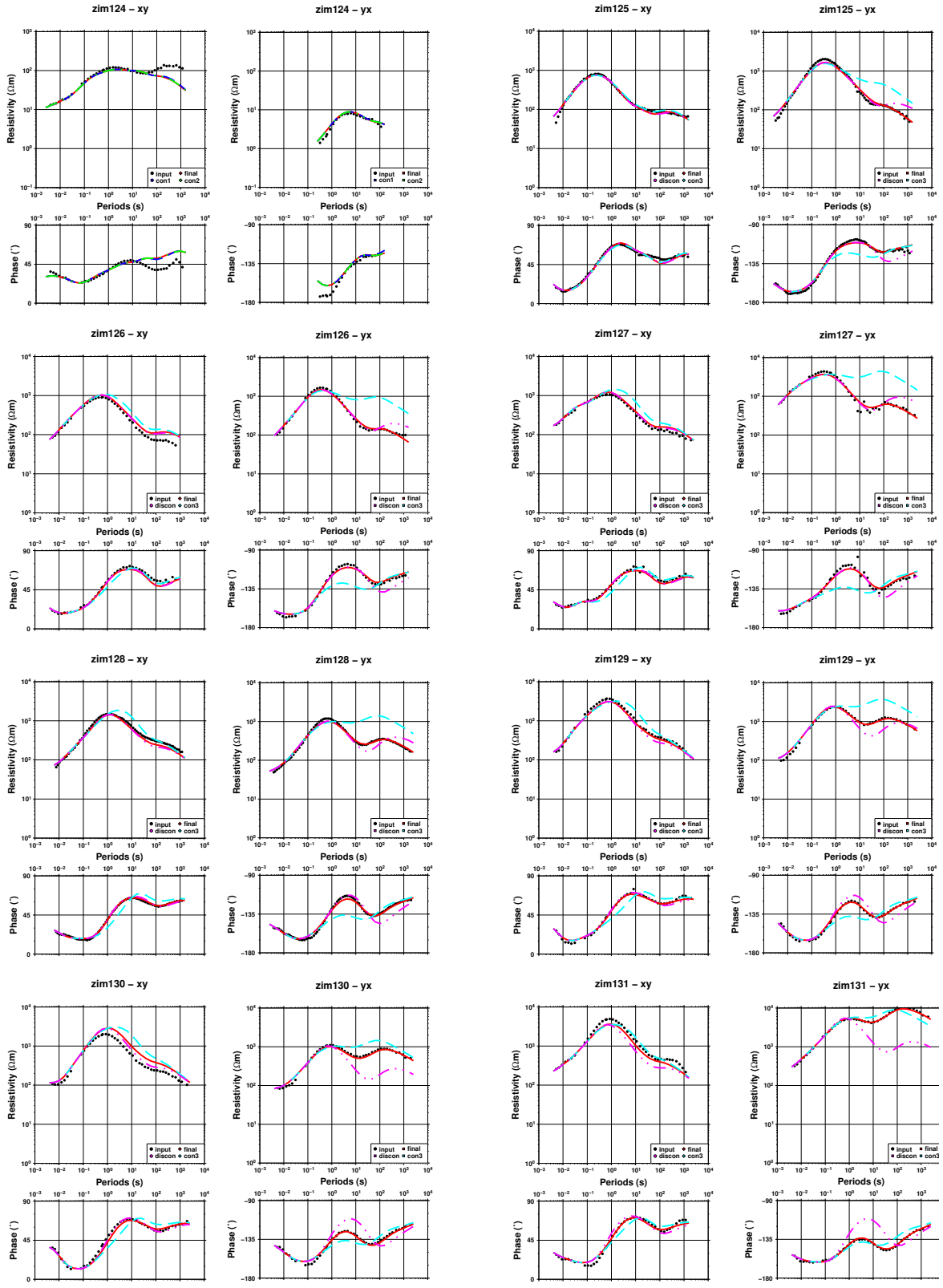

Figure C.14: This figure (Figures C.12/C.13 continued) shows the comparison of the observed data (black dots) and the response curves of the final 2D inversion model (red line) with the response curves obtained from the modified models shown in Figures C.10 and C.11. For each of the models only the response curves of the relevant sites are plotted using the following colour coding: blue - CONNECTED1 (Figure C.10 (a)), green - CONNECTED2 (Figure C.10 (b)), turquoise - CONNECTED3 (Figure C.11 (a)) and pink - DISCONNECTED (Figure C.11 (b)).

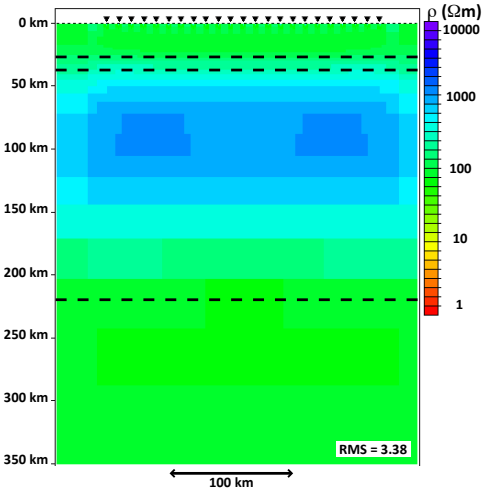

(a) Model: NODYKES A

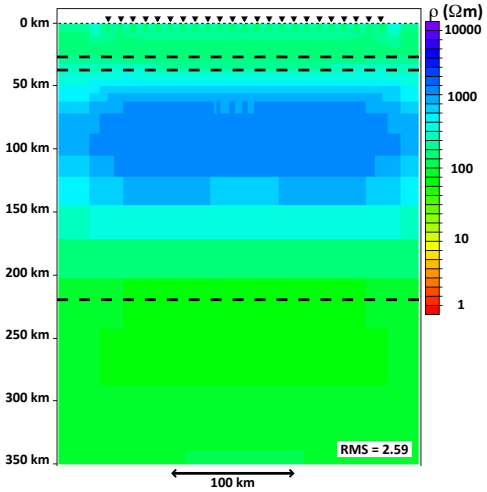

(b) Model: NODYKES B

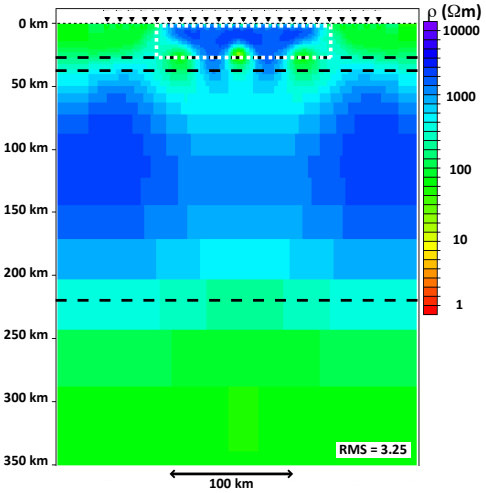

(c) Model: TOPLAYER A

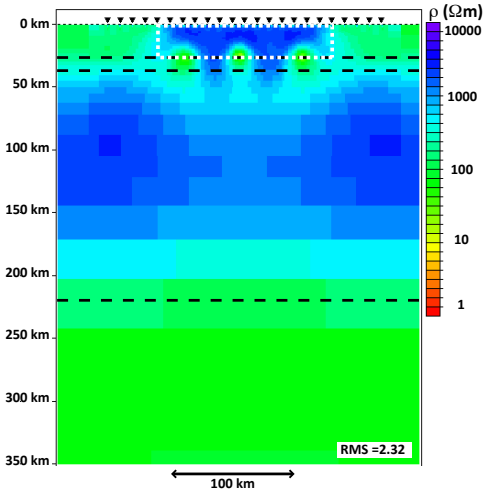

(d) Model: TOPLAYER B

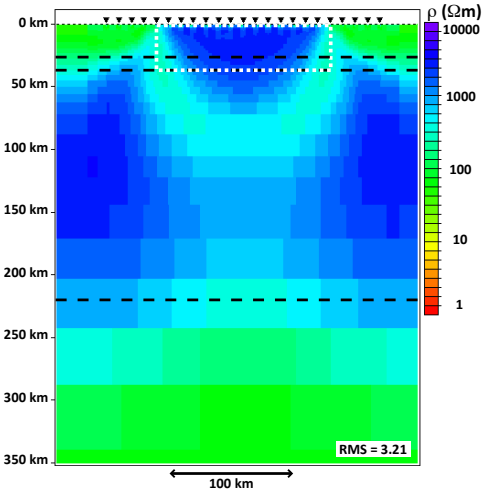

(e) Model: CRUST A

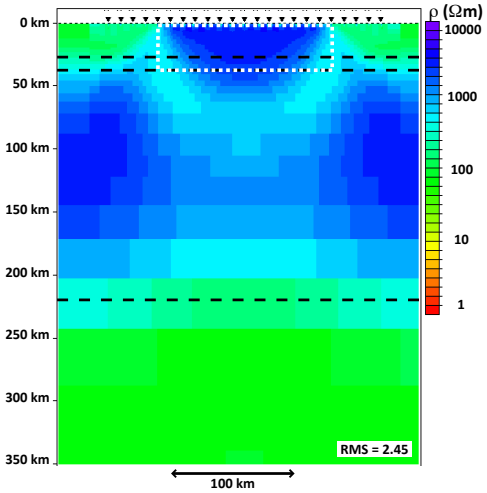

(f) Model: CRUST B

Figure C.15: These figures show the isotropic inversion results of synthetic 2D anisotropic data (calculated using Pek and Verner's (1997) code) simulating dykes of 30000 Ωm in the crust. The white dashed line outlines the area of the anisotropic block representing the dykes and the layered background is illustrated by black dashed lines (for more details on the exact models see Figure 5.14 and Table 5.1).

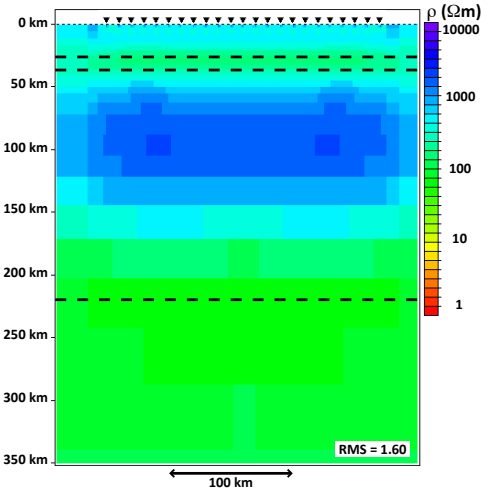

(a) Model: NODYKES C

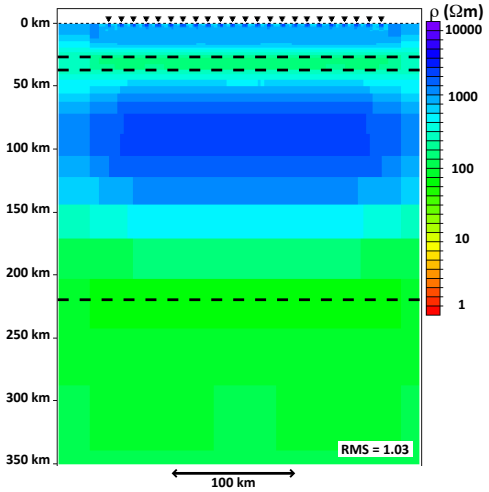

(b) Model: NODYKES D

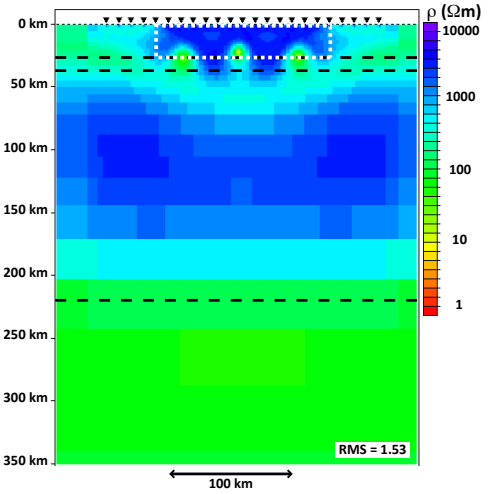

(c) Model: TOPLAYER C

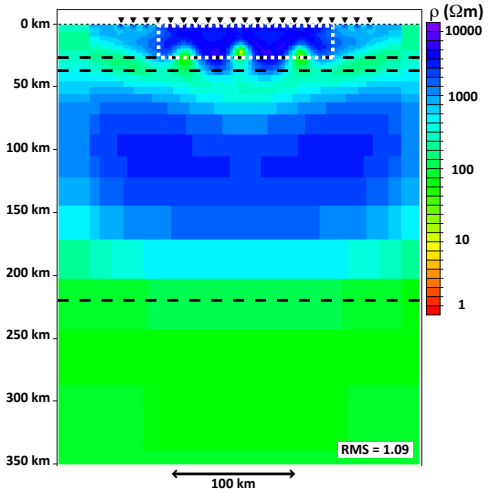

(d) Model: TOPLAYER D

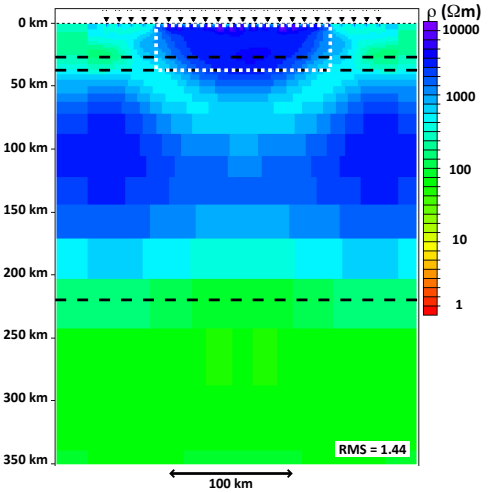

(e) Model: CRUST C

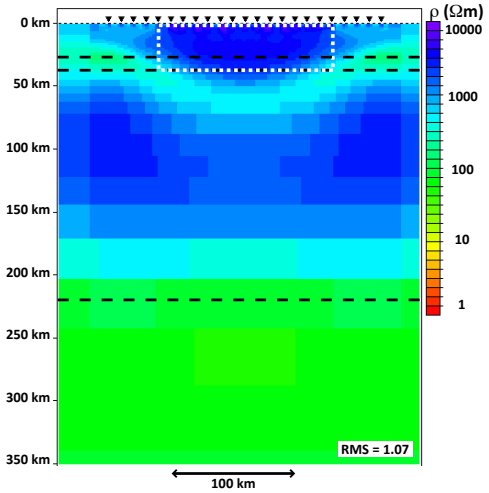

(f) Model: CRUST D

Figure C.16: These figures show the isotropic inversion results of synthetic 2D anisotropic data (calculated using Pek and Verner's (1997) code) simulating dykes of 30000 Ωm in the crust. The white dashed line outlines the area of the anisotropic block representing the dykes and the layered background is illustrated by black dashed lines (for more details on the exact models see Figure 5.14 and Table 5.1).

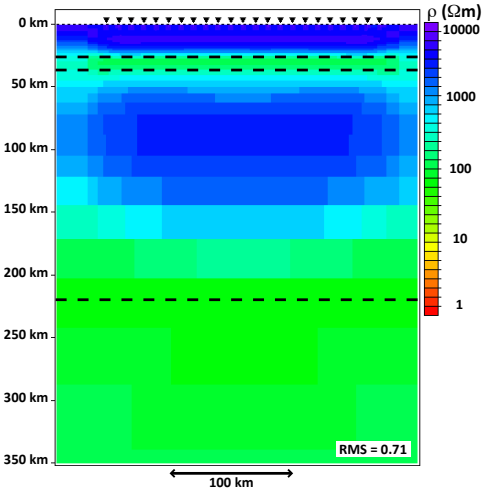

(a) Model: NODYKES E

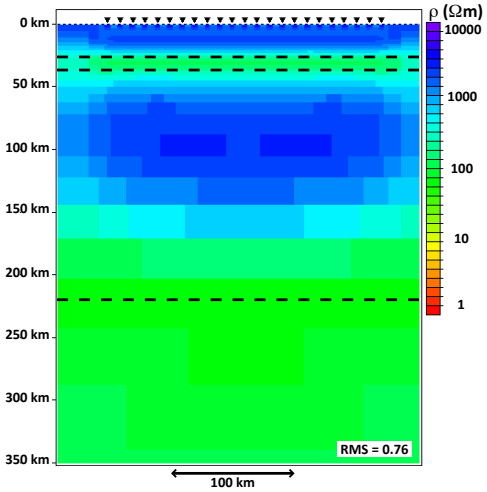

(b) Model: NODYKES F

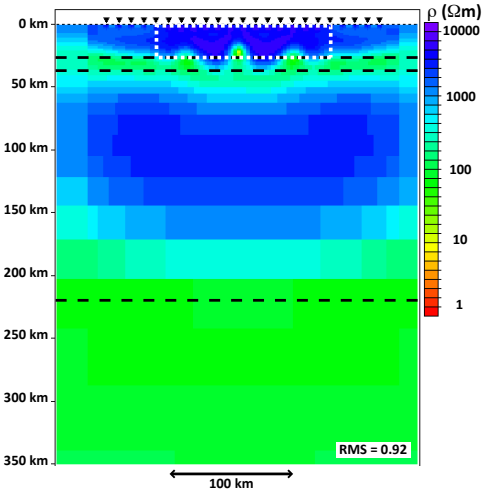

(c) Model: TOPLAYER E

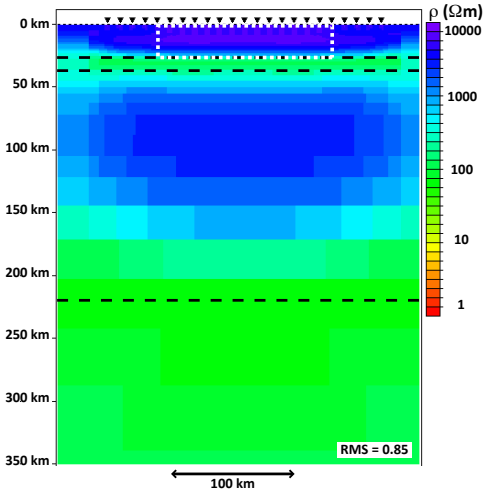

(d) Model: TOPLAYER F

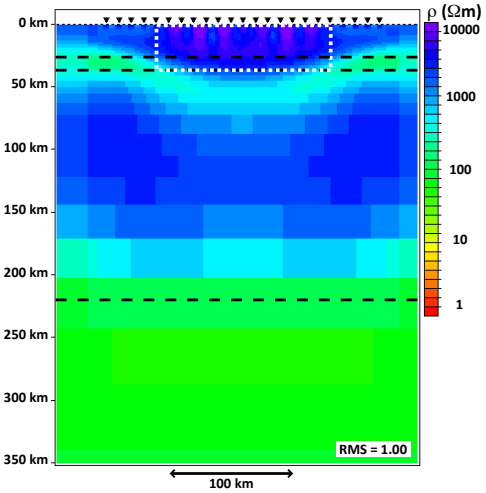

(e) Model: CRUST E

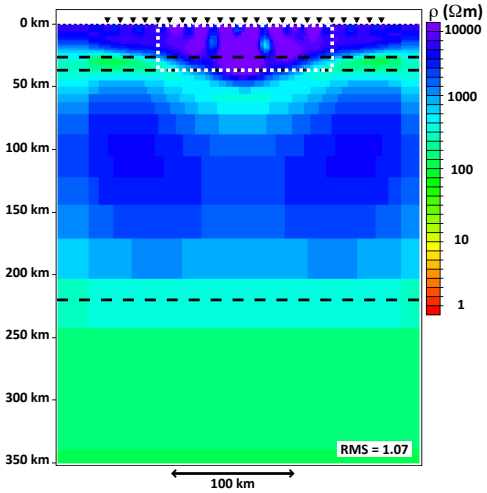

(f) Model: CRUST F

Figure C.17: These figures show the isotropic inversion results of synthetic 2D anisotropic data (calculated using Pek and Verner's (1997) code) simulating dykes of 30000 Ωm in the crust. The white dashed line outlines the area of the anisotropic block representing the dykes and the layered background is illustrated by black dashed lines (for more details on the exact models see Figure 5.14 and Table 5.1).

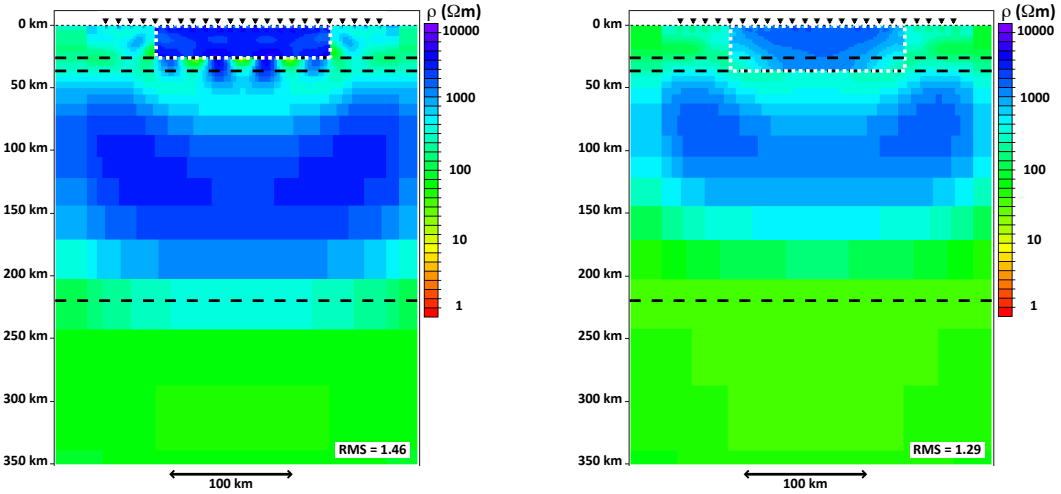

(a) Model: TOPLAYER C with tear zone

(b) Model: CRUST C with tear zone

Figure C.18: These figures show the isotropic inversion results of synthetic 2D anisotropic data of the models TOPLAYERC and CRUSTC (see Figure 5.14 and Table 5.1 for details). The white dashed line outlines the area of the anisotropic block representing the dykes and the layered background is illustrated by black dashed lines. Other than for the inversion results shown in Figures C.15 to C.17, the area of the dykes (white dashed line) was selected to be a tear zone during the inversion.

D

BASIS FUNCTIONS

D.1 EDGE ELEMENT BASIS FUNCTIONS

In Section 6.1 the general formulation of a x-directed edge-element basis function was shown (Equation 6.1). In this appendix all edge-element basis functions of one cell are discussed. The numbering of the edges within a cell is in the following order: x-directed edges first (with y varying faster than z), then y-directed edges (x varies faster than z) and then all z-directed edges (x varying faster than y). Figure D.1 shows a sketch of a cell including the numbering of all edges and the locations of edges with respect to a global Cartesian coordinate system.

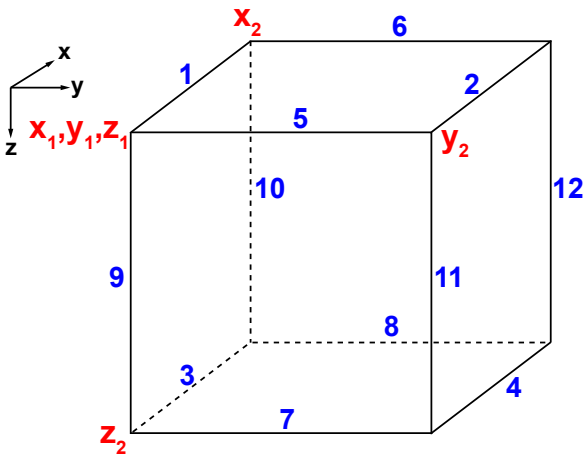

Figure D.1: Sketch of one cell and its numbering of edges and the global mesh coordinates.

The basis functions for such a simple rectangular brick element are for example described by Jin (2002). The x-directed basis functions are given by

$$\begin{aligned} v_1 &= \frac{(y_2 - y)(z_2 - z)}{(y_2 - y_1)(z_2 - z_1)} = \frac{1}{(y_2 - y_1)(z_2 - z_1)} (y_2 - y)(z_2 - z) \\ &= \frac{1}{(y_2 - y_1)(z_2 - z_1)} (y_2 z_2 - z_2 y - y_2 z + yz) \quad , \end{aligned} \tag{D.1}$$

$$\begin{aligned} v_2 &= \frac{(y-y_1)(z_2-z)}{(y_2-y_1)(z_2-z_1)} = \frac{1}{(y_2-y_1)(z_2-z_1)}\,(y-y_1)(z_2-z) \\ &= \frac{1}{(y_2-y_1)(z_2-z_1)}\,(-y_1z_2+z_2y+y_1z-yz) \quad , \end{aligned} \tag{D.2}$$

$$\begin{aligned} v_3 &= \frac{(y_2-y)(z-z_1)}{(y_2-y_1)(z_2-z_1)} = \frac{1}{(y_2-y_1)(z_2-z_1)}\,(y_2-y)(z-z_1) \\ &= \frac{1}{(y_2-y_1)(z_2-z_1)}\,(-y_2z_1+z_1y+y_2z-yz) \quad , \end{aligned} \tag{D.3}$$

and

$$\begin{aligned} v_4 &= \frac{(y-y_1)(z-z_1)}{(y_2-y_1)(z_2-z_1)} = \frac{1}{(y_2-y_1)(z_2-z_1)}\,(y-y_1)(z-z_1) \\ &= \frac{1}{(y_2-y_1)(z_2-z_1)}\,(y_1z_1-z_1y+y_1z-yz) \quad . \end{aligned} \tag{D.4}$$

The basis functions for the x-directed edges are all of the general form

$$v_{1\to4} = G\,(a+by+cz+dyz) \quad , \tag{D.5}$$

where $G = 1/(y_2-y_1)(z_2-z_1)$ and a, b, c and d are constants, which are individual to each edge. Using this general form, $\nabla \times \underline{v}_{1\to4}$ can be written as:

$$\nabla \times \begin{pmatrix} v_{1\to4} \\ 0 \\ 0 \end{pmatrix} = G \begin{pmatrix} 0 \\ \frac{\partial}{\partial z}(a+by+cz+dyz) \\ -\frac{\partial}{\partial y}(a+by+cz+dyz) \end{pmatrix} = G \begin{pmatrix} 0 \\ c+dy \\ -b-dz \end{pmatrix} \tag{D.6}$$

Analogous are the basis functions of the y-directed edges defined as

$$\begin{aligned} v_5 &= \frac{(x_2-x)(z_2-z)}{(x_2-x_1)(z_2-z_1)} = \frac{1}{(x_2-x_1)(z_2-z_1)}\,(x_2-x)(z_2-z) \\ &= \frac{1}{(x_2-x_1)(z_2-z_1)}\,(x_2z_2-z_2x-x_2z+xz) \quad , \end{aligned} \tag{D.7}$$

$$\begin{aligned} v_6 &= \frac{(x-x_1)(z_2-z)}{(x_2-x_1)(z_2-z_1)} = \frac{1}{(x_2-x_1)(z_2-z_1)}\,(x-x_1)(z_2-z) \\ &= \frac{1}{(x_2-x_1)(z_2-z_1)}\,(-x_1z_2+z_2x+x_1z-xz) \quad , \end{aligned} \tag{D.8}$$

$$\begin{aligned} v_7 &= \frac{(x_2-x)(z-z_1)}{(x_2-x_1)(z_2-z_1)} = \frac{1}{(x_2-x_1)(z_2-z_1)}\,(x_2-x)(z-z_1) \\ &= \frac{1}{(x_2-x_1)(z_2-z_1)}\,(-x_2z_1+z_1x+x_2z-xz) \quad , \end{aligned} \tag{D.9}$$

and

$$\begin{aligned} v_8 &= \frac{(x-x_1)(z-z_1)}{(x_2-x_1)(z_2-z_1)} = \frac{1}{(x_2-x_1)(z_2-z_1)}\,(x-x_1)(z-z_1) \\ &= \frac{1}{(x_2-x_1)(z_2-z_1)}\,(x_1z_1-z_1x+x_1z-xz) \quad . \end{aligned} \tag{D.10}$$

The general form of the y-directed basis function is given by

$$v_{5\to 8} = H\,(e + fx + gz + hxz) \quad , \tag{D.11}$$

where $H = 1/\,(x_2 - x_1)\,(z_2 - z_1)$ and e, f, g and h are constants, which are individual to each edge. Using this general equation, $\nabla \times \underline{v}_{5\to 8}$ can be written as:

$$\nabla \times \begin{pmatrix} 0 \\ v_{5\to 8} \\ 0 \end{pmatrix} = H \begin{pmatrix} -\frac{\partial}{\partial z}(e + fx + gz + hxz) \\ 0 \\ \frac{\partial}{\partial x}(e + fx + gz + hxz) \end{pmatrix} = H \begin{pmatrix} -g - hx \\ 0 \\ f + hz \end{pmatrix} \tag{D.12}$$

And finally the z-directed edge basis functions are given by

$$\begin{aligned} v_9 &= \frac{(x_2 - x)\,(y_2 - y)}{(x_2 - x_1)\,(y_2 - y_1)} = \frac{1}{(x_2 - x_1)\,(y_2 - y_1)}\,(x_2 - x)\,(y_2 - y) \\ &= \frac{1}{(x_2 - x_1)\,(y_2 - y_1)}\,(x_2 z_2 - y_2 x - x_2 y + xy) \quad , \end{aligned} \tag{D.13}$$

$$\begin{aligned} v_{10} &= \frac{(x - x_1)\,(y_2 - y)}{(x_2 - x_1)\,(y_2 - y_1)} = \frac{1}{(x_2 - x_1)\,(y_2 - y_1)}\,(x - x_1)\,(y_2 - y) \\ &= \frac{1}{(x_2 - x_1)\,(y_2 - y_1)}\,(-x_1 y_2 + y_2 x + x_1 y - xy) \quad , \end{aligned} \tag{D.14}$$

$$\begin{aligned} v_{11} &= \frac{(x_2 - x)\,(y - y_1)}{(x_2 - x_1)\,(y_2 - y_1)} = \frac{1}{(x_2 - x_1)\,(y_2 - y_1)}\,(x_2 - x)\,(y - y_1) \\ &= \frac{1}{(x_2 - x_1)\,(y_2 - y_1)}\,(-x_2 y_1 + y_1 x + x_2 y - xy) \quad , \end{aligned} \tag{D.15}$$

$$\begin{aligned} v_{12} &= \frac{(x - x_1)\,(y - y_1)}{(x_2 - x_1)\,(y_2 - y_1)} = \frac{1}{(x_2 - x_1)\,(y_2 - y_1)}\,(x - x_1)\,(y - y_1) \\ &= \frac{1}{(x_2 - x_1)\,(y_2 - y_1)}\,(x_1 y_1 - y_1 x + x_1 y - xy) \quad . \end{aligned} \tag{D.16}$$

The z-directed basis function all have the following general form

$$v_{9\to 12} = K\,(i + jx + ky + lxy) \quad , \tag{D.17}$$

where $K = 1/\,(x_2 - x_1)\,(y_2 - y_1)$ and i, j, k and l are constants, which are individual to each edge. Using this general form, $\nabla \times \underline{v}_{9\to 12}$ can be written as

$$\nabla \times \begin{pmatrix} 0 \\ 0 \\ v_{9\to 12} \end{pmatrix} = K \begin{pmatrix} \frac{\partial}{\partial y}(i + jx + ky + lxy) \\ -\frac{\partial}{\partial x}(i + jx + ky + lxy) \\ 0 \end{pmatrix} = K \begin{pmatrix} k + lx \\ -j - ly \\ 0 \end{pmatrix} \tag{D.18}$$

To solve the system of equations calculating the electric field components (Equation 6.10) a multiplication of the curls of the basis functions is required. Using the general form of the

basis functions, the multiplication of $(\nabla \times \underline{\nu}_i) \cdot (\nabla \times \underline{\nu}_j)$ for parallel-directed edges i and j is given by

$$\begin{aligned}
\nabla \times \begin{pmatrix} \nu_{1\to4} \\ 0 \\ 0 \end{pmatrix}_i \cdot \nabla \times \begin{pmatrix} \nu_{1\to4} \\ 0 \\ 0 \end{pmatrix}_j &= G \begin{pmatrix} 0 \\ c_i + d_i y \\ -b_i - d_i z \end{pmatrix} \cdot G \begin{pmatrix} 0 \\ c_j + d_j y \\ -b_j - d_j z \end{pmatrix} \\
&= G^2 \left\{ (c_i + d_i y)(c_j + d_j y) + (-b_i - d_i z)(-b_j - d_j z) \right\} \\
&= G^2 \left(c_i c_j + c_i d_j y + d_i c_j y + d_i d_j y^2 + b_i b_j + b_i d_j z + d_i b_j z + d_i d_j z^2 \right) , \quad \text{(D.19)}
\end{aligned}$$

$$\begin{aligned}
\nabla \times \begin{pmatrix} 0 \\ \nu_{5\to8} \\ 0 \end{pmatrix}_i \cdot \nabla \times \begin{pmatrix} 0 \\ \nu_{5\to8} \\ 0 \end{pmatrix}_j &= H \begin{pmatrix} -g_i - h_i x \\ 0 \\ f_i + h_i z \end{pmatrix} \cdot H \begin{pmatrix} -g_j - h_j x \\ 0 \\ f_j + h_j z \end{pmatrix} \\
&= H^2 \left\{ (-g_i - h_i x)(-g_j - g_j x) + (f_i + h_i z)(f_j + h_j z) \right\} \\
&= H^2 \left(g_i g_j + g_i h_j x + h_i g_j x + h_i h_j x^2 + f_i f_j + f_i h_j z + h_i f_j z + h_i h_j z^2 \right) \quad \text{(D.20)}
\end{aligned}$$

and

$$\begin{aligned}
\nabla \times \begin{pmatrix} 0 \\ 0 \\ \nu_{9\to12} \end{pmatrix}_i \cdot \nabla \times \begin{pmatrix} 0 \\ 0 \\ \nu_{9\to12} \end{pmatrix}_j &= K \begin{pmatrix} k_i + l_i x \\ -j_i - l_i y \\ 0 \end{pmatrix} \cdot \begin{pmatrix} k_j + l_j x \\ -j_j - l_j y \\ 0 \end{pmatrix} \\
&= K^2 \left\{ (k_i + l_i x)(k_j + l_j x) + (-j_i - l_i y)(-j_j - l_j y) \right\} \\
&= K^2 \left(k_i k_j + k_i l_j x + l_i k_j x + l_i l_j x^2 + j_i j_j + j_i l_j y + l_i j_j y + l_i l_j y^2 \right) \quad . \quad \text{(D.21)}
\end{aligned}$$

The mixed term multiplication of $(\nabla \times \underline{\nu}_i) \cdot (\nabla \times \underline{\nu}_j)$ for perpendicular edges i and j is given by

$$\begin{aligned}
\nabla \times \begin{pmatrix} \nu_{1\to4} \\ 0 \\ 0 \end{pmatrix}_i \cdot \nabla \times \begin{pmatrix} 0 \\ \nu_{5\to8} \\ 0 \end{pmatrix}_j &= G \begin{pmatrix} 0 \\ c_i + d_i y \\ -b_i - d_i z \end{pmatrix} \cdot H \begin{pmatrix} -g_j - h_j x \\ 0 \\ f_j + h_j z \end{pmatrix} \\
&= GH(-b_i - d_i z)(f_j + h_j z) \\
&= GH \left(-b_i f_j - b_i h_j z - d_i f_j z - d_i h_j z^2 \right) \quad , \quad \text{(D.22)}
\end{aligned}$$

$$\nabla \times \begin{pmatrix} \nu_{1\to4} \\ 0 \\ 0 \end{pmatrix}_i \cdot \nabla \times \begin{pmatrix} 0 \\ 0 \\ \nu_{9\to12} \end{pmatrix}_j = G \begin{pmatrix} 0 \\ c_i + d_i y \\ -b_i - d_i z \end{pmatrix} \cdot K \begin{pmatrix} k_j - l_j x \\ -j_j - l_j y \\ 0 \end{pmatrix}$$

$$= GK(c_i + d_i y)(-j_j - l_j y)$$

$$= GK\left(-c_i j_j - c_i l_j y - d_i j_j y - d_i l_j y^2\right) \tag{D.23}$$

and

$$\nabla \times \begin{pmatrix} 0 \\ v_{5\to 8} \\ 0 \end{pmatrix}_j \cdot \nabla \times \begin{pmatrix} 0 \\ 0 \\ v_{9\to 12} \end{pmatrix}_j = H \begin{pmatrix} -g_j - h_j x \\ 0 \\ f_j + h_j z \end{pmatrix} \cdot K \begin{pmatrix} k_j - l_j x \\ -j_j - l_j y \\ 0 \end{pmatrix}$$

$$= HK(-g_i - h_i x)(k_j + l_j x)$$

$$= HK\left(-g_i k_j - g_i l_j x - h_i k_j x - h_i l_j x^2\right) \quad . \tag{D.24}$$

D.2 NODAL ELEMENT BASIS FUNCTIONS

In Section 6.1 the general formulation of a nodal-element basis function was given (Equation 6.2). The basis function for a simple rectangular brick element is for example given by Jin (2002) and Figure D.2 shows a sketch of such an example cell, its numbering of all nodes and the locations of the nodes with respect to a global Cartesian coordinate system.

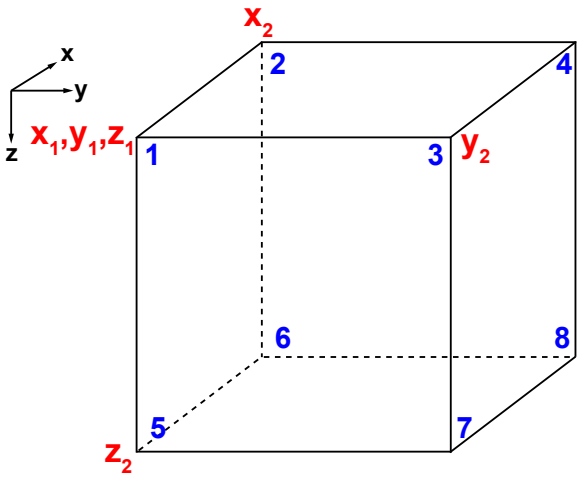

Figure D.2: Sketch of one cell and its numbering of nodes and the global mesh coordinates.

Based on these numbers the nodal-elements u_i (where $i = 1, ..., 8$) are given by

$$\begin{aligned} u_1 &= \frac{(x_2 - x)(y_2 - y)(z_2 - z)}{(x_2 - x_1)(y_2 - y_1)(z_2 - z_1)} = \\ &= \frac{x_2y_2z_2 - y_2z_2x - x_2z_2y - x_2y_2z + z_2xy + y_2xz + x_2yz - xyz}{(x_2 - x_1)(y_2 - y_1)(z_2 - z_1)} \quad , \end{aligned} \tag{D.25}$$

$$\begin{aligned} u_2 &= \frac{(x - x_1)(y_2 - y)(z_2 - z)}{(x_2 - x_1)(y_2 - y_1)(z_2 - z_1)} = \\ &= \frac{-x_1y_2z_2 + y_2z_2x + x_1z_2y + x_1y_2z - z_2xy - y_2xz - x_1yz + xyz}{(x_2 - x_1)(y_2 - y_1)(z_2 - z_1)} \quad , \end{aligned} \tag{D.26}$$

$$\begin{aligned} u_3 &= \frac{(x_2 - x)(y - y_1)(z_2 - z)}{(x_2 - x_1)(y_2 - y_1)(z_2 - z_1)} = \\ &= \frac{-x_2y_1z_2 + y_1z_2x + x_2z_2y + x_2y_1z - z_2xy - y_1xz - x_2yz + xyz}{(x_2 - x_1)(y_2 - y_1)(z_2 - z_1)} \quad , \end{aligned} \tag{D.27}$$

$$\begin{aligned} u_4 &= \frac{(x - x_1)(y - y_1)(z_2 - z)}{(x_2 - x_1)(y_2 - y_1)(z_2 - z_1)} = \\ &= \frac{x_1y_1z_2 - y_1z_2x - x_1z_2y - x_1y_1z + z_2xy + y_1xz + x_1yz - xyz}{(x_2 - x_1)(y_2 - y_1)(z_2 - z_1)} \quad , \end{aligned} \tag{D.28}$$

$$\begin{aligned} u_5 &= \frac{(x_2 - x)(y_2 - y)(z - z_1)}{(x_2 - x_1)(y_2 - y_1)(z_2 - z_1)} = \\ &= \frac{-x_2y_2z_1 + y_2z_1x + x_2z_1y + x_2y_2z - z_1xy - y_2xz - x_2yz + xyz}{(x_2 - x_1)(y_2 - y_1)(z_2 - z_1)} \quad , \end{aligned} \tag{D.29}$$

$$\begin{aligned} u_6 &= \frac{(x - x_1)(y_2 - y)(z - z_1)}{(x_2 - x_1)(y_2 - y_1)(z_2 - z_1)} = \\ &= \frac{x_1y_2z_1 - y_2z_1x - x_1z_1y - x_1y_2z + z_1xy + y_2xz + x_1yz - xyz}{(x_2 - x_1)(y_2 - y_1)(z_2 - z_1)} \quad , \end{aligned} \tag{D.30}$$

$$\begin{aligned} u_7 &= \frac{(x_2 - x)(y - y_1)(z - z_1)}{(x_2 - x_1)(y_2 - y_1)(z_2 - z_1)} = \\ &= \frac{x_2y_1z_1 - y_1z_1x - x_2z_1y - x_2y_1z + z_1xy + y_1xz + x_2yz - xyz}{(x_2 - x_1)(y_2 - y_1)(z_2 - z_1)} \quad , \end{aligned} \tag{D.31}$$

$$\begin{aligned} u_8 &= \frac{(x - x_1)(y - y_1)(z - z_1)}{(x_2 - x_1)(y_2 - y_1)(z_2 - z_1)} = \\ &= \frac{-x_1y_1z_1 + y_1z_1x + x_1z_1y + x_1y_1z - z_1xy - y_1xz - x_1yz + xyz}{(x_2 - x_1)(y_2 - y_1)(z_2 - z_1)} \quad . \end{aligned} \tag{D.32}$$

The nodal basis functions are all of the general form

$$u_{1\to 8} = C\,(a + bx + cy + dz + exy + fxz + gyz + xyz) \quad , \tag{D.33}$$

where $C = 1/\,(x_2 - x_1)\,(y_2 - y_1)\,(z_2 - z_1)$ and a, b, c, d, e, f and g are constants, which are individual to each node. Using this general form, the gradient $\nabla u_{1\to 8}$ can be written as

$$\nabla u_{1\to 8} = C \begin{pmatrix} \frac{\partial}{\partial x} u_{1\to 8} \\ \frac{\partial}{\partial y} u_{1\to 8} \\ \frac{\partial}{\partial z} u_{1\to 8} \end{pmatrix} = C \begin{pmatrix} b + ey + fz + yz \\ c + ex + gz + xz \\ d + fx + gy + xy \end{pmatrix} \quad . \tag{D.34}$$

To solve the system of equations for the approximate potential (Equation 6.24) a multiplication of the gradients of two nodal basis functions is required. Using the general form of the basis functions, the multiplication of $(\nabla u_i) \cdot (\nabla u_j)$ for two nodes i and j is given by

$$\nabla u_i \cdot \nabla u_j = C \begin{pmatrix} b_i + e_i y + f_i z + yz \\ c_i + e_i x + g_i z + xz \\ d_i + f_i x + g_i y + xy \end{pmatrix} \cdot C \begin{pmatrix} b_j + e_j y + f_j z + yz \\ c_j + e_j x + g_j z + xz \\ d_j + f_j x + g_j y + xy \end{pmatrix} \quad , \tag{D.35}$$

if $i = j$ then

$$\begin{aligned} \nabla u_i \cdot \nabla u_i = C^2 \Big((b_i + e_i y + f_i z + yz)^2 \quad &+ \quad (c_i + e_i x + g_i z + xz)^2 \\ &+ \quad (d_i + f_i x + g_i y + xy)^2 \Big) \end{aligned} \tag{D.36}$$

else

$$\begin{aligned} \nabla u_i \cdot \nabla u_j = \quad C^2 \quad &\big\{ (b_i + e_i y + f_i z + yz)(b_j + e_j y + f_j z + yz) \\ &+ \quad (c_i + e_i x + g_i z + xz)(c_j + e_j x + g_j z + xz) \\ &+ \quad (d_i + f_i x + g_i y + xy)(d_j + f_j x + g_j y + xy) \big\} \quad . \end{aligned} \tag{D.37}$$

The right hand side of Equation 6.24 involves the multiplication of a nodal-element and an edge-element basis function, i. e., $u_h \cdot \underline{v}_j \cdot \underline{\hat{n}}$. This product is only non-zero, if the hth node and the jth edge are part of the same cell (or more specific of the same face in this cell), and if $\underline{v}_j$ is parallel to $\underline{\hat{n}}$, i.e.,

$$u_h \cdot \underline{v}_j \cdot \underline{\hat{n}} = \begin{cases} 0 & \text{if } \underline{v}_j \perp \underline{\hat{n}} \text{ and/or } u_h \text{ and } \underline{v}_j \text{ are not part of the same face} \\ t_{h,j} & \text{if } \underline{v}_j \parallel \underline{\hat{n}};\ u_h \text{ and } \underline{v}_j \text{ are part of the same face} \end{cases} \tag{D.38}$$

where for $\underline{\hat{n}}$ in x-direction $t_{h,j}$ (where $h = 1,..,8$ and $j = 1,2,3,4$) is given by (using Equations D.5 and D.33)

$$
\begin{aligned}
t_{1\to8,1\to4} &= u_{1\to8}\cdot v_{1\to4} \\
&= C\left(a_h + b_h x + c_h y + d_h z + e_h xy + f_h xz + g_h yz + xyz\right) \\
&\quad \cdot\ G\left(a_j + b_j y + c_j z + d_j yz\right) \\
&= C\ G(a_h a_j + a_h b_j y + a_h c_j z + a_h d_j yz \\
&\quad +\ b_h a_j x + b_h b_j xy + b_h c_j xz + b_h d_j xyz \\
&\quad +\ c_h a_j y + c_h b_j y^2 + c_h c_j yz + c_h d_j y^2 z \\
&\quad +\ d_h a_j z + d_h b_j yz + d_h c_j z^2 + d_h d_j yz^2 \\
&\quad +\ e_h a_j xy + e_h b_j xy^2 + e_h c_j xyz + e_h d_j xy^2 z \\
&\quad +\ f_h a_j xz + f_h b_j xyz + f_h c_j xz^2 + f_h d_j xyz^2 \\
&\quad +\ g_h a_j yz + g_h b_j y^2 z + g_h c_j yz^2 + g_h d_j y^2 z^2 \\
&\quad +\ a_j xyz + b_j xy^2 z + c_j xyz^2 + d_j xy^2 z^2)\quad .
\end{aligned}
\tag{D.39}
$$

Analogous for a y-directed $\underline{\hat{n}}$ is $t_{h,j}$ (where $h = 1,..,8$ and $j = 5,6,7,8$) given by (using Equations D.11 and D.33)

$$
\begin{aligned}
t_{1\to8,5\to8} &= u_{1\to8}\cdot v_{5\to8} \\
&= C\left(a_h + b_h x + c_h y + d_h z + e_h xy + f_h xz + g_h yz + xyz\right) \\
&\quad \cdot\ H\left(e_j + f_j x + g_j z + h_j xz\right) \\
&= C\ H(a_h e_j + a_h f_j x + a_h g_j z + a_h h_j xz \\
&\quad +\ b_h e_j x + b_h f_j x^2 + b_h g_j xz + b_h h_j x^2 z \\
&\quad +\ c_h e_j y + c_h f_j xy + c_h g_j yz + c_h h_j xyz \\
&\quad +\ d_h e_j z + d_h f_j xz + d_h g_j z^2 + d_h h_j xz^2 \\
&\quad +\ e_h e_j xy + e_h f_j x^2 y + e_h g_j xyz + e_h h_j x^2 yz \\
&\quad +\ f_h e_j xz + f_h f_j x^2 z + f_h g_j xz^2 + f_h h_j x^2 z^2 \\
&\quad +\ g_h e_j yz + g_h f_j xyz + g_h g_j yz^2 + g_h h_j xyz^2 \\
&\quad +\ e_j xyz + f_j x^2 yz + g_j xyz^2 + h_j x^2 yz^2)\quad ,
\end{aligned}
\tag{D.40}
$$

and for a z-directed $\underline{\hat{n}}$ ($t_{h,j}$, where $h = 1,..,8$ and $j = 9,10,11,12$) using Equations D.17 and D.33 yields

$$
\begin{aligned}
t_{1\to8,9\to12} &= u_{1\to8}\cdot v_{9\to12} \\
&= C\left(a_h + b_h x + c_h y + d_h z + e_h xy + f_h xz + g_h yz + xyz\right) \\
&\quad \cdot\ K\left(i_j + j_j x + k_j y + l_j xy\right) \\
&= C\ K(a_h i_j + a_h j_j x + a_h k_j y + a_h l_j xy \\
&\quad +\ b_h i_j x + b_h j_j x^2 + b_h k_j xy + b_h l_j x^2 y \\
&\quad +\ c_h i_j y + c_h j_j xy + c_h k_j y^2 + c_h l_j xy^2 \\
&\quad +\ d_h i_j z + d_h j_j xz + d_h k_j yz + d_h l_j xyz \\
&\quad +\ e_h i_j xy + e_h j_j x^2 y + e_h k_j xy^2 + e_h l_j x^2 y^2 \\
&\quad +\ f_h i_j xz + f_h j_j x^2 z + f_h k_j xyz + f_h l_j x^2 yz \\
&\quad +\ g_h i_j yz + g_h j_j xyz + g_h k_j y^2 z + g_h l_j xy^2 z \\
&\quad +\ i_j xyz + j_j x^2 yz + k_j xy^2 z + l_j x^2 y^2 z)\quad .
\end{aligned}
\tag{D.41}
$$

E

FORWARD MODELLING RESULTS

E.1 ROTATED 2D VERSUS 3D RESPONSES

This appendix belongs to the comparison of the 3D responses with the 2D rotated responses over a simple dyke model as described in Section 7.1.2. Figure 7.4 shows the 3D mesh design and the location of the 1 Ωm dyke embedded in a 100 Ωm homogeneous halfspace as well as the locations of all seven sites. The following figures (Figures E.1 to E.3) show the apparent resistivity curves on top and the phase curves below. All four components are plotted; from left to right xx, xy, yx and then yy. The red stars are the 3D responses and the blue squares represent the 2D responses calculated using the code of Rodi and Mackie (2001) (implemented in Geosystem's software WinGLink®) and rotated by 45°. In general these responses agree very well in all four components. Only site 1 and 2 show small differences, which are most likely related to the rather blocky realisation of the 45° dyke in the 3D model.

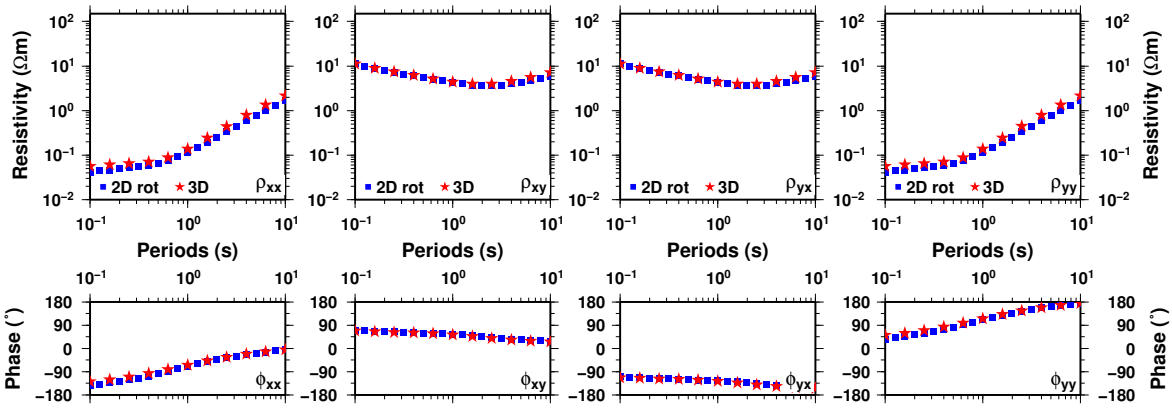

Figure E.1: Resistivity and phase curves for all four components calculated at site 1. The blue squares represent the rotated 2D responses and the red stars are the 3D responses.

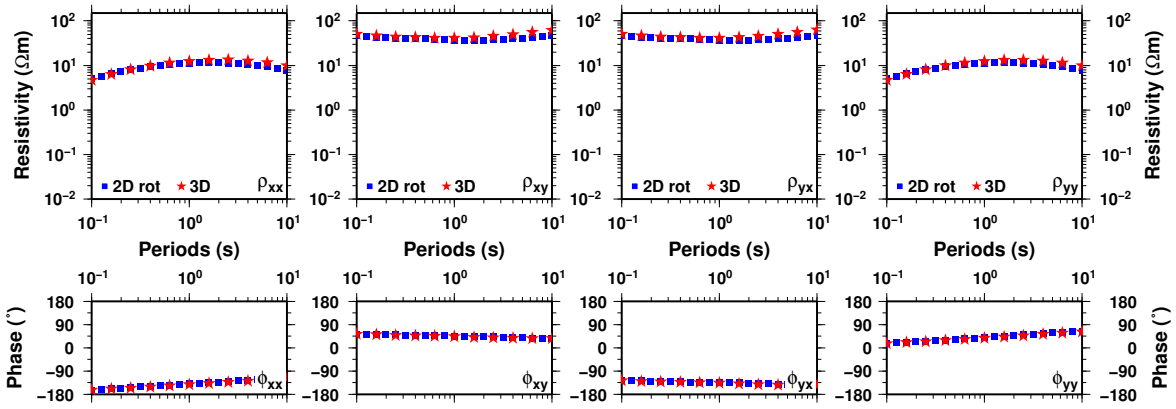

(a) Site 2

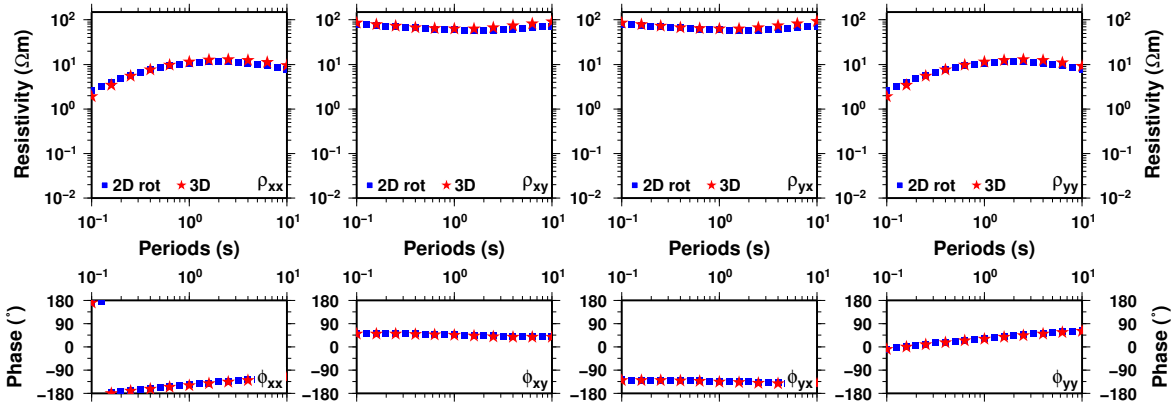

(b) Site 3

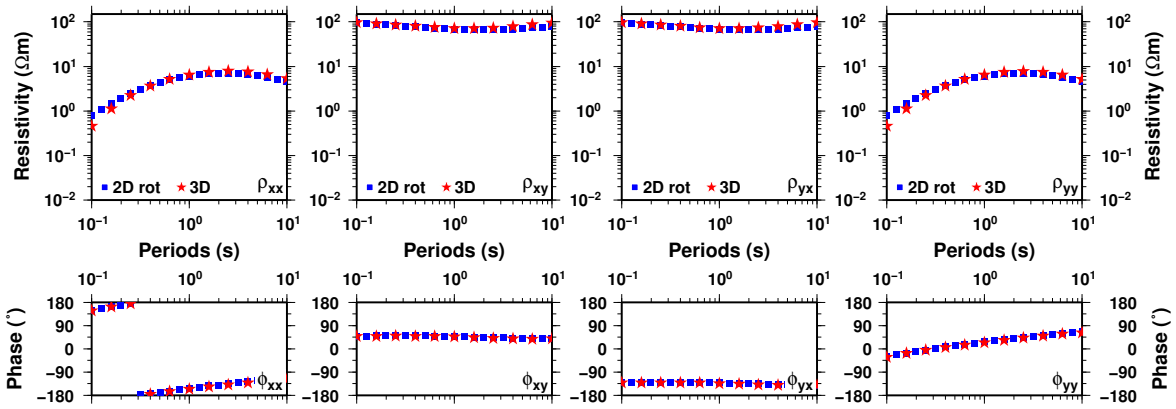

(c) Site 4

Figure E.2: Resistivity and phase curves for all four components calculated at sites 2 (a), 3 (b) and 4 (c). The blue squares represent the rotated 2D responses and the red stars are the 3D responses.

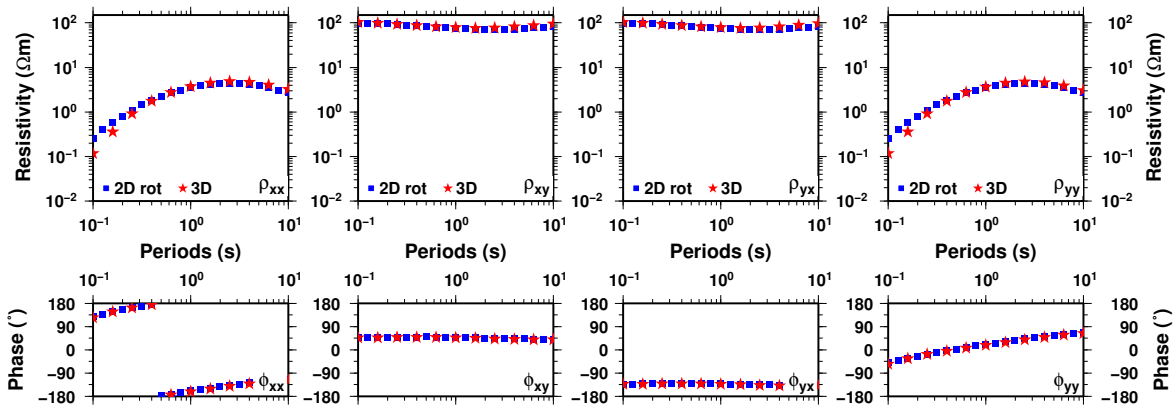

(a) Site 5

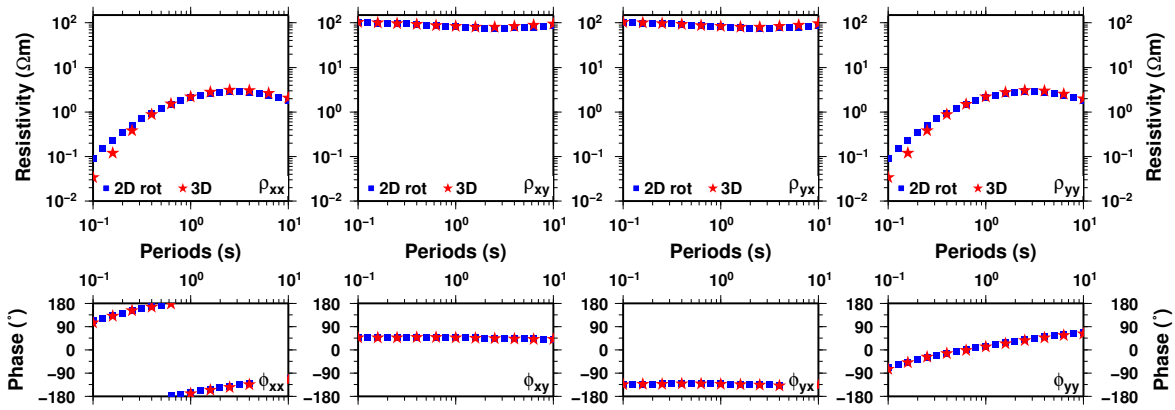

(b) Site 6

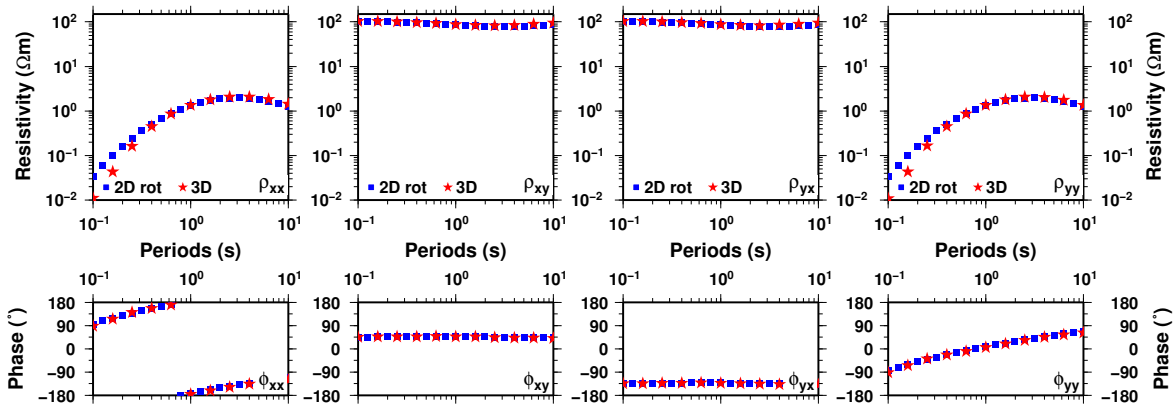

(c) Site 7

Figure E.3: Resistivity and phase curves for all four components calculated at sites 5 (a), 6 (b) and 7 (c). The blue squares represent the rotated 2D responses and the red stars are the 3D responses.

E.2 RESULTS OF THE COMMEMI 3D-1A MODEL

This part of the appendix contains a collection of figures related to the forward tests conducted using the 3D-1A COMMEMI model in Section 7.2.1. The 3D-1A model consists of a 0.5 Ωm block in a homogeneous halfspace of 100 Ωm. Three different sizes of the mesh were used to calculate the forward responses, of which the mesh design is shown here. Figure E.4 shows the mesh for the coarse mesh (46 x 46 x 39 cells with a centre cell width of 250 m), Figure E.5 illustrates the fine mesh (70 x 70 x 39 cells with a centre cell width of 100 m) and finally the very fine mesh (96 x 96 x 39 cells with a centre cell width of 50 m) is shown in Figure E.6.

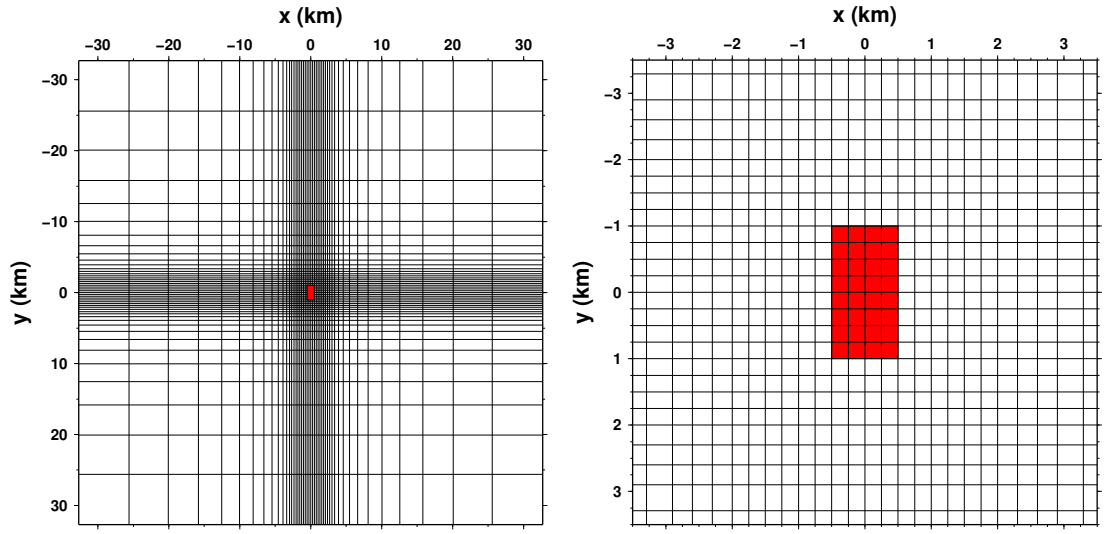

(a) Plan view - complete mesh

(b) Plan view - centre of the mesh

(c) Section view - complete mesh

(d) Section view - centre of the mesh

Figure E.4: Figures showing the mesh design for the 3D-1A coarse mesh in plan view ((a) and (b)) and in section view ((c) and (d)). The mesh consists of 46 x 46 x 39 cells with a centre cell width of 250 m. The red rectangular shows the location of the 0.5 Ωm block of the model and the blue layer indicates the airlayers.

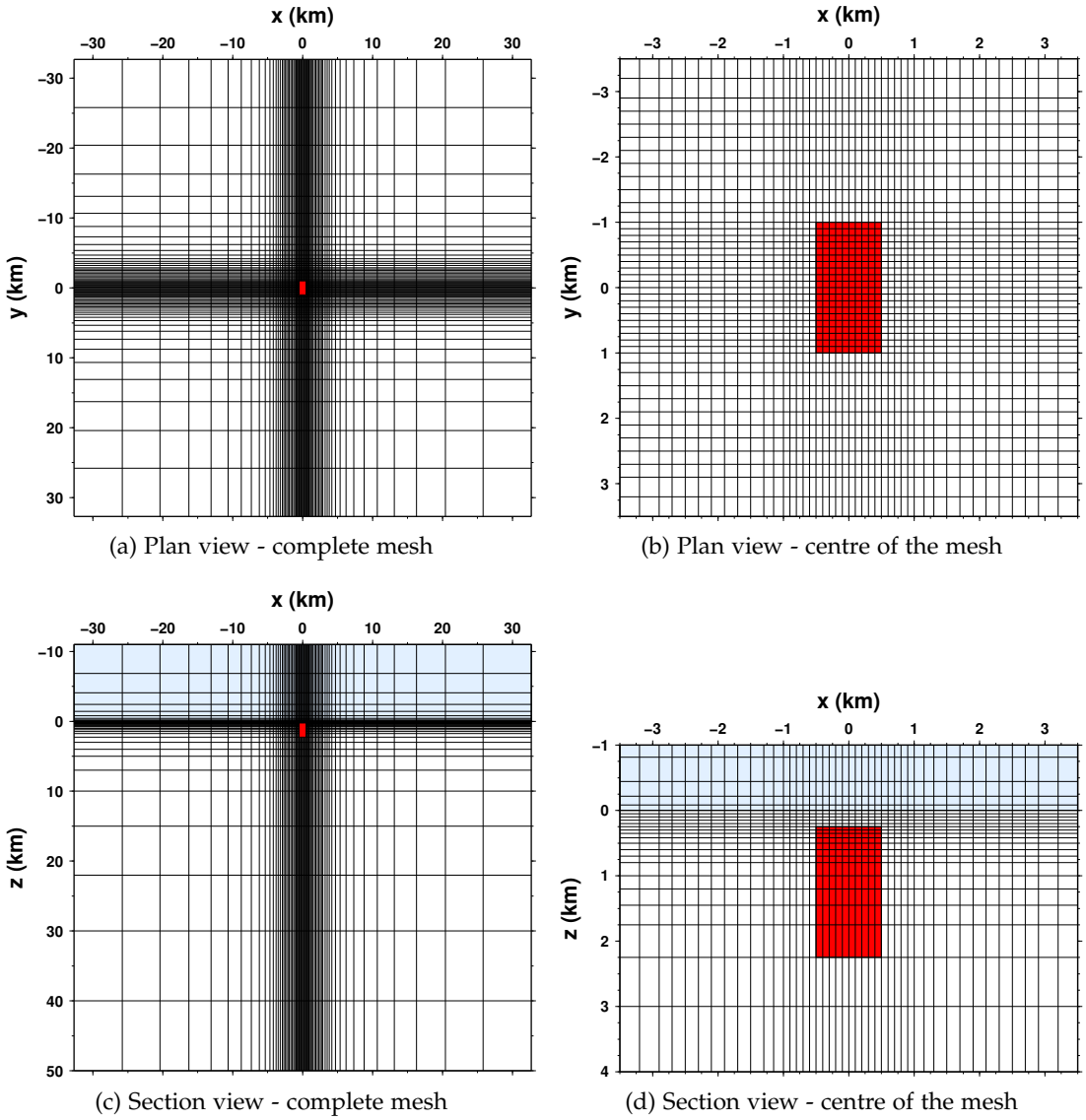

(a) Plan view - complete mesh

(b) Plan view - centre of the mesh

(c) Section view - complete mesh

(d) Section view - centre of the mesh

Figure E.5: Figures showing the mesh design for the 3D-1A fine mesh in plan view ((a) and (b)) and in section view ((c) and (d)). The mesh consists of 70 x 70 x 39 cells with a centre cell width of 100 m. The red rectangular shows the location of the 0.5 Ωm block of the model and the blue layer indicates the airlayers.

Figures E.7, E.8 and E.9 show the comparison of the 3D forward responses (without divergence correction and with correction applied every 10, 20, 50 and 100 iterations) at 0.1 s and 10 s with the results from Zhdanov et al. (1997) for the coarse, fine and very fine mesh, respectively. All figures show that the correction is required to gain reasonable response curves, although it seems that at 10 s it does not matter how often the correction is applied. The corresponding convergence curves for these runs are shown in Figure E.10. Plotted is the preconditioned residual norm (ILU preconditioning with zero fill-in), which is a measure of convergence provided during the iterative procedure by the SPARSKIT solver (Saad, 1990). It can be seen that the convergence is significantly quicker if the divergence correction is applied, and that the convergence tends to be somewhat quicker if the divergence correction is applied more frequently.

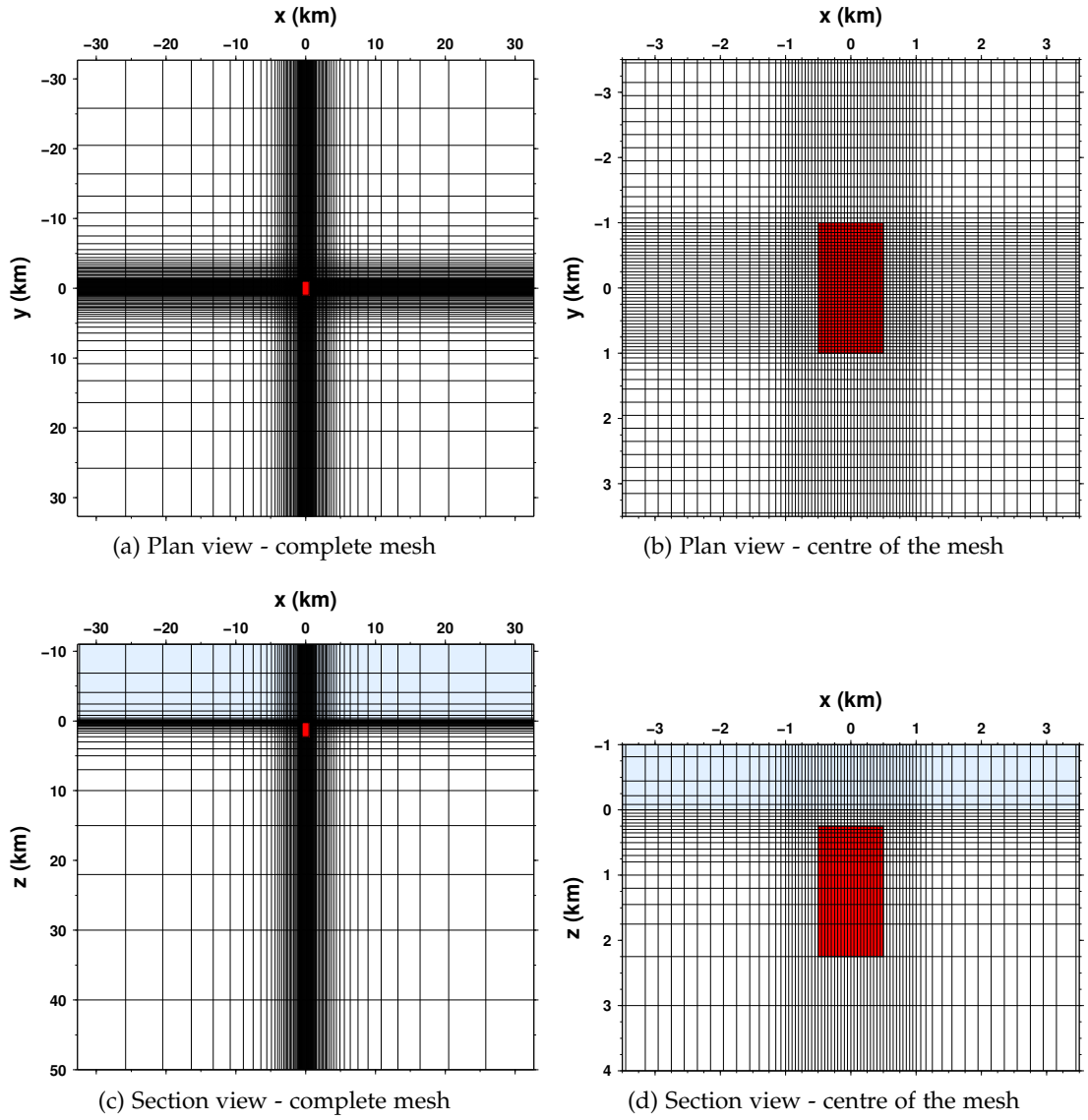

(a) Plan view - complete mesh

(b) Plan view - centre of the mesh

(c) Section view - complete mesh

(d) Section view - centre of the mesh

Figure E.6: Figures showing the mesh design for the 3D-1A very fine mesh in plan view ((a) and (b)) and in section view ((c) and (d)). The mesh consists of 96 x 96 x 39 cells with a centre cell width of 50 m. The red rectangular shows the location of the 0.5 Ωm block of the model and the blue layer indicates the airlayers.

Figures E.11 to E.14 show the horizontal components of the electric field at 275 m depth at 0.1 s and 10 s for both source magnetic field polarizations after 40, 500 and 1000 iterations. The positive effect of the divergence correction to the calculated field is obvious. Figure E.15 to E.18 show the corresponding correction potentials and their gradients (correction fields) for the first application of the correction. The figures show that the correction potential is generated by sources (discontinuities of the normal component of the current density) located over the two faces of the body that are normal to the predominant direction of the electric field.

A comparison of 3D-1A response curves for all three meshes obtained after 100, 200, 400, 600, 800, 1000 and 5000 iteration applying the divergence correction every 20 iterations is shown in Figures E.19 (coarse mesh), Figures E.20 (fine mesh) and Figures E.21 (very fine mesh). While 100 and 200 iterations are not enough to gain a reasonable results, 5000 iterations compared to 1000 iterations can be considered to not be worth the additional costs (computation time). Since 1000 iterations and application of the divergence correction every 20 iterations seems to be the ideal combination for the COMMEMI 3D-1A model, the responses from these settings of all three meshes are shown in Figure E.22. Solid line show the response curve with correction applied and for comparison the response without correction are shown as dashed lines. For more details see Figure 7.12 and corresponding text in Section 7.2.1.

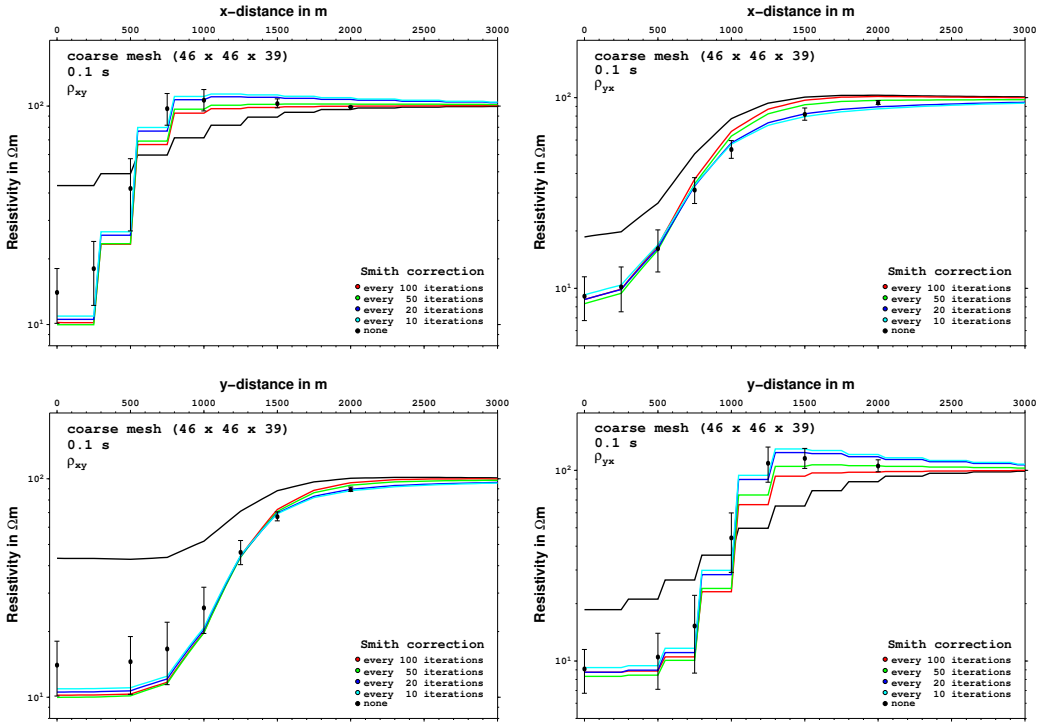

(a) Responses for 0.1 s

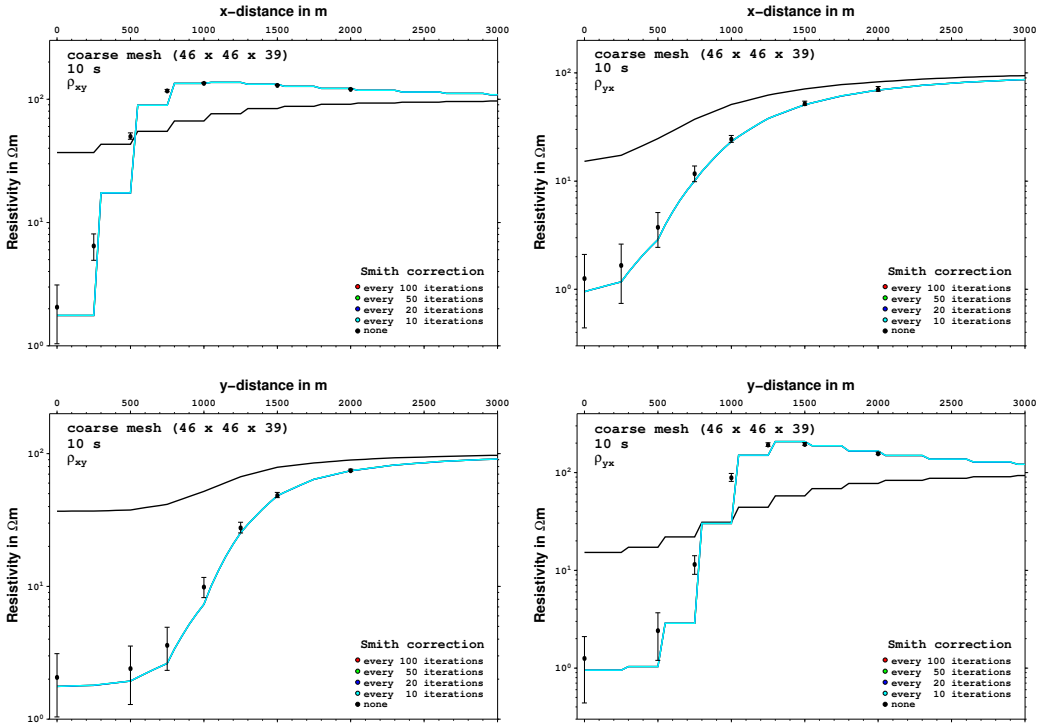

(b) Responses for 10 s

Figure E.7: Figure showing the response curves at 0.1 s (a) and 10 s (b) obtained from the COMMEMI 3D-1A model using a coarse mesh (46 x 46 x 39 cells) and applying the divergence correction every 10, 20, 50 and 100 iterations. The black line shows the response curve calculated without the divergence correction and the symbols with error bars represent the mean value and the standard deviation of the published results from Zhdanov et al. (1997).

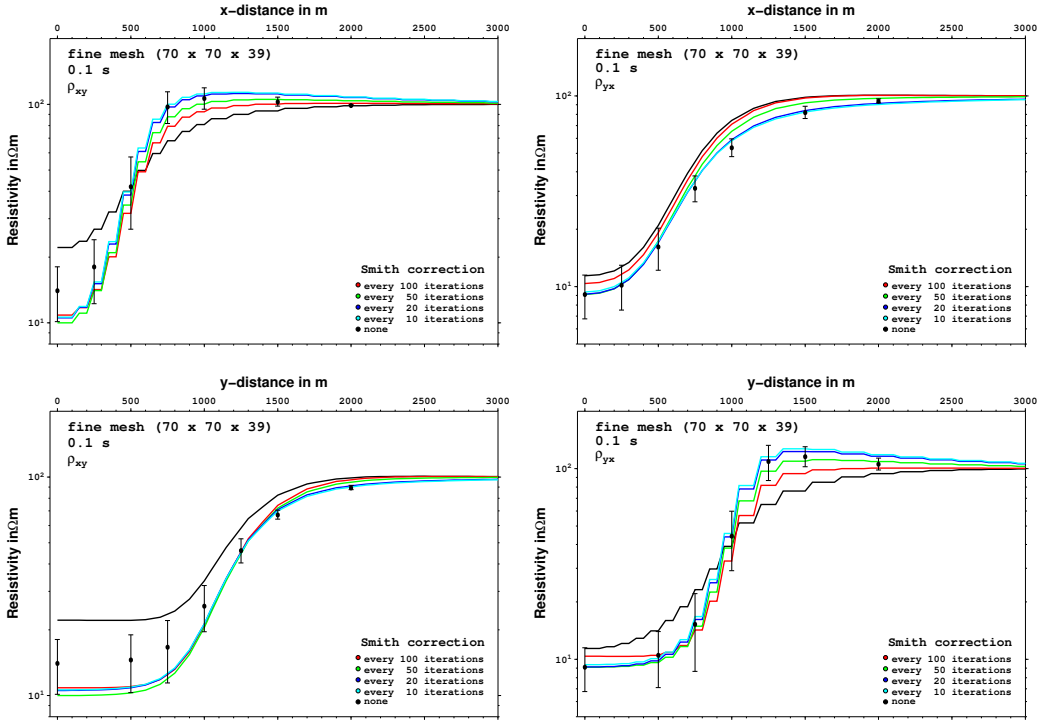

(a) Responses for 0.1 s

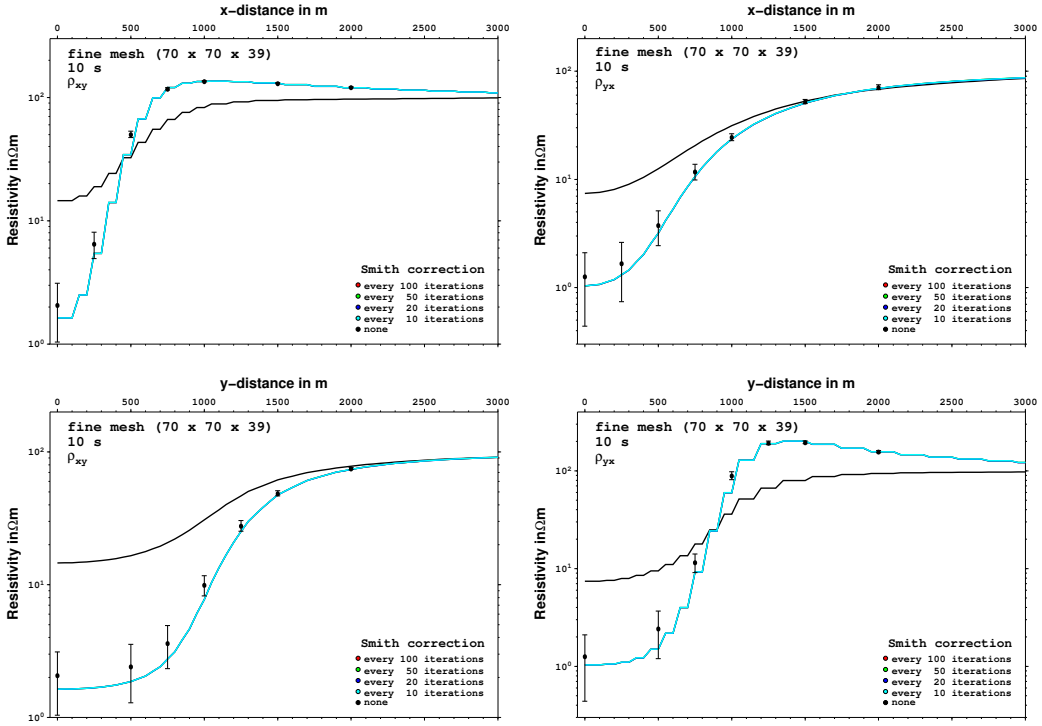

(b) Responses for 10 s

Figure E.8: Figure showing the response curves at 0.1 s (a) and 10 s (b) obtained from the COMMEMI 3D-1A model using a fine mesh (70 x 70 x 39 cells) and applying the divergence correction every 10, 20, 50 and 100 iterations. The black line shows the response curve calculated without the divergence correction and the symbols with error bars represent the mean value and the standard deviation of the published results from Zhdanov et al. (1997).

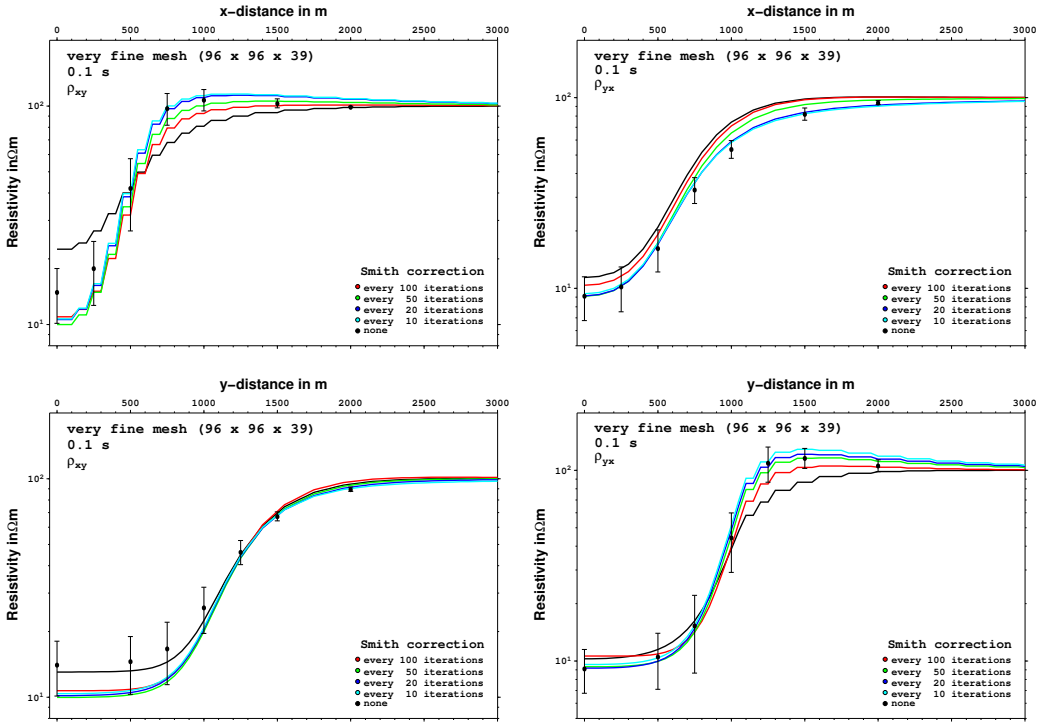

(a) Responses for 0.1 s

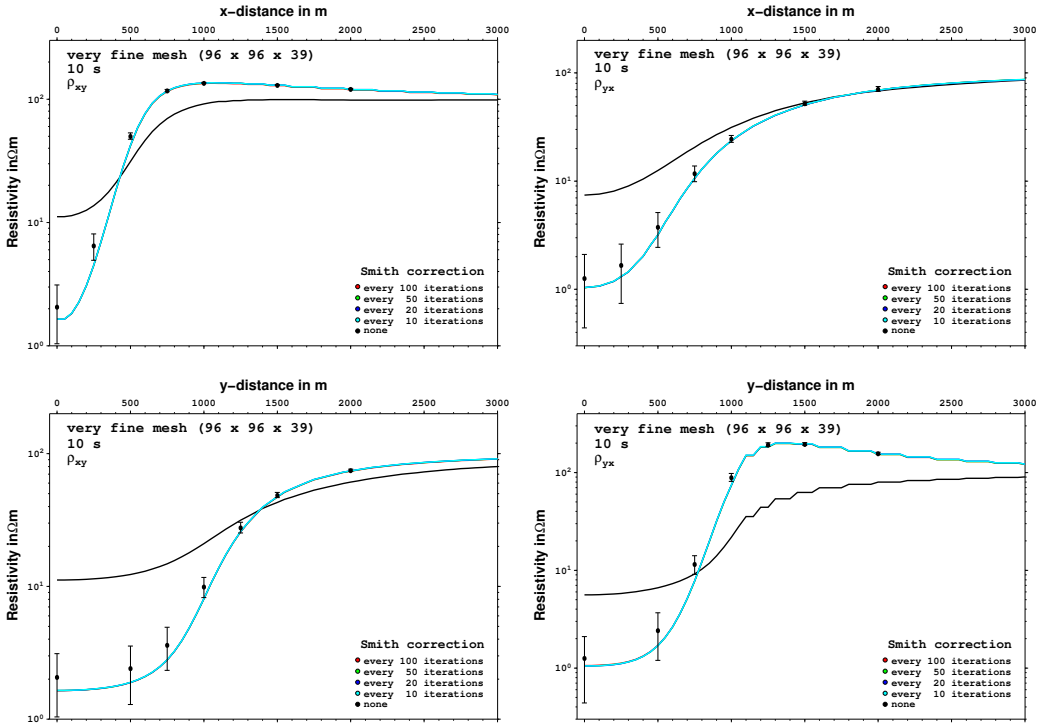

(b) Responses for 10 s

Figure E.9: Figure showing the response curves at 0.1 s (a) and 10 s (b) obtained from the COMMEMI 3D-1A model using a very fine mesh (96 x 96 x 39 cells) and applying the divergence correction every 10, 20, 50 and 100 iterations. The black line shows the response curve calculated without the divergence correction and the symbols with error bars represent the mean value and the standard deviation of the published results from Zhdanov et al. (1997).

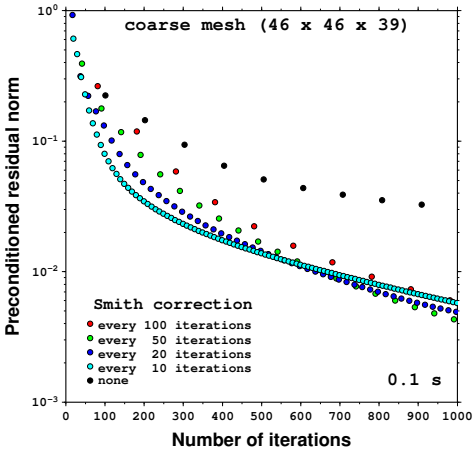

(a) Coarse mesh convergence curve for 0.1 s

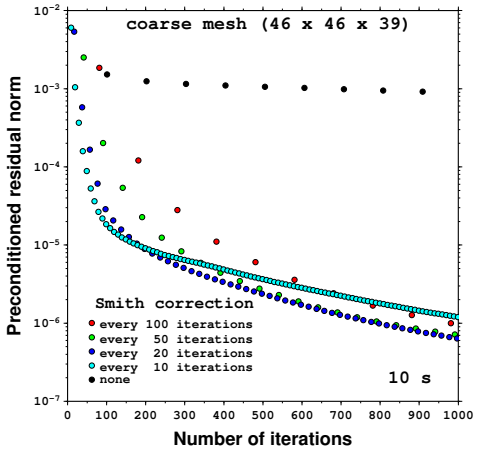

(b) Coarse mesh convergence curve for 10 s

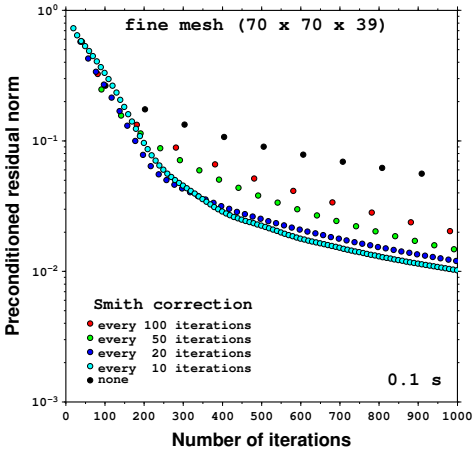

(c) Fine mesh convergence curve for 0.1 s

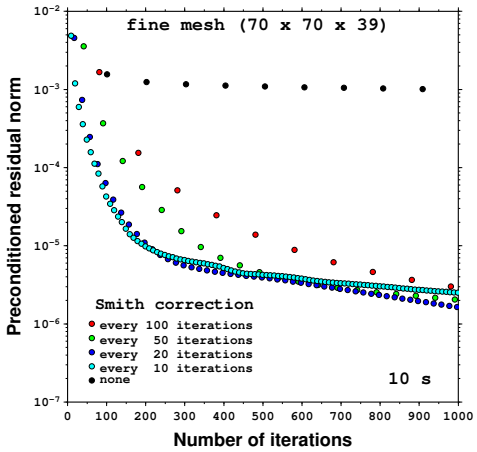

(d) Fine mesh convergence curve for 10 s

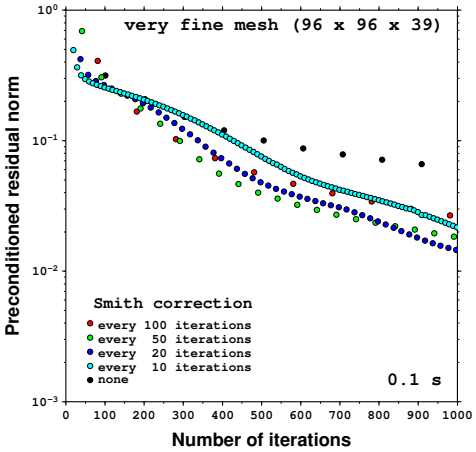

(e) Very fine mesh convergence curve for 0.1 s

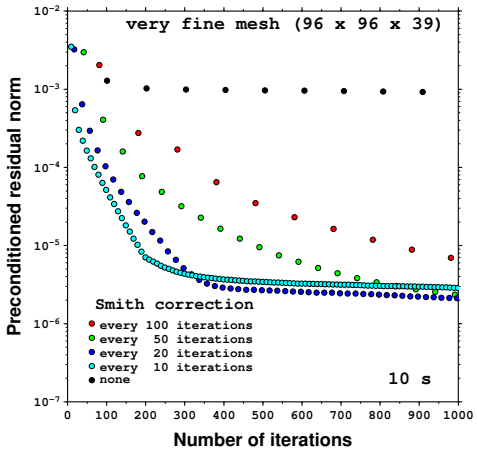

(f) Very fine mesh convergence curve for 10 s

Figure E.10: Figure showing the convergence curves for the coarse mesh (a and b), the fine mesh (c and d) and the very fine mesh (e and f). These curves belong to the calculation of responses curves at 0.1 s (left) and 10 s (right) for the COMMEMI 3D-1A model.

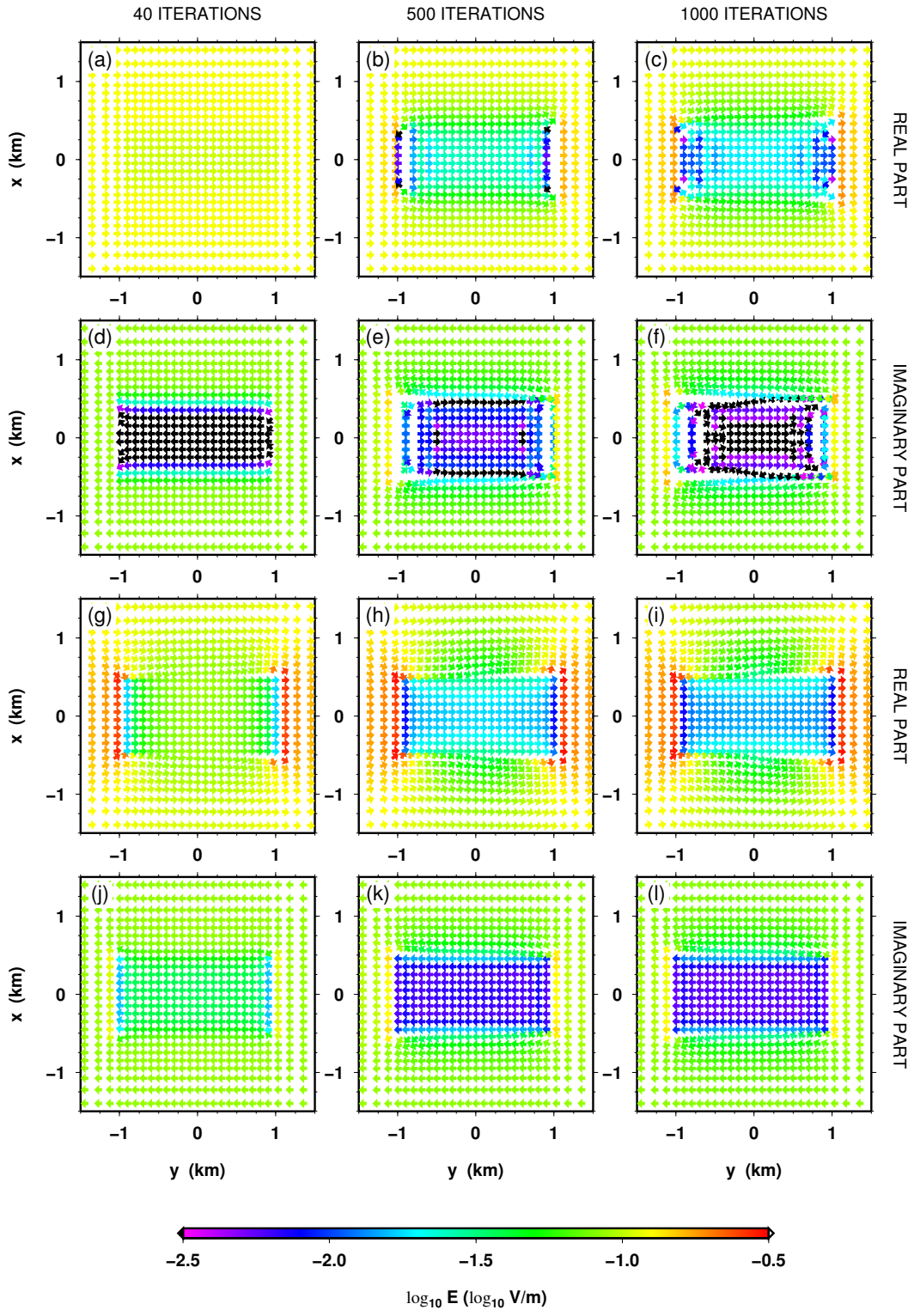

Figure E.11: Horizontal components of the electric field at 0.1 s at a depth of 275 m (x-directed source magnetic field). Panels (a) to (c) show the real and (d) to (f) the imaginary parts of the electric fields for the run without divergence correction, whereas (g) to (i) are the real and (j) to (l) the imaginary parts of the electric fields for the run in which the divergence correction is applied every 20 iterations. The panels on the left show intermediate electric fields after 40 iterations, the middle ones are after 500 iterations and on the right are the final electric fields after 1000 iterations.

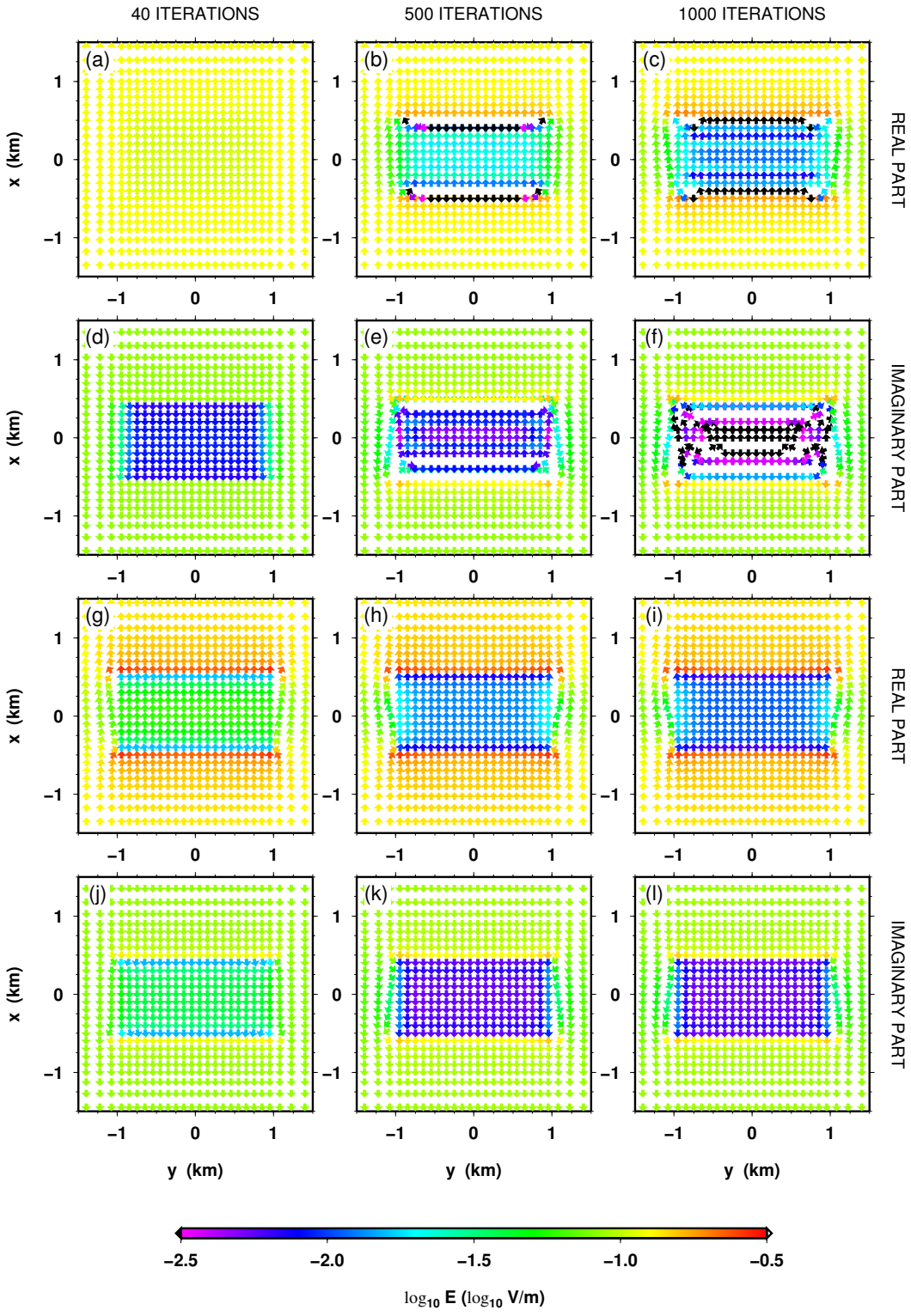

Figure E.12: Horizontal components of the electric field at 0.1 s at a depth of 275 m (y-directed source magnetic field). Panels (a) to (c) show the real and (d) to (f) the imaginary parts of the electric fields for the run without divergence correction, whereas (g) to (i) are the real and (j) to (l) the imaginary parts of the electric fields for the run in which the divergence correction is applied every 20 iterations. The panels on the left show intermediate electric fields after 40 iterations, the middle ones are after 500 iterations and on the right are the final electric fields after 1000 iterations.

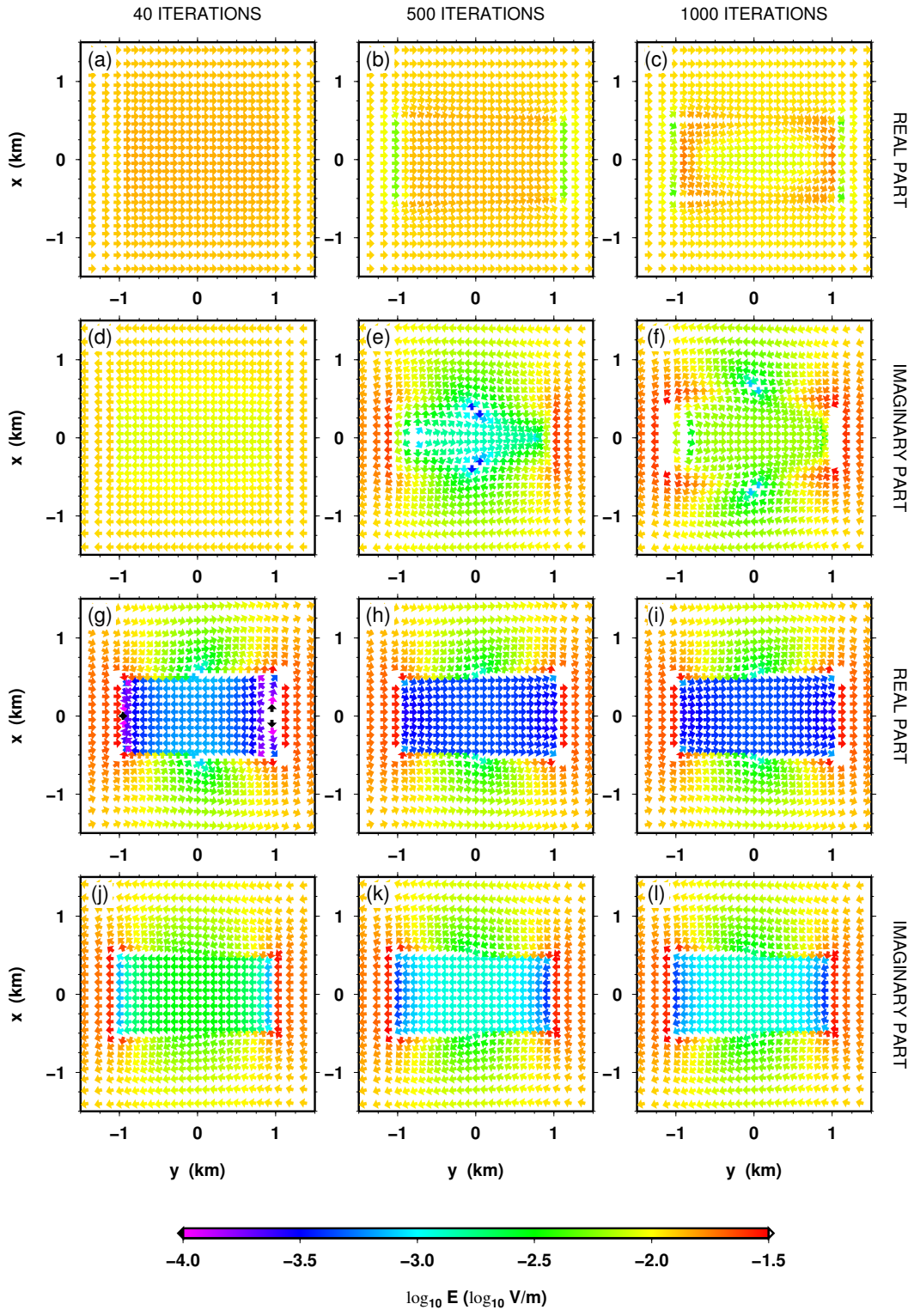

Figure E.13: Horizontal components of the electric field at 10 s at a depth of 275 m (x-directed source magnetic field). Panels (a) to (c) show the real and (d) to (f) the imaginary parts of the electric fields for the run without divergence correction, whereas (g) to (i) are the real and (j) to (l) the imaginary parts of the electric fields for the run in which the divergence correction is applied every 20 iterations. The panels on the left show intermediate electric fields after 40 iterations, the middle ones are after 500 iterations and on the right are the final electric fields after 1000 iterations.

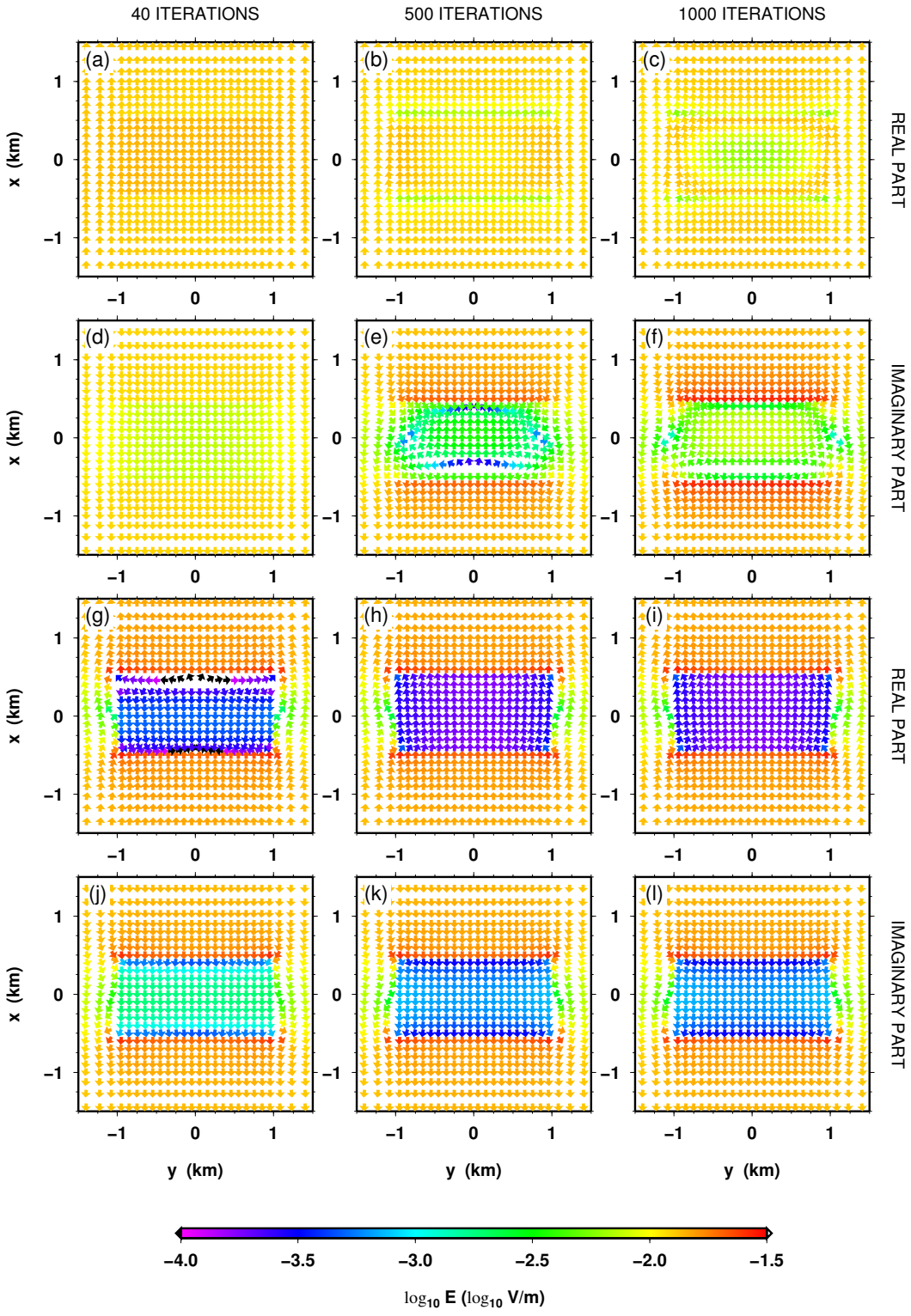

Figure E.14: Horizontal components of the electric field at 10 s at a depth of 275 m (y-directed source magnetic field). Panels (a) to (c) show the real and (d) to (f) the imaginary parts of the electric fields for the run without divergence correction, whereas (g) to (i) are the real and (j) to (l) the imaginary parts of the electric fields for the run in which the divergence correction is applied every 20 iterations. The panels on the left show intermediate electric fields after 40 iterations, the middle ones are after 500 iterations and on the right are the final electric fields after 1000 iterations.

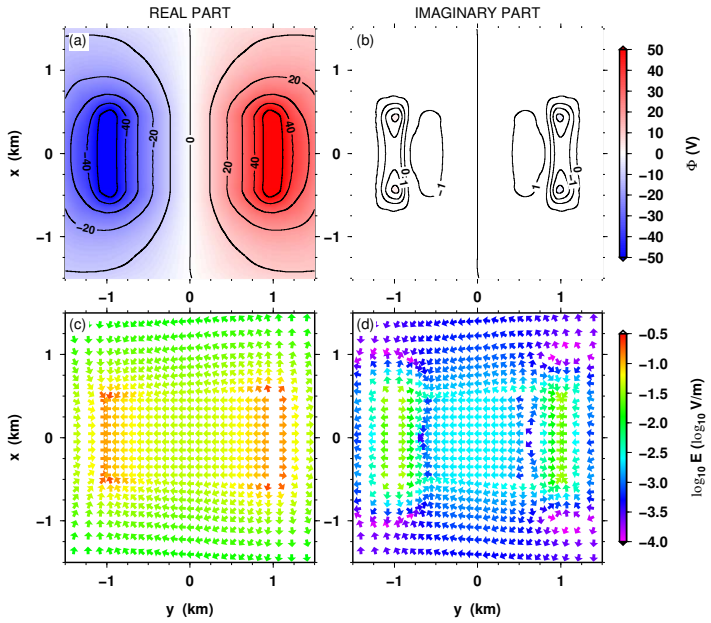

Figure E.15: Divergence correction potential and its gradient at 0.1 s for a x-directed source magnetic field. Panel (a) shows the real and (b) the imaginary parts of the divergence correction potential applied after 20 iterations in the run whose intermediate electric field is shown in Figure E.11 ((g) and (j)). The real (c) and imaginary (d) parts of the horizontal correction electric field are given by the gradient of the correction potential. The potential and field are shown at a depth of 275 m.

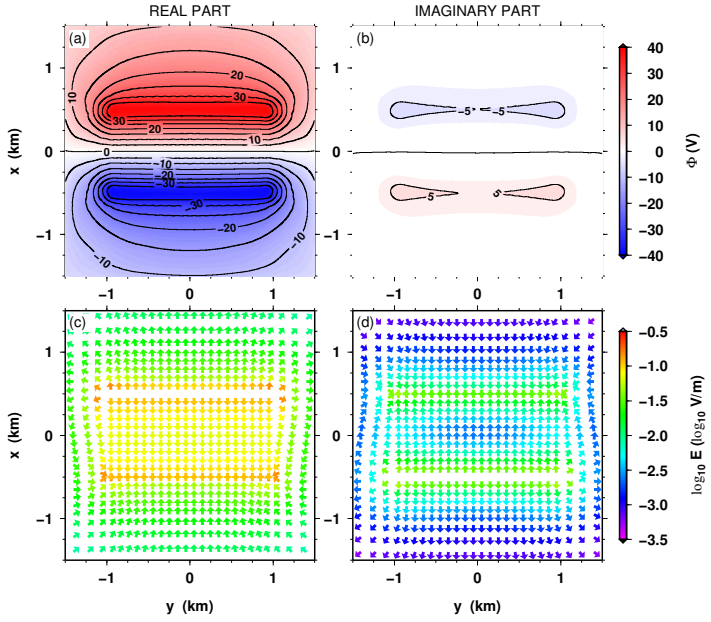

Figure E.16: Divergence correction potential and its gradient at 0.1 s for a y-directed source magnetic field. Panel (a) shows the real and (b) the imaginary parts of the divergence correction potential applied after 20 iterations in the run whose intermediate electric field is shown in Figure E.12 ((g) and (j)). The real (c) and imaginary (d) parts of the horizontal correction electric field are given by the gradient of the correction potential. The potential and field are shown at a depth of 275 m.

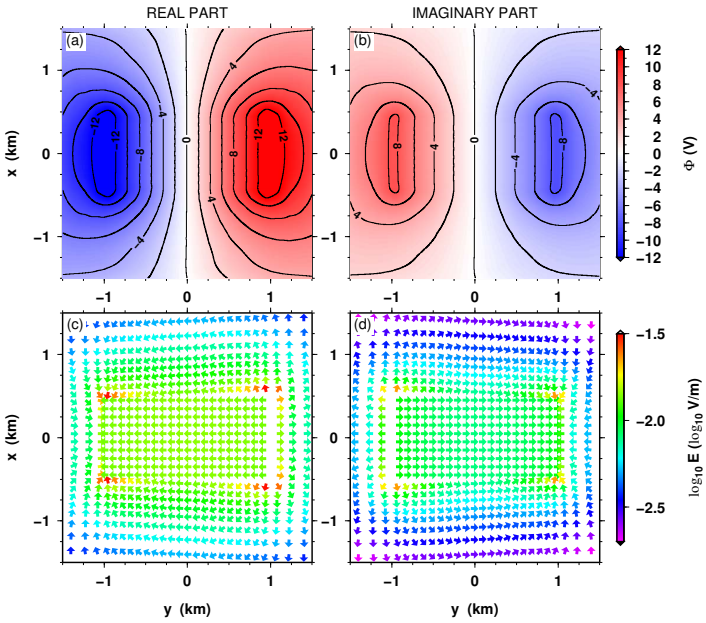

Figure E.17: Divergence correction potential and its gradient at 10 s for a x-directed source magnetic field. Panel (a) shows the real and (b) the imaginary parts of the divergence correction potential applied after 20 iterations in the run whose intermediate electric field is shown in Figure E.13 ((g) and (j)). The real (c) and imaginary (d) parts of the horizontal correction electric field are given by the gradient of the correction potential. The potential and field are shown at a depth of 275 m.

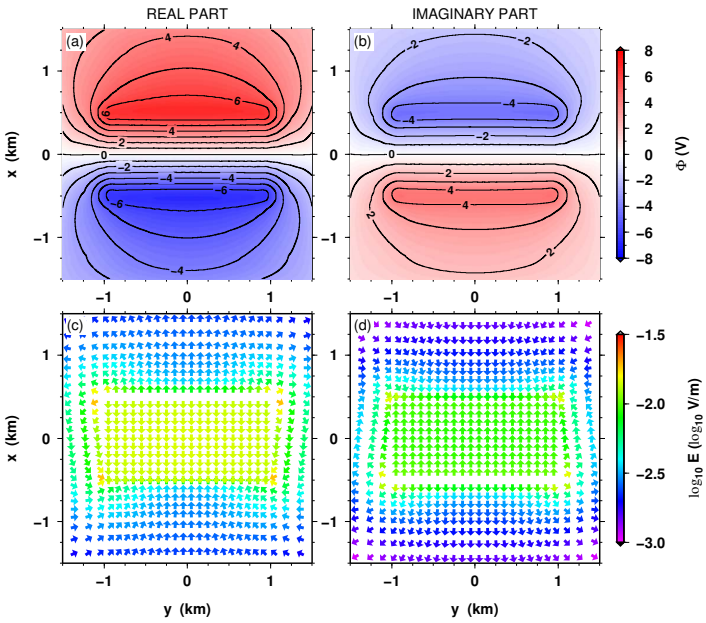

Figure E.18: Divergence correction potential and its gradient at 10 s for a y-directed source magnetic field. Panel (a) shows the real and (b) the imaginary parts of the divergence correction potential applied after 20 iterations in the run whose intermediate electric field is shown in Figure E.14 ((g) and (j)). The real (c) and imaginary (d) parts of the horizontal correction electric field are given by the gradient of the correction potential. The potential and field are shown at a depth of 275 m.

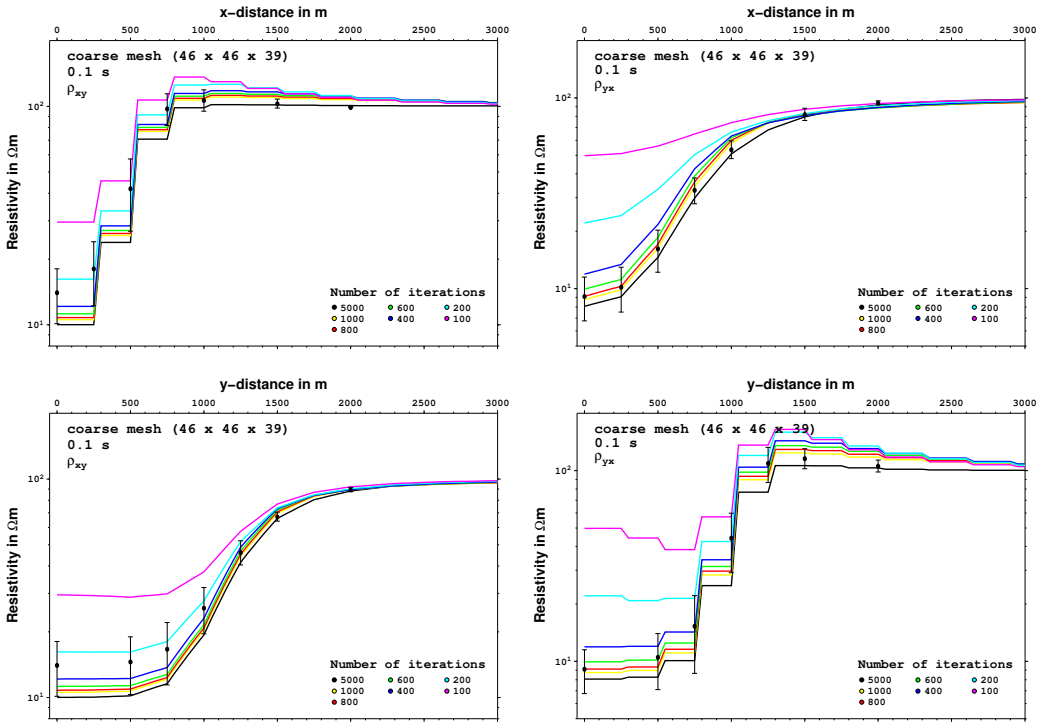

(a) Responses for 0.1 s

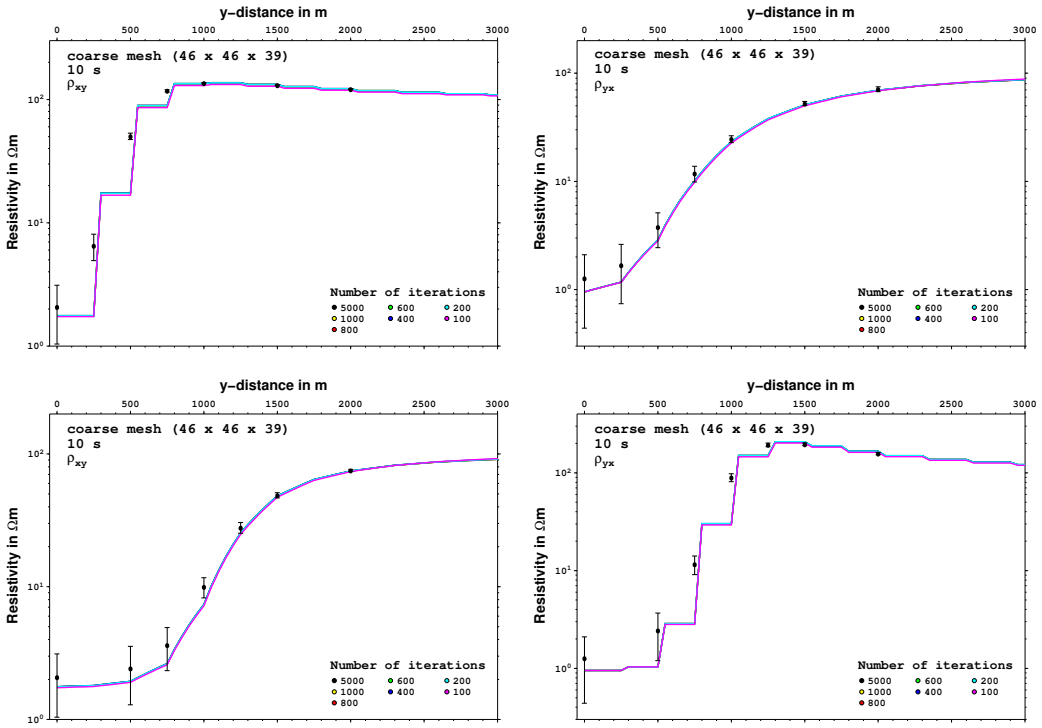

(b) Responses for 10 s

Figure E.19: Figure showing the response curves at 0.1 s (a) and 10 s (b) obtained from the COMMEMI 3D-1A model after 100, 200, 400, 600, 800, 1000 and 5000 iterations (applying the divergence correction every 20 iterations) using a coarse mesh (46 x 46 x 39 cells). The black symbols with error bars represent the mean value and the standard deviation of the published results from Zhdanov et al. (1997).

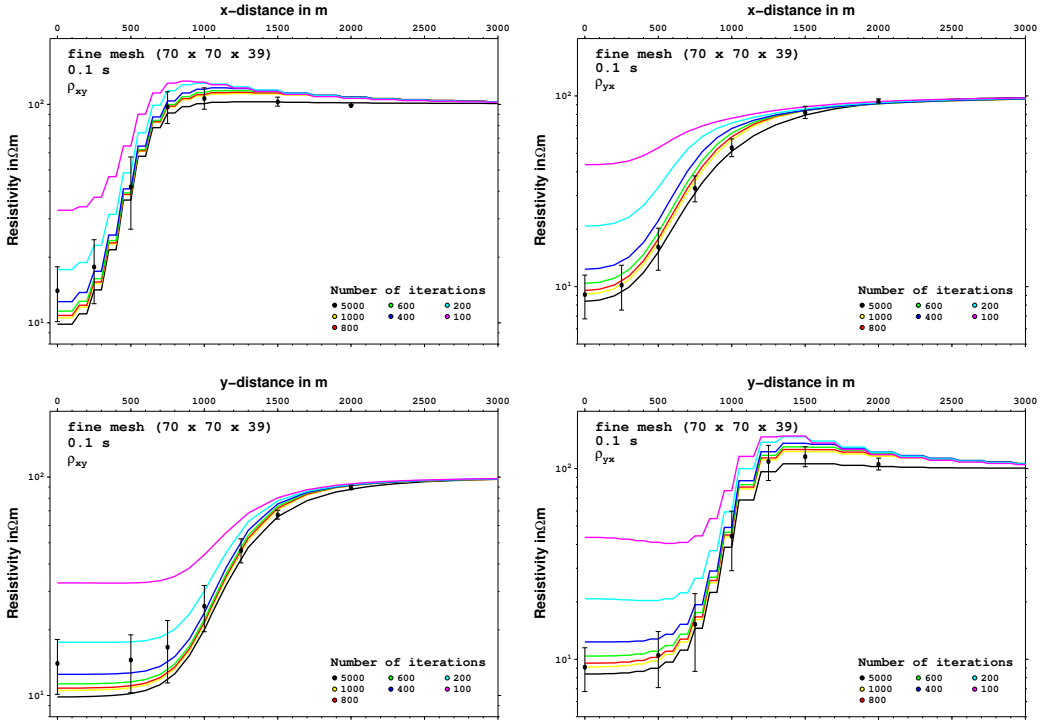

(a) Responses for 0.1 s

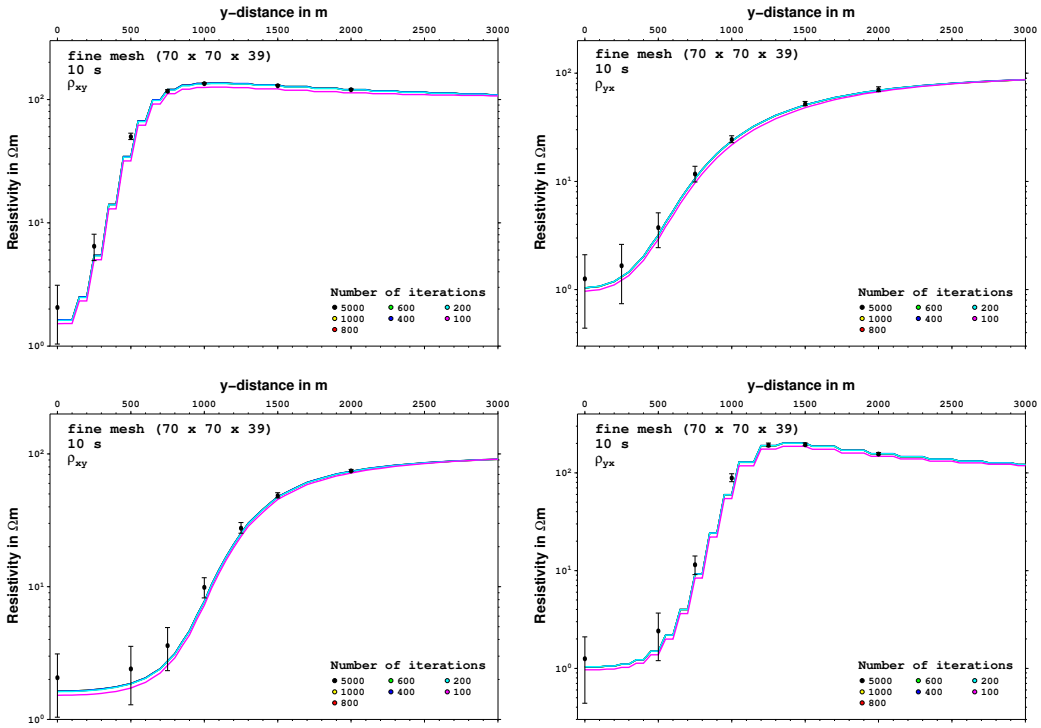

(b) Responses for 10 s

Figure E.20: Figure showing the response curves at 0.1 s (a) and 10 s (b) obtained from the COMMEMI 3D-1A model after 100, 200, 400, 600, 800, 1000 and 5000 iterations (applying the divergence correction every 20 iterations) using a fine mesh (70 x 70 x 39 cells). The black symbols with error bars represent the mean value and the standard deviation of the published results from Zhdanov et al. (1997).

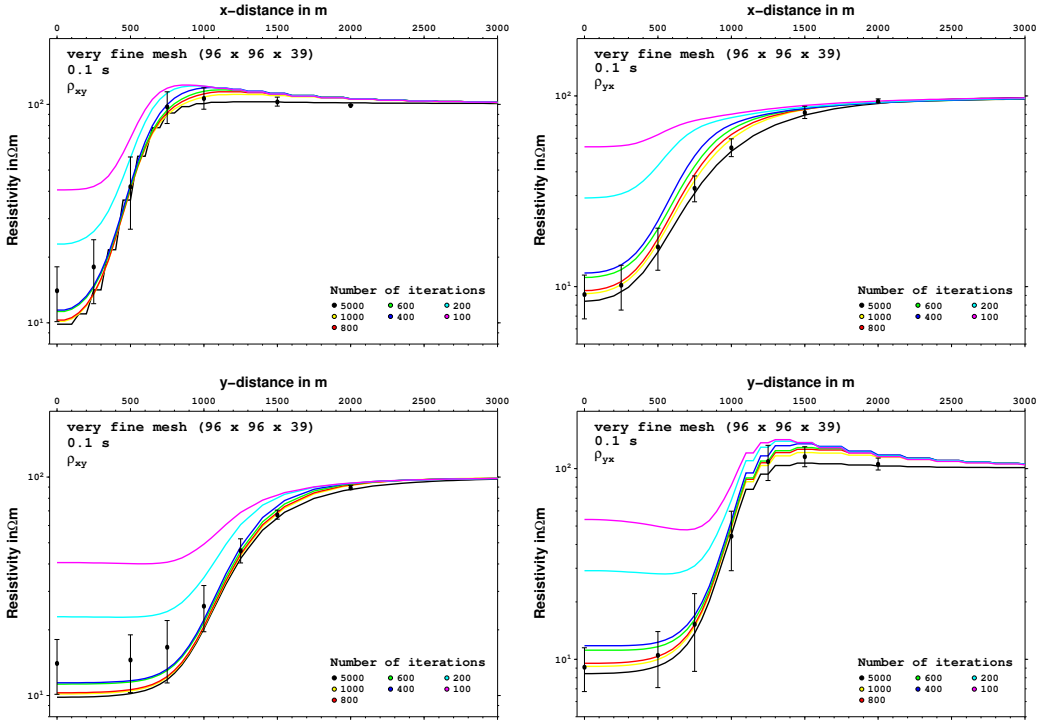

(a) Responses for 0.1 s

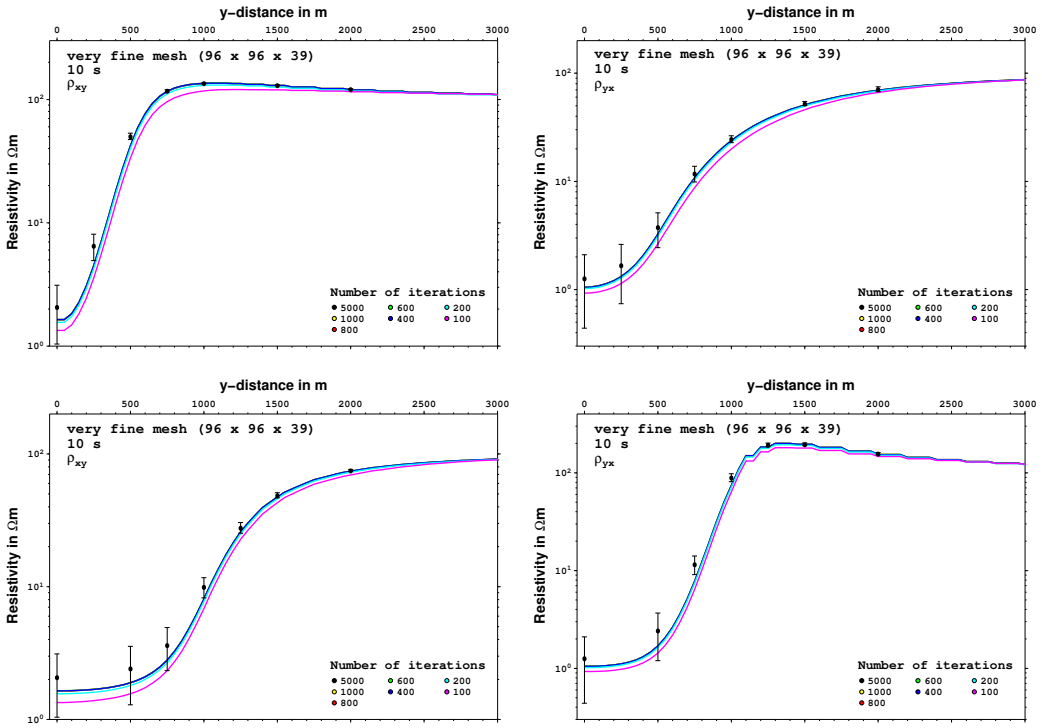

(b) Responses for 10 s

Figure E.21: Figure showing the response curves at 0.1 s (a) and 10 s (b) obtained from the COMMEMI 3D-1A model after 100, 200, 400, 600, 800, 1000 and 5000 iterations (applying the divergence correction every 20 iterations) using a very fine mesh (96 x 96 x 39 cells). The black symbols with error bars represent the mean value and the standard deviation of the published results from Zhdanov et al. (1997).

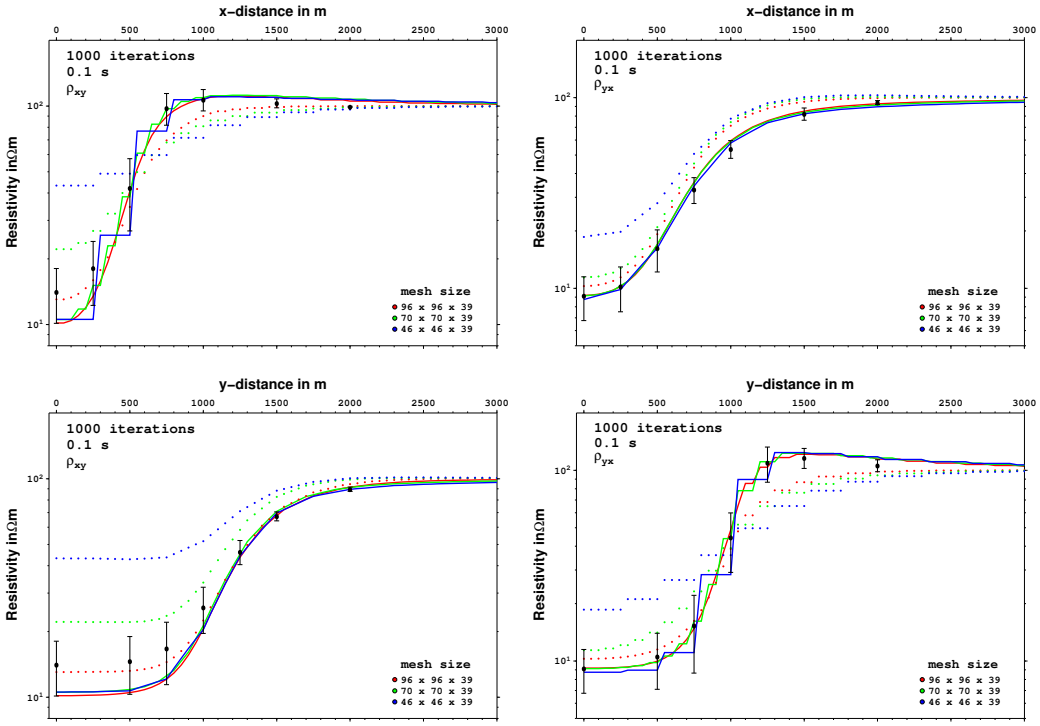

(a) Responses for 0.1 s

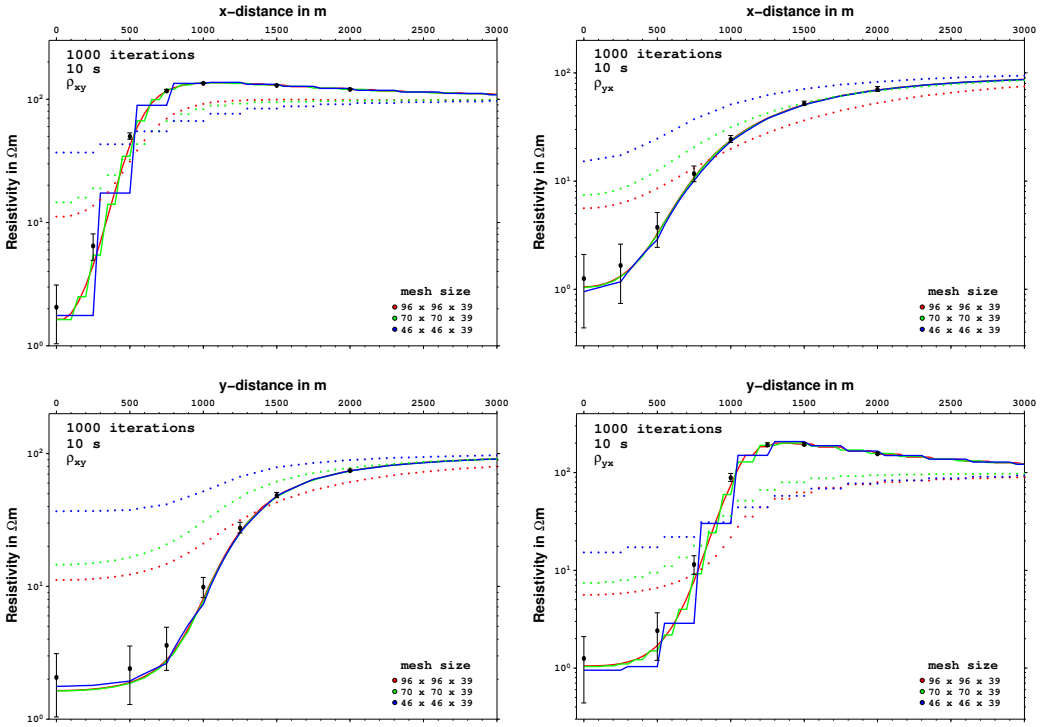

(b) Responses for 10 s

Figure E.22: Figure showing the response curves at 0.1 s (a) and 10 s (b) obtained from the COMMEMI 3D-1A model using three different meshes: coarse mesh (blue), fine mesh (green) and very fine mesh (red). The solid lines are the responses curves after 1000 iterations applying the divergence correction every 20 iterations. For comparison the dashed lines represent the curves after 1000 iterations without any correction being applied. The symbols with error bars represent the mean value and the standard deviation of the published results from Zhdanov et al. (1997).

E.3 RESULTS OF THE COMMEMI 3D-2A MODEL

The COMMEMI 3D-2A model from Zhdanov et al. (1997) was also used to test the forward algorithm in Section 7.2.1. Figure E.23 shows the used mesh and the resistivity structure of the model. As the model is based on a layered-background resistivity distribution, the implemented homogeneous halfspace boundary conditions turned out to not be ideal. Therefore faked 1D boundaries (hard-wired specifically for the 3D-2A example) were tested as well. The resulting response curves at 100 s and 1000 s are shown in Figures 7.14 and 7.15 in comparison to different published results. This appendix contains the plots of the horizontal components of the electric field at 250 m depth after 6000, 40000 and 80000 iterations for both forward implementations using homogeneous halfspace and 1D boundaries (Figures E.24 to E.35). Figures E.36 to E.43 show the corresponding correction potentials and their gradients for the first application of the correction.

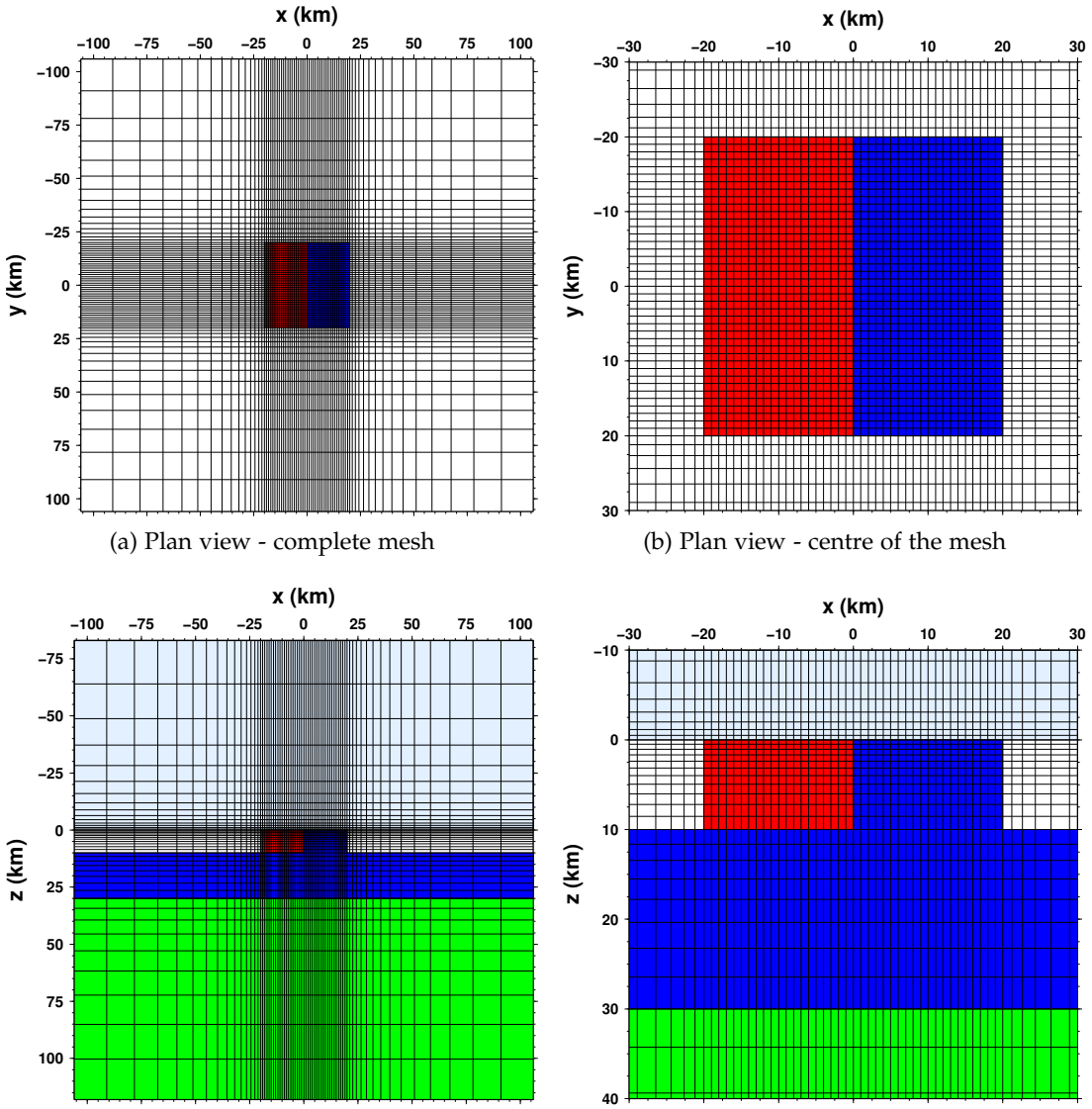

(a) Plan view - complete mesh

(b) Plan view - centre of the mesh

(c) Section view - complete mesh

(d) Section view - centre of the mesh

Figure E.23: Figures showing the mesh design for the 3D-2A mesh in plan view ((a) and (b)) and in section view ((c) and (d)). The mesh consists of 70 x 70 x 43 cells with a centre cell width of 1 km. The resistivity distribution is indicated by colours: red - 1 Ωm, white - 10 Ωm, blue - 100 Ωm, green - 0.1 Ωm and lightblue indicates the airlayer.

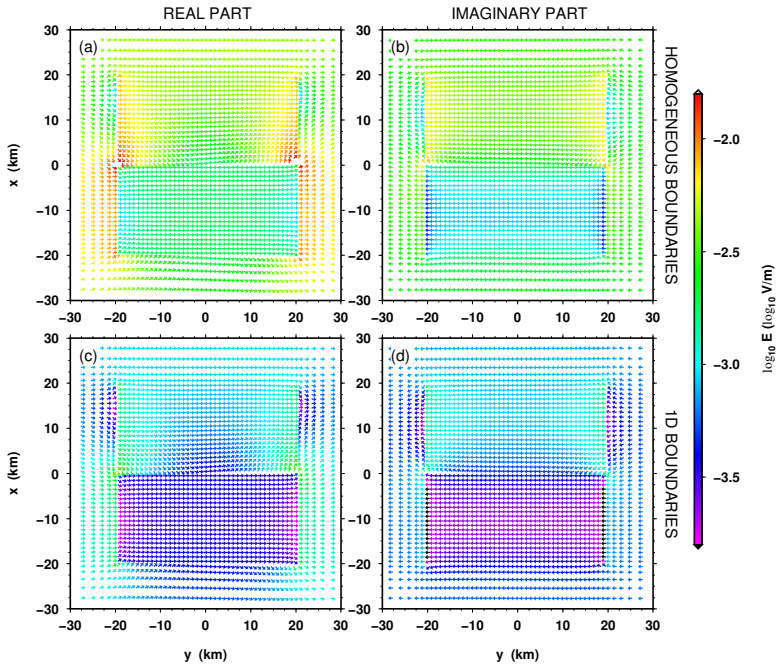

Figure E.24: Horizontal components of the electric field at 100 s at a depth of 250 m (x-directed source magnetic field). Panels (a) and (c) show the real and (b) to (d) the imaginary parts of the electric fields for the run with homogeneous halfspace boundaries ((a) and (b)) and 1D boundaries ((c) and (d)). Shown are the fields after 6000 iterations and the divergence correction is applied every 400 iterations.

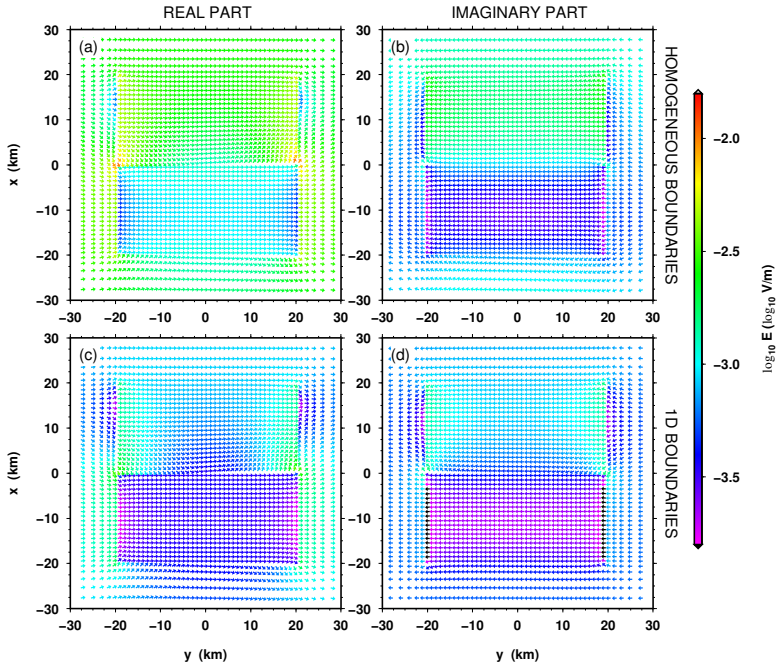

Figure E.25: Horizontal components of the electric field at 100 s at a depth of 250 m (x-directed source magnetic field). Panels (a) and (c) show the real and (b) to (d) the imaginary parts of the electric fields for the run with homogeneous halfspace boundaries ((a) and (b)) and 1D boundaries ((c) and (d)). Shown are the fields after 40000 iterations and the divergence correction is applied every 400 iterations.

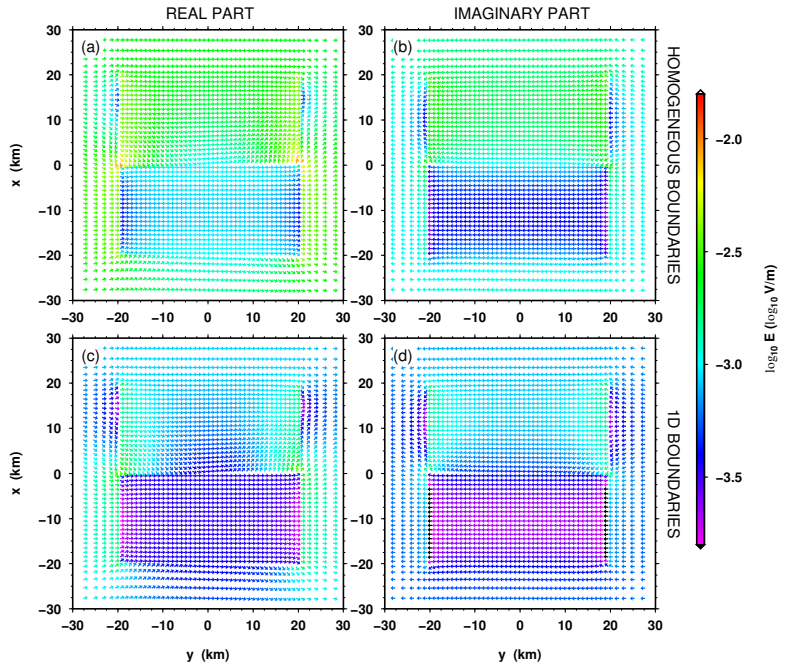

Figure E.26: Horizontal components of the electric field at 100 s at a depth of 250 m (x-directed source magnetic field). Panels (a) and (c) show the real and (b) to (d) the imaginary parts of the electric fields for the run with homogeneous halfspace boundaries ((a) and (b)) and 1D boundaries ((c) and (d)). Shown are the fields after 80000 iterations and the divergence correction is applied every 400 iterations.

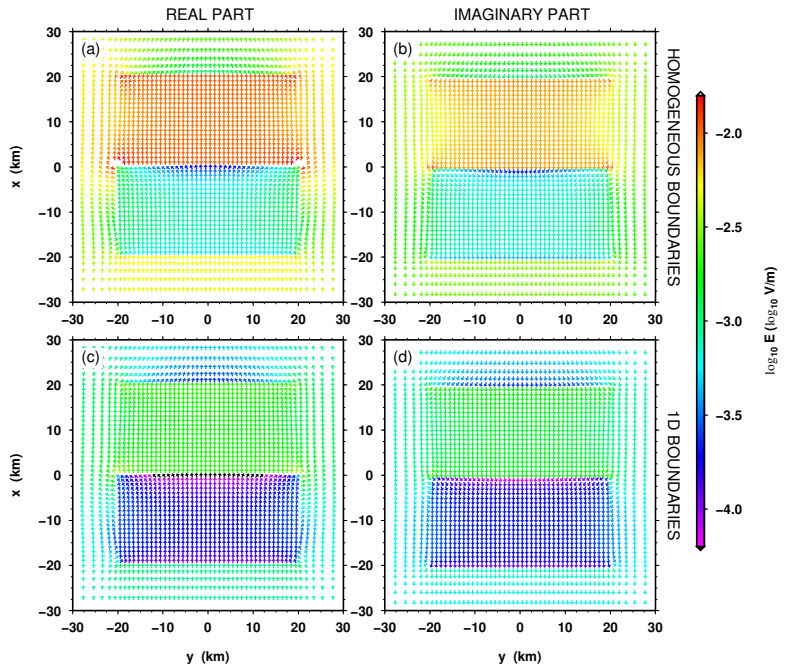

Figure E.27: Horizontal components of the electric field at 100 s at a depth of 250 m (y-directed source magnetic field). Panels (a) and (c) show the real and (b) to (d) the imaginary parts of the electric fields for the run with homogeneous halfspace boundaries ((a) and (b)) and 1D boundaries ((c) and (d)). Shown are the fields after 6000 iterations and the divergence correction is applied every 400 iterations.

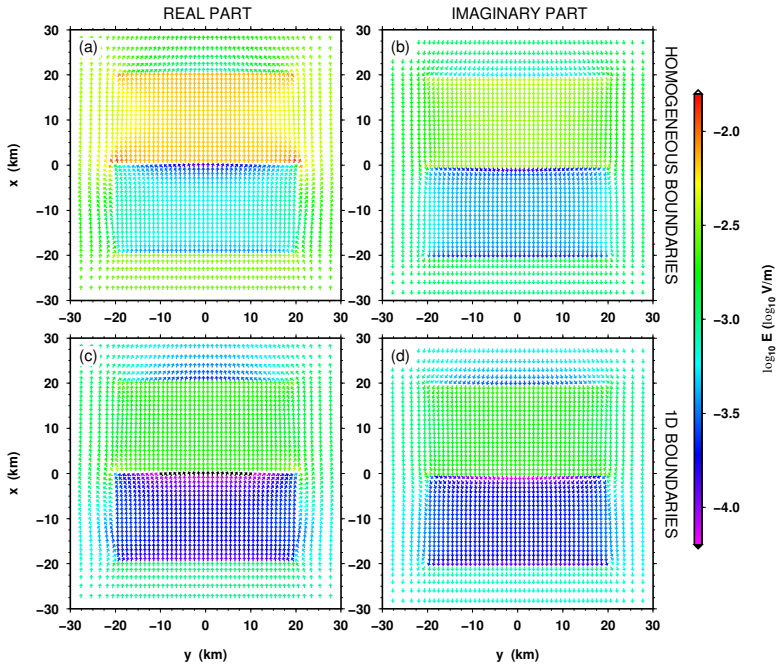

Figure E.28: Horizontal components of the electric field at 100 s at a depth of 250 m (y-directed source magnetic field). Panels (a) and (c) show the real and (b) to (d) the imaginary parts of the electric fields for the run with homogeneous halfspace boundaries ((a) and (b)) and 1D boundaries ((c) and (d)). Shown are the fields after 40000 iterations and the divergence correction is applied every 400 iterations.

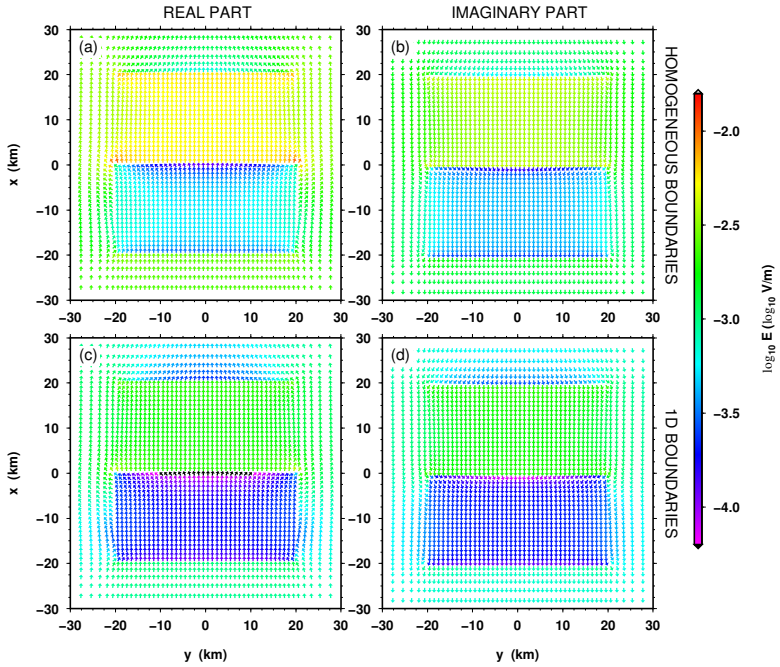

Figure E.29: Horizontal components of the electric field at 100 s at a depth of 250 m (y-directed source magnetic field). Panels (a) and (c) show the real and (b) to (d) the imaginary parts of the electric fields for the run with homogeneous halfspace boundaries ((a) and (b)) and 1D boundaries ((c) and (d)). Shown are the fields after 80000 iterations and the divergence correction is applied every 400 iterations.

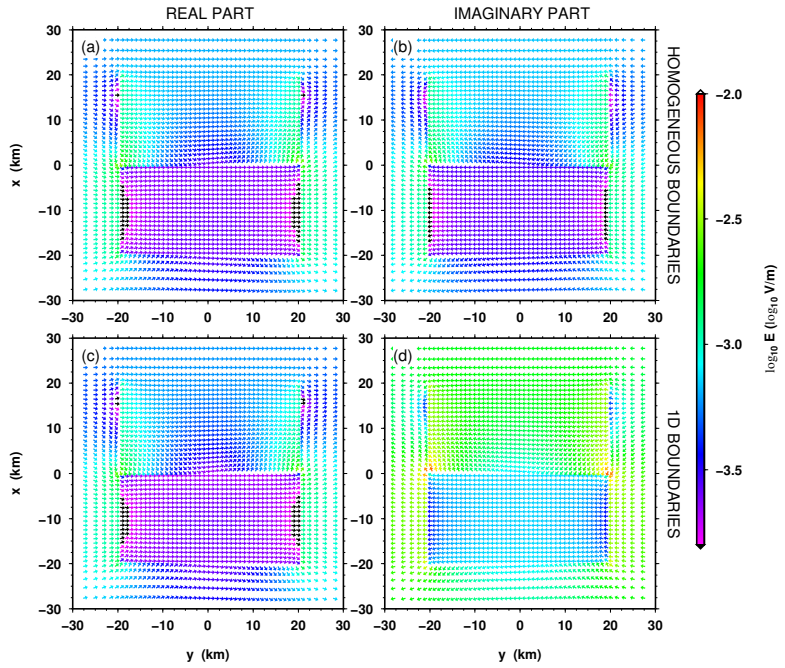

Figure E.30: Horizontal components of the electric field at 1000 s at a depth of 250 m (x-directed source magnetic field). Panels (a) and (c) show the real and (b) to (d) the imaginary parts of the electric fields for the run with homogeneous halfspace boundaries ((a) and (b)) and 1D boundaries ((c) and (d)). Shown are the fields after 6000 iterations and the divergence correction is applied every 400 iterations.

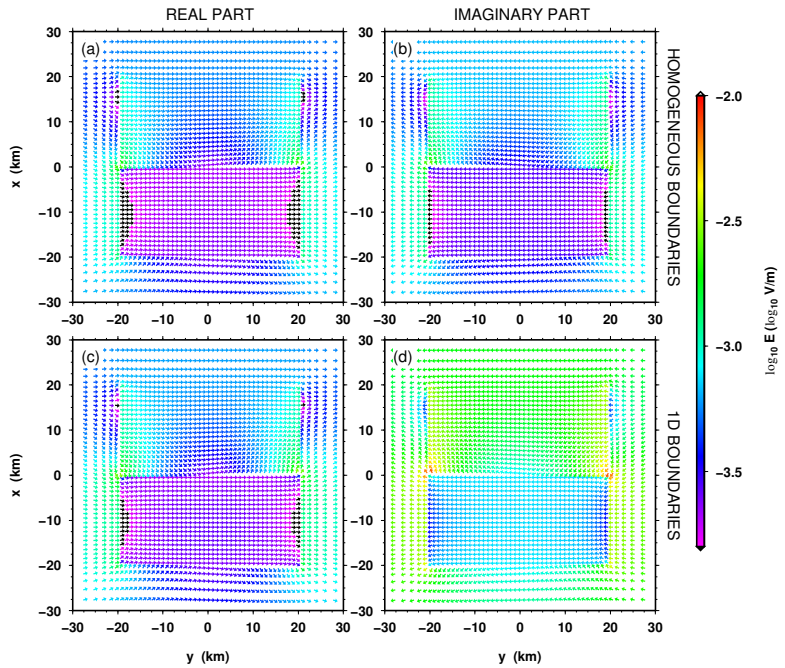

Figure E.31: Horizontal components of the electric field at 1000 s at a depth of 250 m (x-directed source magnetic field). Panels (a) and (c) show the real and (b) to (d) the imaginary parts of the electric fields for the run with homogeneous halfspace boundaries ((a) and (b)) and 1D boundaries ((c) and (d)). Shown are the fields after 40000 iterations and the divergence correction is applied every 400 iterations.

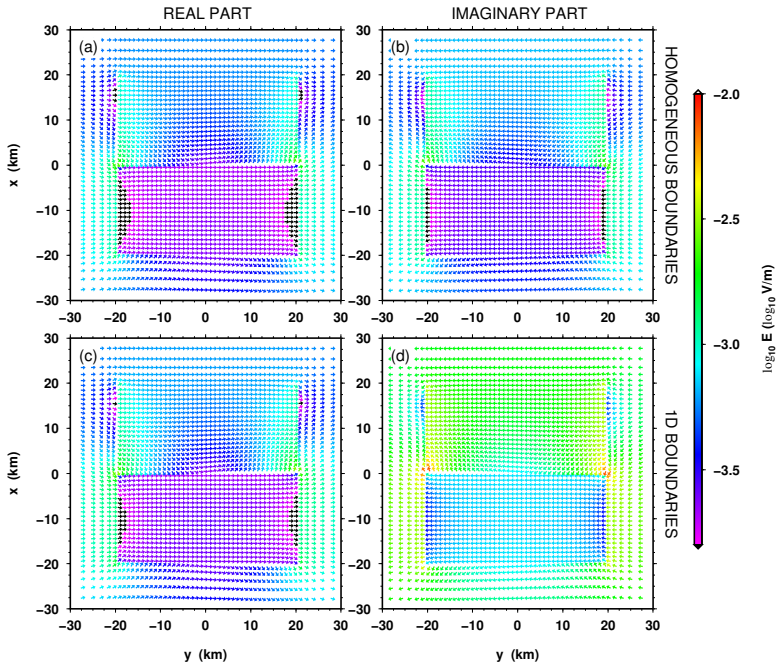

Figure E.32: Horizontal components of the electric field at 1000 s at a depth of 250 m (x-directed source magnetic field). Panels (a) and (c) show the real and (b) to (d) the imaginary parts of the electric fields for the run with homogeneous halfspace boundaries ((a) and (b)) and 1D boundaries ((c) and (d)). Shown are the fields after 80000 iterations and the divergence correction is applied every 400 iterations.

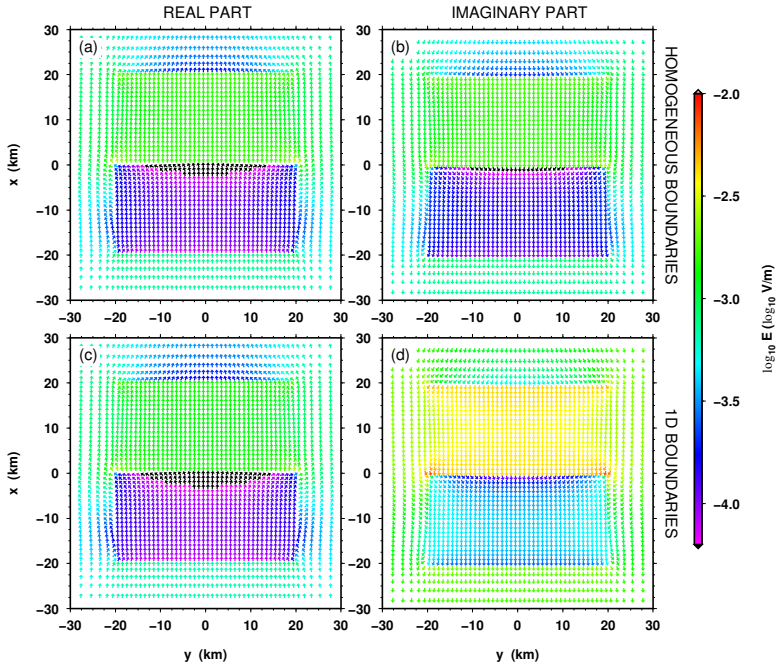

Figure E.33: Horizontal components of the electric field at 1000 s at a depth of 250 m (y-directed source magnetic field). Panels (a) and (c) show the real and (b) to (d) the imaginary parts of the electric fields for the run with homogeneous halfspace boundaries ((a) and (b)) and 1D boundaries ((c) and (d)). Shown are the fields after 6000 iterations and the divergence correction is applied every 400 iterations.

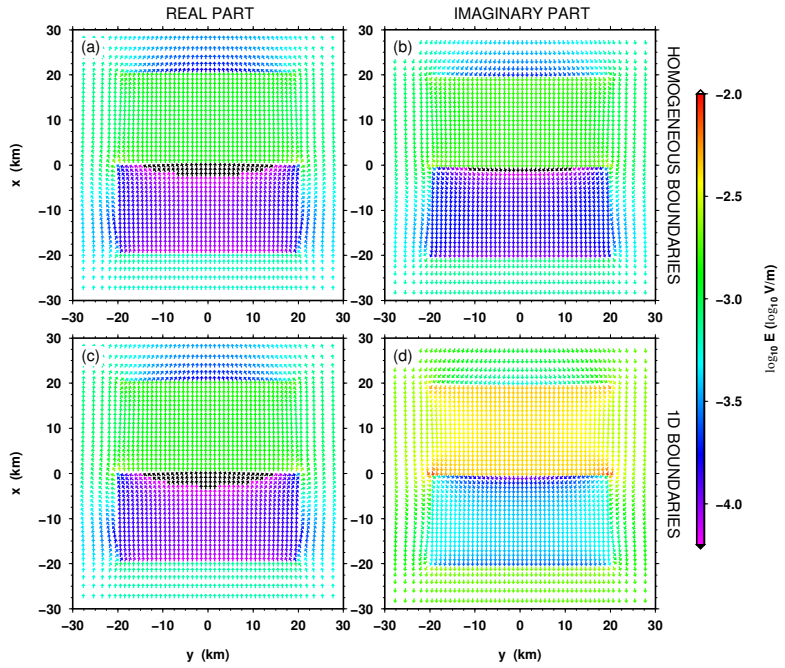

Figure E.34: Horizontal components of the electric field at 1000 s at a depth of 250 m (y-directed source magnetic field). Panels (a) and (c) show the real and (b) to (d) the imaginary parts of the electric fields for the run with homogeneous halfspace boundaries ((a) and (b)) and 1D boundaries ((c) and (d)). Shown are the fields after 40000 iterations and the divergence correction is applied every 400 iterations.

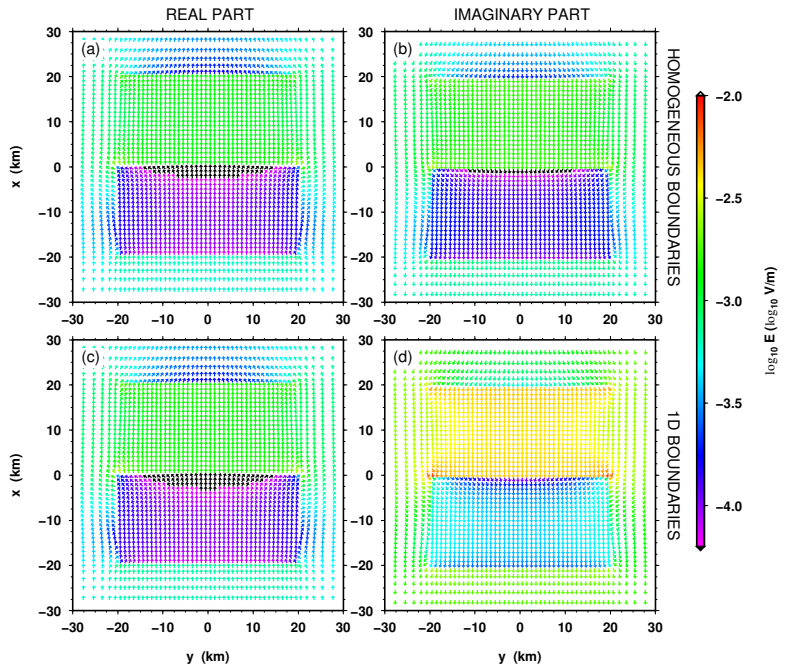

Figure E.35: Horizontal components of the electric field at 1000 s at a depth of 250 m (y-directed source magnetic field). Panels (a) and (c) show the real and (b) to (d) the imaginary parts of the electric fields for the run with homogeneous halfspace boundaries ((a) and (b)) and 1D boundaries ((c) and (d)). Shown are the fields after 80000 iterations and the divergence correction is applied every 400 iterations.

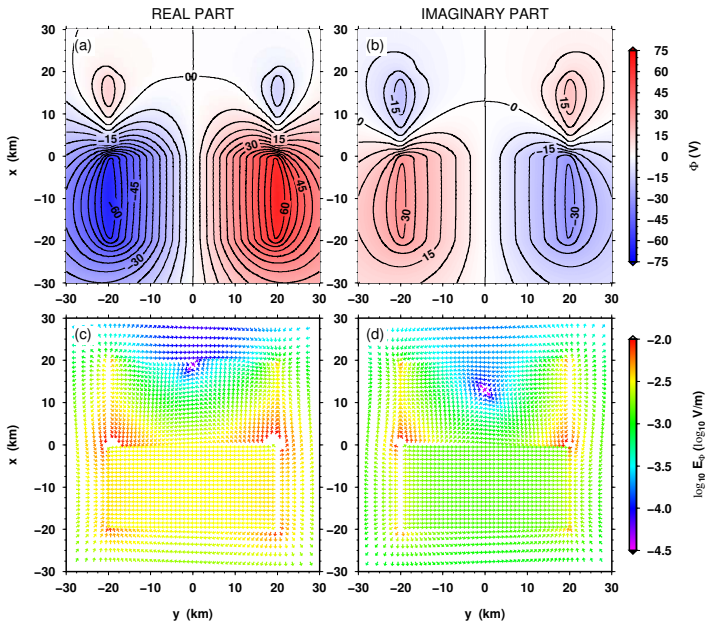

Figure E.36: Divergence correction potential and its gradient of the COMMEMI 3D-2A model at 100 s for a x-directed source magnetic field and homogeneous halfspace boundaries. Panel (a) shows the real and (b) the imaginary parts of the divergence correction potential applied after 400 iterations. The real (c) and imaginary (d) parts of the horizontal correction electric field are given by the gradient of the correction potential. The potential and field are shown at a depth of 250 m.

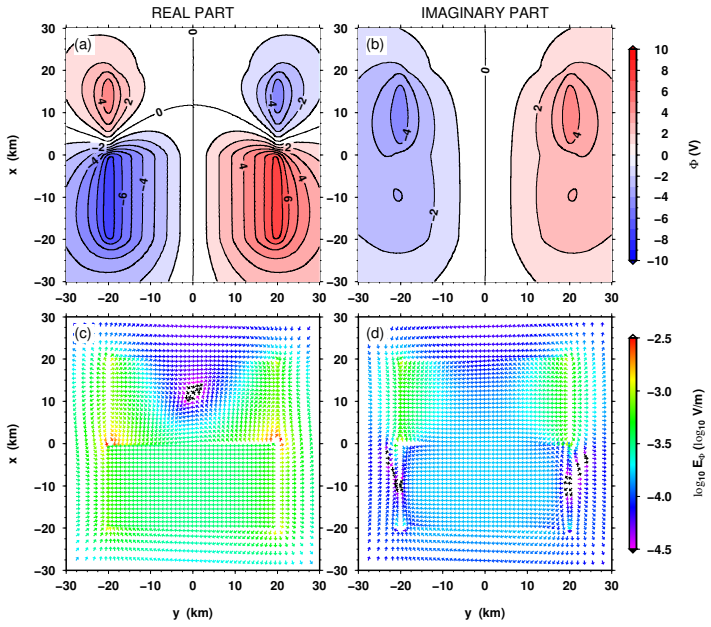

Figure E.37: Divergence correction potential and its gradient of the COMMEMI 3D-2A model at 100 s for a x-directed source magnetic field and 1D boundaries. Panel (a) shows the real and (b) the imaginary parts of the divergence correction potential applied after 400 iterations. The real (c) and imaginary (d) parts of the horizontal correction electric field are given by the gradient of the correction potential. The potential and field are shown at a depth of 250 m.

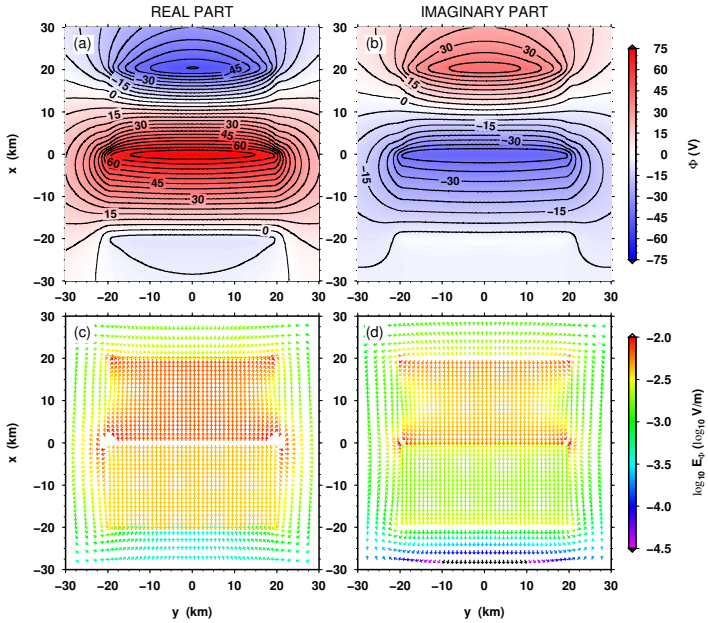

Figure E.38: Divergence correction potential and its gradient of the COMMEMI 3D-2A model at 100 s for a y-directed source magnetic field and homogeneous halfspace boundaries. Panel (a) shows the real and (b) the imaginary parts of the divergence correction potential applied after 400 iterations. The real (c) and imaginary (d) parts of the horizontal correction electric field are given by the gradient of the correction potential. The potential and field are shown at a depth of 250 m.

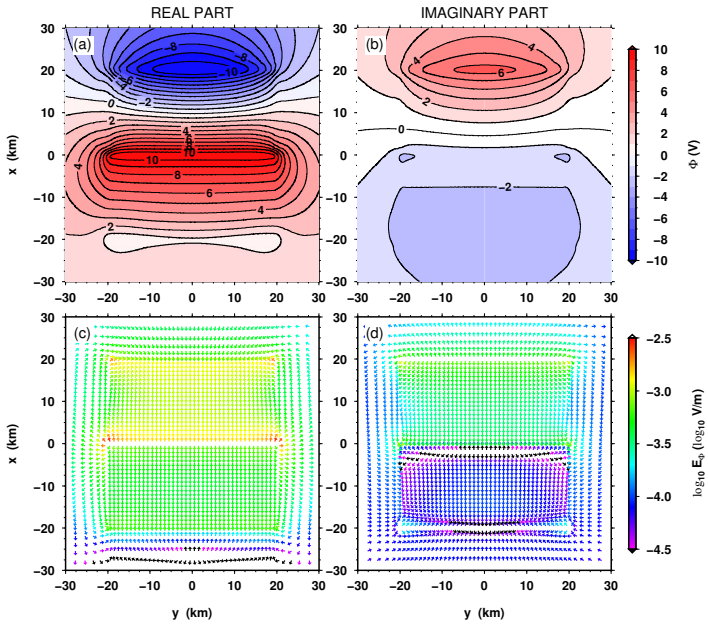

Figure E.39: Divergence correction potential and its gradient of the COMMEMI 3D-2A model at 100 s for a y-directed source magnetic field and 1D boundaries. Panel (a) shows the real and (b) the imaginary parts of the divergence correction potential applied after 400 iterations. The real (c) and imaginary (d) parts of the horizontal correction electric field are given by the gradient of the correction potential. The potential and field are shown at a depth of 250 m.

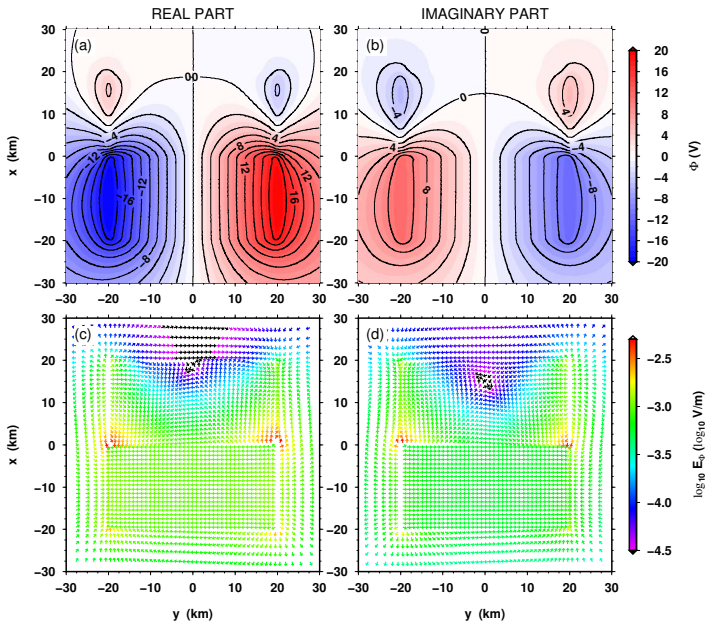

Figure E.40: Divergence correction potential and its gradient of the COMMEMI 3D-2A model at 1000 s for a x-directed source magnetic field and homogeneous halfspace boundaries. Panel (a) shows the real and (b) the imaginary parts of the divergence correction potential applied after 400 iterations. The real (c) and imaginary (d) parts of the horizontal correction electric field are given by the gradient of the correction potential. The potential and field are shown at a depth of 250 m.

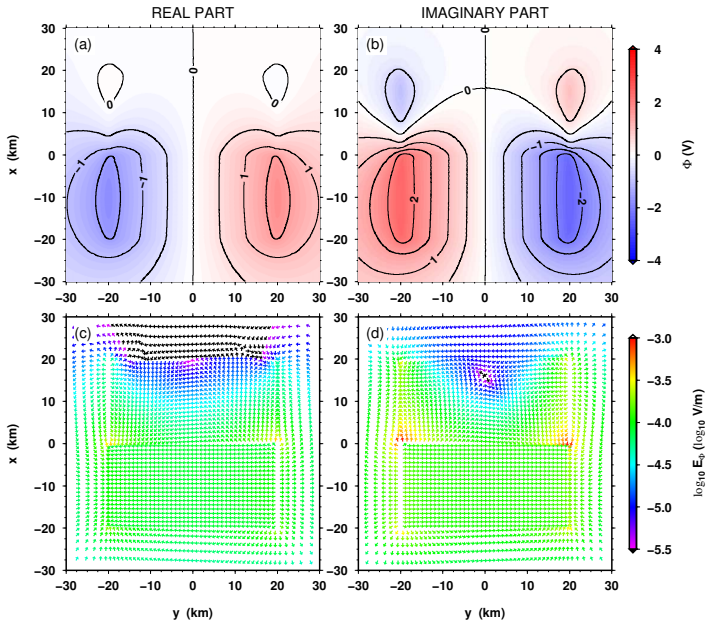

Figure E.41: Divergence correction potential and its gradient of the COMMEMI 3D-2A model at 1000 s for a x-directed source magnetic field and 1D boundaries. Panel (a) shows the real and (b) the imaginary parts of the divergence correction potential applied after 400 iterations. The real (c) and imaginary (d) parts of the horizontal correction electric field are given by the gradient of the correction potential. The potential and field are shown at a depth of 250 m.

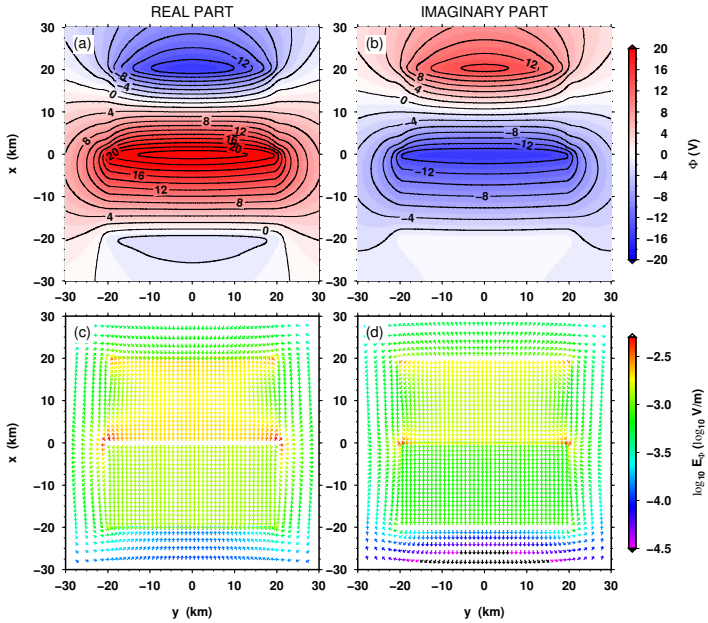

Figure E.42: Divergence correction potential and its gradient of the COMMEMI 3D-2A model at 1000 s for a y-directed source magnetic field and homogeneous halfspace boundaries. Panel (a) shows the real and (b) the imaginary parts of the divergence correction potential applied after 400 iterations. The real (c) and imaginary (d) parts of the horizontal correction electric field are given by the gradient of the correction potential. The potential and field are shown at a depth of 250 m.

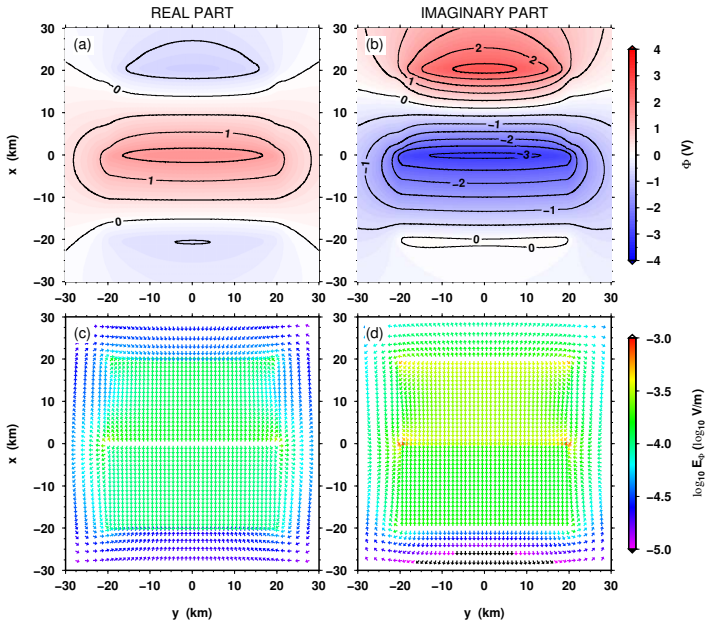

Figure E.43: Divergence correction potential and its gradient of the COMMEMI 3D-2A model at 1000 s for a y-directed source magnetic field and 1D boundaries. Panel (a) shows the real and (b) the imaginary parts of the divergence correction potential applied after 400 iterations. The real (c) and imaginary (d) parts of the horizontal correction electric field are given by the gradient of the correction potential. The potential and field are shown at a depth of 250 m.

E.4 RESULTS OF THE DTM1 MODEL

The Dublin Test Model 1 (DTM1) was used in Section 7.2.2 to test the forward algorithm. The model consists of three blocks of different sizes and resistivities. The model is described in Figure 7.16. Figure E.44 shows the design of the mesh used to calculate forward responses at sites on four profiles (Table 7.4 lists the locations of the 59 sites of the data sets used for comparison). Figure E.45 to Figure E.52 show the resistivity and phase curves for all four components at 100 s and 1000 s as black symbols. These responses match very well the results from five other codes/users (see Section 7.2.2 for references), which are represented by coloured symbols. For the sake of completeness, Figures E.53 to E.56 show the horizontal components of the electric field at 100 s and 1000 s in 5.5 km and 26.4 km depth and the corresponding correction potentials and their gradients are shown in Figures E.57 to E.64.

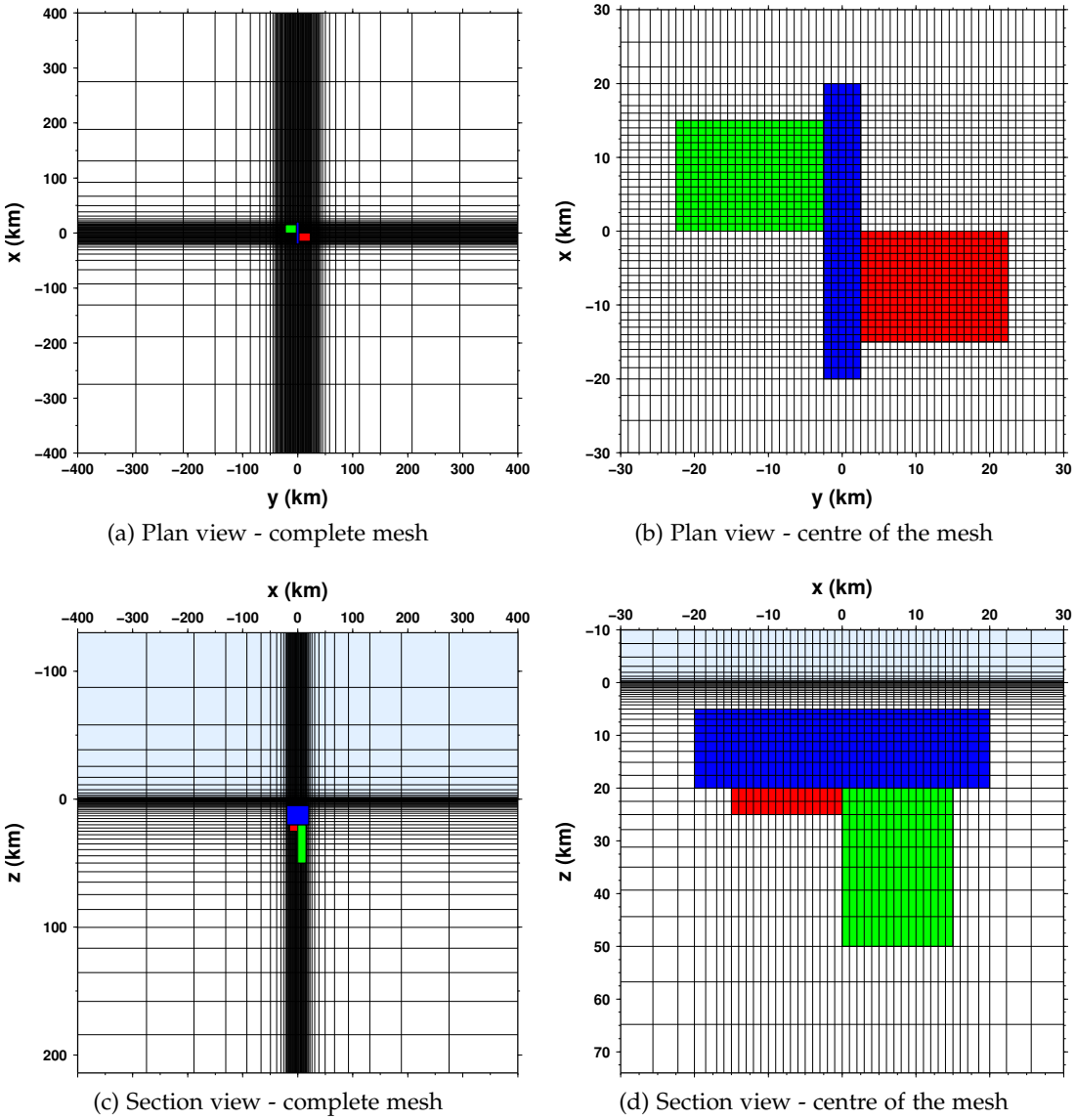

(a) Plan view - complete mesh

(b) Plan view - centre of the mesh

(c) Section view - complete mesh

(d) Section view - centre of the mesh

Figure E.44: Figures showing the mesh design for the DTM1 mesh in plan view ((a) and (b)) and in section view ((c) and (d)). The mesh consists of 91 x 60 x 57 cells with a centre cell width of 1 km. The coloured rectangulars show the location of the three blocks of the model (blue - 10 Ωm, red - 1 Ωm and green - 10 000 Ωm) and the lightblue layer indicates the airlayers.

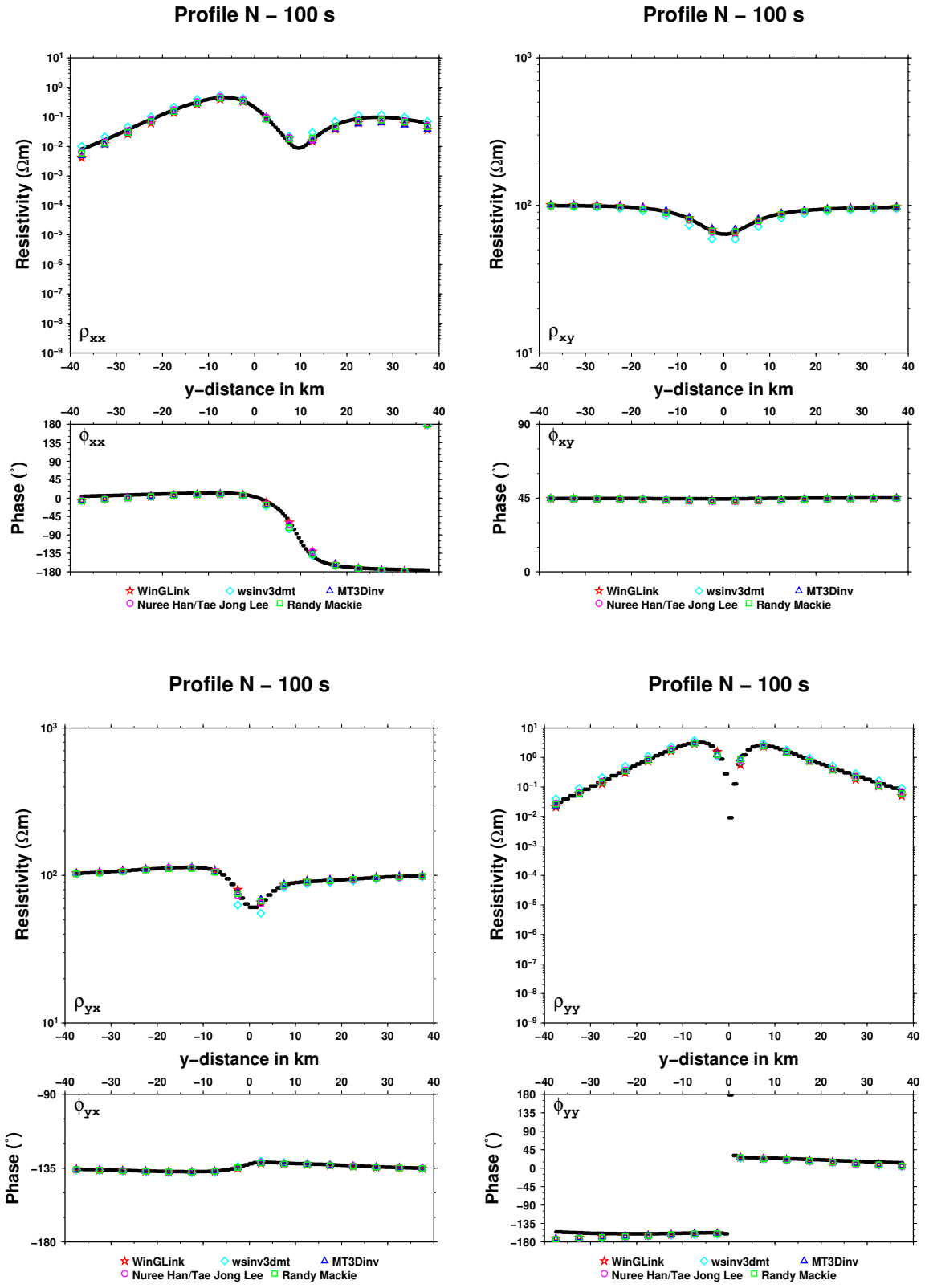

Figure E.45: Figure showing the responses curves (black symbols) of Profile N at 100 s calculated for the Dublin Test Model 1 (DTM1) (see Figure 7.16). Each panel, one each for xx, xy, yx and yy components, shows the apparent resistivity curves on top and the phase curves below. The colour symbols are results from other codes/users (see legend), which are available as reference data sets on MTnet.

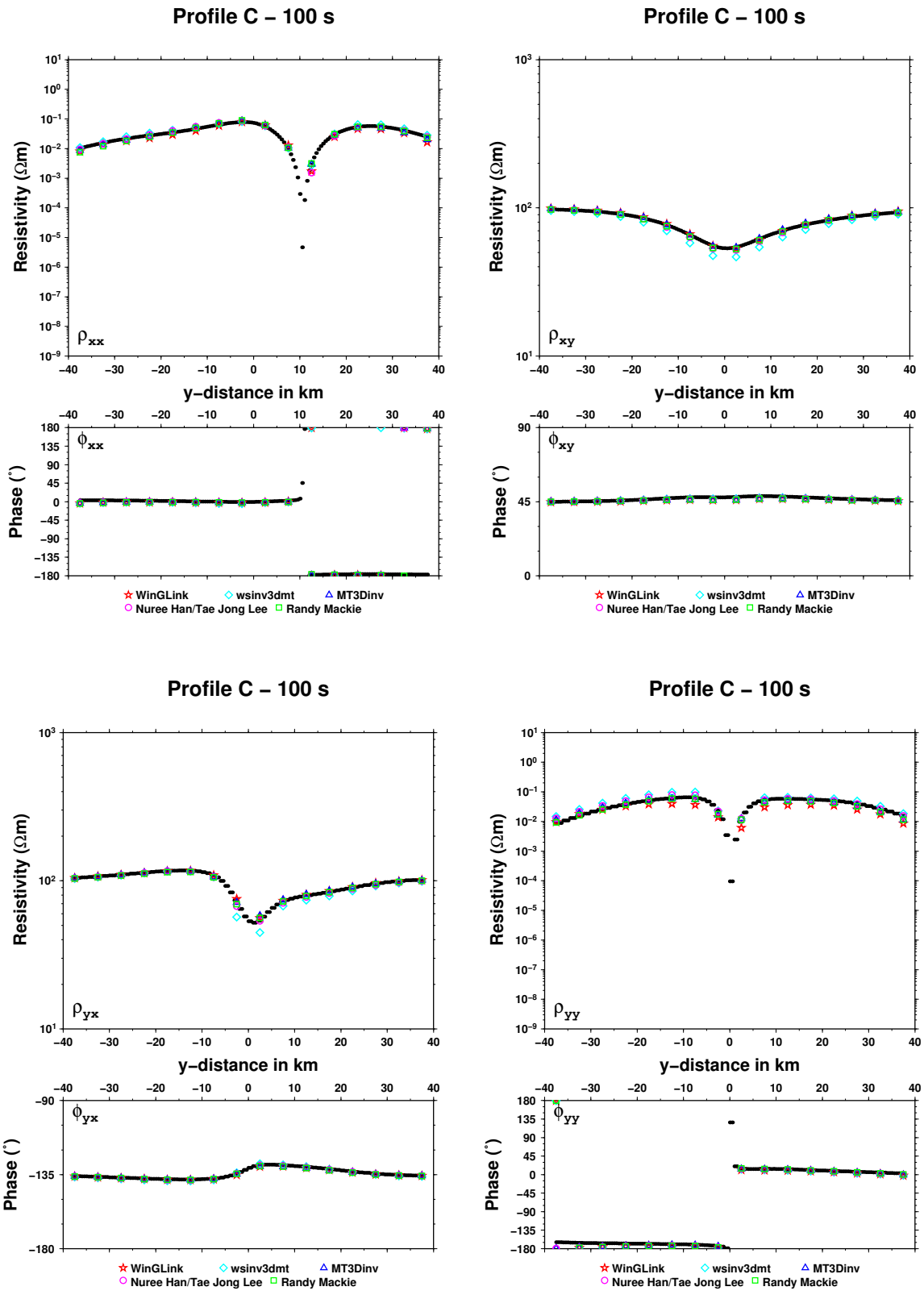

Figure E.46: Figure showing the responses curves (black symbols) of Profile C at 100 s calculated for the Dublin Test Model 1 (DTM1) (see Figure 7.16). Each panel, one each for xx, xy, yx and yy components, shows the apparent resistivity curves on top and the phase curves below. The colour symbols are results from other codes/users (see legend), which are available as reference data sets on MTnet.

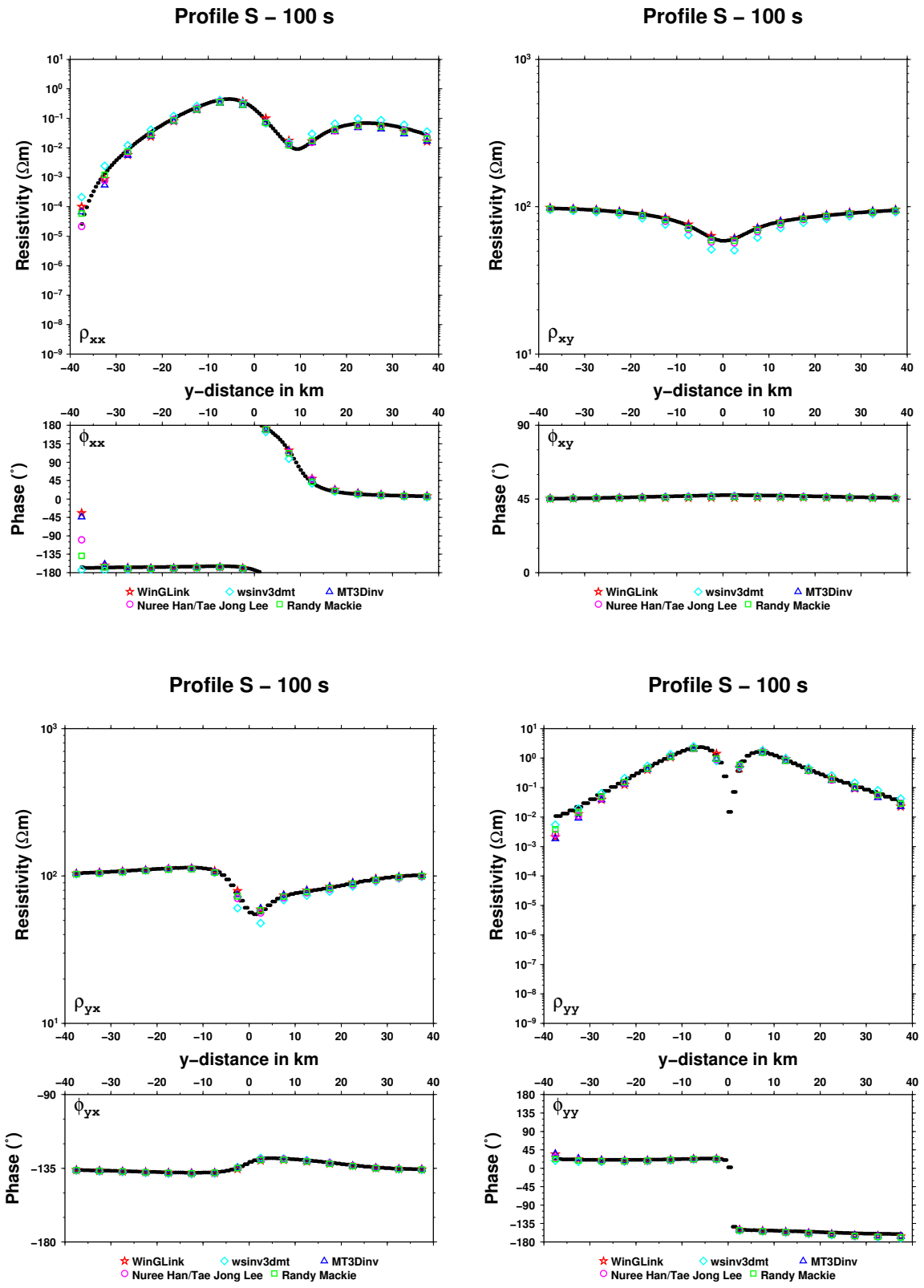

Figure E.47: Figure showing the responses curves (black symbols) of Profile S at 100 s calculated for the Dublin Test Model 1 (DTM1) (see Figure 7.16). Each panel, one each for xx, xy, yx and yy components, shows the apparent resistivity curves on top and the phase curves below. The colour symbols are results from other codes/users (see legend), which are available as reference data sets on MTnet.

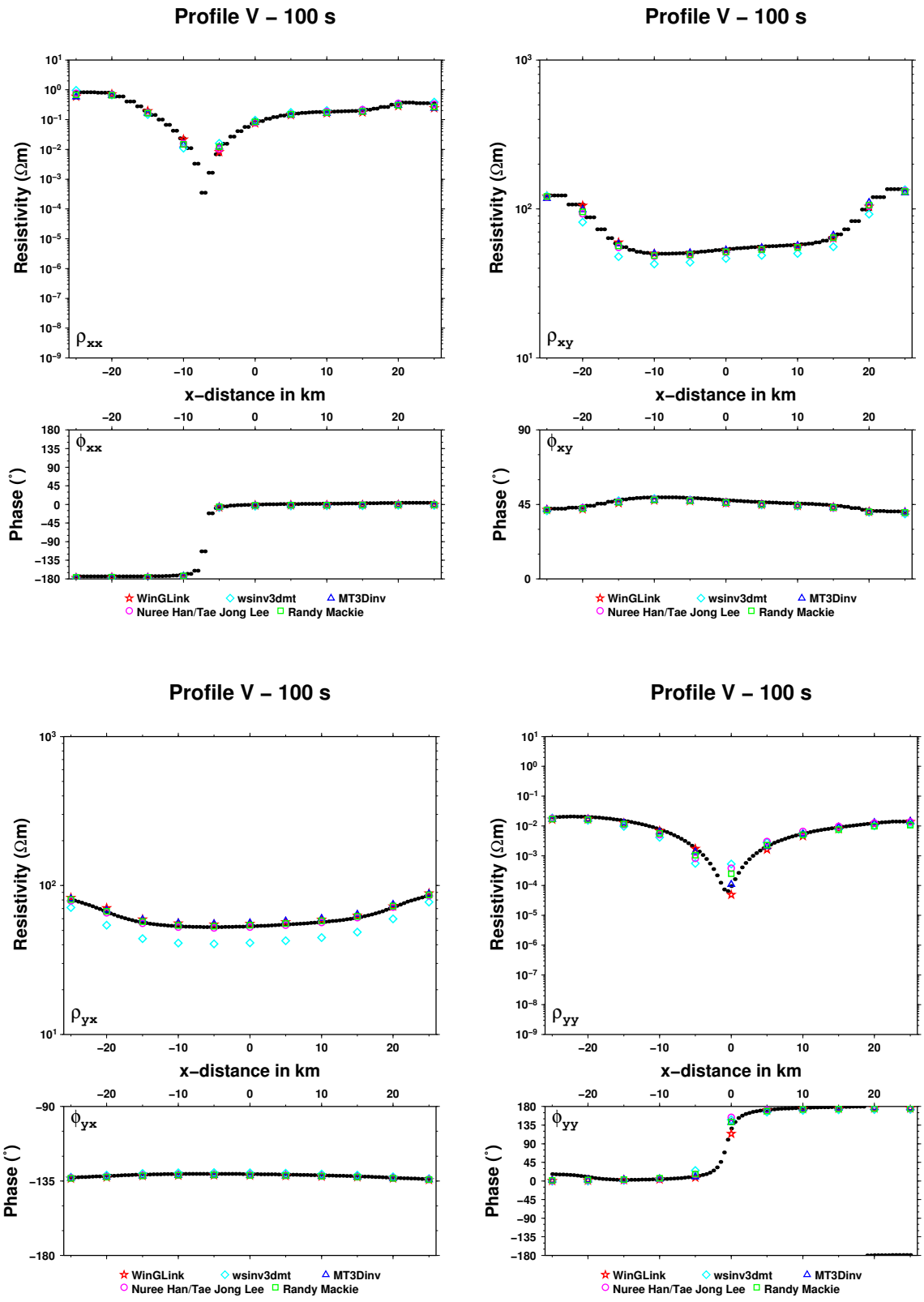

Figure E.48: Figure showing the responses curves (black symbols) of Profile V at 100 s calculated for the Dublin Test Model 1 (DTM1) (see Figure 7.16). Each panel, one each for xx, xy, yx and yy components, shows the apparent resistivity curves on top and the phase curves below. The colour symbols are results from other codes/users (see legend), which are available as reference data sets on MTnet.

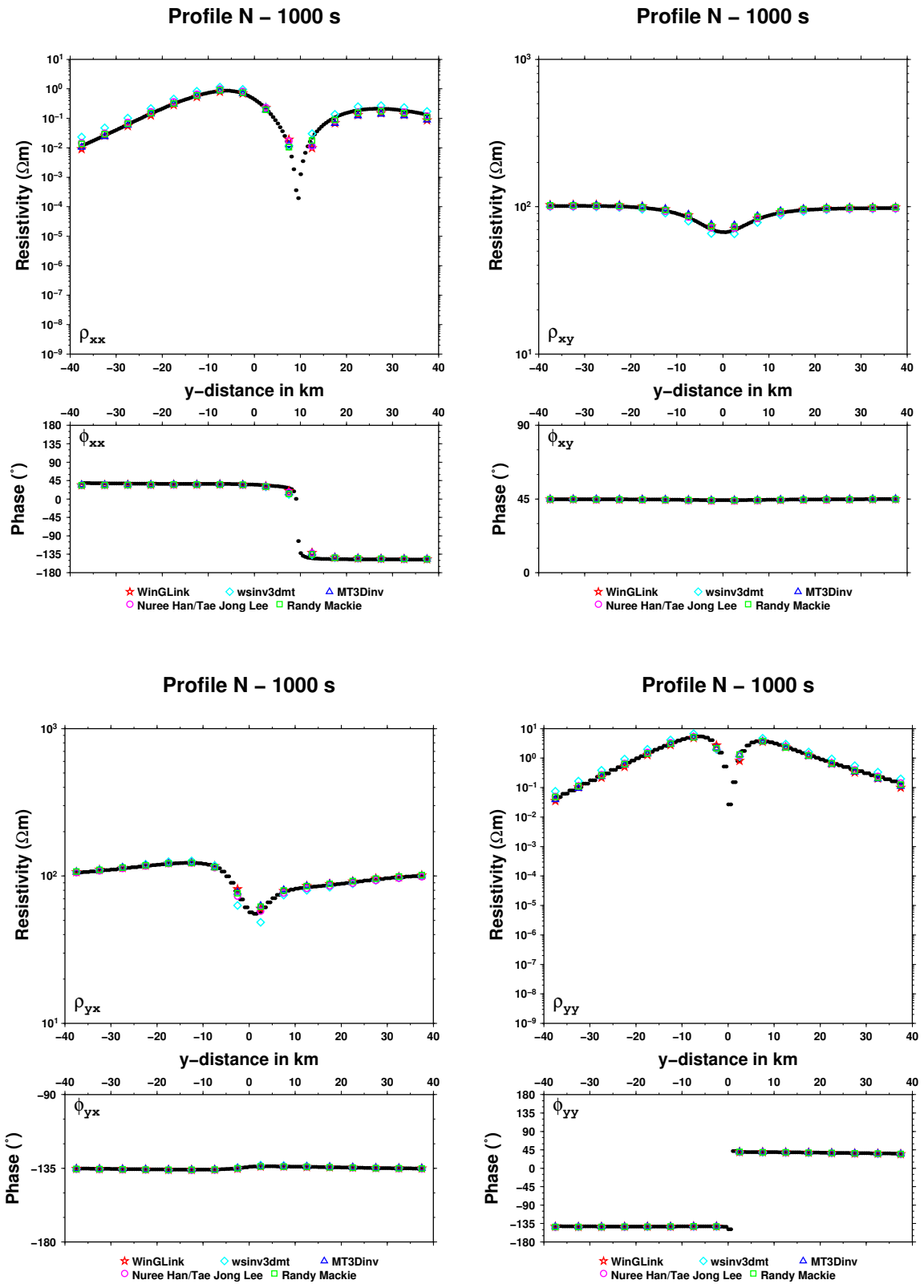

Figure E.49: Figure showing the responses curves (black symbols) of Profile N at 1000 s calculated for the Dublin Test Model 1 (DTM1) (see Figure 7.16). Each panel, one each for xx, xy, yx and yy components, shows the apparent resistivity curves on top and the phase curves below. The colour symbols are results from other codes/users (see legend), which are available as reference data sets on MTnet.

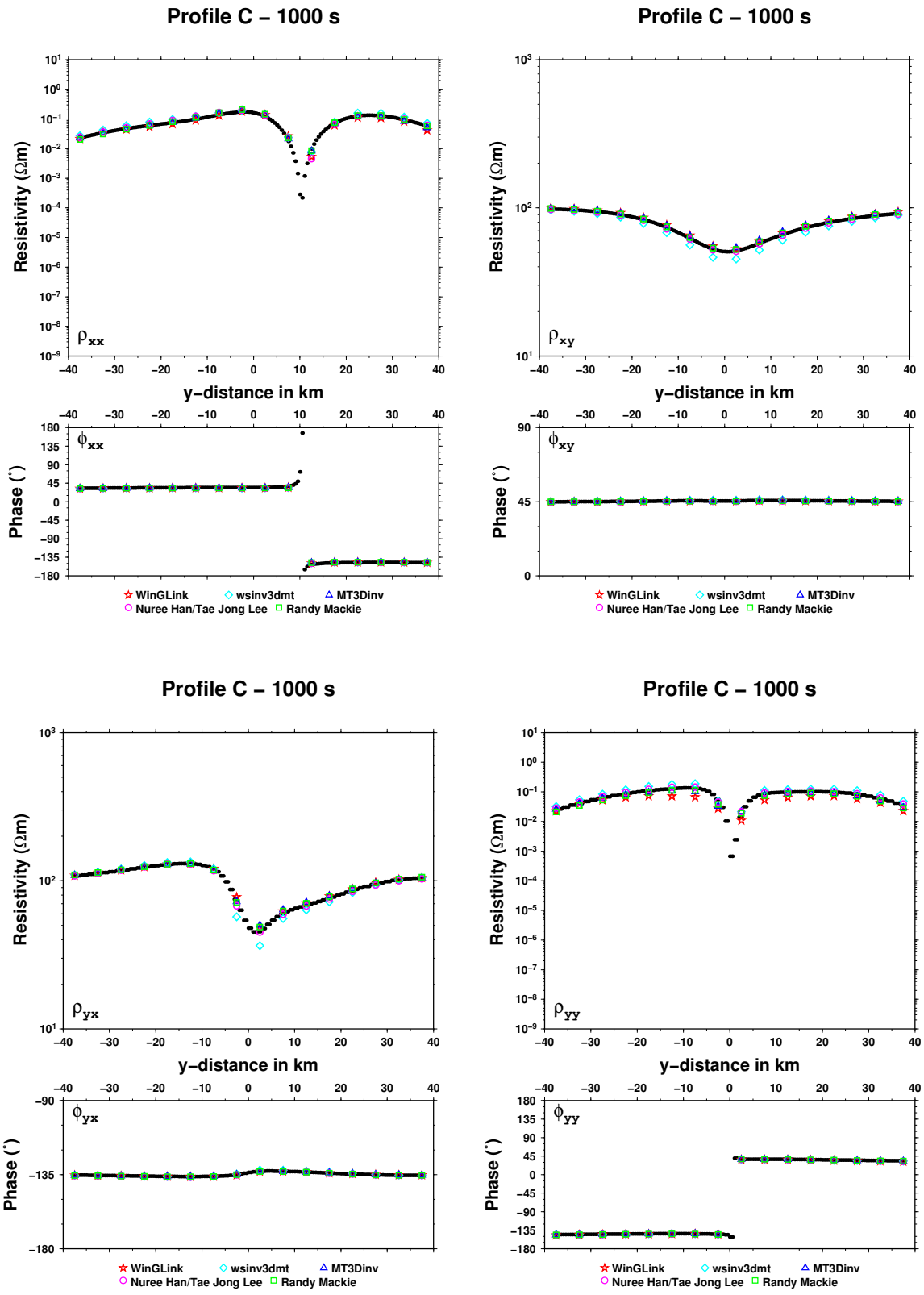

Figure E.50: Figure showing the responses curves (black symbols) of Profile C at 1000 s calculated for the Dublin Test Model 1 (DTM1) (see Figure 7.16). Each panel, one each for xx, xy, yx and yy components, shows the apparent resistivity curves on top and the phase curves below. The colour symbols are results from other codes/users (see legend), which are available as reference data sets on MTnet.

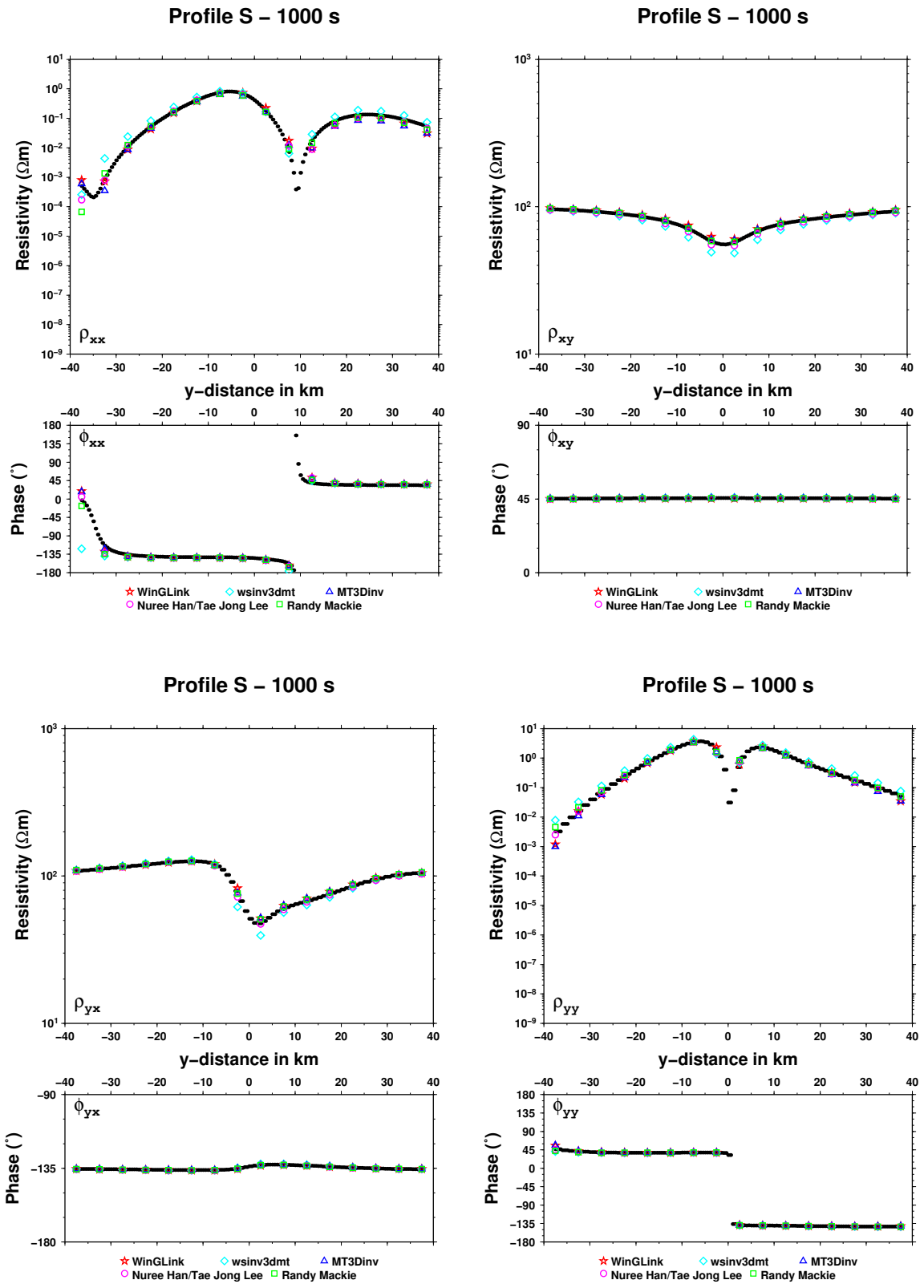

Figure E.51: Figure showing the responses curves (black symbols) of Profile S at 1000 s calculated for the Dublin Test Model 1 (DTM1) (see Figure 7.16). Each panel, one each for xx, xy, yx and yy components, shows the apparent resistivity curves on top and the phase curves below. The colour symbols are results from other codes/users (see legend), which are available as reference data sets on MTnet.

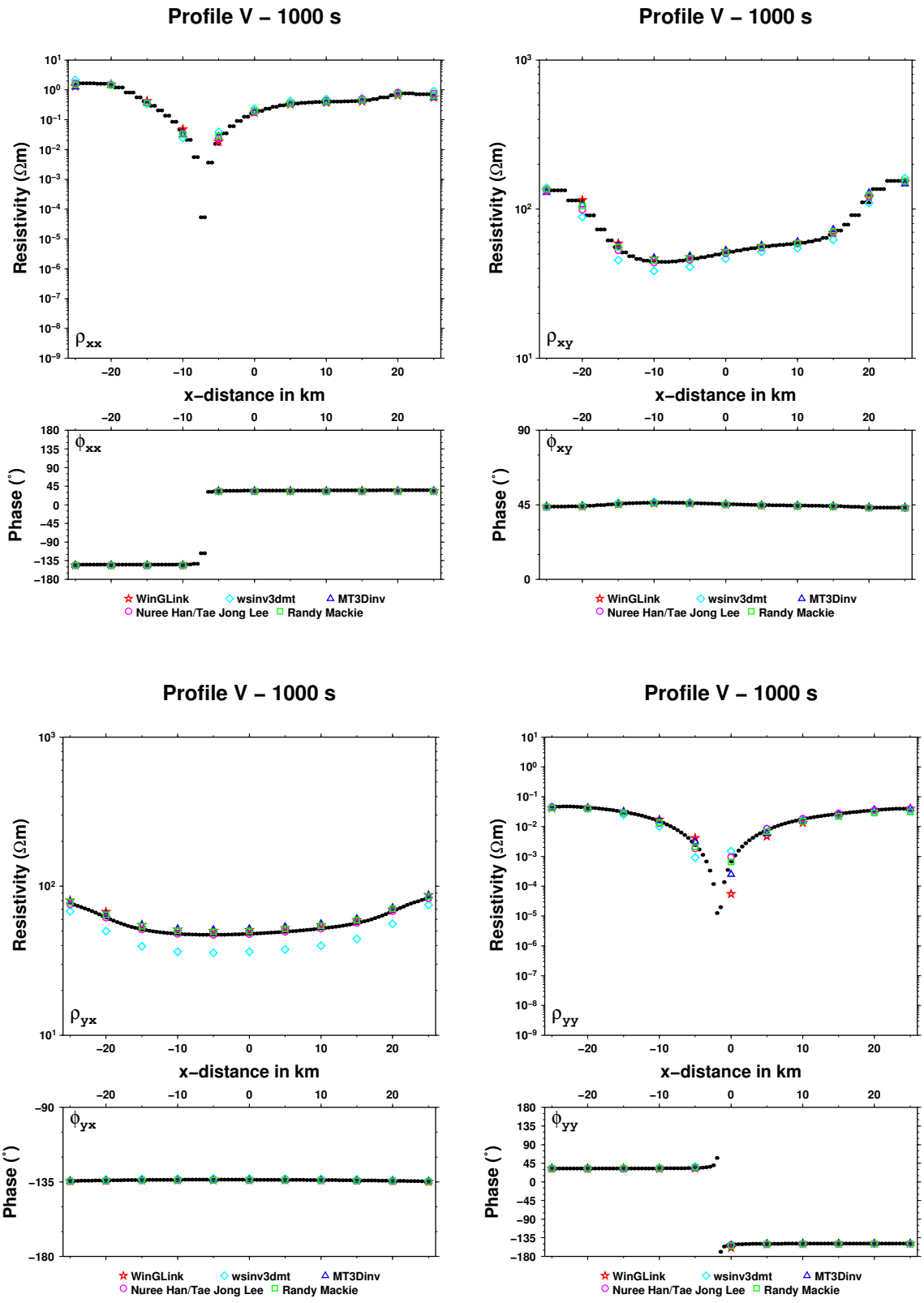

Figure E.52: Figure showing the responses curves (black symbols) of Profile V at 1000 s calculated for the Dublin Test Model 1 (DTM1) (see Figure 7.16). Each panel, one each for xx, xy, yx and yy components, shows the apparent resistivity curves on top and the phase curves below. The colour symbols are results from other codes/users (see legend), which are available as reference data sets on MTnet.

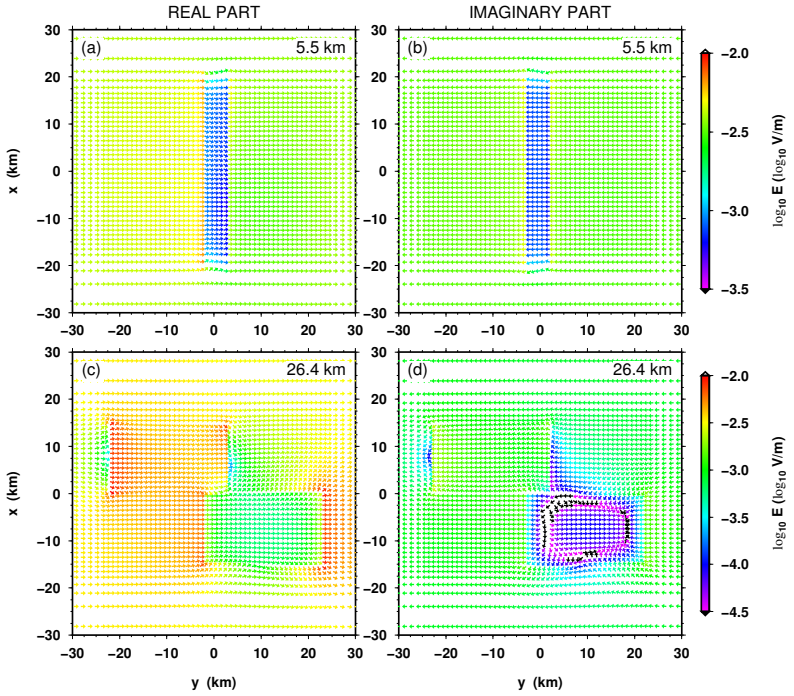

Figure E.53: Horizontal components of the electric field at 100 s at depths of about 5.5 km (top) and 26.4 km (bottom) for a x-directed source magnetic field. Panels (a) and (c) show the real and (b) and (d) the imaginary parts of the electric fields after 1000 iterations applying the divergence correction every 20 iterations.

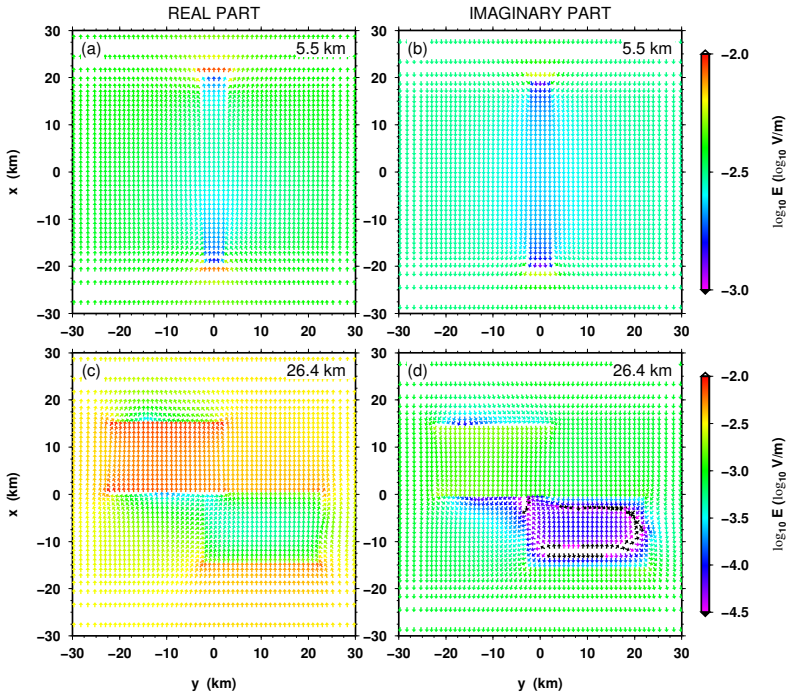

Figure E.54: Horizontal components of the electric field at 100 s at depths of about 5.5 km (top) and 26.4 km (bottom) for a y-directed source magnetic field. Panels (a) and (c) show the real and (b) and (d) the imaginary parts of the electric fields after 1000 iterations applying the divergence correction every 20 iterations.

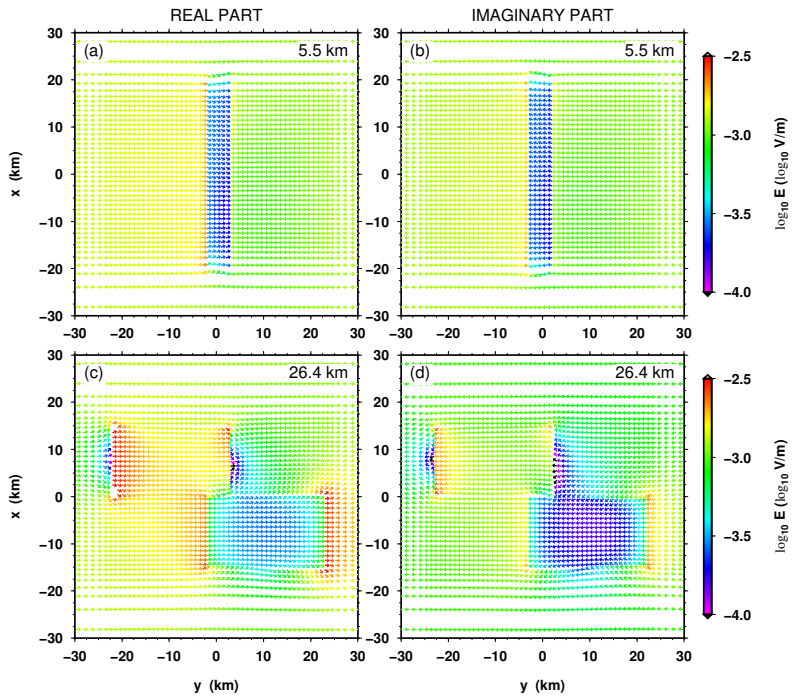

Figure E.55: Horizontal components of the electric field at 1000 s at depths of about 5.5 km (top) and 26.4 km (bottom) for a x-directed source magnetic field. Panels (a) and (c) show the real and (b) and (d) the imaginary parts of the electric fields after 1000 iterations applying the divergence correction every 20 iterations.

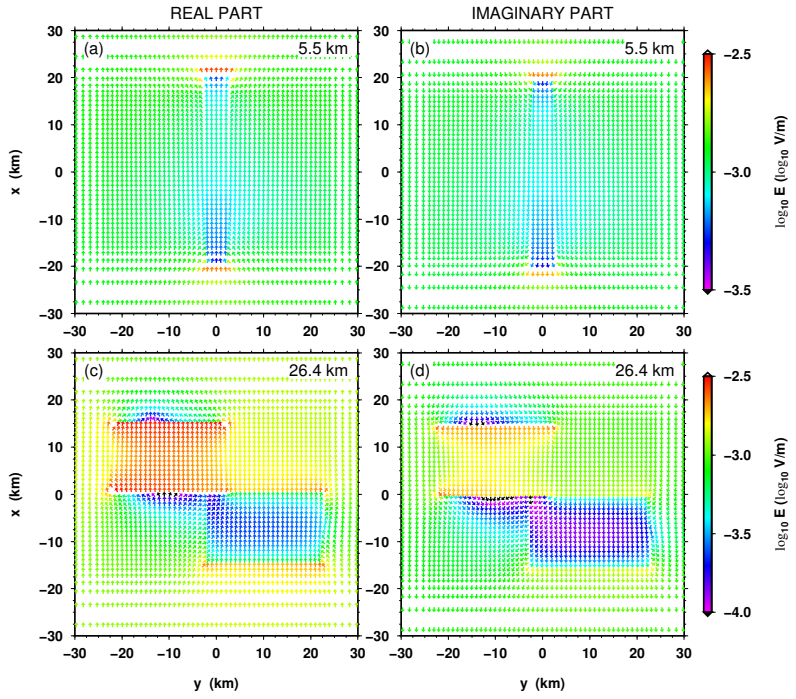

Figure E.56: Horizontal components of the electric field at 1000 s at depths of about 5.5 km (top) and 26.4 km (bottom) for a y-directed source magnetic field. Panels (a) and (c) show the real and (b) and (d) the imaginary parts of the electric fields after 1000 iterations applying the divergence correction every 20 iterations.

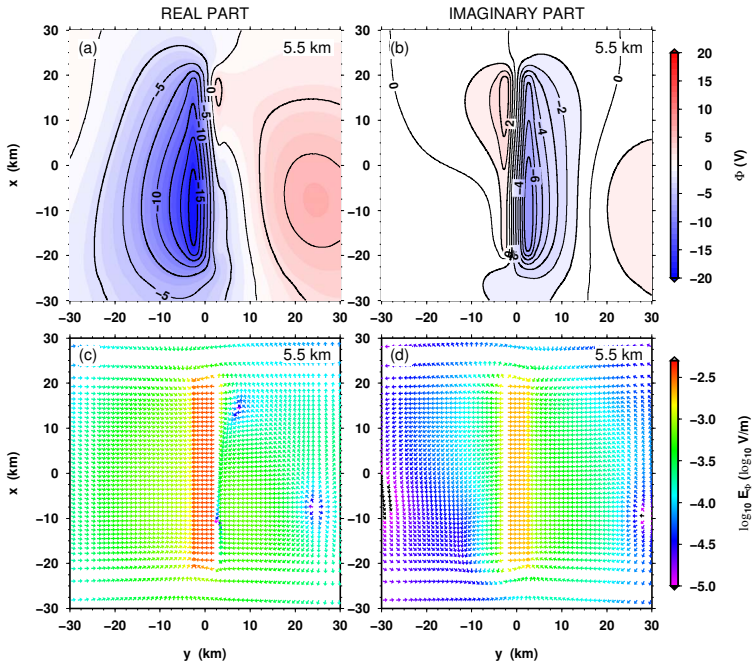

Figure E.57: Divergence correction potential and its gradient at 100 s for a x-directed source magnetic field. Panel (a) shows the real and (b) the imaginary parts of the divergence correction potential applied after 20 iterations. The real (c) and imaginary (d) parts of the horizontal correction electric field are given by the gradient of the correction potential. The potential and the field are shown at a depth of 5.5 km.

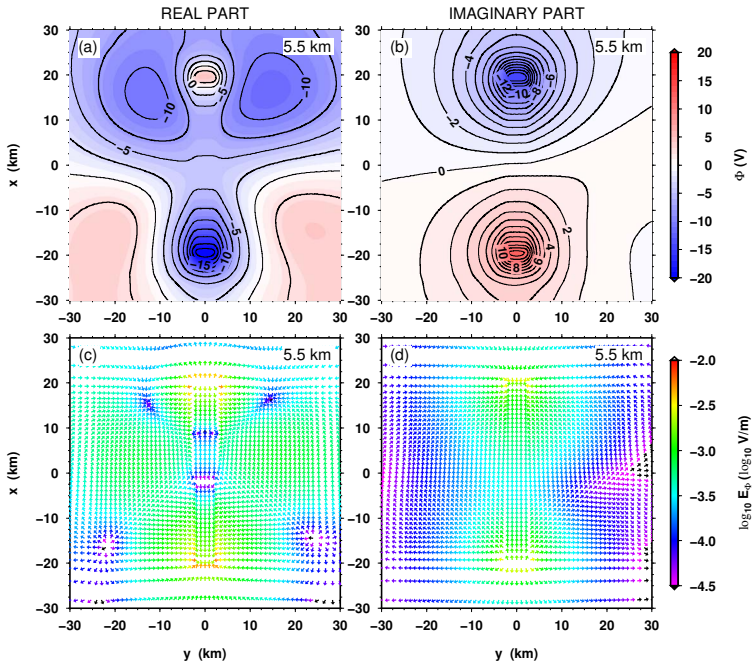

Figure E.58: Divergence correction potential and its gradient at 100 s for a y-directed source magnetic field. Panel (a) shows the real and (b) the imaginary parts of the divergence correction potential applied after 20 iterations. The real (c) and imaginary (d) parts of the horizontal correction electric field are given by the gradient of the correction potential. The potential and the field are shown at a depth of 5.5 km.

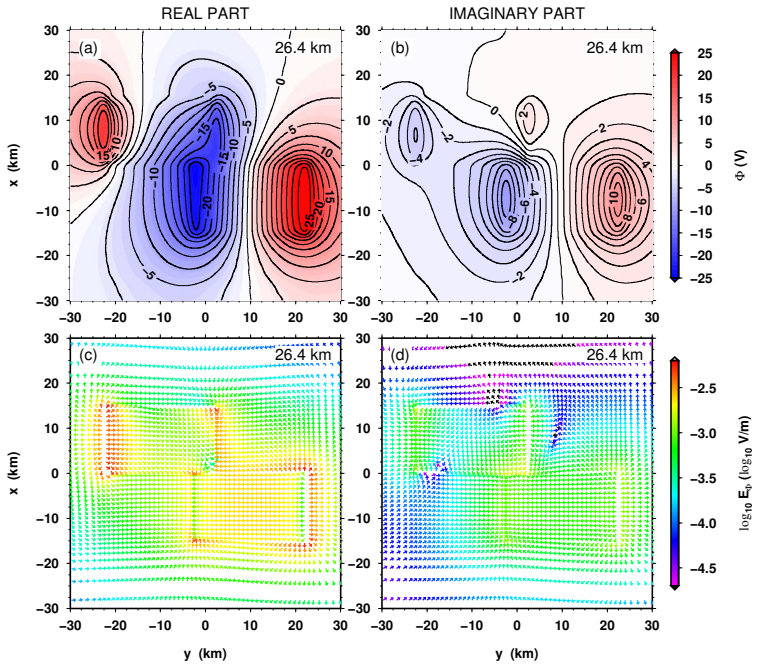

Figure E.59: Divergence correction potential and its gradient at 100 s for a x-directed source magnetic field. Panel (a) shows the real and (b) the imaginary parts of the divergence correction potential applied after 20 iterations. The real (c) and imaginary (d) parts of the horizontal correction electric field are given by the gradient of the correction potential. The potential and the field are shown at a depth of of 26.4 km.

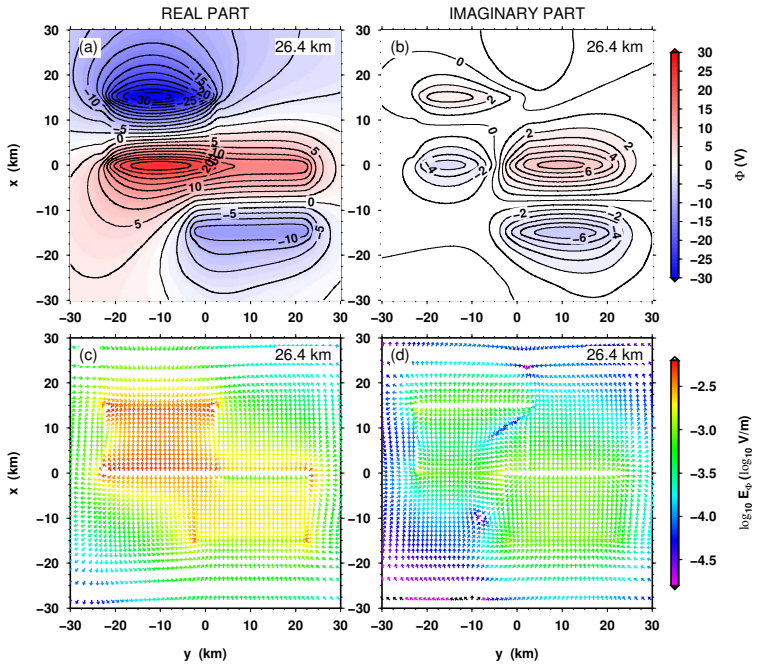

Figure E.60: Divergence correction potential and its gradient at 100 s for a y-directed source magnetic field. Panel (a) shows the real and (b) the imaginary parts of the divergence correction potential applied after 20 iterations. The real (c) and imaginary (d) parts of the horizontal correction electric field are given by the gradient of the correction potential. The potential and the field are shown at a depth of of 26.4 km.

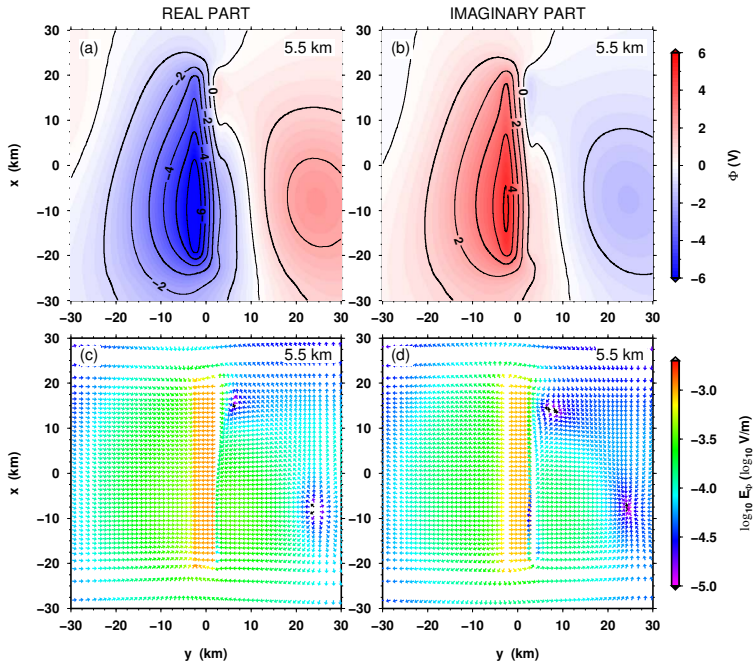

Figure E.61: Divergence correction potential and its gradient at 1000 s for a x-directed source magnetic field. Panel (a) shows the real and (b) the imaginary parts of the divergence correction potential applied after 20 iterations. The real (c) and imaginary (d) parts of the horizontal correction electric field are given by the gradient of the correction potential. The potential and the field are shown at a depth of 5.5 km.

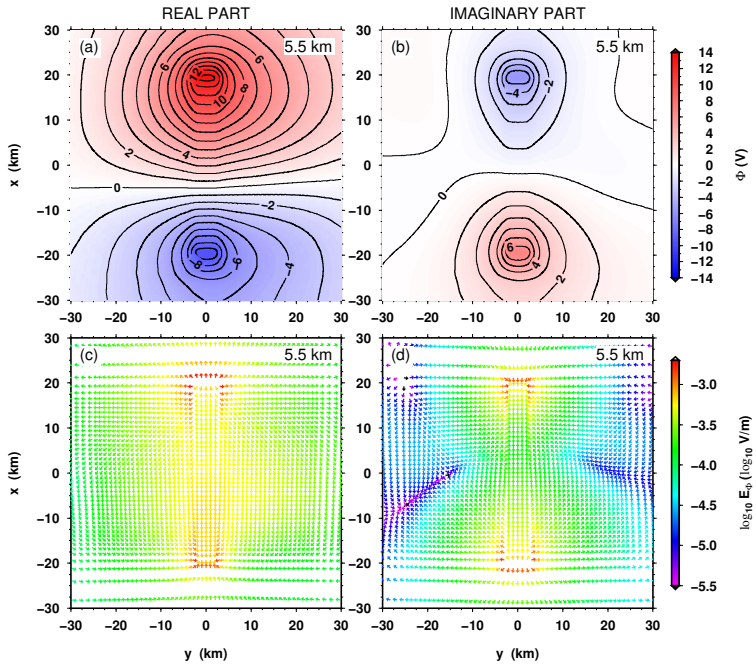

Figure E.62: Divergence correction potential and its gradient at 1000 s for a y-directed source magnetic field. Panel (a) shows the real and (b) the imaginary parts of the divergence correction potential applied after 20 iterations. The real (c) and imaginary (d) parts of the horizontal correction electric field are given by the gradient of the correction potential. The potential and the field are shown at a depth of 5.5 km.

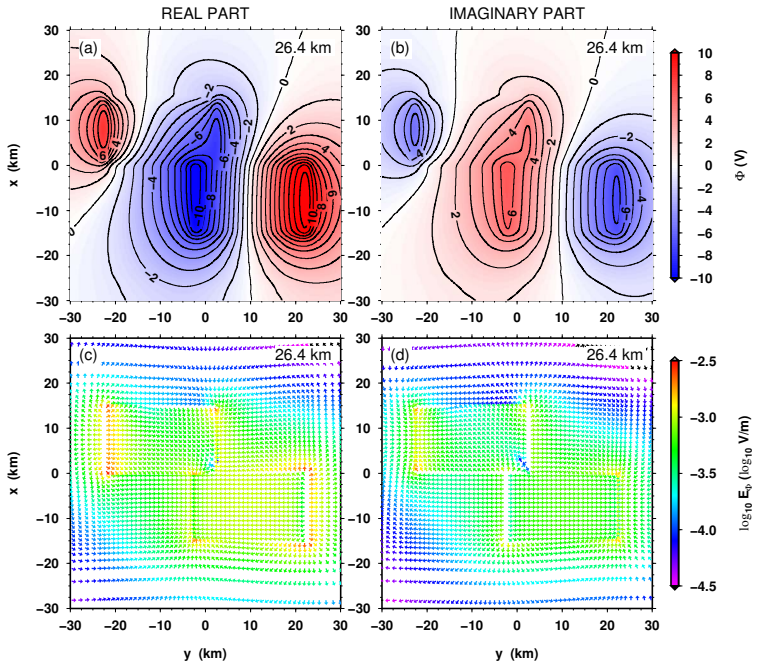

Figure E.63: Divergence correction potential and its gradient at 1000 s for a x-directed source magnetic field. Panel (a) shows the real and (b) the imaginary parts of the divergence correction potential applied after 20 iterations. The real (c) and imaginary (d) parts of the horizontal correction electric field are given by the gradient of the correction potential. The potential and the field are shown at a depth of 26.4 km.

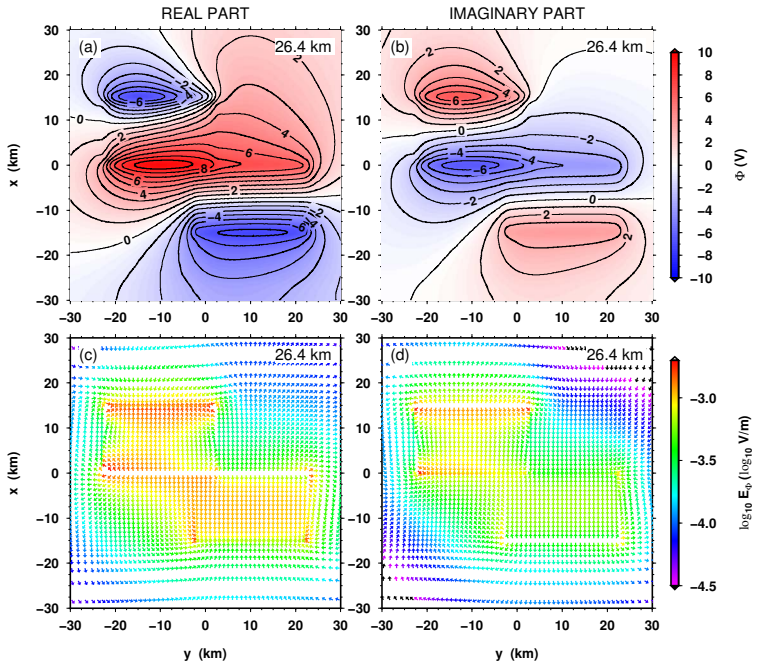

Figure E.64: Divergence correction potential and its gradient at 1000 s for a y-directed source magnetic field. Panel (a) shows the real and (b) the imaginary parts of the divergence correction potential applied after 20 iterations. The real (c) and imaginary (d) parts of the horizontal correction electric field are given by the gradient of the correction potential. The potential and the field are shown at a depth of 26.4 km.

F

DERIVATION OF DERIVATIVES

This Appendix belongs to Chapter 8, which describes the inversion code MCMT3DID. For the inversion process using a Gauss-Newton approach it is essential to determine the derivatives of the objective function with respect to the inversion parameters to generate the needed Jacobian matrix and its transpose. Section F.1 discusses the contribution of using a non-L_2 norm as measure of misfit and model complexity and the equations to calculate the derivatives of the data with respect to the conductivity structure and with respect to the distortion parameters is shown in Sections F.2 and F.3, respectively.

F.1 CONTRIBUTION OF USING A NON-L_2 NORM AS MEASURE OF MISFIT AND MODEL COMPLEXITY

Farquharson and Oldenburg (1998) discussed the contribution of using non-L_2 measures, such as the Huber and Ekblom measures, to the derivatives of the data misfit and model structure compared to using standard L_2 measures. In order to construct a system of equations upon which an iteratively reweighted least-squares routine can be used, Farquharson and Oldenburg (1998) consider a diagonal matrix $\underline{\underline{R}}$ given by

$$\underline{\underline{R}} = \mathrm{diag}\left\{\frac{f'(x_1)}{x_1}, \frac{f'(x_2)}{x_2}, ..., \frac{f'(x_n)}{x_n}\right\} \quad , \tag{F.1}$$

where $f'(x_i)$ is the derivative of the function $f(x_i)$. In the case of MCMT3DID the function $f(x)$ is either the Huber measure or the Ekblom measure. Therefore the derivative of ϕ_s with respect to the conductivity structure is

$$\frac{\partial \phi_s}{\partial \underline{m}} = \underline{\underline{W}}_s^T \, \underline{\underline{R}}_s \, \underline{\underline{W}}_s \, (\underline{m} - \underline{m}_{ref}) \quad , \tag{F.2}$$

where $\underline{\underline{W}}_s$ and $\underline{\underline{W}}_s^T$ are the weighting matrix and its transpose and the elements of the matrix $\underline{\underline{R}}_s$ are given by

$$R_s^{ii} = p\left(\left[W_s^i(m^i - m_{ref}^i)\right]^2 + \varepsilon^2\right)^{p/2-1} \quad . \tag{F.3}$$

Analogous is the derivative of $\underline{\phi_x}$ with respect to the conductivity structure given by

$$\frac{\partial \phi_x^k}{\partial \underline{m}} = \underline{\underline{W}}_x^{T,k} \, \underline{\underline{R}}_x^k \, \underline{\underline{W}}_x^k \, (\underline{m} - \underline{m}_{ref}) \quad , \tag{F.4}$$

where $\underline{\underline{W}}_x^k$ is one of the 13 direction matrices (see Figure 8.2, Section 8.2.2) and the elements of the matrix $\underline{\underline{R}}_x^k$ are given by

$$R_x^{k,ii} = p\left(\left[W_x^{k,i}(m^i - m_{ref}^i)\right]^2 + \varepsilon^2\right)^{p/2-1} \quad . \tag{F.5}$$

The derivative of ϕ_d with respect to the model structure is can be written as

$$\frac{\partial \phi_d}{\partial \underline{m}} = \underline{\underline{J}}_m^T \underline{\underline{W}}_d^T \underline{\underline{R}}_d \underline{\underline{W}}_d \left(\underline{\underline{J}}_m \underline{m} - \underline{d}_{obs}\right) \quad , \tag{F.6}$$

where the elements of the matrix $\underline{\underline{R}}_d$ are given by

$$R_d^{ii} = \begin{cases} 2 & \text{if } |W_d^i(d_{pred}^i - d_{obs}^i)| \leqslant h \\ 2h/|W_d^i(d_{pred}^i - d_{obs}^i)| & \text{if } |W_d^i(d_{pred}^i - d_{obs}^i)| > h \end{cases} \quad . \tag{F.7}$$

Analogous is the derivative of ϕ_d with respect to the distortion parameters given by

$$\frac{\partial \phi_d}{\partial \underline{c}} = \underline{\underline{J}}_c^T \underline{\underline{W}}_d^T \underline{\underline{R}}_d \underline{\underline{W}}_d \left(\underline{\underline{J}}_c \underline{c} - \underline{d}_{obs}\right) \quad . \tag{F.8}$$

And finally the derivative of ϕ_c with respect to the distortion parameters can be written as

$$\frac{\partial \phi_c}{\partial \underline{c}} = \underline{\underline{W}}_c^T \underline{\underline{R}}_c \underline{\underline{W}}_c \left(\underline{c} - \underline{c}_{ref}\right) \quad , \tag{F.9}$$

where the elements of the matrix $\underline{\underline{R}}_c$ are given by

$$R_c^{ii} = \begin{cases} 2 & \text{if } |W_c^i(c_{pred}^i - c_{obs}^i)| \leqslant h \\ 2h/|W_c^i(c_{pred}^i - c_{obs}^i)| & \text{if } |W_c^i(c_{pred}^i - c_{obs}^i)| > h \end{cases} \quad . \tag{F.10}$$

Therefore using non-L_2 norm measures turns Equation 8.18 into

$$\begin{aligned} &\left[\begin{array}{c} \underline{\underline{J}}_m^T \underline{\underline{W}}_d^T \underline{\underline{R}}_d \underline{\underline{W}}_d \underline{\underline{J}}_m \\ +\beta_m \alpha_s \underline{\underline{W}}_s^T \underline{\underline{R}}_s \underline{\underline{W}}_s \\ +\beta_m \textstyle\sum_k \alpha_k \underline{\underline{W}}_k^T \underline{\underline{R}}_x^k \underline{\underline{W}}_k \end{array}\right] \delta \underline{m} = \\ -\ &\underline{\underline{J}}_m^T \underline{\underline{W}}_d^T \underline{\underline{R}}_d \underline{\underline{W}}_d (\underline{d}^n - \underline{d}_{obs}) - \left[\begin{array}{c} \beta_m \alpha_s \underline{\underline{W}}_s^T \underline{\underline{R}}_s \underline{\underline{W}}_s \\ +\beta_m \textstyle\sum_k \alpha_k \underline{\underline{W}}_k^T \underline{\underline{R}}_x^k \underline{\underline{W}}_k \end{array}\right] (\underline{m}^n - \underline{m}_{ref}) \quad , \end{aligned} \tag{F.11}$$

Equation 8.24 becomes

$$\begin{aligned} &\left[\underline{\underline{J}}_c^T \underline{\underline{W}}_d^T \underline{\underline{R}}_d \underline{\underline{W}}_d \underline{\underline{J}}_c + \beta_c \underline{\underline{W}}_c^T \underline{\underline{R}}_c \underline{\underline{W}}_c\right] \delta \underline{c} = \\ -&\underline{\underline{J}}_c^T \underline{\underline{W}}_d^T \underline{\underline{R}}_d \underline{\underline{W}}_d (\underline{d}^n - \underline{d}_{obs}) - \beta_c \underline{\underline{W}}_c^T \underline{\underline{R}}_c \underline{\underline{W}}_c (\underline{c}^n - \underline{c}_{ref}) \quad , \end{aligned} \tag{F.12}$$

and finally Equation 8.32 can be written as

$$\left[\begin{array}{c} \underline{\underline{J}}_g^T\,\underline{\underline{W}}_d^T\,\underline{\underline{R}}_d\,\underline{\underline{W}}_d\,\underline{\underline{J}}_g + \beta_m\alpha_s\,\underline{\underline{V}}_s^T\,\underline{\underline{P}}_s\,\underline{\underline{V}}_s \\ +\beta_m\sum_k \alpha_k\,\underline{\underline{V}}_k^T\,\underline{\underline{P}}_k\,\underline{\underline{V}}_k + \beta_c\,\underline{\underline{V}}_c^T\,\underline{\underline{P}}_c\,\underline{\underline{V}}_c \end{array}\right]\delta\underline{g} = \tag{F.13}$$

$$-\underline{\underline{J}}_g^T\,\underline{\underline{W}}_d^T\,\underline{\underline{R}}_d\,\underline{\underline{W}}_d\,(\underline{d}^n - \underline{d}_{obs}) - \left[\begin{array}{c} \beta_m\alpha_s\,\underline{\underline{V}}_s^T\,\underline{\underline{P}}_s\,\underline{\underline{V}}_s \\ +\beta_m\sum_k \alpha_k\,\underline{\underline{V}}_k^T\,\underline{\underline{P}}_k\,\underline{\underline{V}}_k \\ +\beta_c\,\underline{\underline{V}}_c^T\,\underline{\underline{P}}_c\,\underline{\underline{V}}_c \end{array}\right]\left(\underline{g}^n - \underline{g}_{ref}\right) \quad ,$$

where

$$\underline{\underline{P}}_s = \begin{pmatrix} \underline{\underline{R}}_s & 0 \\ 0 & 0 \end{pmatrix},\ \underline{\underline{P}}_k = \begin{pmatrix} \underline{\underline{R}}_x^k & 0 \\ 0 & 0 \end{pmatrix} \text{ and } \underline{\underline{P}}_c = \begin{pmatrix} 0 & 0 \\ 0 & \underline{\underline{R}}_c \end{pmatrix} \quad .$$

F.2 DERIVATIVES OF THE DATA WITH RESPECT TO THE CONDUCTIVITIES

This part of the appendix shows how the derivatives with respect to the conductivity structure are calculate for data values that are either impedance, tipper or apparent resistivity and phase. The impedance tensor, $\underline{\underline{Z}}$, is related to the calculated electric, $\underline{E}$, and magnetic, $\underline{H}$, fields by

$$\begin{pmatrix} E_x \\ E_y \end{pmatrix} = \begin{pmatrix} Z_{xx} & Z_{xy} \\ Z_{yx} & Z_{yy} \end{pmatrix}\begin{pmatrix} H_x \\ H_y \end{pmatrix} \quad . \tag{F.14}$$

As the inversion code calculates the fields for two different polarisations (here indicated by indices 1 and 2), the impedance tensor is determined by

$$\begin{pmatrix} E_{x1} & E_{x2} \\ E_{y1} & E_{y2} \end{pmatrix} = \begin{pmatrix} Z_{xx} & Z_{xy} \\ Z_{yx} & Z_{yy} \end{pmatrix}\begin{pmatrix} H_{x1} & H_{x2} \\ H_{y1} & H_{y2} \end{pmatrix} \quad . \tag{F.15}$$

The inverse of the matrix $\underline{\underline{H}}$ is given by

$$\begin{pmatrix} H_{x1} & H_{x2} \\ H_{y1} & H_{y2} \end{pmatrix}^{-1} = \frac{1}{H_{x1}H_{y2} - H_{x2}H_{y1}}\begin{pmatrix} H_{y2} & -H_{x2} \\ -H_{y1} & H_{x1} \end{pmatrix} \tag{F.16}$$

and therefore the impedance tensor elements are calculated as

$$\begin{aligned} \begin{pmatrix} Z_{xx} & Z_{xy} \\ Z_{yx} & Z_{yy} \end{pmatrix} &= \begin{pmatrix} E_{x1} & E_{x2} \\ E_{y1} & E_{y2} \end{pmatrix}\begin{pmatrix} H_{x1} & H_{x2} \\ H_{y1} & H_{y2} \end{pmatrix}^{-1} \\ &= \begin{pmatrix} E_{x1} & E_{x2} \\ E_{y1} & E_{y2} \end{pmatrix}\frac{1}{H_{x1}H_{y2} - H_{x2}H_{y1}}\begin{pmatrix} H_{y2} & -H_{x2} \\ -H_{y1} & H_{x1} \end{pmatrix} \\ &= \begin{pmatrix} \frac{E_{x1}H_{y2} - E_{x2}H_{y1}}{H_{x1}H_{y2} - H_{x2}H_{y1}} & \frac{-E_{x1}H_{x2} + E_{x2}H_{x1}}{H_{x1}H_{y2} - H_{x2}H_{y1}} \\ \\ \frac{E_{y1}H_{y2} - E_{y2}H_{y1}}{H_{x1}H_{y2} - H_{x2}H_{y1}} & \frac{-E_{y1}H_{x2} + E_{y2}H_{x1}}{H_{x1}H_{y2} - H_{x2}H_{y1}} \end{pmatrix} \quad . \end{aligned} \tag{F.17}$$

The individual components of the impedance tensor can be written as

$$Z_{xx} = \frac{E_{x1}H_{y2} - E_{x2}H_{y1}}{H_{x1}H_{y2} - H_{x2}H_{y1}} = \frac{E_{x2} - \frac{H_{y2}}{H_{y1}}E_{x1}}{H_{x2} - \frac{H_{y2}}{H_{y1}}H_{x1}} = \frac{E_{x2} - \beta E_{x1}}{H_{x2} - \beta H_{x1}} \quad , \tag{F.18}$$

$$Z_{xy} = \frac{-E_{x1}H_{x2} + E_{x2}H_{x1}}{H_{x1}H_{y2} - H_{x2}H_{y1}} = \frac{E_{x1} - \frac{H_{x1}}{H_{x2}}E_{x2}}{H_{y1} - \frac{H_{x1}}{H_{x2}}H_{y2}} = \frac{E_{x1} - \alpha E_{x2}}{H_{y1} - \alpha H_{y2}} \quad , \tag{F.19}$$

$$Z_{yx} = \frac{E_{y1}H_{y2} - E_{y2}H_{y1}}{H_{x1}H_{y2} - H_{x2}H_{y1}} = \frac{E_{y2} - \frac{H_{y2}}{H_{y1}}E_{y1}}{H_{x2} - \frac{H_{y2}}{H_{y1}}H_{x1}} = \frac{E_{y2} - \beta E_{y1}}{H_{x2} - \beta H_{x1}} \tag{F.20}$$

and

$$Z_{yy} = \frac{-E_{y1}H_{x2} + E_{y2}H_{x1}}{H_{x1}H_{y2} - H_{x2}H_{y1}} = \frac{E_{y1} - \frac{H_{x1}}{H_{x2}}E_{y2}}{H_{y1} - \frac{H_{x1}}{H_{x2}}H_{y2}} = \frac{E_{y1} - \alpha E_{y2}}{H_{y1} - \alpha H_{y2}} \quad , \tag{F.21}$$

where

$$\alpha = -\frac{H_{x1}}{H_{x2}} \quad \text{and} \quad \beta = -\frac{H_{y2}}{H_{y1}} \quad . \tag{F.22}$$

The tipper vector is calculated from the magnetic field components,

$$H_z = (T_x \; T_y) \begin{pmatrix} H_x \\ H_y \end{pmatrix} \tag{F.23}$$

or, written in terms of the two different polarisations (indices 1 and 2),

$$(H_{z1} \; H_{z2}) = (T_x \; T_y) \begin{pmatrix} H_{x1} & H_{x2} \\ H_{y1} & H_{y2} \end{pmatrix} \quad , \tag{F.24}$$

applying the inverse of the matrix containing the lateral magnetic field components (Equation F.16) yields

$$\begin{aligned} \begin{pmatrix} T_x & T_y \end{pmatrix} &= \begin{pmatrix} H_{z1} & H_{z2} \end{pmatrix} \begin{pmatrix} H_{x1} & H_{x2} \\ H_{y1} & H_{y2} \end{pmatrix}^{-1} \\ &= \begin{pmatrix} H_{z1} & H_{z2} \end{pmatrix} \frac{1}{H_{x1}H_{y2} - H_{x2}H_{y1}} \begin{pmatrix} H_{y2} & -H_{x2} \\ -H_{y1} & H_{x1} \end{pmatrix} \\ &= \begin{pmatrix} \frac{H_{z1}H_{y2} - H_{z2}H_{y1}}{H_{x1}H_{y2} - H_{x2}H_{y1}} & \frac{-H_{z1}H_{x2} + H_{z2}H_{x1}}{H_{x1}H_{y2} - H_{x2}H_{y1}} \end{pmatrix} \quad . \end{aligned} \tag{F.25}$$

Applying the ratios α and β yields (in components)

$$T_x = \frac{H_{y2}H_{z1} - H_{y1}H_{z2}}{H_{y2}H_{x1} - H_{y1}H_{x2}} = \frac{H_{z2} - \frac{H_{y2}}{H_{y1}}H_{z1}}{H_{x2} - \frac{H_{y2}}{H_{y1}}H_{x1}} = \frac{H_{z2} + \beta H_{z1}}{H_{x2} + \beta H_{x1}} \tag{F.26}$$

and

$$T_y = \frac{H_{x1}H_{z2} - H_{x2}H_{z1}}{H_{x1}H_{y2} - H_{x2}H_{y1}} = \frac{H_{z1} - \frac{H_{x1}}{H_{x2}}H_{z2}}{H_{y1} + -\frac{H_{x1}}{H_{x2}}H_{y2}} = \frac{H_{z1} + \alpha H_{z2}}{H_{y1} + \alpha H_{y2}} \quad . \tag{F.27}$$

As the ratios α and β depend on the magnetic field components, which themselves depend on the cell conductivities, the derivatives of the ratios with respect to the conductivity of a cell (σ) are given by

$$\frac{\partial \alpha}{\partial \sigma} = \frac{H_{x1}}{(H_{x2})^2}\frac{\partial H_{x2}}{\partial \sigma} - \frac{1}{H_{x2}}\frac{\partial H_{x1}}{\partial \sigma} \tag{F.28}$$

and

$$\frac{\partial \beta}{\partial \sigma} = \frac{H_{y2}}{(H_{y1})^2}\frac{\partial H_{y1}}{\partial \sigma} - \frac{1}{H_{y1}}\frac{\partial H_{y2}}{\partial \sigma} \quad . \tag{F.29}$$

The derivatives of the four components of the impedance tensor with respect to the conductivity of a cell (σ) are given by

$$\begin{aligned}
\frac{\partial Z_{xx}}{\partial \sigma} &= \frac{\frac{\partial}{\partial \sigma}(E_{x2} + \beta E_{x1})(H_{x2} + \beta H_{x1})}{(H_{x2} + \beta H_{x1})^2} \\
&\quad - \frac{(E_{x2} + \beta E_{x1})\frac{\partial}{\partial \sigma}(H_{x2} + \beta H_{x1})}{(H_{x2} + \beta H_{x1})^2} \\
&= \left\{\frac{\partial E_{x2}}{\partial \sigma} + \beta\frac{\partial E_{x1}}{\partial \sigma} + \frac{\partial \beta}{\partial \sigma}E_{x1}\right\}\frac{1}{(H_{x2} + \beta H_{x1})} \\
&\quad - \frac{(E_{x2} + \beta E_{x1})}{(H_{x2} + \beta H_{x1})^2}\left\{\frac{\partial H_{x2}}{\partial \sigma} + \beta\frac{\partial H_{x1}}{\partial \sigma} + \frac{\partial \beta}{\partial \sigma}H_{x1}\right\} \quad ,
\end{aligned} \tag{F.30}$$

$$\begin{aligned}
\frac{\partial Z_{xy}}{\partial \sigma} &= \frac{\frac{\partial}{\partial \sigma}(E_{x1} + \alpha E_{x2})\left(H_{y1} + \alpha H_{y2}\right)}{\left(H_{y1} + \alpha H_{y2}\right)^2} \\
&\quad - \frac{(E_{x1} + \alpha E_{x2})\frac{\partial}{\partial \sigma}\left(H_{y1} + \alpha H_{y2}\right)}{\left(H_{y1} + \alpha H_{y2}\right)^2} \\
&= \left\{\frac{\partial E_{x1}}{\partial \sigma} + \alpha\frac{\partial E_{x2}}{\partial \sigma} + \frac{\partial \alpha}{\partial \sigma}E_{x2}\right\}\frac{1}{\left(H_{y1} + \alpha H_{y2}\right)} \\
&\quad - \frac{(E_{x1} + \alpha E_{x2})}{\left(H_{y1} + \alpha H_{y2}\right)^2}\left\{\frac{\partial H_{y1}}{\partial \sigma} + \alpha\frac{\partial H_{y2}}{\partial \sigma} + \frac{\partial \alpha}{\partial \sigma}H_{y2}\right\} \quad ,
\end{aligned} \tag{F.31}$$

$$\begin{aligned}
\frac{\partial Z_{yx}}{\partial \sigma} &= \frac{\frac{\partial}{\partial \sigma}\left(E_{y2} + \beta E_{y1}\right)(H_{x2} + \beta H_{x1})}{(H_{x2} + \beta H_{x1})^2} \\
&\quad - \frac{\left(E_{y2} + \beta E_{y1}\right)\frac{\partial}{\partial \sigma}(H_{x2} + \beta H_{x1})}{(H_{x2} + \beta H_{x1})^2} \\
&= \left\{\frac{\partial E_{y2}}{\partial \sigma} + \beta\frac{\partial E_{y1}}{\partial \sigma} + \frac{\partial \beta}{\partial \sigma}E_{y1}\right\}\frac{1}{(H_{x2} + \beta H_{x1})} \\
&\quad - \frac{\left(E_{y2} + \beta E_{y1}\right)}{(H_{x2} + \beta H_{x1})^2}\left\{\frac{\partial H_{x2}}{\partial \sigma} + \beta\frac{\partial H_{x1}}{\partial \sigma} + \frac{\partial \beta}{\partial \sigma}H_{x1}\right\}
\end{aligned} \tag{F.32}$$

and

$$\begin{aligned}\frac{\partial Z_{yy}}{\partial \sigma} &= \frac{\frac{\partial}{\partial \sigma}\left(E_{y1}+\alpha E_{y2}\right)\left(H_{y1}+\alpha H_{y2}\right)}{\left(H_{y1}+\alpha H_{y2}\right)^2} \\ &\quad - \frac{\left(E_{y1}+\alpha E_{y2}\right)\frac{\partial}{\partial \sigma}\left(H_{y1}+\alpha H_{y2}\right)}{\left(H_{y1}+\alpha H_{y2}\right)^2} \\ &= \left\{\frac{\partial E_{y1}}{\partial \sigma}+\alpha\frac{\partial E_{y2}}{\partial \sigma}+\frac{\partial \alpha}{\partial \sigma}E_{y2}\right\}\frac{1}{\left(H_{y1}+\alpha H_{y2}\right)} \\ &\quad - \frac{\left(E_{y1}+\alpha E_{y2}\right)}{\left(H_{y1}+\alpha H_{y2}\right)^2}\left\{\frac{\partial H_{y1}}{\partial \sigma}+\alpha\frac{\partial H_{y2}}{\partial \sigma}+\frac{\partial \alpha}{\partial \sigma}H_{y2}\right\} . \end{aligned} \tag{F.33}$$

The derivatives of the electric and magnetic field components with respect to the cell conductivity are the solution of the iterative process within the inversion code. Applying the chain rule, the derivatives of Equations F.18 to F.22 (and F.26 and F.27) with respect to the electric and magnetic field components are required to calculate the derivatives of the data with respect to the conductivity σ. The derivatives of the coefficients α and β with respect to the magnetic field components can be written as

$$\frac{\partial \alpha}{\partial H_{x1}} = -\frac{1}{H_{x2}} , \tag{F.34}$$

$$\frac{\partial \alpha}{\partial H_{x2}} = \frac{H_{x1}}{(H_{x2})^2} , \tag{F.35}$$

$$\frac{\partial \beta}{\partial H_{y1}} = \frac{H_{y2}}{(H_{y1})^2} \quad \text{and} \tag{F.36}$$

$$\frac{\partial \beta}{\partial H_{y2}} = -\frac{1}{H_{y1}} . \tag{F.37}$$

The derivatives of the impedance tensor elements with respect to the electrical and magnetic field components are given by

Z_{xx} component:

$$\frac{\partial Z_{xx}}{\partial E_{x1}} = \frac{\beta}{H_{x2}+\beta H_{x1}} , \tag{F.38}$$

$$\frac{\partial Z_{xx}}{\partial E_{y1}} = 0 , \tag{F.39}$$

$$\frac{\partial Z_{xx}}{\partial H_{x1}} = -\beta\frac{E_{x2}+\beta E_{x1}}{(H_{x2}+\beta H_{x1})^2} , \tag{F.40}$$

$$\frac{\partial Z_{xx}}{\partial H_{y1}} = -\frac{E_{x2}+\beta E_{x1}}{(H_{x2}+\beta H_{x1})^2}\frac{\partial \beta}{\partial H_{y1}}H_{x1} + \frac{1}{H_{x2}+\beta H_{x1}}\frac{\partial \beta}{\partial H_{y1}}E_{x1} , \tag{F.41}$$

$$\frac{\partial Z_{xx}}{\partial E_{x2}} = \frac{1}{H_{x2}+\beta H_{x1}} , \tag{F.42}$$

$$\frac{\partial Z_{xx}}{\partial E_{y2}} = 0 \ , \tag{F.43}$$

$$\frac{\partial Z_{xx}}{\partial H_{x2}} = -\frac{E_{x2}+\beta E_{x1}}{(H_{x2}+\beta H_{x1})^2} \ , \tag{F.44}$$

$$\frac{\partial Z_{xx}}{\partial H_{y2}} = -\frac{E_{x2}+\beta E_{x1}}{(H_{x2}+\beta H_{x1})^2}\frac{\partial \beta}{\partial H_{y2}}H_{x1} + \frac{1}{H_{x2}+\beta H_{x1}}\frac{\partial \beta}{\partial H_{y2}}E_{x1} \ , \tag{F.45}$$

Z_{xy} component:

$$\frac{\partial Z_{xy}}{\partial E_{x1}} = \frac{1}{H_{y1}+\alpha H_{y2}} \ , \tag{F.46}$$

$$\frac{\partial Z_{xy}}{\partial E_{y1}} = 0 \ , \tag{F.47}$$

$$\frac{\partial Z_{xy}}{\partial H_{x1}} = \frac{E_{x1}+\alpha E_{x2}}{(H_{y1}+\alpha H_{y2})^2}\frac{\partial \alpha}{\partial H_{x1}}H_{y2} + \frac{1}{H_{y1}+\alpha H_{y1}}\frac{\partial \alpha}{\partial H_{x1}}E_{x2} \ , \tag{F.48}$$

$$\frac{\partial Z_{xy}}{\partial H_{y1}} = -\frac{E_{x1}+\alpha E_{x2}}{(H_{y1}+\alpha H_{y2})^2} \ , \tag{F.49}$$

$$\frac{\partial Z_{xy}}{\partial E_{x2}} = \frac{\alpha}{H_{y1}+\alpha H_{y2}} \ , \tag{F.50}$$

$$\frac{\partial Z_{xy}}{\partial E_{y2}} = 0 \ , \tag{F.51}$$

$$\frac{\partial Z_{xy}}{\partial H_{x2}} = -\frac{E_{x1}+\alpha E_{x2}}{(H_{y1}+\alpha H_{y2})^2}\frac{\partial \alpha}{\partial H_{x2}}H_{y2} + \frac{1}{H_{y1}+\alpha H_{y2}}\frac{\partial \alpha}{\partial H_{x2}}E_{x2} \ , \tag{F.52}$$

$$\frac{\partial Z_{xy}}{\partial H_{y2}} = -\alpha\frac{E_{x1}+\alpha E_{x2}}{(H_{y1}+\alpha H_{y2})^2} \ , \tag{F.53}$$

Z_{yx} component:

$$\frac{\partial Z_{yx}}{\partial E_{x1}} = 0 \ , \tag{F.54}$$

$$\frac{\partial Z_{yx}}{\partial E_{y1}} = \frac{\beta}{H_{x2}+\beta H_{x1}} \ , \tag{F.55}$$

$$\frac{\partial Z_{yx}}{\partial H_{x1}} = -\beta\frac{E_{y2}+\beta E_{y1}}{(H_{x2}+\beta H_{x1})^2} \ , \tag{F.56}$$

$$\frac{\partial Z_{yx}}{\partial H_{y1}} = -\frac{E_{y2}+\beta E_{y1}}{(H_{x2}+\beta H_{x1})^2}\frac{\partial \beta}{\partial H_{y1}}H_{x1} + \frac{1}{H_{x2}+\beta H_{x1}}\frac{\partial \beta}{\partial H_{y1}}E_{y1} \quad , \tag{F.57}$$

$$\frac{\partial Z_{yx}}{\partial E_{x2}} = 0 \quad , \tag{F.58}$$

$$\frac{\partial Z_{yx}}{\partial E_{y2}} = \frac{1}{H_{x2}+\beta H_{x1}} \quad , \tag{F.59}$$

$$\frac{\partial Z_{yx}}{\partial H_{x2}} = -\frac{E_{y2}+\beta E_{y1}}{(H_{x2}+\beta H_{x1})^2} \quad , \tag{F.60}$$

$$\frac{\partial Z_{yx}}{\partial H_{y2}} = -\frac{E_{y2}+\beta E_{y1}}{(H_{x2}+\beta H_{x1})^2}\frac{\partial \beta}{\partial H_{y2}}H_{x1} + \frac{1}{H_{x2}+\beta H_{x1}}\frac{\partial \beta}{\partial H_{y2}}E_{y1} \quad , \tag{F.61}$$

Z_{yy} component:

$$\frac{\partial Z_{yy}}{\partial E_{x1}} = 0 \quad , \tag{F.62}$$

$$\frac{\partial Z_{yy}}{\partial E_{y1}} = \frac{1}{H_{y1}+\alpha H_{y2}} \quad , \tag{F.63}$$

$$\frac{\partial Z_{yy}}{\partial H_{x1}} = -\frac{E_{y1}+\alpha E_{y2}}{(H_{y1}+\alpha H_{y2})^2}\frac{\partial \alpha}{\partial H_{x1}}H_{y2} + \frac{1}{H_{y1}+\alpha H_{y2}}\frac{\partial \alpha}{\partial H_{x1}}E_{y2} \quad , \tag{F.64}$$

$$\frac{\partial Z_{yy}}{\partial H_{y1}} = -\frac{E_{y1}+\alpha E_{y2}}{(H_{y1}+\alpha H_{y2})^2} \quad , \tag{F.65}$$

$$\frac{\partial Z_{yy}}{\partial E_{x2}} = 0 \quad , \tag{F.66}$$

$$\frac{\partial Z_{yy}}{\partial E_{y2}} = \frac{\alpha}{H_{y1}+\alpha H_{y2}} \quad , \tag{F.67}$$

$$\frac{\partial Z_{yy}}{\partial H_{x2}} = -\frac{E_{y1}+\alpha E_{y2}}{(H_{y1}+\alpha H_{y2})^2}\frac{\partial \alpha}{\partial H_{x2}}H_{y2} + \frac{1}{H_{y1}+\alpha H_{y2}}\frac{\partial \alpha}{\partial H_{x2}}E_{y2} \quad , \tag{F.68}$$

$$\frac{\partial Z_{yy}}{\partial H_{y2}} = -\alpha\frac{E_{y1}+\alpha E_{y2}}{(H_{y1}+\alpha H_{y2})^2} \quad . \tag{F.69}$$

The derivatives of the elements of the tipper vector with respect to the magnetic field components are given by

$$\frac{\partial T_x}{\partial H_{x1}} = -\beta\frac{H_{z2}+\beta H_{z1}}{(H_{x2}+\beta H_{x1})^2} \quad , \tag{F.70}$$

$$\frac{\partial T_x}{\partial H_{y1}} = -\frac{H_{z2}+\beta H_{z1}}{(H_{x2}+\beta H_{x1})^2}\frac{\partial \beta}{\partial H_{y1}}H_{x1} + \frac{1}{H_{x2}+\beta H_{x1}}\frac{\partial \beta}{\partial H_{y1}}H_{z1} \quad , \tag{F.71}$$

$$\frac{\partial T_x}{\partial H_{z1}} = \frac{\beta}{H_{x2}+\beta H_{x1}} \quad , \tag{F.72}$$

$$\frac{\partial T_x}{\partial H_{x2}} = -\frac{H_{z2}+\beta H_{z1}}{(H_{x2}+\beta H_{x1})^2} \quad , \tag{F.73}$$

$$\frac{\partial T_x}{\partial H_{y2}} = -\frac{H_{z2}+\beta H_{z1}}{(H_{x2}+\beta H_{x1})^2}\frac{\partial \beta}{\partial H_{y2}}H_{x1} + \frac{1}{H_{x2}+\beta H_{x1}}\frac{\partial \beta}{\partial H_{y2}}H_{z1} \quad , \tag{F.74}$$

$$\frac{\partial T_x}{\partial H_{z2}} = \frac{1}{H_{x2}+\beta H_{x1}} \tag{F.75}$$

$$\frac{\partial T_y}{\partial H_{x1}} = -\frac{H_{z1}+\alpha H_{z2}}{(H_{y1}+\alpha H_{y2})^2}\frac{\partial \alpha}{\partial H_{x1}}H_{y2} + \frac{1}{(H_{y1}+\alpha H_{y2})^2}\frac{\partial \alpha}{\partial H_{x1}}H_{z2} \quad , \tag{F.76}$$

$$\frac{\partial T_y}{\partial H_{y1}} = -\frac{H_{z1}+\alpha H_{z2}}{(H_{y1}+\alpha H_{y2})^2} \quad , \tag{F.77}$$

$$\frac{\partial T_y}{\partial H_{z1}} = \frac{1}{H_{y1}+\alpha H_{y2}} \quad , \tag{F.78}$$

$$\frac{\partial T_y}{\partial H_{x2}} = -\frac{H_{z1}+\alpha H_{z2}}{(H_{y1}+\alpha H_{y2})^2}\frac{\partial \alpha}{\partial H_{x2}}H_{y2} + \frac{1}{(H_{y1}+\alpha H_{y2})^2}\frac{\partial \alpha}{\partial H_{x2}}H_{z1} \quad , \tag{F.79}$$

$$\frac{\partial T_y}{\partial H_{y2}} = -\alpha\frac{H_{z1}+\alpha H_{z2}}{(H_{y1}+\alpha H_{y2})^2} \quad , \tag{F.80}$$

$$\frac{\partial T_y}{\partial H_{z2}} = \frac{\alpha}{H_{y1}+\alpha H_{y2}} \tag{F.81}$$

The apparent resistivities can be determined from the impedance tensor elements by

$$\rho_{ij} = \frac{1}{\omega\mu}|Z_{ij}|^2 = \frac{1}{\omega\mu}Z_{ij}Z_{ij}^* = \frac{1}{\omega\mu}(\mathrm{Re}\,Z_{ij}+i\mathrm{Im}\,Z_{ij})(\mathrm{Re}\,Z_{ij}-i\mathrm{Im}\,Z_{ij}) \quad , \tag{F.82}$$

and phases are given by

$$Z_{ij} = |Z_{ij}|e^{i\phi_{ij}} \quad . \tag{F.83}$$

Therefore the derivatives of the apparent resistivities with respect to the electrical and magnetic field components (where F stands for any of these field components) can be written as

$$\begin{aligned}
\frac{\partial \rho_{ij}}{\partial F} &= \frac{1}{\omega\mu}\left(\frac{\partial \mathrm{Re}\, Z_{ij}}{\partial F} + \mathrm{i}\,\frac{\partial \mathrm{Im}\, Z_{ij}}{\partial F}\right)\left(\mathrm{Re}\, Z_{ij} - \mathrm{i}\,\mathrm{Im}\, Z_{ij}\right) \\
&\quad + \frac{1}{\omega\mu}\left(\mathrm{Re}\, Z_{ij} + \mathrm{i}\,\mathrm{Im}\, Z_{ij}\right)\left(\frac{\partial \mathrm{Re}\, Z_{ij}}{\partial F} - \mathrm{i}\,\frac{\partial \mathrm{Im}\, Z_{ij}}{\partial F}\right) \\
&= \frac{1}{\omega\mu}\left\{\frac{\partial \mathrm{Re}\, Z_{ij}}{\partial F}\mathrm{Re}\, Z_{ij} - \mathrm{i}\,\frac{\partial \mathrm{Re}\, Z_{ij}}{\partial F}\mathrm{Im}\, Z_{ij} + \mathrm{i}\,\frac{\partial \mathrm{Im}\, Z_{ij}}{\partial F}\mathrm{Re}\, Z_{ij} + \frac{\partial \mathrm{Im}\, Z_{ij}}{\partial F}\mathrm{Im}\, Z_{ij}\right. \\
&\quad \left. + \mathrm{Re}\, Z_{ij}\frac{\partial \mathrm{Re}\, Z_{ij}}{\partial F} - \mathrm{i}\,\mathrm{Re}\, Z_{ij}\frac{\partial \mathrm{Im}\, Z_{ij}}{\partial F} + \mathrm{i}\,\mathrm{Im}\, Z_{ij}\frac{\partial \mathrm{Re}\, Z_{ij}}{\partial F} + \mathrm{Im}\, Z_{ij}\frac{\partial \mathrm{Im}\, Z_{ij}}{\partial F}\right\} \\
&= \frac{2}{\omega\mu}\left\{\mathrm{Re}\, Z_{ij}\frac{\partial \mathrm{Re}\, Z_{ij}}{\partial F} + \mathrm{Im}\, Z_{ij}\frac{\partial \mathrm{Im}\, Z_{ij}}{\partial F}\right\} \quad . \qquad \text{(F.84)}
\end{aligned}$$

The derivatives of the phases with respect to the electric and magnetic field components can be derived using the following equation

$$\begin{aligned}
\frac{\partial \mathrm{Re}\, Z_{ij}}{\partial F} + \mathrm{i}\,\frac{\partial \mathrm{Im}\, Z_{ij}}{\partial F} &= |Z_{ij}| e^{\mathrm{i}\phi_{ij}}\,\mathrm{i}\,\frac{\partial \phi_{ij}}{\partial F} + \frac{\partial |Z_{ij}|}{\partial F} e^{\mathrm{i}\phi_{ij}} \quad , \\
\frac{1}{Z_{ij}}\left\{\frac{\partial \mathrm{Re}\, Z_{ij}}{\partial F} + \mathrm{i}\,\frac{\partial \mathrm{Im}\, Z_{ij}}{\partial F}\right\} &= \frac{1}{|Z_{ij}|}\frac{\partial |Z_{ij}|}{\partial F} + \mathrm{i}\,\frac{\partial \phi_{ij}}{\partial F} \quad , \\
\frac{\mathrm{Re}\, Z_{ij} - \mathrm{i}\,\mathrm{Im}\, Z_{ij}}{(\mathrm{Re}\, Z_{ij})^2 + (\mathrm{Im}\, Z_{ij})^2}\left\{\frac{\partial \mathrm{Re}\, Z_{ij}}{\partial F} + \mathrm{i}\,\frac{\partial \mathrm{Im}\, Z_{ij}}{\partial F}\right\} &= \frac{1}{|Z_{ij}|}\frac{\partial |Z_{ij}|}{\partial F} + \mathrm{i}\,\frac{\partial \phi_{ij}}{\partial F} \quad . \qquad \text{(F.85)}
\end{aligned}$$

Applying $|Z_{ij}| = \sqrt{(\mathrm{Re}\, Z_{ij})^2 + (\mathrm{Im}\, Z_{ij})^2}$ and $|Z_{ij}|^2 = (\mathrm{Re}\, Z_{ij})^2 + (\mathrm{Im}\, Z_{ij})^2$ yields

$$\begin{aligned}
\mathrm{i}\,\frac{\partial \phi_{ij}}{\partial F} &= \frac{1}{|Z_{ij}|}\left(\frac{\mathrm{Re}\, Z_{ij}}{|Z_{ij}|}\frac{\partial \mathrm{Re}\, Z_{ij}}{\partial F} - \mathrm{i}\,\frac{\mathrm{Im}\, Z_{ij}}{|Z_{ij}|}\frac{\partial \mathrm{Re}\, Z_{ij}}{\partial F} + \mathrm{i}\,\frac{\mathrm{Re}\, Z_{ij}}{|Z_{ij}|}\frac{\partial \mathrm{Im}\, Z_{ij}}{\partial F} + \right. \\
&\quad \left. \frac{\mathrm{Im}\, Z_{ij}}{|Z_{ij}|}\frac{\partial \mathrm{Im}\, Z_{ij}}{\partial F} - \frac{\partial |Z_{ij}|}{\partial F}\right) \quad . \qquad \text{(F.86)}
\end{aligned}$$

The derivative of $|Z_{ij}|$ is given by

$$\begin{aligned}
\frac{\partial}{\partial F}\sqrt{(\mathrm{Re}\, Z_{ij})^2 + (\mathrm{Im}\, Z_{ij})^2} &= \frac{1}{2\sqrt{(\mathrm{Re}\, Z_{ij})^2 + (\mathrm{Im}\, Z_{ij})^2}}\left(2\mathrm{Re}\, Z_{ij}\frac{\partial \mathrm{Re}\, Z_{ij}}{\partial F} + \right. \\
&\quad \left. 2\mathrm{Im}\, Z_{ij}\frac{\partial \mathrm{Im}\, Z_{ij}}{\partial F}\right) \\
&= \frac{\mathrm{Re}\, Z_{ij}}{|Z_{ij}|}\frac{\partial \mathrm{Re}\, Z_{ij}}{\partial F} + \frac{\mathrm{Im}\, Z_{ij}}{|Z_{ij}|}\frac{\partial \mathrm{Im}\, Z_{ij}}{\partial F} \qquad \text{(F.87)}
\end{aligned}$$

Substituting Equation F.87 into Equation F.86 yields

$$\begin{aligned}
\mathrm{i}\frac{\partial \phi_{ij}}{\partial F} &= -\mathrm{i}\,\frac{\mathrm{Im}\, Z_{ij}}{|Z_{ij}|^2}\frac{\partial \mathrm{Re}\, Z_{ij}}{\partial F} + \mathrm{i}\,\frac{\mathrm{Re}\, Z_{ij}}{|Z_{ij}|^2}\frac{\partial \mathrm{Im}\, Z_{ij}}{\partial F} \\
\Rightarrow \frac{\partial \phi_{ij}}{\partial F} &= \frac{\mathrm{Re}\, Z_{ij}}{|Z_{ij}|^2}\frac{\partial \mathrm{Im}\, Z_{ij}}{\partial F} - \frac{\mathrm{Im}\, Z_{ij}}{|Z_{ij}|^2}\frac{\partial \mathrm{Re}\, Z_{ij}}{\partial F} \quad . \qquad \text{(F.88)}
\end{aligned}$$

F.3 DERIVATIVES OF THE DATA WITH RESPECT TO THE DISTORTION PARAMETERS

This part of the appendix contains the equations required to calculate the derivatives of the data with respect to the distortion parameters and the comparison of calculated and brute-force $\underline{\underline{J}}_c$ elements for data values in apparent resistivity and phase. Note that the tipper vector remains unaffected by distortion, and that by assumption the impedance tensor $\underline{\underline{Z}}$ is only related to the conductivity structure, which is independent of the distortion. Therefore the data ($\underline{\underline{D}}$), which are affected by galvanic distortion ($\underline{\underline{C}}$), are given by

$$\underline{\underline{D}} = \underline{\underline{C}}\,\underline{\underline{Z}} \tag{F.89}$$

or

$$\begin{aligned}\begin{pmatrix} D_{xx} & D_{xy} \\ D_{yx} & D_{yy} \end{pmatrix} &= \begin{pmatrix} C_{11} & C_{12} \\ C_{21} & C_{22} \end{pmatrix} \begin{pmatrix} Z_{xx} & Z_{xy} \\ Z_{yx} & Z_{yy} \end{pmatrix} \\ &= \begin{pmatrix} C_{11}Z_{xx} + C_{12}Z_{yx} & C_{11}Z_{xy} + C_{12}Z_{yy} \\ C_{21}Z_{xx} + C_{22}Z_{yx} & C_{21}Z_{xy} + C_{22}Z_{yy} \end{pmatrix} ,\end{aligned} \tag{F.90}$$

The different components of the distorted data $\underline{\underline{D}}$ are given by

$$\begin{aligned} D_{xx} &= C_{11}Z_{xx} + C_{12}Z_{yx} \ , \\ D_{xy} &= C_{11}Z_{xy} + C_{12}Z_{yy} \ , \\ D_{yx} &= C_{21}Z_{xx} + C_{22}Z_{yx} \quad \text{and} \\ D_{yy} &= C_{21}Z_{xy} + C_{22}Z_{yy} \ . \end{aligned} \tag{F.91}$$

As the true impedance tensor is independent of the distortion parameters, the derivatives of the distorted data with respect to the distortion parameters can be calculated by

$$\frac{\partial \underline{\underline{D}}}{\partial C_{ij}} = \frac{\partial}{\partial C_{ij}} \left(\underline{\underline{C}}\,\underline{\underline{Z}}\right) = \frac{\partial \underline{\underline{C}}}{\partial C_{ij}} \underline{\underline{Z}} \ . \tag{F.92}$$

The derivatives of each datum (where the datum is an impedance value) with respect to each distortion element are

$$\begin{aligned} \frac{\partial D_{xx}}{\partial C_{11}} &= Z_{xx}, & \frac{\partial D_{xx}}{\partial C_{12}} &= Z_{yx}, & \frac{\partial D_{xx}}{\partial C_{21}} &= 0, & \frac{\partial D_{xx}}{\partial C_{22}} &= 0, \\ \frac{\partial D_{xy}}{\partial C_{11}} &= Z_{xy}, & \frac{\partial D_{xy}}{\partial C_{12}} &= Z_{yy}, & \frac{\partial D_{xy}}{\partial C_{21}} &= 0, & \frac{\partial D_{xy}}{\partial C_{22}} &= 0, \\ \frac{\partial D_{yx}}{\partial C_{11}} &= 0, & \frac{\partial D_{yx}}{\partial C_{12}} &= 0, & \frac{\partial D_{yx}}{\partial C_{21}} &= Z_{xx} \ , & \frac{\partial D_{yx}}{\partial C_{22}} &= Z_{yx}, \\ \frac{\partial D_{yy}}{\partial C_{11}} &= 0, & \frac{\partial D_{yy}}{\partial C_{12}} &= 0, & \frac{\partial D_{yy}}{\partial C_{21}} &= Z_{xy}, & \frac{\partial D_{yy}}{\partial C_{22}} &= Z_{yy}. \end{aligned} \tag{F.93}$$

For each datum being a resistivity value the derivative is given by

$$\frac{\partial \rho_{ij}}{\partial C_{mn}} = \frac{2}{\omega\mu}\left(\mathrm{Re}\, D_{ij}\frac{\partial \mathrm{Re}\, D_{ij}}{\partial C_{mn}} + \mathrm{Im}\, D_{ij}\frac{\partial \mathrm{Im}\, D_{ij}}{\partial C_{mn}}\right) \quad , \tag{F.94}$$

where $i = x, y$, $j = x, y$, $m = 1, 2$ and $n = 1, 2$ (see Equation F.90). Therefore the derivatives with respect to each distortion element are given by

ρ_{xx} component:

$$\frac{\partial \rho_{xx}}{\partial C_{11}} = \frac{2}{\omega\mu}\left(\mathrm{Re}\, D_{xx}\mathrm{Re}\, Z_{xx} + \mathrm{Im}\, D_{xx}\mathrm{Im}\, Z_{xx}\right) , \tag{F.95}$$

$$\frac{\partial \rho_{xx}}{\partial C_{12}} = \frac{2}{\omega\mu}\left(\mathrm{Re}\, D_{xx}\mathrm{Re}\, Z_{yx} + \mathrm{Im}\, D_{xx}\mathrm{Im}\, Z_{yx}\right) , \tag{F.96}$$

$$\frac{\partial \rho_{xx}}{\partial C_{21}} = 0 , \qquad \frac{\partial \rho_{xx}}{\partial C_{22}} = 0 , \tag{F.97}$$

ρ_{xy} component:

$$\frac{\partial \rho_{xy}}{\partial C_{11}} = \frac{2}{\omega\mu}\left(\mathrm{Re}\, D_{xy}\mathrm{Re}\, Z_{xy} + \mathrm{Im}\, D_{xy}\mathrm{Im}\, Z_{xy}\right) , \tag{F.98}$$

$$\frac{\partial \rho_{xy}}{\partial C_{12}} = \frac{2}{\omega\mu}\left(\mathrm{Re}\, D_{xy}\mathrm{Re}\, Z_{yy} + \mathrm{Im}\, D_{xy}\mathrm{Im}\, Z_{yy}\right) , \tag{F.99}$$

$$\frac{\partial \rho_{xy}}{\partial C_{21}} = 0 , \qquad \frac{\partial \rho_{xy}}{\partial C_{22}} = 0 , \tag{F.100}$$

ρ_{yx} component:

$$\frac{\partial \rho_{yx}}{\partial C_{11}} = 0 , \qquad \frac{\partial \rho_{yx}}{\partial C_{12}} = 0 , \tag{F.101}$$

$$\frac{\partial \rho_{yx}}{\partial C_{21}} = \frac{2}{\omega\mu}\left(\mathrm{Re}\, D_{yx}\mathrm{Re}\, Z_{xx} + \mathrm{Im}\, D_{yx}\mathrm{Im}\, Z_{xx}\right) , \tag{F.102}$$

$$\frac{\partial \rho_{yx}}{\partial C_{22}} = \frac{2}{\omega\mu}\left(\mathrm{Re}\, D_{yx}\mathrm{Re}\, Z_{yx} + \mathrm{Im}\, D_{yx}\mathrm{Im}\, Z_{yx}\right) , \tag{F.103}$$

ρ_{yy} component:

$$\frac{\partial \rho_{yy}}{\partial C_{11}} = 0 , \qquad \frac{\partial \rho_{yy}}{\partial C_{12}} = 0 , \tag{F.104}$$

$$\frac{\partial \rho_{yy}}{\partial C_{21}} = \frac{2}{\omega\mu}\left(\mathrm{Re}\, D_{yy}\,\mathrm{Re}\, Z_{xy} + \mathrm{Im}\, D_{yy}\,\mathrm{Im}\, Z_{xy}\right), \tag{F.105}$$

$$\frac{\partial \rho_{yy}}{\partial C_{22}} = \frac{2}{\omega\mu}\left(\mathrm{Re}\, D_{yy}\,\mathrm{Re}\, Z_{yy} + \mathrm{Im}\, D_{yy}\,\mathrm{Im}\, Z_{yy}\right). \tag{F.106}$$

For each datum being a phase value the derivatives are given by

$$\frac{\partial \Phi_{ij}}{\partial C_{mn}} = \frac{\mathrm{Re}\, D_{ij}}{|D_i j|^2}\frac{\partial \mathrm{Im}\, D_{ij}}{\partial C_{mn}} + \frac{\mathrm{Im}\, D_{ij}}{|D_{ij}|^2}\frac{\partial \mathrm{Re}\, D_{ij}}{\partial C_{mn}}, \tag{F.107}$$

where $i = x, y$, $j = x, y$, $m = 1, 2$ and $n = 1, 2$ (see Equation F.90). Therefore the derivatives with respect to each distortion element are given by

Φ_{xx} component:

$$\frac{\partial \Phi_{xx}}{\partial C_{11}} = \frac{\mathrm{Re}\, D_{xx}}{|D_{xx}|^2}\mathrm{Im}\, Z_{xx} - \frac{\mathrm{Im}\, D_{xx}}{|D_{xx}|^2}\mathrm{Re}\, Z_{xx}, \tag{F.108}$$

$$\frac{\partial \Phi_{xx}}{\partial C_{12}} = \frac{\mathrm{Re}\, D_{xx}}{|D_{xx}|^2}\mathrm{Im}\, Z_{yx} - \frac{\mathrm{Im}\, D_{xx}}{|D_{xx}|^2}\mathrm{Re}\, Z_{yx}, \tag{F.109}$$

$$\frac{\partial \Phi_{xx}}{\partial C_{21}} = 0, \qquad \frac{\partial \Phi_{xx}}{\partial C_{22}} = 0, \tag{F.110}$$

Φ_{xy} component:

$$\frac{\partial \Phi_{xy}}{\partial C_{11}} = \frac{\mathrm{Re}\, D_{xy}}{|D_{xy}|^2}\mathrm{Im}\, Z_{xy} - \frac{\mathrm{Im}\, D_{xy}}{|D_{xy}|^2}\mathrm{Re}\, Z_{xy}, \tag{F.111}$$

$$\frac{\partial \Phi_{xy}}{\partial C_{12}} = \frac{\mathrm{Re}\, D_{xy}}{|D_{xy}|^2}\mathrm{Im}\, Z_{yy} - \frac{\mathrm{Im}\, D_{xy}}{|D_{xy}|^2}\mathrm{Re}\, Z_{yy}, \tag{F.112}$$

$$\frac{\partial \Phi_{xy}}{\partial C_{21}} = 0, \qquad \frac{\partial \Phi_{xy}}{\partial C_{22}} = 0, \tag{F.113}$$

Φ_{yx} component:

$$\frac{\partial \Phi_{yx}}{\partial C_{11}} = 0, \qquad \frac{\partial \Phi_{yx}}{\partial C_{12}} = 0, \tag{F.114}$$

$$\frac{\partial \Phi_{yx}}{\partial C_{21}} = \frac{\mathrm{Re}\, D_{yx}}{|D_{yx}|^2}\mathrm{Im}\, Z_{xx} - \frac{\mathrm{Im}\, D_{yx}}{|D_{yx}|^2}\mathrm{Re}\, Z_{xx}, \tag{F.115}$$

$$\frac{\partial \Phi_{yx}}{\partial C_{22}} = \frac{\mathrm{Re}\, D_{yx}}{|D_{yx}|^2}\mathrm{Im}\, Z_{yx} - \frac{\mathrm{Im}\, D_{yx}}{|D_{yx}|^2}\mathrm{Re}\, Z_{yx}, \tag{F.116}$$

Φ_{yy} component:

$$\frac{\partial \Phi_{yy}}{\partial C_{11}} = 0, \qquad \frac{\partial \Phi_{yy}}{\partial C_{12}} = 0, \tag{F.117}$$

$$\frac{\partial \Phi_{yy}}{\partial C_{21}} = \frac{\mathrm{Re}\, D_{yy}}{|D_{yy}|^2}\mathrm{Im}\, Z_{xy} - \frac{\mathrm{Im}\, D_{yy}}{|D_{yy}|^2}\mathrm{Re}\, Z_{xy}, \tag{F.118}$$

$$\frac{\partial \Phi_{yy}}{\partial C_{22}} = \frac{\mathrm{Re}\, D_{yy}}{|D_{yy}|^2}\mathrm{Im}\, Z_{yy} - \frac{\mathrm{Im}\, D_{yy}}{|D_{yy}|^2}\mathrm{Re}\, Z_{yy}, \tag{F.119}$$

In Section 8.3.2 the brute-force comparison of the Jacobian matrix with respect to the distortion parameters for impedance data is illustrated. The same comparison using the same conductivity models (homogeneous halfspace and two blocks in a halfspace, see Figure 8.5) is shown in Figures F.1 and F.2. Figure F.1 shows the true values of the matrix elements, whereas the absolute values of the matrix elements are compared in Figure F.2. Similar to the comparison for data values in impedance the $\underline{\underline{J}}_c$ elements calculated by the code match the brute-force values well.

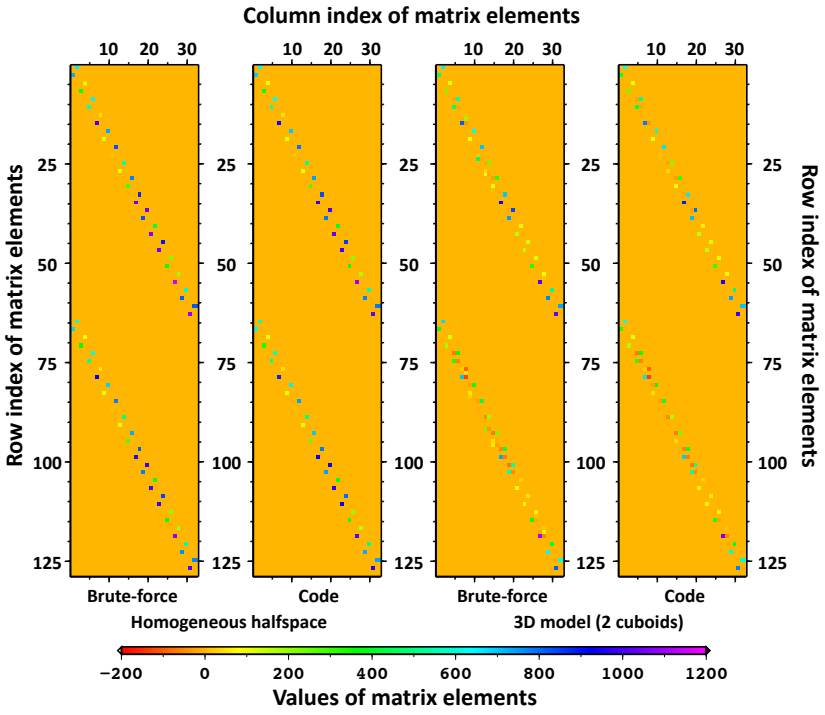

Figure F.1: Figure showing the comparison of the brute-force with the calculated Jacobian matrix, J_c, values for a homogeneous halfspace model (left) and a 3D model as shown in Figure 8.5 (right). Data values are in apparent resistivity and phase.

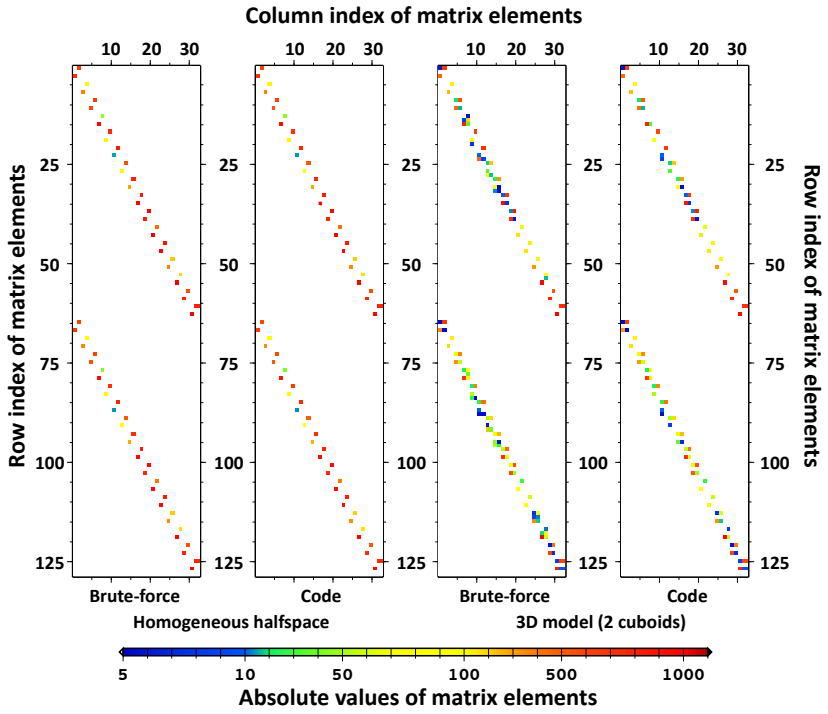

Figure F.2: Figure showing the comparison of the brute-force with the calculated Jacobian matrix, J_c, absolute values for a homogeneous halfspace model (left) and a 3D model as shown in Figure 8.5 (right). Data values are in apparent resistivity and phase. (Note white colour indicate absolute values less than 5.)